Earth Abundant Molecular HX-Splitting Photocatalysts for Solar Energy Storage

Earth Abundant Molecular HX-Splitting Photocatalysts for Solar Energy Storage

A dissertation presented

by

Seung Jun Hwang

to

The Department of Chemistry and Chemical Biology

in partial fulfillment of the requirements

for the degree of

Doctor of Philosophy

in the subject of

Chemistry

Harvard University

Cambridge, Massachusetts

April 2018

Dissertation Advisor: Professor Daniel G. Nocera Seung Jun Hwang

Earth Abundant Molecular HX-Splitting Photocatalysts for Solar Energy Storage

Abstract

Photochemical splitting of hydrohalic acids (HX) into their elemental constituents H_2 and X_2 (2 HX → H_2 + X_2) represents a chemical approach to solar-to-fuels energy conversion. To this end, this thesis has been directed towards developing new chemical platforms that manage both of the requisite two-electron half-reactions of HX splitting: proton reduction and halide oxidation. The thesis work has been devoted to probing the intimate mechanistic details of these two-electron photoreactions. In previous work in the field, the halide oxidation half cycle remains the kinetic bottleneck of a HX photocycle and chemical traps are required to promote halogen extrusion. This heavily mitigates the utility of the photocatalysis for energy storing applications. In addition, heretofore, little progress has been made toward energy storing halogen elimination chemistry with earth-abundant 3*d* metal complexes because of their short excited state lifetimes. Finally, the photochemical M–X bond activation step has not been directly observed in the solid state and its mechanism remains unclear. Each of the aforementioned challenges has been addressed with this thesis work.

A major objective this thesis is to explore new design strategies for efficient halogen photoelimination reactions with earth abundant transition metal complexes. We begin in Chapter 2 by studying diaryl phosphines as photoredox mediator to demonstrate that H_2 evolution catalysis can be achieved via a tandem approach that combines a non-basic photoredox mediator and transition metal catalysts. Next, we examine oxidizing Ni(III)trihalide complexes for

authentic photohalogen elimination via LMCT excited states. We continue in Chapter 3 by exploring the use of ancillary ligands to promote elimination, offering a strategy to circumvent the inherently short-lived excited states of 3*d* metal complexes. We demonstrate HCl-splitting photocatalysis with two closely related bimetallic Rh_2 and Ni_2 catalysts in Chapter 4. Importantly, we directly probe the structural nature of these excited states using low-temperature steady-state photo-crystallography experiments that establish a common chloride-bridged intermediate in halogen elimination reaction. The results of these studies led to the development in Chapter 4 of second generation Rh_2 and Ni_2 photocatalysts, which are more active. We further expand photoreduction chemistry toward Fe(III) metal complexes in Chapter 5 with the synthesis of two families of five-coordinate iron complexes with pyridine diimine (PDI) and phosphine ligand platforms. Through the synthesis and preparation of these compounds, we establish the utility of secondary sphere interactions in efficiently assisting metal-halogen bond activation and sustaining persistent halogen atom radical generation. Photocrystallography experiments on these iron compounds provide the first structural characterization of a Cl•|arene interaction, which is η^1 in nature. Lastly, in Chapter 6, magneto-structural correlation studies of the mononuclear intermediate spin Fe(III) phosphine complexes of Chapter 5 demonstrate the influence of local symmetry on magnetic anisotropy.

Table of Contents

List of Figures

List of Tables

Acknowledgements

First I would like to express my deep appreciation for my advisor Professor Daniel Nocera for his thoughtful guidance and support. I consider myself extremely lucky to have joined Dan's group as he is among the best scientists and educators I have ever met. He takes care of the hard and tedious work, gives us research freedom, and provides us with his creative viewpoints on science. His interdisciplinary research interests as well as fundamental approach to basic science have opened up my mind and I have learned so much about other areas of chemistry by just being part of his lab.

I would also like to thank all of my committee members, Professor Eric Jacobsen and Ted Betley for their insightful discussions. The discussions and questions during the GAC meetings inspired me to think more deeply about my research from different perspectives and I learned a lot in the process.

I am extremely grateful for the friends and colleagues that I gained during graduate school. Especially, I would like to thank my former and current Nocera lab members, who are talented and cooperative. I am especially indebted to two Daves during my Ph.D. journey in the Nocera group. First I thank Dave Powers for being a good friend and mentor. You always called me ‘Seung baby’ and our birthdays were just one month apart. I learned a lot of things from him at the early stages of my Ph.D. This allowed me to settle down in my graduate career smoothly with endless support and patience. I thank Dave Gygi for giving support to my research with his endless passion and having many discussions with me. Gygi, it would be safe to say, that you are one of the best friends as well as colleagues I have met during graduate school. I will miss our time spent together in lab discussing lots of different topics. I thank Andrew Maher and Bryce Anderson for being a part of ‘Team HX’ and letting me learn lots of spectroscopic techniques

particularly laser and EPR experiments. You guys were always welcoming to me whenever I had something to figure out and were ready to listen to my ‘bull-shit’ stories. I am glad that we finally turned these stories into scientifically meaningful data and analysis. I thank Ryan Hadt for helpful discussions on HX splitting projects with calculations. I thank Chris Lemon for his kind support and I respect his work ethic. It was fun to work on beautifully colored Corrole compounds with him. I really thank Yu-Sheng and Shao-Liang for their incredible support and helps in photocrystallography experiments. I was fortunate to have a chance to work at the synchrotron at APS where I got my middle name as ‘speedy’. I was happy to have my Korean Mafia colleagues, Bon Jun and Seungwoo in the Nocera lab. They were always by my side emotionally. I thank Xiaowen for being a good friend as well as a great collaborator. I became an expert in the Chinese cuisine of the Boston area since you joined the group. We used to live in the same apartment building and had great memories together. I am proud that we finally made a successful magnetism collaboration. I thank Dilek for her kind support. I was able to focus on conducting research due to her dedication to the lab. She is an amazing person who is constantly working behind the scenes to keep the lab running. My entire Ph.D. would have been so much harder without her help and support. My thanks also go to Mike Huynh, Dan Graham, Lisa Olshansky, Arturo Pizano, Andrew Ullman, Eric Bloch, Chong Liu, Guillaume Passard, Zamyla Chen, Evan Jones, Tom Keane, Nancy Li, Dan Loh, Charles Margarit, Rui Sun, Ben Zhang, Casey Brodsky, Joe Elias, Brandon Greene, Mengran Liu, British Ben, Matt Nava, Tuncay Ozel, Yangzhong, Serge, Christoph, and Cyrille Costentin. I would also like to thank all my friends who made me enjoy my graduate student life here at Harvard especially Yongho, Jaesung, and Kyungtae.

I would like to thank Professor Sukbok Chang at KAIST. The teaching and training I received from him was the foundation upon which I have pursued further study and research in chemistry. I also would like to thank the Fuel Cell Research Center at KIST especially Professor Soo-Kil Kim and Dr. Sungjong Yoo. It was a time that I could truly feel the joy of research that has fueled my way forward in a research career.

I dedicate this thesis to my family for their encouragement and especially my parents for installing a “can do” mindset. Mom and Dad, thank you for your support, love, and prayer. Yooah, my sister I thank you and my brother in law. Thank you for always being a strong support in my life.

Lastly, I would like to thank Sarah who has put up with many years of living with an erratic schedule and has supported me every step of the way. We met in the 5.04 class at MIT and I instantly fell in love with you. I felt extremely lucky to have you in my life. It was possible to get through my Ph.D journey since you were always with me with warm encouragements. Knowing that we have the rest of our lives together put a lot of perspective into my entire life journey. It will be harder than this for sure, but I believe that we can get through it together.

Ultimately I thank God, you came in my life. Please lead me on a path as you wish.

To my family for their love and support.

Page intentionally left blank

Chapter 1

Introduction

1.1 Introduction

The supply of secure, clean, sustainable energy is among the most important scientific and technical challenges of our time.[1–3] Development of clean and renewable energy sources would have a transformative impact on environmental as well as human health.[4,5] In 2005 it was estimated that particulate air pollution, whose major source in urban environments is automobile exhaust, is to blame for 500,000 deaths each year.[4] Most current methods of energy storage are characterized by low energy densities and consequently they present formidable challenges for the large scale implementation of renewable energy sources. Alternatively, hydrogen-based economies have been proposed as potential clean solutions to meet our energy and environmental needs with a high enough energy density to go to scale. However in order to realize a hydrogen-based fuel economy, clean and renewable sources of hydrogen must be developed. As the reaction of H_2 with CO_2 to make any fuel is effectively thermoneutral,[6] the key challenge from a solar energy conversion point of view is to obtain H_2 renewably. Water (H_2O) and mineral acids (HX) have emerged as logical proton sources for H_2 production, and the hydrogen, generated by proton reduction from these substrates could either be sequestered as a liquid fuel by hydrogenation of small molecule substrates, such as CO_2, or could be used directly in a fuel cell.

$$2H_2O + \text{light} \rightarrow 2H_2 + O_2 \quad (1)$$

$$2HX + \text{light} \rightarrow H_2 + X_2 \quad (2)$$

Whereas the utility of water splitting is well-documented, the utility of HX splitting is less discussed, despite this molecule having the ability to store solar energy in the form of a redox flow battery[7] or chemical fuel.[8] Both H_2O and HX splitting store approximately the same amount of energy (E^o = 1.23 eV and 1.36 eV for H_2O and HCl), respectively shown in equations

(1) and (2). These reactions have three characteristics: they are (1) multielectron, (2) involve coupling redox reactions to protons and (3) involve the formation of high-energy H–H, X–X and O–O bonds.

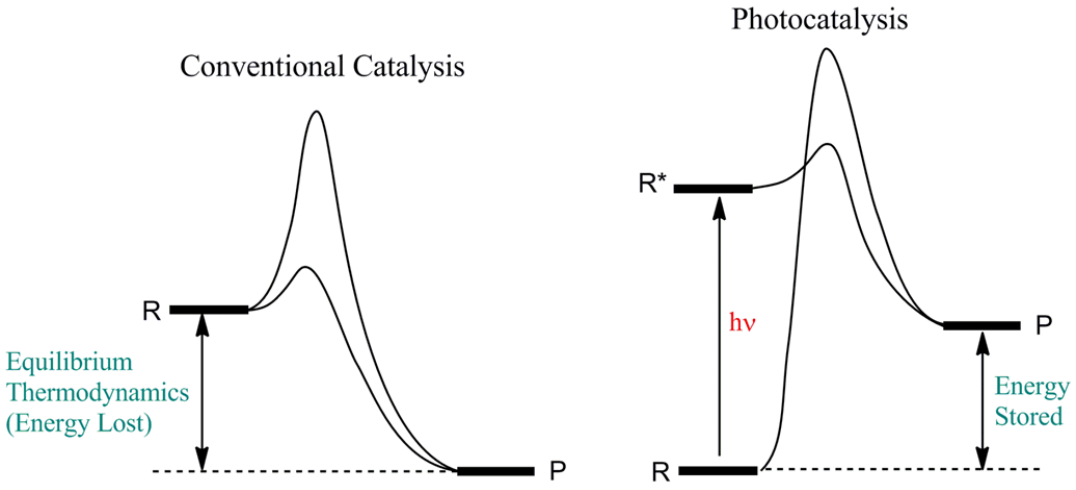

Figure 1.1. Two different reaction coordinate diagrams in conventional catalysis and photocatalysis.

For either source (H_2O or HX), significant fundamental issues confront H_2 generation schemes. Realization of a hydrogen economy requires not only H_2 generation by proton reduction, but also a reaction chemistry needs to be developed to catalytically close the redox cycle; thus O_2 or X_2 generation by water or halide oxidation must accompany H_2 generation.[8] If the link between H_2 generation and carbon-based fuel supplies is to be severed, then the oxidative half of any H_2 generating cycle (M–O or M–X bond activation) must also be solved in any photocycle, preferably using sunlight to drive the reaction, since these reactions are energetically uphill (Figure 1.1).[9]

HX as a substrate for H_2 generation has several advantages over H_2O in terms of catalyst development. Overall, the 2-electron 2-proton transformation in HX splitting is kinetically favored compared to the more mechanistically challenging 4-electron 4-proton coupled

transformation of water splitting. Much higher efficiencies for fuel generation and utilization would be expected since such transformation manages simpler kinetic demands. The design and function of molecular platforms for HX splitting as well as the study of the fundamental principles is needed for the development of these basic processes that underpin oxidation and reduction catalysts are the focus of this thesis. A key advantage of studying molecular systems in HX splitting is their feasibility for detailed mechanistic studies allowing for the development of more efficient catalysts in heterogeneous systems. Molecular platforms that display HX splitting chemistry can also provide further insights into the fundamental aspects of proton coupled electron transfer (PCET) processes, which have far reaching implications in energy storage. Beyond the plethora of information to be gained from fundamental studies, the practical advantages of a $H_2|X_2$ fuel cell over an $H_2|O_2$ fuel cell further strengthen the motivation of HX as a substrate for fuel generation.[10] To date, much higher operating efficiencies have been reported for $H_2|X_2$ fuel cells compared to that of $H_2|O_2$ fuel cells (70 and 50% respectively).[11,12] This is in part due to facile Cl_2 reduction at the cathode as opposed to the sluggish oxygen reduction reaction. Additionally, $H_2|X_2$ fuel cell systems have better stability over $H_2|O_2$ systems since it is well known there are common deleterious side reactions (peroxide formation) for $H_2|O_2$ fuel cells, leading to electrode and membrane degradation within an operating system.[13] Thus, overall, $H_2|X_2$ fuel cells show greater efficiency and stability than $H_2|O_2$ fuel cells. However, it is acknowledged that one of the major drawbacks of an $H_2|X_2$ fuel cell is the corrosive nature of hydrohalic acids as well as generating X_2 (Cl_2 and Br_2) compared to water and O_2, an important consideration for large scale applications.

Figure 1.2 presents a strategy to realizing an authentic two electron H_2 photocycle using HX as a substrate. Two chemical challenges must be addressed in any closed HX splitting cycle:

1) proton reduction to generate H_2, and 2) halide oxidation to liberate X_2 and regenerate the catalyst. HX splitting is an energy storing reaction and is by definition endergonic. In any HX splitting scheme, either one or both of the steps forming H_2 and X_2 production must be uphill in energy and photochemical reactions have been targeted drive HX splitting chemistry. Although finding efficient catalysts, which can manage both requisite half reactions, has been a major challenge, in general, catalyst inefficiencies arise from halide oxidation half reaction. For example, the binuclear rhodium transition metal complexes have been developed for HX splitting photocycles.[14–17] While these complexes are capable of accomplishing HX splitting to H_2, chemical traps are needed to trap halogen radical upon M–X photactivation so as to turn over the photocycle; the excited state of these complexes is not sufficiently oxidizing to drive an authentic elimination of X_2.

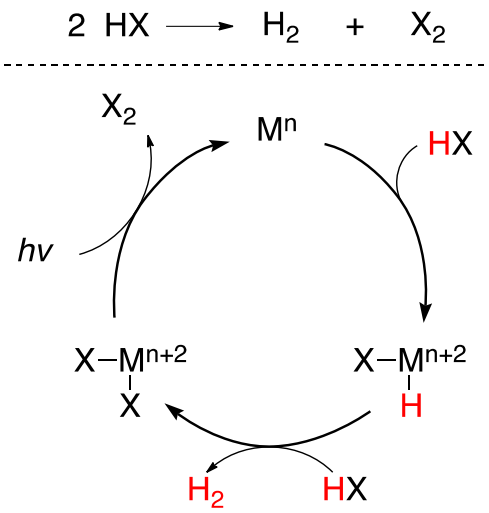

Figure 1.2. Proposed catalytic cycle for HX splitting.

1.2 Major photochemical processes for halogen photoelimination reactions

Electronic excitation into the low-lying M−X σ* orbitals that lead to weakening of the M−X bond is regarded as a common defining factor for promoting halogen photoelimination

chemistry. There are three possible photochemical processes that involve excitations associated with M−X σ* orbitals: LMCT (ligand-to-metal charge transfer), MLCT (metal-to-ligand charge transfer), or MMCT (metal-to-metal charge transfer) (Figure 1.3).

Many high-valent metal complexes in halogen photoelimination reaction utilize excited states with substantial LMCT character. Excitation results in a net transfer of electron density from the halide (X) ligands to the metal center, and in the limiting case the metal is formally reduced by one electron in the excited state and the halogen is oxidized to the radical species. This type of LMCT weakens the M−X bond and promotes elimination of the halogen atom typically as a radical.

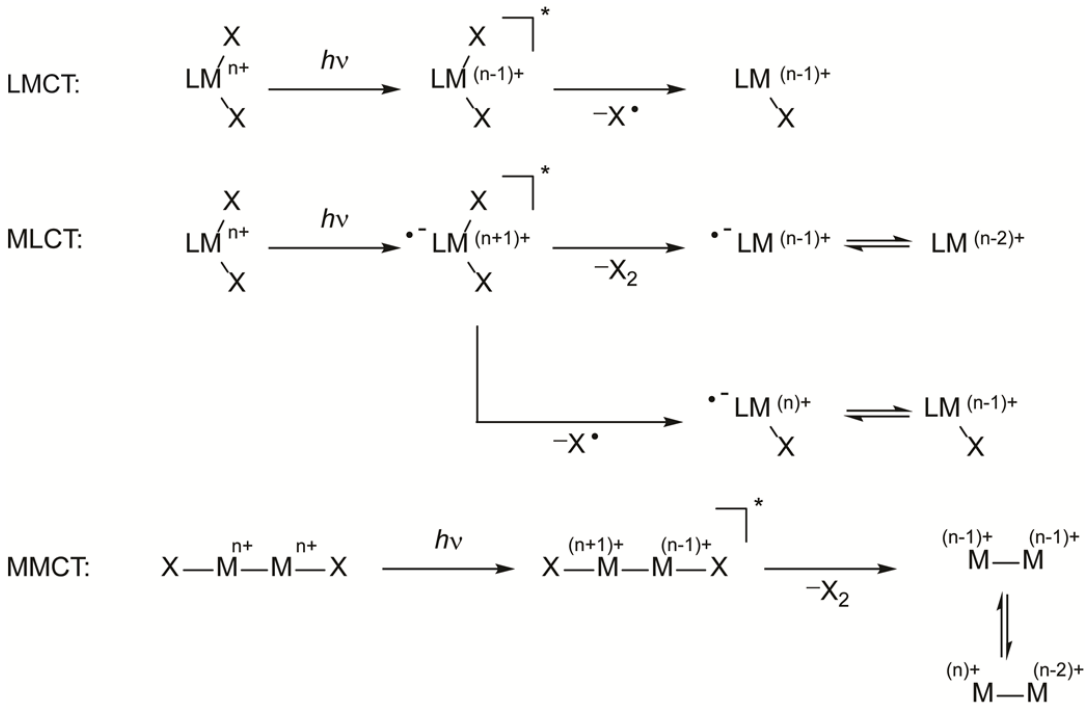

Figure 1.3. Three possible photochemical processes to activate M−X bonds via excitations involving M−X σ* orbitals.

For example, monomeric Pt(IV) complexes supported by monodentate phosphine ligands, such as *trans*-$Pt(PEt_3)_2(R)Br_3$,

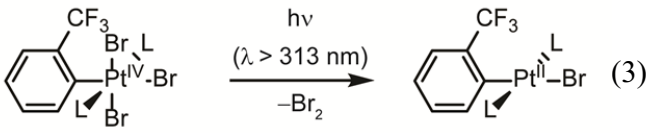

(3)

display an efficient photoelimination of bromine with a 82% quantum yield that is derived from an LMCT excited state (equation (3)).[18]

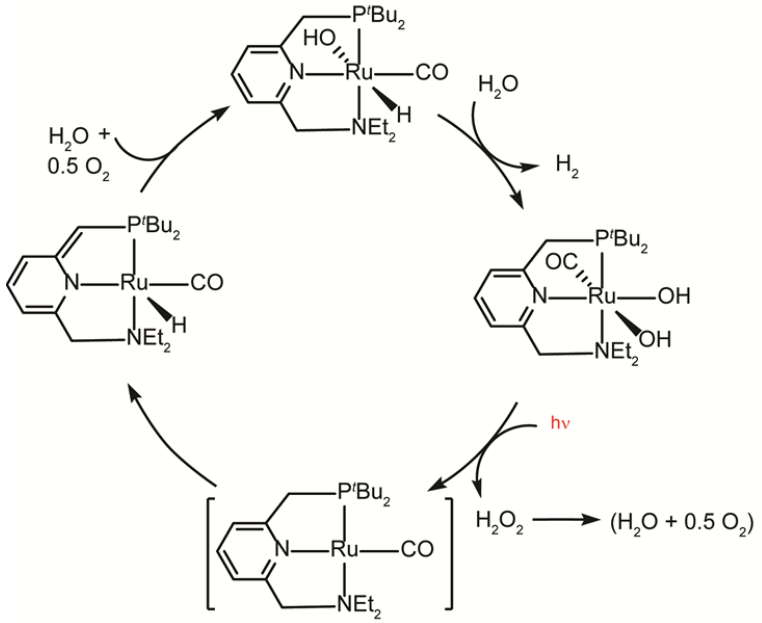

Figure 1.4. Proposed mechanistic pathway for the formation of H_2 and O_2 from water driven by MLCT excited state.

In MLCT photochemistry, the metal is bound by a reducible ligand, and in the excited state, electron density shifts from the metal to this redox-active ligand, resulting in net one-electron oxidation of the metal in the limiting case. Reductive elimination from this higher-oxidation state metal is facile as shown in homogeneous catalysis.[19–21] Though the one-electron reduction pathway is still accessible from the MLCT excited state, multi-electron redox transformations are also feasible. This strategy permits reductive elimination from metal centers, which are not appreciably oxidizing in the ground state. Such MLCT excited state chemistry has

not been fully realized for X_2 elimination but been shown to successfully drive the elimination of hydrogen peroxide from a formal Ru(II) center, coordinated to a redox-active pincer ligand (Figure 1.4).[22]

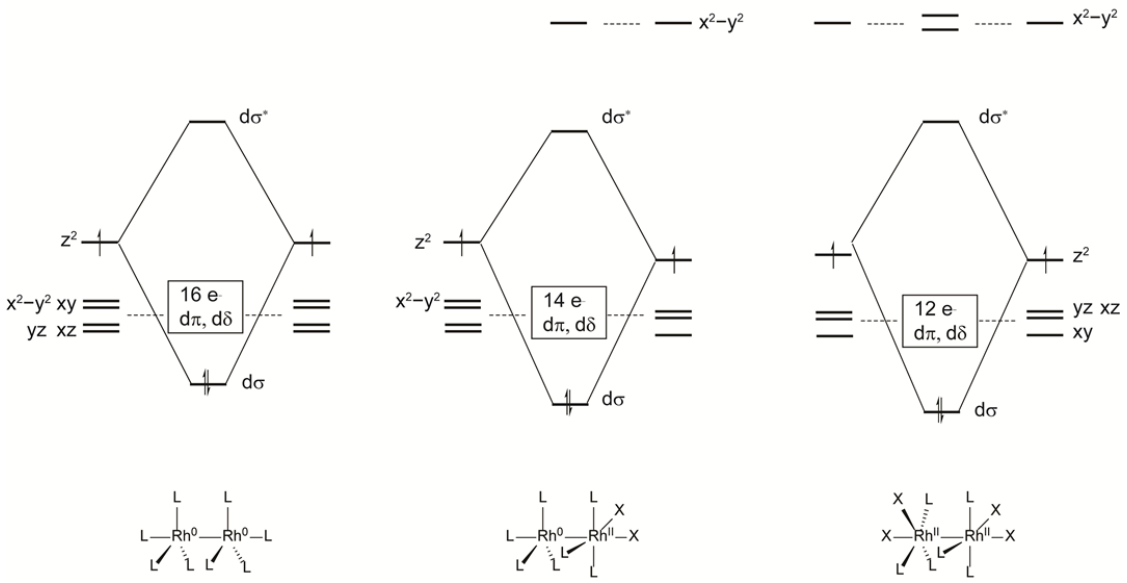

Figure 1.5. A qualitative molecular orbital diagram for the $Rh_2[0,0]$, $Rh_2[0,II]$, and $Rh_2[II,II]$ complexes: importance of metal–metal bond interaction.

Finally, halogen photoelimination via MMCT excitation has been achieved and driven by excitation into the σ* orbitals of metal–metal bond interactions in bimetallic complexes. The excited states of σ* parentage observed for d^7–d^7, d^9–d^7, and d^9–d^9 homo- and hetero-bimetallic dirhodium and diplatinum complexes possess both M–M and M–X antibonding character. Thus the electronic excitation into the empty dσ* orbital is expected to weaken the M–X bonds, thereby promoting halogen elimination.[9,23–26] It is the preservation of the metal–metal bond that engenders a lowest energy dσ* excited state, from which multi-electron photoreactivity may be derived from bimetallic complexes (Figure 1.5).

1.3 Metal complexes promoting halogen photoelimination reactions

The photoreductive elimination of halogens from transition metal complexes is often both the rate limiting and energy storing step in HX photocycles. This necessitates the activation of strong M−X bonds by either of the excited states described in Section 1.2 and shown in Figure 1.3. A great deal of effort has been devoted to identifying molecular platforms that furnish such transformations over the past few decades. Figure 1.6 summarizes these different types of platforms.[18,23–36] Although it is difficult to compare photoefficiencies directly (photochemical quantum yields, Φ_p provided in the Figure 1.6) due to different photochemical conditions, there are noticeable general trends: These complexes (1) are heavily focused on achieving a high oxidation state (2) do not involve first-row metals, and (3) generally require chemical traps for the eliminated halogen atom radical.

1.3.1 High-valent metal centers

For the same reason that highly oxidizing metal centers are good at traditional reductive elimination in homogenous catalysis, they are excellent candidates for two-electron halogen photoelimination. Over the last 20 years, high-valent metal complexes (Pd(IV), Au(III), Cu(III)) have emerged as versatile tools for modern catalytic method development. High-valent catalysis is important for bond-forming chemistry via reductive elimination and consequently is well-poised to drive X–X bond formation by this pathway. For example, Figure 1.7 describes some recent examples of high-valent Ni metal complexes developed for C−C, C−O, and C−X bond formations.[37–39]

Binuclear Metal Complexes

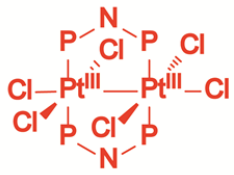

Φ_p = 38% (5.0 M DMBD)
λ_{exc} = 405 nm
dσ*

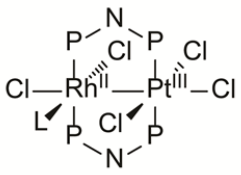

Φ_p = 23% (1.0 M DMBD)
λ_{exc} = 434 nm
LMCT

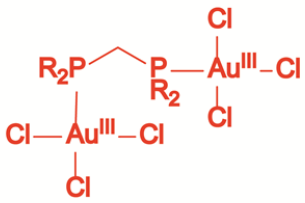

Φ_p = 26% (1.0 M 1-hexene)
λ_{exc} = 320 nm
LMCT

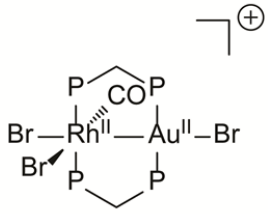

Φ_p = 18% (4.4 M DMBD)
λ_{exc} = 320 nm
MMCT

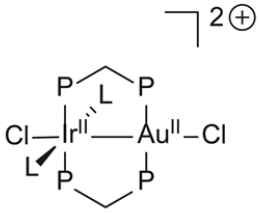

Φ_p = 18% (4.4 M DMBD)
λ_{exc} = 320 nm
MMCT

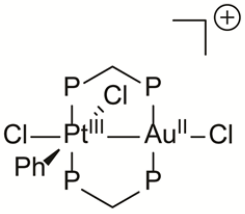

Φ_p = 5.7% (5.0 M DMBD)
λ_{exc} = 405 nm
dσ*

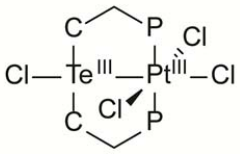

Φ_p = 4.4% (3.3 M DMBD)
λ_{exc} = 350 nm

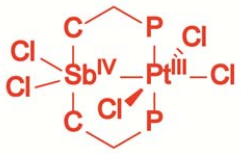

Φ_p = 13.8% (4.4 M DMBD)
λ_{exc} = 320 nm

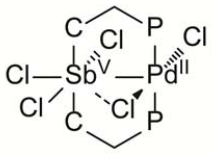

Φ_p = 0.58% (2.0 M Ph_2S)
λ_{exc} = 354 nm

Mononuclear Metal Complexes

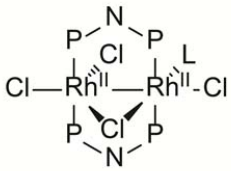

Φ_p = 0.47% (THF)
λ_{exc} = 320 nm

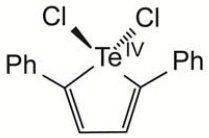

Φ_p = 16.9% (X = Br)
1.6% (X = Cl)
2.3% (X = F)
λ_{exc} = 448 nm (5.0 M DMBD)
LMCT

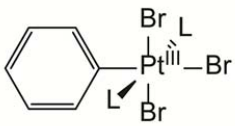

Φ_p = 82% (1.0 M 1-hexene)
λ_{exc} = 313 nm
LMCT

Figure 1.6. The bi-and mono-nuclear complexes studied for halogen photoelimination reaction with their photochemical condition. Complexes that could allow for the solid-state photolysis are labeled with red colors.

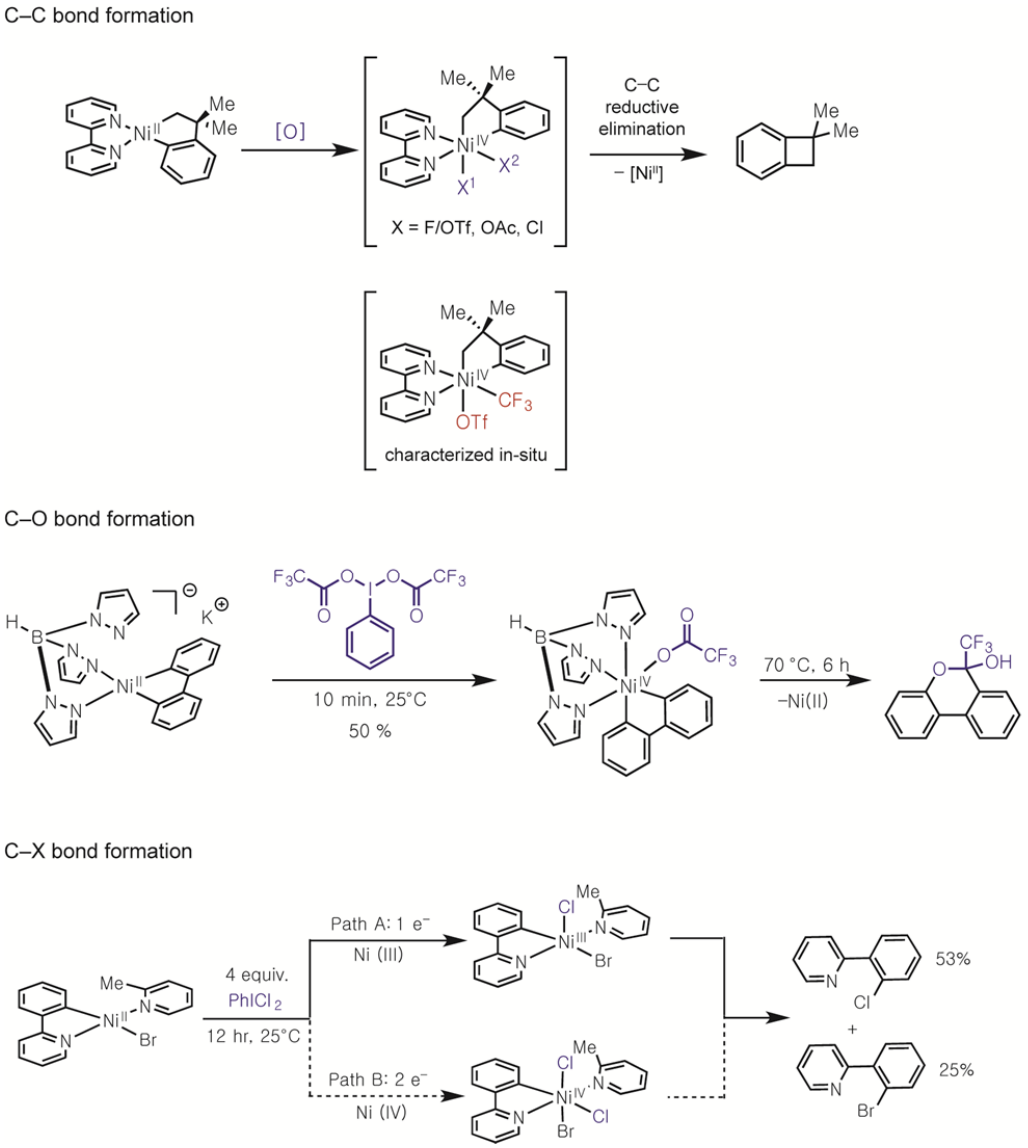

Figure 1.7. Some of recent examples for bond-forming reactions utilized by high-valent Ni catalysts.

Elimination of X—X is distinguished by one major difference from the organic bond forming reactions arising from cross-coupling—reductive elimination of halogen from a metal center is endothermic. Accordingly, research has focused on employing high-valent metal centers coupled to electron withdrawing ligand platforms (or ancillary main group elements as electron reservoirs) to maximize the oxidizing power of the metal center. This is evidenced by

the prevalence of metals centers of formal oxidation state greater than or equal to +3 in the complexes shown in Figure 1.6. The endothermicity of the transformation may be overcome with light excitation, as the internal energy of the overall system is increased upon the complexes' absorption of light as illustrated in Figure 1.1.

Table 1.1. Representative optical electronegativity (χ) data for metals and halide ligands.

Species	**χ**	**Orbital or Symmetry**	**Species**	**χ**	**Orbital or Symmetry**
Fe(II)	1.8	T_d	Cu(III)	2.74-2.8	Planar or Distorted Oh
Fe(III)	2.1	ls	Rh(III)	2.3-2.4	ls
	2.5	hs	Au(III)	2.9	ls square planar
Mn(IV)	2.7-3.0		Pd(II)	2.3-2.4	ls square planar
Co(II)	1.8-1.9	T_d	Pt(IV)	2.6-2.7	ls
Co(III)	2.3	ls	Cl^-	2.89	π orbital
Ni(II)	2.0-2.1	T_d		3.12	σ orbital
	2.2	ls SP	Br^-	2.76	π orbital
Ni(III)	3.05			3.99	σ orbital
Ni(IV)	3.4		I^-	2.60	π orbital
Cu(II)	2.0-2.2	Planar or Distorted O_h		2.87	σ orbital
	2.2-2.5	T_d			

The need for a metal in a high oxidation state that is electronically excited can be explained and predicted by the Jørgensen's scale of optical electronegativity,[40] which was further elaborated by Schmidtke,[41] Schläfer, and Glieman.[42] Most charge transfer photochemistry is initiated by a charge-transfer absorption band (Figure 1.3). It has been proposed that a semi-empirical correlation exists between the energies of charge transfer transition maxima and the

optical electronegativity difference between metal and ligand ($\chi_L - \chi_M$), the *d*-orbital energy difference caused by ligand field splitting (Δ, 10 Dq), the difference in the spin-pairing energy of the central metal in the ground and excited states (δ, SPE), and the Racah parameter B. The energy maximum of the charge-transfer transition is expected to occur according to the following equation (4):

$$\varepsilon_{CT,max} = 35.8(\chi_L - \chi_M) + \Delta + \delta(SPE) + aB \quad (4)$$

These charge transfer transitions should arise at different energies depending on whether (1) the ligand electron involved in the transition has σ or π symmetry with respect to the metal–ligand bond (2) the values of Dq and χ_M are appropriate to the specific metal-centered acceptor orbital involved in the transition, and (3) the acceptor orbital is antibonding or non-bonding (the 10 Dq term will be negligible in the correlative equation if non-bonding metal orbitals are involved in the transition). The SPE, proportional to the Racah parameter B, is typically independent to the complex symmetry and the ligand.

Substituting optical electronegativities listed in Table 1.1 into equation (4) allows for the prediction of the charge transfer transition maxima. For example, we can predict charge transfer transitions (LMCT) from σ and π orbitals of the ligands to the e_g orbitals of the Co(III) ion in $Co(NH_3)_3X^{2+}$ or the e_g or t_{2g} orbitals of Cr(III) in $Cr(NH_3)_5X^{2+}$. For Co(III) complexes, the Δ term for the transition to t_{2g} orbitals has a value of about 28 kJ and a SPE proportional to B ~ 0.75 kJ. Since the optical electronegativity of Cr(III) being smaller than that of Co(III) ($\chi_{Cr} = 1.3$ and $\chi_{Co} = 2.3$) for the same ligand set, values for other parameters (Δ ~ 25.6 KJ, and B ~ 0.2 KJ and thus SPE) do not contribute significantly to the charge transfer maximum and thus the energy maximum of the charge transfer transition is primarily determined simply by χ. Therefore,

a Cr(III) complex of given ligand L exhibits a much higher charge transfer energy when compared to the analogous Co(III) complex.

As exemplified by optical electronegativity values, the focus on metal complexes for halogen photoelimination has been relegated to high-valent second- and third-row transition metal centers ($\chi_{Au(III)}$ = 2.9, $\chi_{Pt(IV)}$ = 2.7). For instance, bimetallic Au_2(III,III) complexes supported by various bidentate phosphine ligands show efficient photoreduction reactivity under irradiation to furnish Au_2(I,I) complexes as photoproducts.[43] It is worth mentioning that LMCT excitation of the Au_2(III,III) centers allows for a four-electron photoreduction of the ligated halogens while photochemically driven M−X bond cleavage is typically limited to one-electron redox transformations, exemplifying the strongly oxidizing nature of the excited state.

1.3.2 First-row transition metals

Beyond higher optical electronegativity values, second- and third-row transition metal complexes possess additional benefits that give rise to rich photochemical reactivity arising from their long-lived excited state lifetimes. Conversely, first-row transition metals typically display extremely short excited state lifetimes that hamper the desired chemistry, instead leading to the undesired back reaction. [44,45] Therefore, additional strategies are required in order to suppress this unproductive back reaction for the realization of halogen photoelimination chemistry with earth abundant elements.

Initial progress has been made towards the goal of accomplishing HX-splitting photocatalysis using complexes based on earth-abundant first-row transition metals particularly with nickel complexes. These were chosen because nickel is known to be active for proton reduction[46,47] as well as having a wide range of accessible oxidation states (0-IV).[48] As an early and rare example, the activation of the M–X bond was found in a binuclear carbene complex,

$[Ni^{II}(\mu\text{-Cl})Cl(IPr)]_2$ (Ipr = 1,3-bis(2,6-diisopropylphenyl)imidazol-2-ylidene) as shown in Figure 1.8.[49] Photolysis of this binuclear Ni complex activates the Ni–Cl bonds sluggishly to furnish $[Ni^{I}(\mu\text{-Cl})(IPr)]_2$ and trapped Cl_2 by solvent. Consistent with this photochemistry, a TD-DFT calculation for a square planar Ni(II) center reveals that light excitation leads to the population of orbitals with σ*(Ni−Cl) character that arises from an LMCT. However, the photoactivation of the M–X bond was neither efficient nor clean leaving room for the improvement.

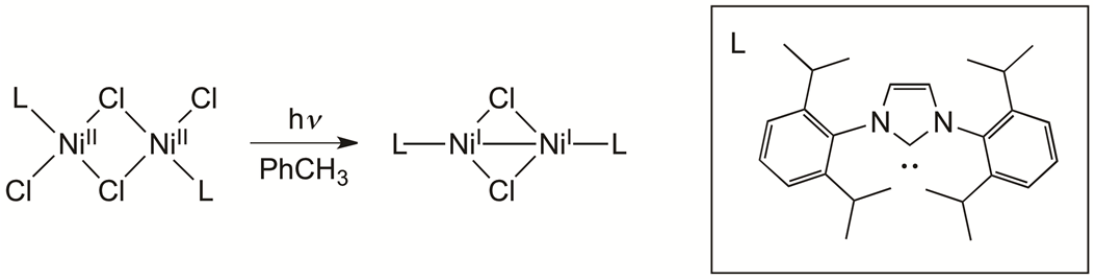

Figure 1.8. The binuclear nickel complexes studied for halogen photoelimination reaction.

There is an additional drawback to utilizing first-row transition metals as HX photocatalysts. The weakening of the M−X bond observed when moving to first-row transition metals is beneficial for the desired reactivity, however, for the same reason, the M−L bond strength will become much weaker compared to that of second- or third-row transition metal complexes leading to a lack of structural rigidity especially under the acidic condition necessary for HX splitting.

As evidenced in Figure 1.3, first-row transition metal complexes are rare and inefficient for halogen photoelimination, making them poor HX photocatalysts. Thus, there is a need to develop inexpensive HX splitting catalysts based on earth-abundant, first-row transition metals. Further, one should choose Ni(III) or Fe(III), as they are good candidates for halogen photoelimination due to their high optical electronegativity ($\chi_{Ni(III)}$ = 3.05 and $\chi_{Fe(III)}$ = 2.5).

1.3.3 Chemical traps for activation of M–X bonds

Chemical traps are commonly required to promote the photoelimination of halogen radicals shown in Figure 1.6 as the exothermic back reaction circumvents authentic (trap-free) X_2 elimination. When traps are thus present, H_2 evolution catalysis can only be achieved.

Chemical traps, such as unsaturated small molecule organic substrates, sequester the halogen in stable halogen-trap adducts, and thus both minimize potential energy storage as well as prevent a closed HX splitting cycle from being realized. Recently, both mono- and binuclear Au complexes as well as bimetallic Pt complexes (Pt_2[III,III] and Pt−Sb[III,IV]) labeled red in Figure 1.6 have been developed which participate in efficient X_2 elimination in the absence of chemical traps. In these cases, the undesired back reaction is avoided by sweeping the generated X_2 gas from the reduced species in the solid state[23,31,43] by using custom quartz vessels such as that shown in Figure 1.9. In this experimental configuration, photochemically generated volatile gaseous products are collected in a second well under static vacuum so the gaseous products may be further analyzed. In a report from the Nocera group regarding the solid-state photochemistry of a tfepma-bridged Pt_2[III,III]Cl_6 complex (tfepma = bis[bis(trifluoroethoxy)phosphino]methylamine, CH_3N-[$P(OCH_2CF_3)_2$]$_2$), photo-evolved Cl_2 was trapped cryogenically and subsequently characterized by in-line mass spectrometry. This experiment established the evolution of Cl_2, but could not quantify the amount of evolved Cl_2.[23] The Gabbaï group has introduced an alternative experimental technique to quantify evolved halogen in solid-state photolysis.[31] The evolved Cl_2 was exposed to a strip of Na metal and the resulting NaCl was quantified by ion chromatography. The quantified Cl_2 yield from Pt–

Sb[III,IV] complex, $Pt^{III}Cl_3Sb^{IV}Cl_2(o\text{-dppp})_2$ (o-dppp = $o(Ph_2P)C_6H_4$) based on the extent of starting material conversion (53%) was determined to be 72%.

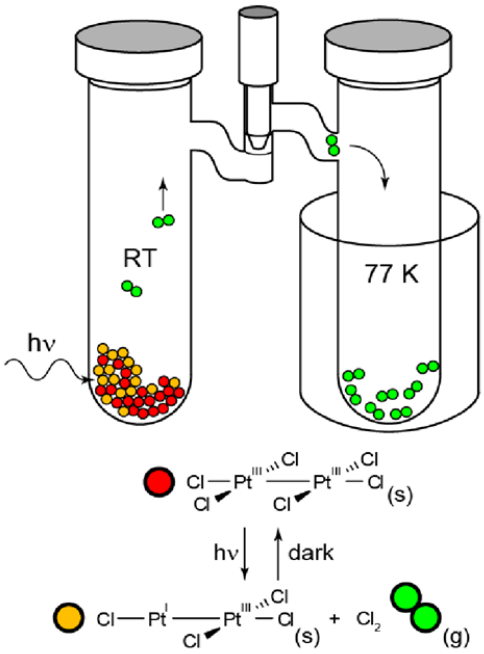

Figure 1.9. Simplified schematic of the apparatus used to perform solid-state photoelimination of halogen gas from metal complexes adapted from ref 9.

1.3.4 Two-electron mixed valency complexes for multi-electron redox phototransformations

One electron mixed valence molecular compounds are typically confined to single electron oxidations and reductions. Following this line of reasoning, two-electron mixed valence compounds should be able to support two-electron reactions, and four when the metal centers are redox cooperative. Two-electron mixed valency is realized when a redox symmetric core is induced to disproportionate, which may be achieved with appropriate ligand design. Bis(difluorophosphino) methylamine (dfpma, $CH_3N(PF_2)_2$) and tfepma are such designed ligands for two-electon mixed valency.[9] These diphosphazane ligands are able to drive the internal disproportionation of binuclear $M_2[I,I]$ cores to $M_2[0,II]$ cores for rhodium[14,17] and iridium.[15,50,51]

DFT calculations show that the unusual two-electron mixed valence core, M^{n}–M^{n+2}, is energetically favored relative to its valence symmetric M^{n+1}–M^{n+1} congener by asymmetric π-donation of the bridgehead amine lone pair to the fluorophosphines. These two-electron mixed valence cores are capable of facilitating a four electron redox chemistry in discrete two-electron steps along the series Rh_2[0,0](dfpma)$_3L_2$, Rh_2[0,II](dfpma)$_3X_2L$, and Rh_2[II,II](dfpma)$_3X_4$.[16,17] Solutions of the Rh_2[0,0] dfpma complex are observed to photocatalytically reduce HCl to H_2 upon light excitation with blue light and the concomitant production of the Rh_2[0,II]X_2 complex. The system is returned to the Rh_2[0,0] starting complex by trapping Cl radicals generated from photochemical M–X bond activation, thus allowing turnover to be achieved. Hydrogen elimination was observed to be facile and neither hydrido nor hydrido-halide intermediates were observed under catalytic conditions (Figure 1.10). While this two-electron mixed valency strategy provides a great opportunity for achieving multi-electron redox transformations, lack of halogen photoelimination reactivity in the absence of chemical traps remains a challenge. Interestingly, this strategy has not been applied to first-row transition metal complexes, thus it would be fundamentally interesting to compare their photoreactivity to that of two-electron mixed valent first-row metal pairs.

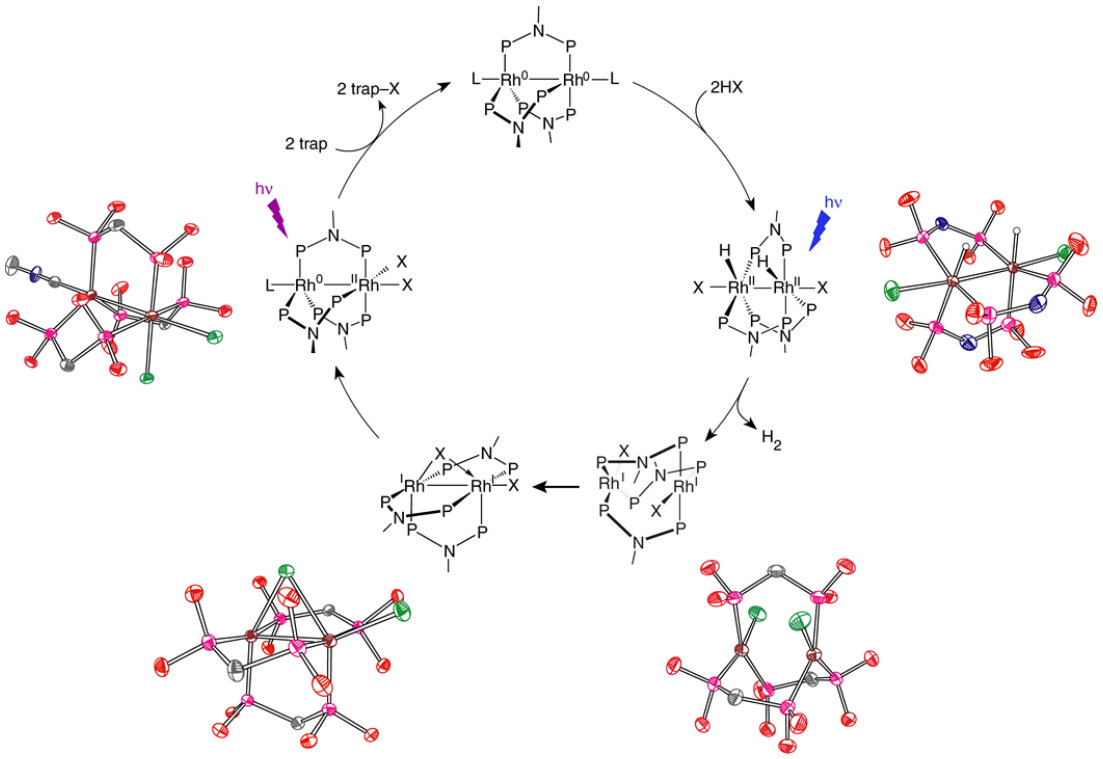

Figure 1.10. Complete photocycle for H_2 generation by the Rh_2 dfpma photocatalyst from nonaqueous solutions containing HCl or HBr adapted from ref 9.

1.4 Scope of thesis

There are no viable alternatives to precious metal complexes for catalyzing HX splitting, and especially M−X photoactivation. In this thesis, we explore the design of first-row transition metal complexes that achieve efficient halogen photoelimination reaction both in solution and in the solid-state. A preeminent question that remains to be addressed is how to overcome the short-excited state lifetime of first-row transition metal complexes and what roles the ligand platform plays in terms of structural, electronic, and secondary coordination sphere effects. The identification of key intermediates utilizing transient absorption (TA) laser spectroscopy and steady-state photocrystallography, coupled with synthetic tools has led us to design more efficient photocatalysts. Starting with Chapter 2, we propose a family of Ni(II)X_2 complexes bearing redox active ligands in an effort to engender MLCT excited states as described in Figure

1.3. Upon photolysis, a diimine-supported Ni(II)X_2 complex accesses excited states in which a formally Ni(III) center is bound to a singly reduced diiminyl radical ligand. Such a complex is expected to be substantially more oxidizing than the Ni(II) ground state complex and may allow for X_2 elimination. The redox activity of diimine ligands bound to nickel are well documented, [52] and the MLCT contribution to the excited state of Ni(II) bisimine complexes has been reported and discussed. [53,54] In support of the proposed MLCT-driven halogen elimination is the recent report by Milstein, who demonstrated O–O bond formation during the photoelimination of H_2O_2 from a Ru(II) complex MLCT excited state.[22] However, we soon realized that the compression of the crystal field upon moving from a second- to first-row metal results in the placement of d-d ligand–field states at lower energy than the charge-separated states. The consequence of this reordering of excited state energies is inherently short excited-state lifetimes for nickel complexes. We therefore introduce a new design strategy in which photochemistry and H_2 evolution roles are separated by tandem redox cycles. Using diaryl phosphines as photoredox mediators, we demonstrate that relatively non-basic phosphines are capable of acting as photoredox mediators under acidic conditions. Catalytic photogeneration of H_2 from HCl has been developed using a combination of non-basic phosphines as photoredox mediators and Ni complexes as H_2 evolution catalysts. While this strategy has been applied for the generation of H_2, it was not able to achieve the halogen photoelimination reaction. Thus in Chapter 3, we employ LMCT excited states (Figure 1.3) for M−X bond photoactivation from oxidizing Ni(III) complexes. These efforts still hinge on developing strategies to overcome the inherently short excited state lifetimes of first-row transition metal based complexes in order to avoid facile energy wasting internal conversion processes. High-yielding, endothermic Cl_2 photoelimination chemistry from mononuclear Ni(III) complexes has been developed utilizing a new strategy

based on secondary coordination sphere effects to suppress the undesired rapid back reaction. On the basis of time-resolved spectroscopy and steady-state photocrystallography experiments, a mechanism involving ligand-assisted halogen elimination is proposed. In these studies to utilize LMCT excited states, we reveal the limitations of the system, primarily that it is confined to one-electron transformations. Thus, the photoproduct Ni(II) species are not active toward proton reduction in the presence of HCl. In Chapter 4, we achieve the halogen photoelimination reaction based on MMCT excited states (Figure 1.3) by unveiling new low-valent binuclear Ni_2[I,I] and Ni_2[I,0] complexes comprising electronically withdrawing ligands. Utilization of metal−metal bonds in a three-fold symmetry provided a strategy to achieve halogen photoelimination from low-valent binuclear Ni centers. The Cl_2 photoelimination has been achieved in the solid-state assisted by short intermolecular distance between two axial Cl atoms in the crystal lattice (3.503 Å). We further design a two electron mixed valency binuclear Ni_2[0,II] complex for the efficient X_2 photoeliminaiton inspired by the photocrystallography results exhibiting the primary photoproduct is bridged halide Ni_2 intermediate. In Chapter 5, using the wealth of electronic and geometric variations of pyridine diimine (PDI) ligands, we expand photoreduction chemistry toward Fe(III) metal complexes employing PDI ligands to understand the fundamental effects of electronics and geometry on the photoefficiency of the halogen elimination reaction. Additionally, we present two families of five-coordinate iron complexes with two-ligand platforms (PDI and monodentate phosphine) that show the utility of secondary sphere arenes to efficiently generate chlorine atom radicals. Further, with careful tailoring of the secondary coordination sphere, we report the first photocrystallographic observation of an arene|chlorine charge transfer complex. In both cases, we establish the effects of secondary coordination sphere interactions with peripheral arenes in the solid-state using photocrystallography, and in the case

of the PDI system we show an increased quantum yield in solution. Overall, we demonstrate the ability to rationally modify and design HX photocatalysts to achieve greater photoefficiency using earth abundant elements. In Chapter 6, in collaboration with the magento-chemist in the group, magneto-structural correlation studies of mononuclear intermediate $S = 3/2$ Fe(III) phosphine complexes, demonstrate the influence of local symmetry on magnetic anisotropy.

1.5 References

1. Nocera, D. G. *ChemSusChem* **2009**, *2*, 387.
2. Nocera, D. G. *Energy Environ. Sci.* **2010**, *3*, 993.
3. Cook, T. R.; Dogutan, D. K.; Reece, S. Y.; Surendranath, Y.; Teets, T. S.; Nocera, D. G. *Chem. Rev.* **2010**, *110*, 6474.
4. Nel, A. *Science* **2005**, *308*, 804.
5. Patz, J. A.; Campbell-Lendrum, D.; Holloway, T.; Foley, J. A. *Nature* **2005**, *438*, 310.
6. K. P. Kuhl, E. R. Cave, D. N. Abram and T. F. Jaramillo, *Energy Environ. Sci.* **2012**, *5*, 7050.
7. Z. Yang, J. Zhang, M. C. W. Kintner-Meyer, X. Lu, D. Choi, J. P. Lemmon and J. Liu, *Chem. Rev.* **2011**, *111*, 3577.
8. A. J. Esswein and D. G. Nocera, *Chem. Rev.* **2007**, *107*, 4022.
9. Nocera, D. G. *Inorg. Chem.* **2009**, *48*, 10001.
10. Thomassen, M.; Sandnes, E.; Børresen, B.; Tunold, R. *J. Appl. Electrochem.* **2006**, *36*, 813.
11. Yeo, R. S.; McBreen, J.; Tseung, A. C. C.; Srinivasan, S. *J. Appl. Electrochem.* **1980**, *10*, 393.
12. Ledjeff, K.; Mahlendorf, F.; Peineche, V.; Heinzel, A. *Electochim. Acta* **1995**, *40*, 315.
13. Thomassen, M.; Børresen, B.; Hagen, G.; Tunold, R.; *J. Appl. Electochem.* **2003**, *33*, 9.

14. Heyduk, A. F.; Macintosh, A. M.; Nocera, D. G. *J. Am. Chem. Soc.* **1999**, *121*, 5023.

15. Heyduk, A. F.; Nocera, D. G. *J. Am. Chem. Soc.* **2000**, *122*, 9415.

16. Heyduk, A. F.; Nocera, D. G. *Science* **2001**, *293*, 1639.

17. Odom, A. L.; Heyduk, A. F.; Nocera, D. G. *Inorg. Chim. Acta* **2000**, *297*, 330.

18. Karikachery, A. R.; Lee, H. B.; Masjedi, M.; Ross, A.; Moody, M. A.; Cai, X.; Chui, M.; Hoff, C. D.; Sharp, P. R. *Inorg. Chem*. **2013**, *52*, 4113.

19. Hickman, A.; Sanford, M. S. *Nature*, **2012**, *484*, 177.

20. Canty, A. J. *Acc. Chem. Res*. **1992**, *25*, 83.

21. e Silva, F. C. S.; Tierno, A. F.; Wengryniuk, S. E. *Molecules*, **2017**, *22*, 780.

22. Kohl, S. W.; Weiner, L.; Schwartsburd, L.; Konstantinovski, L.; Shimon, L. J. W.; Ben-David, Y.; Iron, M. A.; Milstein, D. *Science* **2009**, *324*, 74.

23. Cook, T. R.; Surendranath, Y.; Nocera, D. G. *J. Am. Soc. Chem.* **2009**, *131*, 28.

24. Esswein, A. J.; Veige, A. S.; Nocera, D. G. *J. Am. Chem. Soc.* **2005**, *127*, 16641.

25. Cook, T. R.; Esswein, A. J.; Nocera, D. G. *J. Am. Chem. Soc.* **2007**, *129*, 10094.

26. Teets, T. S.; Lutterman, D. A.; Nocera, D. G. *Inorg. Chem.* **2010**, *49*, 3035.

27. Cook, T. R.; McCarthy, B. D.; Lutterman, D. A.; Nocera, D. G. *Inorg. Chem*. **2012**, *51*, 5152.

28. Teets, T. S.; Neumann, M. P.; Nocera, D. G. *Chem. Commun*. **2011**, *47*, 1485.

29. Cook, T. R.; Esswein, A. J.; Nocera, D. G. *J. Am. Chem. Soc*. **2007**, *129*, 10094.

30. Lin, T.-P.; Gabbaï, F. P. *J. Am. Chem. Soc*. **2012**, *134*, 12230.

31. Yang, H.; Gabbaï, F. P. *J. Am. Chem. Soc*. **2014**, *136*, 10866.

32. Sahu, S.; Gabbaï, F. P. *J. Am. Chem. Soc*. **2017**, *139*, 5035.

33. Carrera, E. I.; McCormick, T. M.; Kapp, M. J.; Lough, A. J.; Seferos, D. S. *Inorg. Chem*. **2013**, *52*, 13779.

34. Carrera, E. I.; Lanterna, A. E.; Lough, A. J.; Scaiano, J. C.; Seferos, D. S. *J. Am. Chem. Soc*. **2016**, *138*, 2678.

35. Carrera, E. I.; Seferos, D. S. *Dalton Trans*. **2015**, *44*, 2092.

36. Powers, D. C.; Chambers, M. B.; Teets, T. S.; Elgrishi, N.; Anderson, B. L.; Nocera, D. G. *Chem. Sci*. **2013**, *4*, 2880.

37. Higgs, A. T.; Zinn, P. J.; Sanford, M. S. *Organometallics* **2010**, *29*, 5446.

38. Camasso, N. M.; Sanford, M. S. *Science* **2015**, *347*, 1218.

39. Meucci, E. A.; Camasso, N. M.; Sanford, M. S. *Organometallics* **2017**, *36*, 247.

40. Jørgensen, C. K. *Progr. Inorg. Chem.* **1962**, *4*, 73.

41. Schmidtke, H.-H. Physical Methods in Advanced Inorganic Chemistry, Hill, H. A. O., Day, P., Eds.; Wiley-Interscience: New York, 1968.

42. Schläfer, H. L.; Gleiman, G. Ligand Field Theory, Chap. 1, Wiley-Interscience: New York, 1969.

43. Teets, T. S.; Nocera, D. G. *J. Am. Chem. Soc*. **2009**, *131*, 7411.

44. McCusker, J. K. *Acc. Chem. Res*. **2003**, *36*, 876.

45. Juban, E. A.; Smeigh, A. L.; Monat, J. E.; McCusker, J. K. *Coord. Chem. Rev*. **2006**, *250*, 1783.

46. Rakowski DuBois, M.; DuBois, D. L. *Chem. Soc. Rev*. **2009**, *38*, 62.

47. Rakowski DuBois, M.; DuBois, D. L. *Acc. Chem. Res*. **2009**, *42*, 1974.

48. Hu, X. *Chem. Sci*. **2011**, *2*, 1867.

49. Lee, C. H.; Lutterman, D. A.; Nocera, D. G. *Dalton Trans.* **2013**, *42*, 2355.

50. Heyduk, A. F.; Nocera, D. G. *Chem. Commun*. **1999**, 1519.

51. Esswein, A. J.; Veige, A. S.; Nocera, D. G. *Organometallics* **2008**, *27*, 1073.

52. de Bruin, B.; Bill, E.; Bothe, E.; Weyhermuller, T.; Wieghardt, K. *Inorg. Chem.* **2000**, *39*, 2936.

53. Servaas, P. C.; Stufkens, D. J.; Oskam, A. *Inorg. Chem.* **1989**, *28*, 1774.

54. Servaas, P. C.; Stufkens, D. J.; Oskam, A. *Inorg. Chem.* **1989**, *28*, 1780.

Chapter 2

Tandem Redox Mediator/Ni(II) Trihalide Complex Photocycle for Hydrogen Evolution from HCl

Parts of this chapter have been published:

Hwang, S.; Powers, D. C.; Maher, A. G.; Nocera, D. G. "Tandem Redox Mediator/Ni(II) Trihalide Complex Photocycle for Hydrogen Evolution from HCl." *Chem. Sci.* **2013**, *54*, 2713–2725.

2.1 Introduction

The photochemical splitting of hydrohalic acids (HX) into H_2 and X_2 is an approach to solar fuel synthesis[1] that stores a comparable amount of energy to water splitting. In addition to the similar energy densities implicit in HX and H_2O splitting chemistries, HX splitting mandates management of only two electrons and two protons, whereas H_2O splitting requires management of four protons and four electrons.[2–5] Photocatalytic HX splitting requires accomplishing multielectron photochemical reactions to activate strong M–X bonds. Typically photoreduction has been the limiting step in HX splitting photocatalysis and often X_2 elimination requires the use of chemical traps for evolved halogen equivalents.[6–17] Attempts at promoting HX splitting with first-row transition metal complexes are attractive given that these metals are typically earth abundant, but have been largely unsuccessful. The challenge of using first-row metal complexes as HX splitting photocatalysts is that photochemical activation of Ni(I) or Ni(II) halides frequently does not lead to photoreduction reactions,[18,19] likely due to the short excited state lifetimes of first-row transition metal complexes.[20–22]

To overcome the short excited state lifetimes typical of first-row complexes, the Nocera group has pursued a photoredox strategy for H_2 evolution from HCl in which the photochemistry and H_2 evolution roles are separated between a photoredox mediator and a hydrogen-evolution catalyst, respectively.[23] This strategy is attractive because because it does not rely on molecular excited states of first-row metal complexes. In the first foray into photoredox catalysis for H_2 evolution, bipyridines were employed as photoredox mediators and Ni polypyridyl complexes as H_2 evolution catalysts. H-atom abstraction (HAA) by the excited state of the bipyridine afforded a pyridinyl radical, which engaged with a Ni(II) halide complex to generate a Ni(I) intermediate via halogen radical abstraction. The resulting Ni(I) complex underwent disproportionation to a

Ni(II) complex and a Ni(0) species, which subsequently engaged in protolytic H_2 evolution. The ability to drive photoreduction reactions by ligand-mediated – and ultimately ligand catalyzed, as ligand is regenerated during proton reduction steps – is an exciting opportunity. The challenge in using bipyridines as photoredox mediators is that the observed excited-state chemistry arises from n → π* excitations. While these efforts demonstrated a synthetic cycle for H_2 evolution, H_2-evolution catalysis was not observed. In the presence of HCl, which is necessarily present during a prospective metal-catalyzed HCl-splitting reaction, the required excitation is unavailable because the involved lone pair on nitrogen is protonated.

To address the challenges of photoredox catalysis for H_2 evolution from HCl, efforts turned to identifying a photoredox mediator that could function under acidic conditions. In this chapter, the role of phosphines as photoredox mediators under acidic conditions will be discussed (pK_a in CH_3CN: PPh_3 = 7.64; pyridine = 12.53).[24] We establish the photochemical homolysis of P–H bonds of 2° phosphines to generate phosphinyl radicals that display sufficient lifetime (~160 μs) to participate in halogen-atom abstraction from a Ni(II) halide complex to furnish a reduced Ni intermediate that participates in an H_2 evolution cycle; the phosphine photoredox mediator is regenerated by HAA from solvent to close the photocycle.[25–27] The H_2-evolution cycle may be closed by thermally promoted protolytic H_2 evolution with HCl.

2.2 Synthesis and Steady-State Photochemistry

We targeted phosphines as potential photoredox mediators for a tandem photoredox / transition metal catalysed H_2-evolution photocycle from HCl based on their demonstrated ability to serve as photochemical H-atom donors.[27] To evaluate the viability of the proposed phosphine-mediated photoredox approach for H_2 evolution, we photolyzed Ni(II) complex $NiCl_2(PPh_3)_2$ (**1**)

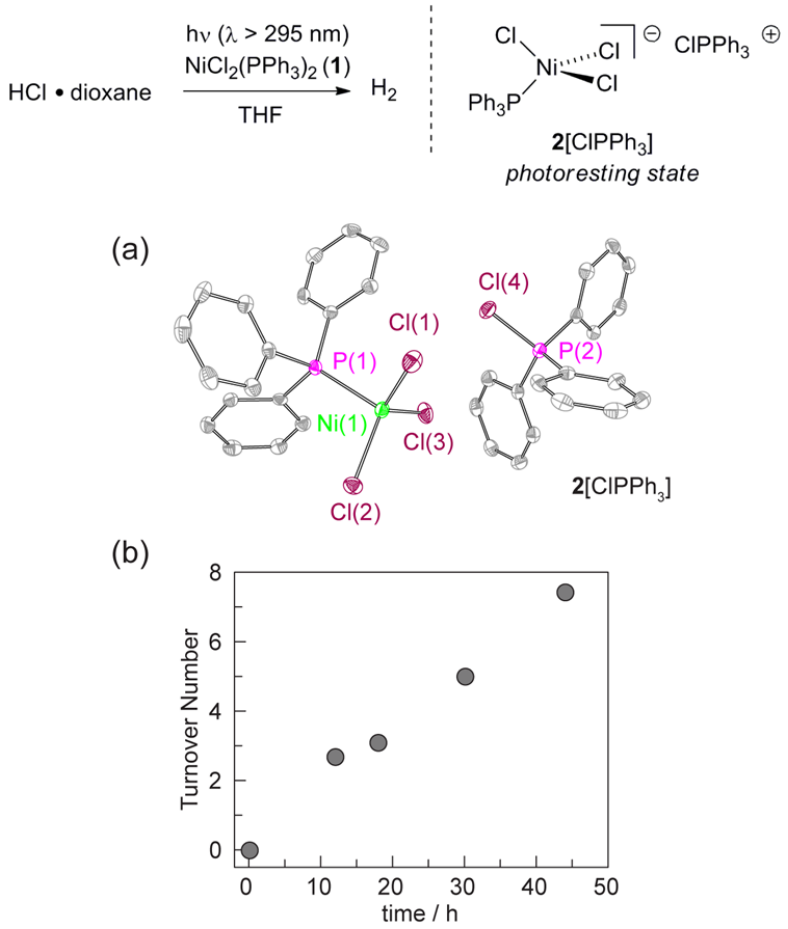

Figure. 2.1. Photolysis of $NiCl_2(PPh_3)_2$ in THF (λ > 295 nm) in the presence of 15 equiv of HCl affords H_2 as well as **2**[$ClPPh_3$]. (a) Thermal ellipsoid plot of **2**[$ClPPh_3$] drawn at the 50% probability level. The hydrogen atoms are omitted for clarity. (b) Time-dependent turnover number (TON) of H_2 produced by a 4.5 mM THF solution of $NiCl_2(PPh_3)_2$ in the presence of 15 equiv HCl (λ > 295 nm).

in THF (λ > 295 nm) in the presence of 1.0 equiv PPh_3 and 15 equiv of HCl. The light beige reaction solution turned pale blue upon photolysis. Analysis of the headspace by gas chromatography (GC) confirmed H_2 as the exclusive gaseous product under these conditions; integration of the chromatogram and comparison to a standard curve revealed that 3.1 turnovers had been achieved in 18 h. $NiCl_2(PPh_3)_2$ participates in ligand dissociation equilibria to release PPh_3 (vide infra),[28] and thus H_2-evolving photocatalysis was also observed in the absence of

exogenous PPh_3. Evaluation of the amount of H_2 evolved as a function of time (Figure. 2.1), showed that in the presence of excess HCl, H_2 evolution continues and 9 turnovers were achieved after 44 h with no signs of deactivation.

During the photolysis of $NiCl_2(PPh_3)_2$, the blue-coloured solution that initially develops persists throughout subsequent H_2 evolution and based on UV-vis measurements, appears to represent the photoresting state of the catalyst system. The pale blue photoproduct was identified as Ni(II) trihalide complex **2**[$ClPPh_3$] by single-crystal X-ray diffraction analysis. In addition, comparison of the in situ UV-vis spectrum obtained during H_2-evolving catalysis with a spectrum obtained from an authentic sample of **2**[$ClPPh_3$], prepared by treatment of $NiCl_2(PPh_3)_2$ with 1.0 equiv of $PhICl_2$ (Figure 2.2), confirmed the identity of the catalyst resting state. Independently isolated complex **2**[$ClPPh_3$] is chemically competent at H_2 generation under above photoreaction conditions.

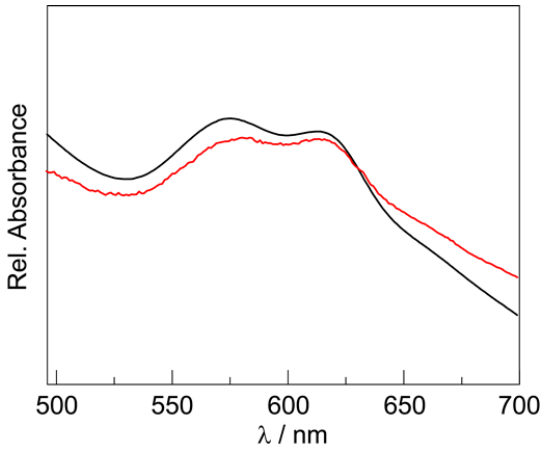

Figure 2.2. UV-vis spectrum of the photolysis of $NiCl_2(PPh_3)_2$ (**1**) in THF ($\lambda > 295$ nm) in the presence of 15 equiv of HCl for 17 h (—, black), and authentic sample of **2**[$ClPPh_3$] (—, red) prepared by treatment of $NiCl_2(PPh_3)_2$ with 1.0 equiv of $PhICl_2$.

Catalyst resting state **2**[$ClPPh_3$] is comprised of a Ni trichloride anion and a phosphonium

cation. In order to establish the roles of both the Ni complex and phosphine in the observed H_2 evolution reaction, **2**[TBA] and phosphonium cation [$ClPPh_3$]OTf were independently prepared. As summarized in Table 2.1, Ni(II) complex **2**[TBA] showed a similar activity toward HCl with 5.0 TON in 18 h. Complex **2**[TBA] also participates in a minor equilibrium with free PPh_3 (vide infra) and thus both catalyst and photoredox mediator are present when **2**[TBA] is employed as the photocatalyst. In contrast, phosphonium salt [$ClPPh_3$]OTf does not produce H_2 under the same reaction conditions. Additionally, neither PPh_3 or [$NiCl_4$][$TEA]_2$ is a competent H_2-evolution catalyst, confirming the necessity of both Ni complex and phosphine for productive H_2 evolution chemistry.

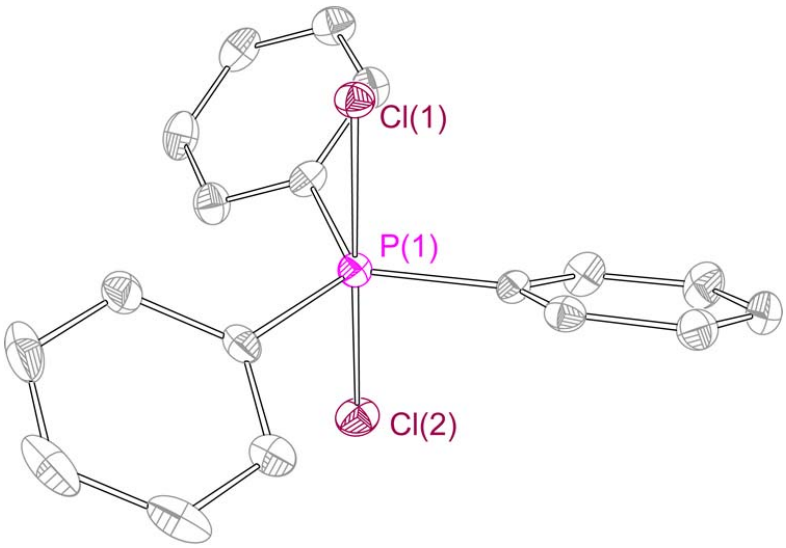

Figure 2.3. Thermal ellipsoid plot of PPh_3Cl_2 drawn at the 50% probability level. H-atoms omitted for clarity.

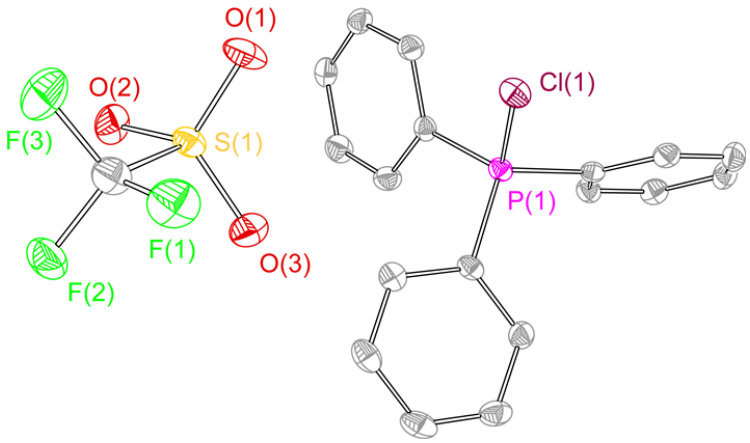

Figure 2.4. Thermal ellipsoid plot of [ClPPh$_3$]OTf drawn at the 50% probability level. H-atoms omitted for clarity.

Table 2.1. TON of H_2 measured in the headspace upon photolysis of designated compounds in the presence of 15 equiv HCl in THF for 18 h.

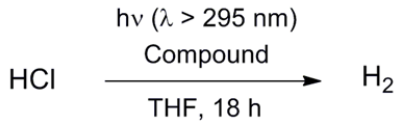

Compound	*TON*
2[ClPPh$_3$]	2.0
PPh$_3$	0
[NiCl$_4$][Et$_4$N]$_2$	0
2[TBA]	5.0
[ClPPh$_3$]OTf	0

2.3 Time-Resolved Photochemical Experiments

In order to probe the contention that photogenerated diphenylphosphinyl radicals could mediate the reduction of a Ni–Cl bond from the Ni(II) trihalide complex, we carried out time-resolved photochemical experiments. On the picosecond timescale, a transient absorption (TA)

difference spectrum obtained by laser flash photolysis (λ_{exc} = 310 nm, THF solutions) of **2**[TBA] exhibits a spectral growth centered at 506 nm with a lifetime of ~700 ps (Figure. 2.5). An identical spectral feature was observed during laser flash photolysis of PPh_3 solutions. This feature was assigned to be that of the singlet excited state of PPh_3, and the observation of this signal in the TA spectrum of **2**[TBA] supports the presence of a minor equilibrium between **2**[TBA] and free PPh_3.[29] Additional support for this ligand dissociation equilibrium is the observation that both **2**[TBA] and PPh_3 both show an emission band centered at 500 nm with a 900 ps lifetime (Figure. 2.6), which is well-matched to reported PPh_3 photophysics.[30] The similar emission lifetimes for both **2**[TBA] and PPh_3 excludes dynamic quenching of the excited $^1PPh_3^*$ species by the Ni complex and suggests that the relatively low steady-state emission intensity observed for **2**[TBA] is due only to a low equilibrium concentration of PPh_3.

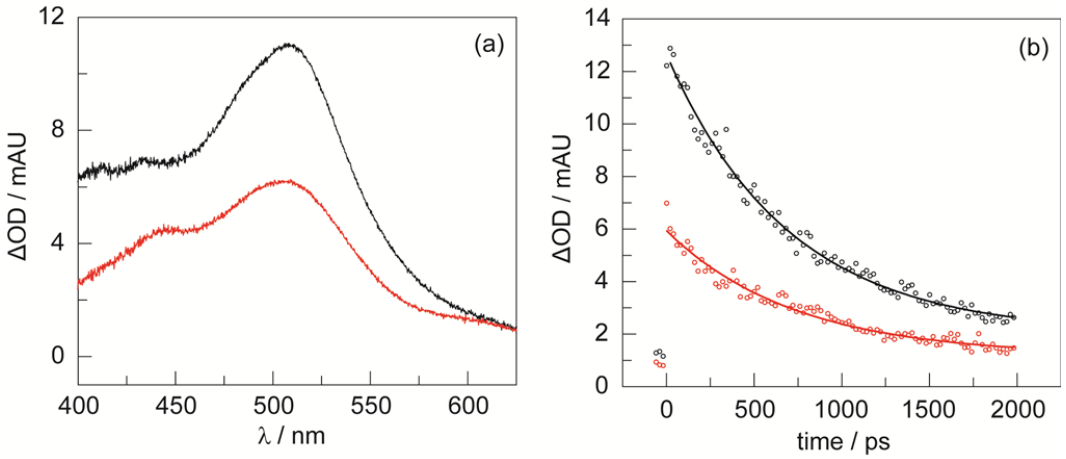

Figure 2.5. (a) Transient absorption spectra obtained by flash laser photolysis (310 nm pump) of Ni complex **2**[TBA] (—, red), and PPh_3 (—, black) in THF at a 2 ps delay. (b) Single wavelength kinetic traces of Ni complex **2**[TBA] (—, red), and PPh_3 (—, black) in THF pumped at 310 nm, centered about 506 nm.

The photochemistry of **2** and PPh_3 were also examined at longer time scales by nanosecond flash photolysis (Figure 2.7). Flash photolysis of either **2**[TEA] (red spectrum,

Figure 2.7) or PPh_3 (black spectrum, Figure 2.7) leads to the observation of TA signals that are ascribed to diphenylphosphinyl radical.[27] The lifetime of the diphenylphosphinyl radical derived from PPh_3 with and without the presence of **2**[TBA] in solution is the same, consistent with no direct reaction between Ni(II) complex and diphenylphosphinyl radical (Figure 2.8). Substantial phosphine consumption is not required for H_2 evolution because the diphenylphosphine generated during catalysis is a competent photoredox carrier. Nanosecond-resolved TA spectra, collected by laser flash photolysis of diphenylphosphine in THF, display the spectral features of diphenylphosphinyl radical (Figure 2.9), confirming that phosphine mediators can be catalytic.[27, 31]

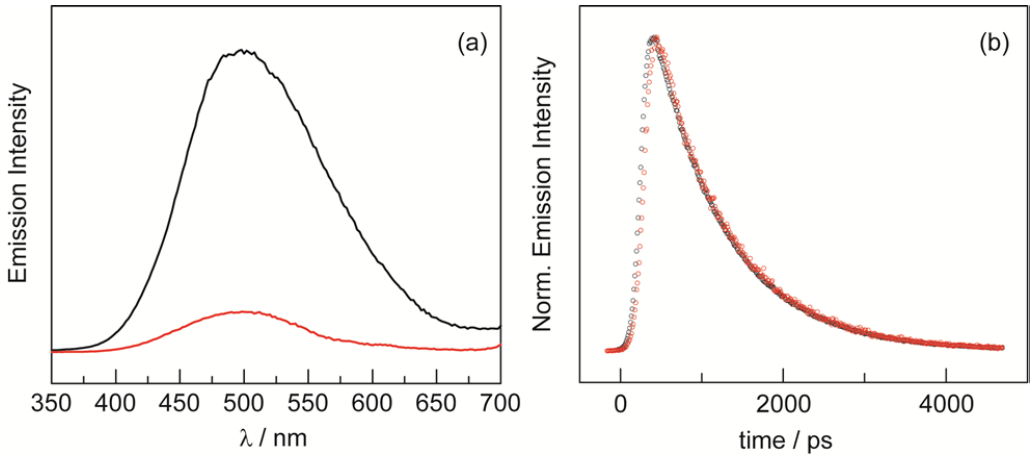

Figure 2.6. (a) Steady-state emission spectra of **2**[TBA] (—, red) and PPh_3 (—, black) in THF. (b) Emission decays of **2**[TBA] (—, red) and PPh_3 (—, black) centered at 500 nm.

That the photogenerated diphenylphosphinyl radical engages in HAA with THF to produce diphenylphosphine is confirmed by the isolation of complex **6**, as a photo-byproduct of the photolysis of Ni complex **2**[TEA]. Complex **6** features two C-bound tetrahydrofuranyl ligands on a phosphorus center and could be derived from reaction of photo-generated diphenylphosphinyl radicals with furanyl radicals derived from HAA chemistry. Additionally we observed (GC-MS) octahydro-2,2'-bifuran (homocoupled THF) as a photochemical byproduct.

While HAA from THF by diphenyl phosphinyl radicals is endothermic (16 kcal/mol uphill based on P–H and C–H bond dissociation energies),[32] irreversible subsequent reactions, such as radical coupling to afford homocoupled THF sequester reactive radical intermediates.[31]

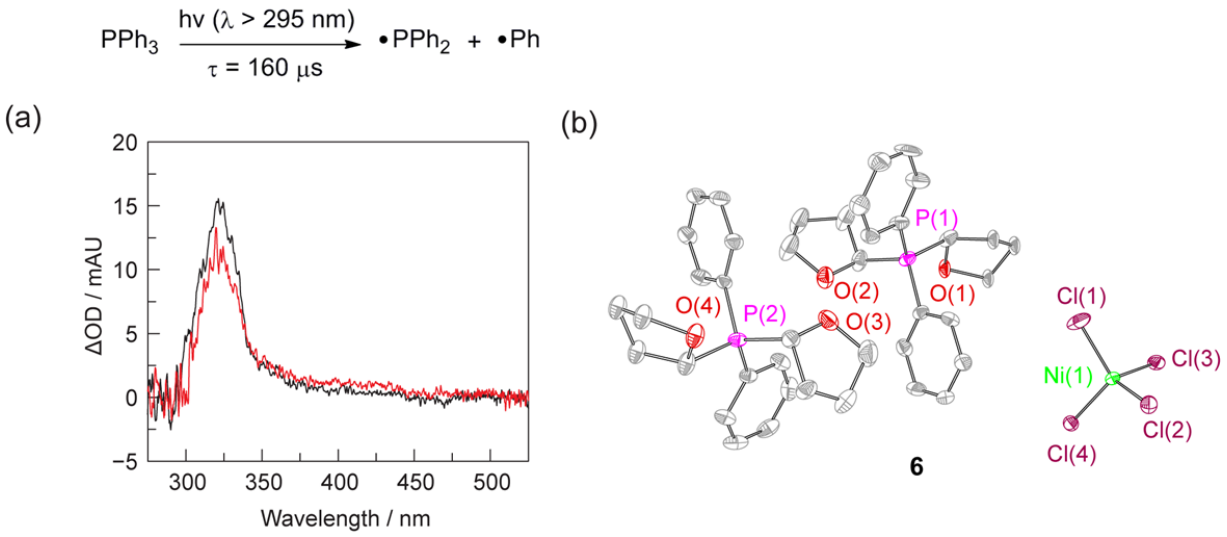

Figure 2.7. (a) Nanosecond transient absorption (TA) spectroscopy of Ni complex **2**[TEA] (—, red) and PPh_3 (—, black) is consistent with formation of diphenylphosphinyl radical. TA spectrum obtained by laser flash photolysis (310 nm pump) of a 1:1 THF:CH_3CN solution recorded at a 1μs delay. (b) Thermal ellipsoid of **6** drawn at the 50% probability level. The hydrogen atoms are omitted for clarity.

The rate for HAA from solvent by photogenerated diphenylphosphinyl is strongly correlated with solvent C–H bond energies.[27, 33] We therefore anticipated that efficiency of the total catalytic process would be dictated by the turnover frequency of the photoredox mediator, which depends on the C–H BDEs of H-atom donor. The turnover frequency (TOF) of hydrogen generation from HCl with Ni complex **2** strongly depends on the solvent we employed, showing a positive correlation to the BDE of solvents: 0.34 h^{-1} TOF in THF, 0.05 h^{-1} TOF in CH_3CN, and 0.02 h^{-1} TOF in C_6H_6 (92, 96, and 112 kcal/mol of C–H BDEs respectively) (See Figure 2.10 for details). [34–36]

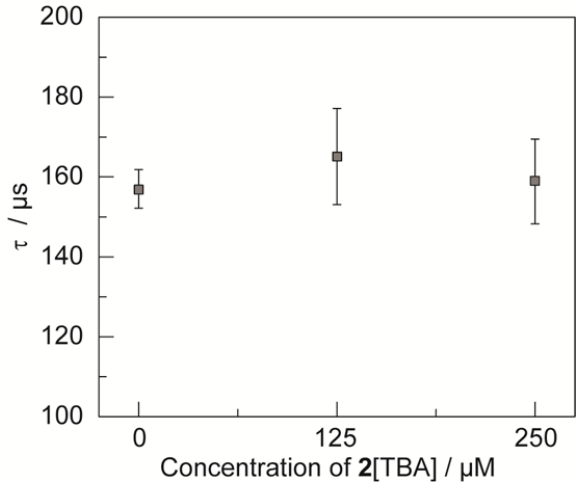

Figure 2.8. The lifetime, τ of the diphenylphosphinyl radical as a function of concentration of Ni complex **2**[TBA] concentration measured by nanosecond laser flash photolysis.

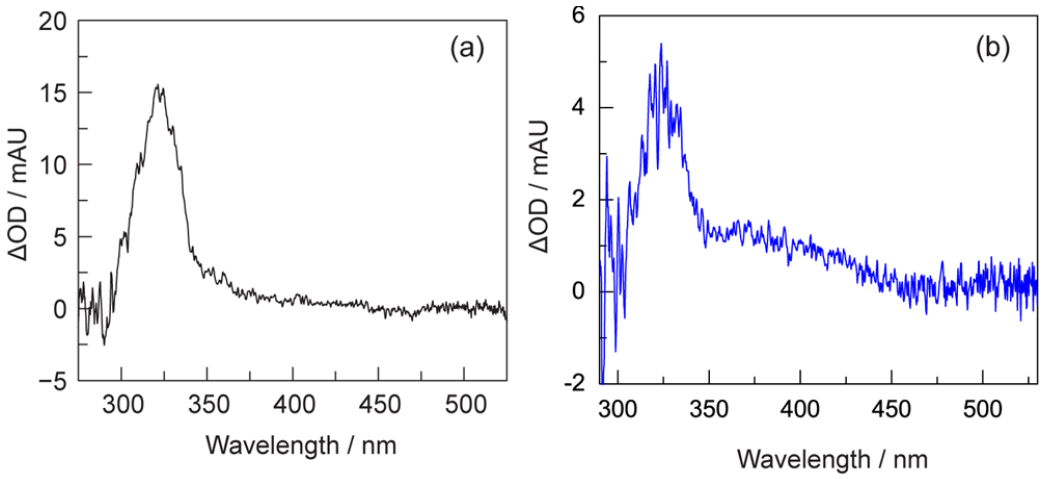

Figure 2.9. Formation of diphenylphosphinyl radical species was observed with nanosecond transient absorption (TA) spectroscopy of (a) triphenylphosphine (▬, black) and (b) diphenylphosphine (▬, blue). TA spectrum obtained by laser flash photolysis (310 nm pump) of THF solution.

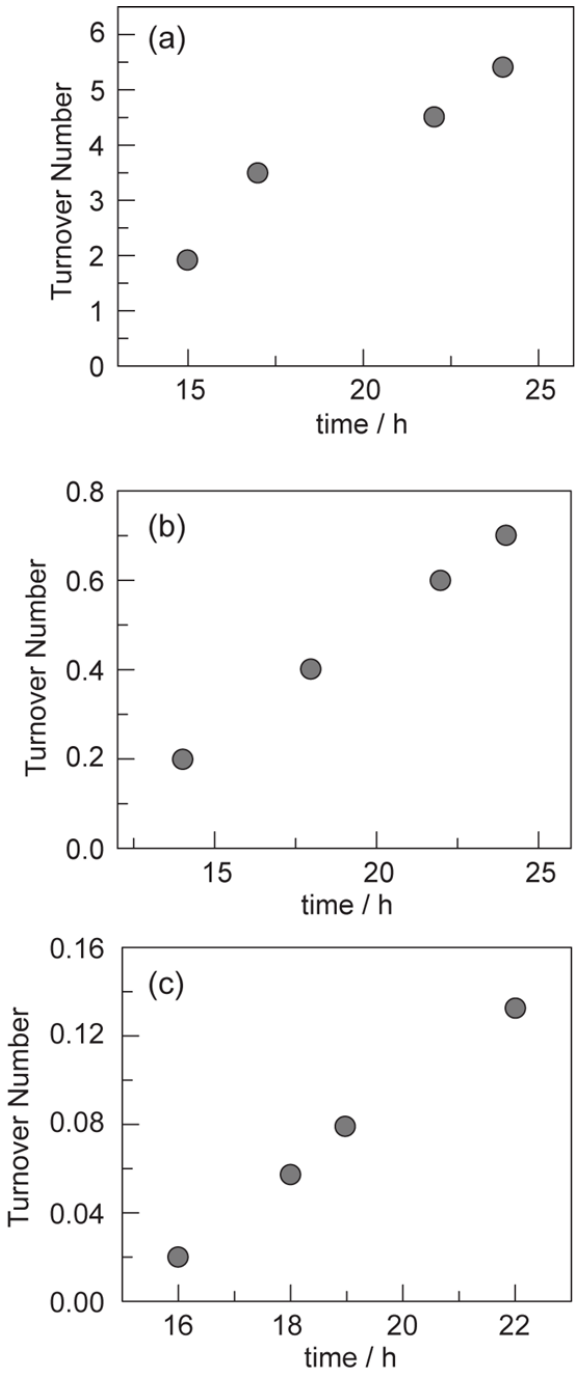

Figure 2.10. (a) Time dependent turnover number (TON) of H_2 produced by photolysis of: (a) **2**[TBA] in THF (λ > 295 nm) in the presence of 15 equiv of HCl; (b) **2**[TBA] in CH_3CN (λ > 295 nm) in the presence of 15 equiv of HCl; and, (c) **2**[TBA] in C_6H_6 (λ > 295 nm) in the presence of 15 equiv of HCl.

2.4 Equilibrium Reactions of Ni(I) intermediates

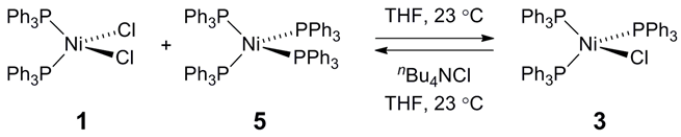

(1)

To probe the potential fate of potential Ni(I) intermediates during catalysis, we examined the chemistry of isolated Ni(I) complexes. Ni(I) complex **3** can be isolated from the comproportionation reaction of $NiCl_2(PPh)_2$ with $Ni(PPh_3)_4$. Based on the $E°(Ni^{II}/Ni^{I})$ and $E°(Ni^{I}/Ni^{0})$ measured by cyclic voltammetry in THF (Figure 2.11), comproportionation is thermodynamically favored. In contrast, in the presence of exogenous chloride ion, added as tetrabutylammonium chloride, disproportionation of Ni(I) complex **3** to Ni(II) complex **1** and Ni(0) complex **5** is observed, as determined by both ^{31}P NMR and electronic absorption spectroscopy (Figure 2.12 and 2.13 respectively). During H_2 evolution photocatalysis, chloride is present in large excess (68 mM) with respect to potential Ni(I) intermediates.

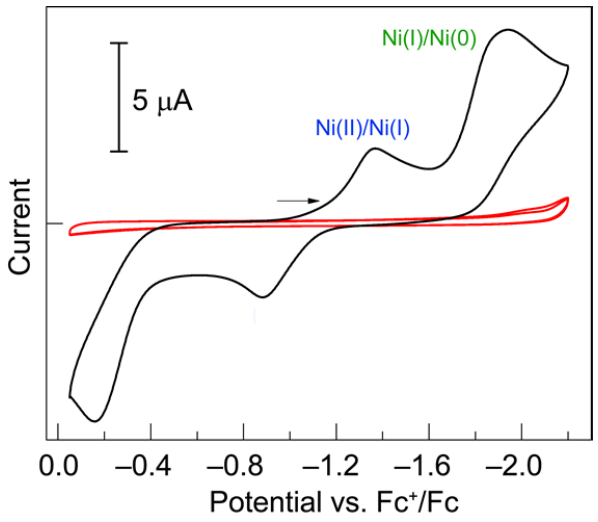

Figure 2.11. Cyclic voltammetry of 1 mM Ni complex **3** (—, black) and solvent background (—, red) measured with 0.1 M $^{n}Bu_4PF_6$ as a electrolyte in THF solution with a scan rate of 100 mV/s. Glassy carbon working electrode, $Ag/AgNO_3$ reference, and Pt wire counter electrode were used. E_p = –1.368 V, (Ni^{II}/Ni^{I}) and –0.885 V, (Ni^{I}/Ni^{II}).

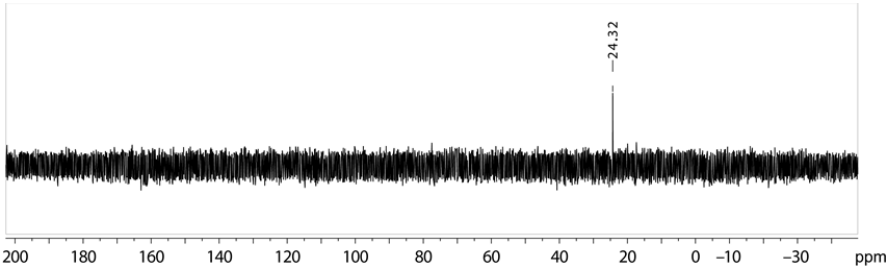

Figure 2.12. ^{31}P NMR spectrum of $NiCl(PPh_3)_3$ (**3**) with 1 equiv of $^{n}Bu_4NCl$ recorded in THF-d_8 at 23 °C. $NiCl(PPh_3)_3$ (**3**) and $NiCl_2(PPh_3)_2$ (**1**) do not display ^{31}P NMR signals.

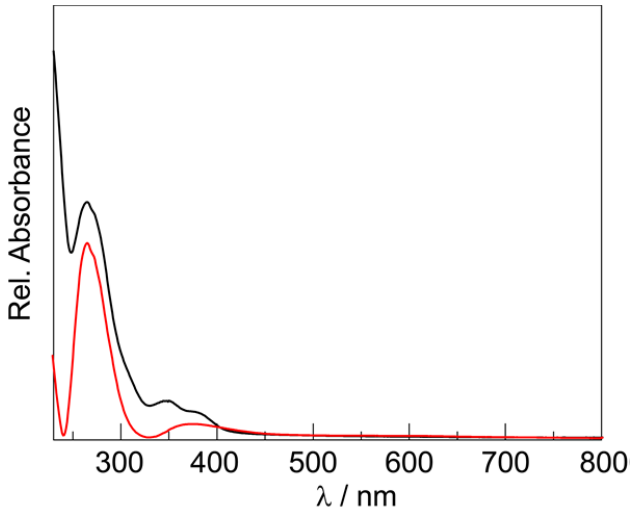

Figure 2.13. UV-vis spectrum of $NiCl(PPh_3)_3$ (**3**) (**—**, black) and $NiCl(PPh)_3$ (**3**) with 1 equiv $^{n}Bu_4Cl$ (**—**, red).

2.5 Thermally Promoted Proton Reduction Reactions

To assess whether the initially produced Ni(I) complex (**3**) or the Ni(0) complex (**5**) generated by disproportionation are active for H_2 production, we examined the stoichiometric H_2-evolution reaction chemistry of Ni(I) and Ni(0) complexes with HCl. The results of these experiments are summarized in Figure 2.14. Treatment of Ni complexes **3**, **4**, and **5** with 15 equiv HCl in THF generates H_2 in 44, 33, and 89% yields, respectively, along with Ni(II) complex **1**,

$NiCl_2(PPh_3)_2$. To gain insight into whether H_2 evolution proceeds by protonation of Ni(I) or Ni(0), generated by disproportionation reactions, electrochemical H_2 evolution was examined using Ni(II) trihalide complex **2**[TEA]. As illustrated in Figure 2.14, Ni complex **2**[TEA] exhibits two electrochemically irreversible waves for the $Ni^{II/I}$ and $Ni^{I/0}$ couples at –1.62 and –1.95 V vs Fc/Fc^+, respectively. In the presence of excess HCl (pK_a = 8.9 in CH_3CN)[37] these two peaks exhibit catalytic cathodic waves. The dominant CV features of the $Ni^{I/0}$ wave in the presence of excess HCl are consistent with Ni^0 being involved in the H_2 generating steps in our photocatalysis.

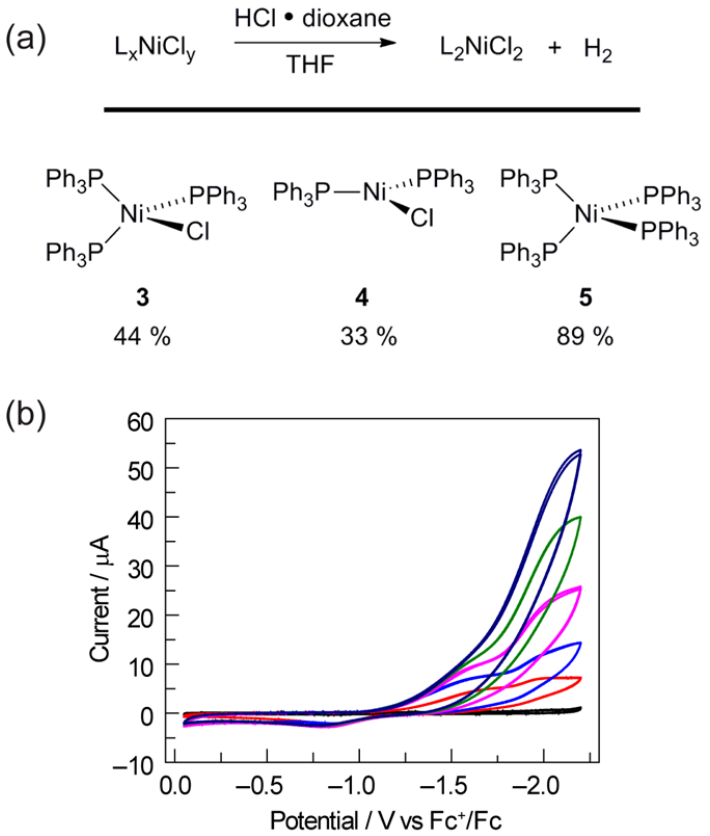

Figure 2.14. (a) Protonation of Ni(I) and Ni(0) complexes afforded Ni(II) chloride as well as H_2. (b) Electrochemical response of electrolyte background (—, black), 1mM Ni complex **2**[TEA] (—, red) to addition of HCl 1.0 equiv (—, blue), 5.0 equiv (—, pink), 9.0 equiv (—, green), 13.0 equiv (—, dark blue) in CH_3CN (0.1 M NBu_4PF_6; Scan rate, 100 mV/s). Glassy carbon working electrode, $Ag/AgNO_3$ reference, and Pt wire counter electrode.

2.6 Discussion

The compression of the crystal field splitting attendant upon moving from a second- to first-row metal results in the placement of d-d ligand–field states at lower energy than the charge-separated states.[38,39] Photoredox catalysis with first row metal complexes is unattainable because of their inherently short excited state lifetimes due to the consequence of this reordering of excited state energies. We have addressed this challenge by employing a tandem catalytic cycle where we use a redox mediator to generate the active metal catalyst. We have been especially committed to realizing such chemistry for energy storage, with HX splitting to H_2 as the target. Therefore, the Nocera group targeted a design strategy in which photochemistry is derived from a photoredox mediator, based on the efficacy of this species to drive redox processes such as CO_2 reduction.[40–42] Specifically, the group initially utilized excited states of bipyridine, which are known to engage in H-atom abstraction (HAA) reactions, to access a reducing pyridinyl radical for substrate reduction. However, efforts to apply this paradigm to H_2 evolution from HCl were not catalytic because the photoredox mediator was basic, and thus protonated in the presence of HCl, and hence exited the cycle.[23] In this chapter we report catalytic photo-generation of H_2 from HCl using a combination of non-basic phosphines as photoredox mediators and Ni complexes as H_2 evolution catalysts. Synthetic studies and time-resolved photochemical studies have defined the salient features of the catalytic cycle: photochemical generation of phosphinyl radicals, formation of a Ni(I) center via halogen-atom abstraction from Ni(II) trihalide complexes, and protolytic H_2 evolution. The results of these investigations establish the tandem nature of the cycle: a H_2 cycle catalyzed by a Ni complex and a photoredox cycle for reduction of Ni–X bonds mediated by phosphinyl radicals. The observation of both photoreduction and hydrogen-evolving protonolysis is the first

demonstration of HX-splitting photochemistry by a first-row transition metal.

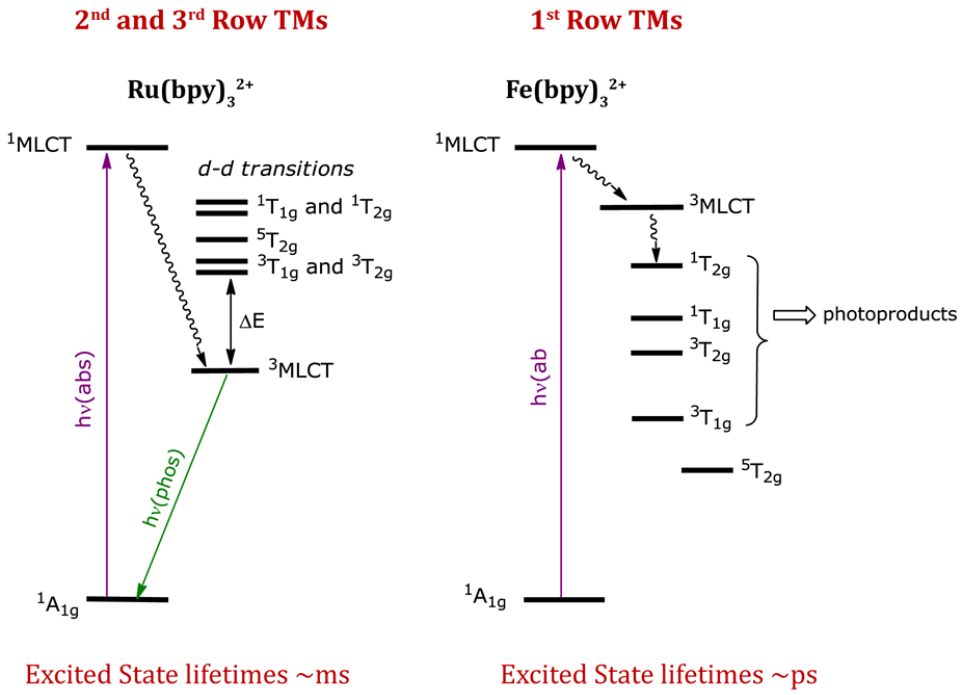

Figure 2.15. Comparison of excited states diagram between 1st and 2nd/3rd row transition metals.

Figure 2.16 illustrates a tandem catalytic cycle that accounts for the photogeneration of H_2 from HCl catalyzed by the Ni phosphine complexes and phosphine photoredox mediators. Diphenyl phosphine is initially formed by photochemical cleavage of the P–C bond and H-atom abstraction from solvent.[27] Photochemical cleavage of the P–H bond in $HPPh_2$ generates an H-atom equivalent and a diphenylphosphinyl radical.[27] The H-atom participates in halogen-atom abstraction with Ni(II) resting state **2** to generate a Ni(I) intermediate while the accompanying diphenylphosphinyl radical participates in C–H abstraction with solvent to regenerate the diphenylphosphine and close the photoredox cycle. Ni(I) intermediate **3** undergoes disproportionation to afford $NiCl_2(PPh_3)_2$ (**1**) and $Ni(PPh_3)_4$ (**5**). Protonolysis of Ni(0) complex **5**

affords H_2 and regenerates Ni(II) dihalide **1**, thus closing the hydrogen evolution cycle. The number of phosphine ligands bound to intermediates in the tandem cycle illustrated in Figure 2.16 is unknown. Isolated complexes **2**[$ClPPh_3$], **3**, **4** and **5**, which display 1 – 4 phosphine ligands per Ni, are all competent catalysts for H_2 evolution and proceed with the same photoresting state (**2**[$ClPPh_3$]), demonstrating ligand dissociation equilibria[28] are established during catalysis (Figure 2.14). Time-resolved photochemical experiments allowed direct observation of the photoredox-carrier diphenylphosphinyl radical and electrochemistry

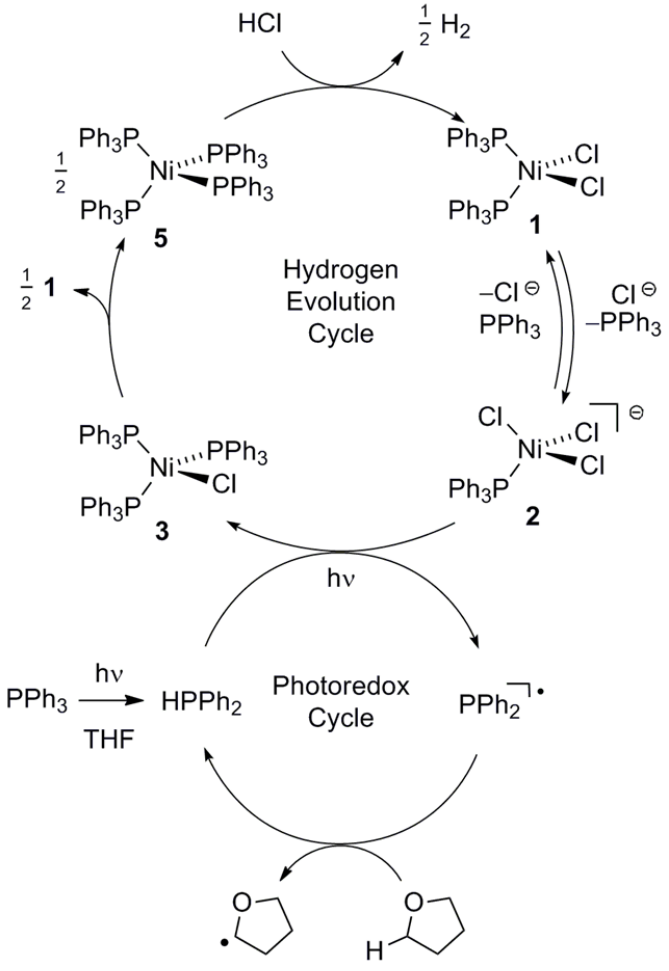

Figure 2.16. Proposed tandem catalytic cycles for H_2-generation with Ni-based H_2-evolution catalysts and phosphine-based photoredox mediators.

experiments suggest that H_2 evolution arises from protonation of Ni(0) intermediates generated by disproportionation of the initially formed Ni(I) photoproduct.

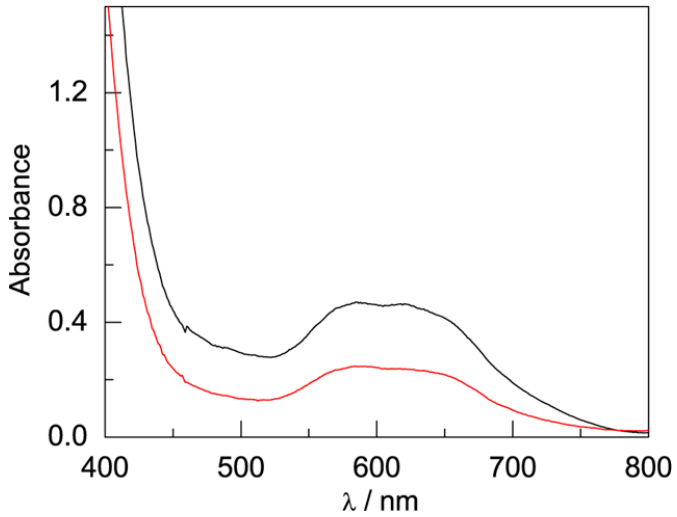

Figure 2.17. UV-vis spectrum of the photolysis of $Ni(PPh_3)_4$ (**5**) in THF ($\lambda > 295$ nm) in the presence of 15 equiv of HCl for 8 h (—, black), and $NiCl(PPh_3)_3$ (**3**) in THF ($\lambda > 295$ nm) in the presence of 15 equiv of HCl for 8 h (—, red).

2.7 Conclusions

As is common for first-row transition metal complexes, nickel halide complexes typically exhibit very short excited state lifetimes. Direct photoactivation of M–X bonds using the molecular excited states of these complexes has proven challenging owing to their lifetimes. To circumvent the limitations imposed by short excited state lifetimes, we have developed a tandem photoredox / transition metal catalysis approach to H_2 evolution in which the chromophore and the H_2-evolution catalyst are localized on different molecules. Using diaryl phosphines as photoredox mediators, we have demonstrated that relatively non-basic phosphines are capable of acting as photoredox mediators under acidic conditions. Robust photocatalytic systems have been developed by combining phosphine photoredox mediators and Ni phosphine H_2-evolution

catalysts. Time-resolved spectroscopy has revealed that phosphines serve as photochemical H-atom donors and activate the M–X bonds of Ni(II) halide complexes via halogen-atom abstraction. The H_2-evolution catalytic cycle is closed by sequential disproportionation of Ni(I) to afford Ni(0) and Ni(II) and protolytic H_2 evolution from the Ni(0) intermediate. The described photoredox strategy is attractive in that independent optimization of photoredox mediator and H_2-evolution catalyst provides multiple handles for system optimization.

2.8 Experimental Details

2.8.1 Materials and Methods

All reactions were carried out in an N_2-filled glovebox. Anhydrous solvents were obtained by filtration through drying columns.[43] NMR chemical shifts are reported in ppm with the residual solvent resonance as internal standard. UV–vis spectra were recorded at 293 K in quartz cuvettes on a Spectral Instruments 400 series diode array and were blanked against the appropriate solvent. $PhICl_2$[44] and $Ni(PPh_3)_2(CH_2{=}CH_2)$[45] were prepared according to reported procedures. $NiCl_2$dme (dme = 1,2-dimethoxyethane) and AgOTf (OTf = trifluoromethanesulfonate) were obtained from Strem Chemicals. Cl_2PPh_3, prepared by treatment of PPh_3 with $PhICl_2$, displayed spectral features identical to those reported in the literature.[46] $NiCl_2(PPh_3)_2$ (**1**), $Ni(PPh_3)_4$ (**5**), tetrabutylammonium chloride ($^nBu_4NCl$), tetraethylammonium chloride ($^nEt_4NCl$), and triphenylphosphine (PPh_3) were obtained from Sigma Aldrich. All chemical were used without further purification. Elemental analysis was obtained by Complete Analysis Laboratories, Inc., New Jersey. Evolved hydrogen was quantified by gas chromatography using a calibration curve derived from adding HCl to known quantities of NaH; over the relevant concentration range, the gas chromatograph response was linear. This

procedure has previously been validated by comparison with Toepler pump combustion analysis.[15]

Physical Methods. NMR spectra were recorded at the Harvard University Department of Chemistry and Chemical Biology NMR facility on a Varian Unity / Inova 600 spectrometer operating at 600 MHz for ^{1}H acquisitions or a or a Varian Mercury 400 spectrometer operating at 375 MHz and 160 MHz for ^{19}F and ^{31}P acquisitions, respectively. NMR chemical shifts are reported in ppm with the residual solvent resonance as internal standard. ^{31}P NMR chemical shifts were referenced to an external 85% H_3PO_4 standard. UV-vis spectra were recorded at 293 K in quartz cuvettes on a Spectral Instruments 400 series diode array and were blanked against the appropriate solvent. Steady-state emission spectra were obtained using a PTI QM 4 Fluorometer, with a 150 W Xe-arc lamp used for excitation (set to 310 nm) and a Hamamatsu R928 photomultiplier tub used for detection. Solution magnetic moments were determined using the Evans method in THF and measured using ^{19}F NMR (hexafluorobenzene added); diamagnetic corrections were estimated from Pascal constants.[47] Steady-state photochemical reactions were performed using a 1000 W high–pressure Hg/Xe arc lamp (Oriel) and the beam was passed through a water–jacketed filter holder containing the appropriate long–pass filter, an iris, and a collimating lens. Structures were collected on a Bruker three-circle platform goniometer equipped with an Apex II CCD and an Oxford cryostream cooling device at 100 K. Radiation was supplied from either a graphite fine focus sealed tube Mo Kα (0.71073 Å) source. Crystals were mounted on a glass fibre using Paratone N oil. Data were collected as a series of φ and/or ω scans. Data were integrated using SAINT and scaled with either a numerical or multi-scan absorption correction using SADABS. The structures were solved by intrinsic phasing methods using SHELXS-97 and refined against F^2 on all data by full matrix least squares with

SHELXL-97. All non-hydrogen atoms were refined anisotropically. Hydrogen atoms were placed at idealized positions and refined using a riding model.

Picosecond transient absorption (TA) experiments were performed using a previously reported home-built Ti:sapphire laser system.[23] The excitation wavelength was set to 310 nm with the power kept between 10-20 μJ/pulse at the sample. The continuum for the probe pulses was generated by focusing an 800 nm beam on a CaF_2 substrate. The reported experiments used a 500 nm blaze grating (300 grooves/mm) and the entrance slit for the monochromator was set to 0.3 mm. The transient absorption spectra reported are averages of 4 replicates of 500 four-spectrum sequences. To remove artifacts in the baseline, spectra were corrected by subtracting an average of 3 spectra taken at negative delays, i.e. time points at which the probe pulse arrives at the sample before the pump pulse. Single-wavelength kinetics traces were obtained by averaging 5 nm spectral windows about the wavelength of interest for each time point. The reported time constants were calculated using a least-squares fit of the data to a monoexponential decay on the OriginPro 8.5 data analysis software. Samples for picosecond TA experiments were prepared using THF in 2.0 mm path-length quartz high-vacuum spectroscopy cells and freeze-pump-thawed for 3 cycles using high-vacuum (1.0×10^{-5} Torr). Nanosecond TA experiments were performed using a modified version of a previously-reported home-built Nd:YAG laser system.[48] In the modified setup, the previously used Triax 320 spectrometer has been replaced by a Horiba iHR320 spectrometer. The output of the Xe-arc lamp was set to 2.0 ms pulses with 30 A current. The reported experiments used a 250 nm blaze grating (300 grooves/mm). For the full-spectrum TA acquisitions, the entrance slit for the monochromator was set to 0.32 mm and the gate time for the CCD was 55 ns. For the single wavelength kinetics TA acquisitions (centered at 320 nm), the entrance and exit slits were set to 0.16 mm, and a 1.0 kV bias was applied to the

photomultiplier tube detector. Error bars for the lifetime data correspond to the standard error of the monoexponential fits. The pump beam (300 nm) was generated from the frequency-doubled 600 nm signal of a Spectra-Physics Quanta-Ray MOPO-700 with FDO–970 option pumped with the 355 nm light from the aforementioned laser. The power of the pump beam was set to 2.4 mJ/pulse. The full TA spectra reported are averages of 200 four-spectrum sequences, and the single wavelength decays are averages of 500 acquisitions. THF or THF:CH_3CN (1:1) solutions of complex **2** and triphenylphosphine were prepared in 20-mL vials sealed with rubber septa in an N_2-filled glovebox. Solutions were flowed through a 3-mm diameter, 1-cm path length flow cell (Starna, type 585.2) using a peristaltic pump and positive argon pressure. Time-resolved emission data was collected using a Hamamatsu C4334 Streak Scope camera, with the 310 nm excitation pulses provided by the Ti:sapphire laser system described above, set to a 1 kHz repetition rate. A 5 ns time window was used, and 5000 exposures were captured for each sample. Samples for both steady-state and time-resolved emission experiments were prepared using THF in 1.0 cm quartz high-vacuum spectroscopy cells in a N_2-atmosphere glovebox.

Preparation of Ni(II) Trihalide Complexes. Complex **2**[$ClPPh_3$]: A solution of $PhICl_2$ (9.1 mg, 3.30×10^{-5} mol, 1.00 equiv) in 1 mL of CH_2Cl_2 was added to a solution of $NiCl_2(PPh_3)_2$ (21.4 mg, 3.30×10^{-5} mol, 1.00 equiv) in 2 mL of CH_2Cl_2 to prompt an immediate colour change from a light beige to blue. The solvent was removed in vacuo, and the resulting solid was treated with pentane. The pentane was decanted, and the resulting solid was dried in vacuo to afford 21.5 mg of title compound (90% yield). ^1H NMR (600 MHz, CD_3CN) δ (ppm): 7.77 (m, 9H), 7.64 (m, 6H). μ_{eff} (CH_3CN) = 4.20 μB. Anal. Calcd. (Found) for $C_{36}H_{30}Cl_4NiP_2$: C, 59.63 (59.53); H, 4.17 (4.09). Crystals suitable for single-crystal diffraction analysis were obtained from a CH_3CN solution of the complex layered with Et_2O.

Complex **2**[TBA]: To a suspension of $NiCl_2$(dme) (40.0 mg, 1.82×10^{-4} mol, 1.00 equiv) in CH_2Cl_2 was added PPh_3 (47.7 mg, 1.82×10^{-4} mol, 1.00 equiv) and $^nBu_4NCl$ (50.6 mg, 1.82×10^{-4} mol, 1.00 equiv) as a solid. The reaction solution immediately turned from yellow to blue. The reaction mixture was stirred at 23 °C for 1 h. The reaction was concentrated to dryness and the residue was taken up in pentane and Et_2O, solvent was decanted, and the residue was dried in vacuo to afford 119 mg of the title complex as a blue solid (98% yield). ^{1}H NMR (600 MHz, CD_3CN) δ (ppm): 3.32 (q, 2H), 1.83 (m, 2H), 1.53 (m, 2H), 1.08 (t, 3H). μ_{eff} (CH_3CN) = 4.02 μB. Anal. Calcd. (Found) for $C_{34}H_{51}Cl_3NNiP$: C, 60.97 (60.93); H, 7.68 (7.58); N, 2.09 (2.06). Complex **2**[TEA] was prepared analogously by substitution of $^nBu_4NCl$ with $^nEt_4NCl$ in 95% yield; ^{1}H NMR (600 MHz, CD_3CN) δ (ppm): 3.48 (q, 2H), 1.45 (t, 3H). μ_{eff} (CH_3CN) = 4.17 μB. Anal. Calcd. (Found) for $C_{26}H_{35}Cl_3NNiP$: C, 56.01 (56.14); H, 6.33 (6.26); N, 2.51 (2.67). Crystals suitable for single-crystal diffraction analysis were obtained from a CH_3CN solution of the complex layered with Et_2O and unit cell data matched literature reports.[49]

Preparation of [ClPPh$_3$]OTf. To a solution of Cl_2PPh_3 (127 mg, 3.81×10^{-4} mol, 1.00 equiv) in CH_2Cl_2 was added AgOTf (98.0 mg, 3.81×10^{-4} mol, 1.00 equiv) as a suspension in CH_2Cl_2. White solid immediately precipitated when AgOTf was added and the reaction mixture was stirred at 23 °C for 1 h before being filtered through Celite. The filtrate was concentrated in vacuo and the residue was taken up in THF and solvent was decanted, and the residue was dried in vacuo to afford 157 mg of the title compound as a white solid (92% yield). ^{31}P NMR (160 MHz, CD_2Cl_2) δ (ppm): 66.4; ^{19}F NMR (275 MHz, CD_2Cl_2) δ (ppm): –78.9. The spectral data is consistent with that reported for $ClPPh_3 \cdot AlCl_4$.[50] Crystals suitable for single-crystal diffraction analysis were obtained from a CH_2Cl_2 solution layered with Et_2O.

Preparation of Ni(II) Tetrachloride Complex [NiCl$_4$][Et$_4$N]$_2$. A solution of $^nEt_4Cl$

(30.2 mg, 1.82×10^{-4} mol, 1.00 equiv) in 2 mL of CH_2Cl_2 was added to a solution of $NiCl_2$(dme) (40.0 mg, 1.82×10^{-4} mol, 1.00 equiv) in 2 mL of CH_2Cl_2 to prompt an immediate colour change from yellow to green. After stirring at 23 °C for 0.5 h, the reaction mixture was concentrated to dryness and the residue was taken up in pentane and solvent was decanted, and the residue was dried in vacuo to afford 77.2 mg of the title compound as a green solid (92% yield). Crystals suitable for single-crystal diffraction analysis were obtained from a CH_3CN solution layered with Et_2O and unit cell data matched literature reports.[51]

Preparation of Ni(I) Complexes. Complex **3**: To a scintillation vial was added Ni(cod)$_2$ (58.0 mg, 2.10×10^{-4} mol, 1.00 equiv) and $NiCl_2$(dme) (46.0 mg, 2.10×10^{-4} mol, 1.00 equiv) as solids, followed by 3 mL of $PhCH_3$. To this solution was added PPh_3 (330 mg, 1. 26×10^{-3} mol, 6.00 equiv) dissolved in 2 mL $PhCH_3$ and the reaction mixture was stirred at 23 °C for 12 h before being filtered through Celite. The filtrate was concentrated in vacuo to a volume of 1.5 mL, layered with hexanes, and cooled to –30 °C to afford yellow crystalline solid (80% yield). ^{1}H NMR (600 MHz, THF-d_8) δ (ppm): 9.51 (br s, 20H), 5.28 (br s, 15H), 4.20 (br s, 10H). μ_{eff} (CH_3CN) = 1.74 μB. Crystals suitable for single-crystal diffraction analysis were obtained from a $PhCH_3$ solution of the complex layered with *n*-hexane and collected unit cell data matched literature reports.[52]

Complex **4**: To a scintillation vial was added $Ni(PPh_3)_2(CH_2{=}CH_2)$ (20.0 mg, 3.30×10^{-5} mol, 1.00 equiv) and $NiCl_2(PPh_3)_2$ (21.4 mg, 3.30×10^{-5} mol, 1.00 equiv) as solids followed by 4 mL of Et_2O. The reaction mixture was stirred at 23 °C for 0.5 h, during which time a yellow precipitate was observed. The mixture was concentrated to dryness and the residue was taken up in pentane and dried in vacuo to afford 18.4 mg of the title complex as a yellow solid (90% yield).[53]

Reaction of $NiCl(PPh_3)_3$ with nBu_4NCl. To a solution of $NiCl(PPh_3)_3$ (3) (14.1 mg, 1.60×10^{-5} mol, 1.00 equiv) in THF-d_8 was added $^{n}Bu_4NCl$ (4.5 mg, 1.6×10^{-4} mol, 1.0 equiv) as a solid at 23 °C. The yellow reaction solution assumed a brown orange color immediately and $Ni(PPh_3)_4$ (5) is observed by ^{31}P NMR (reproduced in Figure S8). Neither $NiCl(PPh_3)_3$ (3) or $NiCl_2(PPh_3)_2$ (1) display ^{31}P NMR signals.

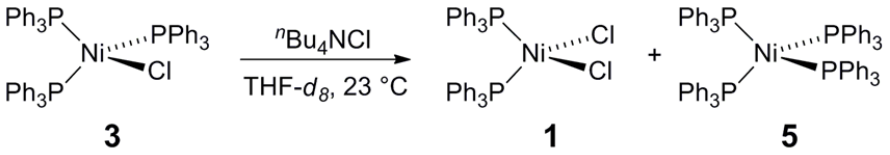

Charaterization of $Ni(PPh_3)_2(CH_2{=}CH_2)$. $Ni(PPh_3)_2(CH_2{=}CH_2)$ were prepared according to reported procedures described above, [54] but NMR data have not been reported in literature ^1H NMR (600 MHz, C_6D_6) δ (ppm): 7.51 (m, 13H), 6.97 (m, 20H), 2.63(s, 4H). (See ^1H NMR data in Figure S6).

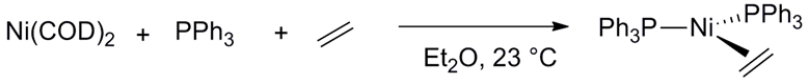

2.8.2 NMR Data

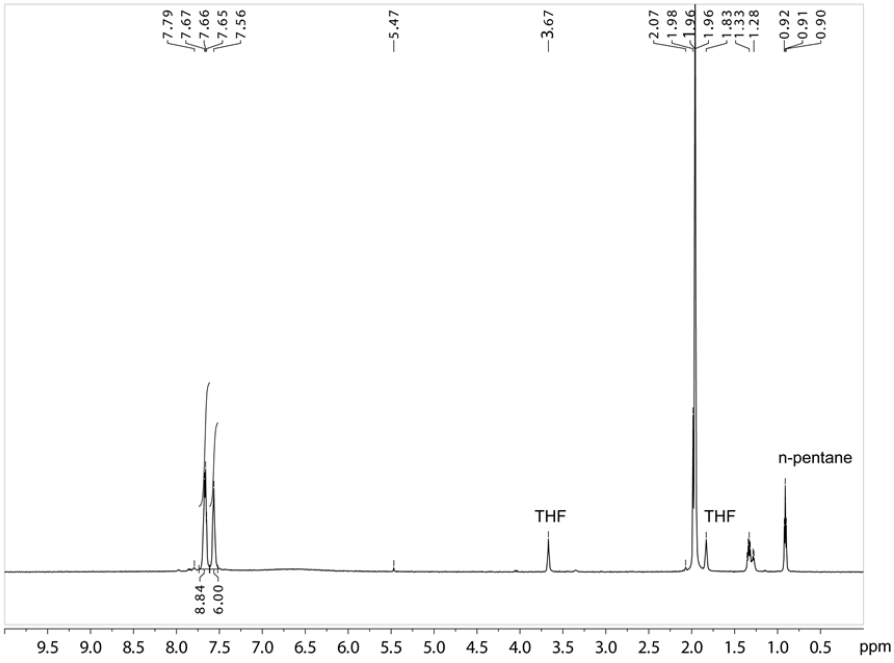

Figure 2.18. ^{1}H NMR spectrum of **2**[ClPPh$_3$] recorded in CD_3CN at 23 °C.

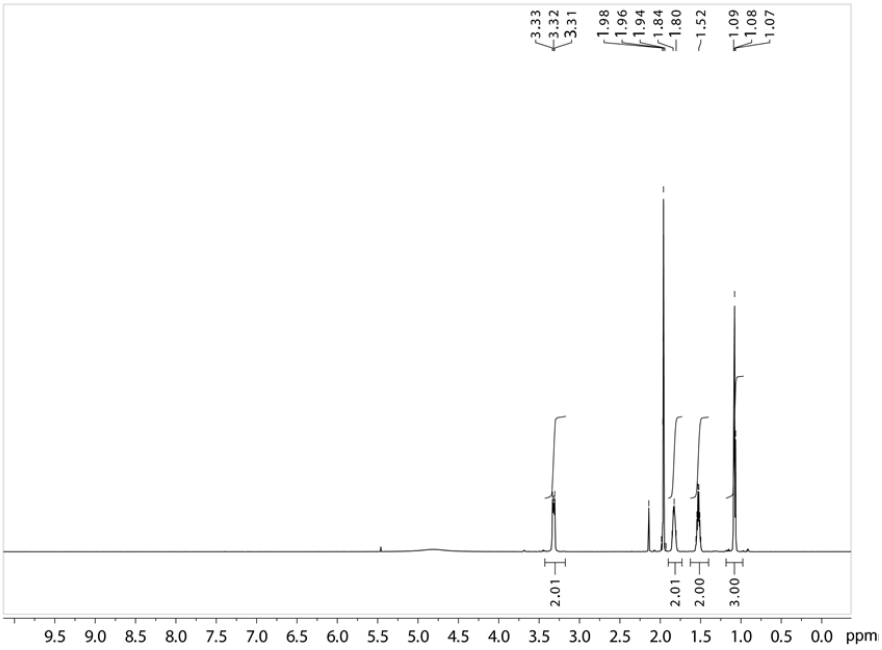

Figure 2.19. ^{1}H NMR spectrum of **2**[TBA] recorded in CD_3CN at 23 °C.

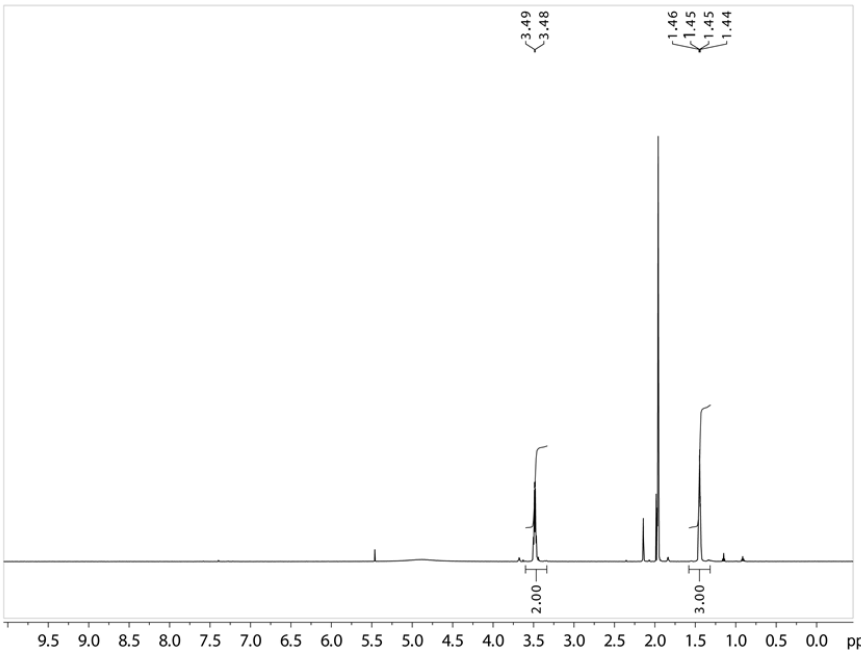

Figure 2.20. ^{1}H NMR spectrum of **2**[TEA] recorded in CD_3CN at 23 °C.

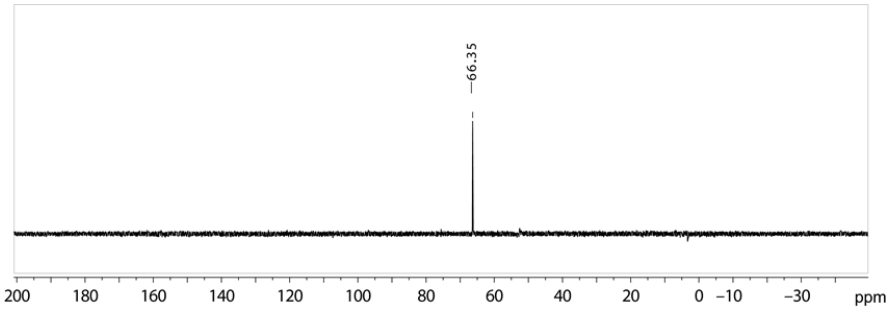

Figure 2.21. ^{31}P NMR spectrum of [ClPPh$_3$]OTf recorded in CD_2Cl_2 at 23 °C.

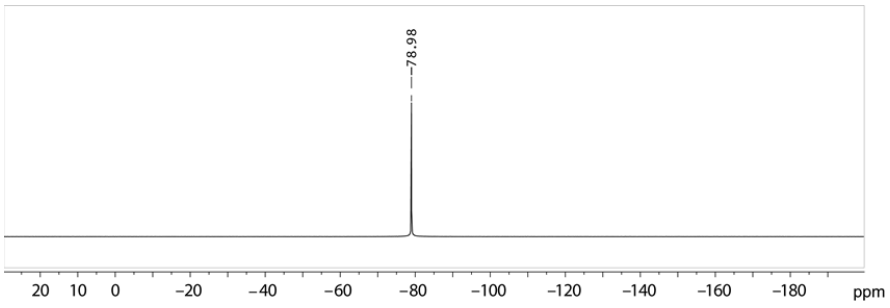

Figure 2.22. ^{19}F NMR spectrum of [ClPPh$_3$]OTf recorded in CD_2Cl_2 at 23 °C.

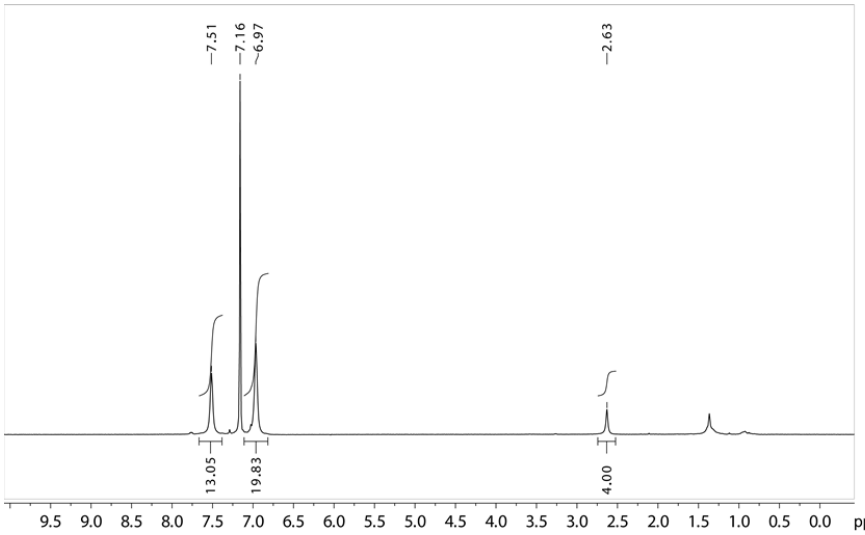

Figure 2.23. ^{1}H NMR spectrum of $Ni(PPh_3)_2(CH_2{=}CH_2)$ recorded in C_6D_6 at 23 °C.

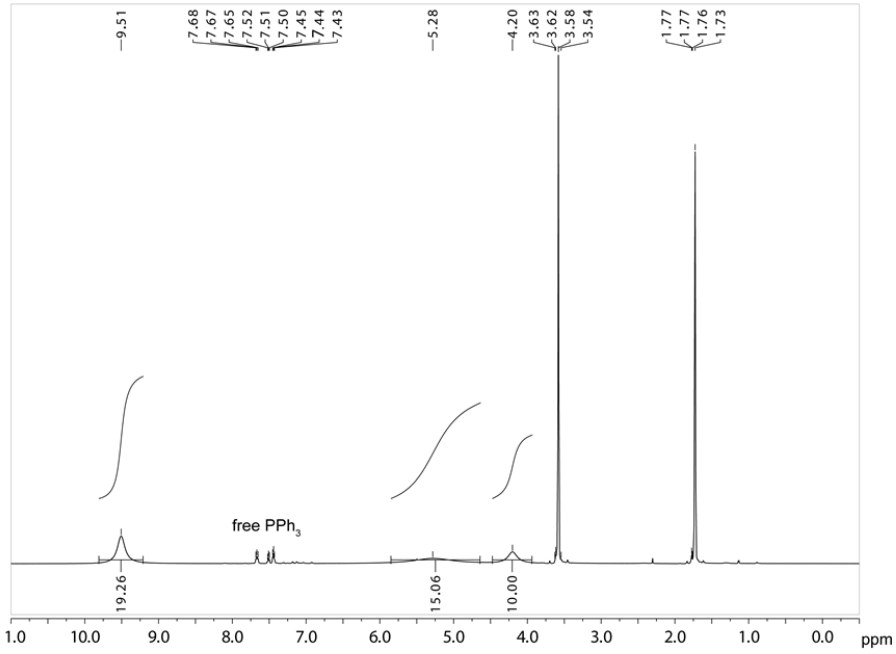

Figure 2.24. ^{1}H NMR spectrum of $NiCl(PPh_3)_3$ (**3**) recorded in THF-d_8 at 23 °C.

2.8.3. X-Ray Data Analysis

Table 2.2. Crystal data and structure refinement for complexes**.**

	2[ClPPh$_3$]	**[NiCl$_4$][PPh$_2$(THF)$_2$]$_2$**	**PPh$_3$Cl$_2$**	**[ClPPh$_3$]OTf**
formula	$C_{36}H_{30}Cl_4NiP_2$	$C_{40}H_{48}Cl_4NiO_4P_2$	$C_{18}H_{15}Cl_2P$	$C_{19}H_{15}ClF_3O_3PS$
CCDC #	992218	992221	992219	992220
fw, g/mol	725.05	855.23	333.17	446.79
temp, K	100(2)	100(2)	100(2)	100(2)
cryst system	Orthorhombic	Monoclinic	Monoclinic	Monoclinic
space group	*Pbca*	*P2(1)/n*	*P2(1)/c*	*P2(1)/n*
color	Blue	Green	White	White
a, Å	17.435(4)	10.1261(8)	13.338(3)	11.255(2)
b, Å	15.662(3)	23.4579(18)	14.376(3)	9.1501(18)
c, Å	24.139(5)	17.8192(14)	8.7454(17)	18.658(4)
α, deg	90	90	90	90
β, deg	90	106.3550(12)	102.53(3)	93.04(3)
γ, deg	90	90	90	90
V, A^3	6591(2)	4061.4(5)	1637.0(6)	1918.7(7)
Z	8	4	4	4
R1[a]	0.0327	0.0593	0.0272	0.0323
wR2[b]	0.0649	0.1236	0.0677	0.0697
GOF[c] (F^2)	1.03	1.016	1.060	1.031
R_{int}	0.0741	0.0668	0.0308	0.0362

[a] $R1_{1/2} = \Sigma||F_o| - |F_c||/\Sigma|F_o|$. [b] $wR2 = (\Sigma(w(F_o^2 - F_c^2)^2)/\Sigma(w(F_o^2)^2))^{1/2}$. [c] $GOF = (\Sigma w(F_o^2 - F_c^2)^2/(n - p))^{1/2}$ where n is the number of data and p is the number of parameters refined.

2.8.4 UV-vis Electronic Absorption Spectroscopy

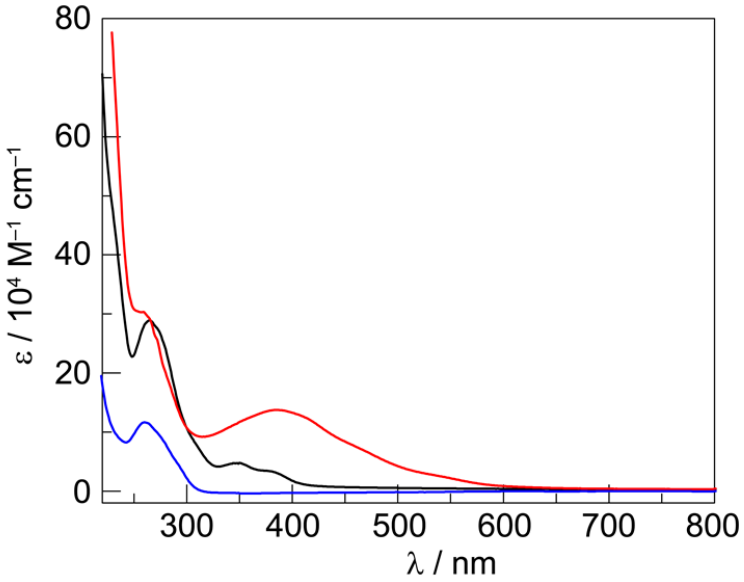

Figure 2.25. Extinction spectra of Ni complexes $NiCl(PPh_3)_3$ (**3**) (—, black), $Ni(PPh_3)_4$ (**5**) (—, red), and **2**[TBA] (—, blue).

2.8.5 Electrochemical Data

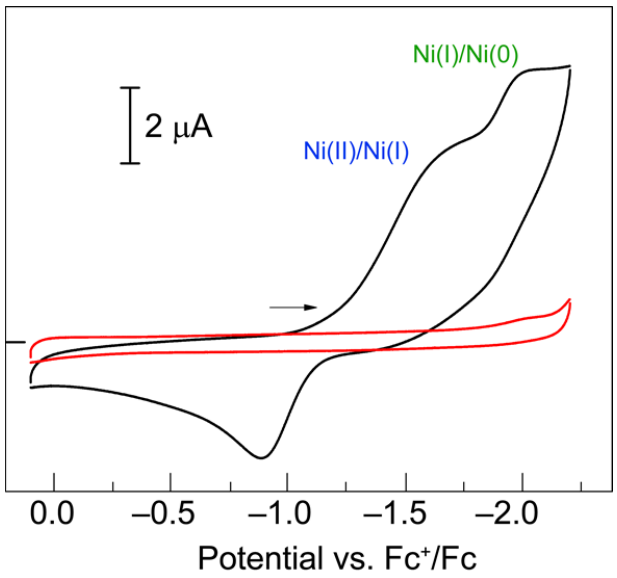

Figure 2.26. Cyclic voltammetry of 1 mM Ni complex **2**[TEA] (—, black) and solvent background (—, red) measured with 0.1 M $^{n}Bu_4PF_6$ as a electrolyte in THF solution with a scan rate of 100 mV/s. Glassy carbon working electrode, $Ag/AgNO_3$ reference, and Pt wire counter electrode were used. E_p = –1.628 V, (Ni^{II}/Ni^{I}) and –0.892 V, (Ni^{I}/Ni^{II}).

2.9 References

1. Esswein, A. J.; Nocera, D. G. *Chem. Rev.* **2007**, *107*, 4022.

2. Nocera, D. G. *Inorg. Chem.* **2009**, ***48***, 10001.

3. Heyduk, A. F.; Nocera, D. G. *Science,* **2001**, *293*, 1639.

4. Esswein, A. J.; Veige, A. S.; Nocera, D. G. *J. Am. Chem. Soc.* **2005**, *127*, 16641.

5. Elgrishi, N.; Teets, T. S.; Chambers, M. B.; Nocera, D. G. *Chem. Commun.* **2012**, *48*, 9474.

6. Cook, T. R.; Surendranath, Y.; Nocera, D. G. *J. Am. Chem. Soc.* **2009**, *131*, 28.

7. Teets, T. S.; Nocera, D. G. *J. Am. Chem. Soc.* **2009**, *131*, 7411.

8. Lin, T.-P.; Gabbaï, F. P. *J. Am. Chem. Soc.* **2012**, *134*, 12230.

9. Yang, H.; Gabbaï, F. P. *J. Am. Chem. Soc.* **2014**, *136*, 10866.

10. Van Zyl, W. E.; L´opez-de-Luzuriaga, J. M.; Fackler Jr, J. P.; Staples, R. J. *Can. J. Chem*. **2001**, *79*, 896.

11. Fackler Jr J. P. *Inorg. Chem*. **2002**, *41*, 6959.

12. Ovens, J. S.; Leznoff, D. B. *Dalton Trans*. **2011**, *40*, 4140.

13. Perera, T. A.; Masjedi, M.; Sharp, P. R. *Inorg. Chem*. **2014**, *53*, 7608.

14. Karikachery, A. R.; Lee, H. B.; Masjedi, M.; Ross, A.; Moody, M. A.; Cai, X.; Chui, M.; Hoff, C. D.; Sharp, P. R. *Inorg. Chem*. **2013**, *52*, 4113.

15. Powers, D. C.; Chambers, M. B.; Teets, T. S.; Elgrishi, N.; Anderson, B. L.; Nocera, D. G. *Chem. Sci.* **2013**, *4*, 2880.

16. Carrera, E. I.; McCormick, T. M.; Kapp, M. J.; Lough, A. J.; Seferos, D. S. *Inorg. Chem.* **2013**, *52*, 13779.

17. For a recent counter-example, see: Powers, D. C.; Hwang, S. J.; Zheng, S.-L.; Nocera, D. G. *Inorg. Chem*. **2014**, *53*, 9122.

18. Lee, C. H.; Lutterman, D. A.; Nocera, D. G. *Dalton Trans*. **2013**, *42*, 2355.

19. Tereniak, S. J.; Marlier, E. E.; Lu, C. C. *Dalton Trans*. **2012**, *41*, 7862.

20. Juban, E. A.; Smeigh, A. L.; Monat, J. E.; McCusker, J. K. *Coord. Chem. Rev*. **2010**, *254*, 2677.

21. Creutz, C.; Chou, M.; Netzel, T. L.; Okumura, M.; Sutin, N. *J. Am. Chem. Soc.* **1980**, *102*, 1309.

22. Lee, C. H.; Cook, T. R.; Nocera, D. G. *Inorg. Chem*. **2011**, *50*, 714.

23. Powers, D. C.; Anderson, B. L.; Nocera, D. G. *J. Am. Chem. Soc.* **2013**, *135*, 18876.

24. Haav, K.; Saame, J.; Kütt, A.; Leito, I. *Eur. J. Org. Chem.* **2012**, 2167.

25. Sakaguchi, Y.; Hayashi, H. *J. Phys. Chem. A* **2004**, *108*, 3421.

26. Versace, D.-L.; Bastida, J. C.; Lorenzini, C.; Cachet-Vivier, C.; Renard, E.; Langlois, V.; Malval, J.-P.; Fouassier, J.-P.; Lalevée, J. *Macromolecules* **2013**, *46*, 8808.

27. Wong, S. K.; Sytnyk, W.; Wan, J. K. S. *Can. J. Chem.* **1971**, *49*, 994.

28. Bontempelli, G.; Magno, F.; Nobili, M. D.; Schiavon, G. *J. Chem. Soc. Dalton Trans.* **1980**, 2288.

29. Sakaguchi, Y.; Hayashi, H. *Chem. Phys. Lett.* **1995**, *245*, 591.

30. Maini, L.; Braga, D.; Mazzeo, P. P.; Ventura, B. *Dalton Trans*. **2012**, *41*, 531.

31. Kaufman, M. L.; Griffin, C. L. *Tetrahedron Lett.* **1965**, *12*, 769.

32. Waterman, R. *Curr. Org. Chem.* **2008**, *12*, 1322.

33. Roth, J. P.; Lovell, S.; Mayer, J. M. *J. Am. Chem. Soc.* **2000**, *122*, 5486.

34. Laarhoven, L. J. J.; Mulder, P.; Wayner, D. D. M. *Acc. Chem. Res.* **1999**, *32*, 342.

35. Cherkasov, A.; Jonsson, M. *J. Chem. Inf. Comput. Sci.* **2000**, *40*, 1222.

36. van Scheppingen, W.; Dorrestijn, E.; Arends, I.; Mulder, P. *J. Phys. Chem. A* **1997**, *101*, 5404.

37. Fourmond, V.; Jacques, P.-A.; Fontecave, M.; Artero, V. *Inorg. Chem.* **2010**, *49*, 10338.

38. Monat, J. E.; McCusker, J. K. *J. Am. Chem. Soc.* **2000**, *122*, 4092.

39. Ferrere, S.; Gregg, B. A. *J. Am. Chem. Soc.* **1998**, *120*, 843.
40. Seshadri, G.; Lin, C.; Bocarsly, A. B. *J. Electroanal. Chem.* **1994**, *372*, 145.

41. Barton, E. E.; Rampulla, D. M.; Bocarsly, A. B. *J. Am. Chem. Soc.* **2008**, *130*, 6342.

42. Cole, E. B.; Lakkaraju, P. S.; Rampulla, D. M.; Morris, A. J.; Abelev, V.; Bocarsly, A. B. *J. Am. Chem. Soc.* **2010**, *132*, 11539.

43. Pangborn, A. B.; Giardello, M. A.; Grubbs, R. H.; Rosen, R. K.; Timmers, F. J. *Organometallics,* **1996**, *15*, 1518.

44. Zhao, X.-F.; Zhang, C. *Synthesis,* **2007**, *4*, 551.

45. Schramm, K. D.; Ibers, J. A. *Inorg. Chem*. **1980**, *19*, 2441.

46. Yano, T.; Hoshino, M.; Kuroboshi, M.; Tanaka, H. *Synlett,* **2010**, *5*, 801.

47. Bain, G. A.; Berry, J. F. *J. Chem. Ed.* **2008**, *85*, 532.

48. Holder, P. G.; Pizano, A. A.; Anderson, B. L.; Stubbe, J.; Nocera, D. G. *J. Am. Chem. Soc.* **2012**, *134*, 1172.

49. Smith, M. C.; Davies, S. C.; Hughes, D. L.; Evans, D. J. *Acta Cryst.* **2001**, *E57*, m509.

50. Schmidpeter, A.; Lochschmidt, S. *Inorg. Syn.* **1990**, *27*, 253.

51. Stucky, G. D.; Folkers, J. B.; Kistenmacher, T. J. *Acta Cryst.* **1967**, *23*, 1064.

52. Ellis, D. D.; Spek, A. L. *Acta Cryst.* **2000**, *C56*, 1067.

53. Norman, N. C.; Orpen, A. G.; Quayle, M. J.; Whittell, G. R. *Acta Cryst.* **2002**, *C58*, m160.

54. Schramm, K. D.; Ibers, J. A. *Inorg. Chem*. **1980**, *19*, 2441.

Chapter 3

Trap-Free Halogen Photoelimination from Mononuclear Ni(III) Complexes Enabled by the Secondary Coordination Sphere

Parts of this chapter have been published:

Hwang, S. J.; Powers, D. C.; Maher, A. G.; Anderson, B. L.; Hadt, R. G.; Zheng, S.-L.; Chen, Y.-S.; Nocera D. G. "Trap-free Halogen Photoelimination from Mononuclear Ni(III) Complexes." *J. Am. Chem. Soc.* **2015**, *137*, 6472–6475.

Hwang, S. J.; Anderson, B. L.; Powers, D. C.; Maher, A. G.; Hadt, R. G.; Nocera D. G. "Halogen Photoelimination from Monomeric Nickel(III) Complexes Enabled by the Secondary Coordination Sphere." *Organometallics,* **2015**, *34*, 4766–4774.

3.1 Introduction

The small-molecule activation reactions that lie at the heart of energy storage and conversion, such as H_2 and H_2O oxidations and H^+, O_2, and CO_2 reductions, are all multi-electron/multi-proton transformations. Development of catalysts to effectively mediate these energy conversion transformations rely on the careful choreography of proton and electron delivery.[1,2] Examples abound in both biological and synthetic catalysis of secondary coordination sphere effects that synchronize the electron and proton. Biological H_2 oxidation in Fe-only hydrogenase is accomplished via cooperation of second-coordination sphere bases, which enforce selective heterolytic cleavage of H_2.[3–5] Similarly, installation of biomimetic proton relays in the secondary-coordination sphere of transition metal complexes, has emerged as a powerfully enabling design element for the development of selective catalysts based on earth-abundant first-row transition elements.[6] Introduction of basic functionality, as either pendant carboxylates (i.e. hangman porphyrin **1**)[7–9] or tertiary amines (i.e. hydrogenase mimic **2**),[10,11] in the secondary coordination sphere of electrocatalysts allows controllable coupling of proton and electron delivery to substrates during electrocatalysis. This strategy has enabled the development of O_2 (Figure 3.1, **1**) and H^+ (Figure 3.1, **1** and **2**) reduction reactions. H-bonding from basic groups in the secondary coordination sphere have also been used in stoichiometric small molecule reactions to generate isolable metal oxido complexes, such as **6** (Figure 3.1, **3**).[12,13]

Against this backdrop, HX-splitting photochemistry (X = Cl, Br) has been advanced as an approach to solar-to-fuels conversion in which proton reduction is coupled to halide oxidation to provide carbon-neutral, closed energy conversion cycles.[14 – 16] Halogen photoelimination reactions are multielectron chemical transformations in which two electrons must be simultaneously managed in the formation of X–X bonds; this bond-forming transformation

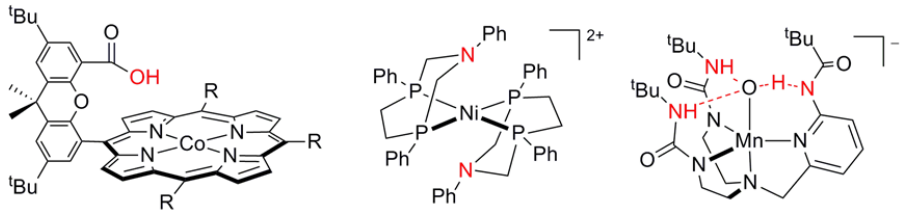

Figure 3.1. Functionality in the secondary coordination sphere that has been useful for promoting multielectron catalysis and stabilization of energetic intermediates.

represents the energy-storing step in HX-splitting cycles. While selective two-electron halogen elimination reactions have been realized for 4d and 5d metal complexes[17–26] and some main-group compounds,[27,28] a similar chemistry is underdeveloped for earth-abundant *3d* metal complexes.[29–31] Additionally, in many cases chemical traps are required to promote halogen extrusion, which inevitably mitigates the utility of these reactions in energy storing catalysis. While trap-free halogen eliminations have begun to be developed for high quantum yield photoreactions,[17,19,22] little progress has been made towards energy-storing halogen elimination chemistry with earth-abundant *3d* metal complexes.

The dearth of photoeliminations from *3d* metal complexes is a reflection of the short intrinsic excited-state lifetimes of these complexes.[32–34] Whereas long-lived charge transfer excited states are frequently encountered in the photochemistry of *4d* and *5d* transition metal complexes, *3d* transition metal complexes typically possess extremely short-lived charge transfer states. These short lifetimes are a consequence of the relatively small crystal field splitting splitting, which results in low-energy ligand-field excited states that provide a mechanism for rapid nonradiative relaxation.[33,34] Strategies to overcome the short lifetimes of *3d* complexes include photoredox chemistry, in which the chromophore and catalyst are decoupled,[35,36] and ligand design strategies aimed at destabilizing low-lying ligand-field states and thus remove

nonradiative pathways for rapid excited-state relaxation.[37] The inherently shorter excited state lifetimes of *3d* metal complexes, as well as their attendant proclivity to participate in one-electron photoredox reactions, contribute to the challenges that must be overcome to achieve energy storage via halogen elimination from first-row complexes.[38–40]

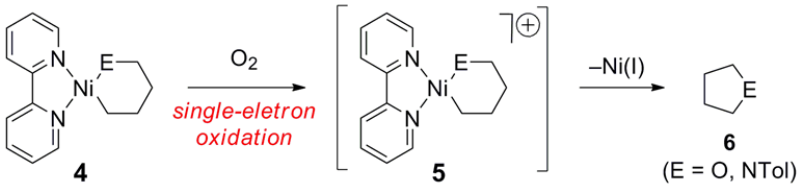

Figure 3.2. Oxidatively induced C–N and C–O reductive elimination reactions from Ni(II) amide and alkoxide complexes pioneered by Hillhouse. The reactions are proposed to proceed via single-electron oxidation to generate Ni(III) complexes followed by reductive elimination.

We have turned our attention to energy storing HX photochemistry that is driven by first-row transition metal complexes under the rubric of two design principles. First, we have targeted mononuclear Ni(III) complexes based on seminal work of Hillhouse that has demonstrated the selective two-electron elimination of C–heteroatom bonds from high oxidation state Ni complexes (Figure 3.2).[41–47] C–N and C–O reductive elimination reactions are sluggish from Ni(II) complexes (i.e. **4** to **6**), but become facile upon one-electron oxidation to Ni(III) (**5**) via single electron transfer to an external oxidant. Given the short excited state lifetimes of first-row complexes, we reasoned that their generation by MLCT excitation would be insufficient to drive the targeted chemistry. Accordingly, we turned our attention to installing Ni(III) into the ground state of the putative photocatalyst. Second, owing to our success in oxygen- and hydrogen-based chemical transformation, we sought to utilize secondary coordination sphere effects to enforce selective halogen elimination from complexes with inherently short excited state lifetimes to circumvent the exothermic back reaction.

In this chapter, a suite of Ni(III) trihalide complexes supported by bidentate phosphine ligands, $NiX_3(LL)$ (LL = bidentate phosphine), that engage in halogen elimination photoreactions both in solution and in the solid state will be described. Time-resolved photochemical studies have identified halogen atom adducts of ligand-based aromatic groups to be intermediates in the elimination reactions. The complexes also participate in high-yielding trap-free halogen elimination, which we have established to be substantially endothermic by solution-phase calorimetry. The excited states responsible for the observed halogen elimination reactions are ligand-to-metal in character, and the ability of these complexes to promote halogen elimination is attributed to the proclivity of the photoeliminating halogen atom to be guided from the primary coordination sphere via a secondary coordination sphere ligand effect arising from an aromatic-halogen interaction.

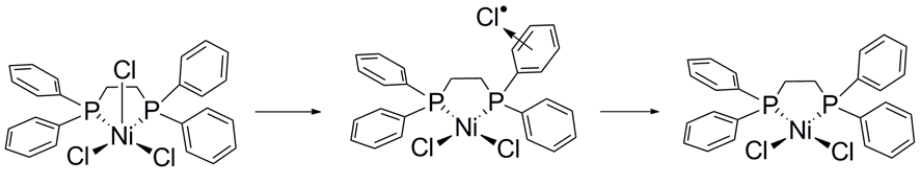

Figure 3.3. Photoextrusion from Ni(III) trichloride **7a** proceeds via initial chlorine radical extrusion, which is stabilized by an arene-to-chlorine-atom charge transfer interaction (**8a**). Subsequent evolution of chlorine affords Ni(II) complex $NiCl_2$(dppe) (**9a**).

3.2 Synthesis and Characterization of Monomeric Ni(III) Complexes

Monomeric Ni(II) dihalide complexes were accessed by treatment of Ni(II) halide starting materials (NiX_2(dme) (X = Cl and Br)) with an equimolar amount of the appropriate bidentate phosphine ligand. Thermal ellipsoid plots of Ni(II) complexes **9c** and **9e** are illustrated in Figure 3.5 and crystallographic data are summarized in Table 3.1.

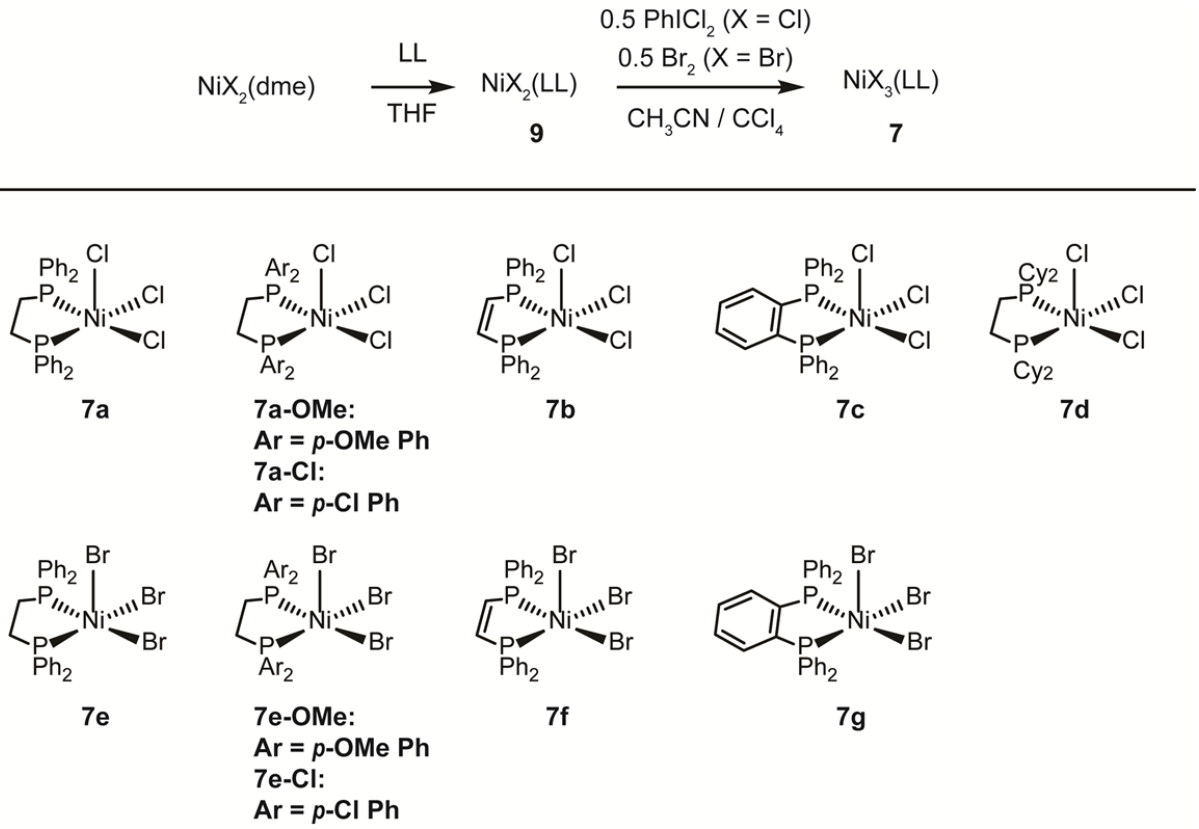

Figure 3.4. Synthesis of Ni(II) and Ni(III) complexes supported by bidentate phosphine ligands.

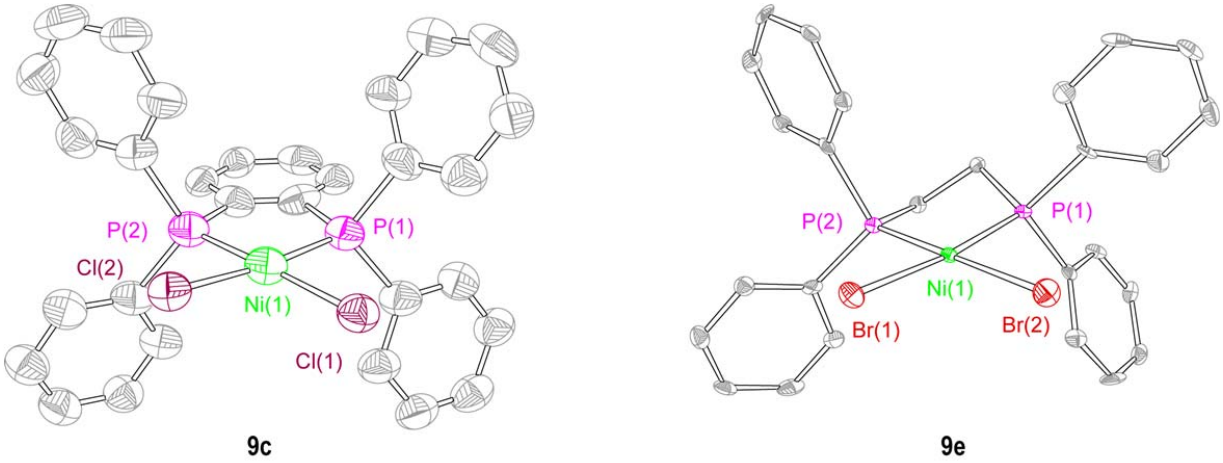

Figure 3.5. Thermal ellipsoid plots of $NiCl_2$(dppb) (**9c**) and $NiBr_2$(dppe) (**9e**) drawn at the 50% probability level. H-atoms and solvents are omitted for clarity.

Table 3.1. Crystal data and structure refinement for **9c** and **9e**.

	$NiCl_2$(dppb) (9c)	**$NiBr_2$(dppe) (9e)**
formula	$C_{30}H_{24}Cl_2NiP_2$	$C_{14}H_{14}BrCl_2\ Ni_{0.50}P$
CCDC #	1401868	1401864
fw, g/mol	576.04	393.39
temp, K	100 (2)	100 (2)
cryst system	Monoclinic	Monoclinic
space group	*Cc*	*P2(1)*
a, Å	15.0451(8)	13.0802(11)
b, Å	9.6692(6),	8.5935(7)
c, Å	18.4342(11)	13.7616(12)
α, deg	90	90
β, deg	104.426(3)	97.5170(14)
γ, deg	90	90
V, A^3	2597.1(3)	1533.6(2)
Z	4	4
R1[a]	0.0861	0.0397
wR2[b]	0.2240	0.0960
GOF[c] (F^2)	1.058	1.051
R_{int}	0.0825	0.0552

[a] $R1_{I/2} = \Sigma||F_o| - |F_c||/\Sigma|F_o|$. [b] $wR2 = (\Sigma(w(F_o^2 - F_c^2)^2)/\Sigma(w(F_o^2)^2))^{1/2}$. [c] $GOF = (\Sigma w(F_o^2 - F_c^2)^2/(n - p))^{1/2}$ where n is the number of data and p is the number of parameters refined.

Oxidation of Ni dichloride complexes **9a**–**9d** with $PhICl_2$ afforded the corresponding monomeric Ni trichloride complexes $NiCl_3$(dppe) (**7a**), $NiCl_3$(dppe-OMe) (**7a-OMe**), $NiCl_3$(dppe-Cl) (**7a-Cl**), $NiCl_3$(dppey) (**7b**), $NiCl_3$(dppb) (**7c**), and $NiCl_3$(dcpe) (**7d**). Using a

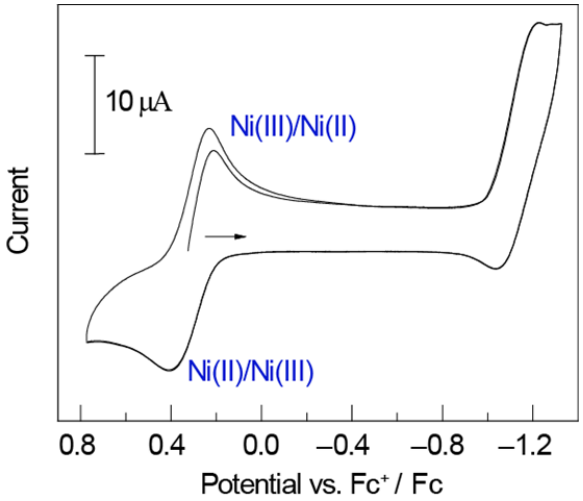

Figure 3.6. Cyclic voltammogram of 1 mM CH_3CN solution of $NiCl_3$(dppe) (**7a**), with 0.1 M $^nBu_4PF_6$ as the supporting electrolyte. Data was recorded at a scan rate of 100 mV/s with a glassy carbon working electrode, $Ag/AgNO_3$ reference, and Pt wire counter electrode.

procedure adapted from Levason,[77] oxidation of Ni(II)Br_2(LL) complexes was accomplished by treatment with 0.5 equiv of Br_2 in CCl_4 to afford $NiBr_3$(dppe) (**7e**), $NiBr_3$(dppe-OMe) (**7e-OMe**), $NiBr_3$(dppe-Cl) (**7e-Cl**), $NiBr_3$(dppey) (**7f**), and $NiBr_3$(dppb) (**7g**). Cyclic voltammetry of Ni(III) compound **7a** in CH_3CN showed a quasi-reversible wave at 0.40 V vs. Fc^+/Fc assigned to the Ni(II)/Ni(III) couple (Figure 3.6). Ni(III) complexes display no ^1H NMR or ^{31}P NMR spectra. Evans method and variable-temperature EPR indicated the complexes are S = ½, as expected for mononuclear d^7 complexes. The EPR spectra of members of the series are shown in Figs. 3.7–3.15. The EPR spectra display pseudo-axial doublet signals with g_x, $g_y > 2$ and g_z ~2.000 and a four-line superhyperfine coupling pattern in the g_z direction (Table 3.2). The superhyperfine coupling is a direct probe of the coupling of the d_z^2 unpaired electron with the nuclear magnetic

moment of the apical halide ligand (I = 3/2 for both Br and Cl) and is a measure of the degree of electron delocalization of the unpaired electron along the apical Ni(III)–X bond.[48] The superhyperfine coupling (A_z) varies depending on the phosphine ligand backbones and arene substituents on the bidentate phosphine ligands; superhyperfine coupling constants are tabulated in Table 3.2.

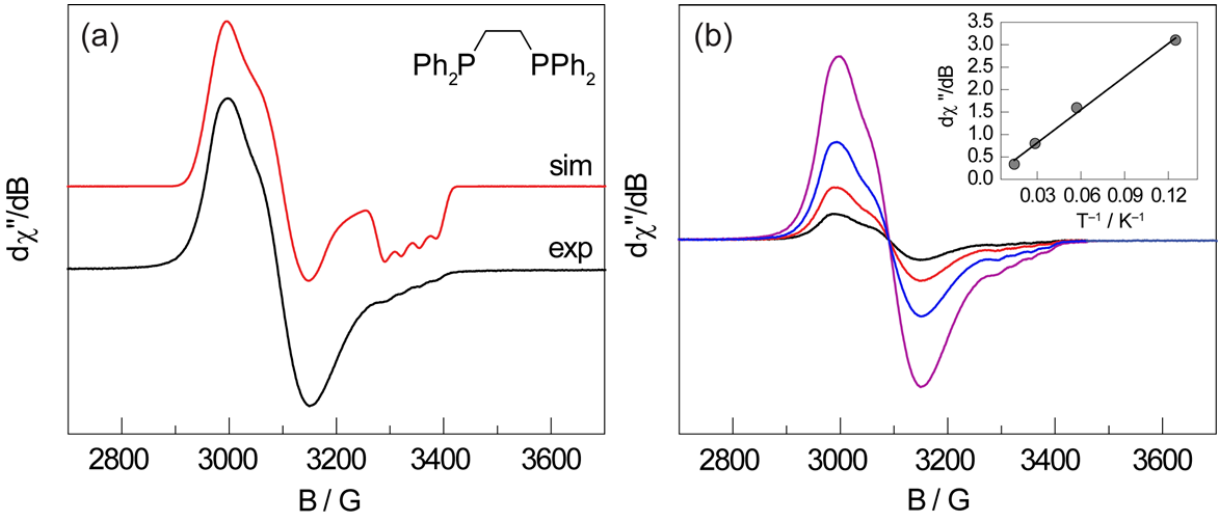

Figure 3.7. (a) EPR spectrum of $NiCl_3$(dppe) (**7a**) recorded at 8.0 K in 1:1 CH_3CN/toluene glass (—, black) and simulated (—, red). (b) EPR spectra of a frozen solution of $NiCl_3$(dppe) (**7a**) in 1:1 CH_3CN/toluene obtained at 70.0 K (—, black) 35.0 K (—, red), 17.5 K (—, blue), and 8.0 K (—, purple). Inset: plot of intensity at 2997 G versus inverse temperature.

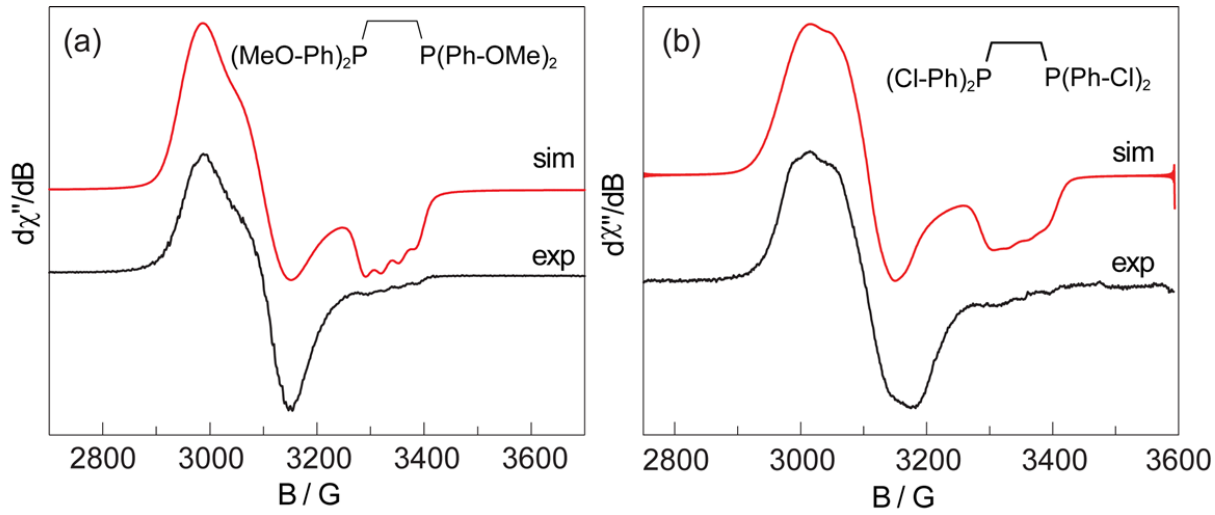

Figure 3.8. (a) EPR spectrum of $NiCl_3$(dppe-OMe) (**7a-OMe**) recorded at 77 K in 1:1 DCM/toluene glass (—, black) and simulated (—, red). (b) EPR spectrum of $NiCl_3$(dppe-Cl) (**7a-Cl**) recorded at 77 K in 1:1 DCM/toluene glass (—, black) and simulated (—, red). For the simulation, the axial hyperfine, $|A_z|$, was fixed to 90 MHz and not optimized.

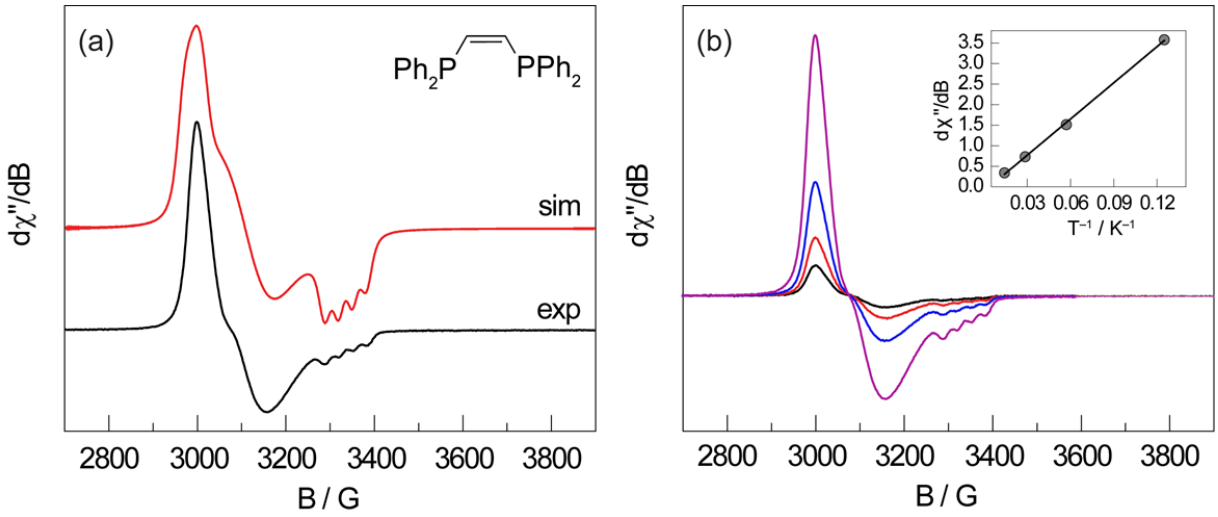

Figure 3.9. (a) EPR spectrum of $NiCl_3$(dppey) (**7b**) recorded at 8.0 K in 1:1 CH_3CN/toluene glass (—, black) and simulated (—, red). (b) EPR spectra of a frozen solution of $NiCl_3$(dppey) (**7b**) in 1:1 CH_3CN/Toluene obtained at 70.0 K (—, black) 35.0 K (—, red), 17.5 K (—, blue), and 8.0 K (—, purple). Inset: plot of intensity at 2999 G versus inverse temperature.

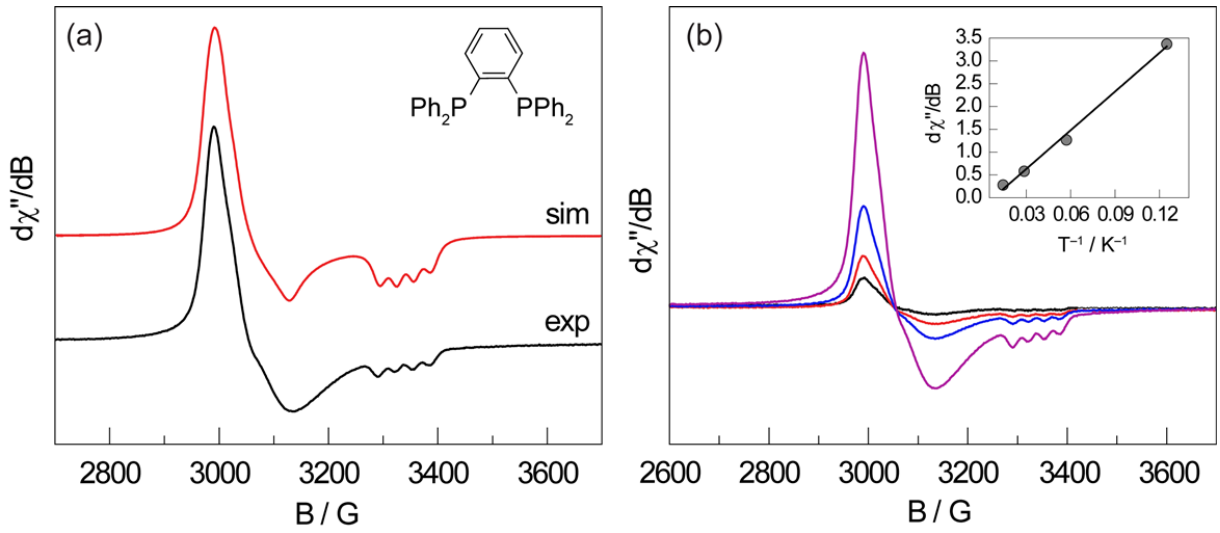

Figure 3.10. (a) EPR spectrum of $NiCl_3$(dppb) (**7c**) recorded at 8.0 K in 1:1 CH_3CN/toluene glass (—, black) and simulated (—, red). (b) EPR spectra of a frozen solution of $NiCl_3$(dppb) (**7c**) in 1:1 CH_3CN/toluene obtained at 70.0 K (—, black) 35.0 K (—, red), 17.5 K (—, blue), and 8.0 K (—, purple). Inset: plot of intensity at 2990 G versus inverse temperature.

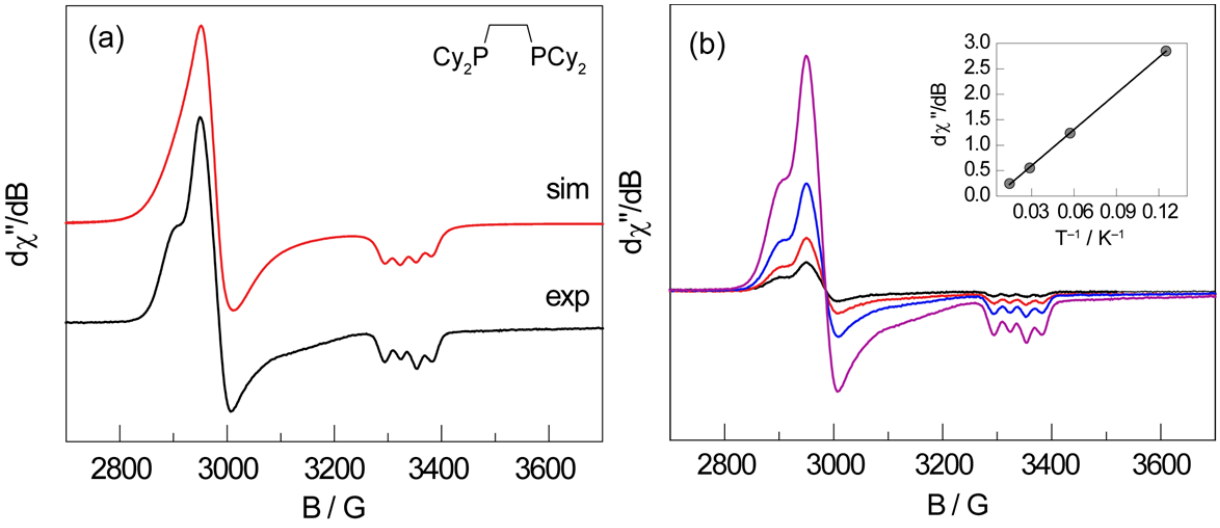

Figure 3.11. (a) EPR spectrum of $NiCl_3$(dcpe) (**7d**) recorded at 8.0 K in 1:1 CH_3CN/toluene glass (—, black) and simulated (—, red). (b) EPR spectra of a frozen solution of $NiCl_3$(dcpe) (**7d**) in 1:1 CH_3CN/toluene obtained at 70.0 K (—, black) 35.0 K (—, red), 17.5 K (—, blue), and 8.0 K (—, purple). Inset: plot of intensity at 2950 G versus inverse temperature.

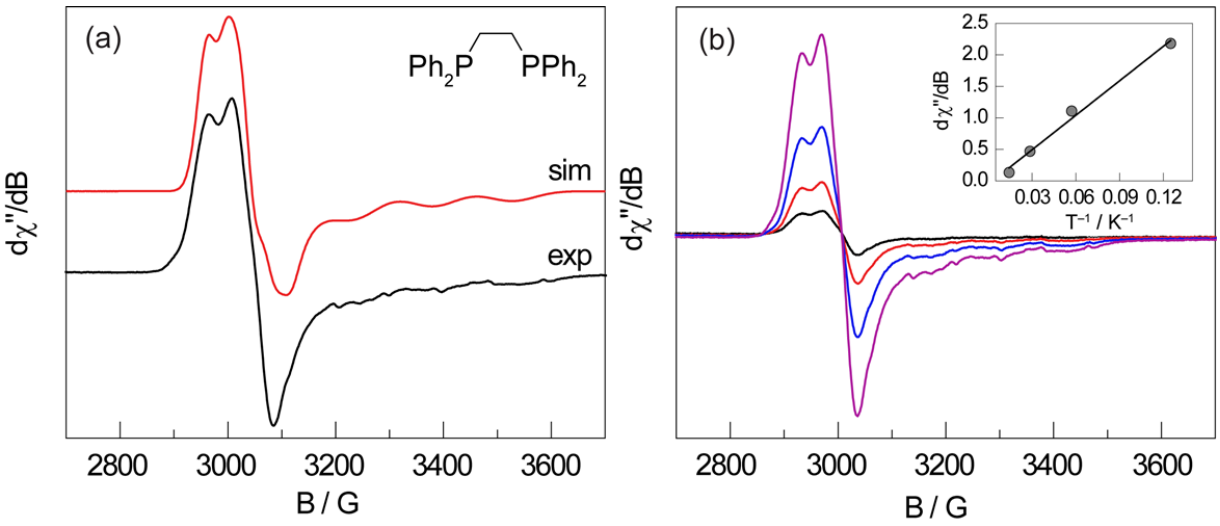

Figure 3.12. (a) EPR spectrum of $NiBr_3$(dppe) (7e) recorded at 8.0 K in 1:1 DCM/toluene glass (—, black) and simulated (—, red). (b) EPR spectra of a frozen solution of $NiBr_3$(dppe) (7e) in 1:1 DCM/toluene obtained at 70.0 K (—, black) 35.0 K (—, red), 17.5 K (—, blue), and 8.0 K (—, purple). Inset: plot of intensity at 2970 G versus inverse temperature.

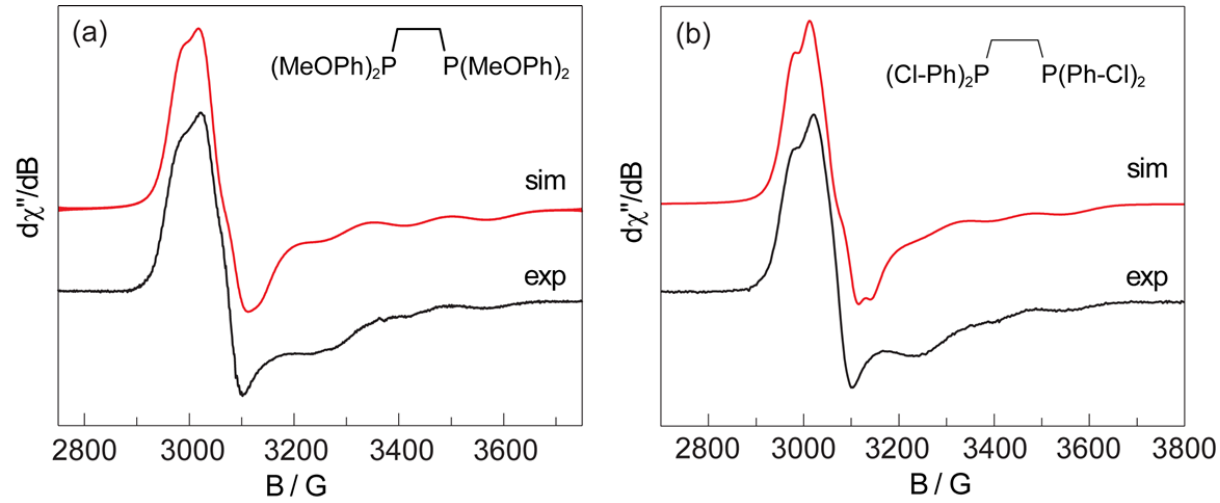

Figure 3.13. (a) EPR spectrum of $NiBr_3$(dppe) (**7e-OMe**) recorded at 77.0 K in 1:1 DCM/toluene glass (—, black) and simulated (—, red). (b) EPR spectrum of $NiBr_3$(dppe-Cl) (**7e-Cl**) recorded at 77.0 K in 1:1 DCM/toluene glass (—, black) and simulated (—, red).

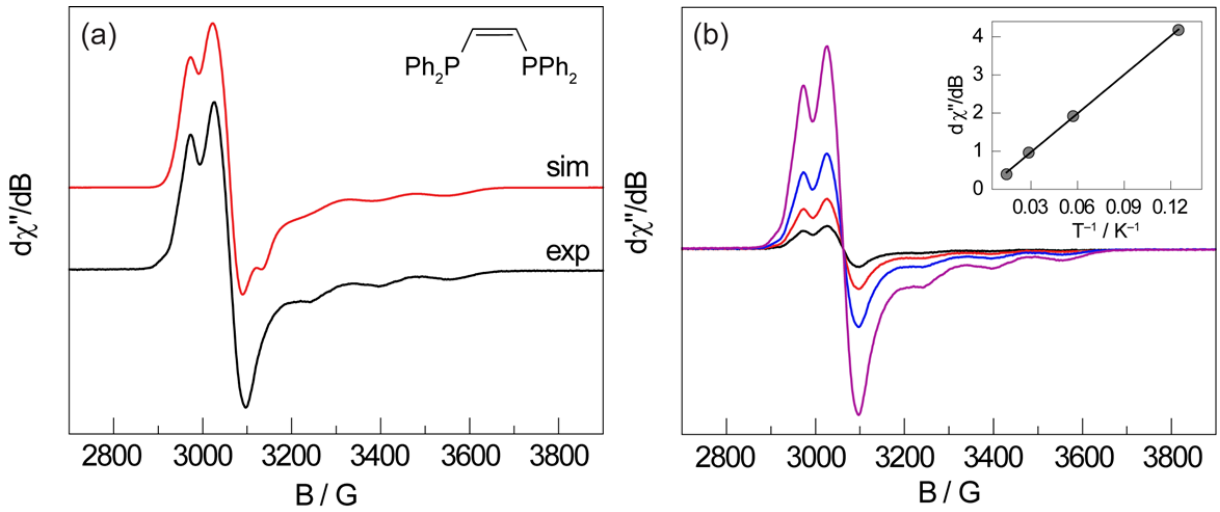

Figure 3.14. (a) EPR spectrum of $NiBr_3$(dppey) (**7f**) recorded at 8.0 K in 1:1 DCM/toluene glass (—, black) and simulated (—, red). (b) EPR spectra of a frozen solution of $NiBr_3$(dppey) (**7f**) in 1:1 DCM/toluene obtained at 70.0 K (—, black) 35.0 K (—, red), 17.5 K (—, blue), and 8.0 K (—, purple). Inset: plot of intensity at 3025 G versus inverse temperature.

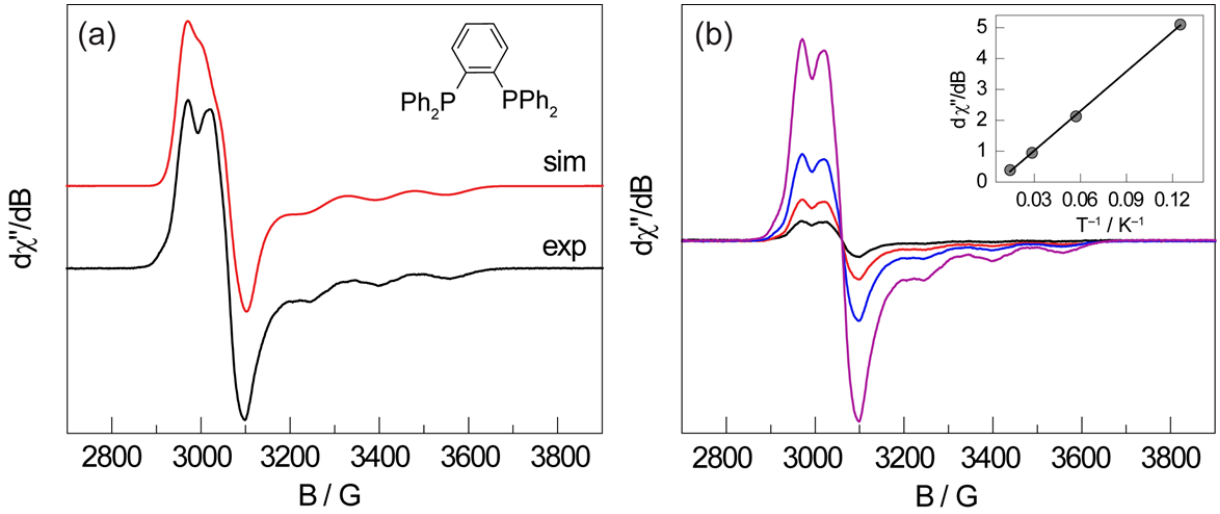

Figure 3.15. (a) EPR spectrum of $NiBr_3$(dppb) (**7g**) recorded at 8.0 K in 1:1 DCM/toluene glass (—, black) and simulated (—, red). (b) EPR spectra of a frozen solution of $NiBr_3$(dppb) (**7g**) in 1:1 DCM/toluene obtained at 70.0 K (—, black) 35.0 K (—, red), 17.5 K (—, blue), and 8.0 K (—, purple). Inset: plot of intensity at 2971 G versus inverse temperature.

Table 3.2. EPR parameters derived from fitting of $NiX_3(LL)$ (**7**) spectra.

Compound	g_x	g_y	g_z	$\|A_z\|$/MHz
7a: $NiCl_3$(dppe)	2.245	2.164	2.012	95
7a-OMe: $NiCl_3$(dppe-OMe)	2.258	2.169	2.017	95
7a-Cl: $NiCl_3$(dppe-Cl)	2.241	2.165	2.01	–
7b: $NiCl_3$(dppey)	2.241	2.155	2.013	92
7c: $NiCl_3$(dppb)	2.232	2.196	2.010	92
7d: $NiCl_3$(dcpe)	2.280	2.260	2.010	81
7e: $NiBr_3$(dppe)	2.203	2.203	2.025	400
7e-OMe: $NiBr_3$(dppe-OMe)	2.208	2.208	2.025	420
7e-Cl: $NiBr_3$(dppe-Cl)	2.201	2.191	2.025	410
7f: $NiBr_3$(dppey)	2.192	2.187	2.024	430
7g: $NiBr_3$(dppb)	2.226	2.176	2.020	420

Single crystal X-ray structures of representative Ni(III) complexes were obtained and indicate a distorted square pyramidal geometry about the Ni center (Figure 3.16), with shorter basal Ni(III)–X bonds and a longer apical Ni(III)–X bond (Table 3.3). For example, the apical Ni–Cl in complex **7c** is 2.287(1) Å whereas the basal Ni–Cl bonds are 2.224(2) and 2.219(2) Å, respectively.

Table 3.3. Selected metrical parameters of $NiBr_3(LL)$ complexes **7e**-**7g** derived from X-ray diffraction data.

LL	Ni–Br_{ap} (Å)	Ni–Br_{basal} (Å)	P1–Ni–P2 (°)	Planarity (°)[a]
dppe	2.4004(10)	2.3625	83.63(6)	34.91
dppey	2.4428(10)	2.3613	87.52(5)	28.87
dppb	2.4410(9)	2.3672	83.64(3)	33.74

[a] 360-(two Br_{ap}–Ni–Br_{basal} + two Br_{ap}–Ni–P_{basal}) (°).

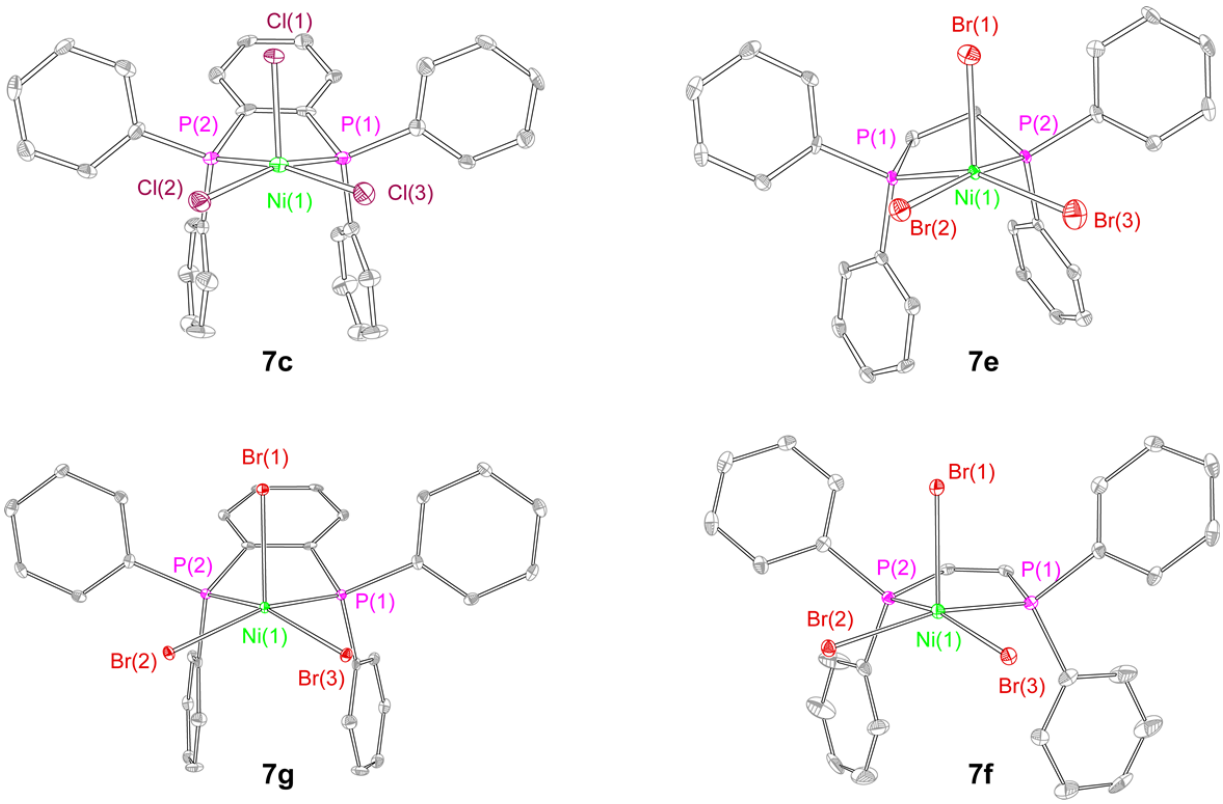

Figure 3.16. Thermal ellipsoid plots of Ni(III) complexes **7c**, **7e**, **7f**, and **7g** in which solvent molecules and H atoms have been removed for clarity. Ellipsoids are drawn at 50% probability.

3.3 UV-vis Absorption Spectroscopy and Photochemistry

The electronic absorption spectra of Ni complexes **7** and **9** are shown in Figures. 3.17–3.24. The spectrum of Ni(II) complex **9c** is representative of the Ni(II) complexes discussed herein, and is dominated by an intense band at 285 nm ($\varepsilon = 2.2 \times 10^4$ M^{-1} cm^{-1}) that is flanked by a shoulder at 335 nm ($\varepsilon = 3.0 \times 10^4$ M^{-1} cm^{-1}) and a much weaker band at 463 nm ($\varepsilon = 1.7 \times 10^3$ M^{-1} cm^{-1}). Oxidation of complex **9c** results in a bathochromic shift of the 335 nm absorption feature to 348 nm ($\varepsilon = 5.2 \times 10^3$ M^{-1} cm^{-1}) and a slight hypsochromic shift of the 463 nm absorption feature to 440 nm ($\varepsilon = 1.8 \times 10^3$ $M^{-1}cm^{-1}$). In addition, a pronounced absorption at 657 nm ($\varepsilon = 1.4 \times 10^3$ M^{-1} cm^{-1}) for complex **7c** is notably absent in Ni(II) complex **9c**. The

profiles of the bromide and chloride Ni(III) complexes are similar, but the former is red-shifted indicating that the absorption spectra of the nickel halide complexes reported here are largely determined by X→Ni(III) charge transfer (Table 3.4).

Irradiation of CH_3CN/CH_2Cl_2 solutions of $NiX_3(LL)$ (**7**) with visible light ($\lambda > 400$ nm) leads to clean conversion to the corresponding reduced $NiX_2(LL)$ (**9**) as determined by both UV-vis and $^{31}P\{^1H\}$ NMR. Well-anchored isosbestic points are observed in most cases studied (Figures 3.17–3.24), and no P-containing side-products were observed by $^{31}P\{^1H\}$ NMR (Figures. 3.25–3.35). Integration of the ^1H NMR spectrum against 1,2-dimethoxyethane as an external standard indicated that Ni(II) complex **9a** was observed in 80% yield. No olefinic traps were required to promote halogen elimination. Cl-based products arising from solution-phase photolysis were not characterized, but photogenerated Cl radicals are expected to participate in H-atom abstraction reactions with either CH_3CN[49,50] or CH_2Cl_2.[51] Halogen photoelimination quantum yields (Φ_p) from each of the Ni(III) complexes were measured actinometrically (against potassium ferrioxalate) and are summarized in Table 3.5.

Table 3.4. UV-vis spectral parameters.

LL	**$NiCl_3(LL)$**	**λ_{max} LMCT** (nm)	**$NiBr_3(LL)$**	**λ_{max} LMCT** (nm)
dppe	**7a**	452/622	**7e**	472/682
dppe-OMe	**7a-OMe**	430/618	**7e-OMe**	462/680
dppe-Cl	**7a-Cl**	336/627	**7e-Cl**	478/691
dppey	**7b**	441/649	**7f**	476/699
dppb	**7c**	453/652	**7g**	479/715
dcpe	**7d**	446/586		

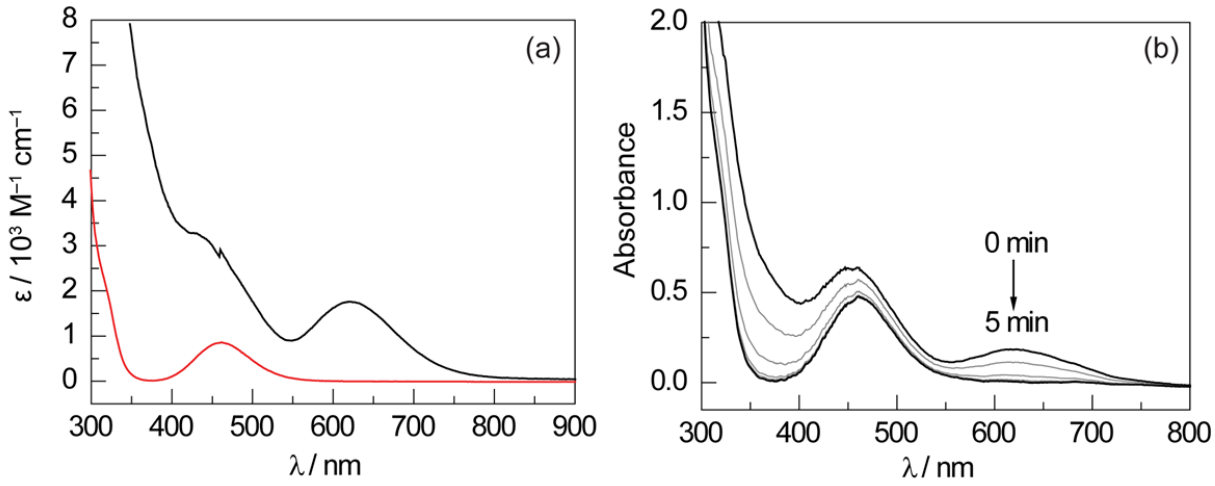

Figure 3.17. (a) Extinction spectra of $NiCl_3$(dppe) (**7a**) (—, black) and $NiCl_2$(dppe) (**9a)** (—, red). (b) Spectral evolution for the photolysis of 0.2 mM of complex **7a** in MeCN (λ_{exc} > 400 nm).

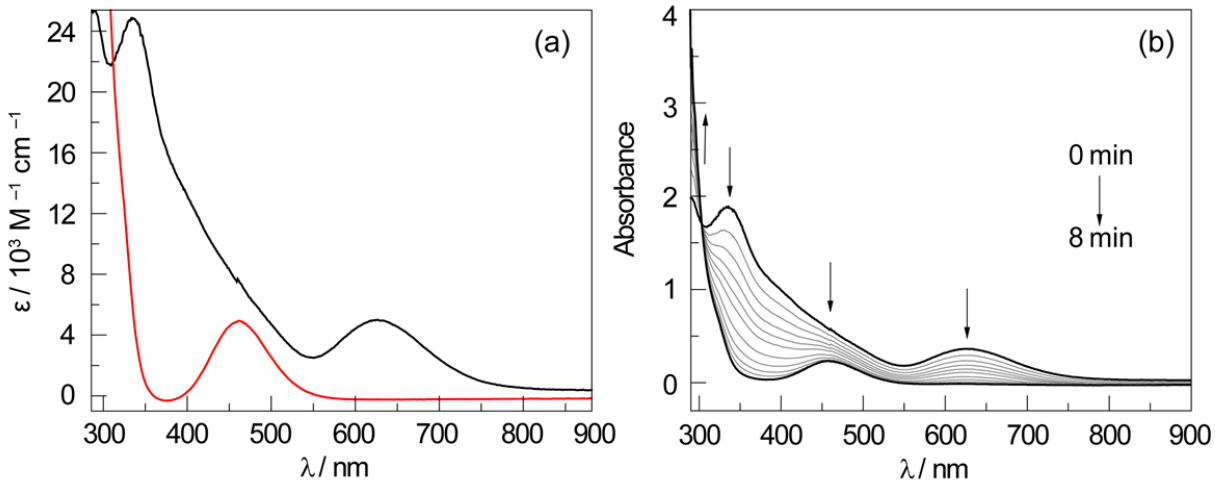

Figure 3.18. (a) Extinction spectra of $NiCl_3$(dppe-Cl) (**7a-Cl**) (—, black) and $NiCl_2$(dppe-Cl) (**9a-Cl**) (—, red). (b) Spectral evolution for the photolysis of $NiCl_3$dppe-Cl (**7a-Cl**) in MeCN (λ_{exc} > 400 nm).

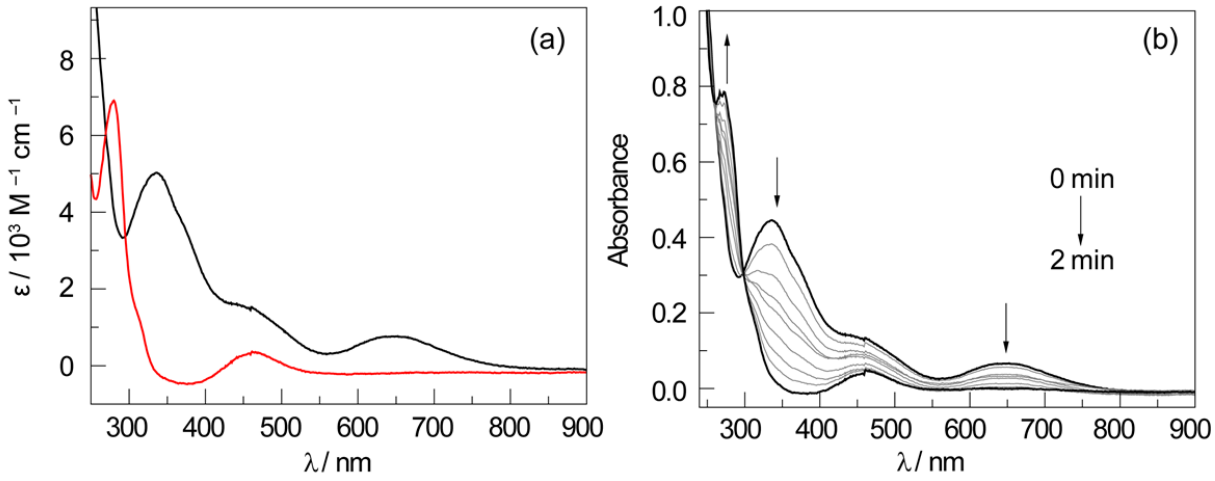

Figure 3.19. (a) Extinction spectra of $NiCl_3$(dppey) (**7b**) (—, black) and $NiCl_2$(dppey) (**9b**) (—, red). (b) Spectral evolution for the photolysis of complex $NiCl_3$(dppey) (**7b**) in MeCN (λ_{exc} > 400 nm).

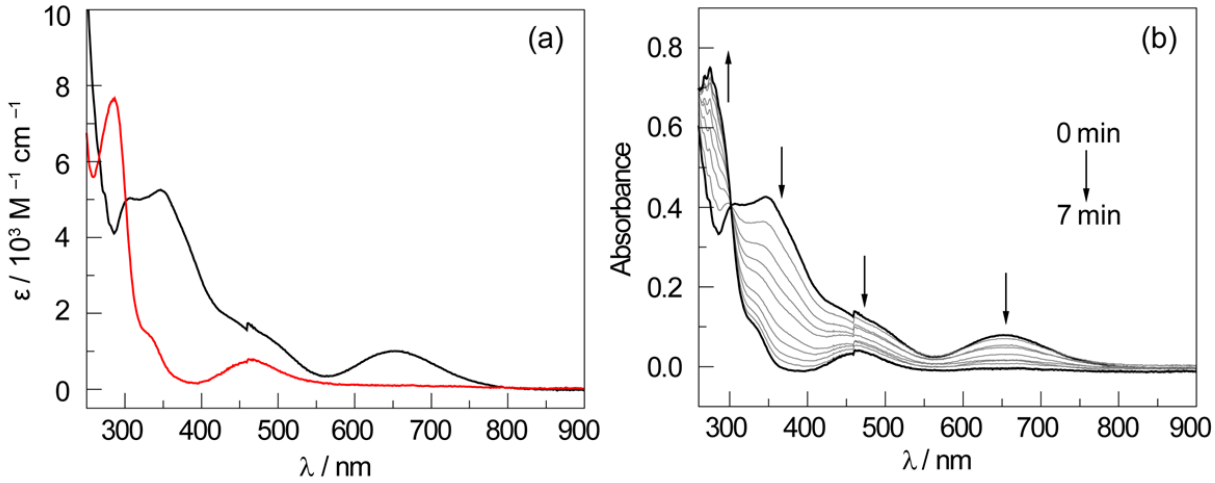

Figure 3.20. (a) Extinction spectra of $NiCl_3$(dppb) (**7c**) (—, black) and $NiCl_2$(dppb) (**9c**) (—, red). (b) Spectral evolution for the photolysis of $NiCl_3$(dppb) (**7c**) in MeCN (λ_{exc} > 400 nm).

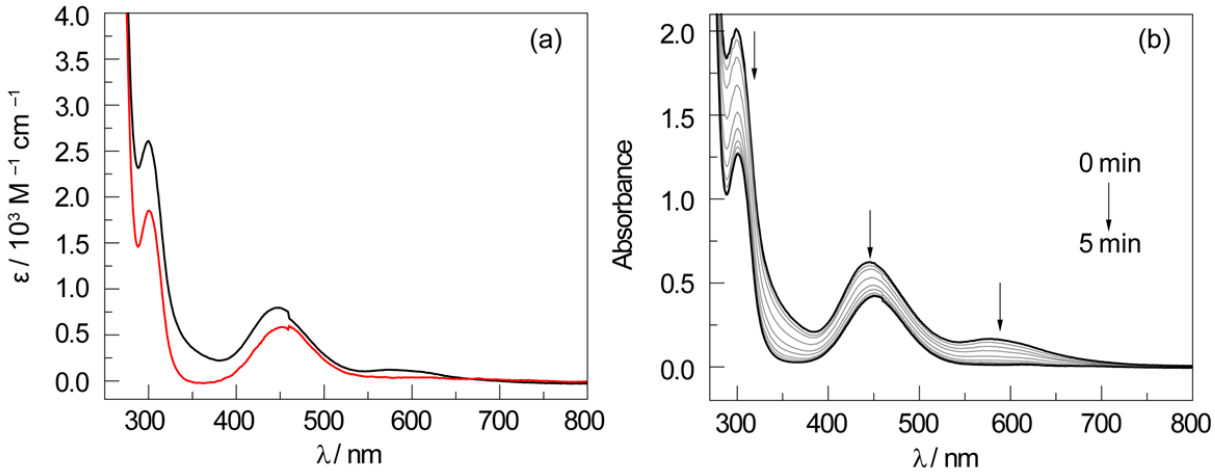

Figure 3.21. (a) Extinction spectra of $NiCl_3$(dcpe) (**7d**) (—, black) and $NiCl_2$(dcpe) (**9d**) (—, red). (b) Spectral evolution for the photolysis of $NiCl_3$(dcpe) (**7d**) in MeCN (λ_{exc} > 400 nm).

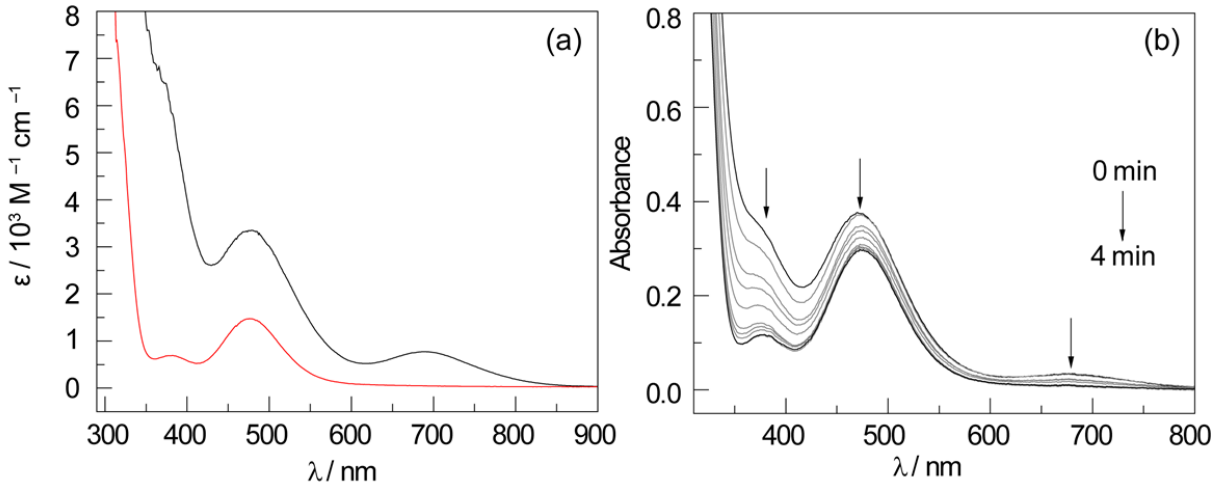

Figure 3.22. (a) Extinction spectra of $NiBr_3$(dppe) (**7e**) (—, black) and $NiBr_2$(dppe) (**9e**) (—, red). (b) Spectral evolution for the photolysis of $NiBr_3$(dppe) (**7e**) in CH_2Cl_2 (λ_{exc} > 400 nm).

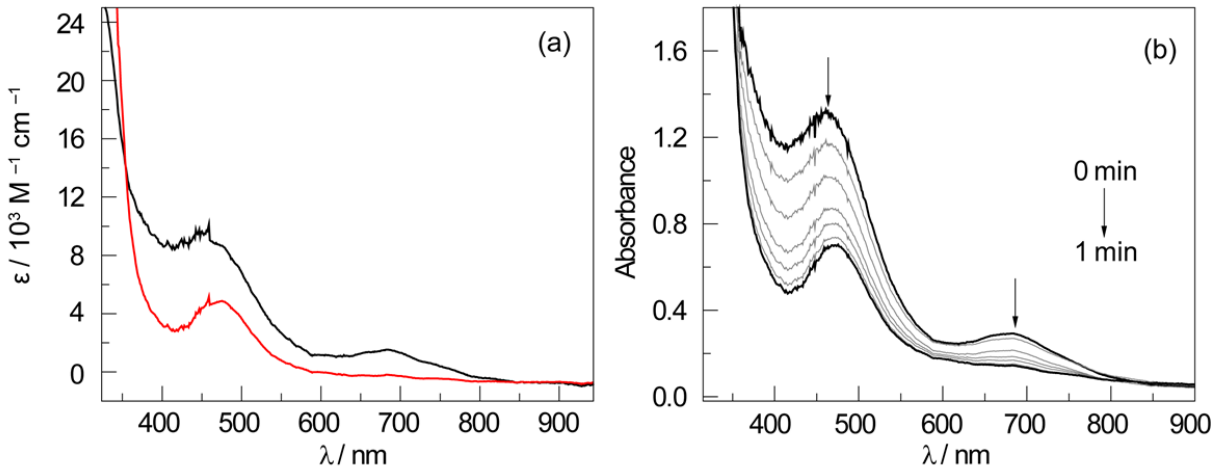

Figure 3.23. (a) Extinction spectra of $NiBr_3$(dppe-OMe) (**7e-OMe**) (—, black) and $NiBr_2$(dppe-OMe) (**9e-OMe**) (—, red). (b) Spectral evolution for the photolysis of $NiBr_3$(dppe-OMe) (**7e-OMe**) in CH_2Cl_2 (λ_{exc} > 400 nm).

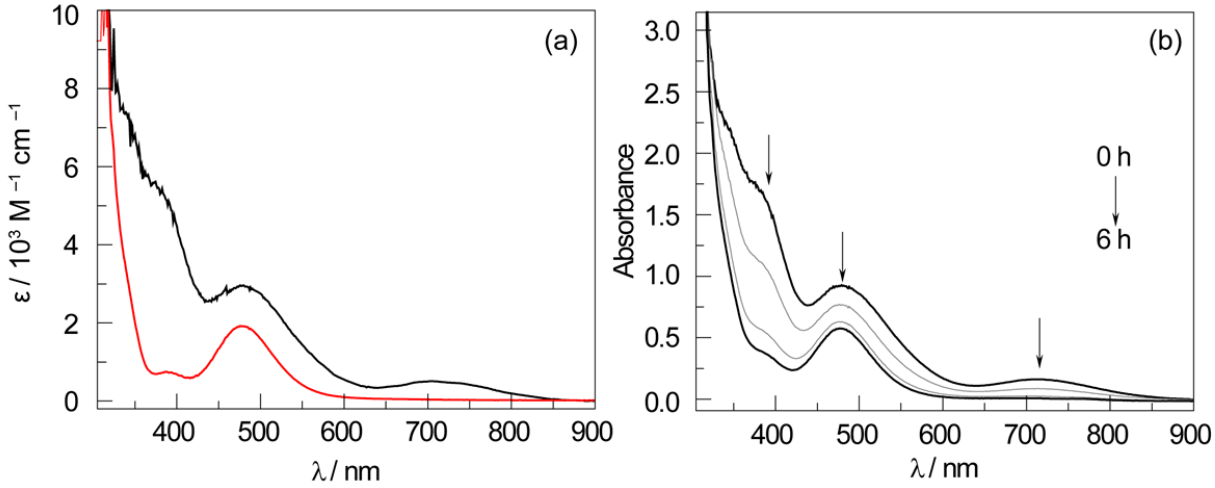

Figure 3.24. (a) Extinction spectra of $NiBr_3$dppb (**7g**) (—, black) and $NiBr_2$(dppb) (**9g**) (—, red). (b) Spectral evolution for the photolysis $NiBr_3$(dppb) (**7g**) in CH_2Cl_2 (λ_{exc} > 400 nm).

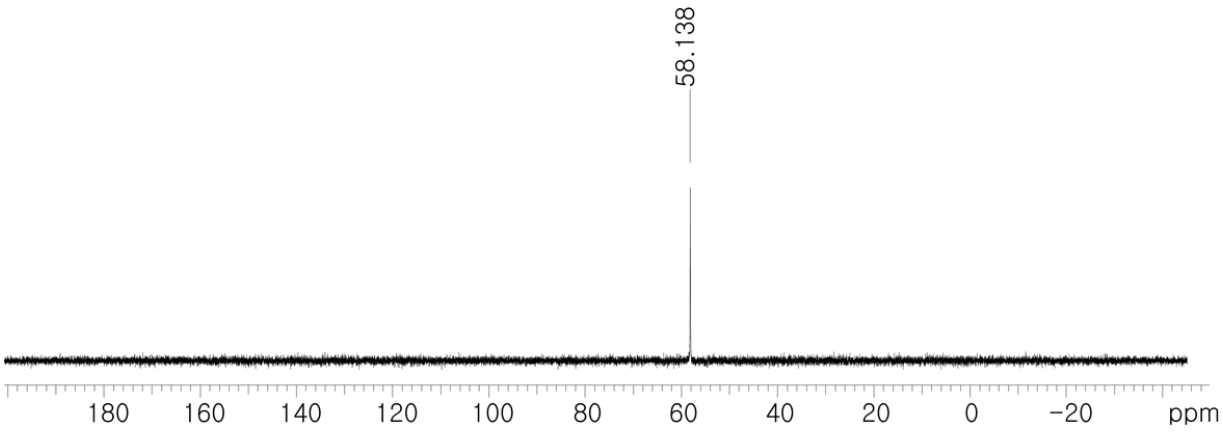

Figure 3.25. $^{31}P\{^{1}H\}$ NMR spectrum of the reaction solution obtained by photolysis of $NiCl_3$(dppe) (**7a**) with visible light ($\lambda > 400$ nm) recorded in CD_2Cl_2 at 23 °C.

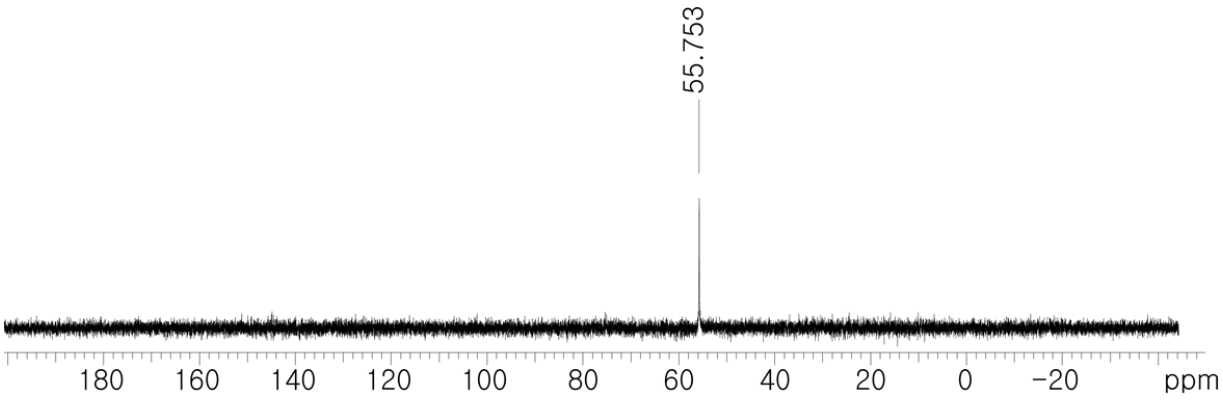

Figure 3.26. $^{31}P\{^{1}H\}$ NMR spectrum of the reaction solution obtained by photolysis of $NiCl_3$(dppe-OMe) (**7a-OMe**) with visible light ($\lambda > 400$ nm) recorded in CD_2Cl_2 at 23 °C.

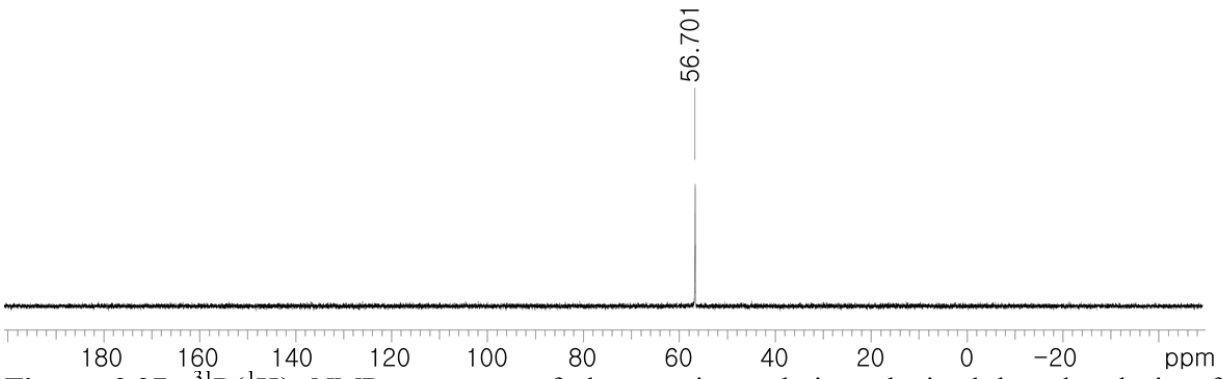

Figure 3.27. $^{31}P\{^{1}H\}$ NMR spectrum of the reaction solution obtained by photolysis of $NiCl_3$(dppe-Cl) (**7a-Cl**) with visible light ($\lambda > 400$ nm) recorded in CD_2Cl_2 at 23 °C.

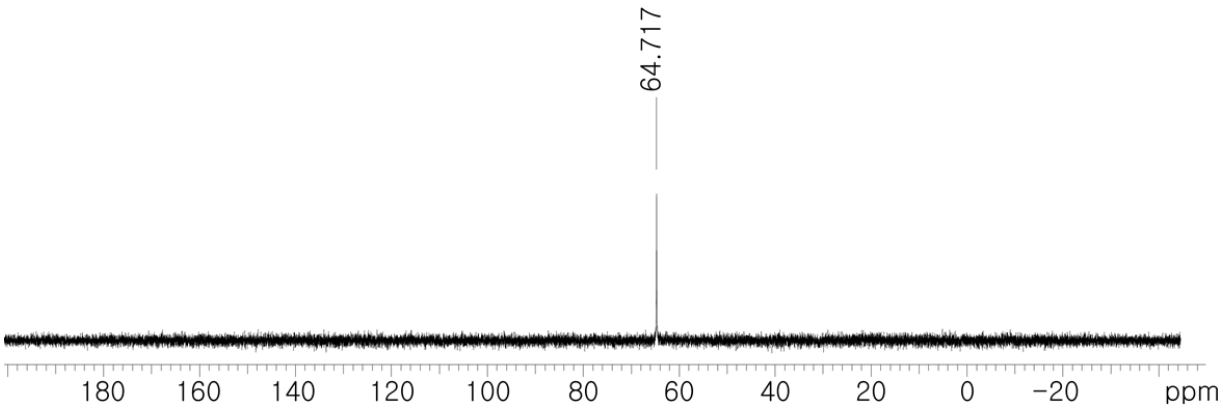

Figure 3.28. $^{31}P\{^{1}H\}$ NMR spectrum of the reaction solution obtained by photolysis of $NiCl_3$(dppey) (**7b**) with visible light ($\lambda > 400$ nm) recorded in CD_2Cl_2 at 23 °C.

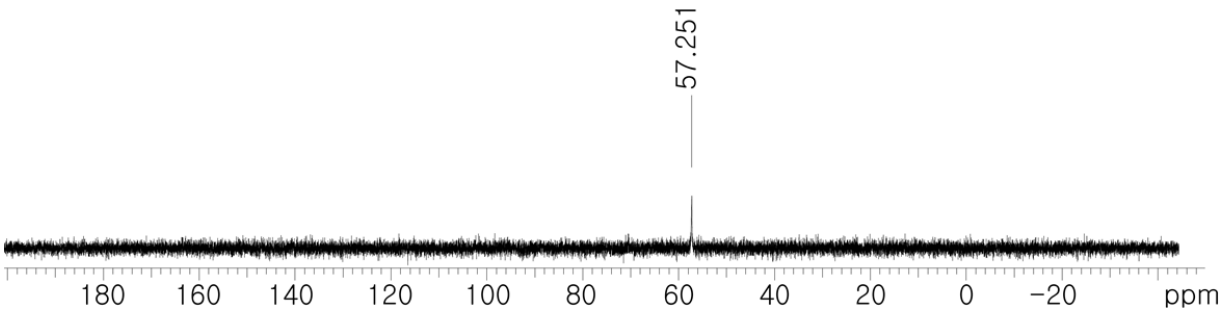

Figure 3.29. $^{31}P\{^{1}H\}$ NMR spectrum of the reaction solution obtained by photolysis of $NiCl_3$(dppb) (**7c**) with visible light ($\lambda > 400$ nm) recorded in CD_2Cl_2 at 23 °C.

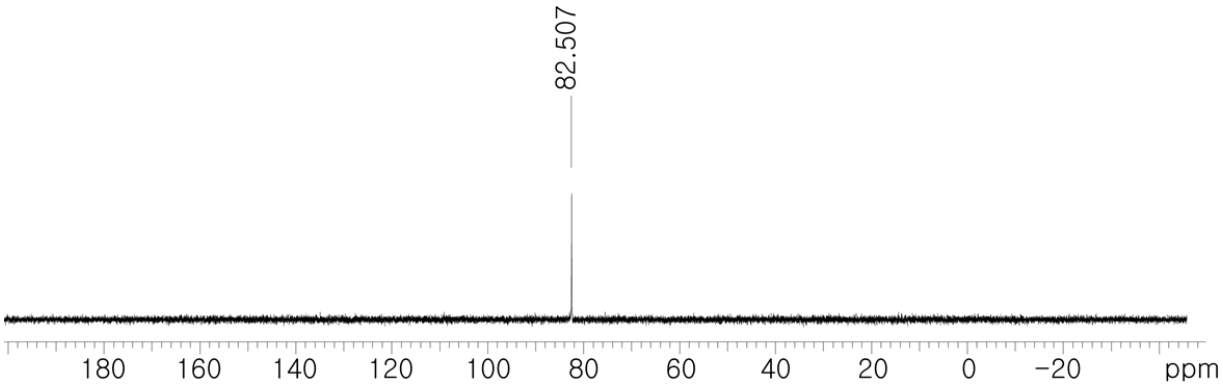

Figure 3.30. $^{31}P\{^{1}H\}$ NMR spectrum of the reaction solution obtained by photolysis of $NiCl_3$(dcpe) (**7d**) with visible light ($\lambda > 400$ nm) recorded in CD_2Cl_2 at 23 °C.

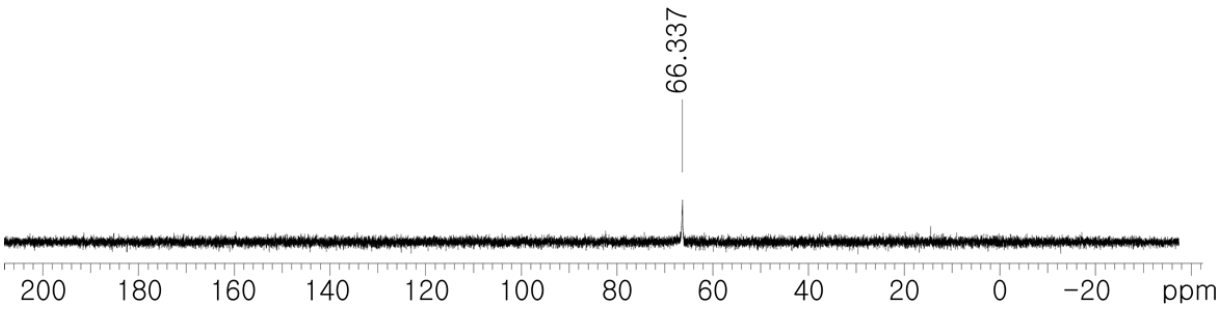

Figure 3.31. $^{31}P\{^{1}H\}$ NMR spectrum of the reaction solution obtained by photolysis of $NiBr_3$(dppe) (**7e**) with visible light ($\lambda > 400$ nm) recorded in CD_2Cl_2 at 23 °C.

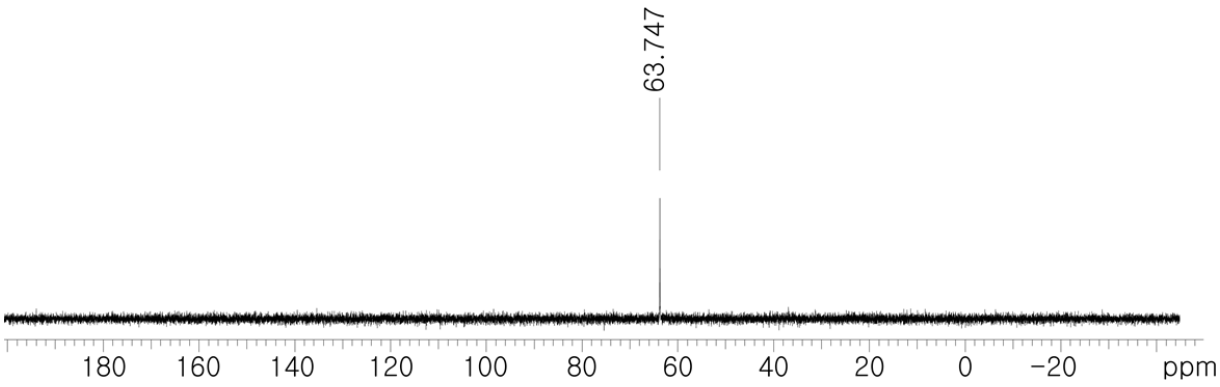

Figure 3.32. $^{31}P\{^{1}H\}$ NMR spectrum of the reaction solution obtained by photolysis of $NiBr_3$(dppe-OMe) (**7e-OMe**) with visible light ($\lambda > 400$ nm) recorded in CD_2Cl_2 at 23 °C.

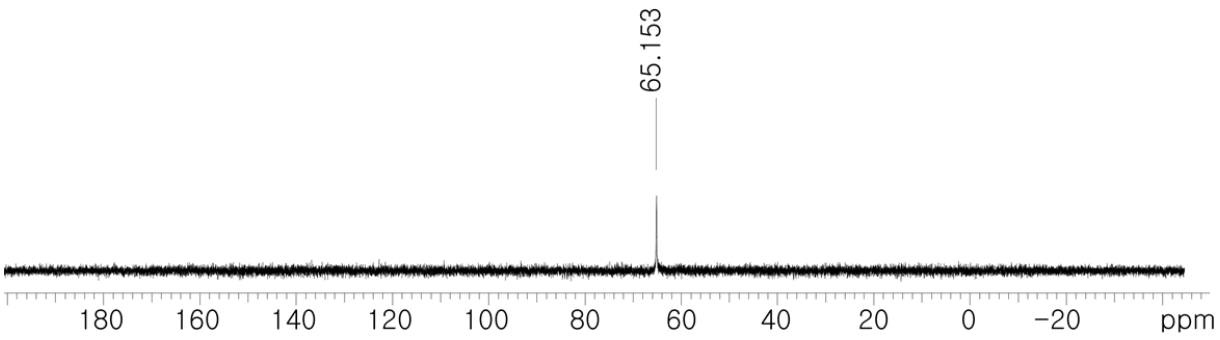

Figure 3.33. $^{31}P\{^{1}H\}$ NMR spectrum of the reaction solution obtained by photolysis of $NiBr_3$(dppe-Cl) (**7e-Cl**) with visible light ($\lambda > 400$ nm) recorded in CD_2Cl_2 at 23 °C.

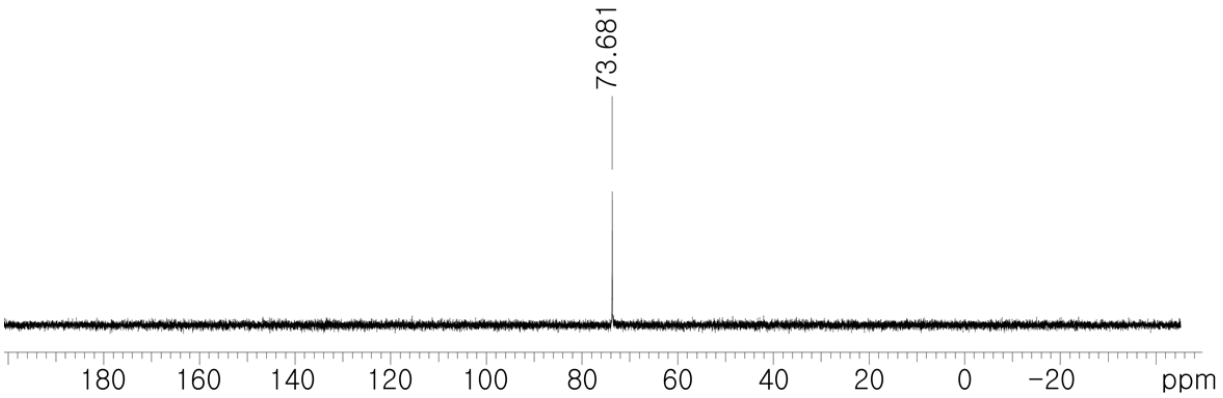

Figure 3.34. $^{31}P\{^{1}H\}$ NMR spectrum of the reaction solution obtained by photolysis of $NiBr_3$(dppey) (**7f**) with visible light (λ > 400 nm) recorded in CD_2Cl_2 at 23 °C.

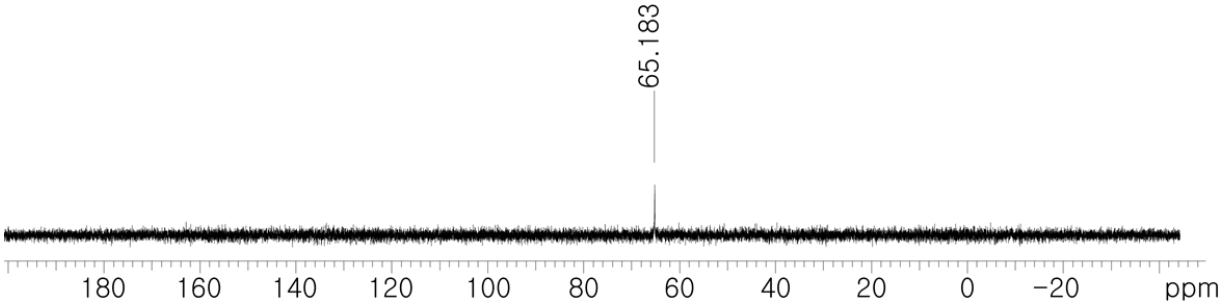

Figure 3.35. $^{31}P\{^{1}H\}$ NMR spectrum of the reaction solution obtained by photolysis of $NiBr_3$(dppb) (**7g**) with visible light (λ > 400 nm) recorded in CD_2Cl_2 at 23 °C.

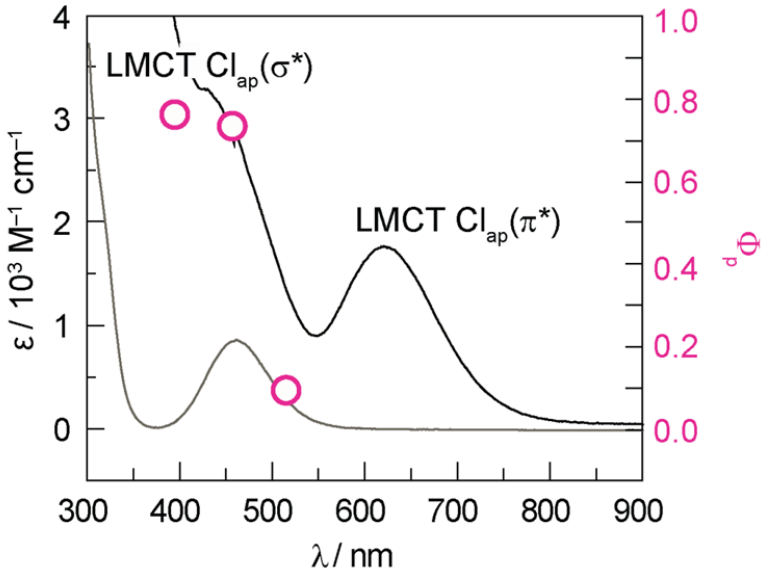

Figure 3.36. Photochemical quantum yields (ϕ) for the reduction of **7a** in CH_3CN as a function of excitation wavelength. The absorption spectra of **7a** and **9a** are included for reference.

Wavelength-dependent quantum yields for halogen elimination from **7a** were measured in CH_3CN against a potassium ferrioxalate standard actinometer and determined to be 77% (370 nm), 76% (434 nm), and 9% (510 nm) (Figure 3.36). These data are consistent with a common, productive excited state that is accessed upon 370 and 434 nm irradiation,[52] indicating rapid internal conversion to a lower energy, photodissociative state. The substantially lower quantum yield at 510 nm indicates that the higher energy LMCT transition (λ_{max} ~ 450 nm) is responsible for efficient halogen photoelimination.

Table 3.5. Quantum yields of NiX_3(LL) halogen elimination photochemistry.[a]

LL	**$NiCl_3$(LL)**	**Φ_p**	**$NiBr_3$(LL)**	**Φ_p**
dppe	**7a**	0.764	**7e**	0.169
dppe-OMe	**7a-OMe**	0.230	**7e-OMe**	0.352
dppe-Cl	**7a-Cl**	0.128	**7e-Cl**	0.056
dppey	**7b**	0.960	**7f**	0.401
dppb	**7c**	0.077	**7g**	0.047
dcpe	**7d**	0.201		
	w/5% C_6H_6 [b]	0.330		
	w/10% C_6H_6 [b]	0.410		
	w/20% C_6H_6 [b]	0.490		
	w/30% C_6H_6 [b]	0.590		
	w/40% C_6H_6 [b]	0.620		

[a] in CH_2Cl_2, λ_{exc} = 370 nm bandpass filter. [b] in CH_3CN with percent addition of benzene.

The presence of an aromatic group in the second coordination sphere significantly enhances Φ_p. The photochemical quantum yield, Φ_p, for cyclohexyl phosphine complex $NiCl_3$(dcpe) is Φ_p(**7d**) = 20.1% whereas that for the dppe complex is Φ_p(**7a**) = 76.4% and near unity for the dppey complex **7b**. We note that the presence of an aromatic solvent increases the Φ_p of **7d.** The addition of benzene to CH_3CN solutions causes Φ_p to increase monotonically until 30% mixtures are attained after which Φ_p levels off at ~60%. Addition of 30% CCl_4 showed no improvement in the photoefficiency (Φ_p = 20.8%), suggesting that a change in solvent dielectric ($\varepsilon(C_6H_6)$ = 2.27 and $\varepsilon(CCl_4)$ = 2.24) is not the source of increased quantum yield for CH_3CN/benzene mixtures. A similar change in Φ_p was also observed for the addition of benzene to solutions of $NiCl_3$(dppb) (**7c**) (Φ_p = 8% in CH_3CN vs Φ_p = 35% with 30% benzene). Halogen photoelimination from substituted dppe-supported NiX_3(LL) complexes was also examined to probe the effects of the electronic properties of the phosphine without modifying the steric environment about the metal center. The quantum yields for para-OMe and para-Cl substituted dppe derivatives were determined to be 35.0% and 5.6% for **7a-OMe** and **7a-Cl**, respectively.

Solid-state irradiation of complex **7a** (~20 Torr, 25 °C) results in the formation of Ni(II) complex **9a (**87% yield based on recovered starting material determined by ^{1}H NMR versus external standard 1,2-dimethoxyethane; Figure 3.37) with concurrent evolution of half an equivalent of Cl_2. Evolved Cl_2 was collected at 77 K and subsequently characterized by mass spectrometric analysis of gaseous reaction products; *m*/*z* corresponding to $^{35,35}Cl_2$, $^{37,37}Cl_2$, $^{35,37}Cl_2$, $^{35}Cl\bullet$, and $^{37}Cl\bullet$ were observed and the measured ratio of ^{35}Cl and ^{37}Cl was good agreement with the natural isotopic abundance for chlorine (Figure 3.38).[53] The yield of evolved Cl_2 was quantified colorimetrically by trapping evolved halogen with *N*,*N*-diethyl-1,4-phenylenediamine sulfate (DPD) to afford the intensely pink radical cation $DPD^{\bullet+}$ (Figure

3.39).[54,55] No reduction of **1a** was observed by ^{1}H NMR, ^{31}P NMR, or UV-vis spectroscopies after heating a powdered sample of complex **1a** at 70 °C in the exclusion of light and moisture, confirming that halogen elimination is photochemically, and not thermally, driven (Figure 3.40).

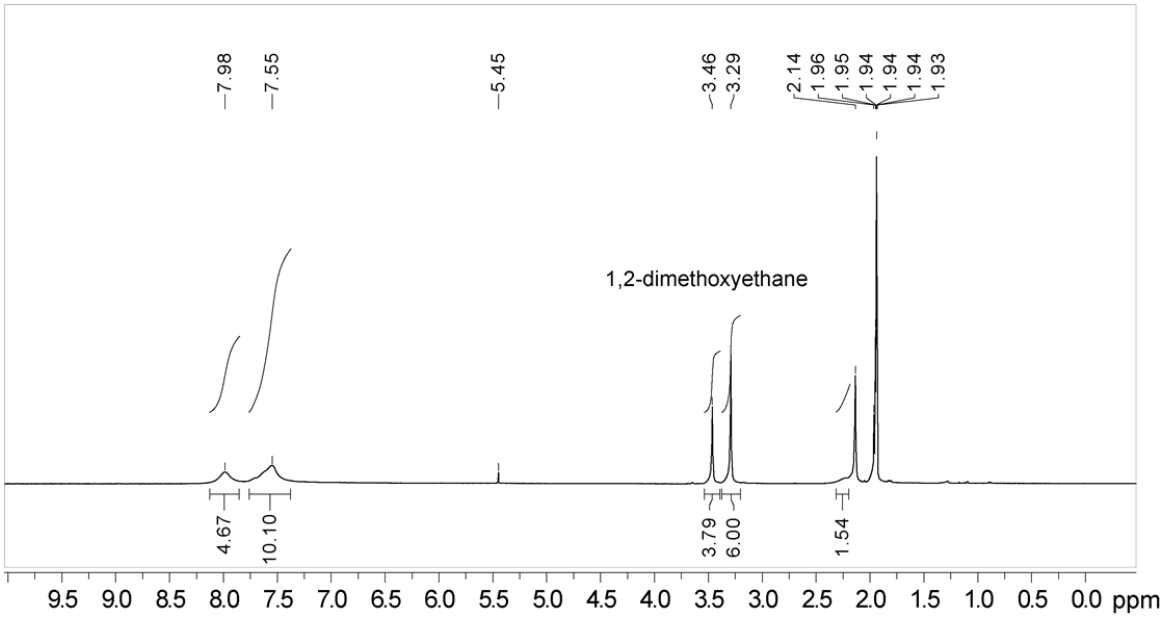

Figure 3.37. ^{1}H NMR spectrum of the photoproducts of solid-state photolysis of **7a** with visible light (λ > 430 nm) recorded in CD_3CN at 23 °C. 1,2-Dimethoxyethane was added as an external standard.

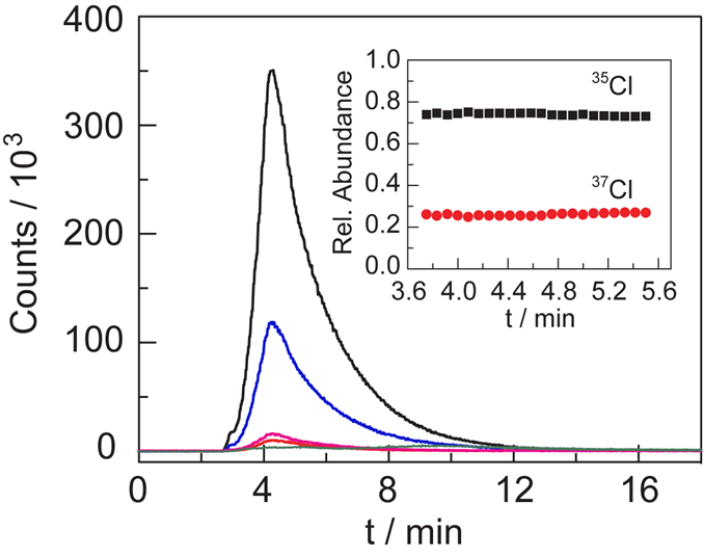

Figure 3.38. Mass spectrometry analysis of the gas evolved from solid-state photolysis of complex **1a**. Traces correspond to ^{35}Cl (black), ^{37}Cl (blue), $^{35}Cl^{35}Cl$ (pink), $^{35}Cl^{37}Cl$ (red), $^{37}Cl^{37}Cl$ (green) mass fragments. Inset: relative abundance of ^{35}Cl (black) and ^{37}Cl (red).

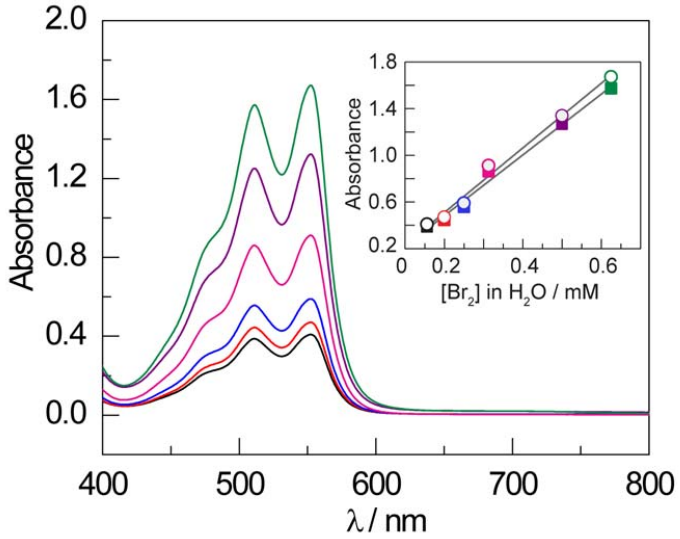

Figure 3.39. UV-vis absorption spectrum, in H_2O, showing formation of DPD $^{\bullet+}$ when DPD is treated with different concentrations of Br_2. The spectrum was recorded at room temperature. Inset shows concentration dependent absorbance, λ_{max} at 552 nm (circles) and λ_{max} at 511 nm (squares).

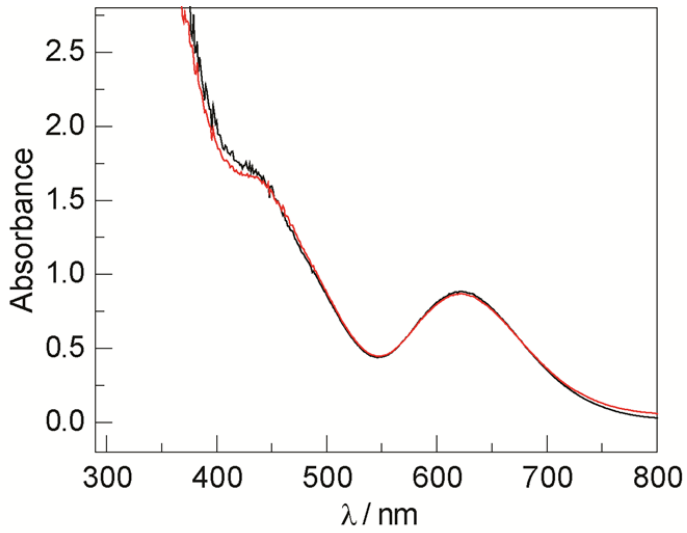

Figure 3.40. Electronic absorption spectra of complex **7a** in MeCN (▬, black) and after heating at 70 °C for 2 d in solid state (▬, red).

3.4 Time-Resolved Photochemistry

Nanosecond-resolved transient absorption (TA) spectroscopy was used to investigate the mechanism of Cl_2 photoelimination from **7a** in solution. Figure 3.41 shows the time evolution of the TA spectrum obtained from laser flash photolysis (355 nm pump) of a CH_3CN solution of Ni(III) complex **7a**. The prompt TA spectrum observed at 40 ns evolves over the course of several microseconds into a spectrum that corresponds to the formation of Ni(II) complex **9a** from Ni(III) complex **7a**; single wavelength kinetics were monitored at 540 nm and provided a lifetime for the TA signal of 3.43 ± 0.05 μs. Figures 3.42–3.58 show the transient absorption (TA) full spectra and single-wavelength kinetics of samples containing Ni(III)Cl_3(LL) complexes **7a**–**c** following laser excitation at 355 nm in CH_3CN. For each sample, the earliest achievable TA difference spectrum acquired (time delay = 40–70 ns) is a superposition of the bleach signal of the starting complex, the absorption of the final product, Ni(II)Cl_2(LL), and any transient species present promptly. The single-wavelength kinetics measurements show changes in absorbance

with lifetimes ranging from 100 ns to 10 μs, depending on the complex, indicating the decay of a transient species to the final Ni(II)Cl_2(LL) photoproduct, as confirmed by the full TA spectra taken at 50 μs. In the case of high quantum yields for halogen elimination, the back-reaction in which the transient decays directly back to the original Ni(III)Cl_3(LL) complex is necessarily negligible.

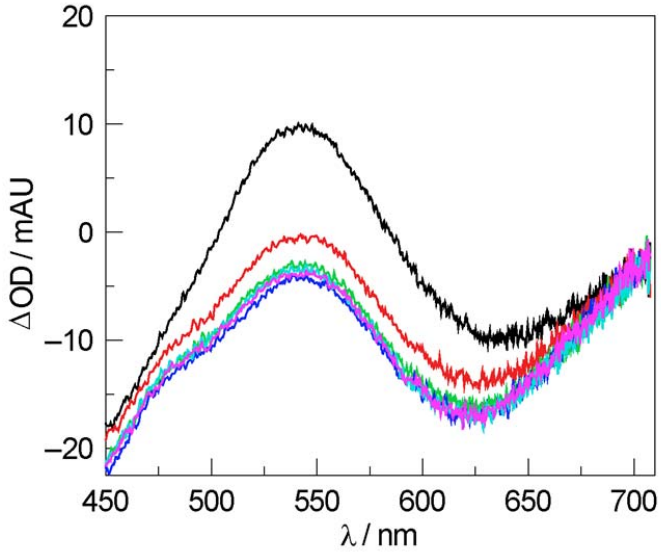

Figure 3.41. Transient absorption spectra obtained by laser flash photolysis of complex **7a** (355 nm pump) as a 0.44 mM solution in MeCN. Transient absorption spectra recorded 40 ns (black), 4 μs (red), 8 μs (green), 12 μs (blue), 16 μs (light blue), and 20 μs (pink) after laser pulse.

Therefore, to a good approximation subtraction of the 50 μs TA spectrum from that of the early spectrum yields the absorption spectrum of the transient species. Accordingly, Figure 3.42 shows the resulting absorption spectrum (blue) for the transient generated from complex **7a**. The spectrum of the transient displays an absorption maximum at 366 nm as well as a broad band with a maximum at 530 nm. We attribute the observed spectral features to an arene-to-chlorine charge transfer adduct between a ligand aryl group and a photogenerated chlorine atom. These spectral features are similar to those of the chlorine-atom charge transfer adduct of benzene

(Figure 3.42, black), generated by either laser flash photolysis or pulse radiolysis.[56–59] The observed spectral features are shifted ~35 nm lower in energy than those in the benzene adduct due to substituent effects (*vide infra*).[59] The chlorine atom-benzene complex has been proposed to be an η^1 π complex based on DFT calculations.[60] This suggests that the observed transient intermediate is a Cl-atom adduct formed with the ligand aryl group. A similar result is obtained for each Ni(III)Cl_3(LL) complex **7a–c** described herein, suggesting that each complex forms a similar transient intermediate.

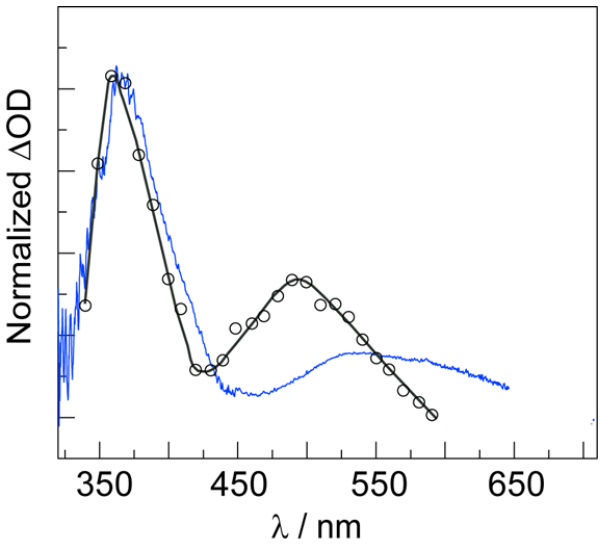

Figure 3.42. Comparison between the absorption spectra of the transient species generated by laser flash photolysis of **7a** (—, blue) and the chlorine-atom charge transfer adduct of benzene (—, black), also generated by laser flash photolysis (data adapted from reference 59, respectively). The blue spectrum is generated by subtracting the TA difference spectrum of a 0.44 mM solution of **7a,** $NiCl_3$(dppe), in CH_3CN acquired at a 50 μs time delay from that acquired at a 40 ns time delay (λ_{exc} = 355 nm). The low energy transient feature shifts to lower energy with the introduction of electron donating substituents of the phenyl ring of dppe along the series.

Further support for the intermediacy of a Cl-atom|aromatic adduct formed along the pathway of the halogen elimination photochemistry of the NiX_3(LL) complexes was obtained by investigating substituted dppe-supported Ni(III) complexes. Charge-transfer complexes between

arenes and halogen atoms are known to display a linear relationship between the absorption energy and the ionization potential of the donor.[56] The λ_{max} of the transient intermediate is perturbed by the presence of substituents on the dppe ligand. As shown in Figures 3.59, the λ_{max} of the transient spectrum red shifts with donor substitution on the aryl ring (**7a**, λ_{max} = 530 nm; **7a-Cl**, λ_{max} = 540 nm; **7a-OMe**, λ_{max} = 610 nm). This observed red shift in the energy of the Cl-atom|aromatic adduct with increasing donor properties of the substituent group is consistent with the spectral trend previously reported for Cl-atom|aromatic adducts as observed by pulse radiolysis experiments.[56]

Given that Φ_p for halogen photoelimination increases with the addition of benzene (Table 3.5), we examined the TA spectrum of complex **7d** in the presence of 30% benzene. The nanosecond-resolved TA spectrum of cyclohexyl phosphine Ni(III) complex **7d** exhibits a weak feature with a maximum at 430 nm. The signal intensity of the observed transient intermediate at 430 nm increases substantially with the addition of benzene to the solution and it slightly red shifts; the time evolution of the transient decay remains essentially unchanged.

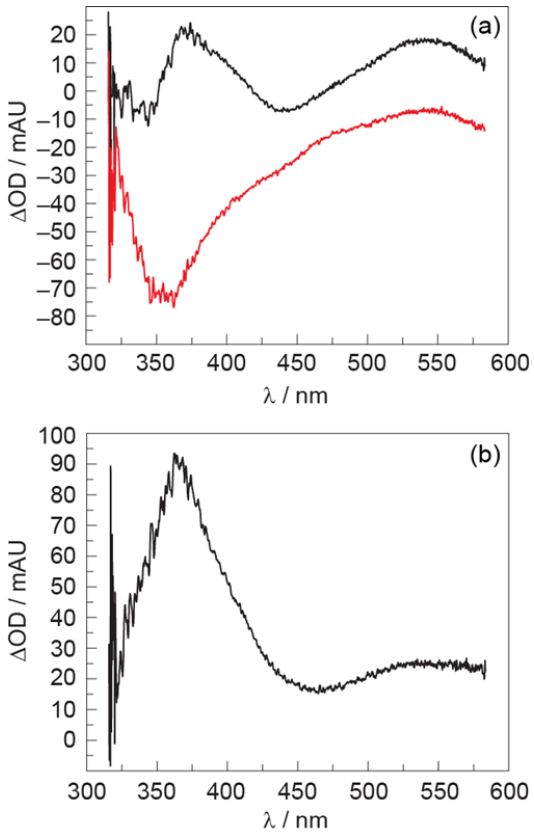

Figure 3.43. Transient absorption spectra obtained by laser flash photolysis (355 nm pump) of $NiCl_3$(dppe) (**7a**) (0.44 mM solution in MeCN). (a) Transient absorption spectra recorded at 50 ns (**—**, black), and 50 μs (**—**, red) after laser pulse. (b) Absorption spectrum of the intermediate species (**8a**) calculated from the difference of TA spectra recorded at 50 ns and 50 μs.

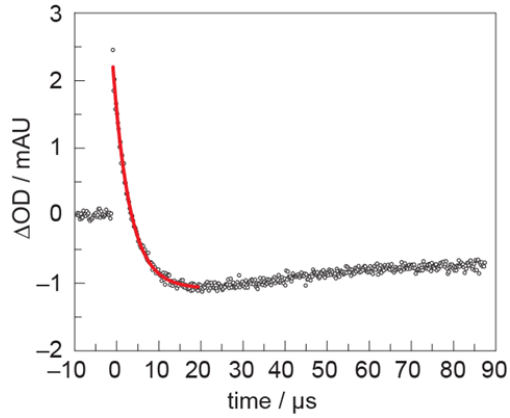

Figure 3.44. Single wavelength kinetic trace of a MeCN solution of $NiCl_3$(dppe) (**7a**) pumped at 355 nm and recorded at 560 nm. Initial component lifetime: $\tau = 4.0 \pm 0.1$ μs.

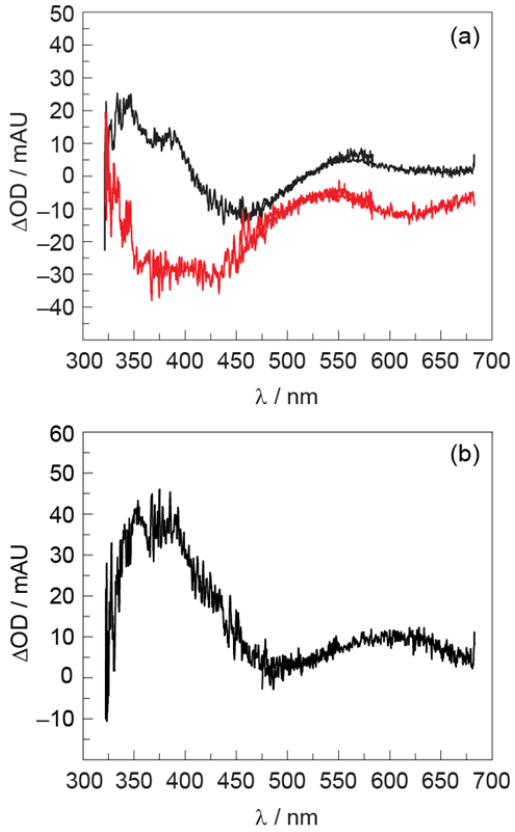

Figure 3.45. Transient absorption spectra obtained by laser flash photolysis (355 nm pump) of $NiCl_3$(dppe-OMe) (**7a-OMe**) (0.44 mM solution in MeCN). TA spectra are composites of spectra acquired with windows centered at 450 and 550 nm. (a) Transient absorption spectra recorded at 70 ns (—, black), and 50 μs (—, red) after laser pulse. (b) Absorption spectrum of the intermediate species (**8a-OMe**) calculated from the difference of TA spectra recorded at 70 ns and 50 μs.

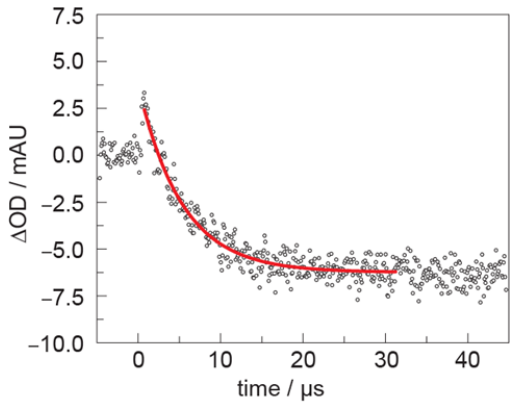

Figure 3.46. Single wavelength kinetic trace of a MeCN solution of $NiCl_3$(dppe-OMe) (**7a-OMe**) pumped at 355 nm and recorded at 600 nm. Initial component lifetime: $\tau = 5.3 \pm 0.2$ μs.

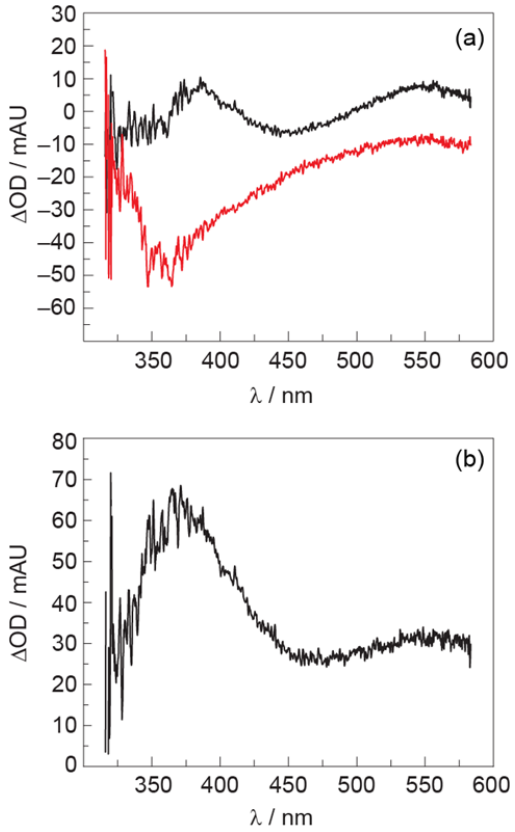

Figure 3.47. Transient absorption spectra obtained by laser flash photolysis (355 nm pump) of $NiCl_3$(dppe-Cl) (**7a-Cl**) (0.44 mM solution in MeCN). (a) Transient absorption spectra recorded at 70 ns (**—**, black) and 50 μs (**—**, red) after laser pulse. (b) Absorption spectrum of the intermediate species (**8a-Cl**) calculated from the difference of TA spectra recorded at 70 ns and 50 μs.

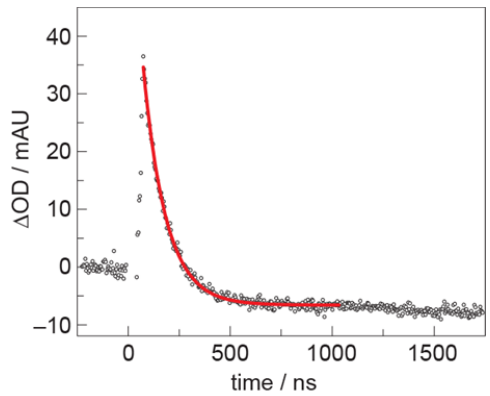

Figure 3.48. Single wavelength kinetic trace of a MeCN solution of $NiCl_3$(dppe-Cl) (**7a-Cl**) pumped at 355 nm and recorded at 550 nm. Initial component lifetime: $\tau = 100 \pm 1$ ns.

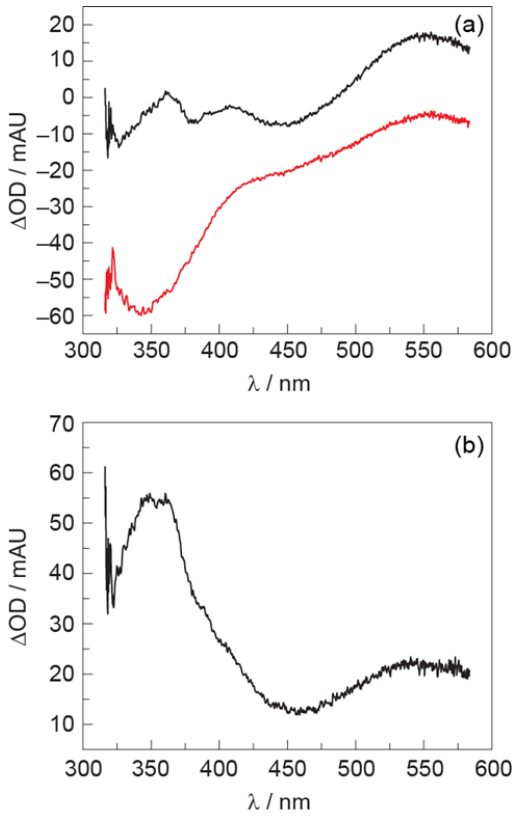

Figure 3.49. Transient absorption spectra obtained by laser flash photolysis (355 nm pump) of $NiCl_3$(dppey) (**7b**) (0.44 mM solution in MeCN). (a) Transient absorption spectra recorded at 50 ns (—, black), and 50 μs (—, red) after laser pulse. (b) Absorption spectrum of the intermediate species (**8b**) calculated from the difference of TA spectra recorded at 50 ns and 50 μs.

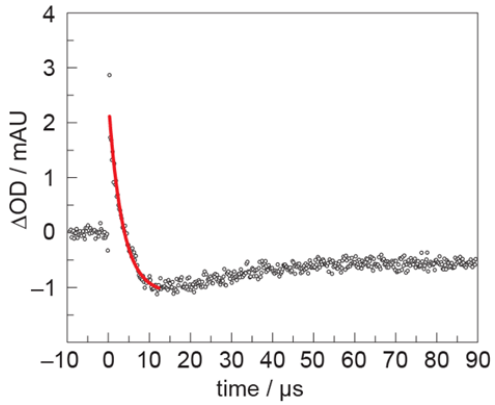

Figure 3.50. Single wavelength kinetic trace of a MeCN solution of $NiCl_3$(dppey) (**7b**) pumped at 355 nm and recorded at 550 nm. Initial component lifetime: $\tau = 3.4 \pm 0.2$ μs.

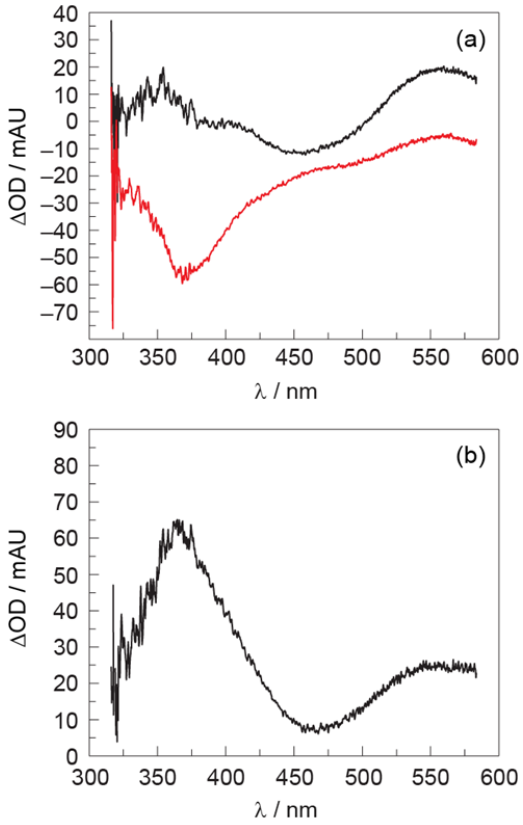

Figure 3.51. Transient absorption spectra obtained by laser flash photolysis (355 nm pump) of $NiCl_3$(dppb) (**7c**) (0.44 mM solution in MeCN). (a) Transient absorption spectra recorded at 300 ns (▬, black), and 50 μs (▬, red) after laser pulse. (b) Absorption spectrum of the intermediate species (**8c**) calculated from the difference of TA spectra recorded at 300 ns and 50 μs.

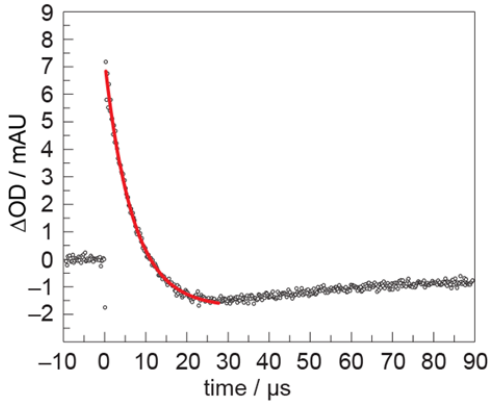

Figure 3.52. Single wavelength kinetic trace of a MeCN solution of $NiCl_3$(dppb) (**7c**) pumped at 355 nm and recorded at 550 nm. Initial component lifetime: $\tau = 6.8 \pm 0.1$ μs.

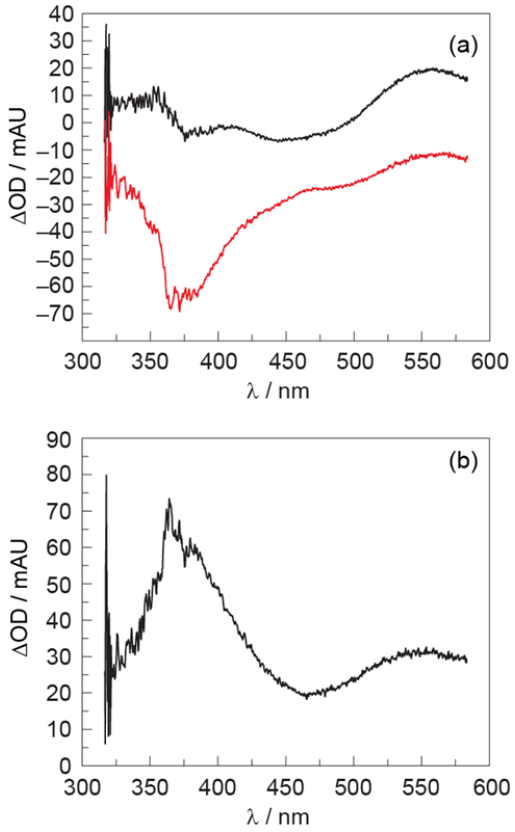

Figure 3.53. Transient absorption spectra obtained by laser flash photolysis (355 nm pump) of $NiCl_3$(dppb) (**7c**) (0.44 mM solution in 30/70 benzene/MeCN). (a) Transient absorption spectra recorded at 300 ns (—, black), and 50 μs (—, red) after laser pulse. (b) Absorption spectrum of the intermediate species (**8c**) calculated from the difference of TA spectra recorded at 300 ns and 50 μs.

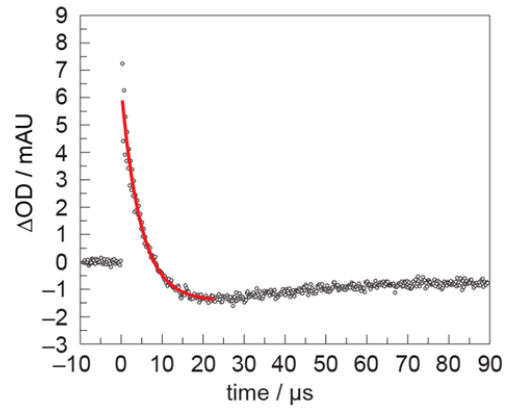

Figure 3.54. Single wavelength kinetic trace of a solution (0.44 mM in 30:70 benzene:MeCN) of $NiCl_3$(dppb) (**7c**) pumped at 355 nm and recorded at 550 nm. Initial component lifetime: $\tau = 4.7 \pm 0.2$ μs.

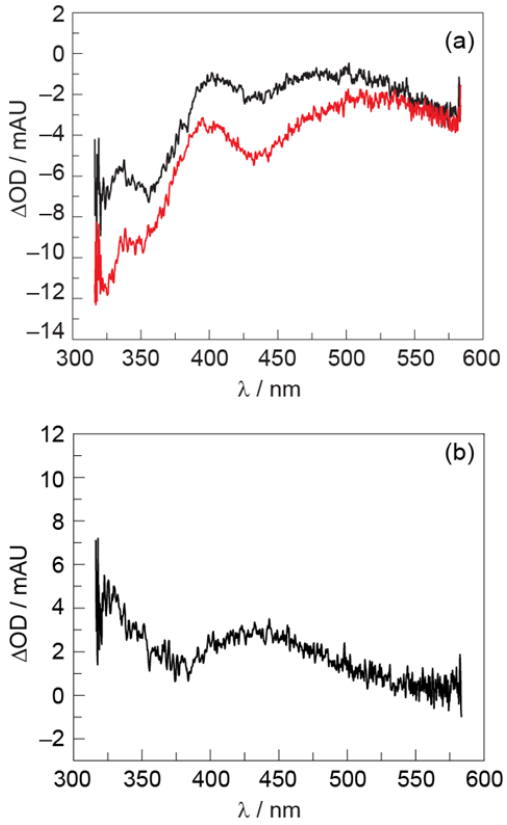

Figure 3.55. Transient absorption spectra obtained by laser flash photolysis (355 nm pump) of $NiCl_3$(dcpe) (**7d**) (0.44 mM solution in MeCN). (a) Transient absorption spectra recorded at 80 ns (**—**, black), and 50 μs (**—**, red) after laser pulse. (b) Absorption spectrum of the intermediate species (**8d**) calculated from the difference of TA spectra recorded at 80 ns and 50 μs.

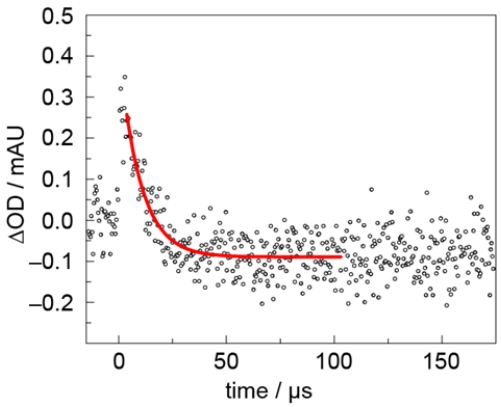

Figure 3.56. Single wavelength kinetic trace of a solution of $NiCl_3$(dcpe) (**7d**) pumped at 355 nm and recorded at 440 nm. Initial component lifetime: $\tau = 9.8 \pm 0.8$ μs.

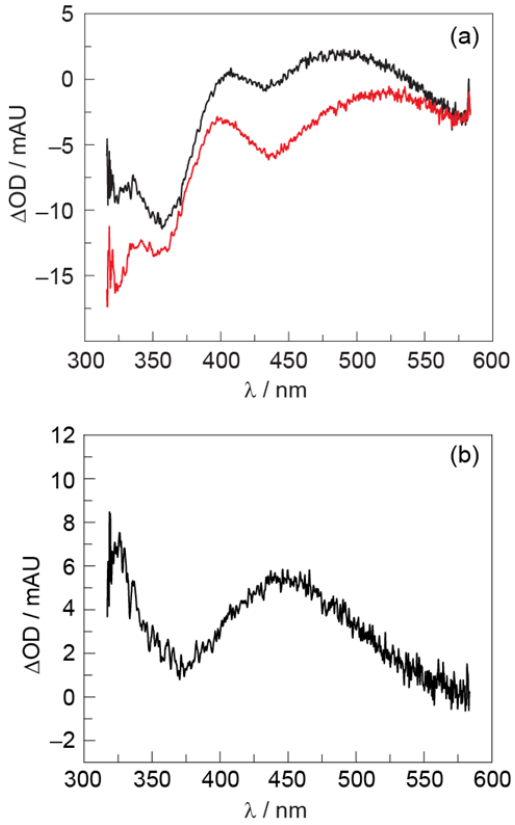

Figure 3.57. Transient absorption spectra obtained by laser flash photolysis (355 nm pump) of $NiCl_3$(dcpe) (**7d**) (0.44 mM solution in 30:70 benzene:MeCN). (a) Transient absorption spectra recorded at 380 ns (—, black), and 50 μs (—, red) after laser pulse. (b) Absorption spectrum of the intermediate species (**8d**) calculated from the difference of TA spectra recorded at 380 ns and 50 μs.

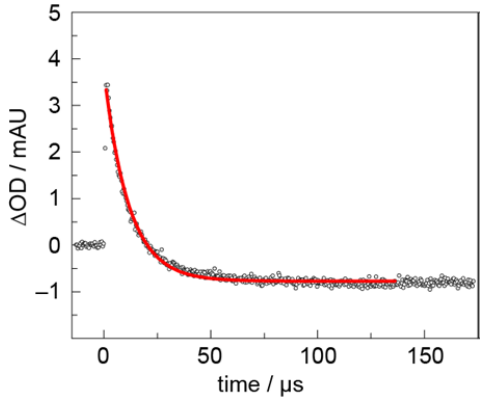

Figure 3.58. Single wavelength kinetic trace of a solution (0.44 mM in 30:70 benzene:MeCN) $NiCl_3$(dcpe) (**7d**) pumped at 355 nm and recorded at 550 nm. Initial component lifetime: $\tau = 11.5 \pm 0.1$ μs.

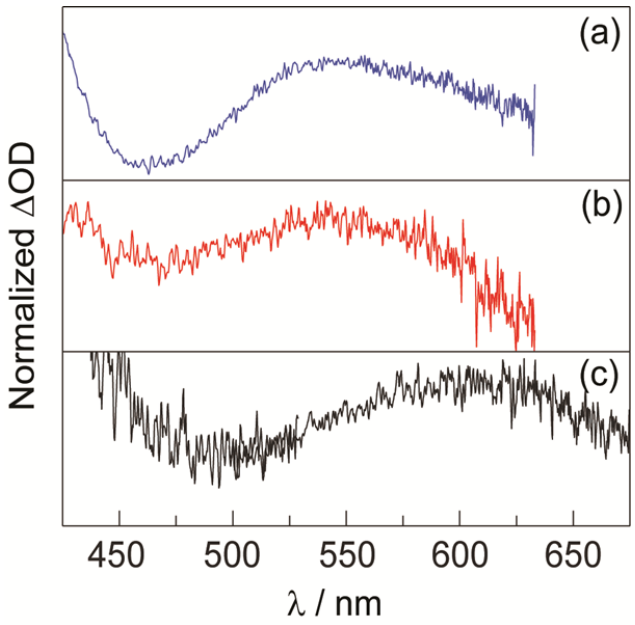

Figure 3.59. Comparison between the absorption spectra of the transient species generated by laser flash photolysis. The low energy transient feature shifts to lower energy with the introduction of electron donating substituents of the phenyl ring of dppe along the series (a) **7a** (—, blue), (b) **7a-Cl** (—, red), and (c) **7a-OMe** (—, black).

3.5 Photocrystallographic Observation of M–X Bond Activation

Steady-state photocrystallography results are consistent with the photoactivation of the apical halogen bond. As we have previously shown for halogen photoelimination reactions from Rh_2 complexes,[61] atomic displacements during solid-state photoreactions can be directly investigated with X-ray diffraction by comparing diffraction with and without irradiation. Such comparison of these diffraction data sets in a photodifference map can indicate the photoinduced atomic displacements in a crystalline sample. Complex **7f**, $NiBr_3$(dppey) (dppey = *cis*-bis(diphenylphosphino)ethylene) was used in these experiments because the bromide ligands have greater electron density as compared to chloride ligands, which makes examination of photoinduced atomic displacement possible at low populations of reaction progress. Complex **7e** was not used in these experiments due to crystallographic disorder in the solid-state structure in

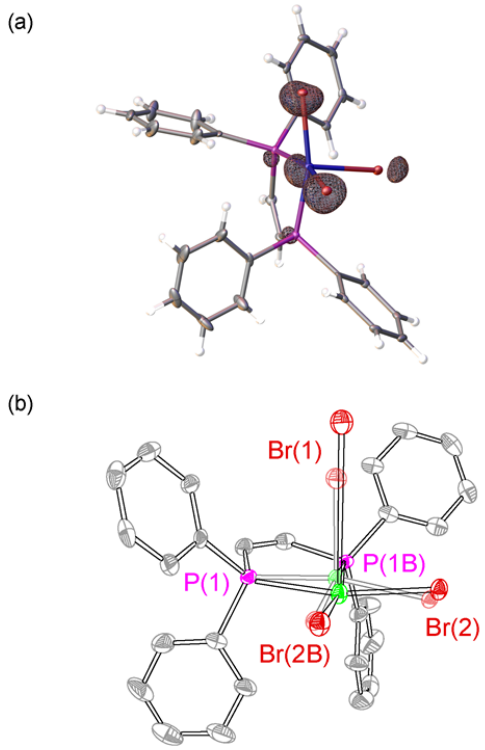

Figure 3.60. (a) Photodifference map obtained for complex **7f** irradiated with a 365 nm LED (5 mW at the crystal) at 15 K. (b) Thermal ellipsoid plot showing the dark structure (faded) and the irradiated structure (bold) generated from **7f**. This plot was generated by normalizing the positions of the P centers in the dark and irradiated structures to focus on the relative motions of the Br ligand. H-atoms and solvent molecules are omitted for clarity. Ellipsoids are drawn at 50% probability.

the dark. The difference map (Figure 3.60 (a)), generated from diffraction data collected prior to and during irradiation (λ = 365 nm) shows the presence of a photoinduced structure populated at 3.5(2)% of the crystal (Figure 3.60 (a)). The photodifference map shows that the apical Ni–Br bond elongates from 2.464(2) to 3.70(4) Å, whereas two basal Ni–Br bonds are crystallographically unchanged (2.3615(7) (dark), and 2.35(5) (photoinduced), indicating apical halide is photochemically labile. The observed structural changes are neither photochemically nor thermally reversible, which is consistent with the photoinduced component arising from irreversible Ni–X scission in the solid state. Crystallinity of the samples is destroyed upon further photolysis, also consistent with the operation of a chemically irreversible solid-state

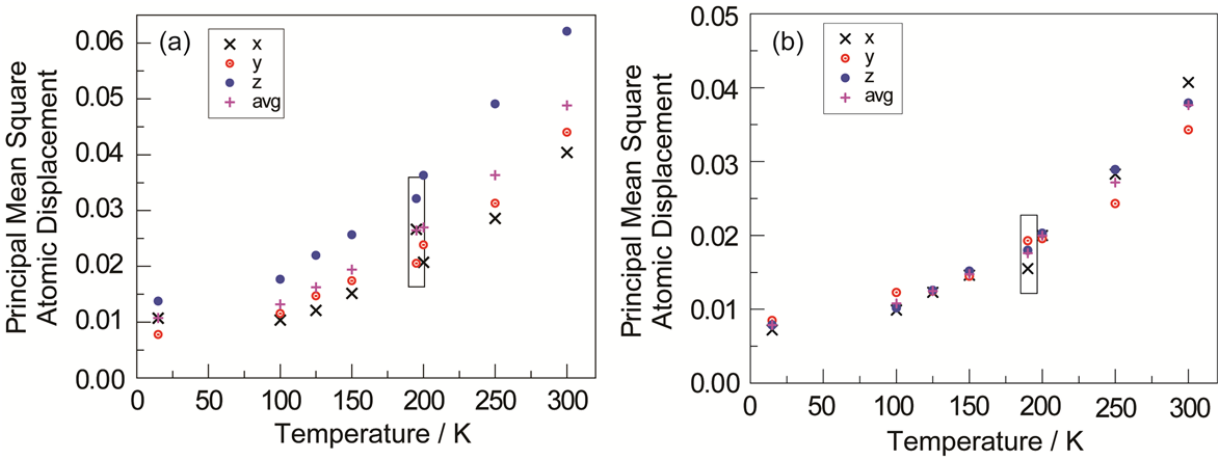

Figure 3.61. Principal mean square atomic displacements (U) for complex **7f** as a function of temperature plotted for (a) apical bromide atom (b) phosphorous atoms in the ligands. Thermal parameters obtained during photocrystallography are highlighted in a box.

reaction. The metrical parameters of **7f** do not exhibit significant temperature dependence, confirming that the photodifference map arises from photochemical, not thermal M–X activation; [62] evaluation of the extent of laser heating on the crystal samples is provided in Figure 3.61.

3.6 Solution-Phase Calorimetry

The chlorine photoelimination enthalpies were determined by solution calorimetry, which was accomplished by addition of $PhICl_2$ as a solid to solutions of $Ni(II)Cl_2(LL)$ complexes (**9**) (Figure 3.62). The enthalpy for chlorination was obtained based on the equations:

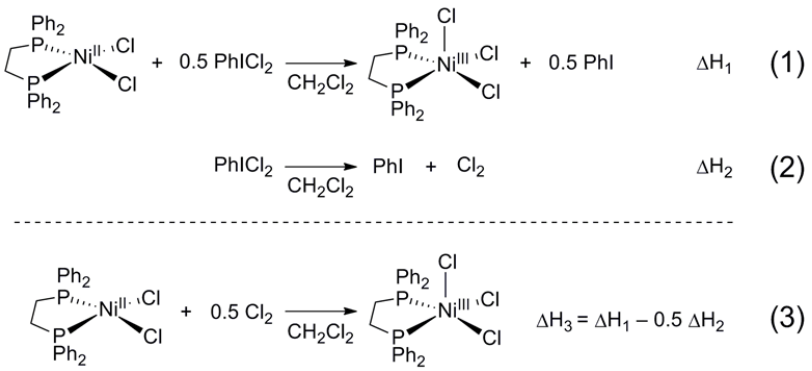

The heat of reaction was measured for Eq. (1). The known heat of reaction of chlorine release from solid $PhICl_2$ was corrected for the enthalpy of solution of the solid $PhICl_2$, which was measured separately. The enthalpies of Cl_2 addition to compounds of **9**, listed in Table 3, were obtained from Eq. (3) and are the average of three independent measurements. All complexes confront endothermic barriers to halogen elimination with complex **7a** possessing significant energy storage capacity for the Cl_2 photoelimination reaction.

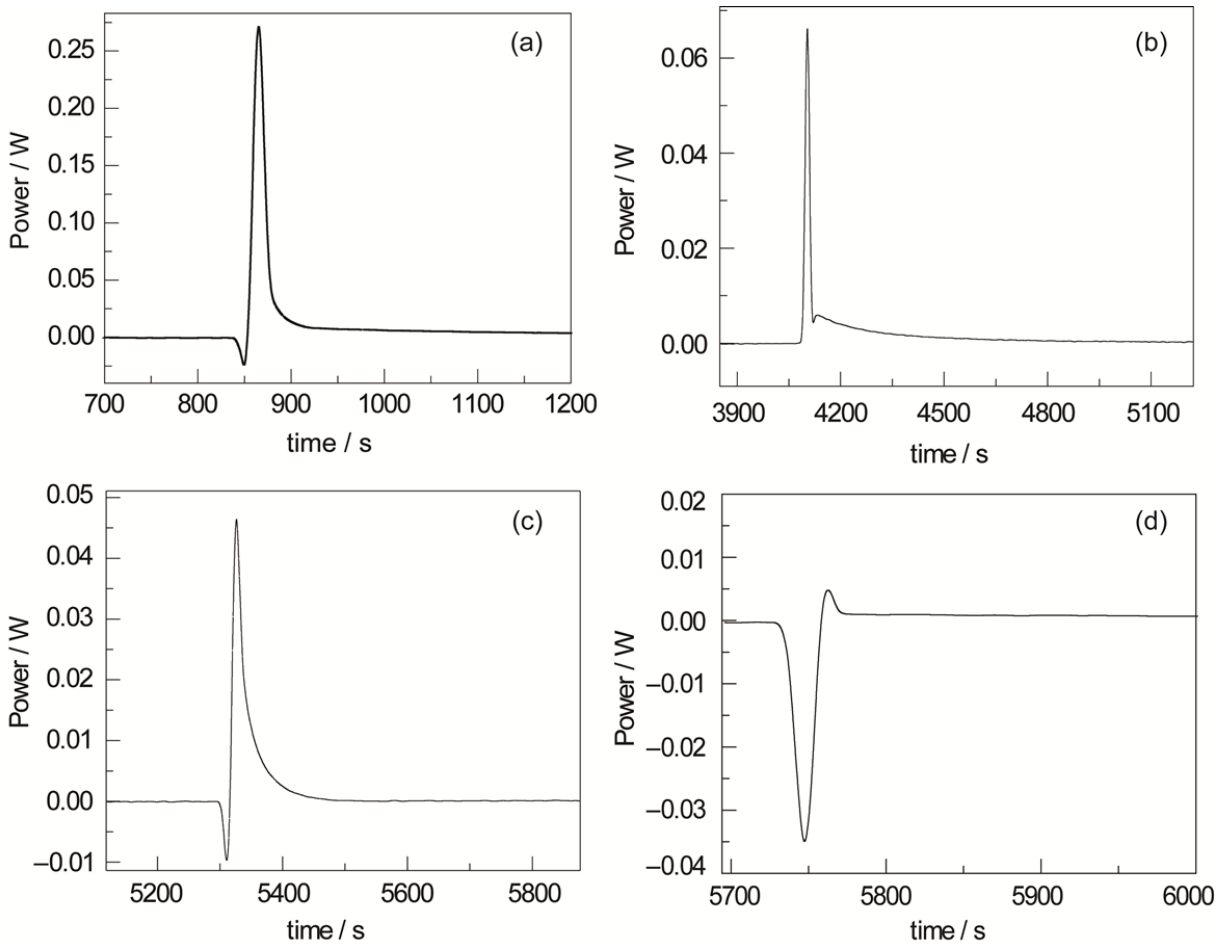

Figure 3.62. Thermogram for reaction of (a) $NiCl_2$(dppe) (**9a**) (b) $NiCl_2$(dppey) (**9b**) (c) $NiCl_2$(dppb) (**9c**) (d) $NiCl_2$(dcpe) (**9d**) and $PhICl_2$ in CH_2Cl_2.

Table 3.6. Reaction enthalpy for chlorination of Ni(II) complexes.

$$NiCl_2(LL) + 0.5\ Cl_2 \longrightarrow NiCl_3(LL)$$

LL	ΔH (kcal mol^{-1})
dppe	–23.7
dppey	–20.8
dppb	–16.7
dcpe	–7.0

3.7 Computational Results

DFT geometry optimization of **7f** was performed as described in the Experimental section. The DFT-based ground state wavefunction is consistent with a Ni(III) center and an unpaired electron/hole residing in an antibonding Ni d_{z2}/halide p_z orbital, which results in a delocalized metal-to-apical-ligand bonding description as indicated by EPR spectroscopy (e.g., DFT-based spin densities of ~0.81 and ~0.23 for Ni(III) and the apical halide, respectively, for **7f**). Additionally, the β-Mayer bond order (MBO) for this complex is calculated to be ~0.44. To gain insight into the nature of the excited states of the Ni(III) compounds, TD-DFT calculations were performed using the optimized geometry of **7f**. The calculated absorption spectrum largely reproduces the spectral features observed in the experimental data (Figure 3.63 and Table 3.7). On the basis of the TD-DFT results, the lower energy absorption feature (~575 nm) arises from an apical Br(p(π))→ Ni(d_{x2-y2}) LMCT, while the higher energy absorption feature (~400–500 nm) largely consists of intense phenyl ring π → Ni(d_{x2-y2}) charge transfer (CT) transitions and weak basal Br(p(π)) → Ni(d_{x2-y2}) LMCTs. These assignments are consistent with the photochemical results in that the lower energy CT feature decays upon irradiation while the higher energy feature persists. Interestingly, an apical Br(p(σ)) → Ni(d_{z2}) LMCT is predicted within the higher energy absorption envelope (~440 nm, state 7, Figure 3.63 and Table 3.7).

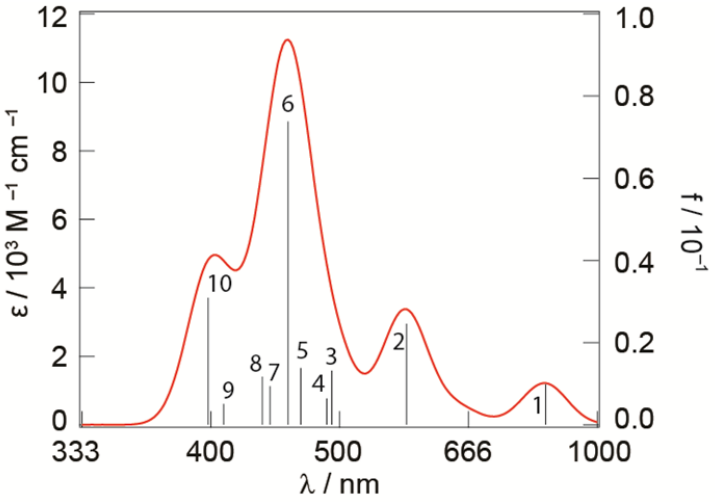

Figure 3.63. Relevant oscillators (oscillator strength > 0.02; solid black bars) from TD–DFT calculations for complex $NiBr_3$(dppey) (**7f**) with simulated absorption spectrum overlaid (solid red line).

Table 3.7. TD-DFT calculated transitions for $NiBr_3$(dppey) (**7f**), (DCM = CH_2Cl_2).

State	λ/nm	Energy/eV	f^a	Contributions	Assignment
1	833	1.48	0.0099	170A → 172A (78%) 168A → 172A (10%)	α(pσ(ap)) → α(d_{x2-y2})
2	575	2.16	0.0246	169B → 172B (29%) 166A → 172A (17%) 168A → 172A (14%)	β(pπ(ap)) → β(d_{x2-y2})
3	493	2.51	0.0132	165A → 172A (48%) 170B → 172B (15%)	α(Phπ) → α((d_{x2-y2})
4	488	2.55	0.0064	157A → 172A (26%) 169B → 172B (21%)	α(pπ(dis)) → α(d_{x2-y2})
5	465	2.67	0.0138	164A → 172A (29%) 164B → 171B (19%) 157A → 172A (12%)	α(Phπ) → α(d_{x2-y2})
6	455	2.73	0.0738	164A → 172A (46%) 164B → 171B (23%)	α(Phπ) → α(d_{x2-y2})
7	440	2.82	0.0096	156B → 171B (30%) 152B → 171B (12%) 165B → 171B (12%)	β(pσ(ap)) → β(d_{z2})
8	435	2.85	0.0117	157A → 172A (18%) 159A → 172A (14%) 160A → 172B (13%) 165B → 172B (11%)	α(pπ (dis)) → α(d_{x2-y2}) + α(Phπ) → α(d_{x2-y2})
9	408	3.04	0.0055	158A → 172A (45%) 164B → 172B (12%)	α(Phπ) → α(d_{x2-y2})

10	398	3.11	0.0316	158A → 172A (16%) 164B → 172B (10%)	α(Phπ) → α($d_{x^2-y^2}$)

[a] Calculated transitions with oscillator strengths greater than 0.0050 are listed.

In a molecular orbital picture, transitions to the unoccupied Ni(d_{z2}) orbital (i.e., the β-LUMO) eliminate any formal Ni-apical halide bond order and would be expected to result in significant destabilization. We therefore explored the nature of the ground and excited state PES for elongation of the Ni–apical halide bond for **7f**. The CH_2Cl_2 corrected PESs for Ni–Br bond loss are given in Figure 3.64, in which the TD-DFT calculated σ → σ* excited state energy is plotted as a function of ligand-metal bond distance. Note that this transition involves excitation of a β p_z/d_{z2} bonding electron to the β p_z/d_{z2} anti-bonding MO, β156 and β171 in Figures 3.65–66. This LMCT state is clearly dissociative,[63] as can be seen from the TD-DFT ground and excited state surfaces, resulting in the formation of a one-electron reduced Ni(II) S=0 metal center and a Br radical.

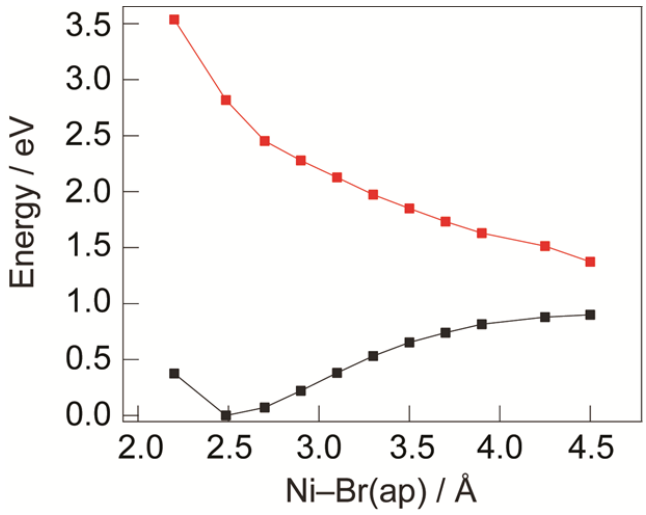

Figure 3.64. CH_2Cl_2 corrected PESs (S = ½) of **7f** as a function of Ni–Br(ap) bond cleavage. Ground state energies are given as black squares, and the energies of the β(pσ(Br(ap))) → β(Ni(d(z^2))) LMCT excited state (7 in Table 3.7) are given as red squares. Note that the PES of this σ → σ* excited state is repulsive and can, upon excitation, result in homolytic cleavage of the Ni(III)–Br bond to a Br radical and a low-spin, S = 0 Ni(II) metal center.

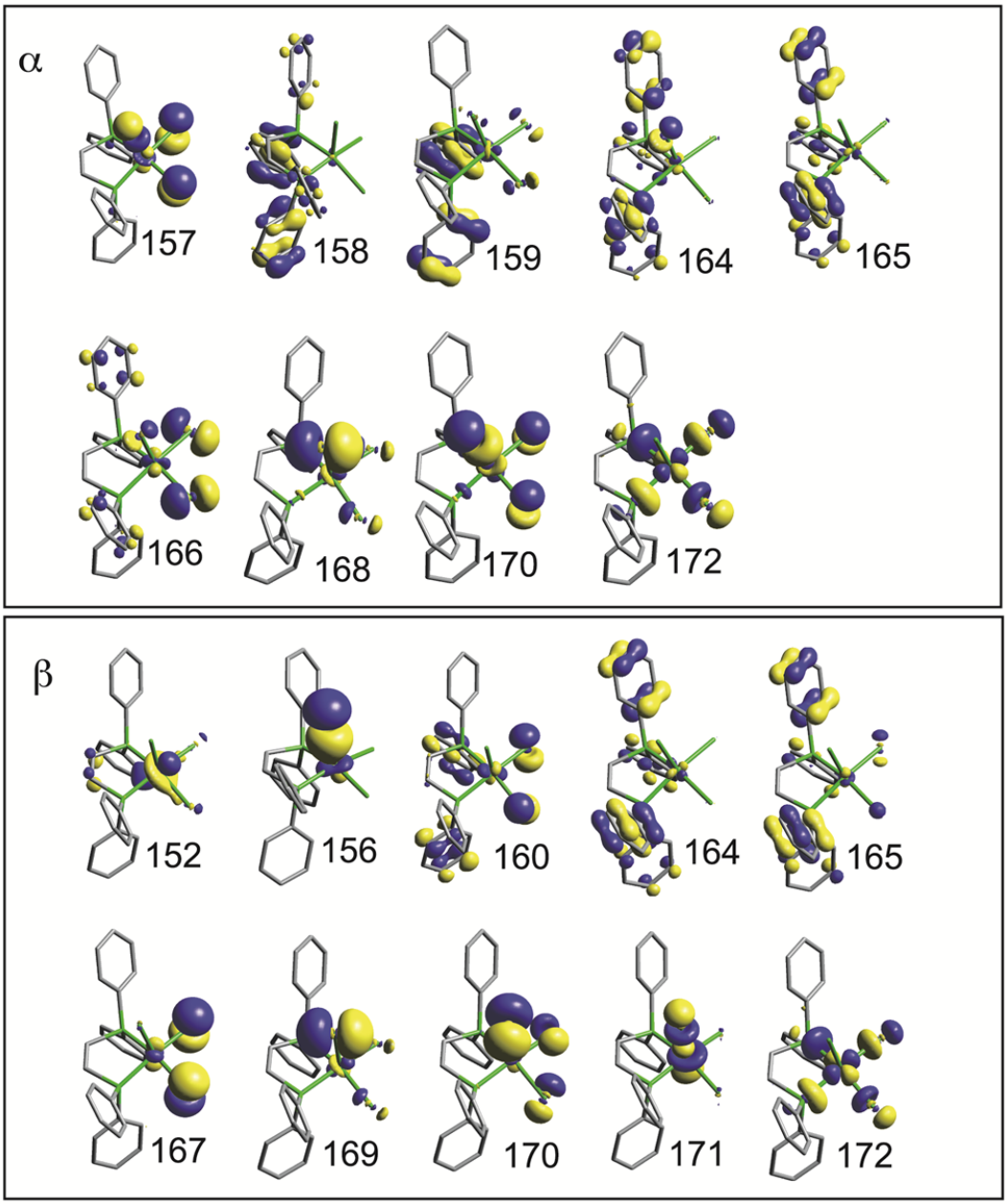

Figure 3.65. Representative molecular orbitals of $NiBr_3$(dppey) (**7f**). Note that state 7 above consists largely of β156 → β171.

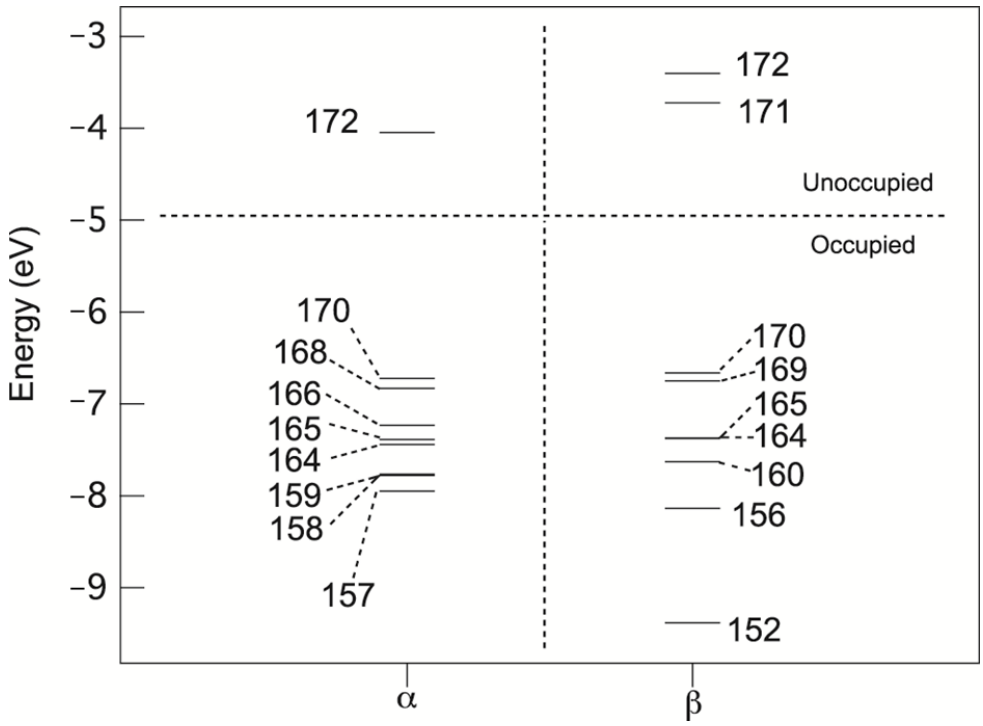

Figure 3.66. Energy levels of frontier molecular orbitals of $NiBr_3$(dppey) (**7f**).

In addition to the PES, we have geometry optimized the resulting Cl-atom|aromatic charge transfer intermediate for both **8a** and **8e**. DFT frequency calculations indicate local energetic minima for both complexes, which is consistent with the TA spectroscopic results and previous reports of the energetics of halogen|arene complexes.[64] The preferred halogen atom|arene interaction is roughly η_1 (C–X distances of ~2.6 and 2.9 Å for the Cl and Br radicals, respectively). Mulliken spin densities are consistent with significant charge transfer, i.e., a closed-shell Ni(II) ion associated to a halide atoms (e.g., spin densities of 0.00, 0.66, and 0.74 for Ni(II), Cl and Br, respectively).

The TD-DFT calculated absorption spectra are given in Figure 3.67. The absorption spectra are consistent with experimental observations (Figure 3.43); there are relatively intense charge transfer features predicted at ~500 and ~550 nm for the Cl and Br adducts, respectively (Figure 3.67). The parentage of these transitions arises from a filled, bonding

halide(p)|arene(p(π)) donor orbitals and the β-LUMO, which is an anti-bonding halide(p)|arene(p(π)) molecular orbital (Figure 3.68 illustrates representative orbital contours).

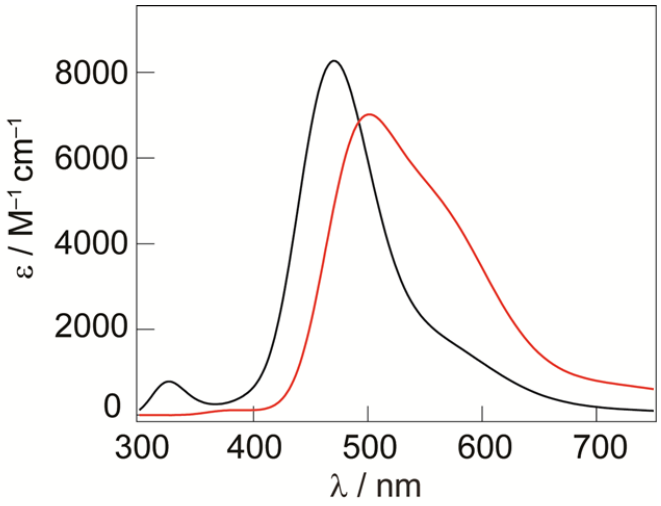

Figure 3.67. Computational results of the charge transfer transitions of NiX_3(dppey) complexes. Gas phase TD-DFT calculated absorption spectra for **8b** (—, black) and **8f** (—, red).

The amount of total electron donation from the phosphine ligand to Ni(III) has been explored using CDA[65] as described in the Experimental section. The values have been computed for all $NiCl_3$(LL) and $NiBr_3$(LL) complexes and are compared to the quantum yields in Fig. 3.69. In general, a positive correlation between Φ_p and electron donation of the phosphine to Ni(III) is observed for $NiCl_3$(LL) and $NiBr_3$(LL) complexes.

It is interesting to note that increased electron donation to Ni(III) should result in a lower Ni(III/II) reduction potential, which would oppose homolytic cleavage of the Ni(III)–X bond. This difference in donation should be reflected in the solution-phase calorimetry measurements. Indeed, the complexes with larger endothermic barriers to halogen elimination generally have higher quantum yields (e.g., **7a**: 23.7 kcal/mol and Φ_p = 0.764 versus **7d**: 7.0 kcal/mol and Φ_p = 0.201). Thus, experiment and theory together emphasize the dual contributions of the secondary

coordination sphere and the excited state relaxation/decay pathways in directing the outcome of the photochemical reactivity.

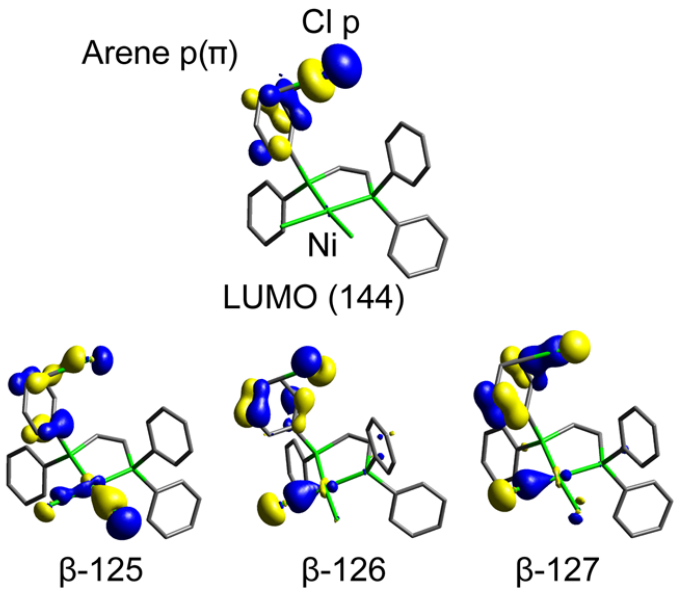

Figure 3.68. Computational results on the $NiCl_3$(dppey) CT complexes. Major molecular orbitals involved in the formation of the absorption features observed around 500 nm for the Cl-based CT complexes. Donor orbitals are along the bottom, and the acceptor β-LUMO is above.

Figure 3.70 illustrates a halogen extrusion mechanism that is consistent with the spectroscopic, photochemical, photocrystallographic and computational experiments. Photon absorption by Ni(III) trihalide complexes **7** provides access to a dissociative LMCT excited state. Participation of ligand-based aromatic substituents via arene-to-chlorine-atom charge transfer stabilizes the photodissociated chlorine atom in the secondary coordination sphere of the metal complexes (intermediate **8**). Steady-state photocrystallography experiments indicate that the apical halide, which displays a substantially longer M–X bond than the basal halide ligands, is selectively eliminated. Intermediate **8** displays a microsecond lifetime, which we propose serves to provide sufficient time to participate in productive elimination chemistry and provides a

mechanism to overcome the short excited state lifetimes of *3d* metal complexes. In solution-phase experiments, the photodissociated chlorine atom is likely intercepted by solvent via H-atom abstraction, while in the solid state in the absence of chemical traps, dimerization affords Cl_2.

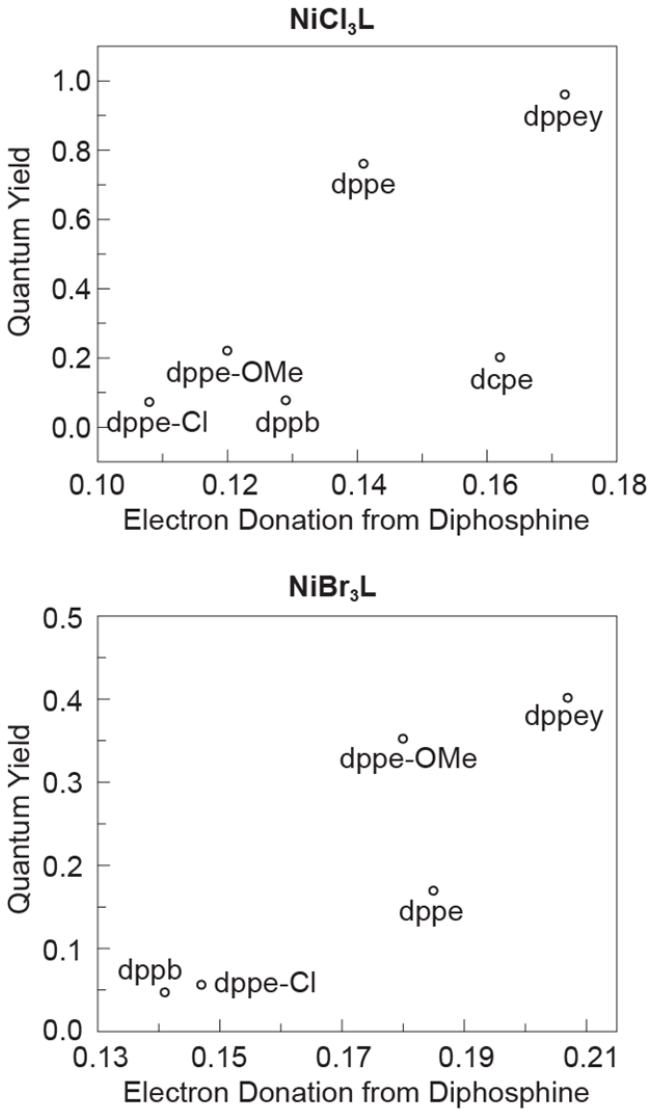

Figure 3.69. Plot of experimental quantum yield versus computed electron donation from the diphosphine backbone to the NiX_3 core.

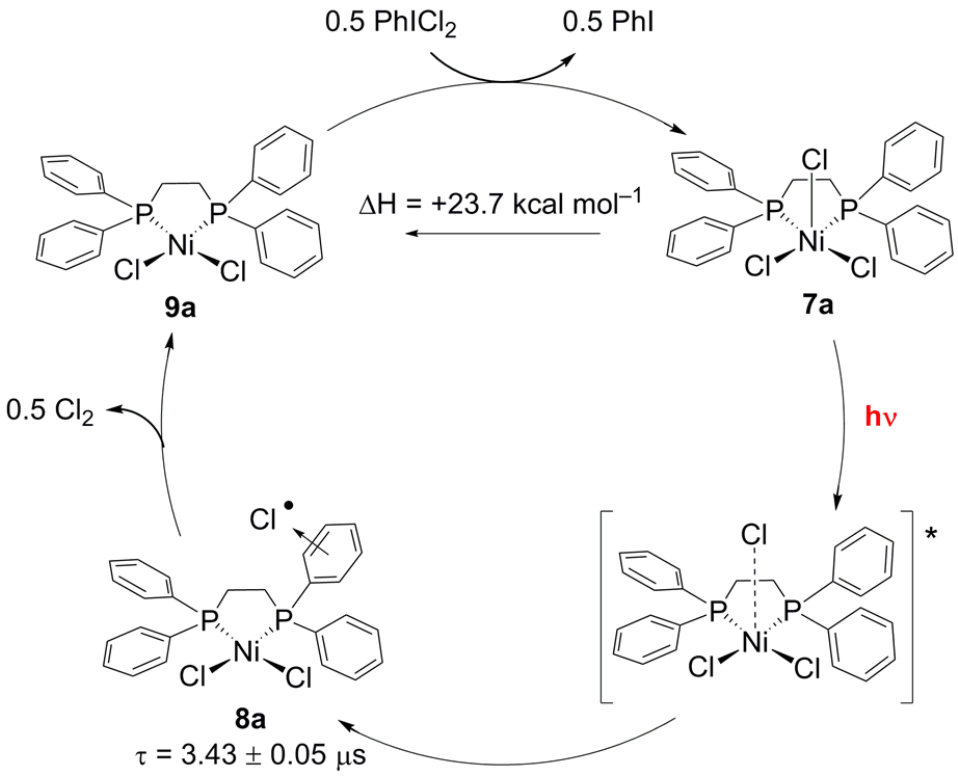

Figure 3.70. Proposed photoreduction of complex **7a** proceeds via a LMCT excited state to furnish the arene-to-Cl charge transfer intermediate **8a**.

3.8 Discussion

The significant oxidizing power of Ni(III) suggested the possibility of developing a halogen elimination photochemistry based on Ni(III) complexes and thus the possibility of developing HX-splitting energy storing cycles. To this end, we targeted $NiX_3(LL)$ complexes (X = Cl, Br; LL = bidentate phosphine) (**7**), which are furnished from the oxidation of corresponding Ni(II) square planar $NiX_2(LL)$ complexes (**9**) with halogen sources. All of the Ni(III) compounds are paramagnetic and possess a square pyramidal primary coordination sphere (Figure 3.16).

Steady-state photolysis of Ni(III) complexes **7** results in their clean conversion to Ni(II) complexes **9**. The solution photochemistry is characterized by tightly anchored isosbestic points, and both UV-vis and ^{31}P NMR indicate that the photoelimination proceeds cleanly (Figures. 3.14–21). All of the complexes demonstrate an efficient halogen elimination photochemistry with quantum yields reaching 96%. In general, Cl_2 photoelimination proceeds at higher quantum efficiencies than Br_2 elimination from homologous complexes (Table 3.5). The origin of this difference in efficiencies between Cl and Br complexes is unclear and under current investigation. In solution, halogen is trapped by H-atom abstraction from solvent and consequently the photoevolved halogen equivalents are not observed.[66,67] The need to trap the eliminated halogen is circumvented when the photochemistry is carried out in the solid state. Solid-state photolysis of thin-films of Ni(III) complexes **7** affords the Ni(II) complexes **9** and molecular halogen, which has been isolated, characterized, and quantified. Solution-phase calorimetry indicates that halogen addition to Ni(II) is substantially exothermic (Table 3.6), and thus photoelimination from $NiX_3(LL)$ compounds represents an energy-storing transformation.

Preliminary transient spectroscopic experiments suggested that halogen photoelimination from $NiCl_3$(dppe) was assisted by a secondary coordination sphere effect involving an arene-to-chlorine-radical charge transfer intermediate. The generality of the proposed intermediate has now been established for the class of Ni(III)X_3(LL) complexes. TA spectra of the intermediate generated by $NiCl_3$(LL) photoexcitation display two distinct spectral features: an absorption in the UV region and a broad absorption in the visible region. The photointermediate observed in the TA spectrum of complexes with unsubstituted aryl phosphines exhibits a UV feature at ~350 nm and a band in the visible region at λ_{max} ~ 550 nm. As shown in Figure 3.42, the spectrum of the intermediates is consistent with that of halogen|aryl CT complexes, though it is red-shifted as compared to simple CT adducts owing to electron donation from the phosphine group. The CT absorption band further red-shifts with the introduction of donor groups on the phenyl phosphine. The TA intermediate of **7a-Cl** and **7a-OMe** (Figures 3.59 (b) and (c)) shifts to 540 nm and 600 nm respectively, consistent with the observed shift of CT bands in arene|Br complexes resulting from aryl substitution with electron donors.[68,]

To probe the influence of aromatic residues on the halogen elimination photochemistry, the phenyl groups of the dppe were replaced with cyclohexyl groups. Complex **7d** participates in solution-phase halogen elimination but with considerably attenuated quantum yield. A transient intermediate of **7d** is observed but it is weak and considerably blue-shifted from **7a**. Halogen atom adducts of cyclohexane are known and as observed here, the signal is weak and the charge transfer band is blue shifted (λ_{max} = 435 nm) due to an increase in ionization energy of cyclohexane as compared to an aromatic group.[69] Due to the predicted blue shift coupled with the clean conversion to starting material upon photolysis, we believe that the intermediate observed in the TA spectrum of **7d** is also a Cl-radical complex, **8d**. Upon the addition of

increasing concentrations of benzene, the quantum yield approaches an asymptotic value of ~60%. We believe that the enhancement in quantum yield is due to specific radical-π interactions, because addition of CCl_4 (similar dielectric to benzene) did not have a measurable influence on Φ_p. When the TA spectrum of complex **7d** is measured in the presence of 30% benzene, the spectral feature exhibits a 15 nm bathochromic shift (λ_{max} = 450 nm) and the rate of decay of the intermediate are essentially unchanged (Figures. 3.52–3.55). The enhancement in Φ_p upon the addition of benzene without a change in the time evolution of the intermediate suggests that benzene is enhancing the initial dissociation of the chlorine radical from the nickel center, but does not react at a competitive rate with generated intermediate. The observed decay rate of ~10^5 s^{-1} is considerably slower than the dissociation rates of ~10^6 s^{-1} observed for Cl-benzene adducts.[59] Therefore, only a small and undetectable concentration of Cl-benzene complex would be formed during the experiment.

The computed excited state PES of **7f** (Figure 3.64) provides further support for rapid halide radical elimination. The excited state PESs are dissociative in both gas phase and dielectric corrected (CH_2Cl_2) calculations suggesting a rapid dissociation of the halide radical from the photoreduced Ni center.[70,71] The fate of the halide radical is then dictated by its subsequent back-reaction or sequestration by solvent. Utilization of secondary coordination interactions with arene ligands appears to provide an effective pathway to guide the halogen atom out of the primary coordination sphere, thereby preventing the energetically favored back-reaction. For the resulting charge transfer intermediate, the nature of the dominant transitions observed in the TA spectra are predicted by TD-DFT calculations as arene to halide charge transfer, consistent with the spectral shift of the absorptions upon perturbation of the arene ring by the addition of methoxy groups.

Examination of the relationship of Φ_p with both reaction enthalpy and super hyperfine coupling reveals that Φ_p is not necessarily correlated with reaction thermodynamics or M–L covalency (Tables 3.6 and 3.2, respectively). However, complexes with larger endothermic barriers do tend to show higher quantum yields (Tables 3.5 and 3.6). Similarly, a positive correlation between ligand donor strength (as determined using CDA analyses) and Φ_p was observed. Generally, the increased Φ_p upon increased endothermicity of ligand loss and electron donation suggests that the important factors governing Φ_p derive from the secondary coordination sphere as well as the relative rates of the various decay pathways of the dissociative electronic excited state. Nonradiative decay pathways have been shown to be sensitive to changes in ligand donor ability[72,73] and appear to be suppressed in the $NiX_3(LL)$ complexes studied by electron rich ligands. These contributions will be the subject of future ultrafast time-resolved spectroscopic investigations.

3.9 Conclusions

Authentic halogen photoelimination from mononuclear Ni(III) complexes has been achieved with visible light. The photoreaction is substantially endothermic; calorimetry experiments have established chlorine elimination stores up to 23.7 kcal mol^{-1}. Photochemical, transient spectroscopic and computational results of the $NiX_3(LL)$ complexes point to the formation of a relatively long-lived (3 μs) transient species derived from a dissociative ligand-to-metal charge transfer (LMCT) excited state. The photodissociative Ni(III)–halogen intermediate is stabilized by the interaction of the photoeliminating halogen atom with an aryl ring of the secondary coordination sphere. The efficiency of the photoelimination can be directly traced to the stability of the charger transfer halogen|aryl adduct. Interactions with aromatic groups of a

coordinating ligand offers a means to suppress rapid back reactions and increase the quantum yield for halogen elimination, which is the critical step in designing photocatalytic HX splitting cycles.

3.10 Experimental Details

3.10.1 Materials and Synthetic Details

All reactions were carried out in an N_2-filled glovebox. Anhydrous solvents were obtained from drying columns and stored over activated molecular sieves.[74] $NiCl_2$(dme) (dme = 1,2-dimethoxyethane), $NiBr_2$(dme), dppb (dppb = bis(diphenylphosphino)benzene), dppey (dppey = *cis*-bis(diphenylphos-phino)ethylene), and $NiCl_2$(dppe) (dppe = 1,2-bis(diphenylphosphino)ethane) were obtained from Strem Chemicals. Bromine, dppe, and dcpe (dcpe = 1,2-bis(dicylohexylphosphino)ethane) were obtained from Sigma Aldrich. $PhICl_2$,[75] dppe-OMe (dppe-OMe = 1,2-*bis*(di-4-methoxyphenyl)phosphine)ethane), and dppe-Cl (dppe-Cl = 1,2-*bis*(di-4-chlorophenyl)phosphine)ethane) were prepared according to literature procedures.[76] Ni(III) complexes (**7**) and Ni(II)complexes (**9**) that are discussed herein are enumerated based on the halide (X) and supporting phosphine (LL) ligand: X = Cl, LL = dppe, **7a**, **9a**; X = Cl, LL = dppe-OMe: **7a-OMe**, **9a-OMe**; X = Cl, LL = dppe-Cl: **7a-Cl**, **9a-Cl**; X = Cl, LL = dppey: **7b**, **9b**; X = Cl, LL = dppb: **7c**, **9c**; X = Cl, LL = dcpe: **7d**, **9d**; X = Br, LL = dppe: **7e**, **9e**; X = Br, LL = dppe-Cl: **7e-Cl**, **9e-Cl**; X = Br, LL = dppe-OMe: **7e-OMe**, **9e-OMe**; X = Br, LL = dppey: **7f**, **9f**; X = Br, LL = dppb: **7g**, **9g**. Complexes **7a**,[77] **7b**,[77] **7c**,[77] , **7e**,[77] **7f**,[77] **7g**,[77] **9a**,[78] **9a-OMe**,[76] **9b**,[79] **9c**,[80] **9d**,[81] **9e**,[78] **9e-OMe**,[82] and **9f**[83] were prepared by according to literature procedures.

Preparation of Ni(II) Dihalide Complexes (NiX_3(LL)). Ni(II) complexes $NiCl_2$(dppe-Cl) (9a-Cl), $NiBr_2$(dppe-Cl) (9e-Cl), and $NiBr_2$(dppb) (9g) were prepared by sequential treatment of NiX_2(dme) (X = Cl and Br) with an equimolar amount of the appropriate phosphine in THF, precipitation with pentane, and isolation by vacuum filtration.

Preparation of Ni(III) Trichloride Complexes ($NiCl_3$(LL)). The following preparation of complex **7a-OMe** is representative of other members of this family. In a scintillation vial was added 60 mg (0.093 mmol) of $NiCl_2$(dppe-OMe) (**9a-OMe**) followed by 2 mL CH_3CN. In a separate vial was added 15.3 mg (0.055 mmol, 0.6 equiv) of $PhICl_2$ and 2 mL CH_3CN. $PhICl_2$ was added dropwise to the solution of **9a-OMe** during which time a color change from orange to green was observed. The solution was stirred with the exclusion of light for 5 min at 23 °C at which time the solvent was removed in vacuo to yield a green solid. The residue was washed with pentane and dried in vacuo to afford 55 mg of the title complex as a green solid (86% yield). EPR (1:1 $CH_3CN/PhCH_3$) g-value: $g_1 = 2.258$; $g_2 = 2.169$; $g_3 = 2.017$. $\mu_{eff} = 2.17$ μB. Complex **7a-Cl** was prepared analogously: green solid; 81% yield. EPR (1:1 $CH_3CN/PhCH_3$) g-value: $g_1 = 2.241$; $g_2 = 2.165$; $g_3 = 2.01$. $\mu_{eff} = 2.13$ μB. Complex $NiCl_3$(dcpe) (**7d**) was prepared analogously except CH_2Cl_2 was used as solvent and Et_2O was used to wash: green solid; 60% yield. EPR (1:1 $CH_3CN/PhCH_3$) g-value: $g_1 = 2.26$; $g_2 = 2.28$; $g_3 = 2.01$. $\mu_{eff} = 2.10$ μB.

Preparation of Ni(III) Tribromide Complexes ($NiBr_3$(LL)). The following preparation of complex **7e-OMe** is representative of other members of this family. A sample of $NiBr_2$(dppe-OMe) (**9e-OMe**) (60 mg, 0.081 mmol) was dissolved in 2 mL of CCl_4. A solution of 0.194 M Br_2 (206μL, 0.041 mmol, 0.5 equiv) in CH_2Cl_2 was added dropwise to give a black solution, which was stirred at 23 °C for 30 min in the dark. The volatiles were removed in vacuo to give the product as a dark brown powder. The residue was washed with pentane and dried in vacuo

(80% Yield). EPR (1:1 CH_2Cl_2/$PhCH_3$) g-value: g_1 = 2.208; g_2 = 2.208; g_3 = 2.025. μ_{eff} = 1.95 μB. Complex **7e-Cl** was prepared analogously: dark brown solid; 77% yield. EPR (1:1 CH_3CN/$PhCH_3$) g-value: g_1 = 2.201; g_2 = 2.191; g_3 = 2.025. μ_{eff} = 1.90 μB.

3.10.2 Physical Measurements

NMR spectra were recorded at the Harvard University Department of Chemistry and Chemical Biology NMR facility on a Varian Unity / Inova 600 spectrometer operating at 600 MHz for ^1H acquisitions and 162 MHz for $^{31}P\{^1H\}$ acquisitions. NMR chemical shifts are reported in ppm with the residual solvent resonance as internal standard. $^{31}P\{^1H\}$ NMR chemical shifts were referenced to an external 85% H_3PO_4 standard. Solution magnetic moments were determined using the Evans method in CH_3CN or CH_2Cl_2 and measured using ^{19}F NMR (hexafluorobenzene added); diamagnetic corrections were estimated from Pascal constants.[84] UV-vis spectra were recorded at 293 K in quartz cuvettes on a Spectral Instruments 400 series diode array blanked against the appropriate solvent. EPR spectra were recorded on a Bruker ELEXIS E-500 or E-580 spectrometer equipped with a Bruker ER4122 SHQE-W1 resonator and an Oxford Instruments ESR 900 cryostat. EPR spectra were simulated using EasySpin 4.5.5 to obtain g-values and hyperfine constants. Isotopic abundance was accounted for by averaging the simulated spectra of all naturally occurring isotopes scaled by their natural abundance. The hyperfine coupling constants presented are that of the most abundant isotope.[85] Electrochemical experiment was recorded at ambient temperature in a glove box with a CH Instrument 760D or 730C potentiostat. Cyclic voltammetry of a 1 mM CH_3CN solution of Ni complex **7a** was measured with a scan rate of 100 mV/s in the dark (0.1 M $^nBu_4PF_6$ as supporting electrolyte). A

glassy carbon working electrode, BASi Ag/AgCl reference, and Pt wire counter electrode were used.

Solution Calorimetry Measurements. *Representative Procedure.* In the glove box, a solution of 0.488 g (0.79 mmol) of $NiBr_2$(dppe) (**9e**) in 100 mL of anhydrous CH_2Cl_2 was prepared. This solution was transferred to a glass cell for the Thermometric 2225 Precision Solution Calorimeter, which was equipped with an ampule-breaking rod. A small glass ampule containing 0.031g Br_2 (0.194 mmol) was added, sealed, and loaded into the calorimeter. Following temperature equilibration (achieved standard deviation of 2 μK after 2 h), the reaction was initiated by breaking the ampoule and rotating the calorimeter to insure complete mixing. Electrical calibrations were run before and after breaking the ampoule. In the case of chloride Ni complexes, the enthalpy of interest was obtained based on the equations described in section 3.6. Measured data based on the reaction of the solid $PhICl_2$ was corrected for the enthalpy of solution of the solid $PhICl_2$, which was measured separately. The enthalpy of solution of iodobenzene and 0.194 M Br_2 in CH_2Cl_2 were also measured for the purposes of a solvation correction. Reported data is the average of three independent measurements.

Photochemistry. Steady-state photochemical reactions were performed using a 1000 W high-pressure Hg/Xe arc lamp (Oriel) and the beam was passed through a water-jacketed filter holder containing the appropriate long-pass filter, an iris and a collimating lens. Samples were photolyzed in a constant-temperature circulating water bath. Photochemical quantum yields (Φ_p) were determined using 370 nm monochromatic light, which was generated with a 370 nm Hg line filter on a 1000 W Hg/Xe arc lamp. Potassium ferrioxalate solution (0.006M) was used as a chemical actinometer.[86] The photo flux was determined from the average of actinometric measurements before and after irradiation of the reaction samples. Each Φ_p determination was

carried out in triplicate on solutions of the complex in CH_2Cl_2 or CH_3CN with benzene. Nanosecond resolved transient absorption (TA) spectroscopy experiments were performed using a system described previously,[87] but with an iHR320 spectrometer. The 355 nm laser pulses (8-10 ns at FWHM) used for excitation were generated using the third harmonic of a 10 Hz Nd:YAG pulsed laser. The white-light continuum was provided by a Xe-arc lamp set to 2.0 ms pulses with 30 A current. A 250 nm or 1000 nm blaze grating (300 grooves/mm) was used for spectral acquisitions centered below 500 nm and above 500 nm, respectively. For full spectrum TA acquisitions, the entrance slit was set to 0.16 mm (3.0 nm resolution) and the gate time for the CCD was 100 ns to 200 ns. For single-wavelength kinetics experiments, the entrance and exit slits were set to 3 nm resolution, and 1.0 kV bias was used for the photomultiplier tube (PMT). PMT outputs were collected and averaged with a 1 GHz oscilloscope (LeCroy 9384CM). The full spectra are averages of 50-200 four-spectrum sequences and the single-wavelength kinetics traces are averages of 500-1000 acquisitions. CH_3CN solutions of complexes **7a**–**7d** were prepared in 100 mL Schlenk flasks in an N_2-filled glovebox. During TA acquisitions the solutions were flowed without recirculation through a 3-mm diameter, 1-cm path length flow cell (Starna, type 585.2) using a peristaltic pump and positive N_2 pressure. Solid-state photolysis experiments were carried out in an "H" shaped reactor custom made by James Glass of Hanover Massachusetts. Films of **7a** were deposited on the wall of one of the chambers by evaporation; samples of 10 to 40 mg were deposited from solutions in CH_2Cl_2. The reaction vessel was evacuated and the sample was then irradiated using a 350 nm long wave pass filter; the second side of the reaction vessel was cooled to 77 K during irradiation. The reactor was periodically rotated so as to present unphotolyzed **7a** to the incident light. After 10 h of irradiation, the two sides of the reactor were separated by closing a Teflon stopcock. Unreacted **7a** was recovered in

45% yield based on ^{1}H NMR spectrum. The liquid nitrogen cooled compartment of the reactor described above was connected to He carrier gas and an in-line mass spectrometer (Agilent Technologies 5975C Mass Selective Detector) and purged for 2 h before data collection. The mass spectrometer was operated in selective ion mode that monitored for 35 (Cl_2 fragment), 37 (Cl_2 fragment), 70 (Cl_2), 72 (Cl_2), 74 (Cl_2), and 44 (CO_2) amu. After a stable baseline was reached, the frozen compartment was rapidly warmed by immersion in water while MS data was collected in real-time. Data were collected until all gas levels returned to their baseline values. The percent abundance for 35 and 37 ions were computed using the following equations: $^{35}Cl = [2 \times {}^{35}Cl + {}^{72}Cl + 2 \times {}^{70}Cl]/[2 \times ({}^{35}Cl + {}^{37}Cl + {}^{70}Cl + {}^{72}Cl + {}^{74}Cl)]$; $^{37}Cl = [2 \times {}^{37}Cl + {}^{72}Cl + 2 \times {}^{74}Cl]/[2 \times ({}^{35}Cl + {}^{37}Cl + {}^{70}Cl + {}^{72}Cl + {}^{74}Cl)]$ (^{n}Cl = counts at n amu). The yield of evolved Cl_2 and Br_2 were quantified colorimetrically by trapping evolved halogen with *N,N*-diethyl-1,4-phenylenediamine sulfate (DPD) to afford the pink radical cation $DPD^{\bullet+}$. Formation of $DPD^{\bullet+}$ was monitored by UV-vis spectroscopy and quantified against a standard curve obtained by addition of known amount of bromine to 5 mM DPD solution in water. As displayed in Figure 3.36, $DPD^{\bullet+}$ radical formation is linearly correlated to the concentration of bromine employed. When DPD was the limiting reagent in oxidation reaction, the amount of $DPD^{\bullet+}$ radical generated was the same for either Br_2 or Cl_2 as the oxidant. Evolved halogen from solid-state photolysis was obtained from the same standard concentration curve. A representative procedure for determining halogen photoevolution yields is as follows: Films of complex **7a** (50 mg) were deposited on the wall of one of the chambers in "H" shaped reactor by evaporation. 5 mM DPD solution in water was then placed in another chamber and the solution was frozen to 77 K while the entire reaction vessel was evacuated. After 12 h of irradiation, the two sides of the reactor were separated by closing a Teflon stopcock and thawing the frozen DPD solution. When

vacuum transferred halogens were completely dissolved in DPD solution, the UV-vis spectrum was taken to calculate the amounts of halogen evolved from photolysis.

X-Ray Crystallographic Details. Single crystals of **7c** were obtained from a CH_2Cl_2 solution layered with toluene. Crystals of **7g** were obtained from a CH_2Cl_2/$PhCH_3$ solution of the complex layered with a small amount of Br_2 in CH_2Cl_2 solution. Diffraction data were collected either on a Bruker three-circle platform goniometer equipped with an Apex II CCD and an Oxford cryostream cooling device (100 K) with radiation from a graphite fine focus sealed tube Mo Kα (0.71073 Å) source or on a vertically mounted Bruker D8 three-circle platform goniometer equipped with an Apex II CCD and an Oxford Diffraction Helijet cooling device (15 K) with synchrotron radiation (0.41328 Å) supplied to ChemMatCARS located at Advances Photon Source (APS), Argonne National Laboratory (ANL). Crystals were mounted on a glass fiber pin using Paratone N oil. Data was collected as a series of φ and/or ω scans. Data was integrated using SAINT and scaled with multi-scan absorption correction using SADABS.[88] The structures were solved by intrinsic phasing using SHELXT (Apex2 program suite v2014.1) and refined against F^2 on all data by full matrix least squares with SHELXL-97.[89] All non-H atoms were refined anisotropically. H atoms were placed at idealized positions and refined using a riding model. Crystal data and refinement statistics are summarized in Table 1 and thermal ellipsoid plots are collected in Fig. 4. X-ray crystal structures of **7c**, **7g**, **9c** and **9e** are available from the Cambridge Crystal Structure Database (1040260, 1040259, 1401868, and 1401864, respectively). Photocrystallography data was collected using 0.41328 Å radiation at 15 K (Oxford Diffraction Helijet) on a vertically mounted Bruker D8 three-circle platform goniometer equipped with an Apex II CCD at ChemMatCARS located at the Advanced Photon Source (APS), Argonne National Laboratory (ANL). Illumination was provided by a Thorlabs 365 nm

LED (M365L2) and was delivered to the sample via a 100 μm (i.d.) fiber optic. Dark structures were solved and refined as described above. For data sets obtained during irradiation, non-H atoms of the product were located in difference Fourier maps, calculated with coefficients F_0(irradiated) − F_0(dark), and then refined with constraints on the product molecule's atomic displacement parameters to the corresponding values of the reactant molecule (EADP instructions of SHELXL97). The percentage of the reactant in the crystal was treated as a variable in the refinements.

Computational Details. All DFT calculations were performed using the Gaussian 09, Revision D.01 software suite.[90] For all calculations, the B3LYP[91–93] hybrid exchange-correlation functional was used in combination with a split basis set (TZVP[94] for Ni, P, and Br; TZV[95] for C and H). Starting geometries for gas-phase optimization were obtained from crystallographic coordinates; frequency calculations were carried out to ensure structures represented energetic minima. Time-dependent DFT (TD-DFT) single point calculations were carried out on the gas-phase geometry optimized models using the same combination of functional and basis sets. Where used, solvation effects were included using the polarized continuum model (PCM). Ground and excited state potential energy surfaces (PESs) for metal-apical halide bond loss were constructed using constrained geometry optimizations coupled to subsequent TD-DFT calculations. Charge decomposition analyses (CDA) were carried out using the AOMix program (revision 6.82).[96] The degree of phosphine ligand donation was calculated using NiX_3 and phosphine ligands as fragments; the degree of phosphine ligand donation was calculated as the difference in total electron donation (sum of all occupied α and β molecular orbitals) from the phosphine ligand to NiX_3 and back-donation between NiX_3 and the phosphine ligand. Wavefunction contours were generated using the β-LUMO program.[97]

3.10.3 NMR data

Complexes **9b**[79] and **9f**[83] have been previously reported, but only $^{31}P\{^{1}H\}$ NMR data has been reported. Complexes **9c**[80] has been reported in the literature but neither ^{1}H or $^{31}P\{^{1}H\}$ NMR data have been reported.

$NiCl_2$(dppe-Cl) (**9a-Cl**): ^{1}H NMR (600 MHz, CD_2Cl_2) δ (ppm): 7.89 (m, 8H), 7.54 (d, $^{3}J_{HH}$ = 7.8 Hz, 8H), 2.15 (d, J_{HP} = 17.4 Hz, 4H); $^{31}P\{^{1}H\}$ NMR (160 MHz, CD_2Cl_2) δ (ppm): 56.7 (s).

$NiCl_2$(dppey) (**9b**): ^{1}H NMR (600 MHz, CD_2Cl_2) δ (ppm): 7.89 (m, 7H), 7.61 (m, 2H), 7.52 (m, 7H), 6.68 (m, 2H); $^{31}P\{^{1}H\}$ NMR (160 MHz, CD_2Cl_2) δ (ppm): 64.7 (s).

$NiCl_2$(dppb) (**9c**): ^{1}H NMR (600 MHz, CD_2Cl_2) δ (ppm): 7.85 (m, 6H), 7.58 (m, 4H), 7.47 (m, 8H), 7.29 (m, 3H), 6.96 (m, 3H); $^{31}P\{^{1}H\}$ NMR (160 MHz, CD_2Cl_2) δ (ppm): 57.3 (s).

$NiBr_2$(dppe) (**9e**): ^{1}H NMR (600 MHz, CD_2Cl_2) δ (ppm): 7.98 (m, 6H), 7.61 (m, 3H), 7.54 (m, 6H), 2.09 (m, 4H); ^{31}P NMR (160 MHz, CD_2Cl_2) δ (ppm): 66.3.

$NiBr_2$(dppe-Cl) (**9e-Cl**): ^{1}H NMR (600 MHz, CD_2Cl_2) δ (ppm): 7.88 (m, 8H), 7.55(d, $^{3}J_{HH}$ = 8.4 Hz, 8H), 2.12 (d, J_{HP} = 17.4 Hz, 4H); $^{31}P\{^{1}H\}$ NMR (160 MHz, CD_2Cl_2) δ (ppm): 65.2 (s).

$NiBr_2$(dppey) (**9f**): ^{1}H NMR (600 MHz, CD_2Cl_2) δ (ppm): 7.90 (m, 8H), 7.60 (m, 3H), 7.52 (m, 4H), 6.83 (m, 2H); $^{31}P\{^{1}H\}$ NMR (160 MHz, CD_2Cl_2) δ (ppm): 73.6 (s).

$NiBr_2$(dppb) (**9g**): ^{1}H NMR (600 MHz, CD_2Cl_2) δ (ppm): 7.75 (m, 4H), 7.62 (m, 8H), 7.25 (m, 10H), 7.00 (m, 4H). $^{31}P\{^{1}H\}$ NMR (160 MHz, CD_2Cl_2) δ (ppm): 65.2 (s).

3.10.4 X-Ray Data Analysis

Table 3.8. Crystal data and structure refinement for complexes **7c, 7e, 7g,** and **7f**.

	$NiCl_3$(dppb) (7c)	**$NiBr_3$(dppe) (7e)**	**$NiBr_3$(dppb) (7g)**	**$NiBr_3$(dppey) (7f)**
formula	$C_{30}H_{24}Cl_3NiP_2$	$C_{27}H_{26}Br_3Cl_2NiP_2$	$C_{16.5}H_{15}Br_{1.5}Cl_3Ni_{0.5}P$	$C_{28}H_{26}Br_3Cl_4NiP_2$
CCDC #	1040260	1040258	1040259	1040261
fw, g/mol	611.49	781.76	499.83	864.67
temp, K	100(2)	100(2)	15(2)	100(2)
cryst system	Monoclinic	Monoclinic	Monoclinic	Orthorhombic
space group	*P2(1)*	*P2(1)/n*	*P2(1)/m*	*Pnma*
color	Green	Black	Black	Black
a, Å	9.7441(9)	13.5432(7)	8.7809(4)	23.482(1)
b, Å	14.730(1)	15.0186(8)	21.401(1)	16.8828(7)
c, Å	10.2714(9)	14.8428(7)	10.6362(5)	7.9874(4)
α, deg	90	90	90	90
β, deg	113.297(2)	111.8000(8)	113.3720(7)	90
γ, deg	90	90	90	90
V, Å^3	1354.1(2)	2803.1(2)	1834.8(2)	3166.6(2)
Z	2	4	4	4
R1[a]	0.0525	0.0433	0.0187	0.0296
wR2[b]	0.0861	0.1086	0.0439	0.0602
GOF[c] (F′)	0.983	1.038	1.039	1.025
R_{int}	0.0678	0.0668	0.0210	0.0456

[a] $R1 = \Sigma||F_o| - |F_c||/\Sigma|F_o|$. [b] $wR2 = (\Sigma(w(F_o^2 - F_c^2)^2)/\Sigma(w(F_o^2)^2))^{1/2}$. [c] $GOF = (\Sigma w(F_o^2 - F_c^2)^2/(n - p))^{1/2}$ where n is the number of data and p is the number of parameters refined.

3.10.5 XYZ Coordinates

Table 3.9. Cartesian coordinates of the geometry-optimized $NiCl_3$(dppe) (**7a**).

Atom Type	x	y	z
Ni	0.061335	–0.65323	1.135742
Cl	0.135629	–2.851292	0.312622
Cl	–1.610794	–0.732096	2.630764
Cl	1.706671	–0.312504	2.633743
P	–1.523559	–0.08222	–0.41261
P	1.597432	–0.106314	–0.433477
C	–2.903612	–1.256235	–0.675578
C	–2.768036	–2.344123	–1.550349
H	–1.83634	–2.521717	–2.065657
C	–3.823729	–3.234864	–1.729887
H	–3.70682	–4.072643	–2.403344
C	–5.017037	–3.058452	–1.029338
H	–5.832758	–3.755469	–1.164997
C	–5.150657	–1.989925	–0.143051
H	–6.066975	–1.857687	0.415385
C	–4.099985	–1.093414	0.039163
H	–4.206356	–0.280472	0.741031
C	–2.325312	1.560004	–0.170754
C	–3.116054	2.102229	–1.199508
H	–3.285112	1.544405	–2.111074
C	–3.705841	3.354589	–1.048529
H	–4.315257	3.760079	–1.844712
C	–3.51655	4.079685	0.130082
H	–3.97819	5.050641	0.247769
C	–2.741481	3.544452	1.156527
H	–2.602	4.09502	2.076603
C	–2.147102	2.28958	1.010883
H	–1.578421	1.865397	1.82416
C	–0.644164	0.101431	–2.071353
H	–1.247308	–0.345345	–2.862079
H	–0.587293	1.172854	–2.26667
C	0.768661	–0.507756	–2.05211
H	1.362443	–0.145548	–2.892813
H	0.720117	–1.59323	–2.108548
C	1.954349	1.700584	–0.530643
C	2.511394	2.249147	–1.699558
H	2.761516	1.614283	–2.538404
C	2.770686	3.614856	–1.784201
H	3.201369	4.023863	–2.688026
C	2.480996	4.450849	–0.703833
H	2.684045	5.510977	–0.770373

C	1.938672	3.913891	0.461723
H	1.721622	4.553859	1.305618
C	1.675037	2.546323	0.551475
H	1.282852	2.132353	1.468102
C	3.227194	–0.938068	–0.44569
C	4.367257	–0.251601	0.001114
H	4.285793	0.762703	0.360972
C	5.610713	–0.878793	–0.006407
H	6.481313	–0.341979	0.344346
C	5.729662	–2.195541	–0.450923
H	6.695436	–2.682347	–0.45093
C	4.597663	–2.887843	–0.880618
H	4.680124	–3.915069	–1.207783
C	3.349126	–2.269698	–0.874248
H	2.474011	–2.834165	–1.155559

Table 3.10. Cartesian coordinates of the geometry-optimized $NiCl_3$(dppe-Cl) (**7a-Cl**).

Atom Type	x	y	z
Ni	0.061513	–0.646215	1.12516
Cl	0.134545	–2.837524	0.289071
Cl	–1.608913	–0.729511	2.616504
Cl	1.704388	–0.293712	2.617731
P	–1.52315	–0.081391	–0.419551
P	1.595897	–0.101366	–0.44125
C	–2.901101	–1.257518	–0.675541
C	–2.765886	–2.350917	–1.543056
H	–1.837445	–2.533258	–2.061826
C	–3.815863	–3.248549	–1.720841
H	–3.7112	–4.091485	–2.386265
C	–4.992129	–3.050507	–1.012285
C	–5.148932	–1.993371	–0.128145
H	–6.067256	–1.871627	0.425152
C	–4.09569	–1.097643	0.042516
H	–4.207385	–0.284785	0.743327
C	–2.330291	1.556966	–0.175123
C	–3.111928	2.108711	–1.205269
H	–3.275026	1.563673	–2.125204
C	–3.706365	3.359059	–1.056192
H	–4.308907	3.781231	–1.845921
C	–3.514478	4.05221	0.132458
C	–2.759258	3.531975	1.171135
H	–2.637221	4.082985	2.091033
C	–2.166342	2.277835	1.014123
H	–1.608361	1.850258	1.833081

C	–0.647504	0.10452	–2.080321
H	–1.247701	–0.346547	–2.870876
H	–0.597508	1.175896	–2.278118
C	0.769796	–0.495975	–2.063398
H	1.360044	–0.125505	–2.902892
H	0.727443	–1.581197	–2.127493
C	1.962182	1.703356	–0.534303
C	2.519968	2.254489	–1.701218
H	2.769704	1.625841	–2.544391
C	2.78483	3.618747	–1.790185
H	3.215289	4.039517	–2.686071
C	2.489549	4.429675	–0.701644
C	1.951112	3.917621	0.468189
H	1.741898	4.565365	1.30559
C	1.687273	2.549561	0.54883
H	1.297428	2.139305	1.46816
C	3.222225	–0.937497	–0.448394
C	4.363629	–0.256803	0.002956
H	4.290401	0.757668	0.363352
C	5.607992	–0.881915	0.003627
H	6.484756	–0.359078	0.353334
C	5.698305	–2.192485	–0.442353
C	4.585951	–2.899594	–0.874756
H	4.678531	–3.925421	–1.196407
C	3.342812	–2.270939	–0.87115
H	2.469927	–2.837304	–1.15495
Cl	7.32541	–3.012366	–0.449294
Cl	–6.369439	–4.221149	–1.244675
Cl	–4.290728	5.688399	0.331442
Cl	2.831489	6.214302	–0.816258

Table 3.11. Cartesian coordinates of the geometry-optimized $NiCl_3$(dppey) (**7b**).

Atom Type	x	y	z
Ni	–0.350287	0.810415	–0.000002
Cl	–0.242371	2.298572	1.676987
Cl	–0.242343	2.298572	–1.676989
Cl	–2.538764	–0.013384	–0.000005
P	0.184386	–0.739266	1.562241
P	0.184386	–0.739268	–1.562241
C	0.204021	–2.347097	0.666437
H	0.266615	–3.267959	1.236786
C	–0.916095	–0.983533	2.998543
C	–2.029309	–1.831589	2.904476
H	–2.264405	–2.318527	1.970154

C	–2.863012	–2.011038	4.005988
H	–3.721215	–2.663707	3.925372
C	–2.604051	–1.336206	5.199217
H	–3.258068	–1.471022	6.049972
C	–1.508912	–0.476569	5.290145
H	–1.314476	0.061195	6.207716
C	–0.666545	–0.295999	4.195632
H	0.169183	0.383544	4.268113
C	1.889751	–0.643611	2.257786
C	2.381348	–1.696988	3.048662
H	1.748514	–2.539007	3.294477
C	3.682514	–1.656535	3.542644
H	4.050107	–2.470533	4.152453
C	4.506967	–0.56652	3.255593
H	5.516468	–0.53532	3.642241
C	4.022835	0.484276	2.479208
H	4.651963	1.337149	2.265239
C	2.720218	0.448998	1.979565
H	2.339862	1.283269	1.410345
C	0.204021	–2.347097	–0.666436
H	0.266615	–3.267961	–1.236783
C	–0.916096	–0.983534	–2.998543
C	–2.029303	–1.831599	–2.904479
H	–2.264395	–2.318544	–1.970161
C	–2.863007	–2.011047	–4.005992
H	–3.721206	–2.663722	–3.925379
C	–2.604052	–1.336206	–5.199216
H	–3.258069	–1.471021	–6.049971
C	–1.50892	–0.47656	–5.29014
H	–1.314489	0.061211	–6.207709
C	–0.666552	–0.295991	–4.195628
H	0.169171	0.383558	–4.268106
C	1.889752	–0.643621	–2.257788
C	2.381335	–1.69699	–3.048682
H	1.74849	–2.538996	–3.294512
C	3.682502	–1.656546	–3.542662
H	4.050084	–2.470538	–4.152486
C	4.506969	–0.566547	–3.255592
H	5.516471	–0.535354	–3.642239
C	4.022851	0.484242	–2.479189
H	4.65199	1.337103	–2.265204
C	2.720233	0.448972	–1.979547
H	2.339888	1.283238	–1.410312

Table 3.12. Cartesian coordinates of the geometry-optimized $NiCl_3$(dppb) (**7c**).

Atom Type	x	y	z
Ni	–0.000033	–0.75484	–0.923544
Cl	–0.000083	–2.669994	0.441758
Cl	–1.668467	–1.105164	–2.385414
Cl	1.668376	–1.105224	–2.385428
P	1.533993	0.271792	0.411835
P	–1.534018	0.271823	0.411844
C	3.179402	–0.485176	0.717005
C	4.349775	0.275263	0.569234
H	4.298502	1.305755	0.25322
C	5.594989	–0.298904	0.823373
H	6.49025	0.29563	0.702254
C	5.685023	–1.631817	1.220769
H	6.652398	–2.076853	1.410489
C	4.523631	–2.39241	1.363069
H	4.586011	–3.430829	1.657751
C	3.274968	–1.829663	1.111035
H	2.381636	–2.430209	1.194119
C	1.873946	2.006056	–0.120134
C	2.120809	2.274874	–1.476976
H	2.095455	1.470621	–2.198257
C	2.406032	3.574878	–1.891219
H	2.594431	3.768551	–2.938203
C	2.442885	4.618576	–0.966679
H	2.664065	5.625711	–1.293155
C	2.192099	4.359622	0.380593
H	2.21634	5.164452	1.102802
C	1.905845	3.062542	0.803933
H	1.7098	2.879232	1.850173
C	0.704175	0.415435	2.055034
C	1.398435	0.496455	3.264889
H	2.478873	0.468535	3.271455
C	0.696709	0.578283	4.469519
H	1.239624	0.624616	5.403467
C	–3.179419	–0.485157	0.717018
C	–4.349813	0.27524	0.569205
H	–4.29857	1.305725	0.253165
C	–5.595012	–0.298962	0.823341
H	–6.49029	0.295539	0.702193
C	–5.685008	–1.631866	1.220773
H	–6.65237	–2.07693	1.41049
C	–4.523594	–2.39242	1.363109
H	–4.585944	–3.430833	1.657814
C	–3.274946	–1.829638	1.111077

H	–2.381595	–2.430155	1.19418
C	–1.873951	2.006093	–0.120121
C	–2.120766	2.274924	–1.476969
H	–2.09539	1.470677	–2.198256
C	–2.405972	3.574932	–1.89121
H	–2.594335	3.768614	–2.938199
C	–2.442853	4.618622	–0.966662
H	–2.664019	5.62576	–1.293137
C	–2.192112	4.359655	0.380616
H	–2.216373	5.16448	1.10283
C	–1.905875	3.062572	0.803954
H	–1.709863	2.879252	1.850198
C	–0.704187	0.415445	2.055039
C	–1.398437	0.496473	3.2649
H	–2.478876	0.468569	3.271475
C	–0.696701	0.578291	4.469524
H	–1.239608	0.624633	5.403477

Table 3.13. Cartesian coordinates of the geometry-optimized $NiCl_3$(dcpe) (**7d**).

Atom Type	x	y	z
Ni	–0.066209	0.04096	1.179332
Cl	0.159949	–2.23898	1.655634
Cl	1.454366	1.18143	2.41639
Cl	–1.791801	0.424849	2.572541
P	1.573426	–0.08126	–0.421207
P	–1.672252	–0.095857	–0.480926
C	2.485858	1.48133	–0.960304
C	1.558256	2.732121	–0.978265
H	0.887255	2.70383	–0.121085
C	2.357598	4.059071	–0.932361
H	2.535112	4.341182	0.108186
C	3.703792	3.928229	–1.657737
H	4.211553	4.893902	–1.700203
C	4.60313	2.882822	–0.94986
H	5.259634	3.382517	–0.233435
C	3.786096	1.804523	–0.189964
H	4.403876	0.919066	–0.063583
C	2.812214	–1.467652	–0.181103
C	3.781254	–1.634011	–1.393635
H	4.108824	–0.668953	–1.784827
C	5.030819	–2.465406	–1.002576
H	5.801684	–1.804019	–0.597184
C	4.686103	–3.535897	0.044486
H	5.551394	–4.176165	0.228996

C	4.207376	–2.886335	1.370243
H	5.04774	–2.789069	2.062068
C	3.578071	–1.48569	1.160983
H	4.355168	–0.721537	1.165754
C	0.676916	–0.628398	–1.980517
H	1.278703	–0.380511	–2.858334
H	0.618906	–1.71626	–1.923746
C	–0.736887	–0.031547	–2.107302
H	–1.305367	–0.55584	–2.879804
H	–0.682361	1.01618	–2.407836
C	–2.741783	–1.642819	–0.551606
C	–3.979048	–1.524456	–1.479061
H	–3.648403	–1.616708	–2.517936
C	–4.990266	–2.65571	–1.145675
H	–5.591371	–2.860717	–2.035775
C	–4.289035	–3.950634	–0.670726
H	–4.915263	–4.817745	–0.890632
C	–2.916231	–4.093166	–1.342243
H	–3.056483	–4.123706	–2.427396
C	–1.960211	–2.927592	–0.956568
H	–1.315193	–2.720146	–1.814128
C	–2.846631	1.379423	–0.617214
C	–4.122736	1.313666	0.295078
H	–4.074354	0.47323	0.98343
C	–4.342614	2.601058	1.109198
H	–3.579089	2.674109	1.884305
C	–4.323771	3.849157	0.211628
H	–4.416487	4.745599	0.828081
C	–3.031428	3.919648	–0.654253
H	–2.476209	4.835082	–0.437645
C	–2.093376	2.71586	–0.426623
H	–1.261848	2.789271	–1.127032
H	–3.293812	3.965768	–1.71571
H	–5.203512	3.832166	–0.438767
H	–5.302398	2.529148	1.626707
H	–4.996936	1.159256	–0.343442
H	–1.670133	2.75406	0.577596
H	–3.17008	1.342774	–1.665615
H	3.526215	2.145319	0.809839
H	5.255474	2.402304	–1.68451
H	1.75619	4.858169	–1.371424
H	0.944149	2.711977	–1.882741
H	3.524803	3.631731	–2.696515
H	2.771281	1.24959	–1.994012

H	3.904778	–4.188736	–0.357343
H	5.455299	–2.921701	–1.900103
H	3.251662	–2.137955	–2.20657
H	2.143064	–2.330662	–0.144719
H	2.905845	–1.25883	1.983546
H	3.475707	–3.53535	1.85475
H	–4.15837	–3.93308	0.414246
H	–2.45108	–5.04117	–1.06516
H	–1.31393	–3.21782	–0.13339
H	–5.68191	–2.30728	–0.37473
H	–4.48325	–0.56707	–1.39378
H	–3.07878	–1.75471	0.482229

Table 3.14. Cartesian coordinates of the geometry-optimized $NiBr_3$(dppe)(**7e**).

Atom Type	x	y	z
Ni	0.043203	–0.510522	0.81754
Br	0.192606	–2.813368	–0.122706
Br	–1.728172	–0.820077	2.386934
Br	1.73111	–0.150477	2.48262
P	–1.545562	0.198766	–0.697734
P	1.591644	0.14845	–0.712378
C	–2.930785	–0.930929	–1.106648
C	–2.768864	–1.952297	–2.054102
H	–1.817987	–2.1027	–2.542197
C	–3.825056	–2.812439	–2.346202
H	–3.686501	–3.599899	–3.07408
C	–5.047207	–2.670844	–1.689185
H	–5.86343	–3.344249	–1.912563
C	–5.210007	–1.666907	–0.734718
H	–6.150371	–1.560647	–0.211808
C	–4.158267	–0.802569	–0.439019
H	–4.290164	–0.038665	0.311856
C	–2.349297	1.819806	–0.334892
C	–3.09795	2.457893	–1.339911
H	–3.23282	1.98554	–2.303851
C	–3.690082	3.695152	–1.100129
H	–4.266502	4.174127	–1.879881
C	–3.545529	4.310424	0.145337
H	–4.008982	5.269596	0.332129
C	–2.812847	3.680149	1.148691
H	–2.708017	4.144696	2.119481
C	–2.216322	2.439872	0.913603
H	–1.677895	1.944978	1.707807

C	–0.642874	0.525282	–2.323012
H	–1.250274	0.177756	–3.159204
H	–0.552613	1.60864	–2.409019
C	0.751304	–0.122334	–2.354658
H	1.354882	0.292999	–3.163451
H	0.673585	–1.198625	–2.495815
C	1.95752	1.958454	–0.721034
C	2.682129	2.514577	–1.790815
H	3.064025	1.881388	–2.580357
C	2.938928	3.882417	–1.833437
H	3.501204	4.296911	–2.659101
C	2.477975	4.713955	–0.810143
H	2.680114	5.775822	–0.843284
C	1.765674	4.170316	0.256211
H	1.414591	4.806387	1.056748
C	1.506649	2.799391	0.303639
H	0.981732	2.383176	1.149534
C	3.228638	–0.664316	–0.814874
C	4.329043	–0.091864	–0.156306
H	4.206501	0.813526	0.418214
C	5.58126	–0.696507	–0.228487
H	6.419838	–0.249681	0.28742
C	5.750075	–1.877994	–0.951045
H	6.722856	–2.347847	–1.001915
C	4.658673	–2.458898	–1.595792
H	4.778797	–3.383418	–2.143346
C	3.40107	–1.862476	–1.52506
H	2.559391	–2.350088	–1.990478

Table 3.15. Cartesian coordinates of the geometry-optimized $NiBr_3$(dppe-OMe) (**7e-OMe**).

Atom Type	x	y	z
Ni	0.056179	–0.575813	0.775392
Br	0.118399	–2.881655	–0.184527
Br	–1.696513	–0.82804	2.386744
Br	1.800272	–0.320191	2.406285
P	–1.541274	0.172755	–0.712594
P	1.591278	0.091897	–0.770766
C	–2.95926	–0.913365	–1.093046
C	–2.854546	–1.94844	–2.040779
H	–1.921516	–2.13147	–2.551638
C	–3.932944	–2.7748	–2.309107
H	–3.860335	–3.574737	–3.030772
C	–5.137783	–2.600965	–1.618275
C	–5.254628	–1.591274	–0.659481

H	–6.169052	–1.447873	–0.105356
C	–4.166284	–0.76115	–0.399178
H	–4.263758	0.005028	0.354879
C	–2.280805	1.811092	–0.32829
C	–3.037721	2.483339	–1.31077
H	–3.213315	2.022816	–2.273837
C	–3.583598	3.730625	–1.058973
H	–4.16725	4.250941	–1.804168
C	–3.389717	4.340112	0.188281
C	–2.652524	3.686371	1.176386
H	–2.501073	4.129461	2.148401
C	–2.104982	2.429228	0.912989
H	–1.564227	1.921132	1.697331
C	–0.662492	0.467012	–2.358052
H	–1.285029	0.103633	–3.175965
H	–0.573438	1.548286	–2.465787
C	0.730232	–0.18154	–2.401185
H	1.326112	0.225641	–3.219908
H	0.650424	–1.259065	–2.5348
C	1.939862	1.898663	–0.754637
C	2.557243	2.505215	–1.858989
H	2.862708	1.910681	–2.709511
C	2.815104	3.874435	–1.883728
H	3.29462	4.306026	–2.748693
C	2.454045	4.662137	–0.78512
C	1.84661	4.071372	0.326755
H	1.587921	4.696301	1.168442
C	1.593392	2.707648	0.341143
H	1.150506	2.260839	1.217957
C	3.220432	–0.716841	–0.903411
C	4.36662	–0.095202	–0.369773
H	4.284041	0.861711	0.122497
C	5.607471	–0.702204	–0.45965
H	6.490765	–0.235544	–0.049634
C	5.732753	–1.955498	–1.071006
C	4.604554	–2.59485	–1.591402
H	4.673951	–3.568812	–2.05007
C	3.358297	–1.97849	–1.498011
H	2.491	–2.509616	–1.857843
O	–6.156274	–3.47933	–1.958423
O	–3.976784	5.58726	0.341416
O	2.661567	6.030599	–0.70237
O	7.01633	–2.478446	–1.10941
C	7.2267	–3.802913	–1.669576
H	8.289917	–3.99093	–1.563879
H	6.663447	–4.557461	–1.117734

H	6.952515	–3.833225	–2.726055
C	–7.41845	–3.412854	–1.241846
H	–7.907707	–2.448166	–1.391279
H	–8.029923	–4.200859	–1.66871
H	–7.275452	–3.595735	–0.175347
C	–3.828709	6.289203	1.605983
H	–4.367328	7.222145	1.478163
H	–4.269502	5.720458	2.42673
H	–2.778843	6.497572	1.820208
C	3.309383	6.72125	–1.804688
H	2.722801	6.638902	–2.721831
H	3.360837	7.760513	–1.497986
H	4.31801	6.338569	–1.97216

Table 3.16. Cartesian coordinates of the geometry-optimized $NiBr_3$(dppe-Cl) (**7e-Cl**).

Atom Type	x	y	z
Ni	0.043697	–0.506619	0.808412
Br	0.190216	–2.800956	–0.14626
Br	–1.724546	–0.816307	2.374903
Br	1.729766	–0.142201	2.46769
P	–1.544265	0.196268	–0.703676
P	1.589934	0.151644	–0.718558
C	–2.930039	–0.933492	–1.106159
C	–2.771097	–1.960259	–2.047814
H	–1.823574	–2.116635	–2.53968
C	–3.823798	–2.824581	–2.33992
H	–3.699548	–3.617002	–3.061718
C	–5.028878	–2.660069	–1.67282
C	–5.212663	–1.667541	–0.721396
H	–6.154911	–1.569499	–0.204779
C	–4.155807	–0.806137	–0.435653
H	–4.291551	–0.042611	0.314582
C	–2.351391	1.814877	–0.340142
C	–3.094205	2.460226	–1.344373
H	–3.227059	1.998577	–2.313359
C	–3.68849	3.697106	–1.10837
H	–4.2609	4.190178	–1.879206
C	–3.53615	4.283584	0.141796
C	–2.820011	3.669765	1.156782
H	–2.728016	4.13782	2.124919
C	–2.226878	2.429771	0.911914
H	–1.696391	1.933299	1.710512

C	–0.645918	0.524313	–2.331587
H	–1.250349	0.171097	–3.167555
H	–0.563621	1.608082	–2.421106
C	0.753779	–0.112915	–2.364515
H	1.353653	0.311552	–3.171214
H	0.683679	–1.188607	–2.513466
C	1.962414	1.960016	–0.72266
C	2.683537	2.520604	–1.791916
H	3.063338	1.895014	–2.588014
C	2.945659	3.887263	–1.837045
H	3.502946	4.314989	–2.656487
C	2.480698	4.691952	–0.804162
C	1.775703	4.171367	0.268971
H	1.43548	4.814265	1.06611
C	1.518669	2.799769	0.306268
H	0.998725	2.385482	1.156156
C	3.225494	–0.662466	–0.817057
C	4.326057	–0.09284	–0.156729
H	4.209695	0.813588	0.417033
C	5.580112	–0.694517	–0.219854
H	6.424521	–0.257902	0.290737
C	5.722413	–1.871198	–0.941397
C	4.652133	–2.469401	–1.589416
H	4.783901	–3.394743	–2.128596
C	3.398522	–1.864738	–1.519654
H	2.560446	–2.356469	–1.986661
Cl	7.36311	–2.658201	–1.032737
Cl	–6.410084	–3.785917	–2.05459
Cl	–4.312161	5.901655	0.454888
Cl	2.818917	6.480239	–0.861923

Table 3.17. Cartesian coordinates of the geometry-optimized $NiBr_3$(dppey) (**7f**).

Atom Type	x	y	z
Ni	–0.390422	0.881042	0
Br	–2.75102	0.101395	0
Br	–0.300137	2.488148	–1.763222
Br	–0.300136	2.488148	1.763221
P	0.158818	–0.677212	1.5714
P	0.158818	–0.677212	–1.5714
C	0.184975	–2.280056	0.66617
H	0.257891	–3.200946	1.235309
C	–0.91757	–0.968407	3.020827
C	–1.997375	–1.859481	2.935664
H	–2.221585	–2.355691	2.003455

C	–2.81144	–2.077771	4.045126
H	–3.64457	–2.762734	3.969535
C	–2.564896	–1.401408	5.239815
H	–3.203473	–1.566397	6.096942
C	–1.500593	–0.503232	5.324669
H	–1.313898	0.033386	6.244527
C	–0.678931	–0.283121	4.221666
H	0.133867	0.423823	4.29145
C	1.872338	–0.598636	2.256192
C	2.346903	–1.646607	3.064644
H	1.696402	–2.467629	3.333828
C	3.653277	–1.627157	3.545964
H	4.006813	–2.436812	4.169729
C	4.500833	–0.563604	3.228802
H	5.514267	–0.548293	3.605977
C	4.03453	0.481681	2.434342
H	4.681616	1.314651	2.196778
C	2.726729	0.466548	1.947517
H	2.363073	1.297327	1.362569
C	0.184975	–2.280056	–0.66617
H	0.257891	–3.200946	–1.23531
C	–0.91757	–0.968407	–3.020827
C	–1.997375	–1.859481	–2.935664
H	–2.221586	–2.355691	–2.003455
C	–2.81144	–2.077771	–4.045126
H	–3.64457	–2.762734	–3.969535
C	–2.564897	–1.401408	–5.239815
H	–3.203474	–1.566397	–6.096942
C	–1.500593	–0.503232	–5.324669
H	–1.313898	0.033385	–6.244528
C	–0.678931	–0.283121	–4.221666
H	0.133867	0.423822	–4.291451
C	1.872338	–0.598636	–2.256193
C	2.346904	–1.646607	–3.064643
H	1.696403	–2.467629	–3.333827
C	3.653278	–1.627156	–3.545963
H	4.006814	–2.436812	–4.169728
C	4.500833	–0.563603	–3.228802
H	5.514267	–0.548292	–3.605977
C	4.034529	0.481683	–2.434342
H	4.681615	1.314653	–2.196779
C	2.726728	0.466549	–1.947517
H	2.363072	1.297328	–1.36257

Table 3.18. Cartesian coordinates of the geometry-optimized $NiBr_3$(dppb) (**7g**).

Atom Type	x	y	z
Ni	0.000012	–0.78015	–0.95512
Br	0.000034	–2.8636	0.428741
Br	–1.75859	–1.16821	–2.52768
Br	1.758619	–1.16819	–2.52768
P	1.534471	0.252698	0.392722
P	–1.53446	0.252686	0.392721
C	3.187049	–0.48474	0.706046
C	4.353874	0.187703	0.312488
H	4.293105	1.143926	–0.18368
C	5.604407	–0.38028	0.551682
H	6.496604	0.145288	0.239959
C	5.703424	–1.62046	1.180593
H	6.674593	–2.06166	1.359433
C	4.545381	–2.29592	1.567577
H	4.613459	–3.26514	2.041983
C	3.291388	–1.73806	1.331313
H	2.399712	–2.28421	1.599765
C	1.86008	2.002525	–0.10936
C	2.006459	2.324372	–1.46821
H	1.918246	1.551481	–2.21787
C	2.279558	3.636448	–1.85331
H	2.391475	3.868486	–2.90348
C	2.402384	4.64164	–0.89508
H	2.61326	5.658392	–1.19765
C	2.249795	4.331235	0.456305
H	2.339836	5.106008	1.205698
C	1.977861	3.022032	0.849193
H	1.855642	2.801864	1.899239
C	0.704118	0.378849	2.038321
C	1.397637	0.460397	3.249068
H	2.477857	0.434287	3.256351
C	0.696573	0.539542	4.454078
H	1.239941	0.585849	5.387783
C	–3.18704	–0.48475	0.706047
C	–4.35386	0.187691	0.312454
H	–4.29308	1.143897	–0.18375
C	–5.6044	–0.38028	0.551652
H	–6.49659	0.145287	0.239899
C	–5.70343	–1.62043	1.180605
H	–6.67461	–2.06162	1.359449
C	–4.5454	–2.29588	1.567631
H	–4.61349	–3.26509	2.042074
C	–3.2914	–1.73804	1.331364

H	–2.39973	–2.28418	1.599853
C	–1.86008	2.002511	–0.10936
C	–2.00646	2.324358	–1.46821
H	–1.91824	1.551468	–2.21787
C	–2.27956	3.636433	–1.85331
H	–2.39148	3.86847	–2.90349
C	–2.4024	4.641624	–0.89508
H	–2.61328	5.658375	–1.19765
C	–2.24981	4.331218	0.456304
H	–2.33986	5.10599	1.205698
C	–1.97787	3.022016	0.849191
H	–1.85566	2.801849	1.899238
C	–0.70411	0.378844	2.038321
C	–1.39763	0.460386	3.249067
H	–2.47785	0.434266	3.256349
C	–0.69657	0.539537	4.454077
H	–1.23994	0.585838	5.387782

Table 3.19. Cartesian coordinates of the geometry-optimized $NiCl_3$(dppey) CT complex (**8b**).

Atom Type	x	y	z
Ni	0.706254	0.949598	0.064267
Cl	0.815857	2.46338	1.697917
Cl	0.491873	2.419744	–1.583055
Cl	–3.844519	–2.949867	1.386988
P	0.819541	–0.654758	1.573421
P	0.692504	–0.593152	–1.504914
C	1.01366	–2.244566	0.664358
H	1.217012	–3.163837	1.204026
C	–0.72765	–0.915114	2.557125
C	–1.236944	–2.18924	2.807539
H	–0.736787	–3.07459	2.446829
C	–2.448724	–2.352863	3.515314
H	–2.766672	–3.342338	3.805044
C	–3.140333	–1.219779	3.991882
H	–4.066263	–1.349422	4.53299
C	–2.633632	0.045881	3.745167
H	–3.159986	0.92242	4.094969
C	–1.437576	0.205712	3.034259
H	–1.053197	1.197343	2.838259
C	2.207908	–0.68222	2.781332
C	2.197294	–1.54124	3.89047
H	1.334254	–2.158828	4.09856
C	3.294322	–1.593203	4.748856
H	3.275078	–2.25467	5.604347

C	4.408208	–0.787179	4.510049
H	5.256843	–0.825164	5.179343
C	4.42025	0.075361	3.414202
H	5.273851	0.714137	3.234766
C	3.325413	0.132423	2.553204
H	3.321482	0.830654	1.729817
C	0.926579	–2.220187	–0.668135
H	1.028398	–3.121135	–1.264485
C	–0.85707	–0.795199	–2.464504
C	–1.917446	–1.541404	–1.927587
H	–1.819397	–2.038762	–0.972651
C	–3.125576	–1.637284	–2.616365
H	–3.936268	–2.209941	–2.188063
C	–3.287774	–0.986709	–3.839251
H	–4.22717	–1.058433	–4.370373
C	–2.240445	–0.232429	–4.370762
H	–2.367449	0.286403	–5.310981
C	–1.030906	–0.12943	–3.687316
H	–0.234931	0.477634	–4.091978
C	2.07684	–0.592227	–2.717222
C	2.149635	–1.580158	–3.713349
H	1.356203	–2.30773	–3.820821
C	3.234606	–1.617657	–4.586545
H	3.279677	–2.378621	–5.353777
C	4.256894	–0.673382	–4.473331
H	5.09752	–0.702552	–5.153219
C	4.187163	0.311986	–3.489638
H	4.969755	1.053375	–3.406475
C	3.102518	0.356008	–2.613498
H	3.032556	1.142129	–1.877249

Table 3.20. Cartesian coordinates of the geometry-optimized $NiBr_3$(dppey) CT complex (**8f**).

Atom Type	x	y	z
Ni	0.082202	1.04576	0.020433
Br	–4.764037	–1.926863	1.296097
Br	–0.287887	2.5841	–1.732616
Br	–0.211521	2.633572	1.753404
P	0.442874	–0.507729	1.552057
P	0.386463	–0.480716	–1.542944
C	0.814893	–2.07363	0.656987
H	1.094237	–2.961224	1.216163
C	–0.965679	–0.982982	2.649021
C	–1.674491	–2.168084	2.444603
H	–1.40088	–2.846803	1.650813

C	–2.769908	–2.497711	3.266125
H	–3.246021	–3.461028	3.160932
C	–3.156399	–1.627625	4.29946
H	–3.999017	–1.881113	4.926478
C	–2.455147	–0.445433	4.501613
H	–2.750035	0.234281	5.288352
C	–1.361702	–0.123982	3.693128
H	–0.829676	0.801661	3.853044
C	1.886657	–0.342128	2.683517
C	2.09528	–1.271544	3.715106
H	1.373127	–2.055937	3.898423
C	3.225758	–1.180692	4.524401
H	3.375739	–1.89802	5.319813
C	4.157329	–0.162808	4.312598
H	5.032531	–0.090591	4.943783
C	3.953088	0.765663	3.292508
H	4.665029	1.563595	3.133218
C	2.822761	0.680014	2.479925
H	2.650897	1.421268	1.713919
C	0.772163	–2.06558	–0.677359
H	1.000715	–2.950684	–1.26258
C	–1.049392	–0.907493	–2.606185
C	–2.063927	–1.735596	–2.102608
H	–1.993181	–2.150759	–1.107201
C	–3.189948	–2.017449	–2.874025
H	–3.96802	–2.649346	–2.469143
C	–3.316875	–1.471201	–4.150833
H	–4.193	–1.686184	–4.747278
C	–2.31773	–0.6358	–4.652061
H	–2.419408	–0.197311	–5.635251
C	–1.191197	–0.347515	–3.884505
H	–0.435374	0.319286	–4.271265
C	1.83955	–0.330521	–2.665196
C	2.099917	–1.326487	–3.621269
H	1.410846	–2.14965	–3.754947
C	3.236906	–1.25199	–4.422616
H	3.425286	–2.021005	–5.159422
C	4.126815	–0.186129	–4.276907
H	5.008182	–0.127855	–4.900989
C	3.872123	0.807037	–3.332354
H	4.551209	1.641413	–3.224179
C	2.734105	0.738529	–2.528264
H	2.522889	1.528188	–1.823158

Table 3.21. Energy of $NiCl_3$(dppe) (**7a**), $NiCl_2$(dppe) (**9a**), and Cl_2 in solvent-corrected energies (Hartree/Particle).

	$NiCl_3$(dppe) (**1a**)	$NiCl_2$(dppe) (**2a**)	Cl_2
Thermal Energy, E	–1234.131607	–1219.130347	–29.939352
Thermal Enthalpy, H	–1234.130662	–1219.129403	–29.938408
Thermal Free Energy, G	–1234.230941	–1219.227849	–29.963937

Table 3.22. Spin densities, population analyses (β-LUMO), Mayer bond orders.[a]

Complex	Ni(d)[b]	X_{ap}(p)b	Ni[c]	X_{ap}[c]	MBO (α/β)
$NiCl_3$(dppe) (**7a**)	65.51	14.78	0.88	0.17	0.633/0.419

[a] All gas-phase values. [b] Values for the β-LUMO (i.e., the unoccupied d_{z2} orbital). [c] Mulliken spin density.

3.11 References

1. Rosenthal, J.; Nocera, D. G. *Acc. Chem. Res.* **2007**, *40*, 543.

2. Rosenthal, J.; Nocera, D. G. Prog. *Inorg. Chem*. **2007**, *55*, 483.

3. Nicolet, Y.; Cavazza, C.; Fontecilla-Camps, J.C. *J. Inorg. Biochem*. **2002**, *91*, 1.

4. Nicolet, Y.; Lemon, B. J.; Fontecilla-Camps, J. C.; Peters, J. W. *Trends Biochem. Sci*. **2000**, *25*, 138.

5. Peters, J. W. *Curr. Opin. Struct. Biol*. **1999**, *9*, 670.

6. Bediako, D. K.; Solis, B. H.; Dogutan, D. K.; Roubelakis, M. M.; Maher, A. G.; Lee, C. H.; Chambers, M. B.; Hammes-Schiffer, S.; Nocera, D. G. *Proc. Natl. Acad. Sci. U.S.A*. **2014**, *111*, 15001.

7. McGuire, R. Jr.; Dogutan, D. K.; Teets, T. S.; Suntivich, J.; Shao-Horn, Y.; Nocera, D. G. *Chem. Sci*. **2010**, *1*, 411.

8. Dogutan, D. K.; McGuire, R., Jr.; Nocera, D. G. *J. Am. Chem. Soc*. **2011**, *133*, 9178.

9. Lee, C. H.; Dogutan, D. K.; Nocera, D. G. *J. Am. Chem. Soc.* **2011**, *133*, 8775.

10. DuBois, M. R.; DuBois, D. L. *Chem. Soc. Rev*. **2009**, *38*, 62.

11. DuBois, M. R.; DuBois, D. L. *Acc. Chem. Res*. **2009**, *42*, 1974.

12. Borovik, A. S. *Acc. Chem. Res*. **2005**, *38*, 54.

13. Park, Y. J.; Matson, E. M.; Nilges, M. J.; Fout, A. R. *Chem. Commun*. **2015**, *51*, 5310.

14. Esswein, A. J.; Nocera, D. G. *Chem. Rev*. **2007**, *107*, 4022.

15. Nocera, D. G. *Inorg. Chem*. **2009**, *48*, 10001.

16. Teets, T. S.; Nocera, D. G. *Chem. Commun*. **2011**, *47*, 9268.
17. Cook, T. R.; Surendranath, Y.; Nocera, D. G. *J. Am. Chem. Soc*. **2009**, *131*, 28.

18. Lin, T.-P.; Gabbaï, F. P. *J. Am. Chem. Soc*. **2012**, *134*, 12230.

19. Yang, H.; Gabbaï, F. P. *J. Am. Chem. Soc*. **2014**, *136*, 10866.

20. Karikachery, A. R.; Lee, H. B.; Masjedi, M.; Ross, A.; Moody, M. A.; Cai, X.; Chui, M.; Hoff, C. D.; Sharp, P. R. *Inorg. Chem*. **2013**, *52*, 4113.

21. Perera, T. A.; Masjedi, M.; Sharp. P. R. *Inorg. Chem*. **2014**, *53*, 7608.

22. Teets, T. S.; Nocera, D. G. *J. Am. Chem. Soc*. **2009**, *131*, 7411.

23. Powers, D. C.; Chambers, M. B.; Teets, T. S.; Elgrishi, N.; Anderson, B. L.; Nocera, D. G. *Chem. Sci*. **2013**, *4*, 2880.

24. Cook, T. R.; Esswein, A. J.; Nocera, D. G. *J. Am. Chem. Soc*. **2007**, *129*, 10094.

25. Cook, T. R.; McCarthy, B. D.; Lutterman, D. A.; Nocera, D. G. *Inorg. Chem*. **2012**, *51*, 5152.

26. Teets, T. S.; Lutterman, D. A.; Nocera, D. G. *Inorg. Chem*. **2010**, *49*, 3035.

27. Carrera, E. I.; Seferos, D. S. *Dalton Trans*. **2015**, *44*, 2092.

28. Carrera, E. I.; McCormick, T. M.; Kapp, M. J.; Lough, A. J.; Seferos, D. S. *Inorg. Chem*. **2013**, *52*, 13779.
29. Kumar, C. V.; Thota, J. *Inorg. Chem*. **2005**, *44*, 825.

30. Buranaprapuk, A.; Malaikaew, Y.; Svasti, J.; Kumar, C. V. *J. Phys. Chem. B* **2008**, *112*, 9258.

31. Jyotsna, T.; Bandara, K.; Kumar, C. V. *Photochem. Photobiol. Sci*. **2008**, *7*, 1531.

32. Creutz, C.; Chou, M.; Netzel, T. L.; Okumura, M.; Sutin, N. *J. Am. Chem. Soc*. **1980**, *102*, 1309.

33. McCusker, J. K. *Acc. Chem. Res*. **2003**, *36*, 876.

34. Juban, E. A.; Smeigh, A. L.; Monat, J. E.; McCusker, J. K. *Coord. Chem. Rev*. **2006**, *250*, 1783.

35. Powers, D. C.; Anderson, B. L.; Nocera, D. G. *J. Am. Chem. Soc*. **2013**, *135*, 18876.

36. Hwang, S. J.; Powers, D. C.; Maher, A. G.; Nocera, D. G. *Chem. Sci*. **2015**, *6*, 917.

37. Fredin, L. A.; Pápai, M.; Rozsályi, E.; Vankó, G.; Wärnmark, K.; Sundström, V.; Persson, P. *J. Phys. Chem. Lett*. **2014**, *5*, 2066.

38. Creutz, C.; Chou, M.; Netzel, T. L.; Okumura, M.; Sutin, N. *J. Am. Chem. Soc*. **1980**, *102*, 1309.

39. McCusker, J. K. *Acc. Chem. Res*. **2003**, *36*, 876.

40. Juban, E. A.; Smeigh, A. L.; Monat, J. E.; McCusker, J. K. *Coord. Chem. Rev*. **2006**, *250*, 1783.

41. Han, R.; Hillhouse, G. L. *J. Am. Chem. Soc*. **1997**, *119*, 8135.

42. Lin, B. L.; Clough, C. R.; Hillhouse, G. L. *J. Am. Chem. Soc.* **2002**, *124*, 2890.

43. Matsunaga, P. T.; Hillhouse, G. L.; Rheingold, A. L. *J. Am. Chem. Soc*. **1993**, *115*, 2075.

44. Koo, K.; Hillhouse, G. L.; Rheingold, A. L. *Organometallics* **1995**, *14*, 456.

45. Koo, K.; Hillouse, G. L. *Organometallics* **1995**, *14*, 4421.

46. Koo, K.; Hillhouse, G. L. *Organometallics* **1996**, *15*, 2669.

47. Matsunaga, P. T.; Mavropoulos, J. C.; Hillhouse, G. L. *Polyhedron* **1995**, *14*, 175.

48. Bruin, B. D.; Hetterscheid, D. G. H.; Koekkoek, A. J. J.; Grützmacher, H. *In Progress in Inorganic Chemistry*; Karlin, K. D., Ed.; J. Wiley and Sons: New York, 2007; Vol. 55, p 247.

49. Kurylo, M. J.; Knable, G. L. *J. Phys. Chem*. **1984**, *88*, 3305.

50. Tyndall, G. S.; Orlando, J. J.; Wallington, T. J.; Sehested, J.; Nielsen, O. J. *J. Phys. Chem*. **1996**, *100*, 660.

51. Sheps, L.; Crowther, A. C.; Elles, C. G.; Crim, F. F. *J. Phys. Chem. A* **2005**, *109*, 4296.

52. Kasha, M. *Discuss. Faraday Soc*. **1950**, *9*, 14.

53. Lide, D. R. *CRC Handbook of Chemistry and Physics*, 85th ed.; CRC Press: Boca Raton, FL, 2004; pp 1-15.

54. Nickel, U.; Chen, Y.-H.; Schenider, S.; Silva, M. I.; Burrows, H. D.; Formosinho, S. J.; *J. Phys. Chem.* **1994**, *98*, 2883.

55. Bader, H.; Sturzenegger, V.; Hoigné, *J. Water Res*. **1988**, *22*, 1109.

56. Bühler, R. E.; Ebert, M. *Nature*, **1967**, *214*, 1220.

57. Strong, R. L.; Rand, S. J.; Britt, J. A. *J. Am. Chem. Soc*. **1960**, *82*, 5053.

58. Bossy, J. M.; Bühler, R. E.; Ebert, M. *J. Am. Chem. Soc*.**1970**, *92*, 1099.

59. Förgeteg, S.; Bérces, T. J. *Photochem. Photobiol., A* **1993**, *73*, 187.

60. Tsao, M.-L.; Hadad, C. M.; Platz, M. S. *J. Am. Chem. Soc*. **2003**, *125*, 8390.

61. Powers, D. C.; Anderson, B. L.; Hwang, S. J.; Powers, T. M.; Pérez, L. M.; Hall, M. B.; Zheng, S.-L.; Chen, Y.-S.; Nocera, D. G. *J. Am. Chem. Soc*. **2014**, *136*, 15346.

62. Schmøkel, M. S. Kamiński, R.; Benedict, J. B.; Coppens, P. *Acta Cryst A* **2010**, *66*, 632.

63. Sokolov, A. Y.; Schaefer III, H. F. *Dalton Trans*. **2011**, *40*, 7571.

64. Tsao, M.-L.; Hadad, C. M.; Platz, M. S. *J. Am. Chem. Soc.* **2003**, *125*, 8390.

65. Dapprich, S.; Frenking, G. *J. Phys. Chem*. **1995**, *99*, 9352.

66. Hendry, D. G.; Mill, T.; Piszkiewicz, L.; Howard, J. A.; Eigenmann, H. K. *J. Phys. Chem. Ref. Data*. **1974**, *3*, 937.

67. Olbregts, J.; Brasseur, G.; Arijs, E. *J. Photochem*. **1984**, *24*, 315.

68. Raner, K. D.; Lusztyk, J.; Ingold, K. U. *J. Phys. Chem*. **1989**, *93*, 564.

69. Alfassi, Z. B.; Huie, R. E.; Mittal, J. P.; Neta, P.; Shoute, L. C. T. *J. Phys. Chem*. **1993**, *97*, 9120.

70. Rosker, M. J.; Dantus, M.; Zewail, A. H. *J. Chem. Phys*. **1988**, *89*, 6113.

71. Roberts, G.; Zewail, A. H. *J. Phys. Chem*. **1991**, *95*, 7973.

72. Della Ciana, L.; Dressick, W. J.; Sandrini, D.; Maestri, M.; Ciano, M. *Inorg. Chem*. **1990**, *29*, 2792.

73. Takizawa, S.; Shimada, K.; Sato, Y.; Murata, S. *Inorg. Chem*. **2014**, *53*, 2983.

74. Pangborn, A. B.; Giardello, M. A.; Grubbs, R. H.; Rosen, R. K.; Timmers, F. J. *Organometallics* **1996**, *15*, 1518.

75. Zielinska, A.; Skulski, L. *Tetrahedron Lett*. **2004**, *45*, 1087.

76. Fawcett, J.; Hope, E. G.; Stuart, A. M.; Sherrington, J. *Inorg. Chim. Acta*. **2006**, *359*, 3535.

77. Gray, L. R.; Higgins, S. J.; Levason, W.; Webster, M. *J. Chem. Soc. Dalton Trans*. **1984**, 459.

78. Zarkesh, R. A.; Hopkins, M. D.; Jordan, R. F. *Eur. J. Inorg. Chem*. **2014**, *2014*, 5491.

79. Bomfim, J. A. S.; de Souza, F. P.; Filgueiras, C. A. L.; de Sousa, A. G.; Gambardella, M. T. P. *Polyhedron*, **2003**, *22*, 1567.

80. Smeets, B. J. J.; Meijer, R. H.; Meuldijk, J.; Vekemans, J. A. J. M.; Hulshof, L. A. *Org. Proc. Res. Dev*. **2003**, *7*, 10.

81. Carroll, M. E.; Barton, B. E.; Gray, D. L.; Mack, A. E.; Rauchfuss, T. B. *Inorg. Chem*. **2011**, *50*, 9554.

82. Angulo, I. M.; Bouwman, E.; Lutz, M.; Mul, W. P.; Spek, A. L. *Inorg. Chem*. **2001**, *40*, 2073.

83. Jarrett, P. S.; Sadler, P. J. *Inorg. Chem*. **1991**, *30*, 2098.

84. Bain, G. A.; Berry, J. F. *J. Chem. Ed*. **2008**, *85*, 532.

85. Stoll, S.; Schweiger, A. J. *Magn. Reson*. **2006**, *178*, 42.

86. Montalti, M.; Credi, A.; Prodi, L.; Gandolfi, M. T. *Handbook of Photochemistry*, 3rd ed.; Taylor and Francis: Boca Raton, 2006.

87. Holder, P. G.; Pizano, A. A.; Anderson, B. L.; Stubbe , J.; Nocera, D. G. *J. Am. Chem. Soc*. **2012**, *134*, 1172.

88. Bruker AXS (2009). Apex II. Bruker AXS, Madison, Wisconsin.

89. Sheldrick, G. M. *Acta Cryst*. **2010**, *D66*, 479.

90. Frisch, M. J.; et al. Gaussian 09, Revision D.01; Gaussian, Inc.: Wallingford, CT, 2009.

91. Stephens, P. J.; Devlin, F. J.; Chabalowski, C. F.; Frisch, M. J. *J. Phys. Chem.* **1994**, *98*, 11623.

92. Lee, C.; Yang, W.; Parr, R. G. *Phys. Rev. B* **1988**, *37*, 785.

93. Becke, A. D. *J. Chem. Phys*. **1993**, *98*, 5648.

94. Schaefer, A.; Huber, C.; Ahlrichs, R. *J. Chem. Phys*. **1994**, *100*, 5829.

95. Schaefer, A.; Horn, H.; Ahlrichs, R. *J. Chem. Phys*. **1992**, *97*, 2571.

96. (a) Gorelsky, S. I.; Lever, A. B. P. *J. Organomet. Chem*. **2001**, *635*, 187−196. (b) Gorelsky, S. I. AOMix: Program for Molecular Orbital Analysis, revision 6.82; http://www.sg-chem.net, Ottawa, ON, 2013.

97. Kieber-Emmons, M. T. Lumo, Version 0.9b; Burlingame, CA, 2011.

Chapter 4

Halide-Bridged Intermediates in Halogen Photoeliminations in Binuclear Rh and Ni Complexes

Parts of this chapter have been published:

Powers, D. C.; Anderson, B. L.; Hwang, S. J.; Powers, T. M.; Pérez, L. M.; Hall, M. B.; Zheng, S.-L.; Chen, Y.-S.; Nocera; D. G. "Photocrystallographic Observation of Halide-Bridged Intermediates in Halogen Photoeliminations" *J. Am. Chem. Soc.* **2014**, *136*, 15346.

Powers, D. C.; Hwang, S. J.; Zheng, S.-L.; Nocera, D. G. "Halide-Bridged Binuclear HX-Splitting Catalysts" *Inorg. Chem.* **2014**, *53*, 9122.

4.1 Introduction

Accomplishing small molecule activation reactions relevant to energy conversion schemes mandates development of catalysis of multi-electron, multi-proton reactions. The multi-electron/multi-proton transformations involved in the splitting of water or hydrohalic acids (HX) to generate energy-rich solar fuels (H_2 and O_2 or X_2) implicitly involve substantial thermodynamic and kinetic barriers.[1–5] Photochemical splitting of HX requires the management of two-electrons and two-protons.[6–9] The Nocera group have developed the design principle of two-electron mixed-valency, $M^n\cdots M^{n+2}$, to promote multi-electron/multi-proton transformations. These endeavors have been guided by the hypothesis that ground-state two-electron mixed valency will give rise to molecular excited states capable of mediating multi-electron photoreactions without participating in the parasitic single-electron transformations that are frequently encountered in inorganic photochemistry.[10,11] Specifically, redox cooperativity may be established between the individual metal centers of a mixed-valence core such that two-electron oxidations may be promoted at a M^{n+2} center and two-electron reductions may be promoted at a M^n center.[12–14] Hydrogen addition and elimination from $M^n\cdots M^{n+2}$ cores is driven through a hydrogen-bridged intermediate (Eq. 1).[15] In this manner, the two-electron mixed valency of the core may be preserved and hence reorganization energy is minimized.

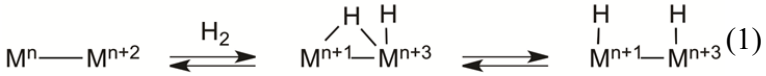

(1)

The challenge in development of HX-splitting chemistry is the halogen elimination half reaction, which has been the bottleneck to development of HX-splitting photochemistry. Only recently has mechanistic information regarding this reaction from dirhodium complexes become available. Nanosecond-resolved transient absorption (TA) spectroscopy of halogen photoelimination reactions from a pair of valence isomers—two-electron mixed-valent complex

1 and valence-symmetric complex **2**—revealed photoelimination via a common intermediate. The Nocera group proposed this intermediate to be Cl-bridged binuclear complex **3**, generated by photoextrusion of an isocyanide ligand (L, Figure 4.1) and migration of a Cl ligand to a bridging position.[16] Intermediate **3** represents an intramolecular analog of ligand-bridged intermediates proposed in binuclear elimination reactions.[17,18]

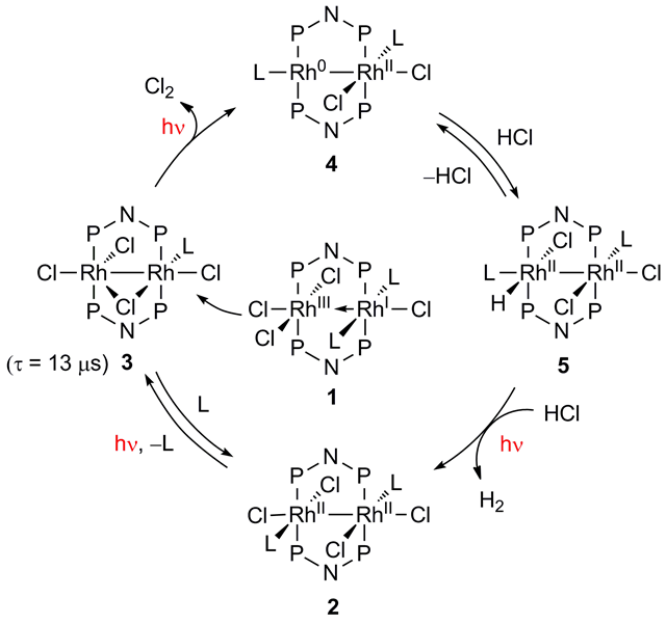

Figure 4.1. HX-splitting catalyzed by **1** proceeds via photoinduced ligand dissociation from catalyst resting state **1**, two-electron photoreduction of chloride-bridged complex **2**, protonation of Rh_2[0,II] complex **3**, and photoinduced H_2 evolution from Rh_2 hydride **4**. Three sequential photochemical steps are involved in the overall cycle; L = 1-adamantylisocyanide, P–N–P = *bis*(trifluoroethoxy)phosphino)methylamine (tfepma).

The ligand-bridged geometry of the two-electron core (i.e. **3)** is reminiscent of hydride-bridged intermediates of the binuclear elimination mechanism described by Norton for binuclear elimination reaction of Os alkyl hydrides.[19–21] In effect, the two-electron mixed valence core permits such an intermediate to be established intramolecularly, thus bypassing the need for a bimolecular reaction to achieve elimination. The potential relevance of such intermediates to

promoting the elimination reactions of more energy intensive processes such as HX splitting has not been investigated. In this Chapter, we now utilize photocrystallography to provide direct information regarding structural changes associated with intermediates of consequence to halogen elimination. Complementary synthesis of a new suite of dirhodium complexes allowed isolation and independent evaluation of the chemistry of the halide-bridged bimetallic complexes. Direct observation of halide-bridged structures establishes binuclear reductive elimination as a critical pathway for metal-halide bond activation.

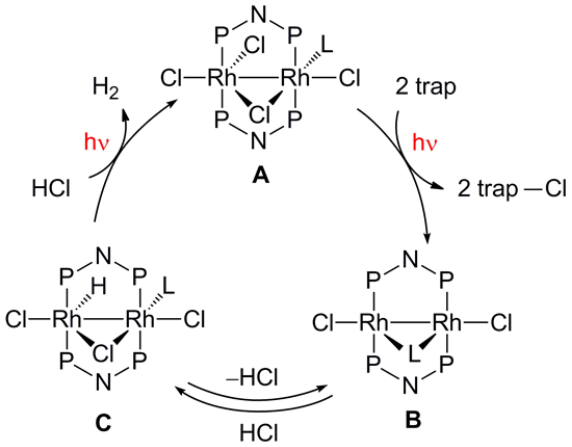

Figure 4.2. A photocycle involving a halide-bridged resting state for HX- has two photochemical steps instead of the three involved in catalysis with complex **1**.

A new family of phosphazane-bridged Rh_2 photocatalysts have been developed where the halide-bridged geometry is designed into the ground state guided by the identification of key intermediate for halogen photoeliminaiton reaction. Photointermediate **3** is short-lived (τ = 13 μs), which is typical of unsaturated structures generated by ligand photo-extrusion chemistry.[22] We hypothesized that if a Rh_2 structure supported by a single monodentate L-type ligand (Rh_2L_1) could be stabilized, the need for photochemically driven ligand dissociation (i.e. conversion of **2** to **3**, Figure 4.1) would be obviated. Stabilization of the chloride-bridged intermediate would

provide a structure poised to directly engage in multielectron photo-elimination chemistry. Accordingly, if a Rh_2L_1 structure were employed as a photocatalyst for HX splitting, the catalysis cycle depicted in Figure 4.2, which relies on two, not three, photochemical steps, could be accomplished.

We also applied this halide bridged two-electron mixed valency strategy to the first-row transition metal complexes. The excited states of $d\sigma^*$ parentage observed for the d^7–d^7, d^9–d^7, and d^9–d^9 homo- and heterobimetallic dirhodium and diplatinum complexes, possess both M–M and M–X antibonding character, such that electronic excitation into the empty dσ* orbital is expected to weaken M–X bonds, thereby promoting halogen elimination.[오류! 책갈피가 정의되어 있지 않습니다.,오류! 책갈피가 정의되어 있지 않습니다.,23–25] Herein, we introduce a system that addresses the challenge of efficient photochemical X_2 elimination at low-valent bimetallic Ni centers.

4.2 Photocrystallography

Thin-film TA spectroscopy was used to establish the homology of solution-phase and solid-state photoreactions. Thin films of complexes **1** and **2**, drop-cast from either THF or CH_2Cl_2 solutions, showed UV-vis absorption spectra that overlaid with solution spectra of **1** and **2** (Figure 4.3). The thin films are polycrystalline based on powder X-Ray diffraction (**1** and **2** (Figure 4.4), but the crystal phase could not be established do to anisotropic orientation of crystallites, which is typical of polycrystalline thin films.[26] TA spectra (λ_{exc} = 355 nm) of these films were recorded at 1 μs delay and show similar features to those observed in solution-phase TA spectra of these complexes, confirming the formation of the same photointermediate in both solution and solid state (Figure 4.5).

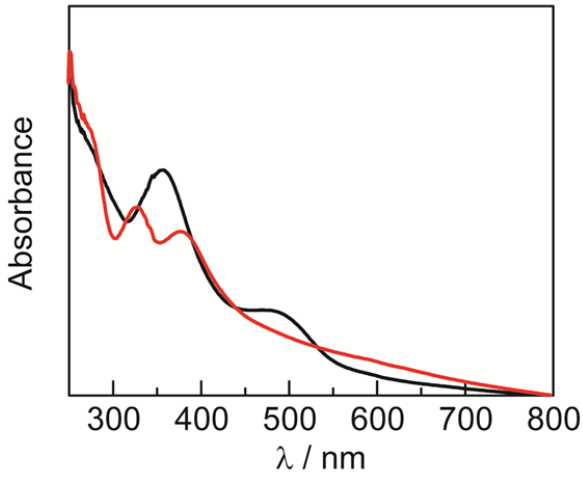

Figure 4.3. Solid-state absorption spectra of Rh_2[I,III] **1** (red) and Rh_2[II,II] complex **2** (black) obtained by measuring the wavelength-dependent absorbance of thin films of **1** and **2** drop cast on glass slides. The same sample preparation was used in measuring TA spectra of thin films.

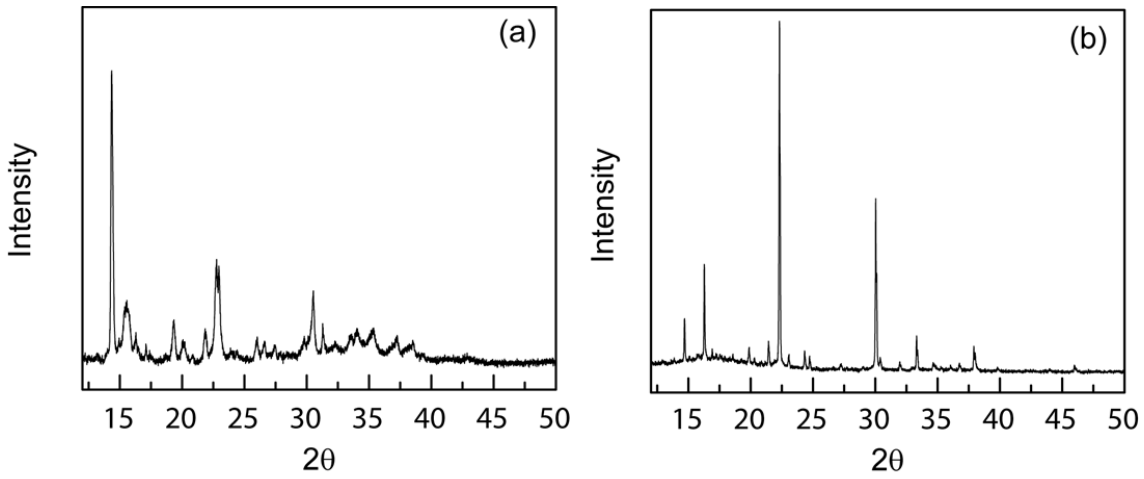

Figure 4.4. Powder diffraction pattern of a thin film of (a) Rh_2[I,III] complex **1** and (b) Rh_2[II,II] complex **2**.

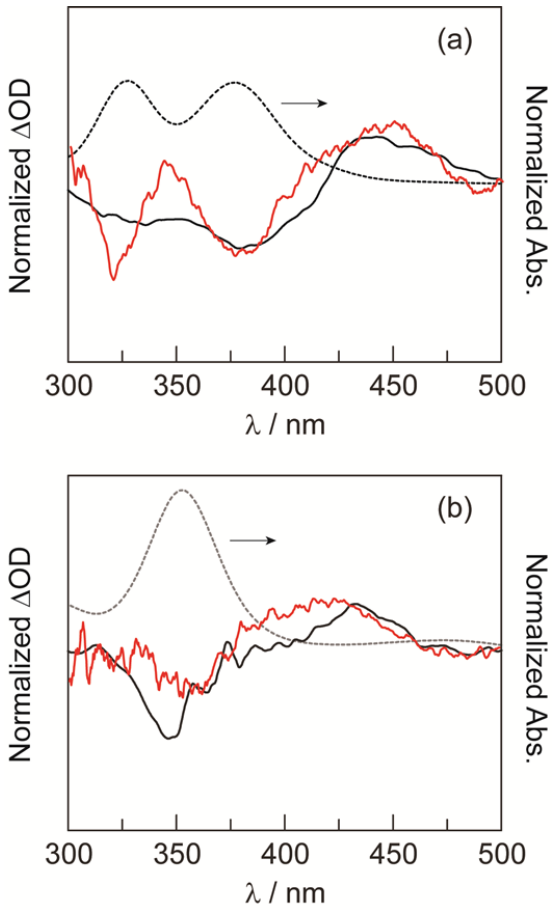

Figure 4.5. UV-vis spectra (dotted black), solution-phase TA spectra (solid black), and thin-film TA spectra (red) of (a) Rh_2[I,III] complex **1** and (b) Rh_2[II,II] complex **2**. TA spectra were obtained by flash laser photolysis (355 nm) and recorded at a 1 μs delay.

Steady-state photocrystallography experiments were performed at the Advanced Photon Source (APS) housed at Argonne National Laboratory (ANL) using synchrotron radiation (0.41328 Å) and a 365 nm LED light source (5 mW power measured at the crystal). A photodifference map was generated by comparing diffraction data obtained for a single crystal of Rh_2[I,III] complex **1** in the dark with diffraction data obtained for the same crystal during irradiation (Figure 4.6a). The crystal was not moved between the acquisitions of the two data sets and thus the orientation matrix was unchanged during the experiment. The difference map showed the presence of a photoinduced structure populated at 5.7(9)% of the crystal.

Examination of the structural perturbations in the photoinduced structure shows ligand reorganization that would be anticipated during a migration of one of the chloride ligands to a bridging position; key metrics include the Rh^1–Rh^2–Cl^3 bond angle, which contracts from 91.05(5) to 83.2(2)° in the photoinduced structure. Concurrent with this, Rh^1–Rh^2–Cl^4 expands from 90.97(5) to 92(2)°. Additionally, Rh^2–Cl^3 which is the bond vector participating in partial migration from terminal to bridging coordination mode elongates from 2.362(2) to 2.66(4) Å (additional metrical parameters are provided in Table 4.1).

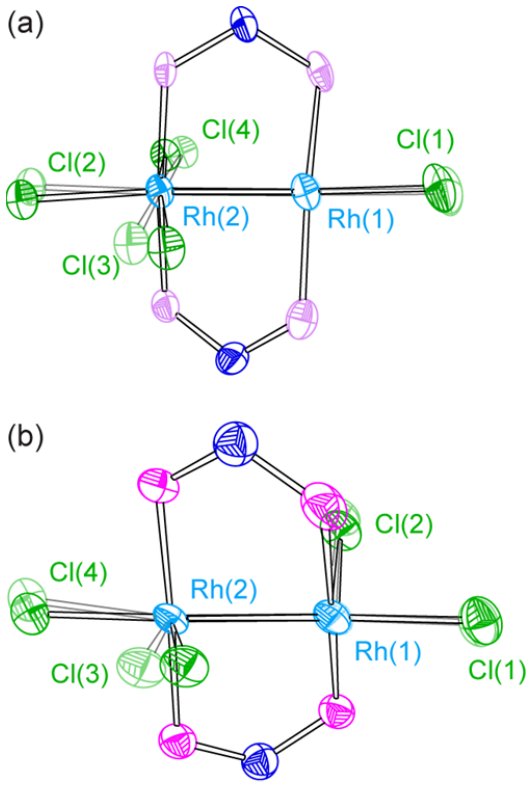

Figure 4.6. Thermal ellipsoid plots of photocrystallography results with photo-induced structures (solid) superimposed on dark structures (faded). (a) Rh_2[I,III] plot; Rh^1–Rh^2–Cl^3 91.05 (5) (dark), 83.2 (2)° (photo-induced). (b) Rh_2[II,II] plot; Rh^1–Rh^2–Cl^3 91.15 (5) (dark), 78 (2)° (light on).

The extent of laser heating of the sample during data acquisition was examined by comparing the size of thermal ellipsoids of atoms not involved in the primary photoreaction (i.e.

N-atoms in the phosphazane ligand) with the size of thermal ellipsoids for the same atoms as a function of temperature.[27] Based on this analysis, laser heating warmed the single crystal of **1** from 15 K to ~250 K (Figure 4.7). The metrical parameters of **1** are not observed to show significant temperature-dependent variation (Table 4.2), confirming that the difference map arises from photochemical, not thermal, effects.

Table 4.1. Comparison of selected metrical parameters for temperature-adjusted dark and photoinduced structures from photocrystallography experiment with Rh_2[I,III] complex **1**.

	Complex **1** (225 K)	photoinduced structure
Rh^1–Cl^1 (Å)	2.494 (2)	2.42 (4)
Rh^2–Cl^2 (Å)	2.435 (2)	2.44 (6)
Rh^2–Cl^3 (Å)	2.362 (2)	2.66 (4)
Rh^2–Cl^4 (Å)	2.364 (2)	2.39 (7)
Rh^1–Rh^2–Cl^3 (°)	91.05 (5)	83.2 (2)
Rh^1–Rh^2–Cl^4 (°)	90.97 (5)	92 (2)

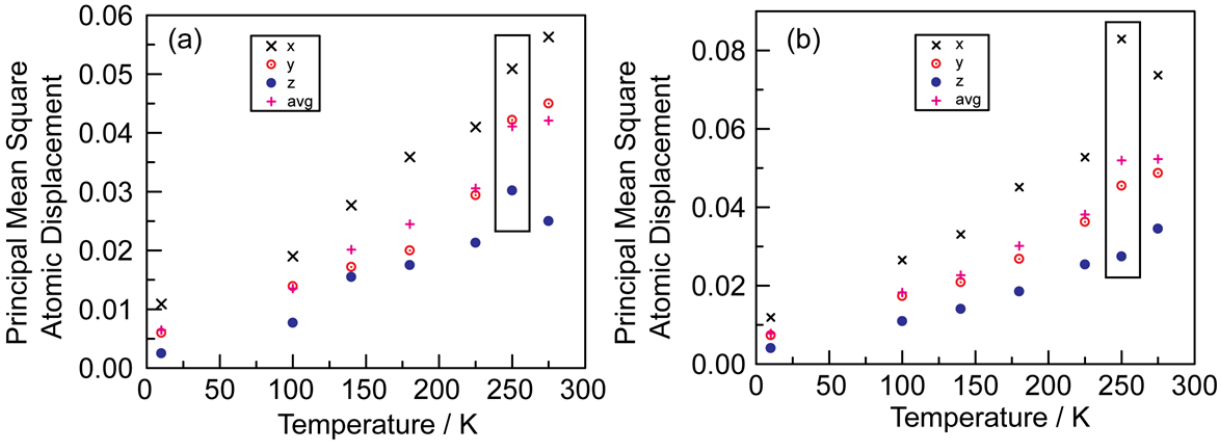

Figure 4.7. Principal mean square atomic displacements (U) for Rh_2[I,III] Complex **1** as a function of temperature plotted for (a) nitrogen atoms in the bridged phosphazane ligands (b) oxygen atoms of the OCH_2CF_3 groups. Thermal parameters obtained during photocrystallography are highlighted in a box.

Table 4.2. Selected metrical parameters for Rh_2[I,III] complex **1** as a function of temperature.

	10 K	100 K	140 K	180 K	225 K	275 K
Rh–Rh (Å)	2.7248 (3)	2.7246 (9)	2.7246 (7)	2.729 (1)	2.7283 (7)	2.749 (2)
Rh^1–Cl^1 (Å)	2.4929 (8)	2.490 (2)	2.493 (2)	2.496 (3)	2.494 (2)	2.509 (3)
Rh^2–Cl^2 (Å)	2.4300 (8)	2.428 (2)	2.431 (2)	2.435 (3)	2.435 (2)	2.448 (3)
Rh^2–Cl^3 (Å)	2.3633 (8)	2.357 (2)	2.359 (2)	2.369 (2)	2.363 (2)	2.387 (2)
Rh^2–Cl^4 (Å)	2.3617 (8)	2.362 (2)	2.359 (2)	2.369 (2)	2.364 (2)	2.388 (2)
Rh^1–Rh^2–Cl^3 (°)	91.26 (2)	91.04 (6)	91.13 (5)	91.13 (6)	91.05 (5)	90.96 (6)
Rh^1–Rh^2–Cl^4 (°)	90.96 (2)	91.17 (6)	91.12 (5)	90.97 (6)	90.97 (5)	90.87 (6)

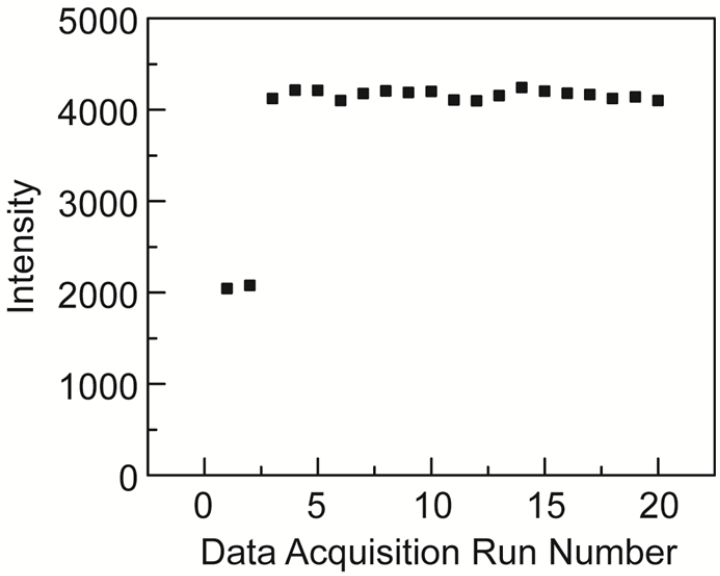

Figure 4.8. Plot of the intensity of spot [9,–1,3] as a function of time. The laser was turned on after the second data point in the above plot.

The photoinduced structure derived from complex **1** was accessed rapidly during irradiation. Comparison of specific reflections from the structures obtained in the dark and under

illumination revealed a set of reflections that showed substantial intensity changes upon irradiation. Examination of these particular reflections as the light was turned on showed that the intensity changes as a step function; the intensity increased rapidly relative to data collection, and then reaches a steady-state value during irradiation (Figure 4.8).

A steady-state photocrystallography experiment was also performed using a single crystal of Rh_2[II,II] complex **2** under identical conditions to the aforementioned experiment with **1** (15 K, 5 mW 365 nm irradiation, 0.41328 Å synchrotron radiation). A photoinduced structure was identified in the photodifference map in which the Rh(1)–Rh(2)–Cl(3) angle contracts from 91.15(5) to 78(2) upon irradiation (Figure 4.6b). Partial migration of Cl(3) towards the bridging position is accompanied by substantial elongation of the Rh–Cl bond (2.378(2) to 2.57(8) Å). The photoinduced geometry could be identified in the photodifference map generated from **2**, but full-molecule disorder in the available single crystals of **2** precluded determination of the population of the photoinduced structure. Variable-temperature crystallography experiments performed on a single crystal of **2** confirm that the observed structural effects are photoinduced, not thermally promoted. Similar to experiments carried out with complex **2**, the photoinduced structure is accessed rapidly relative to data acquisition. Upon cessation of irradiation, the photoinduced structure is no longer observed in the photodifference map, indicating that the photoinduced state is accessed only during steady-state irradiation.

4.3 Synthesis, Characterization and Photochemistry of a new family of Rh_2 complexes

Each of the proposed steps in the targeted photocycle drawn in Figure 4.2: (i) photoreduction of a chloride-bridged binuclear complex to a ligand-bridged Rh_2[I,I] complex, (ii) protonation to afford a chloride-bridged Rh_2 hydride, and (iii) photoevolution of H_2 by

photolysis of the Rh_2 hydrides in the presence of acid, has been independently examined using isolated Rh_2 complexes.

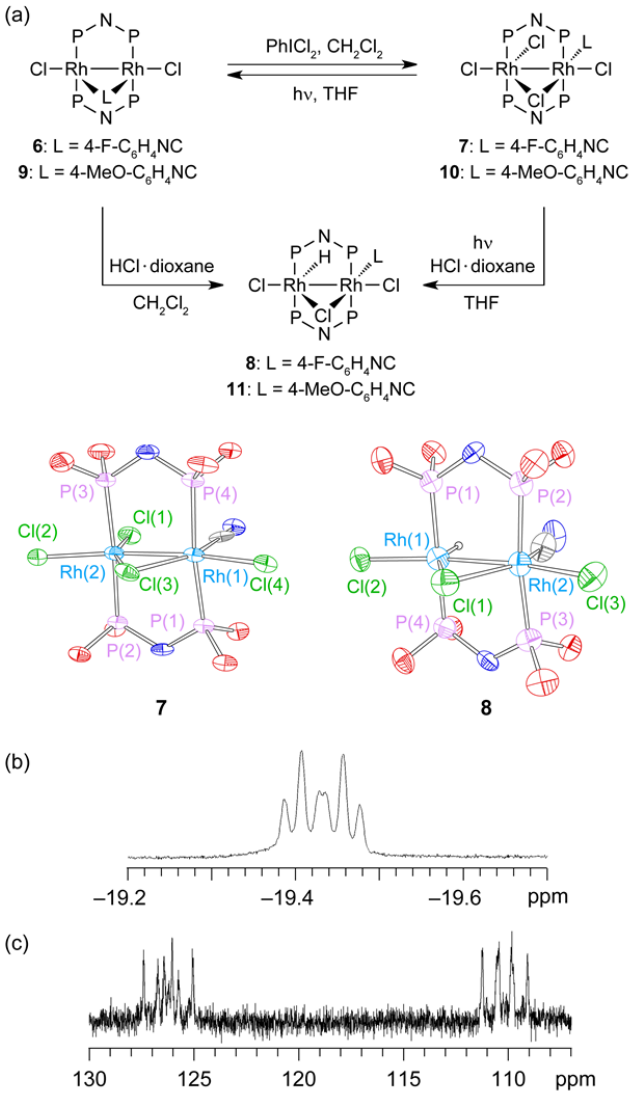

Figure 4.9. (a) Synthetic relationships between Rh_2L_1 chloride complexes. Thermal ellipsoid plots of **7** and **8** drawn at the 50% probability level. The $–CH_2CF_3$, aryl groups and hydrogen atoms are omitted for clarity. Representative bond lengths [Å]: **7**, Rh(1)–Rh(2): 2.6260(8); Rh(1)–Cl(3): 2.423(2); Rh(2)–Cl(3): 2.405(2). **8**, Rh(1)–Rh(2): 2.610(2); Rh(1)–Cl(1): 2.530(3); Rh(2)–Cl(1): 2.467(3). (b) Expansion of the upfield region of the ^1H NMR of Rh_2 hydride **8** showing both $^1J_{Rh–H}$ = 25.0 Hz and $^2J_{P–H}$ = 10.0 Hz.

The suite of Rh_2L_1 complexes needed to interrogate the photocycle of Figure 4.9 was accessed by the sequential treatment of $[RhCl(cod)]_2$ with phosphazane tfepma and substituted aryl isocyanides followed by oxidation with $PhICl_2$; use of 4-F-C_6H_4NC provided ready access to chloride-bridged Rh_2 tetrachloride complex **7**. Photolysis of THF solutions of **7** featuring a terminal isocyanide ligand (ν_{CN} = 2181 cm^{-1}) affords Rh_2[I,I] complex **6** with a bridging isocyanide ligand (ν_{CN} = 1736 cm^{-1}) in 97% yield (Figure 4.10), which establishes the viability of two-electron photo-reduction of (μ-Cl)Rh_2 complexes (step **A** → **B**, Figure 4.2). Photoreduction requires the presence of potential halogen-radical traps (i.e. THF); photolysis of a PhH solution of **8** does not result in photoreduction. Cl-atom trapping by THF via H-atom abstraction (HAA) would generate HCl and a furanyl radical, which could participate in a variety of subsequent transformations.[28,29] The furanyl-radical derived products under these conditions have not been identified.

Treatment of the photogenerated Rh_2[I,I] complex **6** with HCl afforded a new complex, which we assign to be Rh_2 hydride complex **8** (98% yield). The spectral details supporting this assignment are outlined below. ^{1}H NMR spectrum contained signals attributable to one 4-fluorophenylisocyanide ligand, two tfepma ligands, and an additional resonance at –19.40 ppm (dt, $^1J_{Rh–H}$ = 25.0 Hz, $^2J_{P–H}$ = 10.0 Hz), which integrated for a single proton (Figure 4.9b). The $^{31}P\{^1H\}$ NMR spectrum displayed two multiplets, centered at 110 and 126 ppm; a ^{1}H-^{31}P HMQC experiment established coupling of the ^{31}P resonance at 126 ppm to the ^{1}H resonance at –19.40 ppm. The IR spectrum displayed a ν_{CN} = 2171 cm^{-1} (Figure 4.10), consistent with a terminally bound isocyanide ligand.[30–32]

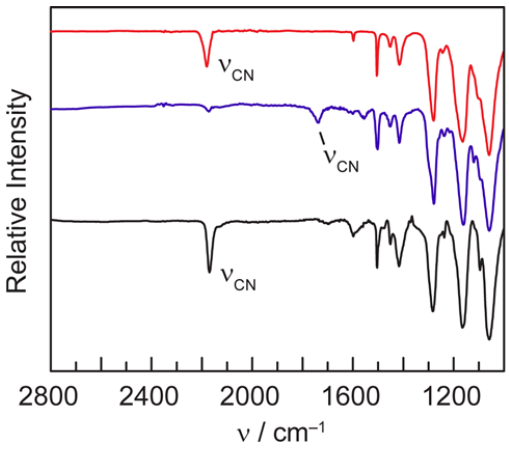

Figure 4.10. IR spectra of Rh_2(I,I) complex **6** (blue, ▬), Rh_2 tetrachloride complex **7** (red, ▬), and Rh_2 hydride complex **8** (black, ▬).

Removal of the reaction solvent and redissolution of the residue afforded a mixture of Rh_2 hydride **8** and Rh_2[I,I] complex **6**. Single crystals of Rh_2 hydride **8** were obtained by layering the reaction mixture with $PhCH_3$ and X-ray diffraction analysis established the molecular structure of **8** to be the chloride-bridged Rh_2 complex shown in Figure 4.9a. The hydride ligand was not located in the difference map, but its presence was inferred by examination of the bond lengths between the bridging chloride ligand and each of the Rh centers; Rh(2)–Cl(1) (trans to isocyanide ligand): 2.467(3) Å while Rh(1)–Cl(1) (trans to hydride ligand): 2.530(3) Å. The asymmetry in the Rh–Cl distances to the bridging ligand is consistent with the strong trans influence of the hydride ligand as compared to the isocyanide ligand.[33] For comparison, Rh–Cl bond distances for chloride-bridged complex **7** are 2.421(2) and 2.404(2) Å, respectively. The oxidative addition of HCl to **6** to generate Rh_2 hydride **8** confirms the viability of the transformation of **B** to **C** in Figure 4.2. Finally, photolysis of **8** in the presence of HCl leads to the evolution of H_2 without consumption of **8** (vide infra, photocatalysis section). Consistent with the requirement for photochemical, not thermal, H_2 evolution, treatment of Rh_2 hydride **8** with excess HCl does not lead to the thermal evolution of H_2. The failure to produce H_2

thermally upon treatment of **8** with HCl is consistent with previous report of diminished hydricity of related Rh_2 hydride complexes.[34]

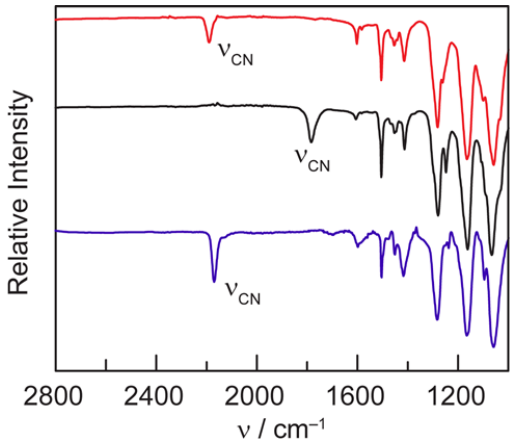

Figure 4.11. IR spectra of Rh_2[I,I] complex **9** (black, ▬), Rh_2 tetrachloride complex **10** (red, ▬), and Rh_2 hydride complex **11** (blue, ▬).

Rh_2L_1 complex **10**, supported by a 4-$MeOC_6H_4NC$ ligand, participates in a similar manifold of photochemical reactions as does Rh_2L_1 complex **7** (Figure 4.9a). Complex **10** undergoes clean photoreduction to Rh[I,I] complex **9**, which can be converted to Rh_2 hydride **11** upon treatment with HCl. The spectral features observed for hydride **11** (^{1}H and ^{31}P{^{1}H} NMR, IR) are similar to those observed for **8**. The ^{1}H NMR spectrum of **11** displays a resonance at –19.44 ppm that integrates for one proton (Figure 4.62), and the IR spectrum of **11** displays a ν_{CN} = 2170 cm^{-1} (Figure 4.11), consistent with a terminally bound isocyanide ligand. In addition, single-crystal X-ray analysis reveals a close structural homology between hydrides **11** and **8**; the Rh–Cl bond trans to the hydride ligand in **11** is 2.5504(7) Å and the Rh–Cl bond trans to the isocyanide ligand is 2.4579(7) Å.

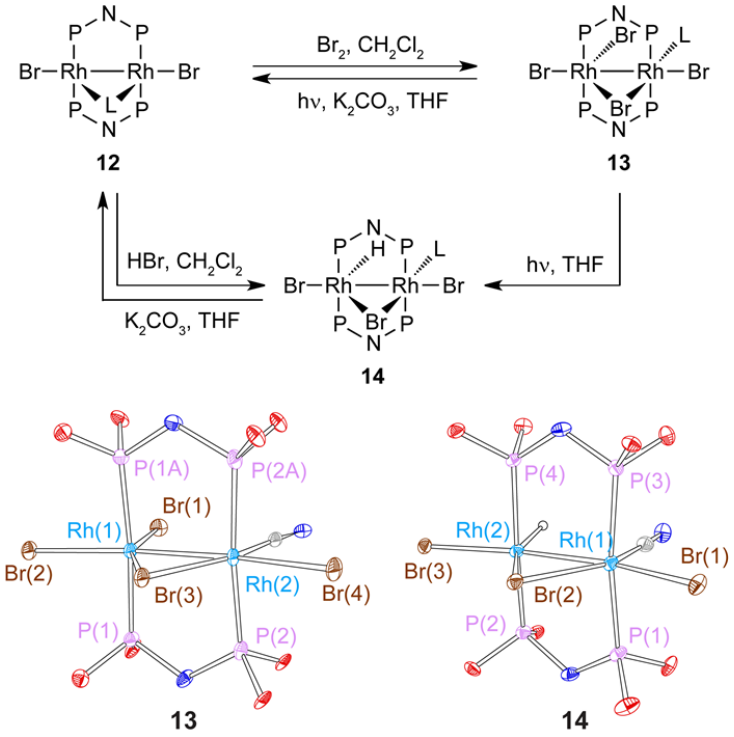

Figure 4.12. Synthetic relationships between Rh_2L_1 bromide complexes. Thermal ellipsoid plots of **13** and **14** drawn at the 50% probability level. The $-CH_2CF_3$, aryl groups and hydrogen atoms are omitted for clarity. Representative bond lengths [Å]: **13**, Rh(1)–Rh(2): 2.651(2); Rh(1)–Br(3): 2.522(2); Rh(2)–Br(3): 2.527(2). **14**, Rh(1)–Rh(2): 2.6309(6); Rh(1)–Br(2): 2.5753(7); Rh(2)–Br(2): 2.5187(7).

The photochemistry of halide-bridged Rh_2L_1 complexes is not specific to Rh_2 chlorides. $Rh_2[I,I]Br_2$ complex **12**, Rh_2Br_4 **13** and Rh_2 hydride **14** are structurally similar to their Rh_2 chloride analogues (Figure 4.12). Notably, the X-ray structure of Rh_2 hydride **14** was determined at 15 K using synchrotron radiation (0.41328 Å) at the Advanced Photon Source housed at Argonne National Laboratory, allowing direct location of the hydride ligand. Consistent with the structures of **8** and **11**, the Rh–Br distance to the bridging bromide is substantially longer trans to the hydride (2.6411(7) Å) than trans to the isocyanide (2.5753 (7) Å).

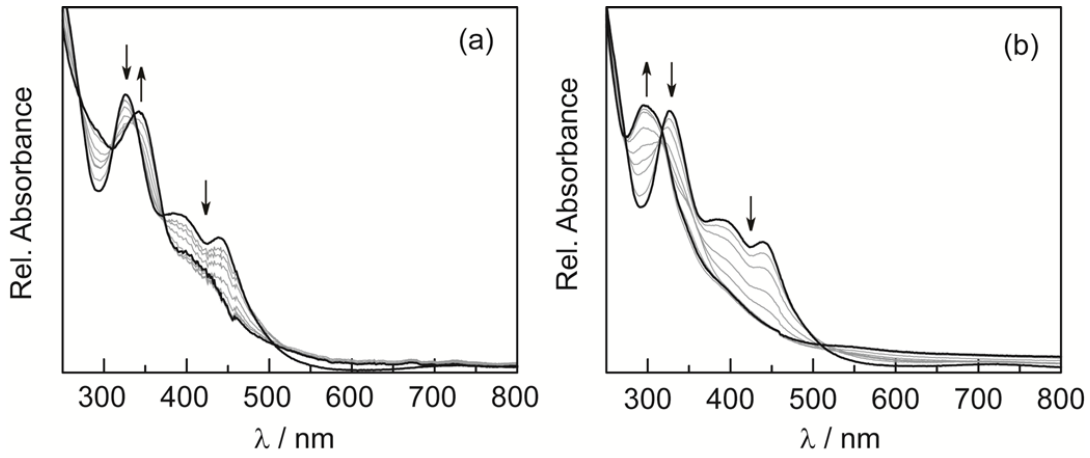

Figure 4.13. (a) Spectral evolution during the photolysis (λ > 295 nm, spectra collected over 100 min) of **13** in THF, which affords Rh_2 hydride **14**, by reaction of photogenerated HBr with Rh_2[I,I] complex **12**. (b) Spectral evolution during the photolysis (λ > 295 nm) of **13** in THF in the presence of K_2CO_3, which affords Rh_2[I,I] complex **14**.

Unlike photolysis of chloride-bridged dirhodium complexes **7** and **10** discussed above, photolysis of **13** does not lead to observation of Rh_2[I,I] complex **12**, but instead leads to the evolution of the spectral features assignable to Rh_2 hydride **14** (Figure 4.13a). Formation of complex **14** can be envisioned as arising from initial photoreduction to Rh[I,I] complex **12** and an equivalent of Br_2. Under high photon flux conditions, Br radical formation would be expected and subsequent reaction of bromine radical with THF would afford HBr and a furanyl radical.[35] Reaction of the photoevolved HBr with Rh_2[I,I] complex **12** would generate observed Rh_2 hydride complex **14**. The Br· implied in such a scheme could arise from either homolysis of photo-evolved Br_2 or directly from complex **13** via two rapid, sequential one-electron reduction steps. The dichotomous photochemical behaviour of chloride-bridged Rh_2 complexes, which undergoes clean photoconversion to Rh_2[I,I] complexes, and bromide-bridged Rh_2 complex **13**, which undergoes photoconversion to hydride **14**, is consistent with the increased acidity of HBr as compared to HCl (pK_a(HCl) = –0.4, pK_a(HBr) = –4.9 in 1,2-dichloroethane).[36,37] When

photolysis of **13** is carried out in the presence of K_2CO_3, added to react with the photogenerated HBr, Rh_2[I,I] bromide complex **12** is observed (Figure 4.13b).

4.4 Photocatalysts

Photocatalysis with halide-bridged complexes was investigated by irradiation of THF solutions of these complexes (1.0 mM Rh_2 catalyst) in the presence of acid (0.1 M). Evolved H_2 was quantified by both gas chromatography (GC) of the headspace gases and Toepler pump combustion analyses. Photolysis of THF solutions of **7** in the presence of HCl led to H_2 evolution. Given that halogen elimination is the efficiency limiting step in all previous HX splitting photocycles that we have studied, we anticipated the dirhodium tetrachloride **7** would be the photoresting state. To the contrary, UV-vis spectra of the H_2-evolution reaction catalyzed by **7** showed the disappearance of the absorption features of **7** and the evolution of the absorption spectrum of Rh_2 hydride **8** (Figure 4.14a). The ^{1}H NMR, IR, and UV-vis spectral features of **8** prepared by treatment of **6** with HCl are identical to those measured for **8** prepared by photolysis of **7** in the presence of HCl. Taken together, the accumulated spectral data establish that the resting state of photocatalysis is dirhodium hydride complex **8**. The change in photoresting state from the maximally chlorinated intermediate (i.e. **1**) to a Rh_2 hydride (i.e. **8**), is consistent with acceleration of halide oxidation relative to proton reduction by stabilizing the ligand-bridged structures required for the halide oxidation half reaction. As is evident from the constant rate of H_2 evolution, and as confirmed by electronic absorption spectroscopy, no catalyst decomposition is detected after 72 h of photolysis (Figure 6a). A catalyst turnover number of 6.8 is attained at 72 h.

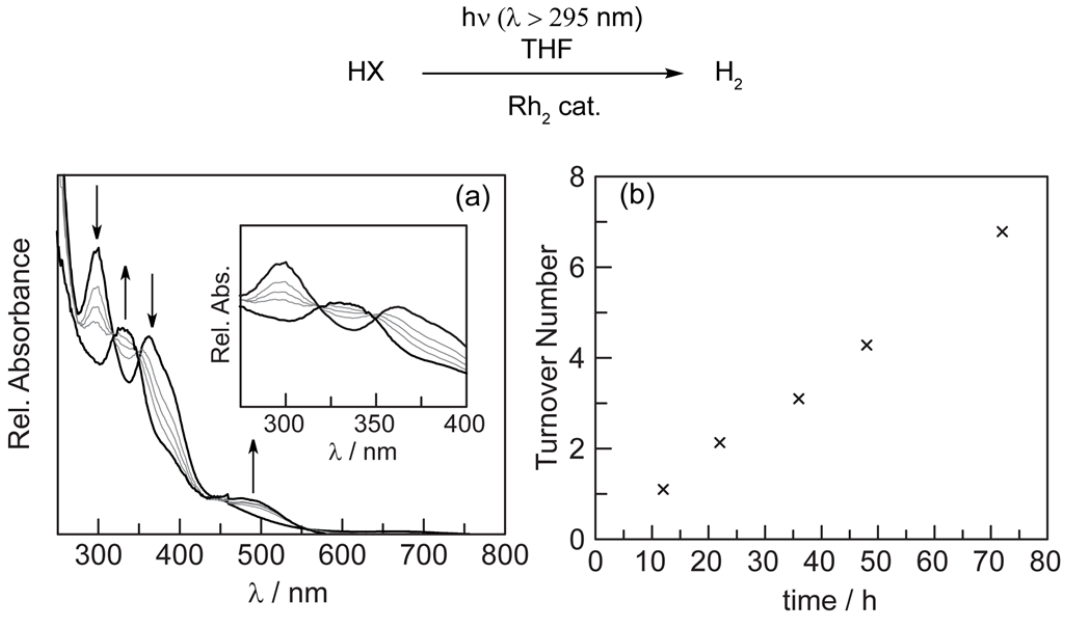

Figure 4.14. (a) Spectral evolution during the photolysis (λ > 295 nm, spectra collected over 75 min) of **7** in THF in the presence of HCl. The spectral features of **7** disappear and the spectral features of Rh_2 hydride **8** evolve with time. Inset: Well-anchored isosbestic points are observed, consistent conversion of **7** to **8** without a steady-state intermediate. (b) Time-dependent H_2 evolution TON (with respect of loading of catalyst **8**) from HCl, catalyzed by chloride-bridged Rh_2 complex **8**; 0.1 M HCl, 1.0 mM Rh_2 cat., λ > 295 nm.

Hydrogen evolution catalysis is also observed when chloride bridged complex **10** is photolyzed in the presence of HCl. Similar to observations with **7** as a precatalyst, photolysis of **10** in the presence of HCl leads to the disappearance of **10** and the evolution of Rh_2 hydride **11** (Figure 4.15). Hydride **11** is the catalyst photoresting state during subsequent H_2 evolution. Similarly, Rh_2 hydride **14** is the photoresting state during H_2 evolution from HBr when either **12** or **13** are employed as the photocatalyst (Figure 4.16).

With a series of Rh_2L_1 complexes in hand, the contention that stabilization of halide-bridged geometries can provide more active HX-splitting photocatalysts could be evaluated. We examined this possibility by measuring the rate of H_2 evolution with Rh_2[II,II] complex **1** as well as chloride-bridged complexes **8** and **11** in the presence of HCl. Tetrachloride complex **1** was

compared with hydridohalide complexes **8**, **11**, and **14** because each of these species represents the catalyst photoresting state during H_2-evolving photocatalysis.

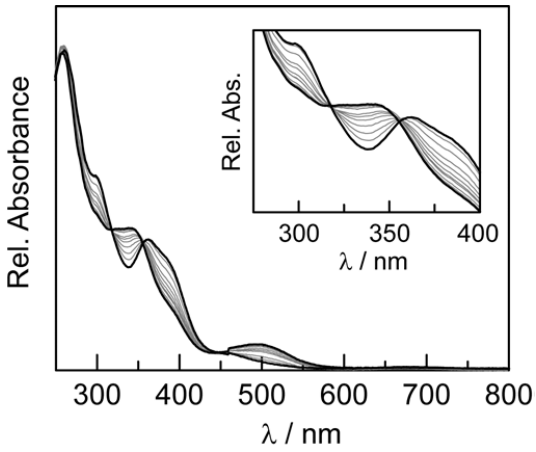

Figure 4.15. Spectral evolution for the photolysis of Rh_2(tfepma)$_2$(*p*-MeO-C_6H_4NC)(μ-Cl)Cl_3 (**9**) in THF (λ > 295 nm) in the presence of HCl·dioxane, which affords Rh_2 hydride **10**. Spectra were collected periodically over 20 min. Inset: Well-anchored isosbestic points were observed in the spectra generated during the photolysis of **9** in the presence of HCl, consistent with the conversion of **9** to **10** proceeding without the build-up of a steady-state intermediate.

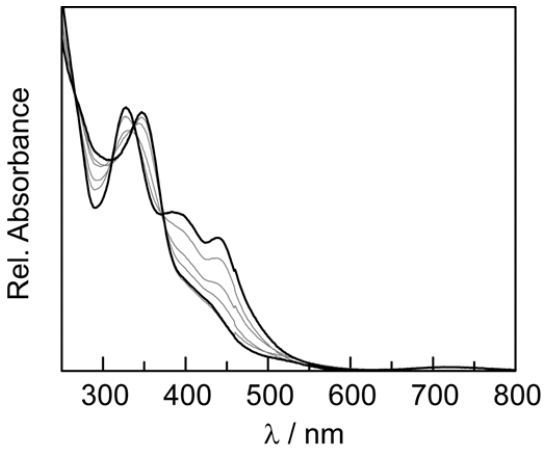

Figure 4.16. a. Spectral evolution for the photolysis of Rh_2(tfepma)$_2$(*p*-F-C_6H_4NC)(μ-Br)Br_3 (**12**) in THF (λ > 295 nm) in the presence of HBr. Spectra were collected periodically over 82 min.

Consistent with Rh_2 hydrides **8**, **11**, and **14** as the catalyst resting states, the H_2 evolution profile does not change if **7**, **10**, or **13** are used as pre-catalysts in lieu of complexes **8**, **11**, and **14**, respectively. To compare the H_2 evolution efficiencies of the catalysts, the amount of H_2 evolved in 24 h was measured using broadband irradiation ($\lambda > 295$ nm). The concentration of catalyst in these experiments (1.0 mM) was such that all of the incident light from the Hg-arc lamp was absorbed (abs ≥ 1.5 for $300 < \lambda < 500$ nm). Single-wavelength studies were not pursued because the overall H_2 evolution efficiency is low, which prevented reliable quantification when single wavelengths were used. We find that Rh_2L_1 complex **8** is 2.3 times more efficient in H_2 evolution than Rh_2L_2 complex **1**; and Rh_2L_1 complex **11** is 4.2 times more efficient at H_2 evolution than is complex **1**. H_2 evolution catalyzed by Br-bridged complex **13** was also found to be 3.5 times faster than H_2 evolution from HCl catalyzed by **1**.

4.5 Ni_2 complexes

Our lab has previously shown that photocrystallography is a powerful tool to witness the motion of bonds in the solid state. Beyond this it has also allowed us to iteratively design better catalysts by understanding the dynamic nature of these catalysts while they interact with light. Early work with the aforementioned dirhodium system showed movement of an axially ligated chloride towards a bridging position, setting the halide up for X_2 elimination. Knowing that this was the intended trajectory of the halide we were able to design a catalyst with the halides pre-oriented in a vicinal configuration, yielding a much higher efficiency for X_2 elimination. Though this system was an early success, it showed modest halide movement, in part likely due to the strength of the Rh–Cl bond and made use of one of the most expensive metals commercially

available. In order to develop catalysts that can be used for the large scale production of X_2, it is imperative that we move towards cheaper earth abundant metals such as nickel.

Further, halogens such as Cl_2 and Br_2 are not only good ways to store solar energy but have been valuable feedstock chemicals for the radical and electrophilic halogenation of small molecules since the 1800s. The storage and transportation of these corrosive and toxic gases/liquids poses a problem to their de-centralized use as well as their use in smaller scale pilot operations. Additionally, halogens made on scale using electrolysis methods starting from brine solutions represent a large energetic input beyond what is required to drive halogenation reactions. If halogens and halogen atom radicals could instead be generated *in-situ* and on-site using a stable halide source and light it could present a drastic improvement in safety, transportation and storage cost, as well as energy efficiency. The use of light in radical halogenations as well as other large scale organic processes is well established and has even grown recently.

To this end, we have aimed to replicate our work with this successful rhodium system using a similar two electron mixed valence system composed of a bimetallic nickel compound bridged by three chelating phosphines (dppm (dppm = $CH_2(PPh_2)_2$ and tfepma (tfepma = $((CF_3CH_2O)_2P)_2NCH_3$)). We wanted to make use of photocrysallography to see if similar design elements could be implicated in this system and if a trend could be constructed to push catalyst design further. Finally, we studied the solution and solid state elimination of Cl• and Cl_2 from these nickel compounds. It should be noted that the ligands used in this system are thermally robust and can be manufactured on scale from commercially viable chemicals. Despite the air sensitive nature of these ligands they can be generated i*n situ* from $Ni(cod)_2$ and the respective phosphine, eliminating the need for catalyst storage.

4.6 Synthesis and Characterization of Ni_2 complexes

Comproportionation of $Ni(cod)_2$ and $NiCl_2(PPh_3)_2$, (cod = 1,5-cyclooctadiene) with 3 equivalent of the phosphazane tfepma ligand yields the diamagnetic $Ni_2[I,I](tfepma)_3Cl_2$ complex **15**. The bromide analog complex **16** was also prepared in an analogous way from $NiBr_2(PPh_3)_2$. Treatment of **15** or **16** with 2 equivalents of CN^tBu in THF affords the one electron reduced paramagnetic $Ni_2[I,0](tfepma)_3(CN^tBu)(X)$ complexes **17** (X = Cl) and **18** (X = Br).

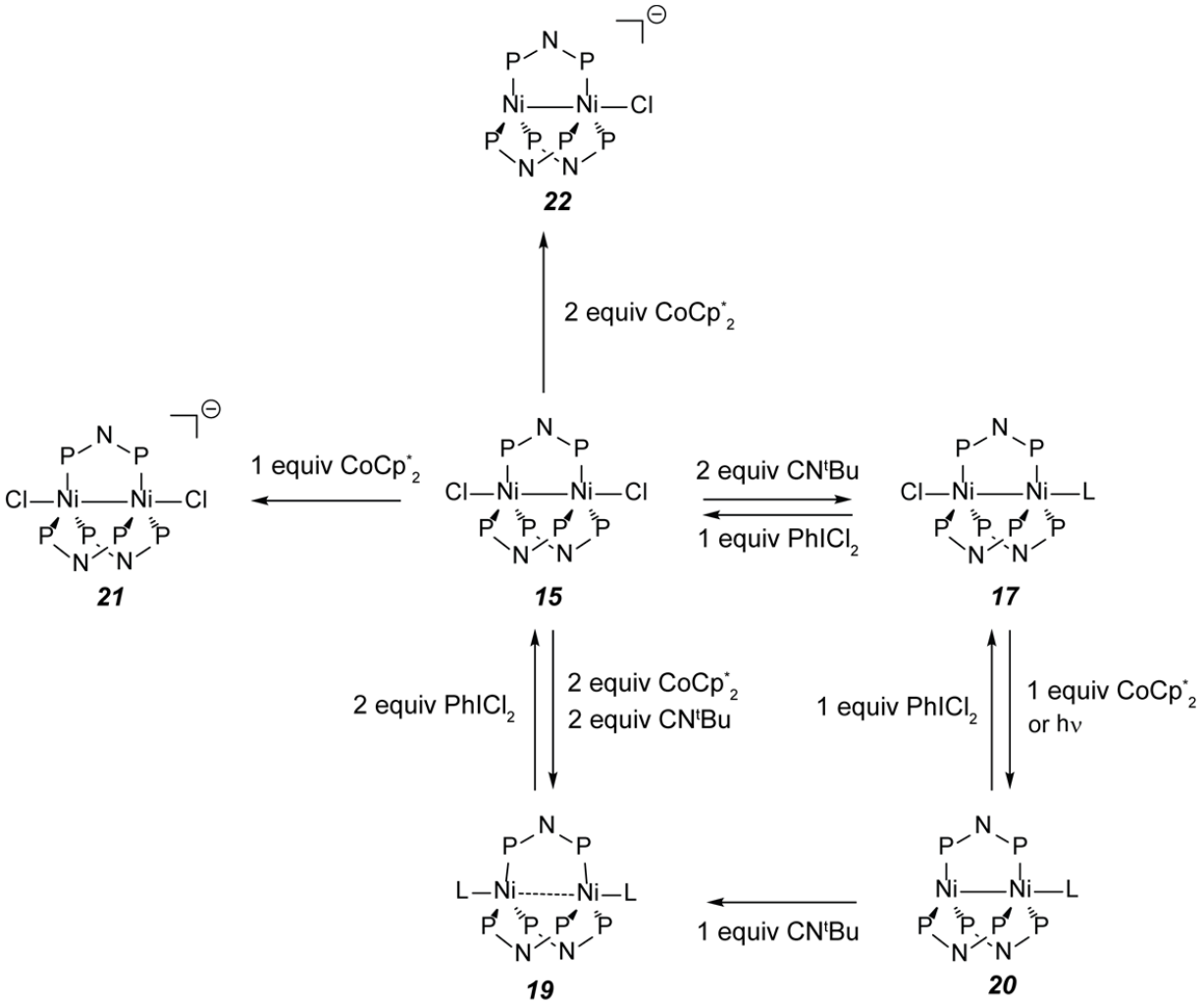

Figure 4.17. Synthetic relationships between tfepma bridged Ni_2 complexes.

The paramagnetic complexes **17** and **18** display no resonances in the ^{1}H NMR and $\{^{1}H\}^{31}P$ NMR spectrum. EPR spectroscopy (Figure 4.18) indicates the complexes are S = ½, as expected for a binuclear d^{9}–d^{10} complex with additional hyperfine couplings to phosphorus and halide atoms, which demonstrates that the unpaired electron occupies the dσ* orbital. As shown in Figure 4.19, the IR spectra of complexes **17** and **18** show a ν_{CN} = 2152 and 2145 cm^{-1} respectively, consistent with a terminally bound isocyanide ligand.

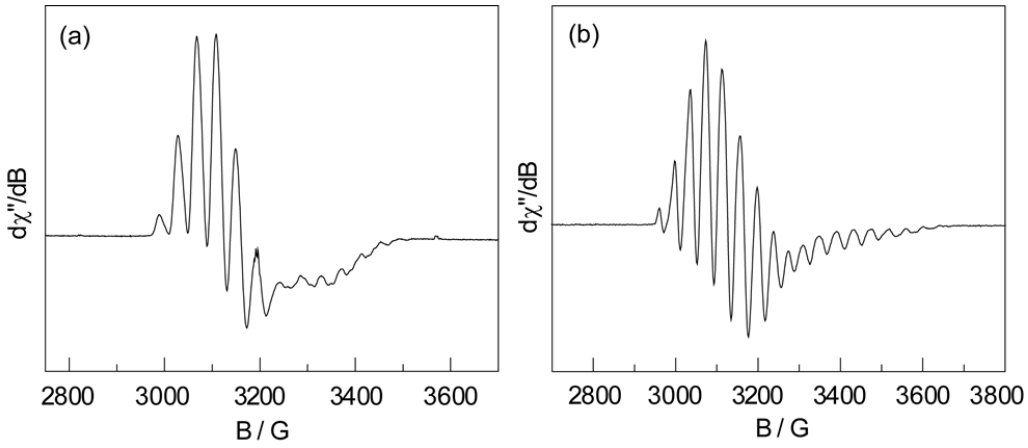

Figure 4.18. EPR spectra of Ni_2[I,0] complexes (a) **17** and (b) **18** recorded at 77.0 K in 2–MeTHF glass.

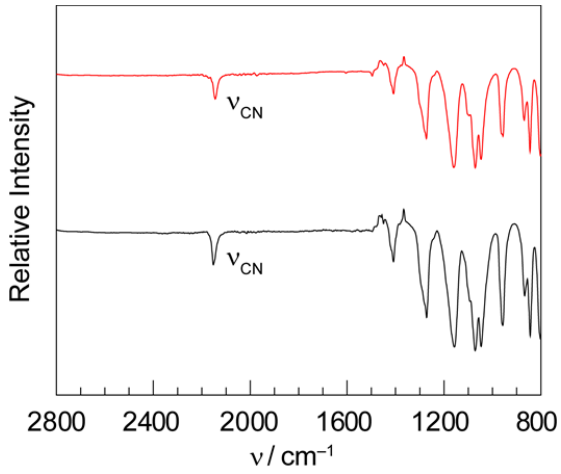

Figure 4.19. IR spectra of Ni_2[I,0] complex **17** (▬, black), and Ni_2[I,0] complex **18** (▬, red).

Treatment of **17** with 0.5 equivalents of iodobenzene dichloride, ($PhICl_2$), in C_6H_6 regenerates **15**. The molecular structure of complex **15** has been determined by X-ray diffraction, and shows a pseudo-D_{3h} symmetry with three bridging tfepma ligands and two five-coordinate nickel centers in a trigonal bipyramidal environment (Figure 4.20). A Ni–Ni distance of 2.5905(10) Å is observed for complex **15**, indicating a formal metal–metal bond that is consistent with previously reported d^9–d^9 binuclear Ni complexes.[38,39] The molecular structure of complex **17** shown in Figure 4.4 confirms the spectral findings of a bimetallic core that possesses an approximate C_{3v} symmetry, with two asymmetric trigonal bipyramidal Ni centers featuring isocyanide and chloride ligands. The Ni–Ni and Ni–Cl distances of 2.8687(3) and 2.4291(5) Å in complex **17** are elongated in comparison to those of complex **15**, 2.5905(10) and 2.2601(13) Å respectively, thereby confirming the population of the dσ* orbital, which possesses anti-bonding character with respect to the Ni–Ni and Ni–Cl bonds.

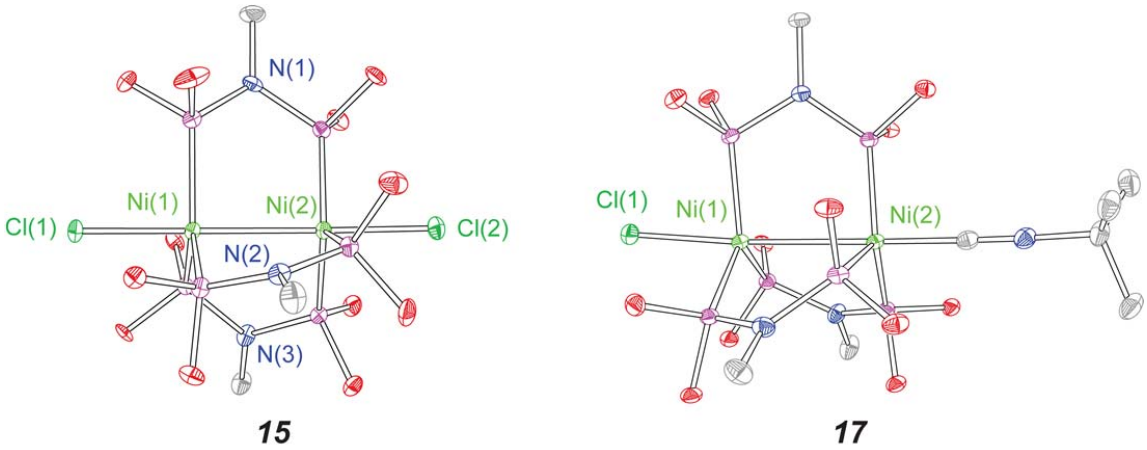

Figure 4.20. Thermal ellipsoid plots of **15** and **17** drawn at 50% probability. H atoms and $-CH_2CF_3$ groups have been removed for clarity.

The two electron reduced $Ni_2[0,0](tfepma)_3(CN^tBu)_2$ complex **19** is obtained when **15** is treated with both 2 equivalents of $CoCp^*_2$ ($CoCp^*_2$ = bis(cyclopentadienyl)cobalt(II)) and 2

equivalents of CN^{t}Bu. The isocyanide bound Ni_2[0,0](tfepma)$_3$(CN^{t}Bu) complex **6** was prepared analogously from treatment of **17** with 1 equivalent of $CoCp^*_2$ in THF. In the absence of isocyanide, treatment of the Ni_2[I,I] complex **15** with 1 or 2 equivalent of $CoCp_2^*$ afforded the [Ni_2[I,0](tfepma)$_3Cl_2$][$CoCp_2^*$] complex **21** and [Ni_2[0,0] (tfepma)$_3$Cl][$CoCp_2^*$], complex **22**, respectively. Complex **19** and **20** feature terminal isocyanide ligand stretching frequencies (ν_{CN} = 2094 and 2150 cm^{-1}, respectively) in the IR spectra (Figure 4.21) consistent with dppm (bis(diphenylphosphino)methane**)** bridged dinuclear nickel complexes reported by Kubiak.[40,41] The molecular structure of both **19** and **20** have been characterized by single crystal X-ray diffraction, and are illustrated in Figure 4.22. The structure of complex **5** shows two distorted tetrahedral Ni(0) centers bridged by three tfepma ligands, where the Ni–Ni distance is 3.810 Å, thereby confirming the absence of a significant Ni–Ni interaction, as expected for two d^{10} metal centers. Interestingly, complex **20** features a coordinatively unsaturated Ni(0) center and displays a much shorter Ni–Ni distance of 2.6413(6) Å., which suggests some degree of polarized Ni(0)/Ni(0) interaction. The formation of a dative bond from the electron rich unsaturated Ni(1) to the electron poor isocyanide-bound Ni(2) could justify the short Ni–Ni bond distance. Treatment of **20** with 1 equivalent of CN^{t}Bu affords complex **19**, as confirmed by $\{^1H\}^{31}P$ NMR spectoscopy. Chemical oxidation of complex **19** and **20** using $PhICl_2$ as a solid chlorine surrogate yields complex **15** and **17,** respectively. X-ray crystallography confirms the structures of **21** and **22**, as shown in Figure 4.23. Both complexes **21** and **22** represent the anionic binuclear Ni complexes with decamethylcobaltocenium ([$CoCp_2^*$]$^+$) as an outer sphere cation. The chloride ligands coordinate to the Ni metal centers to saturate the coordination environment.

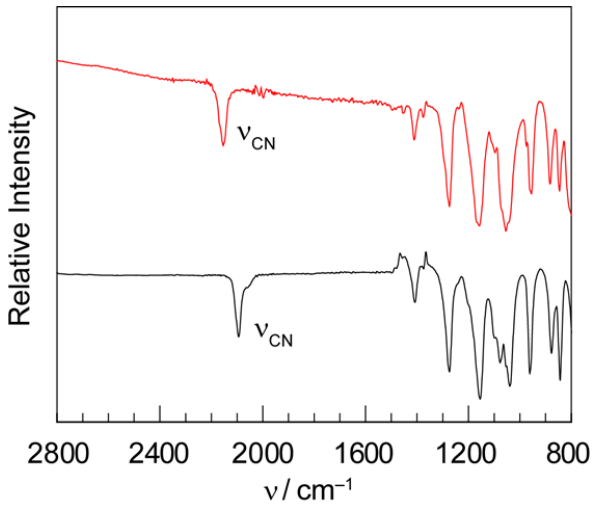

Figure 4.21. IR spectra of Ni_2[0,0] complex **19** (—, black), and Ni_2[0,0] complex **20** (—, red).

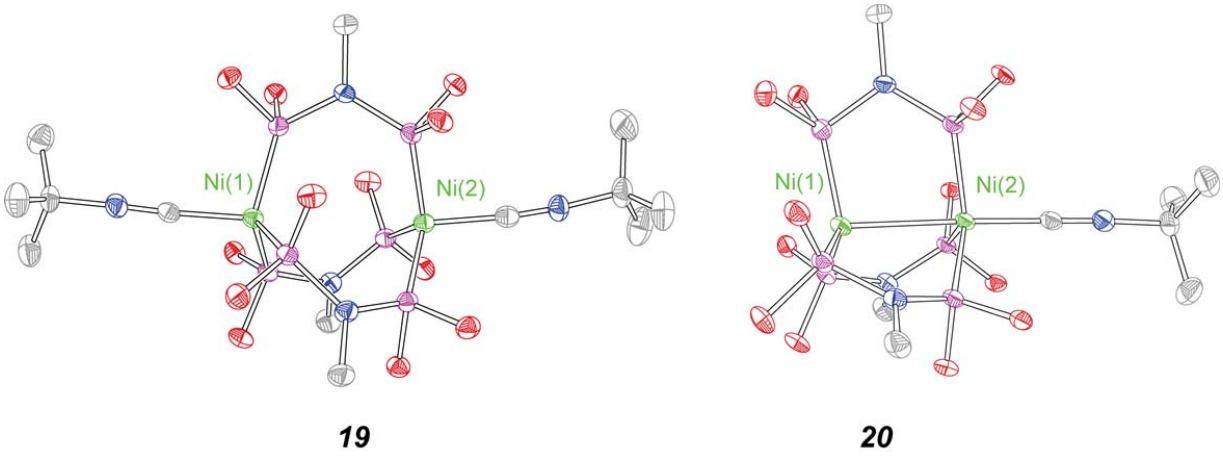

Figure 4.22. Thermal ellipsoid plots of **19** and **20** drawn at the 50% probability level. The $-CH_2CF_3$, and hydrogen atoms are omitted for clarity.

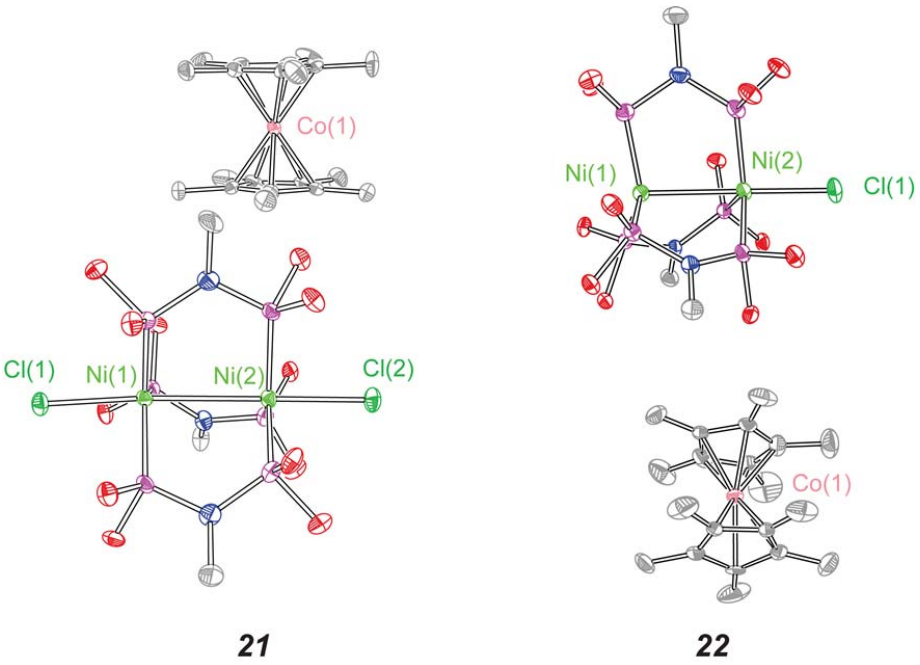

Figure 4.23. Thermal ellipsoid plots of **21** and **22** drawn at the 50% probability level. The $-CH_2CF_3$, and hydrogen atoms are omitted for clarity.

4.7 UV-vis Absorption Spectroscopy and TDDFT

The absorption spectra of complex **15** and **16** are presented in Figure 4.24a. Both complexes exhibit a distinct and intense absorption band in the near-UV that is influenced primarily by the nature of the halide. The absorption maximum of dichloride complex **15** appears at 401 nm, whereas the maximum of the dibromide analogue **16** is red-shifted to 426 nm. Time-dependent density functional theory (TD-DFT) calculated absorption spectra of **15** and **16** are given in Figure 4.24b and satisfactorily reproduce the experimental trend. The TD-DFT calculated states of **15** and **16** are also given in Tables 4.3 and 4.4 respectively, and the prominent absorption bands can be assigned to a combination of halide ligand-to-metal charge transfer (LMCT) and metal-to-metal charge transfer (MMCT) transitions (all donor and acceptor orbitals are given in Figures 4.25 and 4.26).

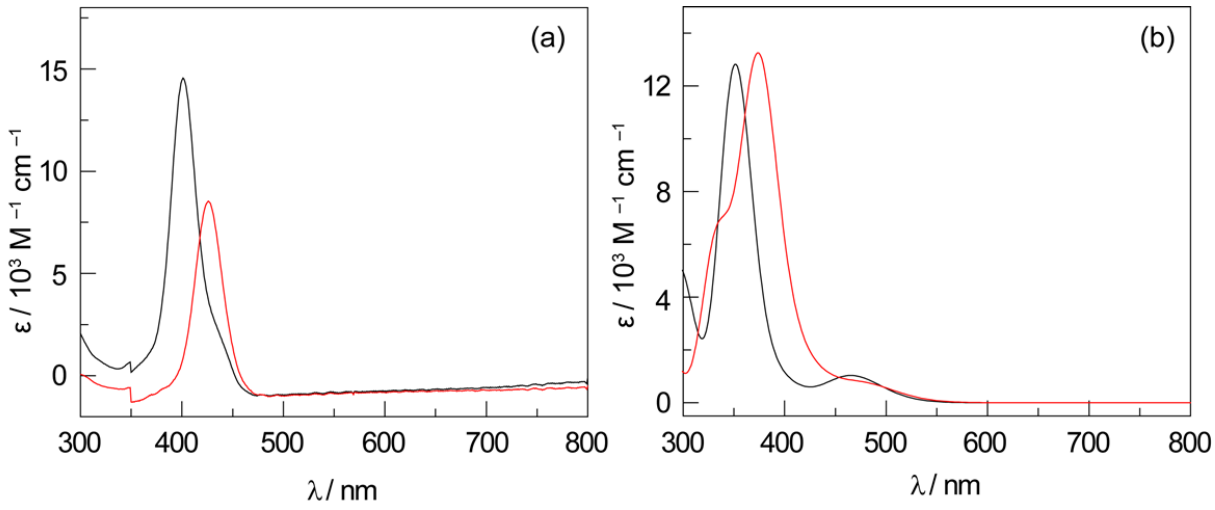

Figure 4.24. (a) Extinction spectra of Ni_2[I,I] complexes **15** (—, black) and complex **16** (—, red). (b) TD-DFT calculated absorption spectra for complexes **15** (—, black) and **16** (—, red).

Table 4.3. TD-DFT calculated transitions for Ni_2[I,I](tfepma)$_3Cl_2$ (**15**).[a]

State	λ (nm)	Energy (cm^{-1})	*f*	Contributions	Assignment
13	394	25,400	0.0117	404α → 409α (71%) 402β → 409β (25%)	Cl(1)(p(z)) → Ni(2)(dz^2) + Cl(2)(p(z)) → Ni(1)(dz^2)
16	351	28,500	0.1753	402β → 409β (70%) 404α → 409α (25%)	Cl(2)(p(z)) → Ni(1)(dz^2) + Cl(1)(p(z)) → Ni(2)(dz^2)
27	302	33,100	0.0388	396β → 409β (75%)	Cl(1)(p(z)) → Ni(1)(dz^2)
28	296	33,800	0.0143	396α → 409α (65%)	Cl(1)(p(z)) → Ni(1)(dz^2)

[a] Calculated transitions with oscillator strengths greater than 0.03 and energies less than ~300 nm. If multiple contributions are present for calculated states, only individual contributions representing ~25% are listed. The Cl(p(z))/Ni($d(z^2)$) LMCT states are bolded. Note that states 13 and 16 undergo configuration interaction; this results in some intensity borrowing for state 13, and thus it is included here.

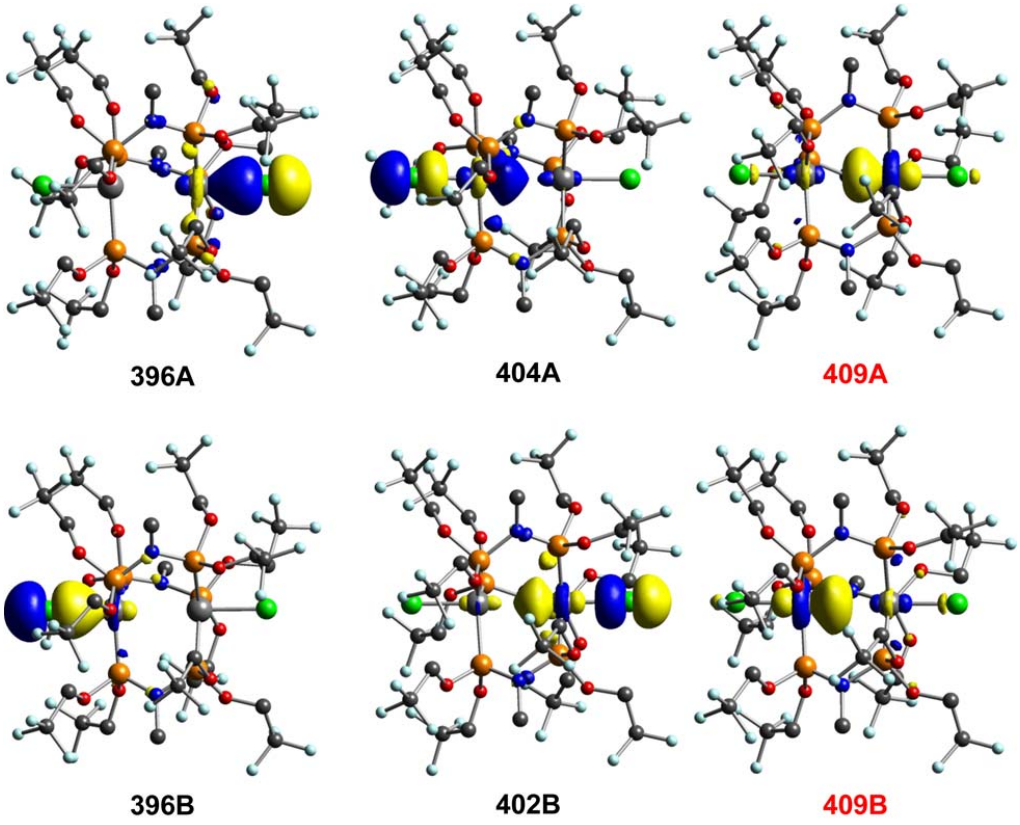

Figure 4.25. Donor (black labeled) and acceptor (red labeled) molecular orbitals of complex **15**.

Table 4.4. TD-DFT calculated transitions for $Ni_2[I,I](tfepma)_3Br_2$ (**16**).[a]

State	λ (nm)	Energy (cm^{-1})	*f*	Contributions	Assignment
13	418	23,900	0.0180	422β → 427β (75%) 420α → 427α (21%)	Br(1)(p(z)) → Ni(2)(dz^2) + Br(2)(p(z)) → Ni(1)(dz^2)
18	374	26,700	0.1739	420α → 427α (72%) 422β → 427β (72%)	Br(2)(p(z)) → Ni(1)(dz^2) + Br(1)(p(z)) → Ni(2)(dz^2)
23	336	29,700	0.0571	417α → 427α (77%)	Br(1)(p(z)) → Ni(1)(dz^2)
24	328	30,500	0.0315	416β → 427β (67%)	Br(2)(p(z)) → Ni(2)(dz^2)

[a] Calculated transitions with oscillator strengths greater than 0.03 and energies less than ~300 nm. If multiple contributions are present for calculated states, only individual contributions representing at least ~25% are listed. The Br(p)/Ni(d(z^2)) LMCT states are bolded. Note that states 13 and 18 undergo configuration interaction; this results in some intensity borrowing for state 13, and thus it is included here.

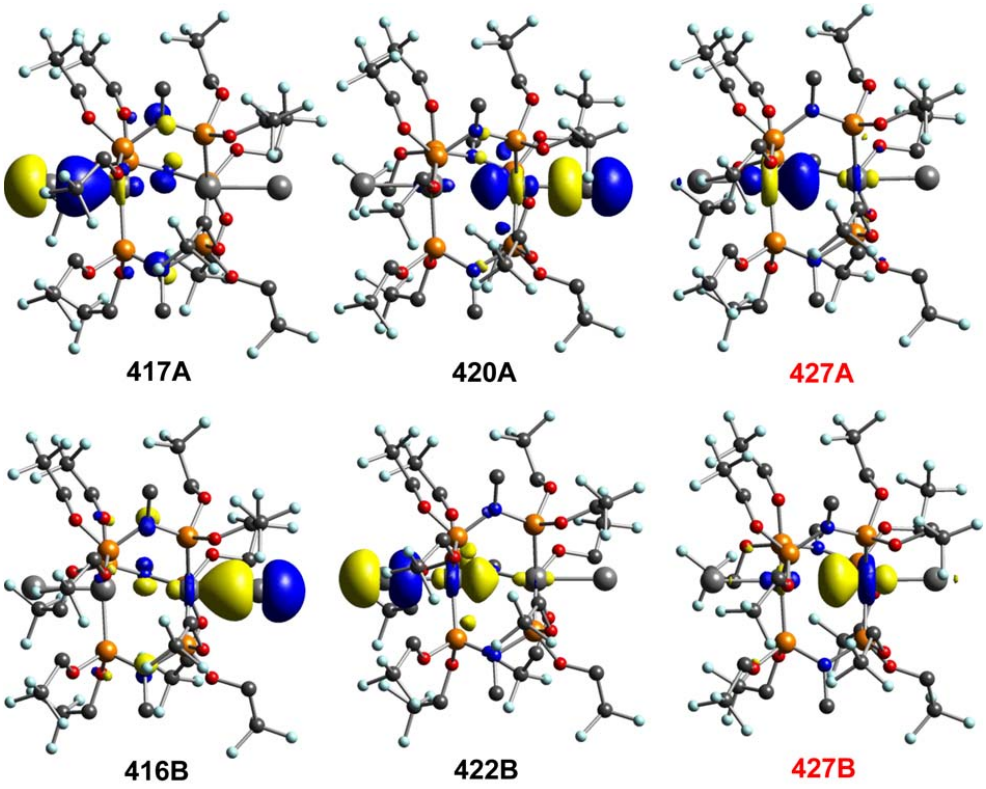

Figure 4.26. Donor (black labeled) and acceptor (red labeled) molecular orbitals of complex **16**.

In contrast, the d^9-d^{10} complex **17** has an absorption spectrum that exhibits a low energy band at ~650 nm and additional bands in the ~325 – 400 nm range and > 300 nm (Figure 4.27a). These absorption bands also shift to lower energy in the bromide complex **18**. TD-DFT calculations suggest the low energy feature is clearly MMCT, while the 350 – 400 nm range consists of mixed MMCT and metal-to-ligand CT (MLCT), with the ligand character largely being low-lying unoccupied phosphine p character (Figure 4.27b). A chloride-based Cl(p(z)) → Ni(dz^2) LMCT transition is found at ~270 nm, thus predicted to be within the higher energy absorption band(s) with energies > 300 nm (Table 4.5). This LMCT transition red-shifts to ~300 nm in the bromide analog **18** (Table 4.6).

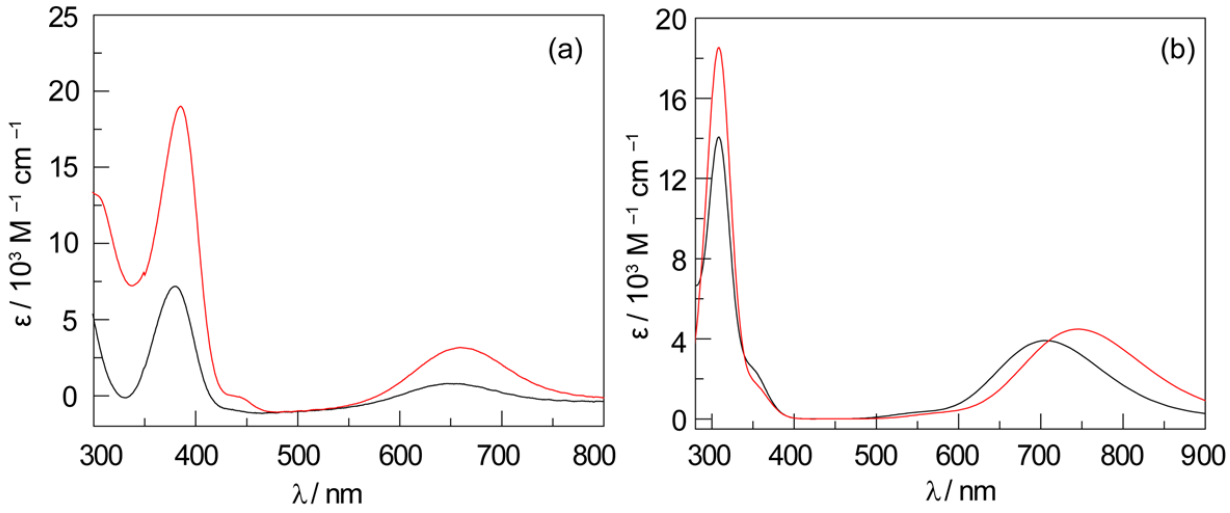

Figure 4.27. (a) Extinction spectra of Ni_2[I,0] complexes **17** (—, black) and complex **18** (—, red). (b) TD-DFT calculated absorption spectra for complexes **17** (—, black) and **18** (—, red).

Table 4.5. TD-DFT calculated transitions for Ni_2[0,I](tfepma)$_3$(CH_3CN)Cl (**17**).[a]

State	λ (nm)	Energy (cm^{-1})	*f*	Contributions	Assignment
5	706	14,200	0.0539	410β → 411β (87%)	σ → σ*
10	350	28,500	0.0307	410β → 412β (51%)	σ → P(unoccupied(p))
14	311	32,100	0.0539	410α → 412α (25%)	Ni(d) → P(unoccupied(p))
15	310	32,300	0.0537	409α → 412α (37%)	Ni(d) → P(unoccupied(p))
16	309	32,400	0.0587	411α → 412α (23%)	Ni(d) → P(unoccupied(p))
37	**272**	**36,800**	**0.0302**	**396β → 411β (68%)**	**Cl(p(z)) → Ni(2)(dz^2)**

[a] Calculated transitions with oscillator strengths greater than 0.03 and energies less than ~270 nm. If multiple contributions are present for calculated states, only individual contributions representing ≥ 25% are listed. The Cl(p(z))/Ni(d(z^2)) LMCT state is bolded.

Table 4.6. TD-DFT calculated transitions for Ni_2[0,I](tfepma)$_3$(CH_3CN)Br (**18**).[a]

State	λ (nm)	Energy (cm^{-1})	*f*	Contributions	Assignment
5	745	13,400	0.0617	419β → 420β (89%)	σ → σ*
15	313	32,000	0.0848	419β → 421β (17%)	σ → P(unoccupied(p))
16	311	32,100	0.0912	420α → 421α (30%)	Ni(d) → P(unoccupied(p))
21	**299**	**33,500**	**0.0325**	**410β → 420β (81%)**	**Br(p(z)) → Ni(2)(dz^2)**

[a] Calculated transitions with oscillator strengths greater than 0.01 and energies less than ~300 nm. If multiple contributions are present for calculated states, only individual contributions representing ≥ 25% are listed. The Br(p(z))/Ni(d(z^2)) LMCT state is bolded.

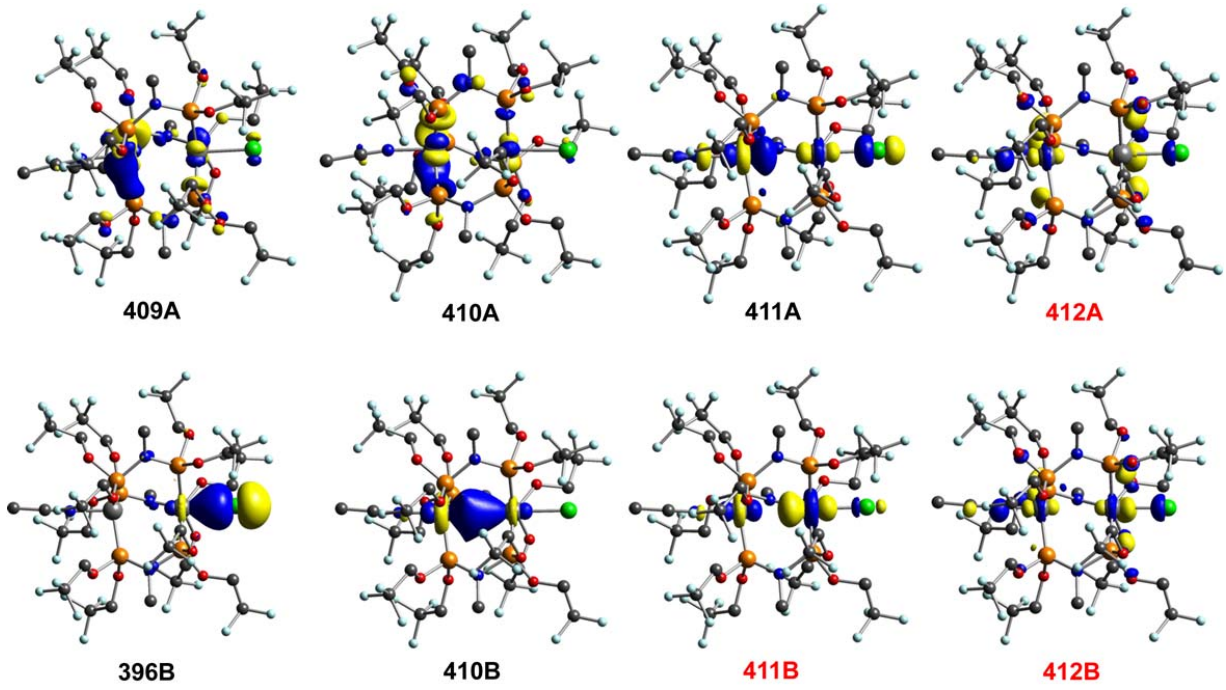

Figure 4.28. Donor (black labeled) and acceptor (red labeled) molecular orbitals of complex **17**.

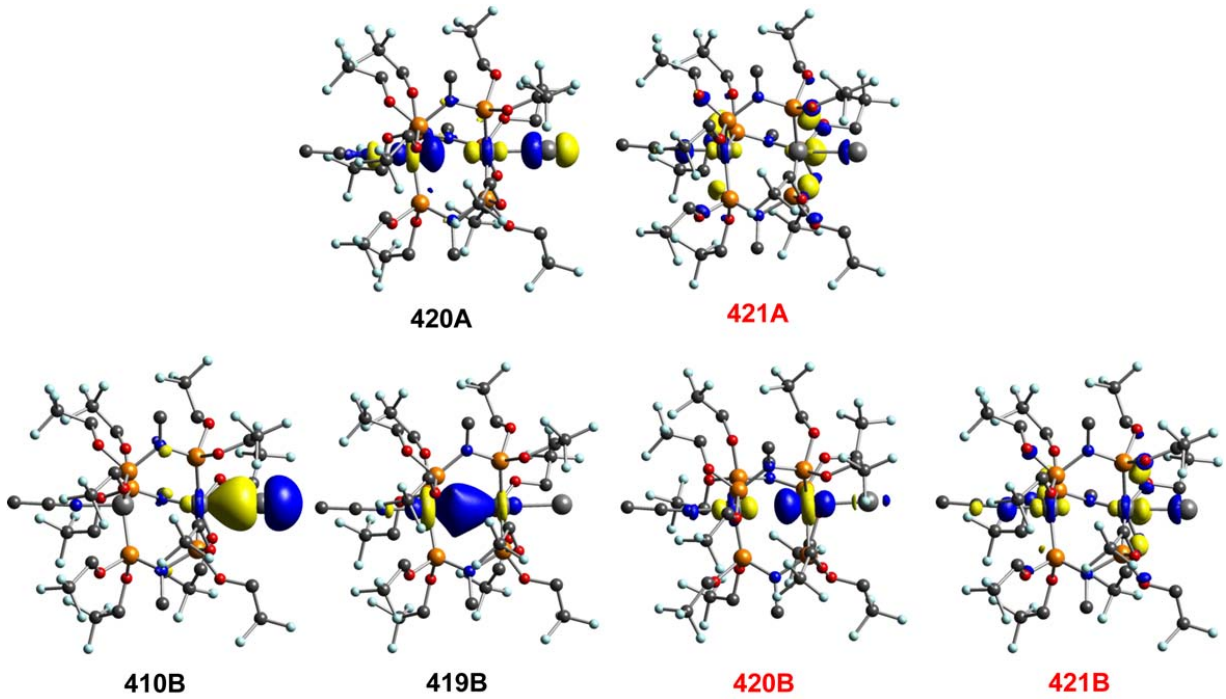

Figure 4.29. Donor (black labeled) and acceptor (red labeled) molecular orbitals of complex **18**.

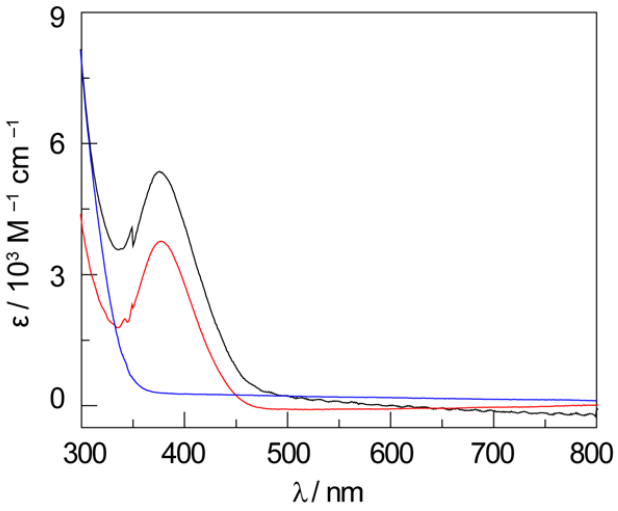

Figure 4.30. Extinction spectra of Ni(0) complexes **19** (—, red), **20** (—, black), and **23** (—, blue).

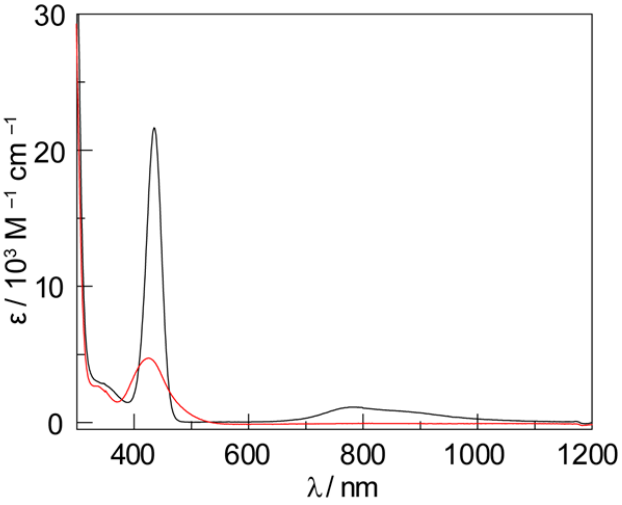

Figure 4.31. Extinction spectra of Ni complexes **21** (—, black) and **22** (—, red).

4.8 Steady-State Photochemistry

Steady-state photolysis with a 1000 W Hg/Xe lamp (λ > 320 nm) of the Ni_2[I,I] complex **15** in solvent containing weak C–H bonds such as THF (C–H BDE = 92 kcal mol^{-1}) [42] leads to the generation of a light green-colored solution over the course of the reaction (Figure 4.32). The comparison of the *in situ* UV-vis and EPR spectra obtained from steady-state photolysis of

complex **15** in THF with a spectrum from an independently prepared sample of the complex **21** confirmed the identity of the putative photoproduct as the one electron reduced anionic $Ni_2[I,0]Cl_2$ complex as depicted in Figure 4.32 and 4.34. This one electron photoreduction reaction was further supported by the reversible nature of complex **15** observed in cyclic voltammetry (Figure 4.33).

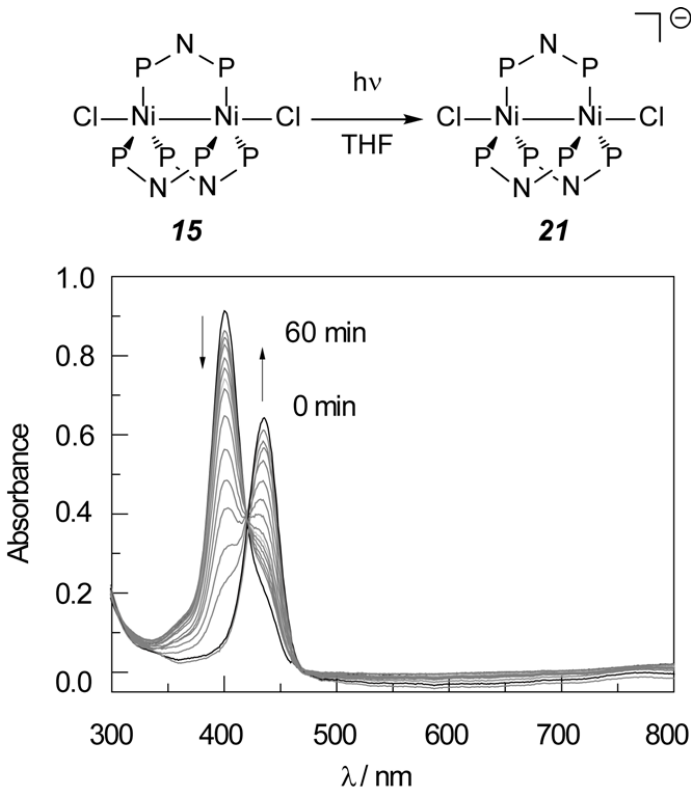

Figure 4.32. Spectra evolution during photolysis (λ > 320 nm) of $Ni_2[I,I]Cl_2$ complex **15** in THF.

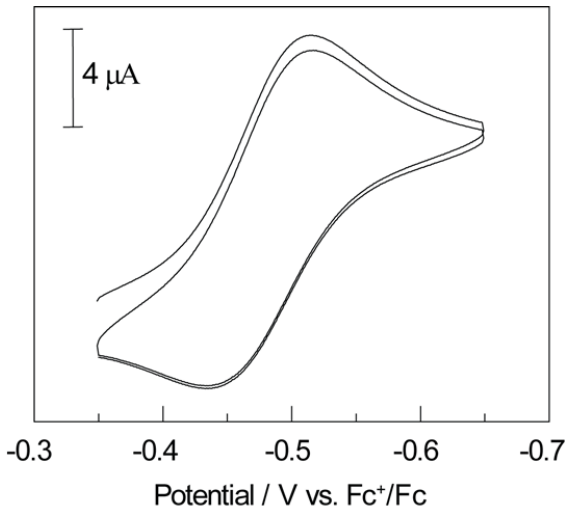

Figure 4.33. Cyclic voltammetry of 1 mM Ni complex **15** (—, black) measured with 0.1 M $^{n}Bu_4PF_6$ as a electrolyte in CH_3CN solution with a scan rate of 100 mV/s. Pt working electrode, $Ag/AgNO_3$ reference, and Pt wire counter electrode were used.

When the photolysis (λ > 320 nm) is run in hexafluorobenzene, the green solution becomes colorless (Figure 4.35). The identity of the colorless photoproduct was established to be $Ni(tfepma)_2$ (**23**) by comparison with an independent sample prepared by treatment of Ni(0) with 2 equivalents of tfepma. ^1H, $\{^1H\}^{31}P$ NMR, and electronic spectroscopies were used to characterize complex **23**, and X-ray crystallographic analysis of a single crystal established **23** to be a pseudo-tetrahedral Ni(0) structure shown in Figure 4.36. The photogenerated Cl radicals are expected to evolve Cl_2 gas, as H-atom abstraction is hampered in the absence of solvent C–H bonds. Thus, the excitation of a Ni–Ni $d_z^2d_z^2$ $d\sigma \rightarrow d\sigma^*$ transition photoactivates the Ni–X bonds to extrude Cl• along with the formation of tfepma-bridged d^{10}–d^{10} binuclear $Ni_2[0,0]$ species that ultimately decomposes into 4-coordinate Ni complex **23**.[43]

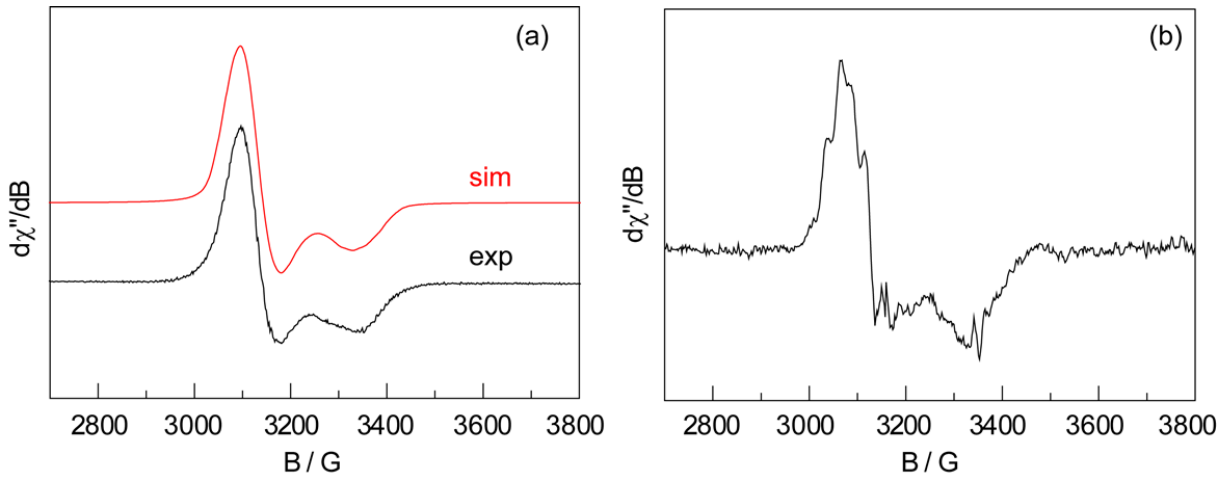

Figure 4.34. EPR spectra of (a) Ni_2[I,0] complex **21** recorded at 77.0 K in $PhCH_3$ glass. (b) Photoproduct of complex **15** in THF recorded at 77.0 K in $PhCH_3$ glass.

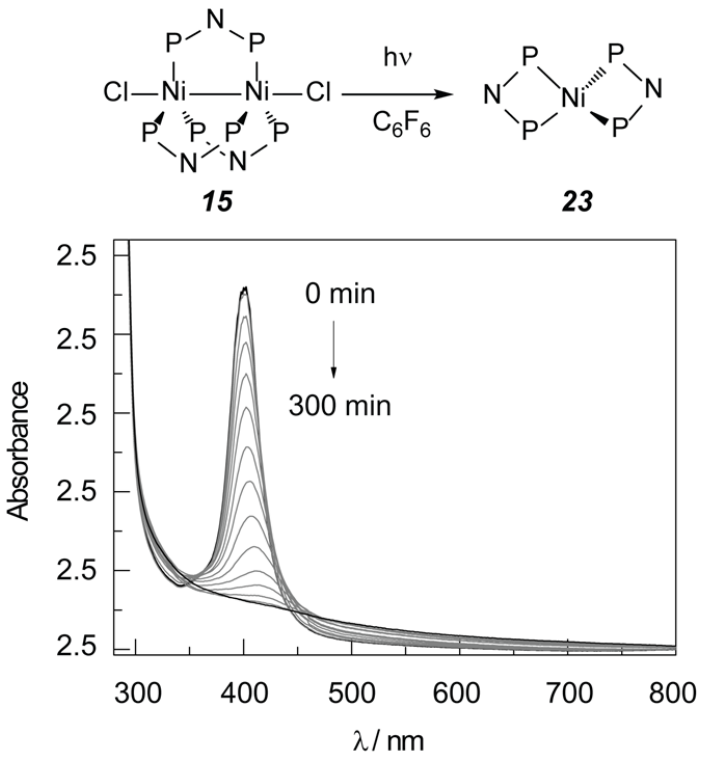

Figure 4.35. Spectra evolution during photolysis (λ > 320 nm) of Ni_2[I,I]Cl_2 complex **15** in C_6F_6.

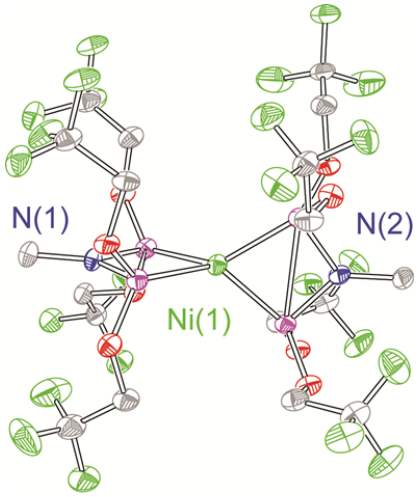

Figure 4.36. Thermal ellipsoid plot of $Ni(tfepma)_2$ (**23**) in which H-atoms have been removed for clarity. Ellipsoids are drawn at 50% probability.

Although steady-state photolysis of the Ni_2[I,I] complex **15** in two different solvents (THF and C_6F_6) afforded different photoproducts, photoreduction of binuclear Ni_2 complexes was observed in both cases. Solution-state photolysis of complex **15** in THF led to rapid conversion to the one-electron reduced paramagnetic Ni_2 complex, as confirmed by *in situ* UV-vis and EPR. We propose that one of the tfepma ligands is protonated from photochemically generated HCl; a free chloride ion is generated, which proceeds to react with the photoreduced neutral Ni_2[I,0]Cl to furnish the anionic Ni_2[I,0]Cl_2. This is corroborated by the fact that the photoreduction process becomes more efficient upon addition of base (2,6-lutidine or 2,6-di-*tert*-butylpyridine). Identical UV-vis and EPR spectra were obtained for the photoproduct of complex **15** in THF and complex **21,** establishing the identity of the putative photoproduct as anionic Ni_2[I,0]Cl_2. We further prepared another anionic Ni_2[I,0] complex, **24,** with a phosphonium cation by the comproportionation reaction between $Ni(cod)_2$ and $NiCl_2(P^iPr_3)_2$ in the presence of 3 equiv of tfepma ligand. The molecular structure of **24** shows an identical binuclear Ni_2[I,0]Cl_2

core structure (Ni–Ni: 2.862 Å and 2.807 Å for complex **21** and **24**; Ni–Cl: 2.431 Å and 2.429 Å respectively) (Figure 4.37).

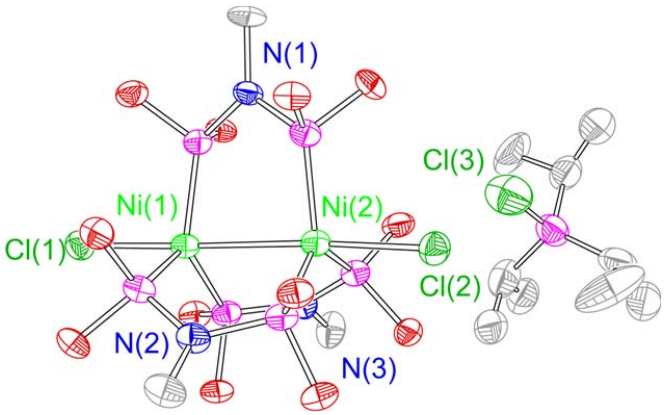

Figure 4.37. Thermal ellipsoid plots of **24** drawn at the 50% probability level. The $–CH_2CF_3$, and hydrogen atoms are omitted for clarity.

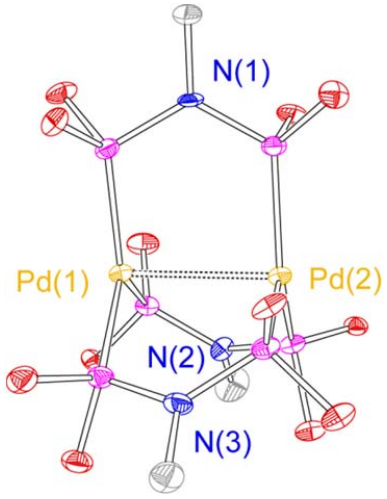

Figure 4.38. Thermal ellipsoid plots of Pd_2[0,0] complex **25** drawn at the 50% probability level. The $–CH_2CF_3$, and hydrogen atoms are omitted for clarity.

The absorption spectrum of complex **24** displays a distinct intense band at 435 nm that is consistent with the spectrum obtained from steady-state photolysis of complex **15** in THF**.** While HCl was photochemically generated via a HAA from the weak C–H bonds of THF (C–H BDE =

92 kcal mol^{-1}), the HAA reaction is hampered in C_6F_6 due to its lack of C–H bonds. Thus, photolysis of complex **15** in C_6F_6 eliminates Cl_2 to furnish the tfepma-bridged d^{10}–d^{10} Ni_2[0,0] complex. Unfortunately, we were not able to isolate this photoproduct since it is not thermally stable. The identity of the photoproduct was established to be mononuclear Ni complex **23**. Even though second- and third-row metals (Pd and Pt) showed a weak metal–metal bond interactions in the analgous d^{10}–d^{10} system ranging from 2.652 to 3.353 Å, the lack of efficient metal–metal orbital overlap in the coordinatively unsaturated environment of the binuclear Ni_2 complex lead to decomposition into four-coordinate **23** as the final photoproduct. This can be seen by structural analysis of the Pd_2 analog complex (**25)** bridged by three tfepma ligands. Synthesis of the tfepma-bridged Pd_2[0,0] complex was accomplished by stirring the free tfepma ligands with $Pd_2(dba)_3$ (dba = dibenzylideneacetone) in benzene for 3h. The molecular structure of complex has been determined by X-ray diffraction, and shows a two three-coordinate palladium centers along with weak Pd–Pd bond interaction (Pd(1)–Pd(2): 2.817 Å) (Figure 4.38). However, de novo synthesis of Ni_2[0,0] was not successful from $Ni(cod)_2$ or reduction of complex **15**, leading us to assume that it is not isolable due to the preference of nickel for the four coordinate tetrahedral environment as well as the weaker M–L bond strength experienced upon moving from 2^{nd}- or 3^{rd}-row to 1^{st}-row transition metals.

Decomposition pathway to the monomeric Ni complex under photolysis of complex **15** was inhibited when additional exogenous supporting ligand was employed. Solution-phase photolysis (λ_{exc} > 400 nm) of Ni_2Cl_2 complex **15** in C_6H_6 in the presence of 1.0 equiv of *tert*-butyl isocyanide led to the rapid conversion to the one-electron reduced Ni_2 complex **17**, as established by monitoring the reaction by UV-vis spectroscopy (Figure 4.39a). Further photolysis of Ni_2Cl complex **17** in C_6H_6 results in the disappearance of the UV-vis features of **17**

and the evolution of features attributable to the reduced $Ni_2(0,0)$ complex **20**, the product of a two-electron photoreduction (Figure 4.39b). The second photochemical step was noticeably sluggish compared to the first photoreduction.

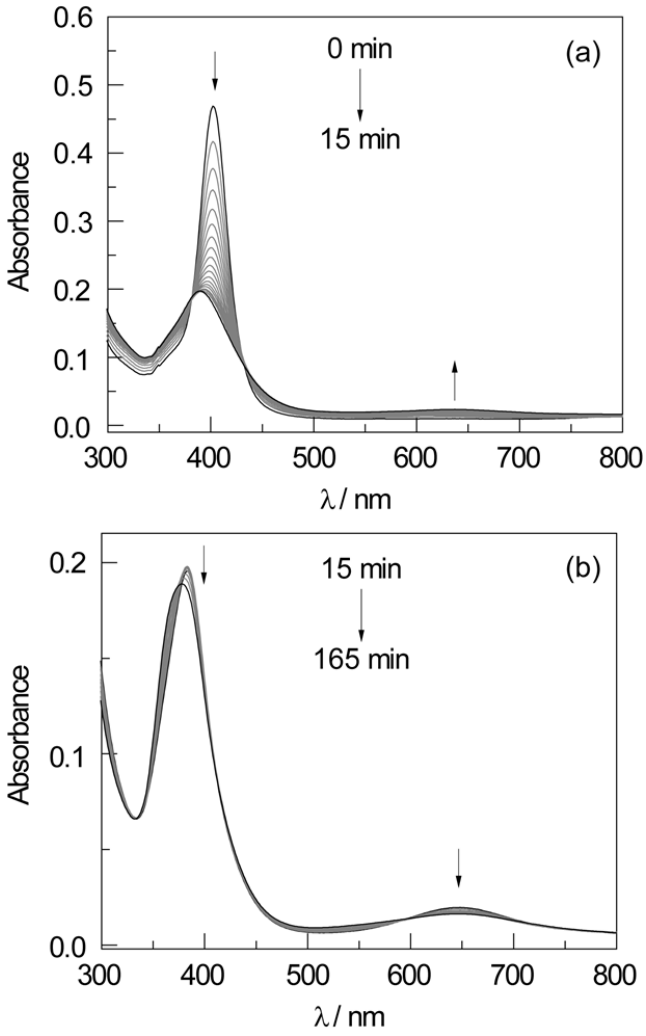

Figure 4.39. Spectral evolution for the photolysis of Ni_2 complex **15** in C_6H_6 in the presence of 1equiv CN^tBu ($\lambda > 380$ nm). (a) During the first 15 min, complex **15** is converted to one-electron reduced Ni_2 complex **17**. (b) Subsequently, **17** is converted to $Ni_2[0,0]$ complex **20**, the product of halogen photoelimination.

Photolysis of a THF solution of **17** ($\lambda > 320$ nm) resulted in the consumption of **17** and clean formation of **20** (Figure 4.20). The photochemical action spectrum was constructed by

measuring wavelength-dependent (260, 315, 370, 410, 540 nm) quantum yields (Φ) for halogen elimination from **17** in THF against a potassium ferrioxalate standard actinometer (Figure 4.40).[44,45] These data indicate that the photoefficiency is greatest exciting the higher energy LMCT band (~270 nm).

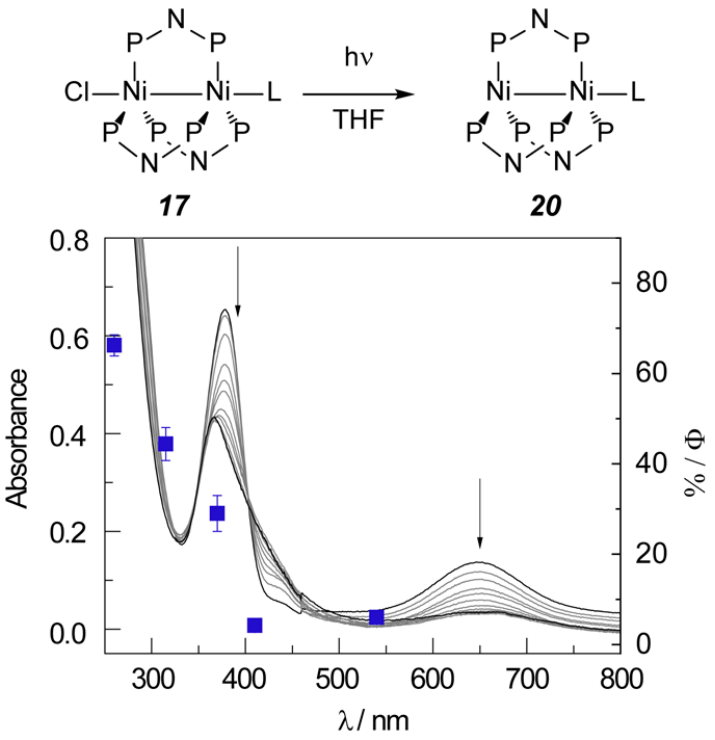

Figure 4.40. Steady-state photolysis of a complex **17** (λ > 320 nm) in THF and photochemical quantum yields (Φ) as a function of excitation wavelength.

4.9 Photocrystallographic Observation of M–X Bond Activation

Building upon our previous photocrystallography experiments to identify intermediates during the halogen photoelimiantion, steady-state photocrystallography techniques were used to probe the photoinduced structural changes in complex **15** and **17**. The nature of the stepwise photoreduction process followed by the $Ni_2(I,I)Cl_2$ complex **15** to the $Ni_2(0,0)$ complex **20** is unveiled by steady-state photocrystallography experiments summarized in Figure 4.41.

Diffraction data collected prior to and during irradiation (λ_{exc} = 300 nm, 20 K) were used to generate a photodifference map, showing the presence of a photoinduced structure populated at 8.6% of the overall crystals. Examination of the structural perturbations in the primary photoproduct shows the photoactivation of one of the axial Ni–Cl(1) bonds: 2.1993(6) (dark) to 2.3948(14) (photoinduced) (Figure 4.41a). Unlike this substantial elongation of the Ni–Cl(1) bond in the photoinduced structure, the remaining axial Ni–Cl(2) and Ni(1)–Ni(2) bonds were not observed to change in the photodifference map. Steady-state photocrystallography experiments were also performed using a single crystal of the Ni_2(I,0)Cl complex **17** under identical conditions as those of the aforementioned experiment with **15**. The photodifference map demonstrated an axial Ni–Cl bond elongatation from 2.4127(9) to 2.495(3) Å, while the Ni–Ni bond significantly contracts from 2.9264(6) to 2.600(2) Å, the known bond length for the ground state of complex **20** (Figure 4.41b). The excited state is therefore a mixture of photoeliminated Cl• and photoproduct **20**. Variable-temperature crystallography of single crystals of **15** and **17** revealed that the metrical parameters do not significantly vary with temperature, confirming that the observed structural changes are not caused by a thermal process over the temperature range of 20-300 K (Figure 4.42 and Table 4.7 and 4.8). These photocrystallography results described offer evidence that the overall X_2 elimination from Ni_2(I,I)Cl_2 complexes in three-fold symmetry proceeds via consecutive stepwise X• photoelimination by LMCT excitation, consistent with solution-phase photolysis experiments.

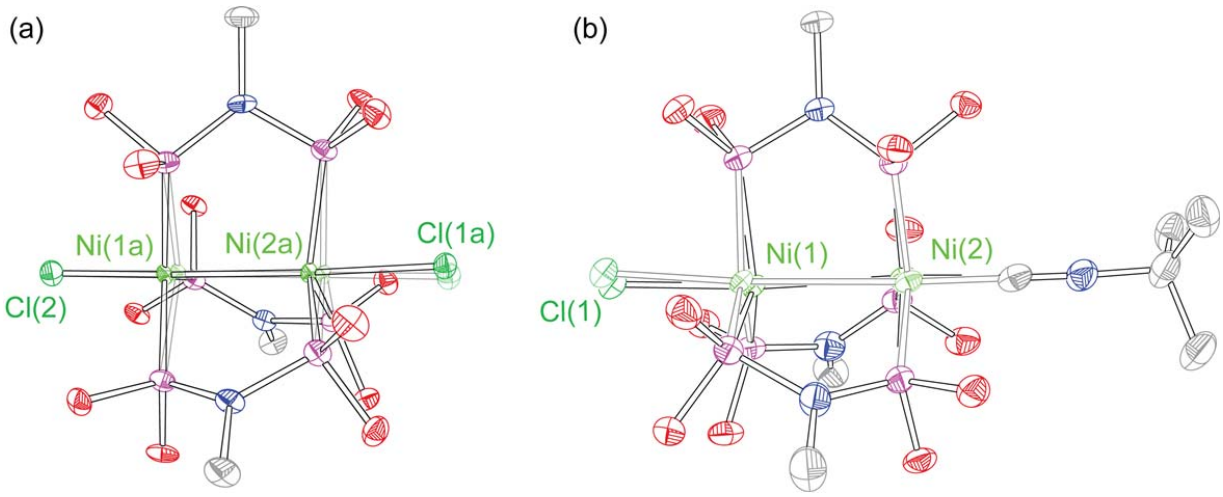

Figure 4.41. Thermal ellipsoid plot showing the dark structure (faded) and the irradiated structure (bold) generated from (a) $Ni_2[I,I]Cl_2$ complex **15** and (b) $Ni_2[I,0]$ complex **17**. This plot was generated by normalizing the positions of the Ni centers in the dark and irradiated structures to focus on the relative motions of the Cl ligands. H-atoms, and OCH_2CF_3 groups are omitted for clarity. Ellipsoids are drawn at 50% probability.

As described in the earlier parts of this Chapter, phosphazane-bridged binuclear Rh_2 complexes have been proposed to facilitate ligand rearrangements to ligand-bridged intermediates owing to the ligand's ability to accommodate two-electron changes at the metal core with minimal reorganization energy. Previously carried out photocrystallography experiments support this hypothesis by showing the prevalence of halide-bridged intermediates that preceded M–X bond activation for X_2 elimination. Although the solid state imposes constraints on the requisite ligand-bridged intermediates, we have leveraged the volatility of carbonyl ligands to allow for the isolation of halide-bridged structures during an interrupted binuclear elimination. We hoped to utilize these findings to develop next generation catalysts for efficient X_2 photoeliminaiton with binuclear Ni complexes by bypassing the stepwise X• elimination process. Thus, we conducted photocrystallographic experiments with the novel compound $Ni_2(CO)(dppm)_2Cl_2$ **25** (isoelectronic to complex **15**) to confirm the presence of Cl-bridged bimetallic cores as a common intermediate between the nickel and rhodium compounds.

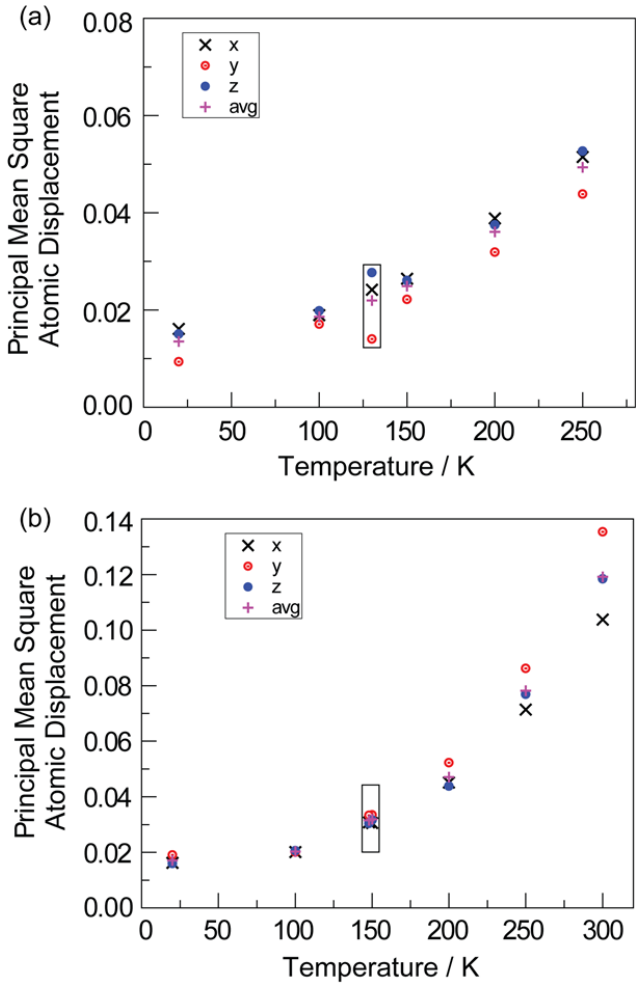

Figure 4.42. Principal mean square atomic displacements (U) for (a) $Ni_2[I,I]Cl_2$ Complex **15** and (b) $Ni_2[I,0]Cl$ Complex **17** as a function of temperature plotted for oxygen atoms of the OCH_2CF_3 groups in the bridged phosphazane ligands. Thermal parameters obtained during photocrystallography are highlighted in a box.

Table 4.7. Selected metrical parameters for Ni_2[I,I] complex **15** as a function of temperature**.**

	Ni–Ni (Å)	Ni^1–Cl^1 (Å)	Ni^2–Cl^2 (Å)
20 K	2.5919(5)	2.2623(8)	2.2598(8)
100 K	2.5990(17)	2.269(3)	2.264(3)
150 K	2.5810(16)	2.256(3)	2.253(3)
200 K	2.599(2)	2.275(3)	2.270(3)
250 K	2.604(2)	2.271(3)	2.269(4)

Table 4.8. Selected metrical parameters for Ni_2[I,0] complex **17** as a function of temperature**.**

	Ni–Ni (Å)	Ni^1–Cl^1 (Å)	Ni^2–C^2 (Å)
20 K	2.8687(3)	2.4292(5)	1.888(2)
100 K	2.8609(7)	2.4156(11)	1.865(4)
150 K	2.8618(8)	2.4166(12)	1.876(5)
200 K	2.8658(7)	2.4172(13)	1.871(5)
250 K	2.8726(11)	2.422 (2)	1.866 (8)
300 K	2.8622(16)	2.428(3)	1.850(13)

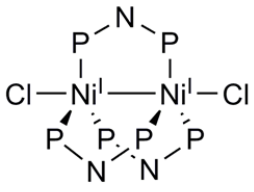

15

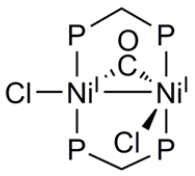

26

The $Ni_2(CO)(dppm)_2Cl_2$ complex **26** was prepared by the comproportionation reaction of $Ni_2(CO)_3(dppm)_2$ and $NiCl_2(dppm)_2$ as described in the literature.[46] The solid-state structure shows two bridging dppm ligands with metal–metal single bonds (2.617 Å) comparable to the

one observed in complex **15** (2.591 Å) and other dppm-bridged dinickel complexes.(REF) Although complex **15** and **26** are isoelectronic d^9–d^9 binuclear nickel dihalide complexes, there are major differences between their structures: (1) complex **26** is bridged with a volatile CO ligand, replacing one of bidentate phosphine ligands in Complex **15** (2) complex **15** has 3-fold symmetry and the nickel centers are in identical geometric environments while complex **26** exhibits an asymmetric A-frame structure. Thus, the Ni–Ni–Cl angles ranges from 179.52(4) in **15** to 104.21(6) in **26**, resulting in a much shorter Cl–Cl bond distance in complex **26** (7.115 and 5.516 Å for complexes **15** and **26** respectively). As aforementioned, the photolability of the carbonyl ligands provides an additional coordination site for the Cl atoms so structural insights into the nature of the primary photoproduct were interrogated using photocrystallography

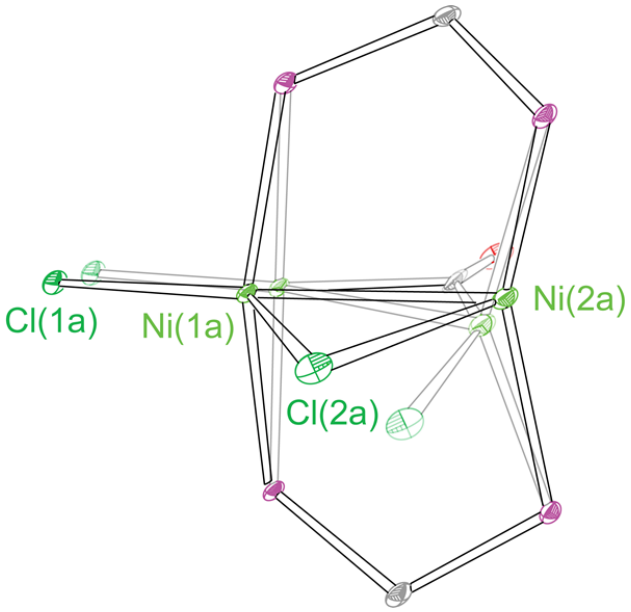

Figure 4.43. Thermal ellipsoid plot showing the dark structure (faded) and the irradiated structure (bold) generated from complex **26** This plot was generated by normalizing the positions of the Ni centers in the dark and irradiated structures to focus on the relative motions of the Cl ligands. H-atoms, solvent molecue, and -Ph groups are omitted for clarity. Ellipsoids are drawn at 50% probability.

After excitation of crystals of complex **26** ($Ni_2(CO)(dppm)_2Cl_2$) with a 365 nm LED light source, 1.48(9) % of the crystal was populated with a photoinduced structure obtained from the photodifference map. It is important to note that atoms with the most electron density (Ni and Cl) are the only ones that can be resolved in the photoinduced structure especially with such low percentage populations. Nevertheless a dramatic structural perturbation was observed for Cl(2) (Figure 4.43), as it migrated to a bridging position (Cl(2)–Ni(2)–Ni(1) bond angle contracting from 104.59(2) to 56.3(12)° in the photoinduced structure). Additionally, as Cl(2) approaches the bridging position, the Ni(2)–Cl(2) bond lenghtelongates from 2.2672(7) to 3.14(5) Å, while the Ni(1)–Cl(2) bond length significantly contracts from 3.8736(7) to 2.76(5) Å. (additional metrical parameters are provided in Table 4.9). It should be noted that this chloride ligand migration to the bridging position from a terminal coordination position is consistent with the observation and characterization of Cl-bridged intermediates in the related Rh_2 complexes. Further, this represents a much larger halide atom movement in the solid state than what was observed in the rhodium system. Although structural perturbation toward Cl-bridged intermediates was found in the photoinduced structures of two Rh_2 complexes by photocrystallography, transient absorption spectroscopy, computational modeling, and direct synthesis of the proposed intermediate complexes were required to confirm the Cl-bridged. Conversely, in the case of binuclear Ni complex **25**, the Cl-bridged intermediate was clearly revealed in the photoinduced structure as a primary photoproduct.

Table 4.9. Comparison of selected metrical parameters for dark and photoinduced structures from photocrystallography experiment with Ni_2 complex **26**.

	Dark structure	photoinduced structure
Ni^1–Ni^2 (Å)	2.6197(4)	2.63 (4)
Ni^1–Cl^1 (Å)	2.2373(6)	2.45(12)

Ni^1–Cl^2 (Å)	3.8736(7)	2.76(5)
Ni^2–Cl^2 (Å)	2.2688(6)	3.14(5)
Cl^1–Ni^1–Ni^2 (°)	162.76(2)	153(4)
Cl^1–Ni^1–Cl^2 (°)	128.36(2)	135(4)
Ni^2–Ni^1–Cl^2 (°)	34.529(11)	71.2(13)
Cl^2–Ni^2–Ni^1 (°)	104.59(2)	123.7(12)
Ni^2–Cl^2–Ni^1 (°)	40.880(13)	52.5(10)

We hypothesized that if a Ni_2 structure has Cl-bridged or two-electron mixed valence $Ni(0,II)Cl_2$, the need for photochemically driven ligand dissociation and chloride movement would be circumvented, thus bypassing the undesired stepwise X• elimination. Therefore, a new design was pursed aiming to make a related compound with vicinal dichloride ligands.

4.10. Synthesis, Characterization and Photochemistry of Mixed Valence Ni_2 Complexes

The series of mixed valence $Ni_2[0,II]Cl_2$ complexes needed to interrogate the proposed X_2 photoeliminaiton was accessed by synthesis of a new Ni[0,0] complex bridged by two phosphazane ligand, followed by oxidation with $PhICl_2$.

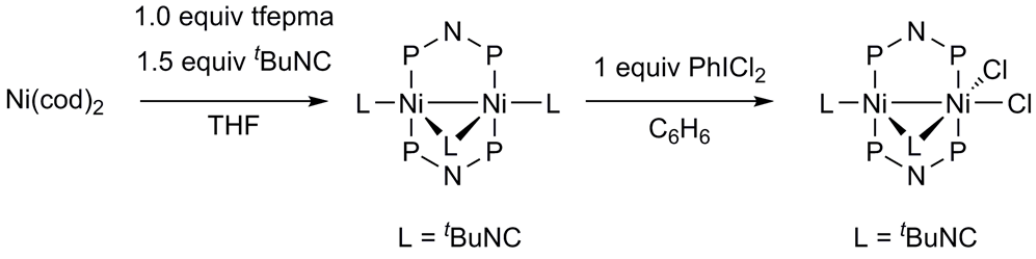

Entry into this series of $Ni_2[0,0]$ complexes **27** was gained by treatment of $Ni(cod)_2$ with 2 equiv of tfepma in the presence of 3 equiv of ^{t}BuNC in THF, resulting in the formation of $Ni_2[0,0](tfepma)_2(^t BuNC)_3$ in 85% yield. Additional isocyanide supporting ligands were key to

accessing the $Ni_2(0,0)$ complexes bridged only by two tfepma phosphazane ligands rather than three for $Ni_2[0,0]$ complexes **19** and **20**.

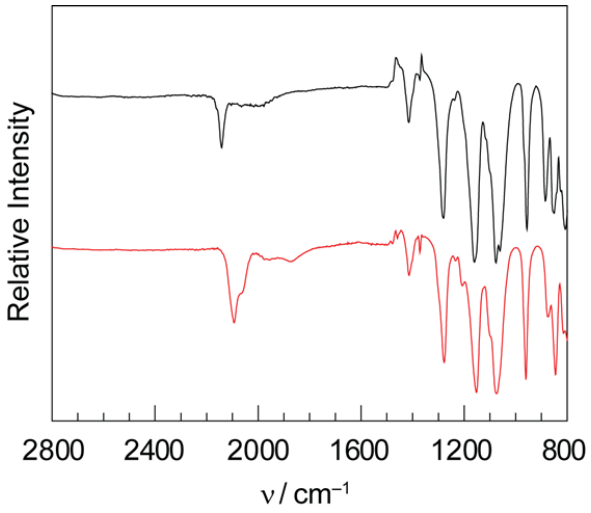

Figure 4.44. IR spectra of $Ni_2[0,0]$ complex **27** (—, red) and $Ni_2[0,II]Cl_2$ complex **28** (—, black).

The $Ni_2[0,0]$ complex **27** reveals a diamagnetic ^1H NMR spectrum containing signals attributable to two tfepma ligands as well as one bridging and two terminal *tert*-butyl isocyanide ligands (Figure 4.89). The $^{31}P\{^1H\}$ NMR spectrum, however, displayed one singlet at 155.5 ppm, indicating all four tfepma phosphorus nuclei are equivalent at 25˚C (Figure 4.90). The IR spectrum displayed a ν_{CN} = 2093 and 1870 cm^{-1}, consistent with a bridging and terminal isocyanide ligands (Figure 4.44).[40,41] The solid-state structure of complex **27** was characterized by X-ray diffraction analysis, exhibiting two tetrahedrally coordinated Ni(0) centers and supporting other spectral features observed for complex **27** (Figure 4.45). Two-electron mixed valence $Ni_2[0,II]$ $(tfepma)_2(^tBuNC)_2Cl_2$ complex **28** was then prepared by treatment of $PhCH_3$ solutions of the $Ni_2[0,0](tfepma)_2(^tBuNC)_3$ complex **27** with 1 equiv of $PhICl_2$. The diamagnetic $Ni_2[0,II]$ complex **28** shows a broad ^1H NMR spectrum and a silent $^{31}P\{^1H\}$ NMR spectrum at

ambient temperature (Figure 4.92). The IR spectrum shows a ν_{CN} = 2141 and 1986 cm^{-1} which is similar to compound **27** (Figure 4.44). Single crystals of complex **28** were obtained by layering Et_2O solutions of **28** with pentane, and X-ray diffraction analysis established the molecular structure of **28** to be the two-electron mixed valence Ni_2Cl_2 complex shown in Figure 4.45.

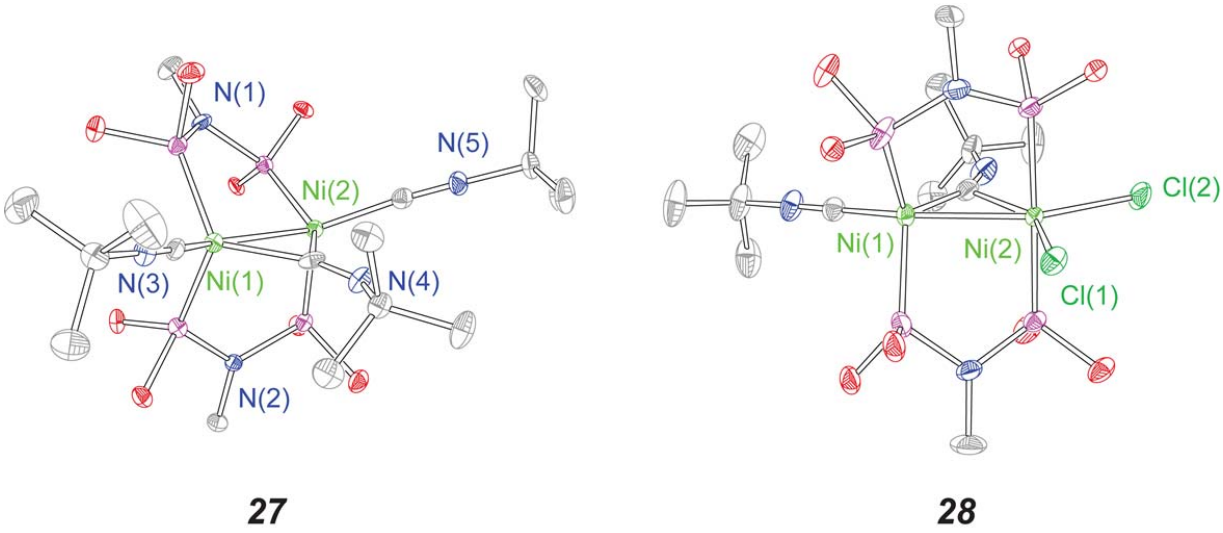

Figure 4.45. Thermal ellipsoid plots of **27** and **28** drawn at 50% probability. H atoms and $-CH_2CF_3$ groups have been removed for clarity.

Unlike stepwise photochemical reactions of Ni_2 complex **15** discussed above, photolysis of **28** in C_6H_6 leads to the clean evolution of the spectral features assigned to the two-electron reduced Ni_2[0,0] complex **19** without the build-up of any intermediates, suggesting photochemical X_2 elimination (Figure 4.46).

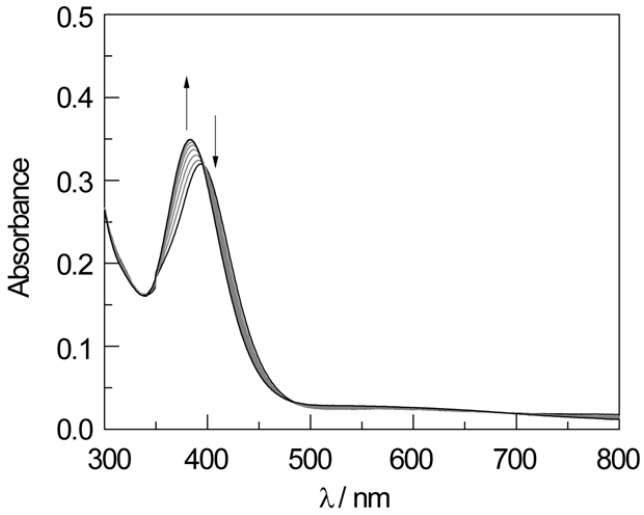

Figure 4.46. Spectra evolution during photolysis (λ > 320 nm) of $Ni_2[0,II]Cl_2$ complex **28** in C_6H_6 in the presence of 1 equiv of tfepma.

4.11 Solid-State Photolysis

Trap-free solid-state halogen photoelimination reactions have been previously observed in mono- and binuclear complexes of Pt(III)[62,64] and Au(III)[63] as well as in mononuclear Ni(III) complexes.[47,48] Solid-state photolysis from binuclear Ni complexes were pursued motivated by the steady-state photolysis of complex **15** in C_6F_6. Irradiation (~20 Torr, 20 °C, λ > 305 nm) of complexes **1**5 in the solid-state for 18 hours results in the formation of compound **23** along with the evolution of Cl_2 gas. The evolved Cl_2 was treated with N,N-diethyl -1,4-phenylenediamine sulfate (DPD) and the resulting $DPD^{\cdot+}Cl^-$ was analyzed colorimetrically to give 80% yield for Cl_2 from **15** based on the extent of starting material conversion (23%) (Figure 4.47). We propose that Cl_2 was formed by the oxidation of Ni–Cl bond with photochemically generated Cl• from neighboring Ni_2 complex due to their close intermolecular Cl–Cl bond distance (3.513 Å) (Figure 4.48).

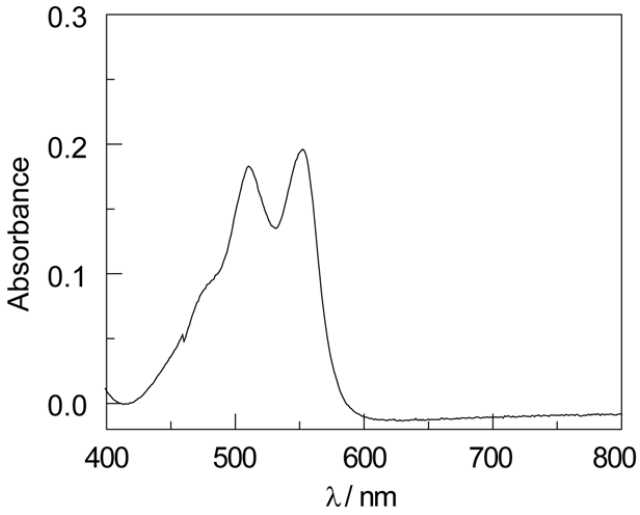

Figure 4.47. UV-vis absorption spectra, showing formation of $[DPD]^{\bullet+}$ when the trapped Cl_2 from solid state photolysis of **15** is treated with DPD.

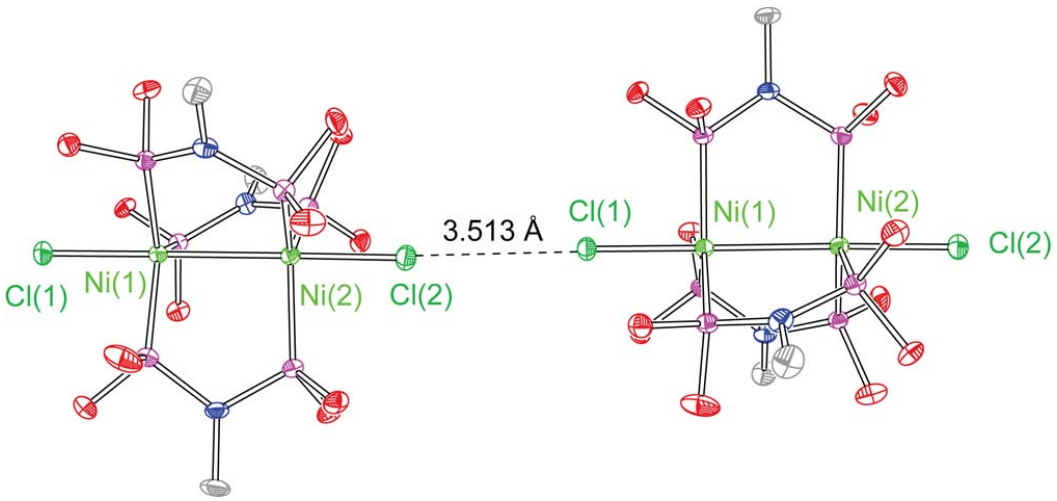

Figure 4.48. Thermal ellipsoid plots of **15** with neighboring molecule drawn at 50% probability. H atoms and $-CH_2CF_3$ groups have been removed for clarity.

4.12 Thermally Promoted Proton Reduction Reactions

After completing the first half-photocycle of the HX-splitting cycle with binuclear Ni complexes, the viability of proton reduction by the photoreduced Ni(0) complexes was examined. Treatment of Ni complexes **19** and **20** with 50 equiv HCl in THF affords Ni complexes **17**

respectively, which were identified by UV-vis spectroscopy, along with the formation of 5% H_2 as a gaseous product (Figure 4.49). The low yield of H_2 observed can be attributed to undesirable reactions with the tfepma ligand, as same species were identified in ^{1}H NMR for reactions of tfepma/complex **23** with HCl (Figure 4.50 and 4.51). We suspect that the ligand is reduced to afford radical cationic species, as observed in previous studies of mononuclear Ni(0) complexes supported by the reducing 2,2′-biquinoline ligand.[49] This assumption was also confirmed by the observation that monomeric Ni(0) complex with more electronically donating ligand afforded more hydrogen upon treatment with HCl (Table 4.6). The strength of the M–L bond is reduced when moving to 1st row transition metals, which causes the discrepancy in the stability of tfepma bridged-metal complexes towards HCl between 1st row and 2nd/ 3rd row metal complexes.[12,13 ,50]

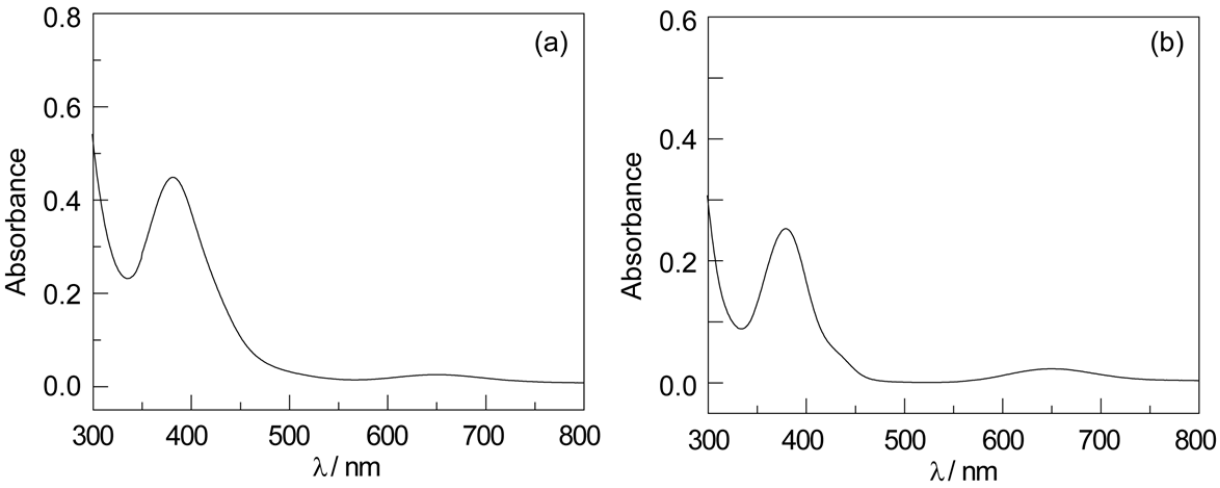

Figure 4.49. UV-vis absorption spectra of (a) **19** and (b) **20** in THF in the reaction with 50 equiv HCl.

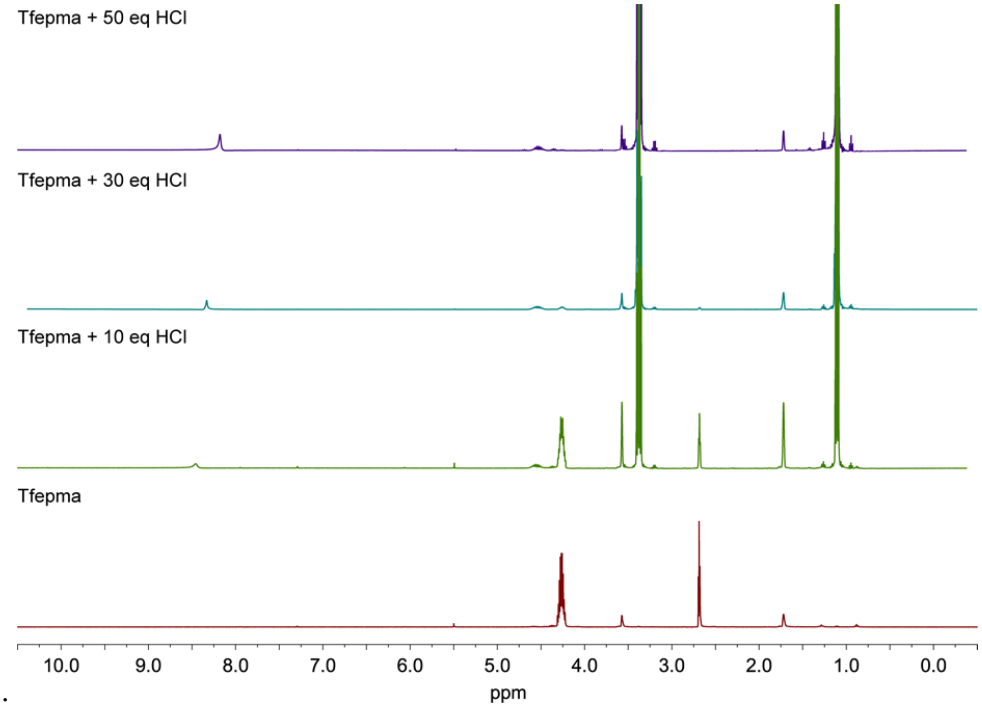

Figure 4.50. ^{1}H NMR spectra of tfepma and their reactions with different amounts of HCl (10, 30, and 50 equiv) recorded in THF–d_8 at 23 °C.

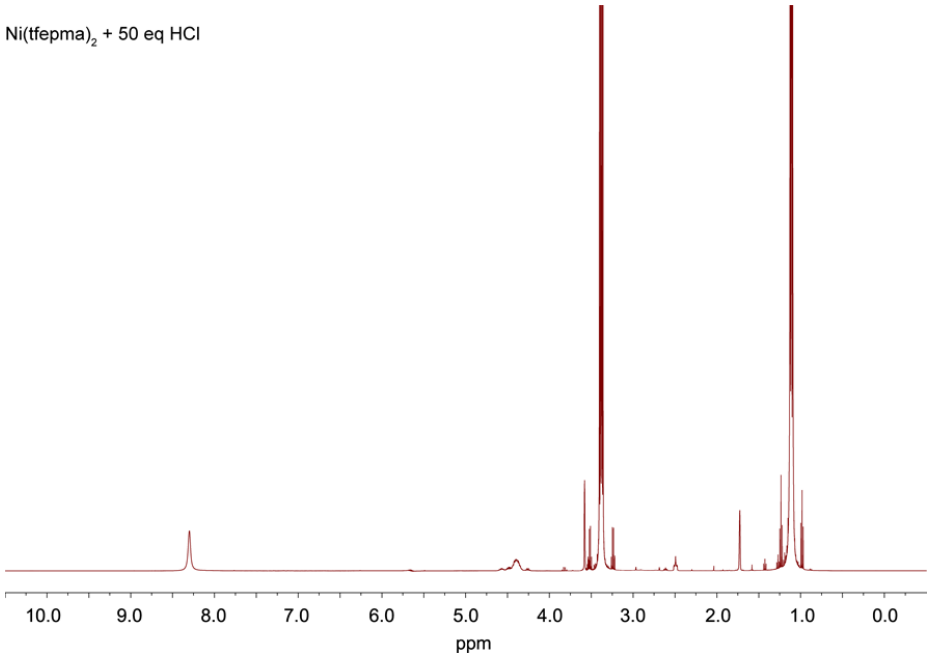

Figure 4.51. ^{1}H NMR spectrum of reaction of $Ni_2(tfepma)_2$ (**23**) with 50 equiv HCl recorded in THF–d_8 at 23 °C.

Table 4.10. H_2 generation yield from protonation reactions of Ni(0) complexes supported by various ligands with 10 equiv of HCl.

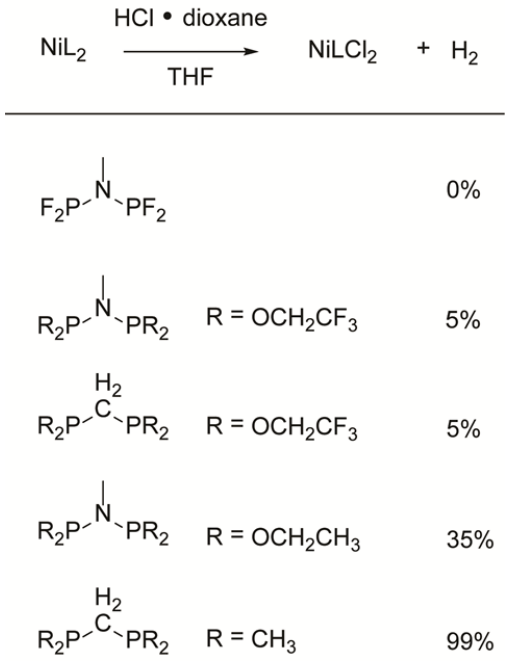

We clearly observed that the formation of hydrogen by reaction of HCl with Ni(0) complexes is strongly influenced by the electronic nature of the supporting ligands as depicted in Table 4.10. Since dmpm supported Ni(0) complexes afforded quantitative amounts of H_2 from HCl (Figure 4.52), this new suite of the Ni_2 complexes supported by bidentate phosphine ligand (dmpm: bis(dimethylphosphino)methane) was prepared to test their feasibility for closing the HX photocycle. The $Ni_2[I,I]Cl_2$ complex bridged with three dmpm ligand (**29**) was prepared by the comproportionation reaction between $Ni(cod)_2$ and $NiCl_2(PPh_3)_2$ in the presence of 3 equiv of bidentate phosphine ligand. When complex **29** was treated with two equiv of HCl, dimeric Ni tetrachloride complex **32** with two bridging dmpm ligands was obtained along with the generation of H_2 as a gaseous product. Interestingly, complex **32** reacts with hydrogen atom (H•) donors such as Bu_3SnH to generate a new purple Ni dimeric complex **34**. Dimeric compound **34** showed a different spin state (S = ½ confirmed by EPR) and UV-vis compared to the non-H

bridged complex **29**. Both Ni complex **29** and **34** were characterized by single X-ray diffraction and exhibited an elongated Ni–Ni bond distance, 3.231 Å for complex **34** compared to 3.06 Å for **29**, (Figure 4.53). Additionally, new peaks were identified by IR for complex **34**, (822, 941, and 1109 cm^{-1}) which are well matched to the frequency of bridging hydrides based on DFT calculations.

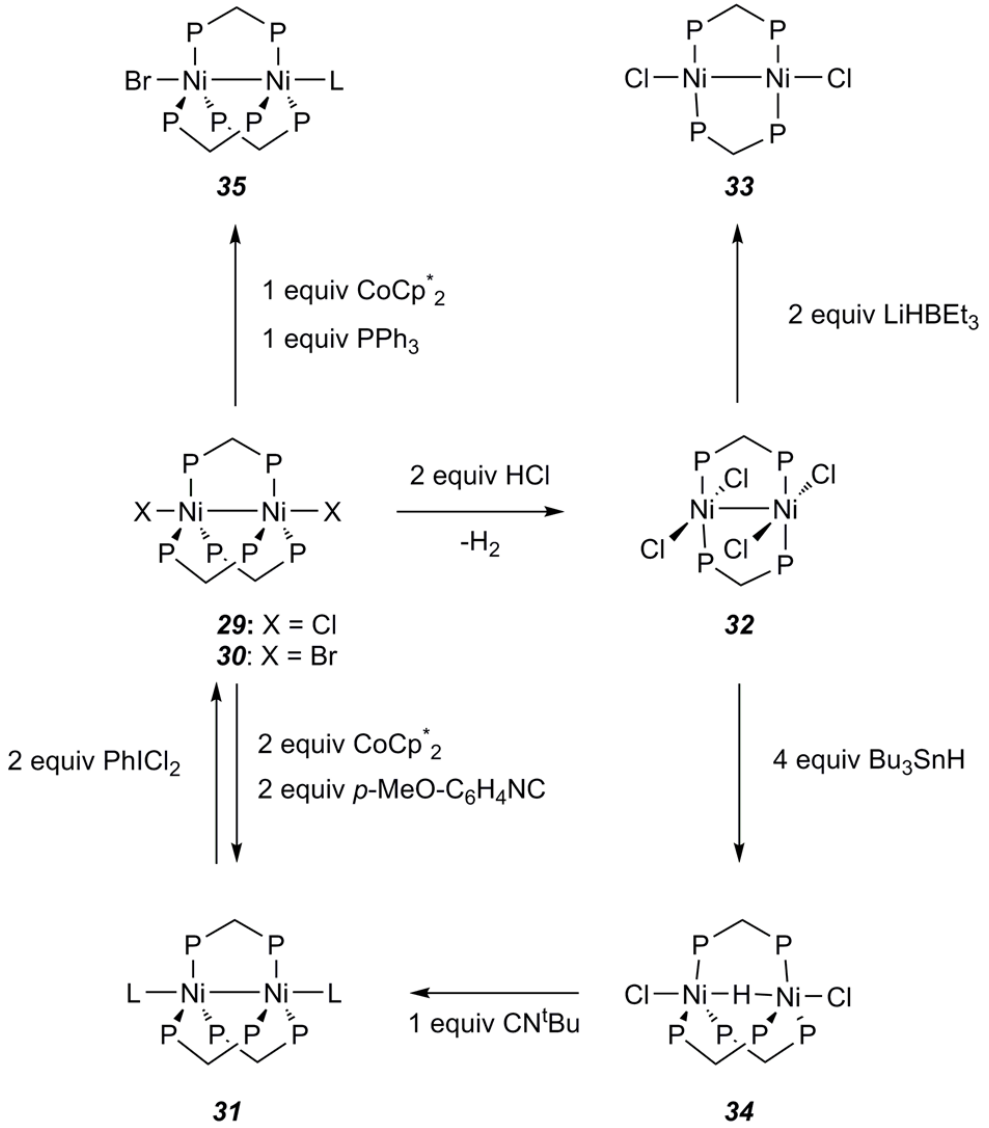

Figure 4.52. Synthetic relationships between dppm bridged Ni_2 complexes.

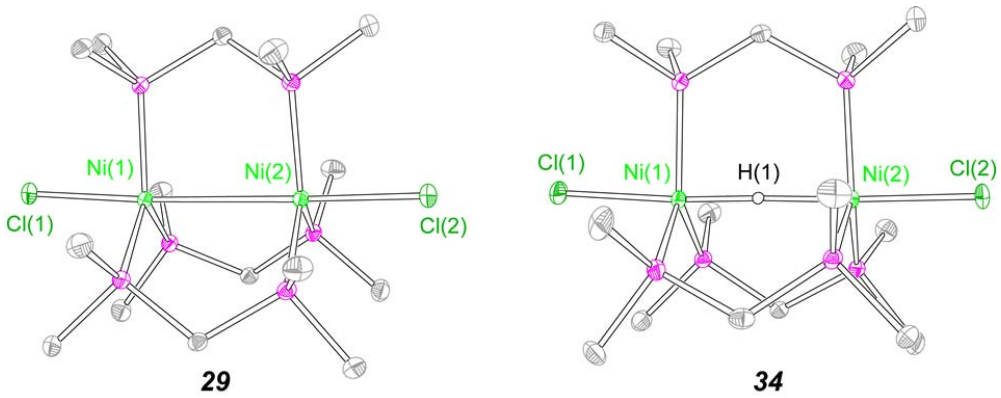

Figure 4.53. Thermal ellipsoid plots of **29** and **34** drawn at 50% probability. H atoms have been removed for clarity except bridged hydride in **34**.

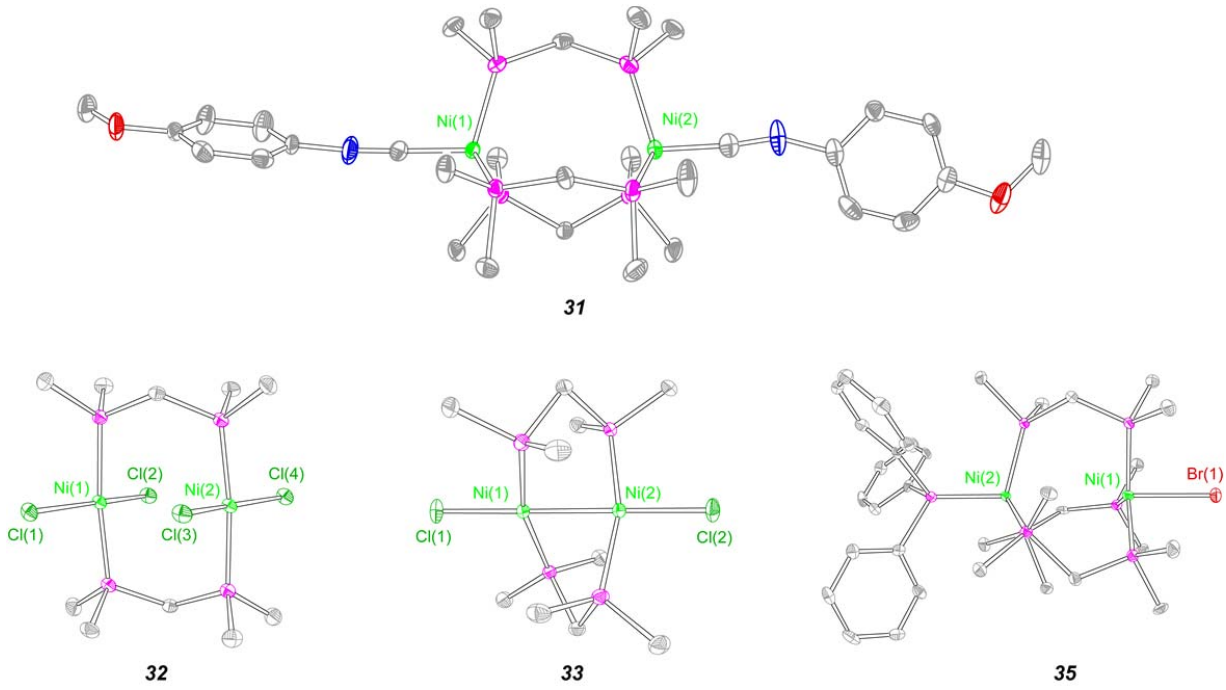

Figure 4.54. Thermal ellipsoid plots of **31**, **32**, **33** and **35** drawn at 50% probability. H atoms have been removed for clarity.

4.13. Outlook: Ligand Design for Halogen Photoelimination from Bimetallic Nickel Complexes

Based on the conclusions from this study on halogen photohalogenation from low-valent bimetallic Ni_2 complexes, we decided to rationally design a new ligand platform that would compile all the structural and electronical requirements to afford Ni complexes that would be efficient at both halogen photoelimination and H_2 production. The three-fold symmetric, low-valent Ni_2 complexes **15** and **17** was shown to be efficient at halogen photoelimination, but the resulting zero-valent Ni complexes, **20** and **23** was unable to achieve efficient H_2 production due to the lability of the tfepma ligand, which can interfere with the reaction. We therefore envisioned a ligand system that would conserve the structural features of the Ni_2 complexes, but that would provide additional stability to the photoreduced zero-valent nickel complex to allow for more efficient H_2 production.

The *tris*((6-(diphenylphosphino)pyridin-2-yl)methyl)amine, TPPA ligand was selected, because we believed that it would stabilize low valent nickel centers in a three-fold symmetry similar to that of Ni_2 complex **15** and **17**, and also provide an additional atrane motif to stabilize the resultant zero-valent nickel species. The diphenyl phosphine groups help with halogen photoelimination, since we previously showed in the Chapter 3 that Ph groups in the second coordination sphere can trap photogenerated chlorine atoms and prevent back reaction with the reduced Ni center. The TPPA ligand was synthesized in three steps from commercially available starting materials, in an overall yield of 10%. First, radical bromination of 2-bromo-6-methylpyridine afforded 2-bromo-6-bromomethylpyridine, which can be trimerized to give *tris*((6-bromopyridin-2-yl)methyl)amine. Further reaction with $KPPh_2$ yields the [TPPA] ligand, which was structurally characterized by X-ray diffraction, as well as ^{1}H, ^{13}C and $^{31}P\{^{1}H\}$ NMR spectroscopy.

The low valent Ni_2 complex, [TPPA]$Ni_2Cl(NiCl_4)_{0.5}$ was isolated from the reaction between $NiCl_2(PPh_3)_2$, $Ni(COD)_2$ and TPPA. The molecular structure of [TPPA]$Ni_2Cl(NiCl_2)_{0.5}$ was determined using X-ray diffraction, thereby revealing a cationic [TPPA]Ni_2Cl species with a bimetallic nickel moiety in a three-fold symmetric environment, in which one Ni is part of the atrane motif. Photolysis of Ni_2 complex with ($\lambda > 320$ nm) showed gradual disappearance of the starting material and formation of a new species, leading us to believe that the compound undergoes halogen photoelimination. We plan to study this system using photocrystallography, transient absorption spectroscopy, and DFT calculations to get insights into the halogen photoelimination mechanism. Our attempts to access the zero-valent [TPPA]Ni_2 species show promising results, as the product from the reaction between $Ni(cod)_2$ and [TPPA] can be isolated and produces H_2 in the presence of HCl. Further studies will include NMR and EPR spectroscopy to follow the formation of the different Ni species formed and to monitor the H_2 production.

4.14 Discussion

Photochemical HX splitting, in which H^+ reduction to H_2 is coupled to X^- oxidation to X_2, offers a paradigm for the construction of a closed-, carbon-neutral, cycle for solar energy conversion. Halogen elimination accounts for the majority of the energy stored in HX splitting cycles and this half-reaction typically has been the roadblock to development of authentic HX-splitting photocatalysis.[10] When halogen elimination is achieved, chemical traps are frequently required to sequester the evolved halogen.[51 – 55] The use of chemical traps provides a thermodynamic driving force for photoreduction and obviates significant energy storage. Trap-

free halogen elimination chemistry has been realized in the solid-state,[62–64] but as of yet, no system is available for which both proton reduction and solid-state halide oxidation are facile.

The Nocera group has developed dirhodium complexes on the hypothesis that mixed-valent complexes will give rise to the requisite multielectron photoreactions. Families of phosphazane-bridged complexes have been developed and they display the targeted multielectron chemistry, but catalysts that accomplish authentic HX splitting to afford both H_2 and X_2 in the absence of chemical traps have proven elusive. Rational development of new HX-splitting platforms has been limited by a dearth of information regarding the mechanism of halogen elimination, thus establishing an imperative for an understanding of the critical steps preceding halogen elimination.

To this end, the results reported herein provide direct insight into the nature of intermediates that promote halogen elimination from bimetallic centers. Halogen elimination proceeds from a common photointermediate for HX splitting photocatalysis that is promoted by either Rh_2[I,III] complex **1** or Rh_2[II,II] complex **2** . Solution-phase, nanosecond-resolved TA spectroscopy has provided evidence for this photointermediate, but its structure has not been established.[16] We have employed photocrystallography to directly probe photoinduced structural changes associated with halogen photoelimination by X-ray diffraction.[56–61] Such experiments are particularly attractive given that solid-state halogen elimination reactions provide inroads to authentic halogen elimination reactions.[62–64] To use photocrystallography reliably to gain insight into the structures of reaction intermediates in solution, the same photointermediates must be accessed in the solid state. The thin-film, nanosecond-resolved TA measurements shown in Figure 2 establish the homology of solution-phase and solid state intermediates; the same TA line shape is generated in solution-phase and solid-state experiments. The nature of this

photoreduction intermediate that is common to complexes **1** and **2** is unveiled by the steady-state photocrystallography experiments summarized in Figure 3. Both Rh_2[I,III] complex **1** and Rh_2[II,II] complex **2** display photoinduced structures characteristic of partial halide migration to a bridging position.

The two-step reaction sequence – ligand loss to generate a ligand-bridged intermediate followed by two electron photoreduction – represents an intramolecular example of the two steps of canonical binuclear elimination mechanisms. Binuclear reductive elimination reactions, originally defined in context of elimination of alkanes and aldehydes from binuclear metal alkyl or acyl complex,[65,66] are proposed to proceed via 1) generation of an open coordination site on the metal alkyl complex by either ligand dissociation or migratory insertion, 2) intermolecular reaction of the unsaturated fragment with a metal hydride to generate a hydride-bridged intermediate, and 3) migration of the alkyl or acyl group onto the bridging hydride to generate the observed organic products as well as binuclear transition metal complexes (Eq. 1).[67–69] Such binuclear elimination has been proposed for complexes based on most of the transition metal series,[70–75] and it is proposed to be operative during both Co- and Rh-catalyzed hydroformylation reactions under some conditions.[17,76–83] We have previously proposed a binuclear reductive elimination mechanism for the H_2 evolution step of HX splitting catalysis with phosphazane-bridged Ir_2 complexes.[84]

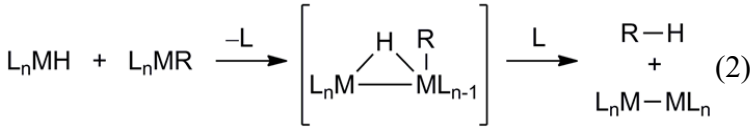

(2)

Based on the results shown in Figures 4.2, 4.9 and 4.13, we now observe that a similar mechanism may be operative for halogen photoelimination.

Overall, we report the successful use of photocrystallography to design a nickel analogue of our previously successful rhodium system that efficiently and cleanly eliminates X_2. We were further able to show substantial halide atom movement by photocrystallography, confirming that the operative mechanism of photoactivation to be the movement of a terminally bound halide to a bridging position. As the field of organic photoredox catalysis blossoms, photocrystallography stands to yield significant mechanistic insight into the generation of reactive radical intermediates and iteratively the design of better catalysts. This will be of particular interest as the field moves into regio- and enatioselective photo-catalysis.

4.15 Conclusions

Ligand photo-dissociation can generate reactive, unsaturated transition metal fragments poised to participate in challenging bond making and breaking reactions. Binuclear reductive elimination reactions have been proposed to proceed through ligand-bridged intermediates, which are generated from unsaturated transition metal fragments. Based on the hypothesis that reactive ligand-bridged intermediates are critical to halogen photoelimination reactions from binuclear Rh and Ni complexes, we have synthesized a family of halide-bridged binuclear Rh complexes and two-electron mixed valence Ni complex. In the case of Rh_2 system, the hypothesis that more efficient H_2 evolution catalysis could be achieved by removing the need for ligand photodissociation prior to halogen elimination reactions was interrogated by evaluating photoevolution of H_2 with the newly synthesized monoisocyanide complexes. Further comparison of the H_2 evolution efficacy of halide-bridged catalysts with coordinatively saturated complexes reveals the halide-bridged structures to be 2–4 times more efficient. We also designed the new Ni complex based on our photocrystallographic observation that halide-bridged

binuclear complex is common intermediate for the halogen photoelimination. Two-electron mixed valence Ni[0,II]Cl_2 complex showed the one-step X_2 elimination rather than consecutive two X• elimination observed for the Ni_2[I,I]Cl_2 complexes in the 3-fold symmetry.

4.16 Experimental Details

4.16.1 Materials and Synthetic Details

All reactions were carried out in an N_2-filled VAC atmospheres glovebox. Anhydrous solvents were obtained from Pure System Technology drying columns backed by argon gas.[85] $Ni(cod)_2$ was obtained from Strem Chemicals, while $NiCl_2(PPh_3)_2$, $NiBr_2(PPh_3)_2$, CN^tBu, and $CoCp^*_2$ were obtained from Sigma Aldrich. All chemicals were used without purification. Complexes **1**, **2**,[14] **5**, **6**, **7**, **9**, **10**,[16] **26**,[46] tfepma,[86] and $PhICl_2$[87] were prepared as previously described.

Rh_2(tfepma)$_2$(CO)$_2Cl_4$. To a solution of $[Rh(CO)_2Cl]_2$ (44.0 mg, 1.13×10^{-4} mol, 1.00 equiv) in $PhCH_3$ (5 mL) at 23 °C was added tfepma (110 mg, 2.26×10^{-4} mol, 2.00 equiv) dropwise as a $PhCH_3$ (1 mL) solution. The reaction mixture was stirred at 23 °C for 1 h during which time evolution of bubbles was observed and the color of the reaction mixture turned from orange to dark red. $PhICl_2$ (46.6 mg, 1.70×10^{-4} mol, 1.50 equiv) was added as a solid. ^{31}P NMR analysis of an aliquot of the reaction mixture showed the presence of two ^{31}P NMR signals (multiplets at 105.3 - 104.5 and 102.2 - 101.5 ppm) in a 2:1 ratio, assigned as due to *trans* and *cis*, respectively. Heating the reaction mixture to 70 °C for 2 h resulted in the conversion of *trans* to *cis* isomer. The reaction mixture was cooled to –30 °C for 1 h at which time a precipitate was observed. Solvent was decanted, the residue washed with pentane, and dried in vacuo to afford 123 mg of the title complex as a yellow solid in 79% yield. *Trans*: ^{1}H NMR (C_6D_6, 23 °C)

δ(ppm): 4.86 - 4.83 (m, 8H), 4.51 - 4.46 (m, 4H), 4.36 - 4.31 (m, 4H), 2.58 (pseudoquintet, J = 3.9 Hz, 6H). ^{31}P NMR (C_6D_6, 23 °C) δ(ppm): 105.3 - 104.5 (m, 4P). ^{19}F NMR (C_6D_6, 23 °C) δ(ppm): –74.68 (t, J = 7.9 Hz, 12F), –75.09 (t, J = 7.9 Hz, 12F). IR: ν_{CN} = 2082 cm^{-1}. Crystals of *cis* suitable for single-crystal diffraction analysis were obtained from a THF solution layered with pentane at –30 °C and crystals of *trans* suitable for single-crystal diffraction analysis were obtained from a CH_2Cl_2 solution layered with hexane at –30 °C.

Rh_2(tfepma)$_2$AdNC(μ-Cl)Cl_3 (3). A thin-film of **Rh_2(tfepma)$_2$(CO)$_2Cl_4$** (52.0 mg, 3.44 × 10^{-4} mol, 1.00 equiv) was deposited on the wall of a two-chamber photoreaction vessel and was dried in vacuo for 12 h. Broad-band photolysis of the thin film with a 100 W Hg lamp was carried out for 4 h under dynamic vacuum (20 mTorr). The residue was taken up in CH_2Cl_2, layered with pentane, and cooled to –30 °C for 1 h, at which time solvent was decanted. The residue was dried in vacuo to afford 48.0 mg of complex **3** as a yellow solid (94% yield). ^{1}H NMR (CD_2Cl_2, 23 °C) δ(ppm): 4.93 - 4.83 (m, 4H), 4.82 - 4.67 (m, 6H), 4.62 - 4.54 (m, 2H), 4.51 - 4.45 (m, 2H), 4.36 - 4.27 (m, 2H), 3.02 (pseudoquintet, J = 3.9 Hz, 6H), 2.13 (br s, 3H), 2.09 (s, 6H), 1.72 - 1.64 (m, 6H). ^{31}P NMR (CD_2Cl_2, 23 °C) δ(ppm): 116.5 - 114.4 (m, 2P), 113.2 - 111.1 (m, 2P). ^{19}F NMR (C_6D_6, 23 °C) δ(ppm): –74.64 (t, J = 7.9 Hz, 6F), –75.30, –75.4 (m, 18F). IR: ν_{CN} = 2199 cm^{-1}. Crystals of **3** suitable for single-crystal diffraction analysis were obtained by cooling a saturated CH_2Cl_2 / hexanes solution of **3** to –30 °C.

Rh_2(tfepma)$_2$(*p*-F-C_6H_4NC)(μ-Cl)Cl_2H (8). To a solution of Rh_2(tfepma)$_2$(μ-*p*-F-C_6H_4NC)Cl_2 (**5**) (31.0 mg, 2.28 × 10^{-5} mol, 1.00 equiv) in THF (0.5 mL) at 23 °C was added HCl·dioxane (4.0 M, 0.10 mL, 3.4 × 10^{-4} mol, 15 equiv) in one portion. The color of the reaction mixture turned from orange to dark red. Solution characterization (^{1}H NMR, ^{19}F NMR, ^{31}P NMR and UV-vis) was carried out using the reaction solution without further purification because

removal of solvent afforded a mixture of Rh_2 hydride **8** and Rh_2[I,I] complex **6**. Based on integration of the ^{1}H NMR spectrum against hexamethylbenzene (internal standard), the yield of **8** was 95%. ^{1}H NMR (400 MHz, CD_2Cl_2) δ (ppm): 7.26 (dd, J = 9.2 Hz, J = 4.9 Hz, 2H), 7.18 (dd, J = 7.9 Hz, J = 7.9 Hz, 2H), 4.93–4.61 (m, 1H), 4.40–4.38 (m, 2H), 3.01 (pseudoquintet, J = 3.9 Hz, 6H), –19.40 (dt, J = 25.0 Hz, J = 10.0 Hz, 1H). ^{31}P NMR (121.5 MHz, CD_2Cl_2) δ (ppm): 127.4–125.1 (m, 2P), 111.2–109.1 (m, 2P). ^{19}F NMR (275 MHz, CD_2Cl_2) δ (ppm): –81.9, –82.3 (m, 24F), –114.1 (m, 1F). IR: ν_{CN} = 2171 cm^{-1}. Crystals suitable for single-crystal diffraction analysis were obtained from a THF solution layered with pentane at –30 °C. Satisfactory combustion analysis could not be obtained because **7** was not stable to evacuation of solvent.

Rh_2(tfepma)$_2$(*p*-MeO-C_6H_4NC)(μ-Cl)Cl_2H (11). To a solution of Rh_2(tfepma)$_2$(μ-*p*-MeO-C_6H_4NC)Cl_2 (**9**) (38.8 mg, 2.23 × 10^{-5} mol, 1.00 equiv) in THF (0.5 mL) at 23 °C was added HCl·dioxane (4.0 M, 0.10 mL, 3.4 × 10^{-4} mol, 15 equiv) in one portion. The color of the reaction mixture turned from orange to dark red. Solution characterization (^{1}H NMR, ^{19}F NMR, ^{31}P NMR and UV-vis) was carried out using the reaction solution without further purification because removal of solvent afforded a mixture of Rh_2 hydride **11** and Rh_2[I,I] complex **9**. Based on integration of the ^{1}H NMR spectrum against hexamethylbenzene (internal standard), the yield of **11** was 90%. ^{1}H NMR (400 MHz, CD_2Cl_2) δ (ppm): 7.18 (d, J = 8.8 Hz, 2H), 6.93 (d, J = 8.8 Hz, 2H), 4.92–4.87 (m, 2H), 4.81–4.70 (m, 6H), 4.70–4.56 (m, 6H), 4.40–4.32 (m, 2H), 3.85 (s, 3H), 2.98 (pseudoquintet, J = 3.3 Hz, 6H), –19.44 (td, J = 35.6 Hz, J = 10.9 Hz, 1H). ^{31}P NMR (121.5 MHz, THF-d_8) δ (ppm): 134.5–132.1 (m, 2P), 118.3–116.2 (m, 2P). IR: ν_{CN} = 2170 cm^{-1}. Crystals suitable for single-crystal diffraction analysis were obtained from a THF solution layered with $PhCH_3$ at –30 °C. Satisfactory combustion analysis could not be obtained because **10** was not stable to evacuation of solvent.

Rh_2(tfepma)$_2$(μ-*p*-F-C_6H_4NC)Br_2 (12). To a solution of [Rh(cod)Br]$_2$ (114 mg, 1.96 × 10^{-4} mol, 1.00 equiv) in THF (4.0 mL), tfepma (191 mg, 3.93 × 10^{-4} mol, 2.00 equiv) and *p*-fluorophenylisocyanide (47.6 mg, 3.93 × 10^{-4} mol, 2.00 equiv) were added sequentially. The dark red reaction solution was stirred at 23 °C for 4 h. Solvent was removed in vacuo and the residue was taken up in THF (1 mL) and hexanes (10 mL). The supernatant was removed and the solid residue was dried in vacuo to afford 203 mg of the title complex (70.8% yield) as an orange solid. ^{1}H NMR (600 MHz, CD_2Cl_2) δ (ppm): 7.29 (dd, *J* = 8.9 Hz, *J* = 4.8 Hz, 2H), 7.03 (dd, *J* = 8.7 Hz, *J* = 8.7 Hz, 2H), 4.68–4.56 (m, 16H), 2.79 (pseudoquintet, *J* = 3.5 Hz, 6H). ^{31}P NMR (121.5 MHz, CD_2Cl_2) δ (ppm): 129.0 (m, 4P). ^{19}F NMR (275 MHz, CD_2Cl_2) δ (ppm): –75.3, –75.2 (m, 24F), –115.3 (m, 1F). IR: ν_{CN} = 1735 cm^{-1}. Crystals suitable for single-crystal diffraction analysis were obtained from a CH_2Cl_2 solution layered with $PhCH_3$ at –30 °C.

Rh_2(tfepma)$_2$(*p*-F-C_6H_4NC)(μ-Br)Br_3 (13). To a solution of Rh_2(tfepma)$_2$(μ-*p*-F-C_6H_4NC)Br_2 (**12**) (15.8 mg, 1.08 × 10^{-5} mol, 1.00 equiv) in CH_2Cl_2 (1.5 mL) at 23 °C was added Br_2 (2.2 mg, 0.70 μL, 1.4 × 10^{-5} mol, 1.3 equiv) as a solution in CH_2Cl_2 (0.5 mL). The color of the reaction solution turned from orange to red. After stirring for 30 min at 23 °C, solvent was removed in vacuo to afford 17.4 mg of the title complex (99.3% yield) as a dark orange solid. ^{1}H NMR (400 MHz, CD_2Cl_2) δ (ppm): 7.50 (dd, *J* = 4.7 Hz, *J* = 1.9 Hz, 2H), 7.48 (dd, *J* = 4.6 Hz, *J* = 4.6 Hz, 2H), 4.95–4.86 (m, 4H), 4.82–4.68 (m, 8H), 4.55–4.48 (m, 2H), 4.44–4.36 (m, 2H), 3.01 (pseudoquintet, *J* = 3.5 Hz, 6H). ^{31}P NMR (121.5 MHz, CD_2Cl_2) δ (ppm): 110.9 (m, 4P). ^{19}F NMR (275 MHz, CD_2Cl_2) δ (ppm): –74.8 (t, *J* = 9.2 Hz, 6F), –75.1 (m, 12F), –75.2 (t, *J* = 9.2 Hz, 6F), –106.4 (m, 1F). IR: ν_{CN} = 2190 cm^{-1}. Crystals suitable for single-crystal diffraction analysis were obtained from a CH_2Cl_2 solution layered with $PhCH_3$ at –30 °C.

Rh_2(tfepma)$_2$(*p*-F-C_6H_4NC)(μ-Br)Br_2H (14). To a solution of Rh_2(tfepma)$_2$(μ-*p*-F-C_6H_4NC)Br_2 (**12**) (32.7 mg, 2.23×10^{-5} mol, 1.00 equiv) in CH_2Cl_2 at 23 °C was added sat. HBr in CH_2Cl_2 (0.5 M, 0.20 mL, 8.6×10^{-5} mol, 4.0 equiv) in one portion. The color of the reaction mixture turned from orange to dark red. Solution characterization (^{1}H NMR, ^{19}F NMR, ^{31}P NMR and UV-vis) was carried out using the reaction solution without further purification because removal of solvent afforded a mixture of Rh_2 hydride **14** and Rh_2[I,I] complex **12**. Based on integration of the ^{1}H NMR spectrum against hexamethylbenzene (added as internal standard), the yield of **14** was 95%. ^{1}H NMR (600 MHz, CD_2Cl_2) δ (ppm): 7.24 (dd, *J* = 9.3 Hz, *J* = 5.0 Hz, 2H), 7.16 (dd, *J* = 7.9 Hz, *J* = 7.9 Hz, 2H), 4.88–4.72 (m, 8H), 4.68–4.59 (m, 6H), 4.40 – 4.34 (m, 2H), 2.97 (pseudoquintet, *J* = 3.8 Hz, 6H), –18.30 (dt, *J* = 21.6 Hz, *J* = 10.1 Hz, 1H). ^{31}P NMR (121.5 MHz, CD_2Cl_2) δ (ppm): 117.5 (m, 2P), 99.9 (m, 2P). ^{19}F NMR (275 MHz, CD_2Cl_2) δ (ppm): –74.5 (m, 24F), –107.0 (m, 1F). IR: ν_{CN} = 2171 cm^{-1}. Crystals suitable for single-crystal diffraction analysis were obtained from a CH_2Cl_2 solution layered with $PhCH_3$. Satisfactory combustion analysis could not be obtained because **13** was not stable to evacuation of solvent.

Ni_2(tfepma)$_3Cl_2$ (15). To a solution of Ni(cod)$_2$ (40 mg, 0.145 mmol, 1.0 equiv) in THF (4 mL) $NiCl_2(PPh_3)_2$ (95 mg, 0.145 mmol, 1.0 equiv) and tfepma (213 mg, 0.435 mmol, 3.0 equiv) were added sequentially. The dark green reaction solution was stirred at 23 ^{o}C for 1 hr. Solvent was removed in vacuo, and the residue was taken up in pentane (20 mL). The supernatant was removed, and the solid residue was dried in vacuo to afford 194 mg of the title complex (81% yield) as a green solid. ^{1}H NMR (THF-d_8, 23 ^{o}C) δ (ppm): 3.10 (br, 9H), 4.63 (br, 24H). ^{31}P{^{1}H} NMR (THF-d_8, 23 ^{o}C) δ (ppm): 117.3 (s, 6P). ^{19}F NMR (THF-d_8, 23 ^{o}C) δ (ppm): −75.8 (s, 24F). %CHN calcd for $C_{27}H_{33}Cl_2F_{36}N_3Ni_2O_{12}P_6$: C 19.66, H 2.02, N 2.55; found: C

19.82, H 2.01, N 2.53. Crystals suitable for single-crystal diffraction analysis were obtained from a $PhCF_3$ solution at −30 °C.

Ni_2(tfepma)$_3Br_2$ (16). To a solution of $Ni(cod)_2$ (40.0 mg, 0.145 mmol, 1.00 equiv) in THF (4 mL) $NiBr_2(PPh_3)_2$ (108 mg, 0.145 mmol, 1.00 equiv) and tfepma (213 mg, 0.435 mmol, 3.00 equiv) were added sequentially. The dark green reaction solution was stirred at 23 °C for 1 hr. Solvent was removed in vacuo, and the residue was taken up in pentane (20 mL). The supernatant was removed, and the solid residue was dried in vacuo to afford 233 mg of the title complex (92.5% yield) as a green solid. ^{1}H NMR (400 MHz, THF-d_8, 23 °C) δ (ppm): 3.16 (br, 9H), 4.67 (br, 24H). ^{31}P{^{1}H} NMR (121.5 MHz, THF-d_8, 23 °C) δ (ppm): 116.4 (br, 6P). ^{19}F NMR (275 MHz, THF-d_8, 23 °C) δ (ppm): −75.7 (s, 24F). %CHN calcd for $C_{27}H_{33}Br_2F_{36}N_3Ni_2O_{12}P_6$: C 18.65, H 1.91, N 2.42; found: C 18.78, H 1.69, N 2.42.

Ni_2(tfepma)$_3$(CN^{t}Bu)Cl (17). A sample of **15** (150 mg, 0.091 mmol, 1.00 equiv) was dissolved in 1.5 mL of THF. A solution of CN^{t}Bu (16 mg, 0.182 mmol, 2.00 equiv) in 0.5 mL of THF was added, and the pine solution was stirred at 23 °C for 2 hr. The solution was concentrated in vacuo to give a dark green residue. The residue was taken up in $PhCH_3$, and cooled to −30 °C for 24 h, at which time 103 mg of complex **17** was isolated as a blue crystalline solid (66.9% yield). The corresponding Ni complex **17** is silent in both ^{1}H and ^{31}P{^{1}H} NMR. IR: ν_{CN} = 2152 cm^{-1}. %CHN calcd for $C_{32}H_{42}ClF_{36}N_4Ni_2O_{12}P_6$: C 22.64, H 2.49, N 3.30; found: C 22.76, H 2.46, N 3.26. Crystals suitable for single-crystal diffraction analysis were obtained from a $PhCH_3$ solution at –30 °C.

Ni_2(tfepma)$_3$(CN^{t}Bu)Br (18). A sample of **16** (150 mg, 0.086 mmol, 1.00 equiv) was dissolved in 1.5 mL of THF. A solution of CN^{t}Bu (15.0 mg, 0.173 mmol, 2.00 equiv) in 0.5 mL of THF was added, and the pine solution was stirred at 23 °C for 2 hr. The solution was

concentrated in vacuo to give a dark green residue. The residue was taken up in $PhCH_3$, and cooled to −30 °C for 24 h, at which time 94.0 mg of complex **18** was isolated as a blue crystalline solid (62.7% yield). The corresponding Ni complex **18** is silent in both ^{1}H and $^{31}P\{^{1}H\}$ NMR. IR: ν_{CN} = 2145 cm^{-1}. %CHN calcd for $C_{32}H_{42}BrF_{36}N_4Ni_2O_{12}P_6$: C 22.07, H 2.43, N 3.22; found: C 22.13, H 2.20, N 3.19. Crystals suitable for single-crystal diffraction analysis were obtained from a $PhCH_3$ solution at –30 °C.

Ni_2(tfepma)$_3$(CN^{t}Bu)$_2$ (19). A suspension of **15** (200 mg, 0.128 mmol, 1.00 equiv) in 2 mL of THF was combined with a solution of CN^{t}Bu (21.0 mg, 0.257 mmol, 2.00 equiv) in 2 mL of THF. The resulting mixture was added to a solution of $CoCp^*_2$ (85.0 mg, 0.257 mmol, 2.00 equiv) in 2 mL THF. A yellow solid formed immediately, and the mixture was stirred for 6 hr, at which time the precipitate was removed by filtration through glass fiber. The solution was concentrated to dryness, and the resulting yellow solid was suspended in 6 mL of Et_2O at –30 °C overnight. The supernatant was decanted, and 140 mg of complex **19** was isolated as a light yellow crystalline solid (62.8% yield). ^{1}H NMR (400 MHz, $PhCD_3$-d_8, 23°C) δ (ppm): 0.90 (t, *J* = 4.0 Hz, 5H), 1.02 (s, 8H), 1.12 (s, 5H), 2.41 (s, 5H), 2.75 (s, 4H), 4.19 (m, 24H). $^{31}P\{^{1}H\}$ NMR (121.5 MHz, $PhCD_3$-d_8, 23 °C) δ (ppm): 150.02 (s, 6P). ^{19}F NMR (275 MHz, THF-d_8, 23 °C) δ (ppm): −75.07 (s, 8F), −74.90 (s, 16H). IR: ν_{CN} = 2094 cm^{-1}. %CHN calcd for $C_{37}H_{51}F_{36}N_5Ni_2O_{12}P_6$: C 25.47, H 2.95, N 4.01; found: C 25.31, H 2.99, N 3.91. Crystals suitable for single-crystal diffraction analysis were obtained from an Et_2O solution at −30 °C.

Ni_2(tfepma)$_3$(CN^{t}Bu) (20). A sample of **17** (50.0 mg, 0.029 mmol, 1.00 equiv) was dissolved in 1.5 mL of THF. A solution of $CoCp_2^*$ (9.7 mg, 0.029 mmol, 1.00 equiv) in 2 mL of THF was added, and the resulting yellow solution was stirred at 23 °C for 6 hr, at which time the precipitate was filtered through glass fiber. The solution was concentrated to dryness, and the

resulting yellow solid was suspended in 5 mL of $PhCH_3$ at −30 °C overnight. The supernatant was decanted, and 24.0 mg of complex 6 was isolated as a yellow crystalline solid (49.9% yield). ^{1}H NMR (400 MHz, $PhCD_3$-d_8, 23°C) δ (ppm): 1.12 (s, 9H), 2.40 (s, 9H), 4.14 (m, 24H). The corresponding Ni complex **6** is silent in $^{31}P\{^1H\}$ NMR. ^{19}F NMR (275 MHz, $PhCD_3$-d_8, 23 °C) δ (ppm): −75.6 (s, 3F), −74.8 (s, 21F). IR: ν_{CN} = 2150 cm^{-1}. %CHN calcd for $C_{32}H_{42}F_{36}N_4Ni_2O_{12}P_6$: C 23.13, H 2.55, N 3.37; found: C 23.47, H 2.43, N 3.21. Crystals suitable for single-crystal diffraction analysis were obtained from a $PhCH_3$ solution at −30 °C.

$[Ni_2(tfepma)_3Cl_2][CoCp^*_2]$ (21). To a solution of **15** (150 mg, 0.091 mmol, 1.00 equiv) was dissolved in 2 mL THF. A solution of $CoCp_2^*$ (31.3 mg, 0.091 mmol, 1.00 equiv) in 2 mL of THF was added, and the light green solution was stirred at 23 °C for 2 hr. The solution was concentrated in vacuo to give a light green residue. The residue was taken up in $PhCF_3$, and cooled to −30 °C for 24 h, at which time 70.0 mg of complex **21** was isolated as a light green crystalline solid (38.9% yield). EPR ($PhCH_3$, 77K) g-value: g_1 = 2.176; g_2 = 2.143; g_3 = 2.012. %CHN calcd for $C_{47}H_{63}Cl_2CoF_{36}N_3Ni_2O_{12}P_6$: C 28.52, H 3.21, N 2.12; found: C 28.50, H 3.08, N 2.14. Crystals suitable for single-crystal diffraction analysis were obtained from a $PhCF_3$ solution at −30 °C.

$[Ni_2(tfepma)_3Cl][CoCp^*_2]$ (22). To a solution of **15** (120 mg, 0.077 mmol, 1.00 equiv) was dissolved in 3 mL THF. A solution of $CoCp_2^*$ (50.8 mg, 0.154 mmol, 2.00 equiv) in 3 mL of THF was added. A yellow solid formed immediately, and the mixture was stirred for 4 hr, at which time the precipitate was removed by filtration through glass fiber. The solution was concentrated to dryness, and the resulting yellow solid was suspended in 6 mL of Et_2O at −30 °C overnight. The supernatant was decanted, and 81 mg of complex **22** was isolated as an orange crystalline solid (54.0% yield). ^{1}H NMR (500 MHz, CD_2Cl_2, 23°C) δ (ppm): 1.71 (s, 30H), 2.70

(s, 9H), 4.28 (dd, J = 65, 195 Hz, 24H). $^{31}P\{^{1}H\}$ NMR (121.5 MHz, CD_2Cl_2, 23 °C) δ (ppm): 138.42–140.76 (m, 3P), 151.12–153.45 (m, 3P). %CHN calcd for $C_{47}H_{63}ClCoF_{36}N_3Ni_2O_{12}P_6$: C 29.05, H 3.27, N 2.16; found: C 28.67, H 3.39, N 2.10. Crystals suitable for single-crystal diffraction analysis were obtained from an Et_2O solution at −30 °C.

Ni(tfepma)$_2$ (23). To a suspension of $Ni(cod)_2$ (120 mg, 0.439 mmol, 1.00 equiv) in THF was added to a solution of tfepma (423 mg, 0.867 mmol, 2.00 equiv) in 2 mL THF. The reaction mixture was stirred for 3 h at which time solvent was removed in vacuo to give beige colored residue. The residue was washed with pentane and dried in vacuo to afford 425 mg of the title complex as a white solid (93.8% yield). ^{1}H NMR (400 MHz, THF-d_8, 23°C) δ (ppm): 2.50 (m, 9H), 4.41 (m, 24H). $^{31}P\{^{1}H\}$ NMR (121.5 MHz, THF-d_8, 23 °C) δ (ppm): 136.2 (s, 4P). ^{19}F NMR (275 MHz, THF-d_8, 23 °C) δ (ppm): −75.9 (t, J = 5.5 Hz, 24F). %CHN calcd for $C_{18}H_{22}F_{24}N_2NiO_8P_4$: C 20.93, H 2.15, N 2.71; found: C 21.09, H 2.09, N 2.62. Crystals suitable for single-crystal diffraction analysis were obtained from a $PhCH_3$ solution layered with pentane at −30 °C.

[Ni$_2$(tfepma)$_3$Cl$_2$][^{i}Pr$_3$PCl] (24). To a solution of $Ni(cod)_2$ (37.5 mg, 0.137 mmol, 1.0 equiv) in THF (4 mL) $NiCl_2(^iPr_3P)_2$ (61.7 mg, 0.137 mmol, 1.0 equiv) and tfepma (234 mg, 0.480 mmol, 3.5 equiv) were added sequentially. The light green reaction solution was stirred at 23 °C for 1 hr. Solvent was removed in vacuo, and the residue was taken up in pentane (20 mL). The supernatant was removed, and the solid residue was dried in vacuo to afford 114 mg of the title complex (45% yield) as a green solid. Crystals suitable for single-crystal diffraction analysis were obtained from a Et_2O solution layered with pentane at −30 °C.

Pd$_2$(tfepma)$_3$ (25). To a solution of $Pd_2(dba)_3$ (150 mg, 0.164 mmol, 1.0 equiv) in benzene (4 mL) solution of tfepma (320 mg, 0.656 mmol, 4.0 equiv) in benzene were added

dropwise. The orange reaction solution was stirred at 23 °C for 3 hr. Solvent was removed in vacuo, and the residue was taken up in pentane (20 mL). The supernatant was removed, and the solid residue was dried in vacuo to afford 178 mg of the title complex (65% yield) as an orange red solid. Crystals suitable for single-crystal diffraction analysis were obtained from a benzene solution at ambient temperature.

Ni_2(tfepma)$_2$(CN^tBu)$_3$ (27). To a solution of $Ni(cod)_2$ (300 mg, 1.11 mmol, 1.0 equiv) in THF (4 mL) at 23°C was added tfepma (532 mg, 1.11 mmol, 1.0 equiv) dropwise as a THF (4 mL) solution. To the resulting reaction mixture was added *tert*-butyl isocyanide (136 mg, 1.64 mmol, 1.5 equiv) dropwise as a THF (4 mL) solution. The reaction mixture was stirred at 23°C for 2 hr. The solvent was removed in vacuo, and the residue was taken up in Et_2O (1 mL) and pentane (3 mL). The supernatant was removed, and the solid residue was dried in vacuo to afford 228 mg of the title complex (85.0% yield) as a yellow solid. ^{1}H NMR (400 MHz, C_6D_6) δ (ppm): 1.0 (s, 18 H), 1.2 (s, 9 H), 2.6 (s, 6 H), 4.08 (m, 12 H), 4.35 (m, 4H). ^{31}P{^{1}H} NMR (121.5 MHz, C_6D_6) δ (ppm): 155.5 (m, 4P). IR: ν_{CN} = 2091.78 cm^{-1}, ν = 1831.25 cm^{-1}. ν = 1590.20 cm^{-1}. Crystals suitable for single-crystal diffraction analysis were obtained from a Et_2O solution layered with pentane at −30 °C.

Ni_2(tfepma)$_2$(CN^tBu)$_2Cl_2$ (28). To a solution of Ni_2(tfepma)$_2$(*tert*-butyl-NC)$_3$ (150 mg, 0.111 mmol, 1.0 equiv) in THF (4 mL) at 23°C was added a solution of $PhICl_2$ (33.5 mg, 0.122 mmol, 1.1 equiv) in THF (2 mL). The reaction mixture was stirred at 23°C for 1 hr, and the color of the reaction mixture changed from light orange to greenish purple. The solvent was removed in vacuo and the residue was taken up in Et_2O (3 mL) and pentane (1 mL) and cooled to −30 °C for one hour. The supernatant was removed and the solid residue was dried in vacuo to afford 106 mg of the title complex (72% yield) as a dark green solid. ^{1}H-NMR (400 MHz, C_6D_6) δ

(ppm): 0.83-1.13 (br, 18 H), 2.55 (s, 6 H), 3.56 (br, 3 H), 4.33 (br, 13H). IR ν_{CN}:= 2141 cm^{-1}, ν = 1986 cm^{-1}. Crystals suitable for single-crystal diffraction analysis were obtained from a Et_2O solution layered with pentane at −30 °C.

$Ni_2Cl_2(dmpm)_3$ (29). To a solution of $Ni(cod)_2$ (37.5 mg, 0.137 mmol, 1.0 equiv) in THF (4 mL) $NiCl_2(PPh_3)_2$ (89.6 mg, 0.137 mmol, 1.0 equiv) and dmpm (65.3 mg, 0.480 mmol, 3.5 equiv) were added sequentially. The dark red reaction solution was stirred at 23 °C for 1 hr. Solvent was removed in vacuo, and the residue was taken up in pentane (20 mL). The supernatant was removed, and the solid residue was dried in vacuo to afford 65.4 mg of the title complex (80% yield) as a red solid. ^1H NMR (400 MHz, C_6D_6-d_6, 23 °C) δ (ppm): 3.81 (br, 6H), 2.60 (br, 36H). The corresponding Ni complex is silent in $^{31}P\{^1H\}$ NMR. Crystals suitable for single-crystal diffraction analysis were obtained from a THF solution layered with pentane at −30 °C.

$Ni_2Br_2(dmpm)_3$ (30). To a solution of $Ni(cod)_2$ (150 mg, 0.548 mmol, 1.0 equiv) in THF (6 mL) $NiBr_2(PPh_3)_2$ (407 mg, 0.548 mmol, 1.0 equiv) and dmpm (224 mg, 1.64 mmol, 3.0 equiv) were added sequentially. The dark red reaction solution was stirred at 23 °C for 1 hr. Solvent was removed in vacuo, and the residue was taken up in pentane (20 mL). The supernatant was removed, and the solid residue was dried in vacuo to afford 319 mg of the title complex (85% yield) as a red-brown solid. ^1H NMR (400 MHz, C_6D_6-d_6, 23 °C) δ (ppm): 9.60 (br, 6H), 6.90 (br, 36H). The corresponding Ni complex is silent in $^{31}P\{^1H\}$ NMR.

$Ni_2(dmpm)_3$(*p*-MeO-$C_6H_4NC)_2$ (31). A suspension of **$Ni_2Br_2(dmpm)_3$** (50.0 mg, 0.073 mmol, 1.0 equiv) in 2 mL of THF was combined with a solution of *p*-OMe-C_6H_4NC (19.5 mg, 0.146 mmol, 2.0 equiv) in 2 mL of THF. The resulting mixture was added to a solution of $CoCp^*_2$ (48 mg, 0.146 mmol, 2.0 equiv) in 2 mL THF. A yellow solid formed immediately, and

the mixture was stirred for 2 hr, at which time the precipitate was removed by filtration through glass fiber. The solution was concentrated to dryness, and the resulting yellow solid was suspended in 6 mL of Et_2O at −30 °C overnight. The supernatant was decanted, and 36.4 mg of title complex was isolated as a light yellow crystalline solid (63% yield). ^{1}H NMR (400 MHz, C_6D_6-d_6, 23°C) δ (ppm): 7.13 (dd, *J* = 12.0 Hz, 4H), 6.56 (dd, *J* = 12.0 Hz, 4H), 3.57 (t, *J* = 8.0 Hz, 6H), 3.20 (s, 6H), 1.38 (s, 36H). ^{31}P{^{1}H} NMR (121.5 MHz, C_6D_6-d_6, 23 °C) δ (ppm): −10.78 (s, 6P). Crystals suitable for single-crystal diffraction analysis were obtained from an Et_2O solution at −30 °C.

$Ni_2Cl_4(dmpm)_2$ (32). To a suspension of $NiCl_2$(dme) (50.0 mg, 0.227 mmol, 1.00 equiv) in THF was added dmpm (30.9 mg, 0.227 mmol, 1.00 equiv) as a solid. The mixture was stirred at 23 °C for 2 h, during which time an orange precipitate was observed. The mixture was concentrated to dryness and the residue was washed with pentane and dried in vacuo to afford 55.5 mg of the title complex as a orange solid (92% yield). Crystals suitable for single-crystal diffraction analysis were obtained from a CH_2Cl_2 solution layered with pentane at −30 °C.

$Ni_2Cl_2(dmpm)_2$ (33). A suspension of **$Ni_2Cl_4(dmpm)_2$** (80.0 mg, 0.151 mmol, 1.0 equiv) in 2 mL of THF was combined with a 1.0 M solution of $LiEt_3BH$ (0.302 mL, 0.302 mmol, 2.0 equiv) in 2 mL of THF. The dark black blue reaction solution was stirred at 23 °C for 2 hr. Solvent was removed in vacuo, and the residue was taken up in pentane (20 mL). The supernatant was removed, and the solid residue was dried in vacuo to afford 60.5 mg of the title complex (87% yield) as a black-blue solid. ^{1}H NMR (400 MHz, $PhCD_3$-d_8, 23°C) δ (ppm): 1.84 (t, *J* = 5.0 Hz, 4H), 1.45 (br, 24H). ^{31}P{^{1}H} NMR (121.5 MHz, CD_2Cl_2-d_2, 23 °C) δ (ppm): 195.55 (s, 4P). Crystals suitable for single-crystal diffraction analysis were obtained from a THF solution layered with pentane at −30 °C.

$Ni_2(\mu\text{-}H)Cl_2(dmpm)_3$ (34). To a suspension of **$Ni_2Cl_4(dmpm)_2$** (80.0 mg, 0.151 mmol, 1.0 equiv) in 4 mL $PhCH_3$ was added a solution of Bu_3SnH (175 mg, 0.602 mmol, 4.0 equiv) in 2 mL of $PhCH_3$. The resulting suspension was stirred at 23 ^oC for 17 hr in the dark. The volatiles were then removed on a vacuo, and the residue was washed with pentane. The remaining solids were extracted with benzene and filtered. The solvents were removed under vacuo to afford 26.3 mg of the title complex (30% yield) as a violet solids. Crystals suitable for single-crystal diffraction analysis were obtained from a THF solution layered with pentane at −30 ^oC.

$Ni_2Br(dmpm)_3(PPh_3)$ (35). A suspension of **$Ni_2Br_2(dmpm)_3$** (50.0 mg, 0.073 mmol, 1.0 equiv) in 2 mL of THF was combined with a solution of PPh_3 (19.1 mg, 0.073 mmol, 1.0 equiv) in 2 mL of THF. The resulting mixture was added to a solution of $CoCp^*_2$ (24.0 mg, 0.073 mmol, 1.0 equiv) in 2 mL THF. A yellow solid formed immediately, and the mixture was stirred for 2 hr, at which time the precipitate was removed by filtration through glass fiber. The green solution was concentrated to dryness, and the resulting yellow solid was suspended in 6 mL of pentane at –30 °C overnight. The supernatant was decanted, and 22.2 mg of the tile complex was isolated as a light yellow crystalline solid (35% yield). Crystals suitable for single-crystal diffraction analysis were obtained from a pentane solution at −30 ^oC.

4.16.2 Physical Measurements

NMR spectra were recorded on a Varian Mercury 400 NMR spectrometer at the Harvard University Department of Chemistry and Chemical Biology Laukien-Purcell Instrumentation Center. ^1H spectra were internally referenced to the residual solvent signal (δ = 1.72 and 3.58 for THF in THF-d_8),[88] while $^{31}P\{^1H\}$ and ^{19}F NMR spectra were externally referenced to 85% H_3PO_4 and 1:1 solution of $CFCl_3$ and $CDCl_3$ respectively. EPR spectra were recorded on a

Bruker ELEXIS E-580 spectrometer equipped with a Bruker ER4122 SHQE-W1 resonator and an Oxford Instruments ESR 900 cryostat. UV–vis absorption spectra were acquired at 293 K in quartz cuvettes using a Cary 5000 spectrometer (Agilent) and were blanked against the appropriate solvent. Steady-state photochemical reactions were performed using a 1000 W high-pressure Hg/Xe arc lamp (Oriel). The beam was passed through a water-jacketed filter holder containing the appropriate long pass filter then through an iris and collimating lens before entering the sample, which was in a quartz cuvette placed in a water-jacketed sample holder to maintain a constant temperature. IR spectra were recorded on a PerkinElmer Spectrum 400 FT-IR/FT-FIR Spectrometer outfitted with a Pike Technologies GladiATR attenuated total reflectance accessory with a monolithic diamond crystal stage and pressure clamp. Samples were suspended in Nujol for all IR measurements. Evolved hydrogen was determined by gas chromatography using a calibration curve derived from adding HCl to known quantities of NaH; over the relevant concentration range, the gas chromatograph response was linear.

X-ray Crystallographic Details. X-ray structures of complexes and variable-temperature (VT) X-ray data were collected on a Bruker three-circle platform goniometer equipped with an Apex II CCD and an Oxford cryostream cooling device operating between 100-300 K. Radiation was from a graphite fine focus sealed tube Mo Kα (0.71073 Å) source. Crystals were mounted on a glass fiber pin using Paratone N oil. Data was collected as a series of φ and/or ω scans. Data was integrated using SAINT and scaled with multi-scan absorption correction using SADABS.[89] The structures were solved by intrinsic phasing using SHELXT (Apex3 program suite v2016.1.0) and refined against F^2 on all data by full matrix least squares with SHELXL-97.[90] All non-hydrogen atoms were refined anisotropically. H atoms were placed at idealized positions and refined using a riding model.

Photocrystallography data was collected using 0.41328 Å radiation at temperature of 20 K (Oxford Diffraction Helijet) on a vertical mounted Bruker D8 three-circle platform goniometer equipped with an Apex II CCD at ChemMatCARS located at Advances Photon Source (APS), Argonne National Laboratory (ANL). Illumination was provided by a Thor Labs 300 nm LED (M300F2) and was delivered to the sample via a 200 μm ID fiber optic. Dark structures were solved and refined as described above. For data sets obtained during irradiation, non-H atoms of the product were located in difference-Fourier maps, calculated with coefficients F_0(irradiated)–F_0(dark), and then refined with restraints on the product molecule's bond lengths and constraints of the atomic displacement parameters to the corresponding values of the reactant molecule (SADI and EADP instructions of SHELXL97). The percentage of the reactant in the crystal was treated as a variable in the refinements.

Computational Details. All DFT calculations were carried out using Gaussian 09, revision A.01,[91] software installed on the Blues cluster at Argonne National Laboratory. Geometry optimizations were carried out using the spin unrestricted B3LYP functional[92] in combination with a 6-311G(d) basis set for Ni and all ligated atoms and a 6-31G(d) basis set for all other atoms.[93,94,95,96] The broken symmetry formalism was used for antiferromagnetically coupled Ni(I,I) states.[97,98] Frequency calculations were carried out to ensure structures represented energetic minima. Single point energy calculations were also carried out using the B3LYP functional and a split basis set (6-311+G(d) for Ni and all ligated atoms and a 6-31G(d) basis set for all other atoms). Orbital surfaces were generated using the β-LUMO program[99] and TDDFT calculations were visualized using the SWizard program (revision 4.6) using band-shapes with half-widths of 3000 cm^{-1}.[100,101] Solvation (THF) was included in single point calculations using the polarized continuum model (PCM).

4.16.3 NMR data

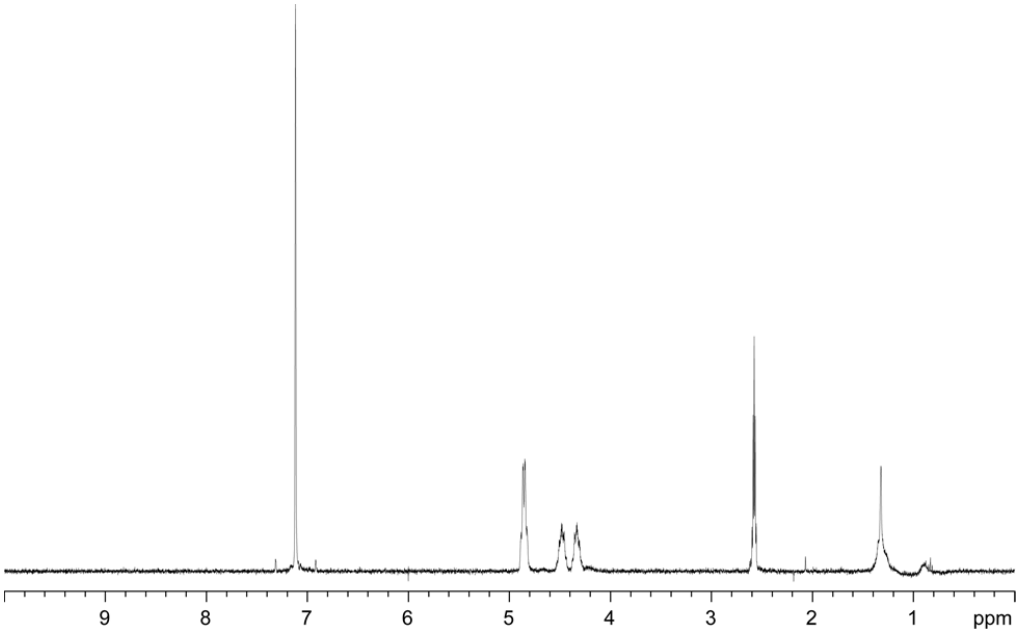

Figure 4.55. ^{1}H NMR spectrum of *trans*-$Rh_2(CO)_2Cl_4(tfepma)_2$ (*trans*) recorded in C_6D_6 at 23 °C.

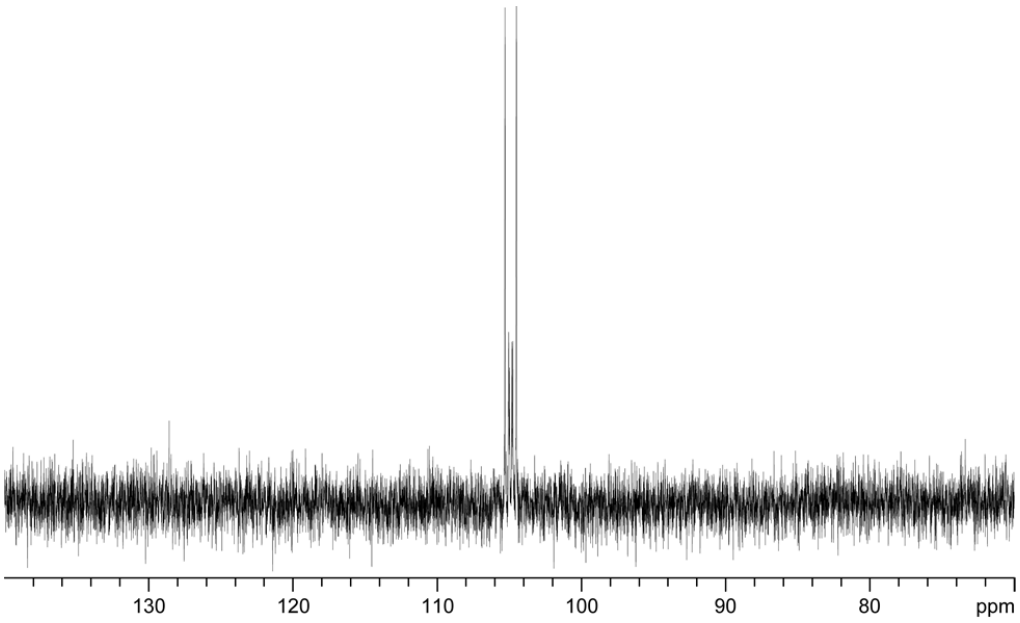

Figure 4.56. ^{31}P NMR spectrum of *trans*-$Rh_2(CO)_2Cl_2(tfepma)_2$ (*trans*) recorded in C_6D_6 at 23 °C.

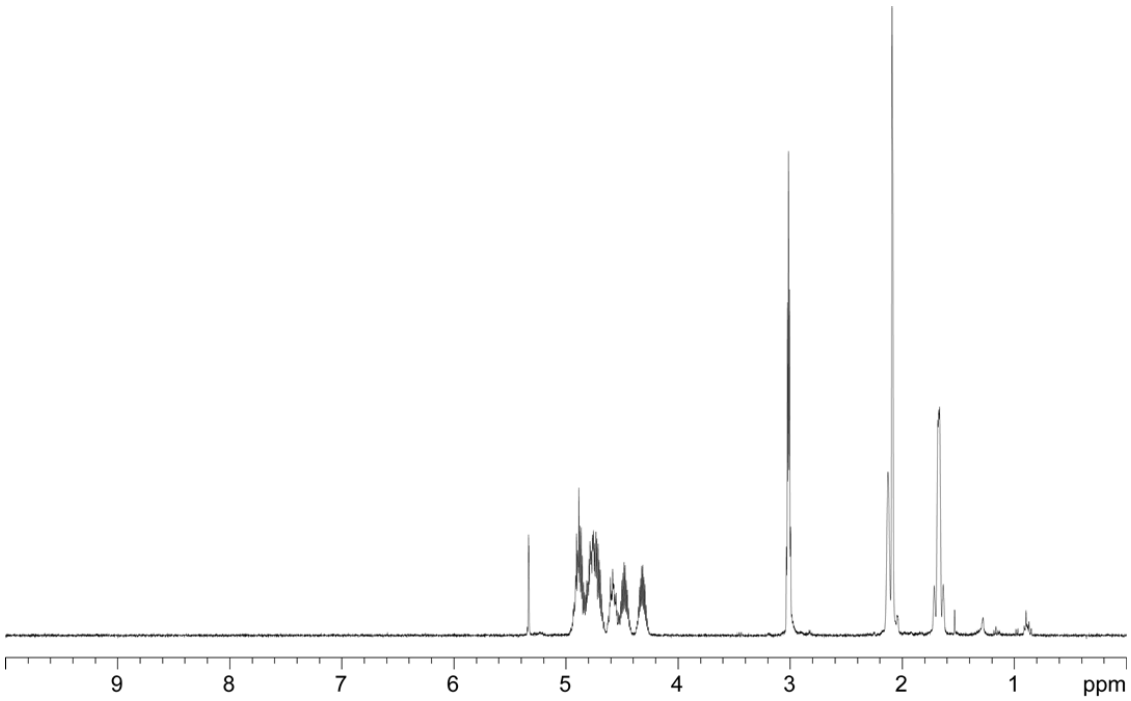

Figure 4.57. ^{1}H NMR spectrum of $Rh_2(AdNC)(tfepma)_2(\mu\text{-}Cl)Cl_3$ (**3**) recorded in CD_2Cl_2 at 23 °C.

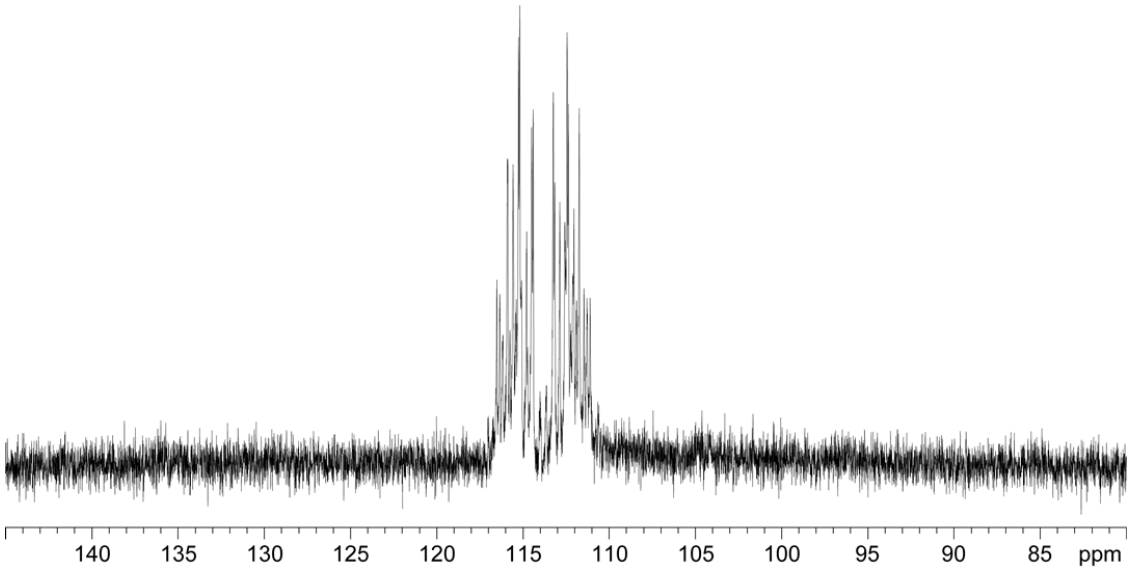

Figure 4.58. ^{31}P NMR spectrum of $Rh_2(AdNC)(tfepma)_2(\mu\text{-}Cl)Cl_3$ (**3**) recorded in CD_2Cl_2 at 23 °C.

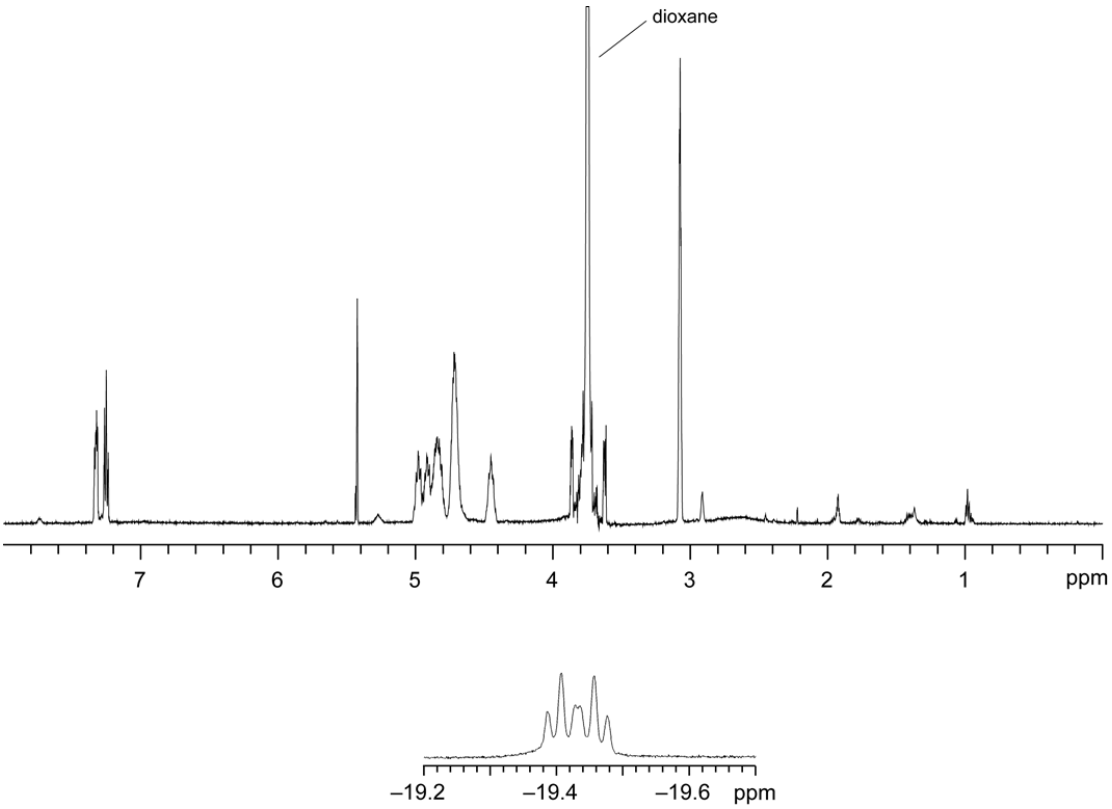

Figure 4.59. ^{1}H NMR spectrum of complex **8** recorded in CD_2Cl_2 at 23 °C. The spectrum was recorded in the presence of excess HCl·dioxane because removal of solvent and redissolution of the residue led to the observation of a mixture of hydride **8** and Rh_2[I,I] complex **6**.

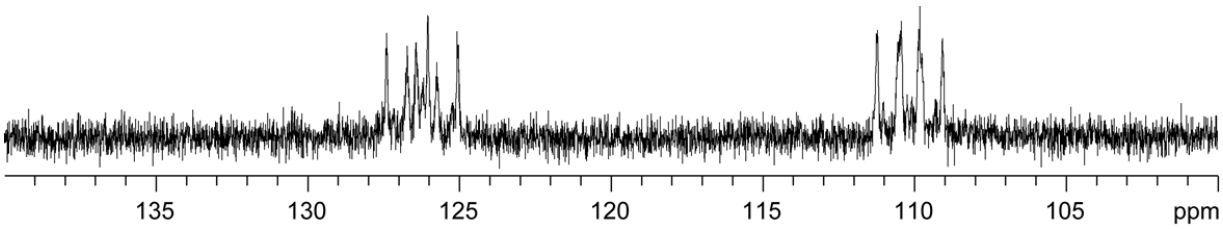

Figure 4.60. ^{31}P NMR spectrum of complex **8** recorded in CD_2Cl_2 at 23 °C. The spectrum was recorded in the presence of excess HCl·dioxane because removal of solvent and re-dissolution of the residue led to the observation of a mixture of hydride **8** and Rh_2[I,I] complex **6**.

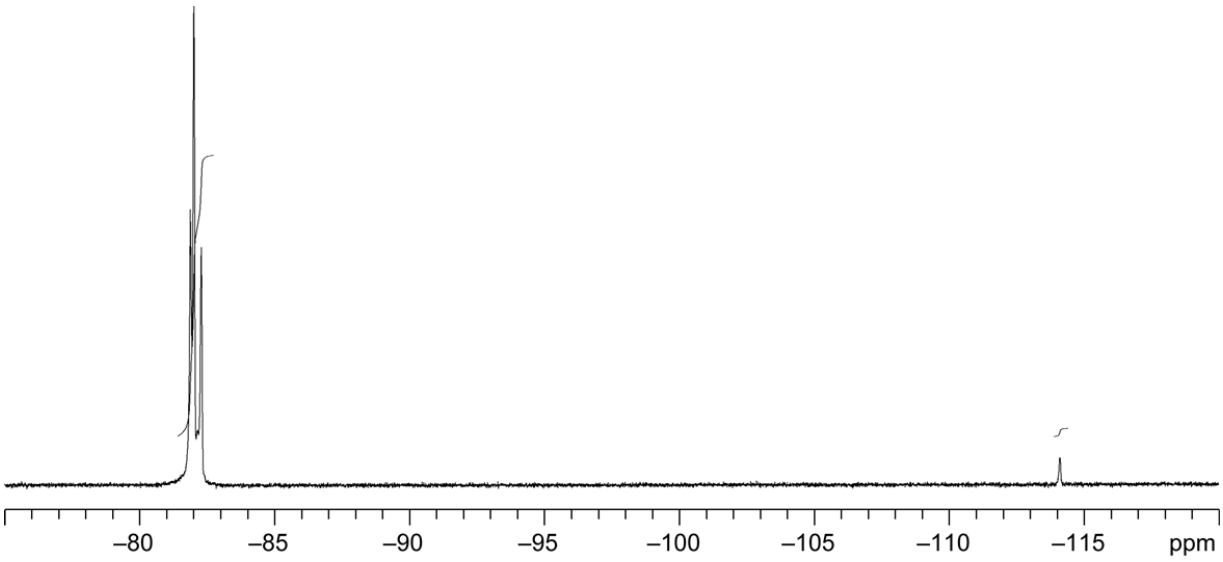

Figure 4.61. ^{19}F NMR spectrum of complex **8** recorded in CD_2Cl_2 at 23 °C. The spectrum was recorded in the presence of excess HCl·dioxane because removal of solvent and re-dissolution of the residue led to the observation of a mixture of hydride **8** and Rh_2[I,I] complex **6**.

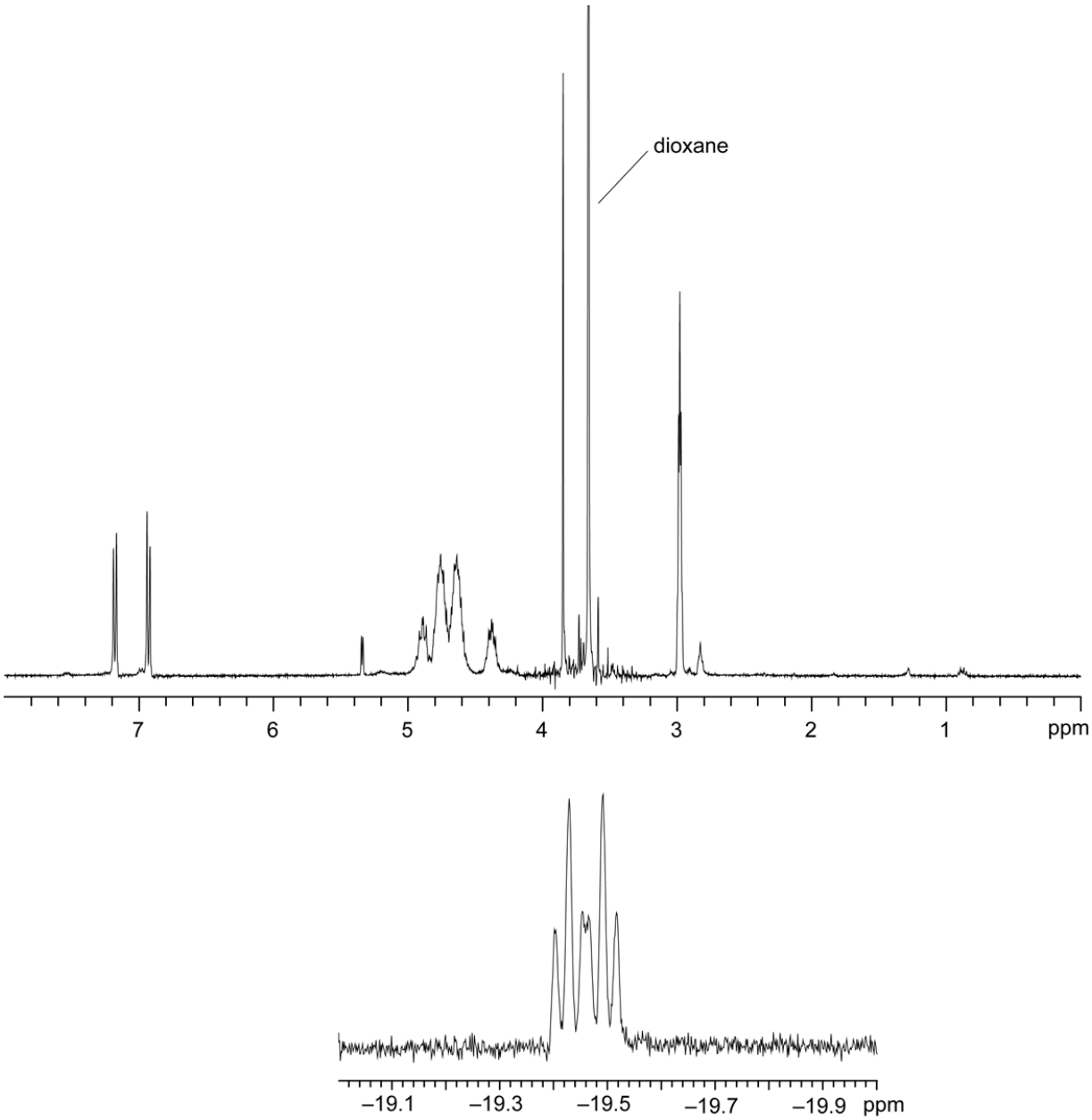

Figure 4.62. ^{1}H NMR spectrum of complex **11** recorded in CD_2Cl_2 at 23 °C. The spectrum was recorded in the presence of excess HCl·dioxane because removal of solvent and re-dissolution of the residue led to the observation of a mixture of hydride **11** and Rh_2[I,I] complex **9**.

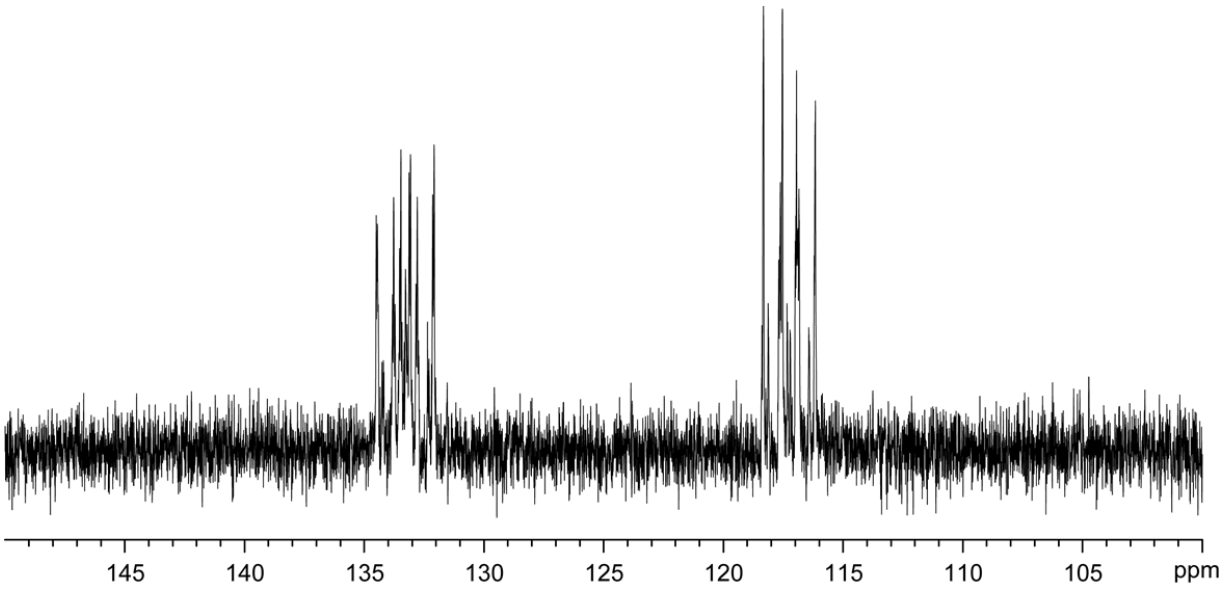

Figure 4.63. ^{31}P NMR spectrum of complex **11** recorded in CD_2Cl_2 at 23 °C. The spectrum was recorded in the presence of excess HCl·dioxane because removal of solvent and re-dissolution of the residue led to the observation of a mixture of hydride **11** and Rh_2[I,I] complex **9**.

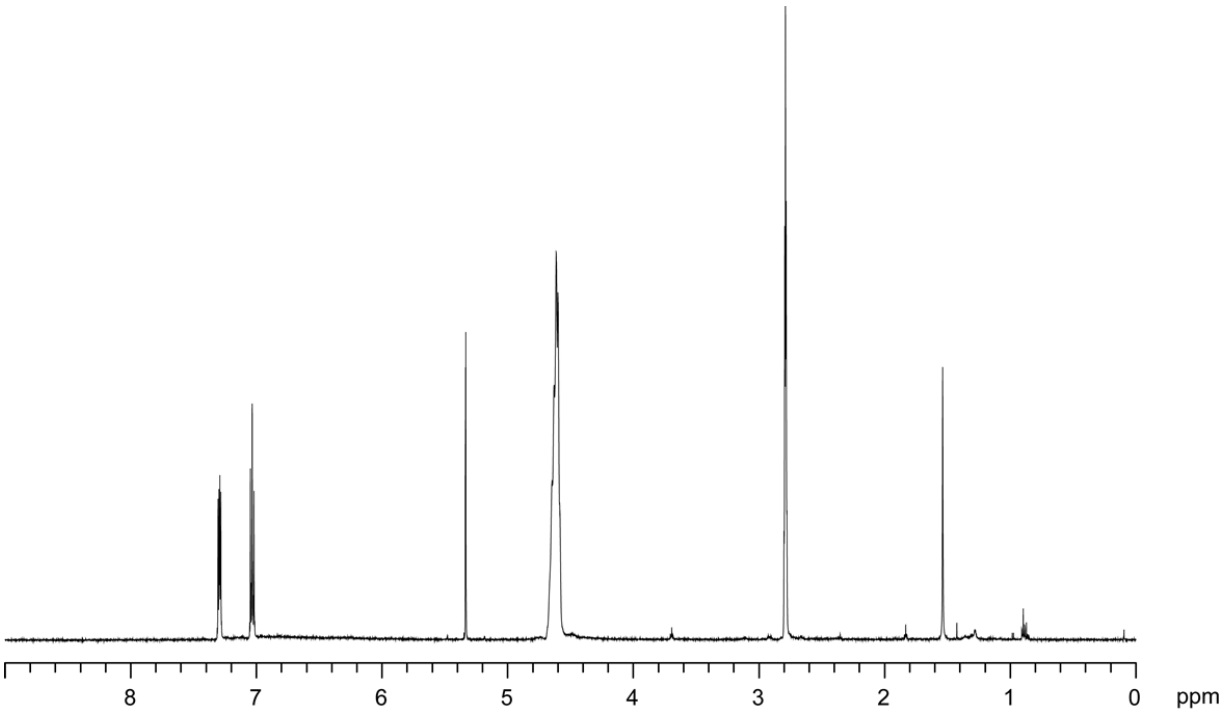

Figure 4.64. ^{1}H NMR spectrum of Rh_2[I,I] bromide complex **12** recorded in CD_2Cl_2 at 23 °C.

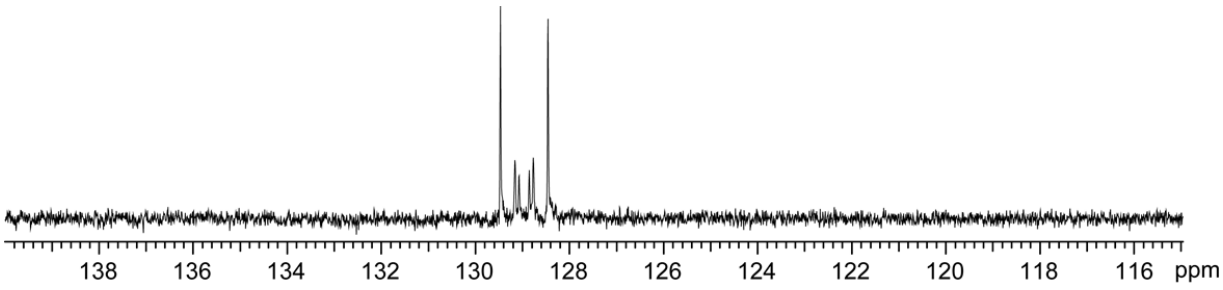

Figure 4.65. ^{31}P NMR spectrum of Rh_2[I,I] bromide complex **12** recorded in CD_2Cl_2 at 23 °C.

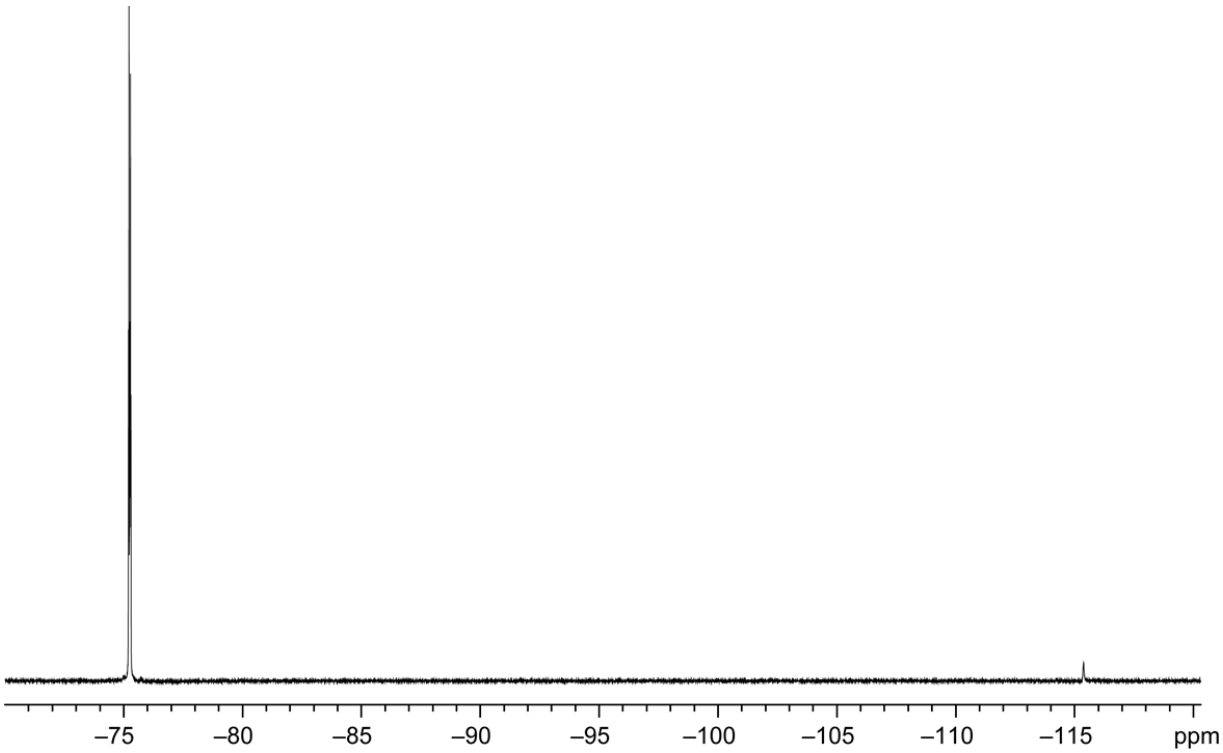

Figure 4.66. ^{19}F NMR spectrum of Rh_2[I,I] bromide complex **12** recorded in CD_2Cl_2 at 23 °C.

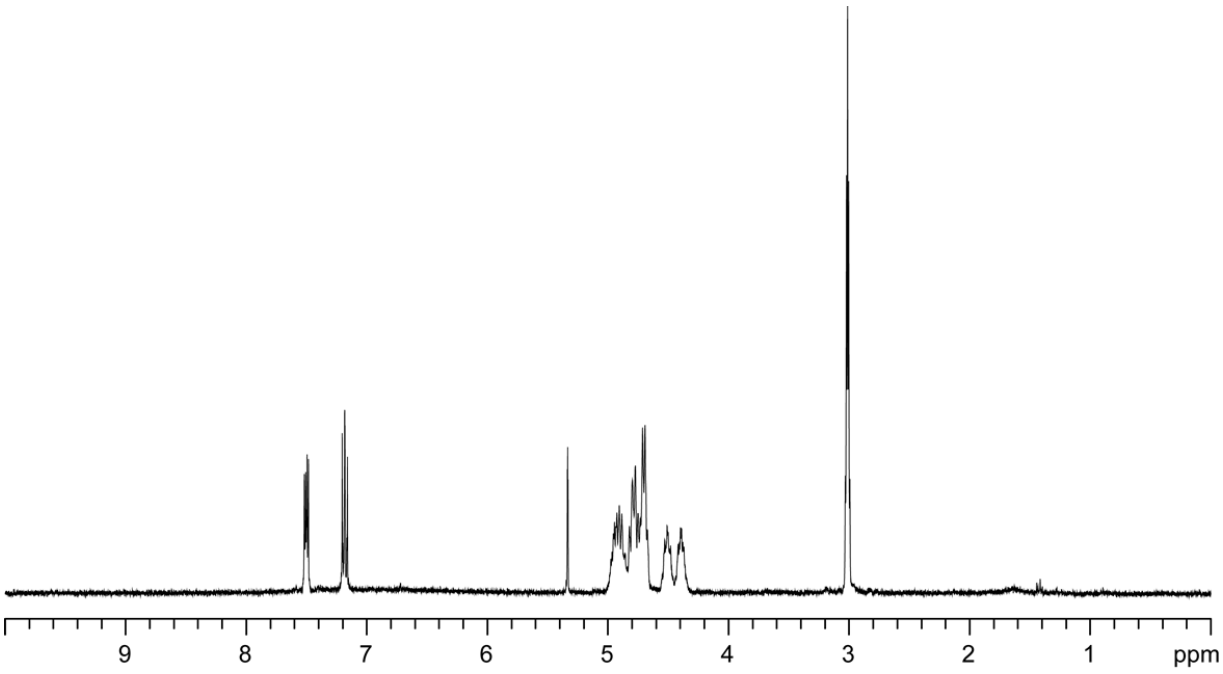

Figure 4.67. ^{1}H NMR spectrum of complex **13** recorded in CD_2Cl_2 at 23 °C.

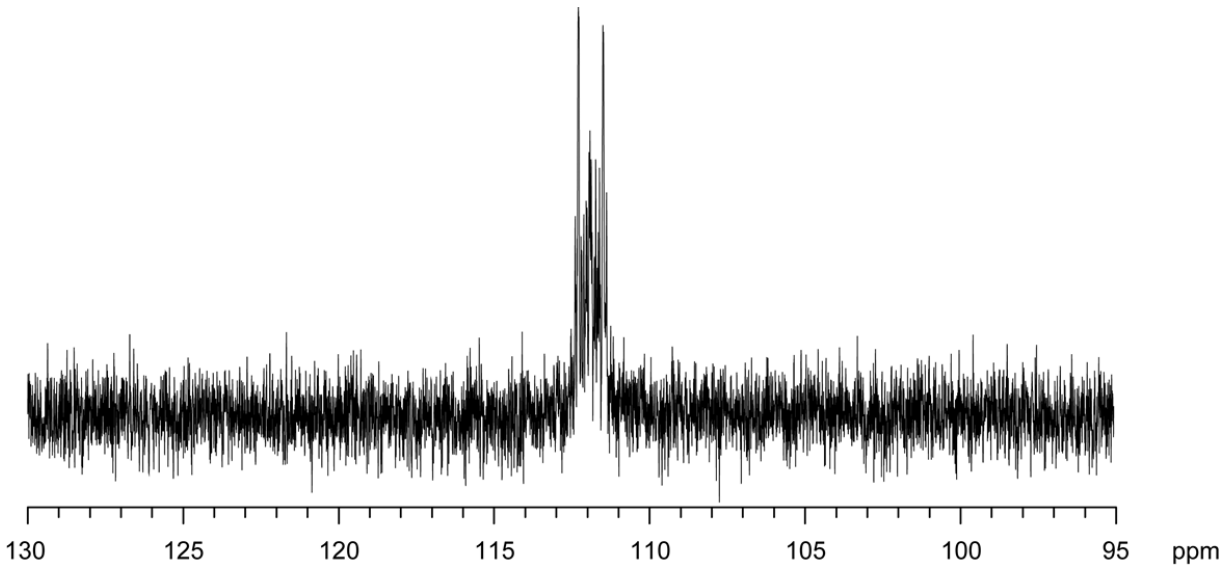

Figure 4.68. ^{31}P NMR spectrum of complex **13** recorded in CD_2Cl_2 at 23 °C.

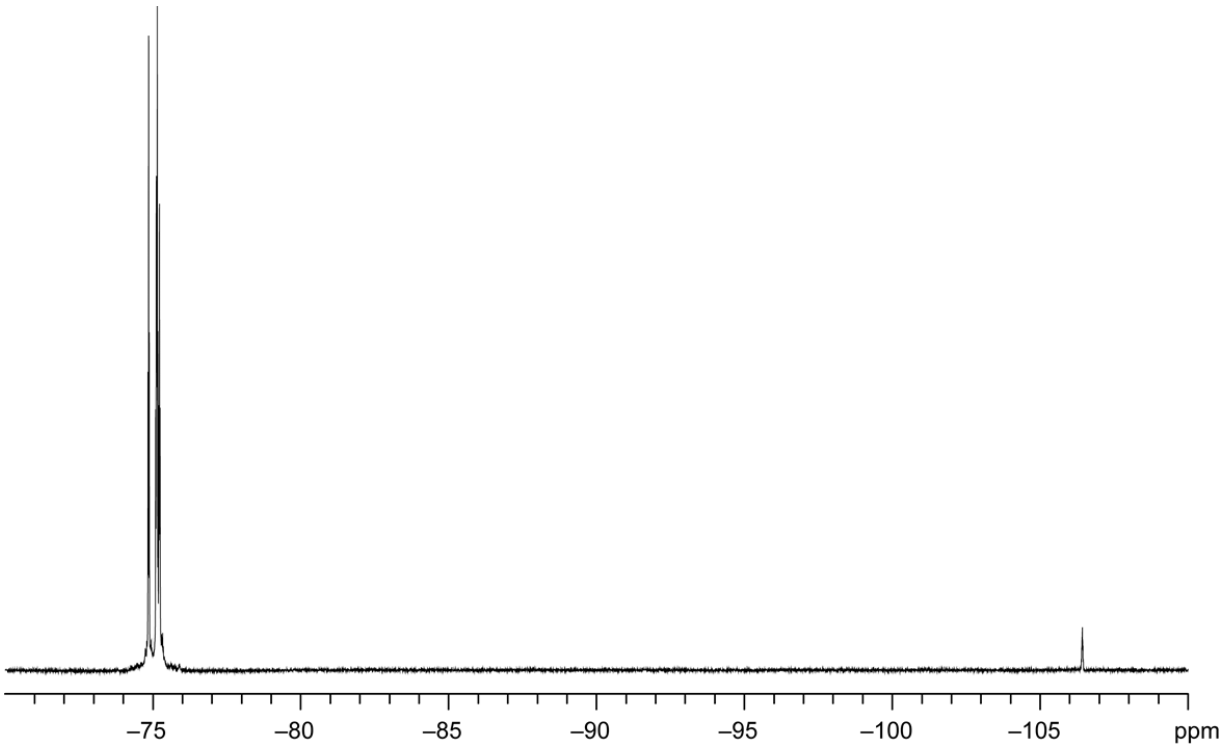

Figure 4.69. ^{19}F NMR spectrum of complex **13** recorded in CD_2Cl_2 at 23 °C.

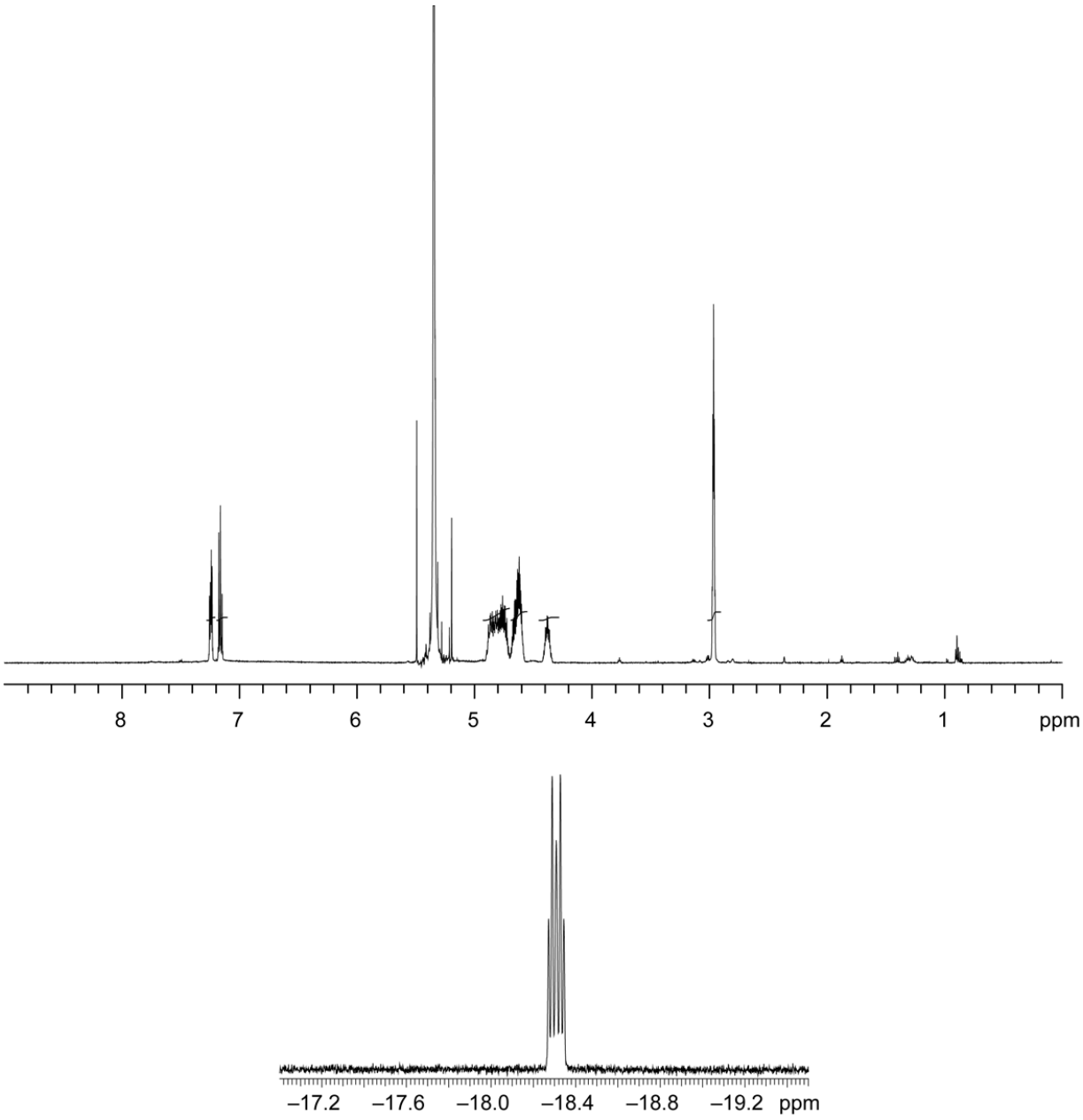

Figure 4.70. ^{1}H NMR spectrum of complex **14** recorded in CD_2Cl_2 at 23 °C. The spectrum was recorded in the presence of excess HBr in CH_2Cl_2 because removal of solvent and re-dissolution of the residue led to the observation of a mixture of hydride **14** and Rh_2[I,I] complex **12**.

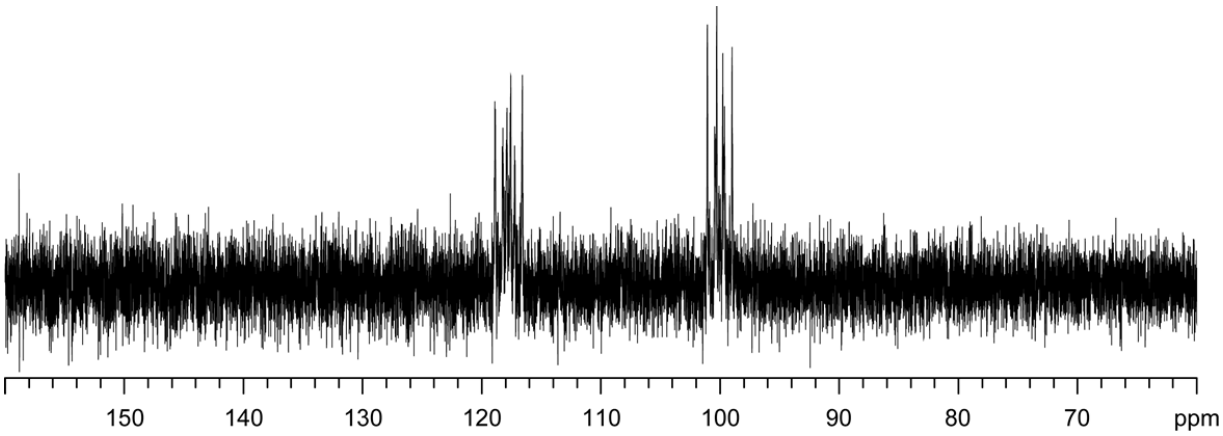

Figure 4.71. ^{31}P NMR spectrum of complex **14** recorded in CD_2Cl_2 at 23 °C. The spectrum was recorded in the presence of excess HBr in CH_2Cl_2 because removal of solvent and re-dissolution of the residue led to the observation of a mixture of hydride **14** and Rh_2[I,I] complex **12**.

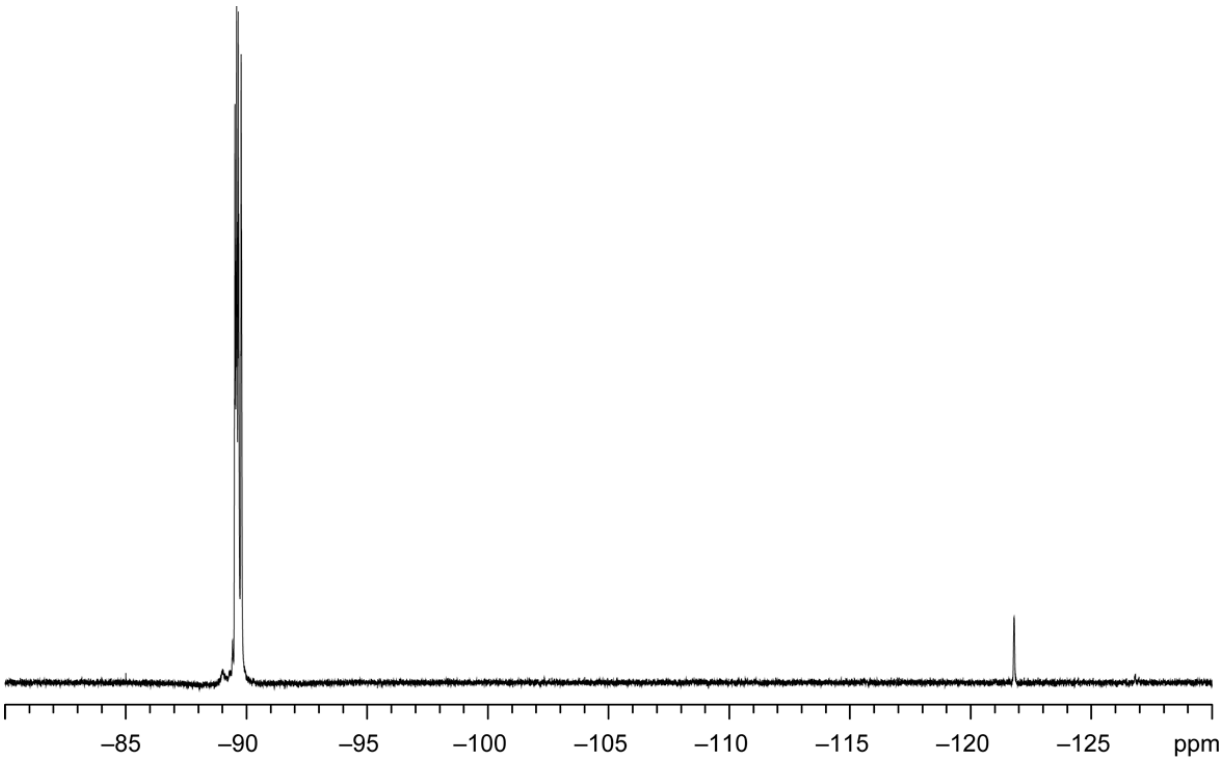

Figure 4.72. ^{19}F NMR spectrum of complex **14** recorded in CD_2Cl_2 at 23 °C. The spectrum was recorded in the presence of excess HBr in CH_2Cl_2 because removal of solvent and re-dissolution of the residue led to the observation of a mixture of hydride **14** and Rh_2[I,I] complex **12**.

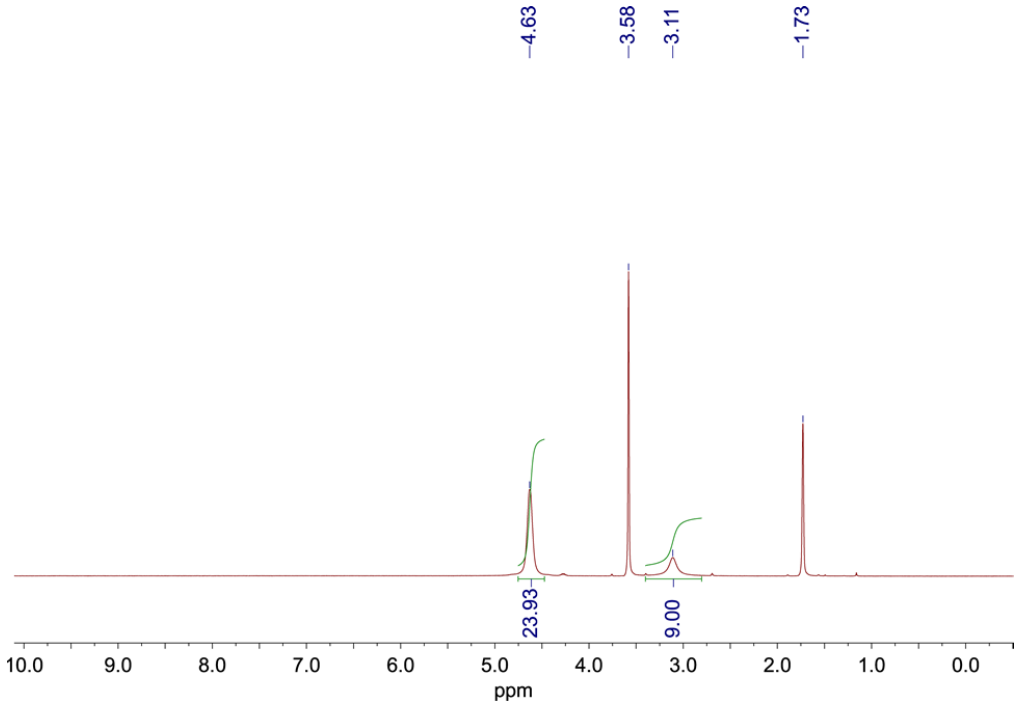

Figure 4.73. ^{1}H NMR spectrum of $Ni_2(tfepma)_3Cl_2$ (**15**) recorded in THF–d_8 at 23 °C.

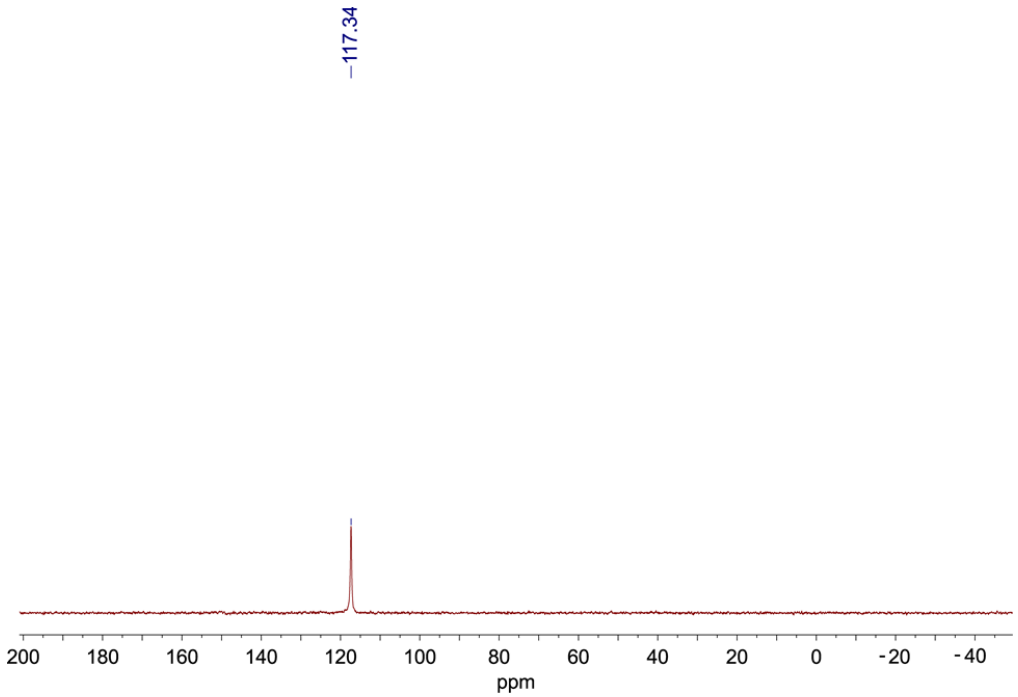

Figure 4.74. $^{31}P\{^{1}H\}$ NMR spectrum of $Ni_2(tfepma)_3Cl_2$ (**15**) recorded in THF–d_8 at 23 °C.

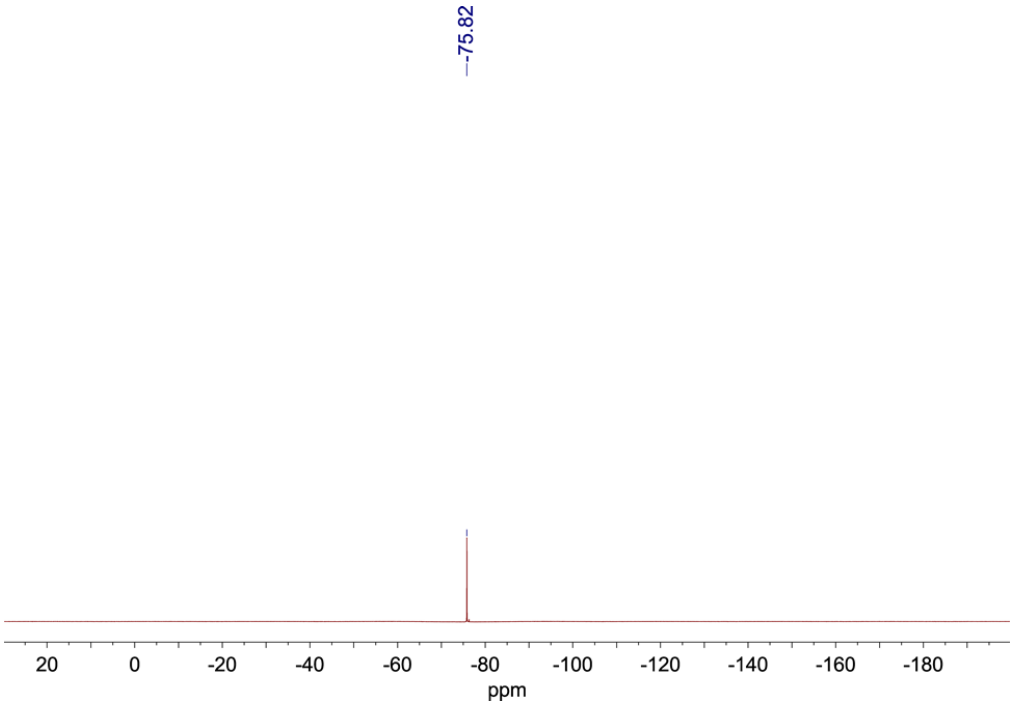

Figure 4.75. ^{19}F NMR spectrum of $Ni_2(tfepma)_3Cl_2$ (**15**) recorded in THF–d_8 at 23 °C.

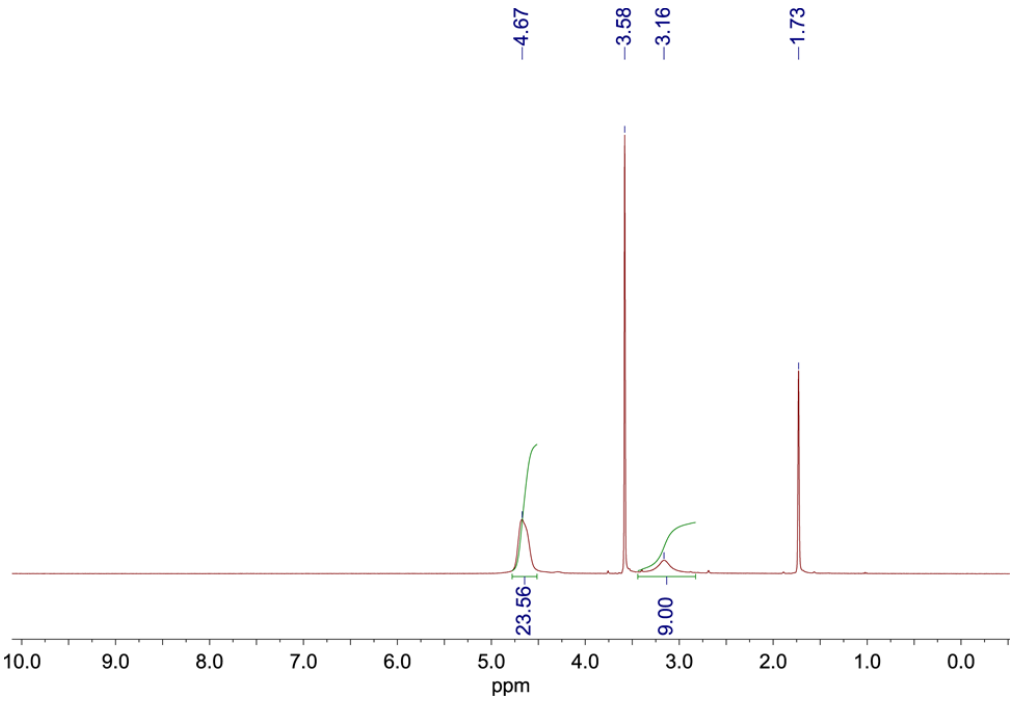

Figure 4.76. ^{1}H NMR spectrum of $Ni_2(tfepma)_3Br_2$ (**16**) recorded in THF–d_8 at 23 °C.

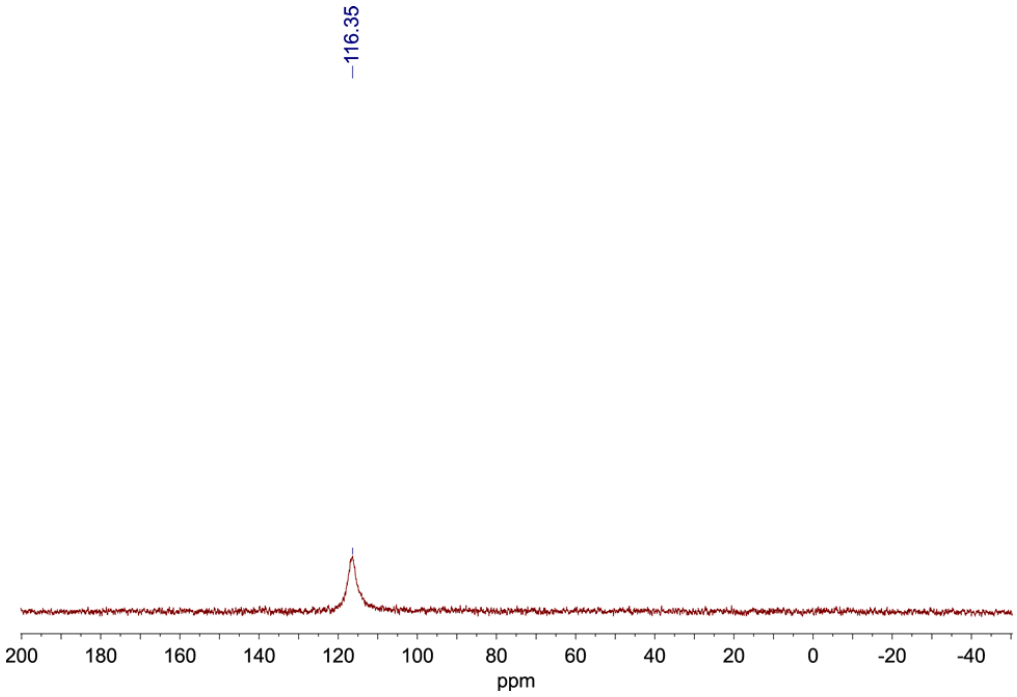

Figure 4.77. $^{31}P\{^{1}H\}$ NMR spectrum of $Ni_2(tfepma)_3Br_2$ (**16**) recorded in THF–d_8 at 23 °C.

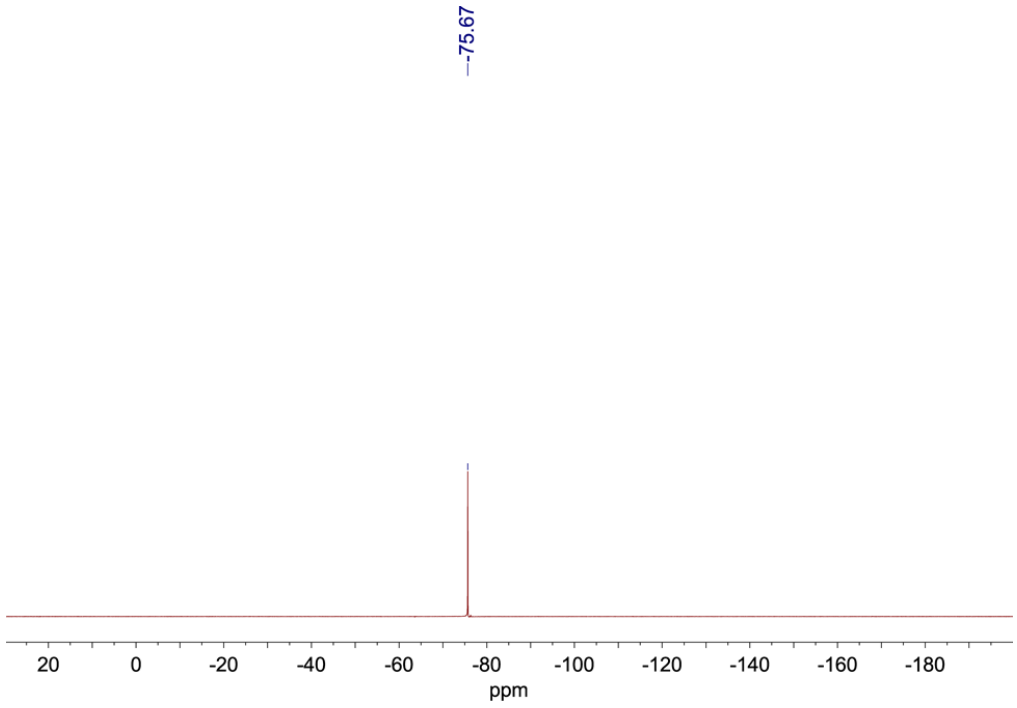

Figure 4.78. ^{19}F NMR spectrum of $Ni_2(tfepma)_3Br_2$ (**16**) recorded in THF–d_8 at 23 °C.

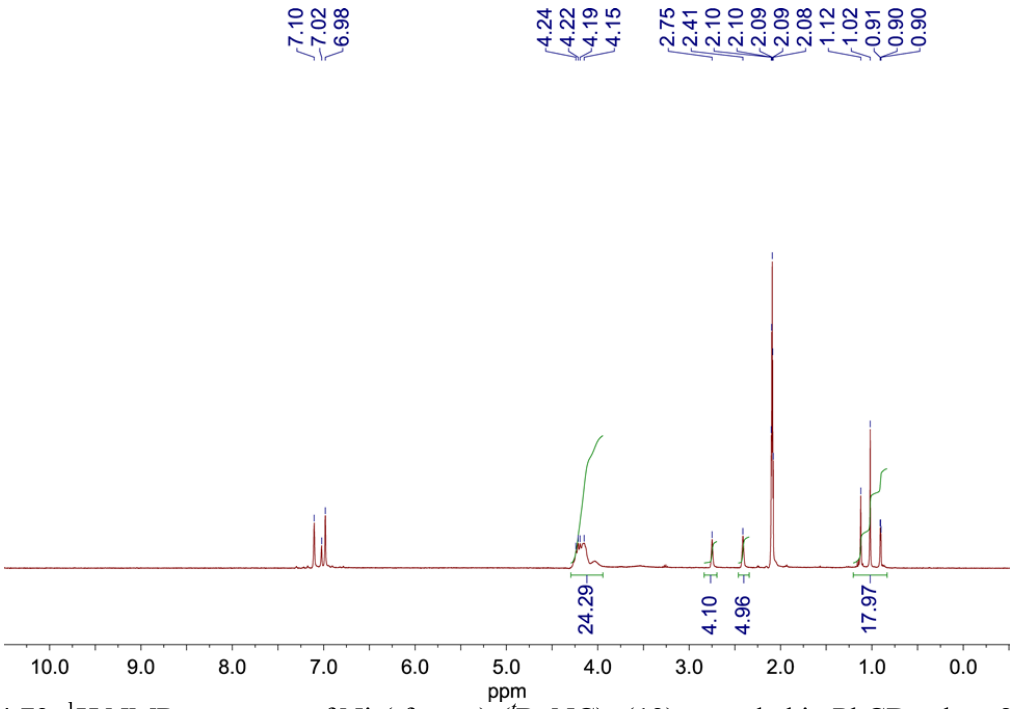

Figure 4.79. ^{1}H NMR spectrum of $Ni_2(tfepma)_2(^tBuNC)_2$ (**19**) recorded in $PhCD_3$–d_8 at 23 °C.

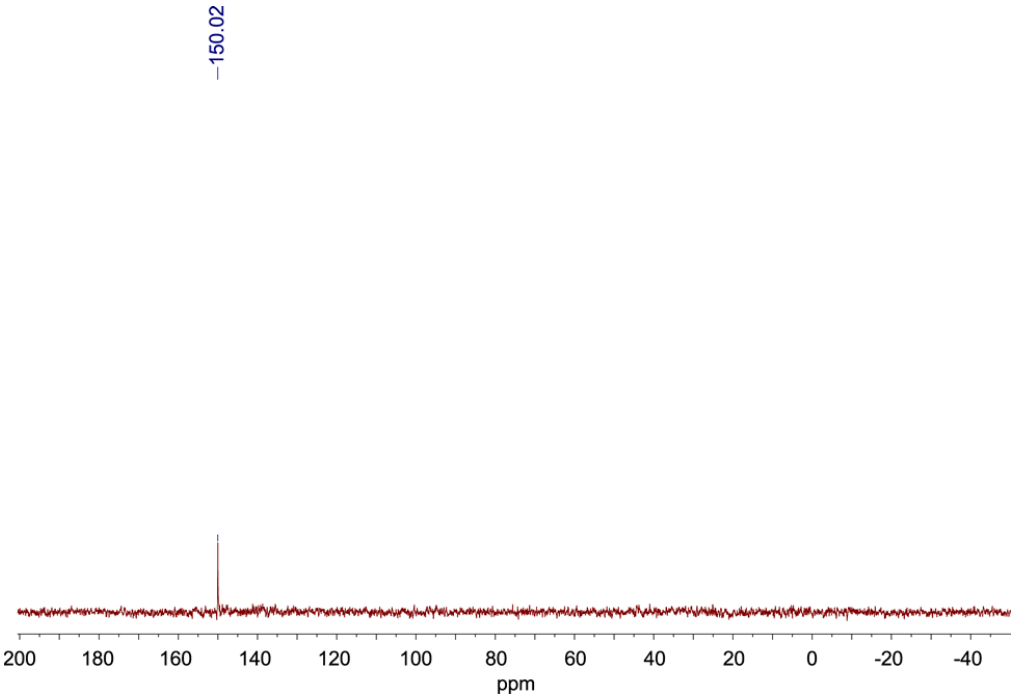

Figure 4.80. $^{31}P\{^{1}H\}$ NMR spectrum of $Ni_2(tfepma)_2(^tBuNC)_2$ (**19**) recorded in $PhCD_3$–d_8 at 23 °C.

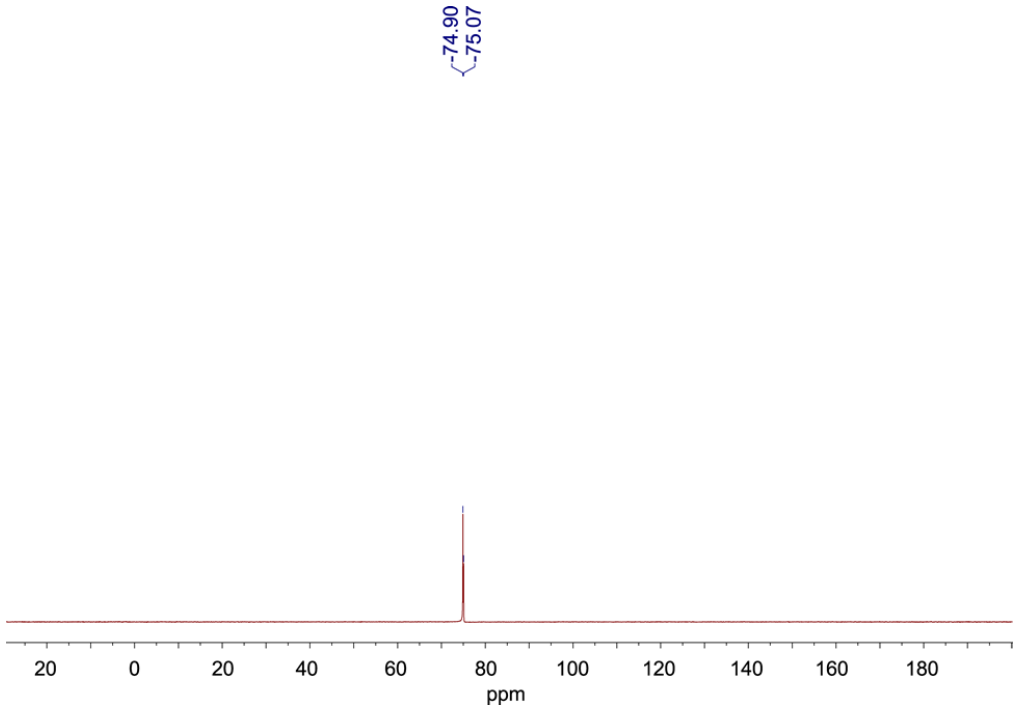

Figure 4.81. ^{19}F NMR spectrum of $Ni_2(tfepma)_2(^tBuNC)_2$ (**19**) recorded in $PhCD_3$–d_8 at 23 °C.

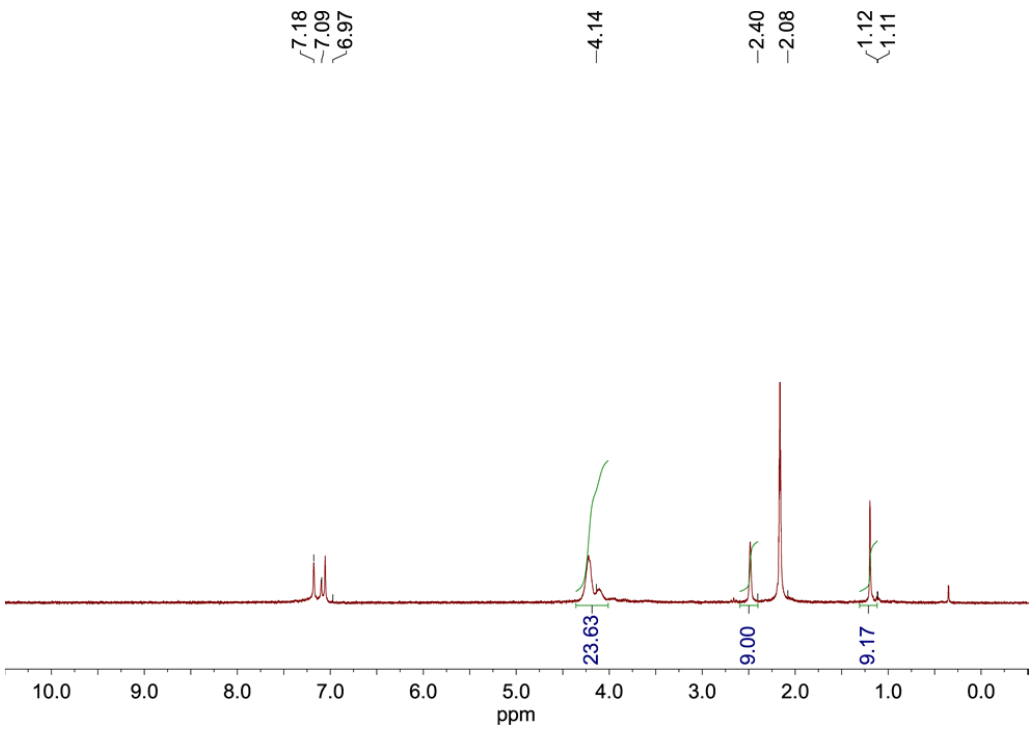

Figure 4.82. ^{1}H NMR spectrum of $Ni_2(tfepma)_3(^tBuNC)$ (**20**) recorded in $PhCD_3$–d_8 at 23 °C.

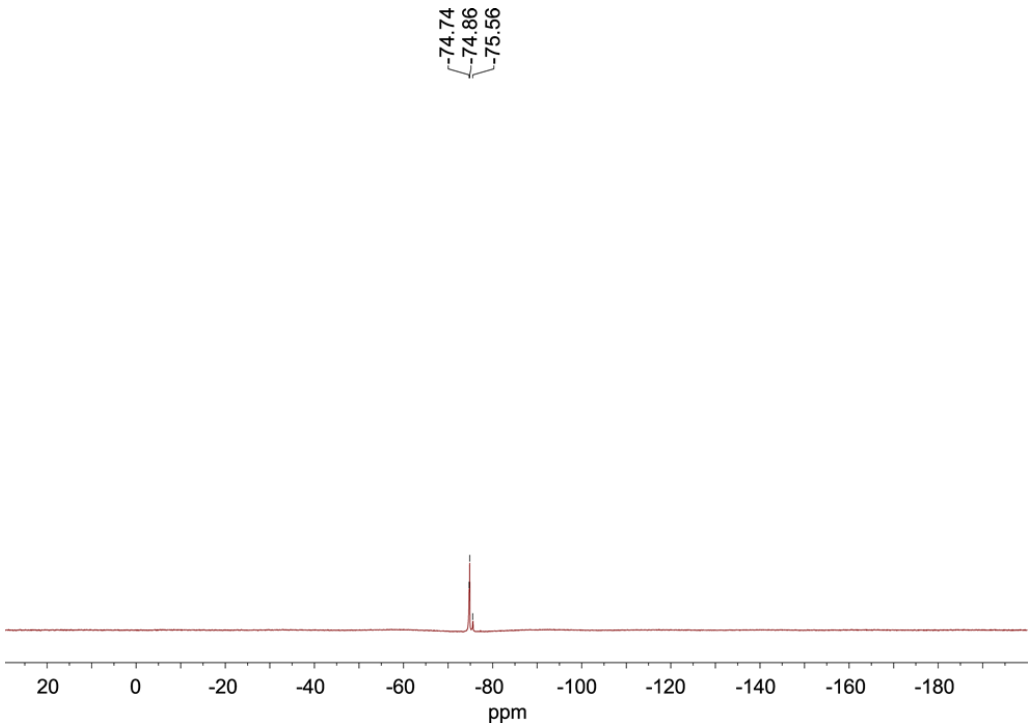

Figure 4.83. ^{19}F NMR spectrum of $Ni_2(tfepma)_3(^tBuNC)$ (**20**) recorded in $PhCD_3$–d_8 at 23 °C.

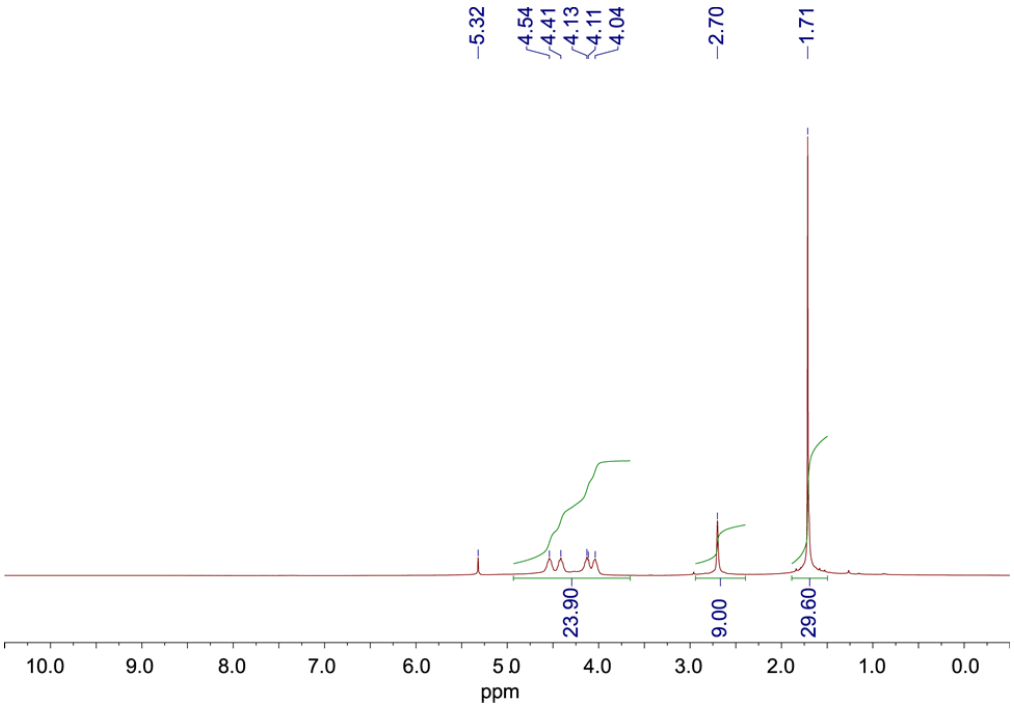

Figure 4.84. ^1H NMR spectrum of $[Ni_2(tfepma)_3Cl][CoCp_2^*]$ (**22**) recorded in CD_2Cl_2 at 23 °C.

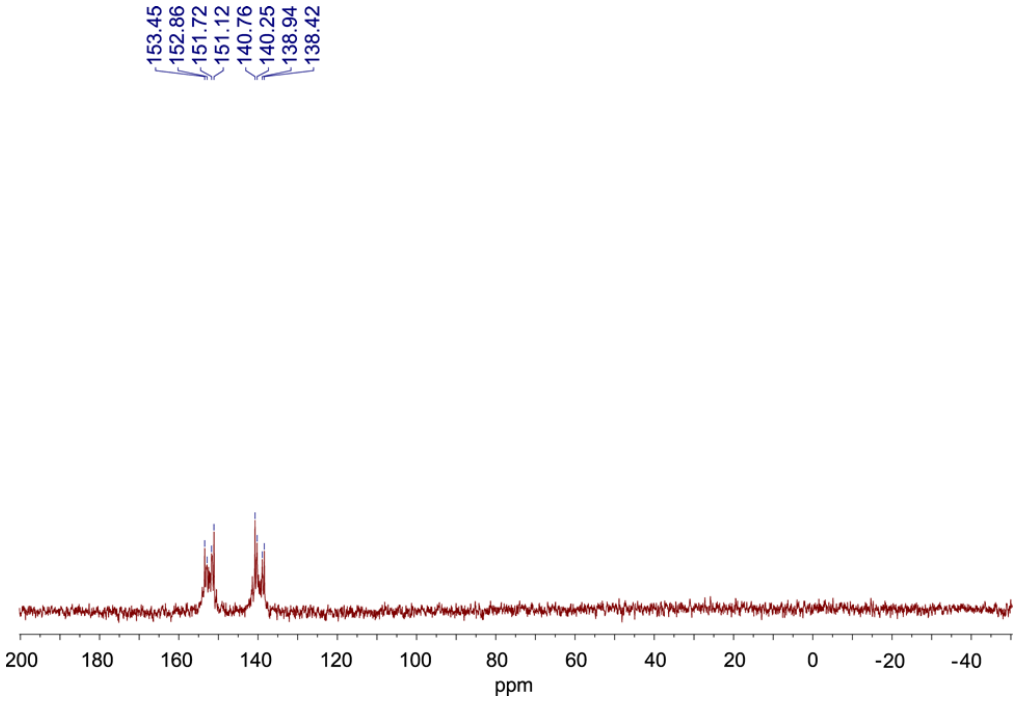

Figure 4.85. $^{31}P\{^{1}H\}$ NMR spectrum of $[Ni_2(tfepma)_3Cl][CoCp_2^*]$ (**22**) recorded in CD_2Cl_2 at 23 °C.

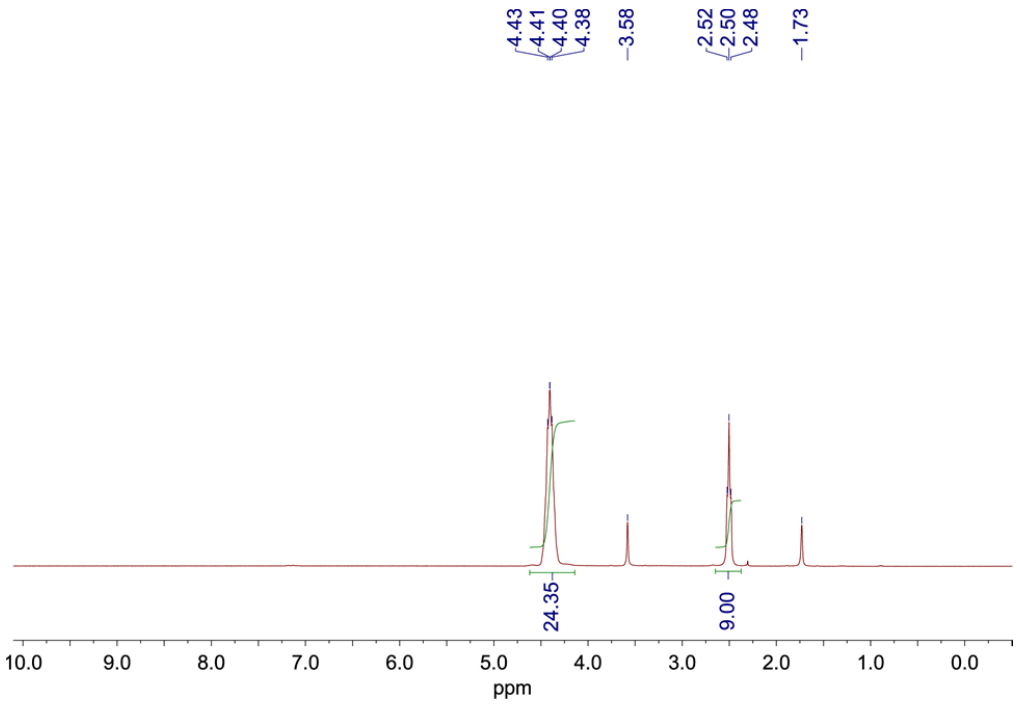

Figure 4.86. ^{1}H NMR spectrum of $Ni_2(tfepma)_2$ (**23**) recorded in THF–d_8 at 23 °C.

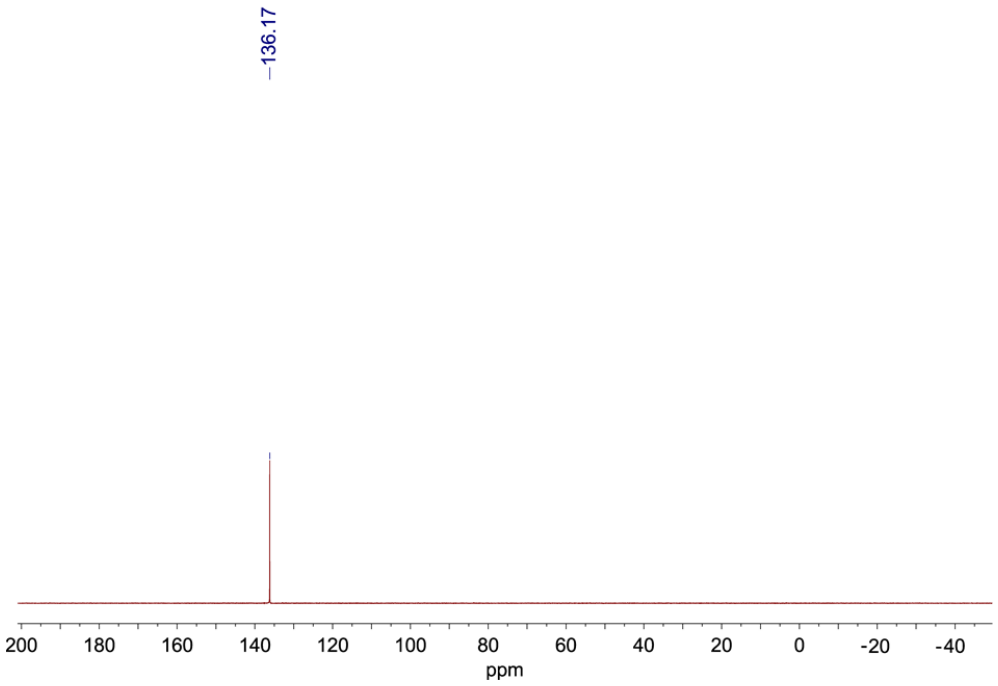

Figure 4.87. $^{31}P\{^{1}H\}$ NMR spectrum of $Ni_2(tfepma)_2$ (**23**) recorded in THF–d_8 at 23 °C.

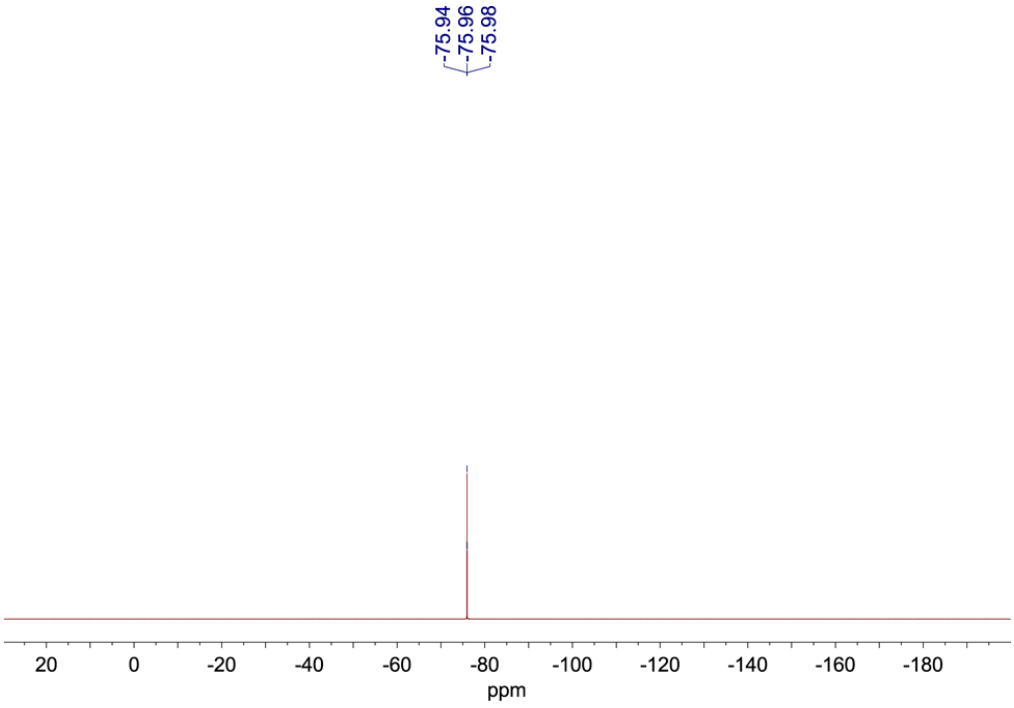

Figure 4.88. ^{19}F NMR spectrum of $Ni_2(tfepma)_2$ (**23**) recorded in THF–d_8 at 23 °C.

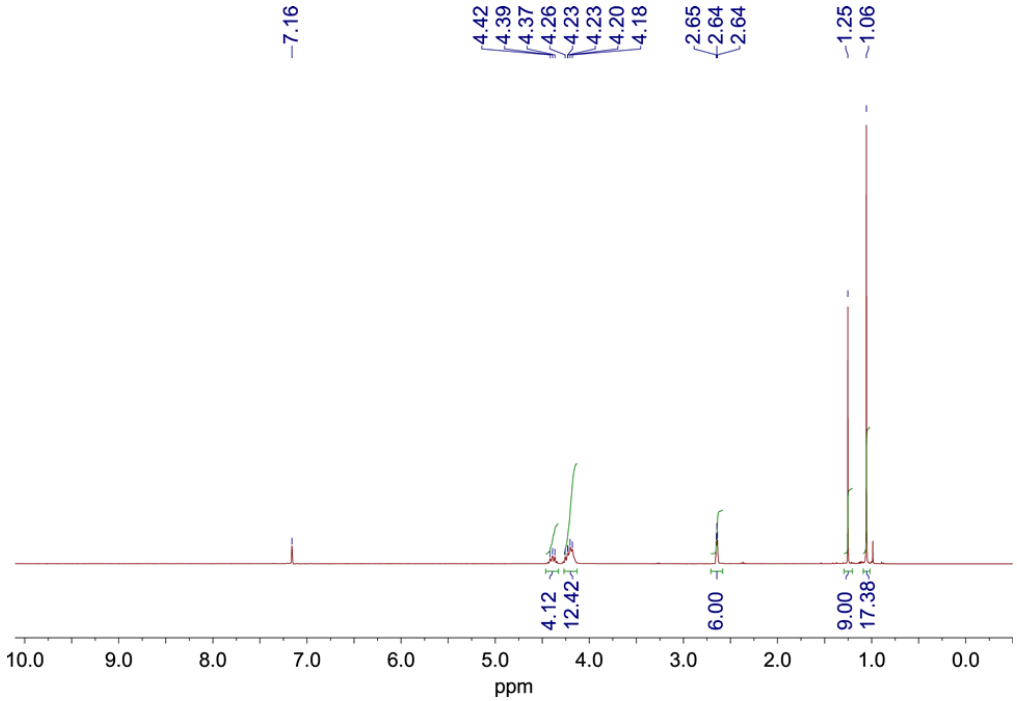

Figure 4.89. ^{1}H NMR spectrum of $Ni_2(tfepma)_2(^tBuNC)_3$ (**27**) recorded in C_6D_6–d_6 at 23 °C.

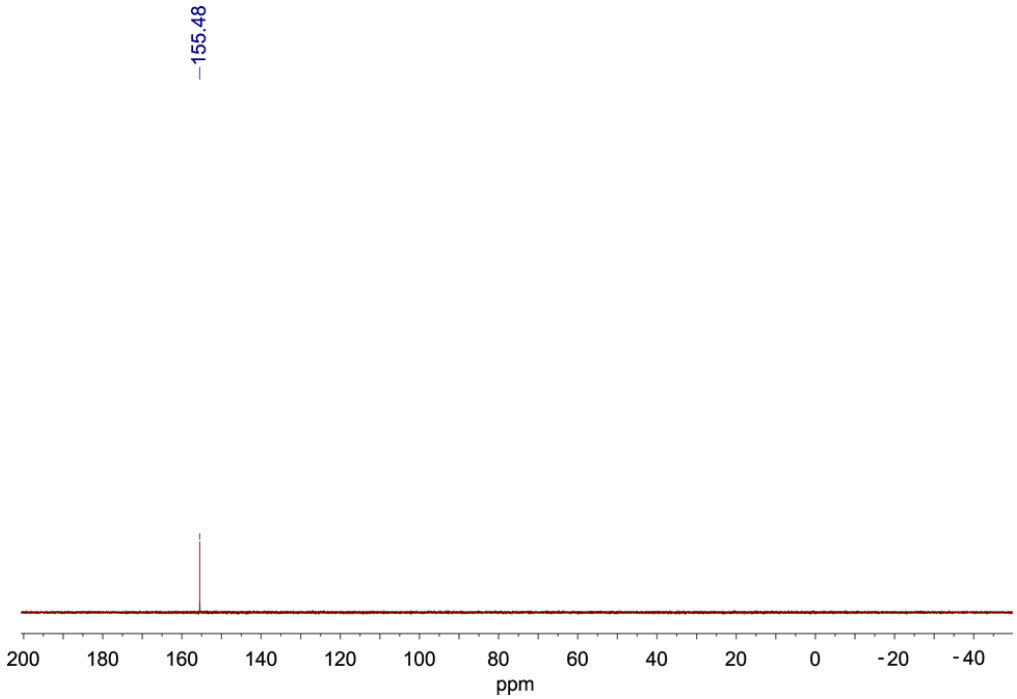

Figure 4.90. $^{31}P\{^{1}H\}$ NMR spectrum of $Ni_2(tfepma)_2(^tBuNC)_3$ (**27**) recorded in C_6D_6–d_6 at 23 °C.

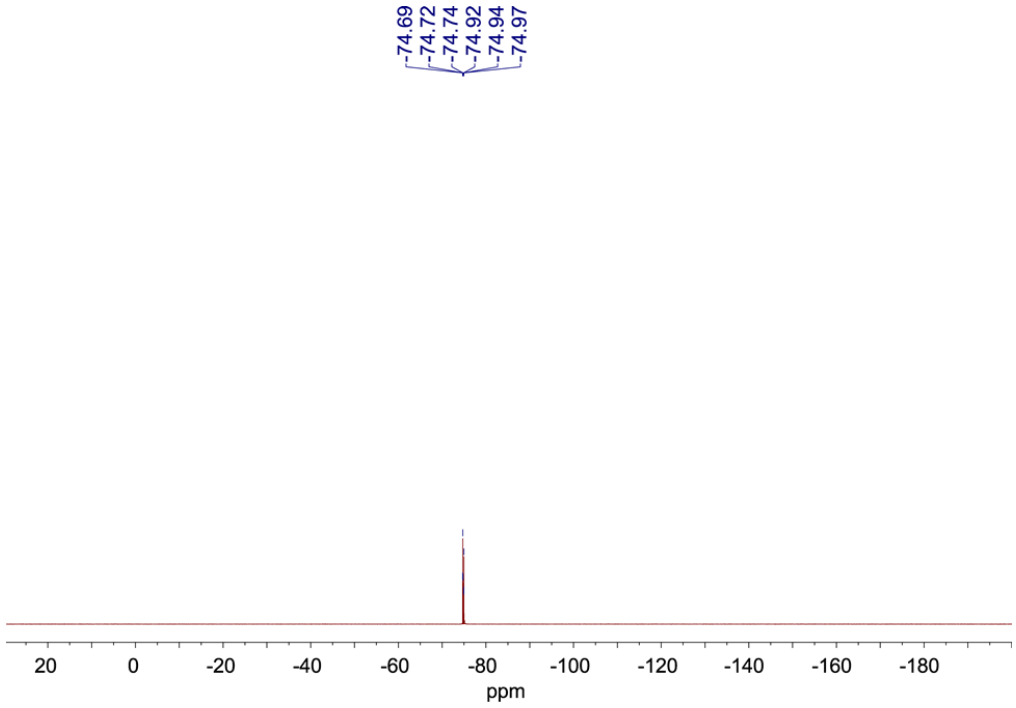

Figure 4.91. ^{19}F NMR spectrum of $Ni_2(tfepma)_2(^tBuNC)_3$ (**27**) recorded in C_6D_6–d_6 at 23 °C.

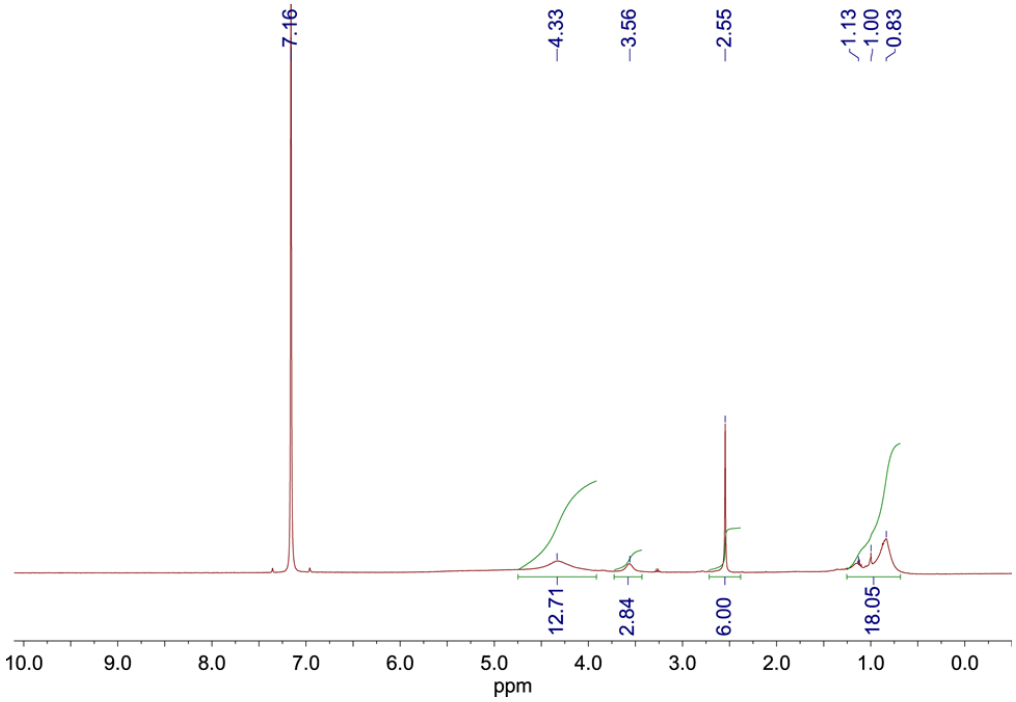

Figure 4.92. ^{1}H NMR spectrum of $Ni_2(tfepma)_2(^tBuNC)Cl_2$ (**28**) recorded in C_6D_6–d_6 at 23 °C.

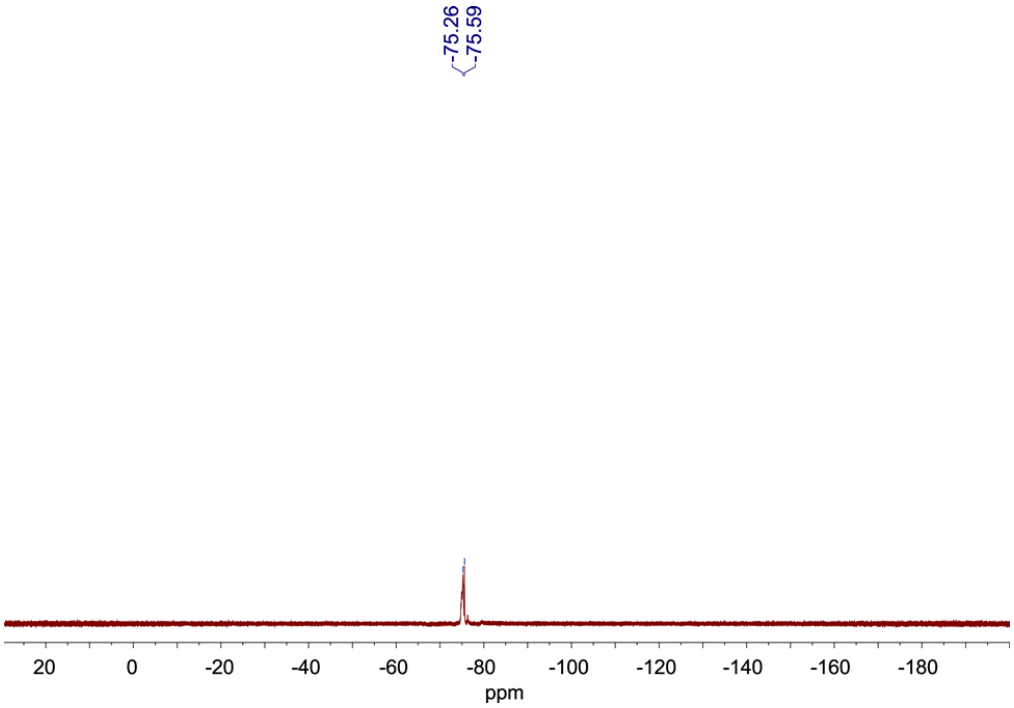

Figure 4.93. ^{19}F NMR spectrum of $Ni_2(tfepma)_2(^tBuNC)Cl_2$ (**28**) recorded in C_6D_6–d_6 at 23 °C.

4.16.4 X-Ray Data Analysis

Table 4.11. X-ray experimental details for complex **15** (CCDC 1573297).

Crystal Data	
Chemical formula	$C_{27}H_{33}Cl_2F_{36}N_3O_{12}P_6Ni_2$
Fw, g/mol	1649.70
Crystal system, space group	monoclinic, *P2(1)/n*
Temperature (K)	100(2)
a, *b*, *c* (Å)	13.3268 (6), 21.4825 (9), 19.9225 (8)
α, β, γ (°)	90, 103.407 (2), 90
V (Å^3)	5548.2 (4)
Z	4
Radiation type	Cu *Kα*
μ (mm^{-1})	5.034
Crystal size (mm)	0.09 × 0.09 × 0.09
Data collection	
Diffractometer	Bruker *APEX*-II CCD
Absorption correction	Multi-scan, *SADABS*
T_{min}, T_{max}	0.6601, 0.6714
No. of measured, independent and observed [$I > 2\sigma(I)$] reflections	72734, 9611, 7143
R_{int}	0.0771
$(\sin \theta/\lambda)_{max}$ (Å^{-1})	0.597
Refinement	
$R[F^2 > 2\sigma(F^2)]$, $wR(F^2)$, S	0.0529, 0.1197, 1.025
No. of reflections	9611
No. of parameters	752
No. of restraints	4
H-atom treatment	H atoms treated by a mixture of independent and constrained refinement
Dr_{max}, Dr_{min} (e Å^{-3})	1.302, –1.858

Table 4.12. X-ray experimental details for complex **17** (CCDC 1573296).

Crystal Data	
Chemical formula	$C_{16}H_{21}Cl_{0.5}F_{18}N_2O_6P_3Ni$
Fw, g/mol	848.69
Crystal system, space group	monoclinic, *Cc*
Temperature (K)	20(2)
a, *b*, *c* (Å)	19.5339(7), 18.5682(7), 17.0119(6)
α, β, γ (°)	90, 93.4750(10), 90
V (Å^3)	6159.0(4)
Z	8
Radiation type	synchrotron
μ (mm^{-1})	0.229
Crystal size (mm)	0.01 × 0.01 × 0.01
Data collection	
Diffractometer	Bruker *APEX*-II CCD
Absorption correction	Multi-scan, *SADABS*
T_{min}, T_{max}	0.9977, 0.9977
No. of measured, independent and observed [$I > 2\sigma(I)$] reflections	81586, 17528, 16390
R_{int}	0.0316
$(\sin \theta/\lambda)_{max}$ (Å^{-1})	0.714
Refinement	
$R[F^2 > 2\sigma(F^2)]$, $wR(F^2)$, S	0.0280, 0.0647, 1.069
No. of reflections	17528
No. of parameters	844
No. of restraints	2
H-atom treatment	H atoms treated by a mixture of independent and constrained refinement
Dr_{max}, Dr_{min} (e Å^{-3})	0.383, –0.398

Table 4.13. X-ray experimental details for complex **19** (CCDC 1573295).

Crystal Data	
Chemical formula	$C_{41}H_{59}F_{36}N_5O_{13}P_6Ni_2$
Fw, g/mol	1817.17
Crystal system, space group	monoclinic, *P2(1)/n*
Temperature (K)	100(2)
a, *b*, *c* (Å)	17.0917(6), 19.2332(7), 21.7568(8)
α, β, γ (°)	90, 98.277(2), 90
V (Å^3)	7077.6(4)
Z	4
Radiation type	Cu *Kα*
μ (mm^{-1})	3.350
Crystal size (mm)	0.34 × 0.30 × 0.10
Data collection	
Diffractometer	Bruker *APEX*-II CCD
Absorption correction	Multi-scan, *SADABS*
T_{min}, T_{max}	0.3920, 0.7306
No. of measured, independent and observed [$I > 2\sigma(I)$] reflections	12281, 12281, 9840
R_{int}	0.0603
$(\sin \theta/\lambda)_{max}$ (Å^{-1})	0.596
Refinement	
$R[F^2 > 2\sigma(F^2)]$, $wR(F^2)$, S	0.0458, 0.1314, 1.082
No. of reflections	12281
No. of parameters	939
No. of restraints	0
H-atom treatment	H atoms treated by a mixture of independent and constrained refinement
Dr_{max}, Dr_{min} (e Å^{-3})	1.006, –0.578

Table 4.14. X-ray experimental details for complex **20** (CCDC 1573294).

Crystal Data	
Chemical formula	$C_{32}H_{42}F_{36}N_4O_{12}P_6Ni_2$
Fw, g/mol	1661.94
Crystal system, space group	monoclinic, *P2(1)/n*
Temperature (K)	100(2)
a, *b*, *c* (Å)	12.7662(8), 24.7569(16), 18.8199(12)
α, β, γ (°)	90, 96.566(2), 90
V (Å^3)	5909.0(7)
Z	4
Radiation type	synchrotron
μ (mm^{-1})	0.229
Crystal size (mm)	0.02 × 0.01 × 0.01
Data collection	
Diffractometer	Bruker *APEX*-II CCD
Absorption correction	Multi-scan, *SADABS*
T_{min}, T_{max}	0.9954, 0.9977
No. of measured, independent and observed [$I > 2\sigma(I)$] reflections	10570, 10570, 8965
R_{int}	0.0659
$(\sin \theta/\lambda)_{max}$ (Å^{-1})	0.598
Refinement	
$R[F^2 > 2\sigma(F^2)]$, $wR(F^2)$, S	0.0574, 0.1438, 1.128
No. of reflections	10570
No. of parameters	849
No. of restraints	10
H-atom treatment	H atoms treated by a mixture of independent and constrained refinement
Dr_{max}, Dr_{min} (e Å^{-3})	0.985, –1.164

Table 4.15. X-ray experimental details for complex **21** (CCDC 1573292).

Crystal Data	
Chemical formula	$C_{47}H_{63}Cl_2CoF_{36}N_3Ni_2P_6O_{12}$
Fw, g/mol	1979.07
Crystal system, space group	Triclinic, *P-1*
Temperature (K)	100(2)
a, *b*, *c* (Å)	19.0168(16), 21.1124(16), 39.175(3)
α, β, γ (°)	90.020(3), 90.369(3), 104.856(3)
V (Å^3)	15202(2)
Z	8
Radiation type	Mo *Kα*
μ (mm^{-1})	1.045
Crystal size (mm)	0.25 × 0.17 × 0.10
Data collection	
Diffractometer	Bruker *APEX*-II CCD
Absorption correction	Multi-scan, *SADABS*
T_{min}, T_{max}	0.6311, 0.7452
No. of measured, independent and observed [$I > 2\sigma(I)$] reflections	326906, 53494, 39373
R_{int}	0.1276
$(\sin\theta/\lambda)_{max}$ (Å^{-1})	0.597
Refinement	
$R[F^2 > 2\sigma(F^2)]$, $wR(F^2)$, S	0.0882, 0.1706, 1.153
No. of reflections	53494
No. of parameters	4299
No. of restraints	1335
H-atom treatment	H atoms treated by a mixture of independent and constrained refinement
Dr_{max}, Dr_{min} (e Å^{-3})	1.06, –1.19

Table 4.16. X-ray experimental details for complex **22** (CCDC 1573291).

Crystal Data	
Chemical formula	$C_{25.5}H_{36.22}Cl_{0.5}Co_{0.5}F18N1.5Ni6.5P_3$
Fw, g/mol	1008.59
Crystal system, space group	Triclinic, *P-1*
Temperature (K)	100(2)
a, *b*, *c* (Å)	12.4520(17), 16.687(2), 19.576(3)
α, β, γ (°)	81.849(4), 79.992(4), 88.833(4)
V (Å^3)	3965.2(9)
Z	4
Radiation type	Mo *Kα*
μ (mm^{-1})	0.971
Crystal size (mm)	0.26 × 0.20 × 0.09
Data collection	
Diffractometer	Bruker *APEX*-II CCD
Absorption correction	Multi-scan, *SADABS*
T_{min}, T_{max}	0.7870, 0.9142
No. of measured, independent and observed [$I > 2\sigma(I)$] reflections	103008, 13843, 10629
R_{int}	0.0665
$(\sin \theta/\lambda)_{max}$ (Å^{-1})	0.598
Refinement	
$R[F^2 > 2\sigma(F^2)]$, $wR(F^2)$, S	0.0436, 0.0947, 1.080
No. of reflections	13843
No. of parameters	1111
No. of restraints	88
H-atom treatment	H atoms treated by a mixture of independent and constrained refinement
Dr_{max}, Dr_{min} (e Å^{-3})	0.867, –0.573

Table 4.17. X-ray experimental details for complex **23** (CCDC 1573293).

Crystal Data	
Chemical formula	$C_{18}H_{22}F_{24}N_2NiO_8P_4$
Fw, g/mol	1032.97
Crystal system, space group	Triclinic, *P-1*
Temperature (K)	100(2)
a, *b*, *c* (Å)	12.3361(19), 12.555(2), 13.665(2)
α, β, γ (°)	86.692(2), 72.296(2), 60.745(2)
V (Å^3)	1748.5(5)
Z	2
Radiation type	Mo *Kα*
μ (mm^{-1})	0.405
Crystal size (mm)	0.21 × 0.18 × 0.09
Data collection	
Diffractometer	Bruker *APEX*-II CCD
Absorption correction	Multi-scan, *SADABS*
T_{min}, T_{max}	0.8303, 0.9192
No. of measured, independent and observed [$I > 2\sigma(I)$] reflections	25972, 6196, 3673
R_{int}	0.1239
$(\sin \theta/\lambda)_{max}$ (Å^{-1})	0.597
Refinement	
$R[F^2 > 2\sigma(F^2)]$, $wR(F^2)$, S	0.0573, 0.1122, 0.982
No. of reflections	6196
No. of parameters	516
No. of restraints	0
H-atom treatment	H atoms treated by a mixture of independent and constrained refinement
Dr_{max}, Dr_{min} (e Å^{-3})	1.154, –0.517

Table 4.18. X-ray experimental details for complex **24**.

Crystal Data	
Chemical formula	$C_{36}H_{52}Cl_3F_{36}N_3Ni_2O_{12}P_7$
Fw, g/mol	1843.37
Crystal system, space group	Orthorhombic, *P2(1)2(1)2(1)*
Temperature (K)	100(2)
a, *b*, *c* (Å)	12.7101(4), 18.6488(5), 28.6407(8)
α, β, γ (°)	90, 90, 90
V (Å^3)	6788.7(3)
Z	4
Radiation type	Cu *Kα*
μ (mm^{-1})	4.759
Crystal size (mm)	0.12 × 0.15 × 0.17
Data collection	
Diffractometer	Bruker *APEX*-II CCD
Absorption correction	Multi-scan, *SADABS*
T_{min}, T_{max}	0.4984, 0.5990
No. of measured, independent and observed [$I > 2\sigma(I)$] reflections	27265, 10384, 4838
R_{int}	0.1314
$(\sin \theta/\lambda)_{max}$ (Å^{-1})	0.597
Refinement	
$R[F^2 > 2\sigma(F^2)]$, $wR(F^2)$, S	0.0870, 0.1916, 0.857
No. of reflections	10384
No. of parameters	881
No. of restraints	0
H-atom treatment	H atoms treated by a mixture of independent and constrained refinement
Dr_{max}, Dr_{min} (e Å^{-3})	1.099, –0.960

Table 4.19. X-ray experimental details for complex **27**.

Crystal Data	
Chemical formula	$C_{28}H_{40}Cl_2F_{24}N_4Ni_2O_8P_4$
Fw, g/mol	1328.89
Crystal system, space group	Monoclinic, *P2(1)/n*
Temperature (K)	100(2)
a, *b*, *c* (Å)	12.3710(7), 16.8266(10), 24.4105(13)
α, β, γ (°)	90, 94.9278(17), 90
V (Å^3)	5062.6(5)
Z	4
Radiation type	Mo *Kα*
μ (mm^{-1})	1.111
Crystal size (mm)	0.08 × 0.12 × 0.21
Data collection	
Diffractometer	Bruker *APEX*-II CCD
Absorption correction	Multi-scan, *SADABS*
T_{min}, T_{max}	0.8002, 0.9164
No. of measured, independent and observed [$I > 2\sigma(I)$] reflections	69568, 8986, 7430
R_{int}	0.0563
$(\sin \theta/\lambda)_{max}$ (Å^{-1})	0.596
Refinement	
$R[F^2 > 2\sigma(F^2)]$, $wR(F^2)$, S	0.0410, 0.0769, 1.070
No. of reflections	8986
No. of parameters	759
No. of restraints	104
H-atom treatment	H atoms treated by a mixture of independent and constrained refinement
Dr_{max}, Dr_{min} (e Å^{-3})	0.686, –0.664

Table 4.20. X-ray experimental details for complex **28**.

Crystal Data	
Chemical formula	$C_{33}H_{48}F_{24}N_5Ni_2O_8P_4$
Fw, g/mol	1340.06
Crystal system, space group	Monoclinic, *P2(1)/n*
Temperature (K)	100(2)
a, *b*, *c* (Å)	12.646(3), 23.048(5), 18.358(4)
α, β, γ (°)	90, 92.665(4), 90
V (Å^3)	5345(2)
Z	4
Radiation type	Mo *Kα*
μ (mm^{-1})	0.957
Crystal size (mm)	0.17 × 0.21 × 0.24
Data collection	
Diffractometer	Bruker *APEX*-II CCD
Absorption correction	Multi-scan, *SADABS*
T_{min}, T_{max}	0.8029, 0.8543
No. of measured, independent and observed [$I > 2\sigma(I)$] reflections	40041, 9452, 6804
R_{int}	0.0834
$(\sin \theta/\lambda)_{max}$ (Å^{-1})	0.509
Refinement	
$R[F^2 > 2\sigma(F^2)]$, $wR(F^2)$, S	0.0539, 0.1262, 1.036
No. of reflections	9452
No. of parameters	696
No. of restraints	0
H-atom treatment	H atoms treated by a mixture of independent and constrained refinement
Dr_{max}, Dr_{min} (e Å^{-3})	1.107, –0.654

Table 4.21. X-ray experimental details for complex **29**.

Crystal Data	
Chemical formula	$C_{15}H_{42}Cl_2Ni_2P_6$
Fw, g/mol	596.63
Crystal system, space group	Monoclinic, *P2(1)*
Temperature (K)	100(2)
a, *b*, *c* (Å)	9.7129(7), 12.5434(9), 11.2088(8)
α, β, γ (°)	90, 94.8900(10), 90
V (Å^3)	1360.63(17)
Z	4
Radiation type	Mo *Kα*
μ (mm^{-1})	1.934
Crystal size (mm)	0.11 × 0.20 × 0.26
Data collection	
Diffractometer	Bruker *APEX*-II CCD
Absorption correction	Multi-scan, *SADABS*
T_{min}, T_{max}	0.6363, 0.8097
No. of measured, independent and observed [$I > 2\sigma(I)$] reflections	20664, 4820, 4643
R_{int}	0.0204
$(\sin \theta/\lambda)_{max}$ (Å^{-1})	0.596
Refinement	
$R[F^2 > 2\sigma(F^2)]$, $wR(F^2)$, S	0.0191, 0.0381, 0.986
No. of reflections	4820
No. of parameters	238
No. of restraints	1
H-atom treatment	H atoms treated by a mixture of independent and constrained refinement
Dr_{max}, Dr_{min} (e Å^{-3})	0.232, –0.198

Table 4.22. X-ray experimental details for complex **31**.

Crystal Data	
Chemical formula	$C_{31}H_{56}N_2Ni_2O_2P_2$
Fw, g/mol	792.02
Crystal system, space group	Monoclinic, *Cc*
Temperature (K)	100(2)
a, *b*, *c* (Å)	24.188(4), 9.8307(16), 18.954(3)
α, β, γ (°)	90, 119.873(3), 90
V (Å^3)	3908.1(11)
Z	4
Radiation type	Mo *Kα*
μ (mm^{-1})	1.238
Crystal size (mm)	0.11 × 0.20 × 0.23
Data collection	
Diffractometer	Bruker *APEX*-II CCD
Absorption correction	Multi-scan, *SADABS*
T_{min}, T_{max}	0.7638, 0.8758
No. of measured, independent and observed [$I > 2\sigma(I)$] reflections	21737, 6943, 6441
R_{int}	0.0391
$(\sin \theta/\lambda)_{max}$ (Å^{-1})	0.595
Refinement	
$R[F^2 > 2\sigma(F^2)]$, $wR(F^2)$, S	0.0348, 0.0740, 1.034
No. of reflections	6943
No. of parameters	402
No. of restraints	0
H-atom treatment	H atoms treated by a mixture of independent and constrained refinement
Dr_{max}, Dr_{min} (e Å^{-3})	0.382, –0.214

Table 4.23. X-ray experimental details for complex **32**.

Crystal Data	
Chemical formula	$C_{11}H_{30}Cl_6Ni_2P_4$
Fw, g/mol	616.35
Crystal system, space group	Monoclinic, *P2(1)/n*
Temperature (K)	100(2)
a, *b*, *c* (Å)	8.1778(6), 17.2180(12), 17.2450(12)
α, β, γ (°)	90, 91.0260(10), 90
V (Å^3)	2427.8(3)
Z	4
Radiation type	Mo *Kα*
μ (mm^{-1})	2.470
Crystal size (mm)	0.15 × 0.17 × 0.20
Data collection	
Diffractometer	Bruker *APEX*-II CCD
Absorption correction	Multi-scan, *SADABS*
T_{min}, T_{max}	0.6379, 0.7082
No. of measured, independent and observed [$I > 2\sigma(I)$] reflections	19727, 4297, 3426
R_{int}	0.0444
$(\sin \theta/\lambda)_{max}$ (Å^{-1})	0.595
Refinement	
$R[F^2 > 2\sigma(F^2)]$, $wR(F^2)$, S	0.0287, 0.0609, 0.999
No. of reflections	4297
No. of parameters	216
No. of restraints	0
H-atom treatment	H atoms treated by a mixture of independent and constrained refinement
Dr_{max}, Dr_{min} (e Å^{-3})	0.539, –0.473

Table 4.24. X-ray experimental details for complex **33**.

Crystal Data	
Chemical formula	$C_{10}H_{28}Cl_2Ni_2P_4$
Fw, g/mol	460.52
Crystal system, space group	Tetragonal, *P(-4)C2*
Temperature (K)	100(2)
a, *b*, *c* (Å)	12.7849(10), 12.7849(10), 12.2545(9)
α, β, γ (°)	90, 90, 90
V (Å^3)	2003.0(3)
Z	4
Radiation type	Mo *Kα*
μ (mm^{-1})	2.450
Crystal size (mm)	0.15 × 0.27 × 0.33
Data collection	
Diffractometer	Bruker *APEX*-II CCD
Absorption correction	Multi-scan, *SADABS*
T_{min}, T_{max}	0.5032, 0.7101
No. of measured, independent and observed [$I > 2\sigma(I)$] reflections	28369, 1776, 1716
R_{int}	0.0162
$(\sin \theta/\lambda)_{max}$ (Å^{-1})	0.594
Refinement	
$R[F^2 > 2\sigma(F^2)]$, $wR(F^2)$, S	0.0152, 0.0346, 1.090
No. of reflections	1776
No. of parameters	86
No. of restraints	0
H-atom treatment	H atoms treated by a mixture of independent and constrained refinement
Dr_{max}, Dr_{min} (e Å^{-3})	0.210, –0.132

Table 4.25. X-ray experimental details for complex **34**.

Crystal Data	
Chemical formula	$C_{15}H_{43}Cl_2Ni_2P_6$
Fw, g/mol	579.64
Crystal system, space group	Monoclinic, *P2(1)*
Temperature (K)	100(2)
a, *b*, *c* (Å)	9.6865(6), 12.6129(7), 11.2211(7)
α, β, γ (°)	90, 94.5540(10), 120
V (Å^3)	1366.61(14)
Z	4
Radiation type	Mo *Kα*
μ (mm^{-1})	1.925
Crystal size (mm)	0.14 × 0.16 × 0.24
Data collection	
Diffractometer	Bruker *APEX*-II CCD
Absorption correction	Multi-scan, *SADABS*
T_{min}, T_{max}	0.6509, 0.7690
No. of measured, independent and observed [$I > 2\sigma(I)$] reflections	10975, 4759, 4471
R_{int}	0.0301
$(\sin \theta/\lambda)_{max}$ (Å^{-1})	0.595
Refinement	
$R[F^2 > 2\sigma(F^2)]$, $wR(F^2)$, S	0.0272, 0.0506, 0.948
No. of reflections	4759
No. of parameters	242
No. of restraints	1
H-atom treatment	H atoms treated by a mixture of independent and constrained refinement
Dr_{max}, Dr_{min} (e Å^{-3})	0.386, –0.256

Table 4.26. X-ray experimental details for complex **35**.

Crystal Data	
Chemical formula	$C_{41}H_{73}BrNi_2O_2P_7$
Fw, g/mol	1012.11
Crystal system, space group	Monoclinic, *P2(1)/n*
Temperature (K)	100(2)
a, *b*, *c* (Å)	9.860(2), 37.094(5), 13.2261(14)
α, β, γ (°)	90, 94.965(5), 90
V (Å^3)	4819.2(13)
Z	6
Radiation type	Mo *Kα*
μ (mm^{-1})	1.875
Crystal size (mm)	0.04 × 0.07 × 0.15
Data collection	
Diffractometer	Bruker *APEX*-II CCD
Absorption correction	Multi-scan, *SADABS*
T_{min}, T_{max}	0.7675, 0.9322
No. of measured, independent and observed [$I > 2\sigma(I)$] reflections	8498, 8498, 6576
R_{int}	0.0834
$(\sin \theta/\lambda)_{max}$ (Å^{-1})	0.595
Refinement	
$R[F^2 > 2\sigma(F^2)]$, $wR(F^2)$, S	0.0550, 0.0982, 1.042
No. of reflections	8498
No. of parameters	490
No. of restraints	0
H-atom treatment	H atoms treated by a mixture of independent and constrained refinement
Dr_{max}, Dr_{min} (e Å^{-3})	1.061, –0.614

4.16.5 XYZ Coordinates

Table 4.27. Cartesian coordinates of the geometry-optimized $Ni_2(tfepma)_3Cl_2$ (**15**).

Atom Type	x	y	z
Ni	0.502119	-0.88521	-0.67205
Ni	-0.74429	1.315993	0.980747
Cl	-1.72882	3.049889	2.272445
Cl	1.470632	-2.58879	-1.95064
P	-0.92439	-2.28229	0.376628
P	2.444131	-0.32359	0.32556
P	-0.20123	0.268027	-2.47986
P	0.997521	1.147115	2.383027
P	-0.60415	2.635763	-0.83149
P	-2.53165	-0.01393	1.250999
O	-1.39278	-3.63321	-0.4021
F	-1.87741	-5.92393	-1.87378
F	5.005249	-0.32241	-2.577
O	3.332699	0.719433	-0.57797
O	3.574499	-1.48248	0.495943
F	-3.18153	-4.82252	-3.23311
F	1.493304	-4.39741	3.335926
F	6.601095	1.038462	-1.97031
O	-1.99853	3.414289	-1.16032
F	5.375623	-3.57477	0.483614
F	-3.6971	-5.00609	-1.11995
F	-1.76536	-2.46882	-4.78442
F	2.0136	-1.81456	4.443402
F	-3.22198	-1.41862	-6.02602
O	-0.23626	-3.00861	1.677451
O	0.738248	0.641684	3.930947
F	-3.69371	-1.90505	-3.95201
F	1.314426	-5.33566	1.381929
O	0.633188	0.110259	-3.86825
F	4.709854	1.828062	-2.71903
F	3.934418	4.169473	-1.09746
O	1.676183	2.586816	2.738559
F	1.110573	-0.95593	6.223277
F	0.144986	-2.63826	5.223061
F	2.073187	-0.43624	-6.15379
F	3.77208	0.719093	-5.41817
F	1.858798	1.696803	-5.79976
F	0.323425	-6.22573	3.111272
F	-4.60828	4.277069	-1.36518
F	-6.33029	0.140865	-0.90319
F	4.294646	-4.57193	2.095633

O	-3.97898	0.445281	0.607745
O	0.378007	3.96002	-0.78841
O	-3.01487	-0.12592	2.804309
F	5.210586	-2.61868	2.42817
N	-2.43878	-1.67534	0.901022
O	-1.65047	-0.26834	-3.03769
F	-3.27304	5.18608	-2.82283
F	-5.18132	0.270329	-2.75435
F	-3.97801	6.35032	-1.1167
F	2.447807	5.634714	-1.73373
F	2.435704	5.243921	2.786195
N	2.406475	0.319328	1.913619
F	3.635622	3.963843	4.072807
F	-4.84667	-1.37923	-1.36041
F	-4.81576	-1.21647	4.563138
F	2.471358	3.660012	-2.63917
N	-0.32968	1.971892	-2.3724
C	-1.91937	-3.55597	-1.7314
H	-1.10275	-3.45761	-2.44923
H	-2.61852	-2.7237	-1.83543
F	-5.24972	0.748182	5.408856
C	5.267994	0.850693	-1.97522
F	2.159795	5.312468	4.948291
C	-2.66985	-4.84756	-1.98979
F	-3.2409	-0.08864	5.554161
C	-2.7087	-1.51059	-4.78497
C	0.650578	-5.06211	2.518825
C	3.624735	0.454855	2.753832
H	4.335533	-0.32128	2.473795
H	3.349254	0.305107	3.79873
H	4.068635	1.447155	2.639077
C	0.835969	-1.49417	5.025375
C	-0.61546	-4.26364	2.252088
H	-1.2511	-4.83889	1.578066
H	-1.12201	-4.08569	3.204287
C	4.755201	0.874411	-0.54431
H	5.236356	0.065642	0.006556
H	4.999477	1.843415	-0.10178
C	1.336011	3.422022	3.844234
H	1.342616	2.855693	4.777742
H	0.358345	3.885898	3.69452
C	2.648705	4.332693	-1.47995

C	2.439095	0.563134	-5.33641
C	2.053844	0.290039	-3.89564
H	2.550491	-0.61964	-3.55111
H	2.360662	1.143673	-3.28788
C	-5.11919	-0.05752	-1.44529
C	-0.51759	2.839428	-3.56411
H	-0.04735	2.36489	-4.42399
H	-0.02071	3.794182	-3.38612
H	-1.57938	3.018922	-3.7516
C	-2.13915	-0.16066	-4.37857
H	-1.34387	0.102263	-5.07685
H	-2.94238	0.580145	-4.41026
C	0.011332	-0.56477	4.153839
H	-0.20375	-1.09446	3.221949
H	-0.92852	-0.33639	4.66017
C	-3.54497	-2.55984	1.350733
H	-3.49402	-3.4985	0.800874
H	-4.49625	-2.07881	1.119551
H	-3.48805	-2.73813	2.427753
C	-3.56929	5.130359	-1.50885
C	-4.32477	0.024339	4.753486
C	4.550267	-3.38217	1.523435
C	-2.37406	4.703997	-0.67993
H	-1.56687	5.425181	-0.82239
H	-2.65203	4.657925	0.375399
C	3.244385	-2.73619	1.103491
H	2.734045	-3.376	0.380749
H	2.625275	-2.59922	1.992837
C	-3.98627	0.702832	3.441021
H	-4.89223	0.778602	2.836383
H	-3.58048	1.69885	3.632515
C	-4.04582	0.781444	-0.77648
H	-3.10501	0.580779	-1.29613
H	-4.29576	1.838805	-0.88297
C	1.736807	3.813539	-0.38314
H	2.005707	2.769818	-0.20173
H	1.907	4.387839	0.529292
C	2.406553	4.493146	3.910502

Table 4.28. Cartesian coordinates of the geometry-optimized $Ni_2(tfepma)_3Br_2$ (**16**).

Atom Type	x	y	z
Ni	1.104692	-0.69704	-0.2846
Ni	-1.42068	0.889797	0.34996
Br	-3.4984	2.190407	0.85784
Br	3.147783	-1.98775	-0.79926
P	0.346903	-2.21971	1.191065
P	2.241616	1.099364	0.460696
P	0.372202	-0.74651	-2.41306
P	-0.17879	2.161229	1.712701
P	-1.55237	1.375603	-1.83237
P	-2.31854	-1.01996	1.115029
O	0.758175	-3.7832	0.986775
F	1.725504	-6.32581	0.520518
F	5.023337	1.695001	-2.32067
O	2.704933	2.07635	-0.77404
O	3.713009	0.875872	1.125206
F	0.33888	-6.59738	-1.14228
F	2.69063	-1.62204	4.848179
F	5.487343	3.821246	-2.15499
O	-3.0308	1.100527	-2.46426
F	6.236579	0.289967	2.067791
F	-0.41674	-6.30417	0.884287
F	0.860025	-4.51758	-3.5222
F	1.65622	1.084242	4.804482
F	-0.63196	-4.81615	-5.08723
O	1.016585	-2.01033	2.674179
O	-0.49728	2.131903	3.330642
F	-1.23314	-4.77672	-2.98982
F	3.506209	-3.05944	3.434177
O	1.458148	-0.82563	-3.62472
F	3.644511	3.171575	-3.12668
F	1.501927	5.009526	-2.62736
O	-0.38184	3.761769	1.478242
F	0.06215	1.827218	6.080587
F	0.311645	-0.32249	5.799814
F	3.502661	-1.13169	-5.46039
F	4.077897	0.96049	-5.22913
F	2.10898	0.440533	-6.01537
F	2.651024	-3.75213	5.31955
F	-5.59573	0.309476	-3.09316
F	-5.14212	-3.61647	-1.00928
F	5.40803	-0.56874	3.895074
O	-3.61902	-1.65347	0.322802
O	-1.39946	2.948663	-2.30223

O	-3.01057	-0.87114	2.584291
F	5.118281	1.546718	3.443399
N	-1.34222	-2.37549	1.439039
O	-0.42497	-2.14444	-2.73714
F	-4.47902	1.060499	-4.80295
F	-3.81362	-3.49061	-2.73645
F	-6.04379	2.285142	-3.90121
F	-0.36921	5.14307	-3.74312
F	-0.98178	6.28331	0.536351
N	1.521396	2.114589	1.638257
F	0.455752	6.287765	2.169475
F	-3.05024	-4.16746	-0.8035
F	-4.23587	-2.18774	4.664585
F	0.865502	3.363454	-3.91651
N	-0.62685	0.525299	-2.98
C	0.513874	-4.4418	-0.26
H	1.296584	-4.184	-0.97639
H	-0.4675	-4.18438	-0.66377
F	-5.87601	-0.74846	4.662303
C	4.494341	2.91361	-2.11143
F	-1.60302	6.915735	2.529106
C	0.548963	-5.93372	0.008386
F	-3.84171	-0.09128	5.093295
C	-0.39856	-4.23015	-3.89802
C	2.520639	-2.85363	4.325479
C	2.285799	3.152869	2.378448
H	3.332475	2.857242	2.42505
H	1.904293	3.210178	3.398982
H	2.17887	4.12927	1.899513
C	0.37478	0.8782	5.185235
C	1.148159	-3.00835	3.690993
H	1.07041	-4.01425	3.276908
H	0.388311	-2.84733	4.460542
C	3.796532	3.000437	-0.76379
H	4.518817	2.75903	0.017058
H	3.413926	4.016884	-0.63554
C	-1.23976	4.626106	2.219211
H	-1.11061	4.483204	3.293787
H	-2.28391	4.461943	1.942703
C	0.429057	4.311496	-3.05612
C	3.060802	0.087795	-5.11725
C	2.527683	0.122367	-3.69851

H	3.32224	-0.16025	-3.00533
H	2.181469	1.135381	-3.48283
C	-3.89879	-3.30056	-1.40227
C	-0.94614	0.715179	-4.41915
H	-0.11813	0.342763	-5.02013
H	-1.05687	1.782267	-4.61626
H	-1.87633	0.205438	-4.68266
C	-0.61738	-2.73149	-4.02766
H	0.093186	-2.34	-4.75667
H	-1.64513	-2.55683	-4.35735
C	-0.57017	0.874204	3.997838
H	-0.27544	0.04521	3.348537
H	-1.58982	0.705857	4.349154
C	-1.94293	-3.51108	2.187
H	-1.29284	-4.37971	2.097057
H	-2.90564	-3.7591	1.737526
H	-2.09558	-3.24784	3.236594
C	-5.04893	1.420311	-3.63436
C	-4.58401	-0.92734	4.334119
C	5.183562	0.307166	2.899631
C	-4.04964	2.069739	-2.69729
H	-3.64339	2.963352	-3.1748
H	-4.54468	2.339283	-1.76131
C	3.89353	-0.06035	2.193031
H	3.976671	-1.07127	1.789029
H	3.076374	-0.00881	2.915775
C	-4.39407	-0.65883	2.854258
H	-5.01831	-1.34884	2.283275
H	-4.67626	0.372546	2.630764
C	-3.54415	-1.85941	-1.08583
H	-2.54008	-1.67708	-1.4786
H	-4.2491	-1.19543	-1.58946
C	-0.27314	3.701201	-1.85703
H	0.458446	3.081125	-1.33148
H	-0.60787	4.498575	-1.19085
C	-0.83313	6.041047	1.857351

Table 4.29. Cartesian coordinates of the geometry-optimized $Ni_2(tfepma)_3(CN^tBu)Cl$ (**17**).

Atom Type	x	y	z
Ni	0.550199	-0.92436	-0.74374
Ni	-0.75761	1.337685	0.99062
Cl	-1.78852	3.104948	2.3439
P	-0.83236	-2.17304	0.318642
P	2.326488	-0.29511	0.279542
P	-0.19614	0.25472	-2.37345
P	0.958069	1.181714	2.37899
P	-0.64086	2.660373	-0.77924
P	-2.51351	0.013057	1.257649
O	-1.29224	-3.55047	-0.47635
F	-1.53828	-5.72247	-2.17526
F	5.060075	-0.28219	-2.51384
O	3.271779	0.725224	-0.62401
O	3.485859	-1.46875	0.444012
F	-3.22086	-4.77805	-3.1906
F	1.512172	-4.42369	3.270452
F	6.596497	1.115813	-1.84165
O	-2.01533	3.464253	-1.15339
F	4.790099	-3.85394	-0.0784
F	-3.35652	-5.27314	-1.06857
F	-1.72721	-2.38289	-4.88468
F	2.048303	-1.78119	4.518408
F	-3.22029	-1.27488	-6.02858
O	-0.14421	-2.95863	1.607305
O	0.740712	0.635106	3.928827
F	-3.65239	-1.91306	-3.98795
F	1.267787	-5.35499	1.320338
O	0.650875	0.133609	-3.79524
F	4.728048	1.860647	-2.68661
F	3.919264	4.197987	-1.12033
O	1.693482	2.590109	2.769931
F	1.015382	-0.96206	6.244162
F	0.160771	-2.66265	5.178193
F	2.546499	-1.43393	-5.10136
F	3.915029	0.262885	-5.18437
F	1.979201	0.365353	-6.18391
F	0.246254	-6.18789	3.060349
F	-4.63429	4.313169	-1.3015
F	-6.33209	0.222124	-0.94207
F	4.25519	-4.60885	1.896521
O	-3.98181	0.420886	0.604487
O	0.366933	3.978004	-0.79153
O	-3.03476	-0.17537	2.798103

F	5.497604	-2.82454	1.70358
N	-2.36753	-1.641	0.868045
O	-1.62269	-0.31929	-2.99199
F	-3.32335	5.266768	-2.75198
F	-5.14827	0.324548	-2.7717
F	-4.01382	6.383727	-1.00913
F	2.436005	5.721077	-1.60779
F	2.425849	5.253611	2.786592
N	2.351002	0.338747	1.869735
F	3.59679	4.013321	4.136532
F	-4.89341	-1.34402	-1.38431
F	-4.81909	-1.23851	4.590615
F	2.440443	3.836325	-2.68744
N	-0.3743	1.959137	-2.31124
C	-1.99164	-3.44174	-1.71084
H	-1.32691	-3.12461	-2.51732
H	-2.82875	-2.74225	-1.64623
F	-5.2185	0.733683	5.434825
C	5.268611	0.906281	-1.90459
F	2.082103	5.364523	4.937266
C	-2.52932	-4.82069	-2.0375
F	-3.21779	-0.1259	5.554856
C	-2.69013	-1.43862	-4.80177
C	0.624059	-5.04071	2.466664
C	3.587444	0.45172	2.68198
H	4.302497	-0.3027	2.352771
H	3.340525	0.261382	3.727591
H	4.023574	1.450509	2.595933
C	0.825917	-1.4945	5.027551
C	-0.59542	-4.17529	2.199223
H	-1.26621	-4.72588	1.538103
H	-1.08529	-3.96373	3.153791
C	4.679404	0.919125	-0.50421
H	5.153561	0.122789	0.071392
H	4.880805	1.893609	-0.05057
C	1.309804	3.442569	3.846171
H	1.294103	2.894347	4.791004
H	0.331654	3.893515	3.661431
C	2.628405	4.400714	-1.47012
C	2.618435	-0.08038	-5.08704
C	2.025307	0.495151	-3.81732
H	2.566489	0.086332	-2.96261

H	2.155636	1.581194	-3.8244
C	-5.1173	-0.01093	-1.46151
C	2.937532	-4.02023	-3.04989
C	-0.56537	2.80121	-3.51751
H	-0.20827	2.256055	-4.39159
H	0.025469	3.712766	-3.41155
H	-1.61701	3.070357	-3.64391
C	-2.12776	-0.11584	-4.30969
H	-1.34481	0.196024	-5.0025
H	-2.93733	0.619153	-4.28824
C	0.028774	-0.58387	4.113467
H	-0.12307	-1.11867	3.171256
H	-0.94233	-0.38217	4.570598
C	-3.44447	-2.56556	1.30314
H	-3.33882	-3.51526	0.779508
H	-4.40943	-2.13159	1.036574
H	-3.41263	-2.72163	2.384644
C	-3.60136	5.175191	-1.43466
C	-4.31025	-0.00194	4.767148
C	4.447494	-3.48851	1.180108
C	-2.39417	4.735367	-0.632
H	-1.59405	5.46693	-0.7655
H	-2.65902	4.661885	0.425545
C	3.191867	-2.64224	1.19122
H	2.378368	-3.21357	0.740374
H	2.92711	-2.41312	2.226867
C	-3.98288	0.667735	3.448435
H	-4.89891	0.752417	2.859424
H	-3.56496	1.660953	3.630467
C	-4.02852	0.78694	-0.77011
H	-3.08876	0.570343	-1.28604
H	-4.2516	1.851997	-0.86507
C	1.726606	3.78865	-0.41524
H	1.989685	2.730075	-0.33817
H	1.918698	4.276034	0.543371
C	2.366838	4.525066	3.924443
H	3.764412	-4.2998	-2.38937
H	2.374307	-4.91788	-3.32359
H	3.335168	-3.55376	-3.95602
N	1.427573	-2.30545	-1.78798
C	2.076776	-3.07186	-2.35828

Table 4.30. Cartesian coordinates of the geometry-optimized $Ni_2(tfepma)_3(CN^tBu)Br$ (**18**).

Atom Type	x	y	z
Ni	1.157805	-0.70593	-0.33687
Ni	-1.45928	0.912321	0.353519
Br	-3.60305	2.231279	0.908809
P	0.368781	-2.08299	1.104874
P	2.118334	1.073438	0.385008
P	0.326062	-0.72174	-2.31218
P	-0.24042	2.165037	1.706806
P	-1.61192	1.406326	-1.79475
P	-2.33177	-0.98066	1.101966
O	0.832842	-3.65915	0.897412
F	2.083375	-6.02132	0.150069
F	5.045639	1.715931	-2.1713
O	2.627328	2.083871	-0.82742
O	3.628497	0.835682	1.027977
F	0.392379	-6.54056	-1.12438
F	2.747493	-1.61775	4.774686
F	5.456957	3.857166	-2.06026
O	-3.0758	1.146593	-2.48034
F	6.004796	-0.48949	1.561623
F	0.11282	-6.30084	1.027438
F	0.867524	-4.42205	-3.63468
F	1.655422	1.105986	4.845007
F	-0.69216	-4.70536	-5.1352
O	1.060557	-1.91845	2.603925
O	-0.49462	2.124315	3.343842
F	-1.18385	-4.79	-3.01153
F	3.477713	-3.10335	3.363916
O	1.418279	-0.80614	-3.55894
F	3.704136	3.129511	-3.13716
F	1.516514	4.984404	-2.6286
O	-0.38717	3.78341	1.51772
F	0.009979	1.763101	6.101459
F	0.332744	-0.36835	5.767154
F	4.117578	-1.35867	-3.99768
F	4.413965	0.653915	-4.78549
F	3.033229	-0.71687	-5.76991
F	2.590634	-3.74028	5.254099
F	-5.65349	0.358437	-3.07219
F	-5.16054	-3.59135	-1.07765
F	5.445331	-0.69327	3.65975
O	-3.6229	-1.66974	0.322447
O	-1.41772	2.969561	-2.31364
O	-3.01087	-0.91879	2.589973

F	5.678236	1.287959	2.774212
N	-1.30474	-2.31616	1.386317
O	-0.44179	-2.14444	-2.67264
F	-4.57743	1.174203	-4.77782
F	-3.79635	-3.44503	-2.77403
F	-6.12944	2.35762	-3.80248
F	-0.37014	5.197501	-3.7031
F	-0.9786	6.301441	0.559555
N	1.464116	2.088423	1.596558
F	0.391195	6.309714	2.249417
F	-3.07832	-4.16182	-0.83882
F	-4.25117	-2.23094	4.655977
F	0.820708	3.398633	-3.96006
N	-0.68458	0.520555	-2.92265
C	0.454299	-4.35376	-0.28451
H	1.023495	-4.00503	-1.1489
H	-0.6125	-4.24859	-0.49693
F	-5.85996	-0.75725	4.686908
C	4.476429	2.935263	-2.05084
F	-1.68596	6.917782	2.528611
C	0.767247	-5.81878	-0.053
F	-3.80992	-0.15145	5.117941
C	-0.42495	-4.16439	-3.93151
C	2.500637	-2.83791	4.259694
C	2.265079	3.103304	2.325821
H	3.315892	2.812804	2.306809
H	1.934706	3.132325	3.36527
H	2.137443	4.094921	1.884223
C	0.368485	0.851468	5.184989
C	1.125385	-2.91703	3.619717
H	0.997199	-3.92063	3.211362
H	0.37359	-2.71645	4.388501
C	3.678279	3.044961	-0.76284
H	4.352998	2.856714	0.073741
H	3.256779	4.05216	-0.6979
C	-1.29011	4.631135	2.219992
H	-1.2095	4.484142	3.299377
H	-2.31955	4.458384	1.896606
C	0.417148	4.324047	-3.05672
C	3.493379	-0.30334	-4.57493
C	2.378926	0.232625	-3.69915
H	2.79748	0.527716	-2.73547

H	1.946576	1.117908	-4.17535
C	-3.90742	-3.27375	-1.43659
C	5.212337	-2.5914	-1.12685
C	-0.98934	0.684003	-4.36519
H	-0.22637	0.170842	-4.951
H	-0.96254	1.745816	-4.6159
H	-1.97861	0.285899	-4.6035
C	-0.69541	-2.67026	-3.97341
H	-0.03846	-2.23036	-4.72517
H	-1.74445	-2.51408	-4.24025
C	-0.54798	0.85023	3.976742
H	-0.2112	0.048515	3.313202
H	-1.56814	0.637838	4.303666
C	-1.85538	-3.48187	2.122483
H	-1.16908	-4.32306	2.03043
H	-2.80777	-3.76517	1.671126
H	-2.02086	-3.23836	3.175133
C	-5.12309	1.491032	-3.58397
C	-4.57316	-0.95745	4.34656
C	5.238418	0.033378	2.54877
C	-4.10779	2.113265	-2.64688
H	-3.72152	3.028359	-3.1011
H	-4.58351	2.344265	-1.69045
C	3.769641	0.015954	2.181052
H	3.468107	-1.01375	1.98116
H	3.186007	0.392826	3.025432
C	-4.38422	-0.66876	2.871204
H	-5.03199	-1.3323	2.294121
H	-4.64115	0.373303	2.66505
C	-3.54899	-1.84183	-1.0883
H	-2.54291	-1.6561	-1.47364
H	-4.24942	-1.16635	-1.58427
C	-0.27528	3.69023	-1.86509
H	0.455312	3.041911	-1.37332
H	-0.57934	4.476544	-1.1701
C	-0.8824	6.051271	1.884277
H	5.880373	-2.15957	-0.37481
H	5.227479	-3.68232	-1.03957
H	5.553369	-2.30396	-2.12576
N	2.813545	-1.64693	-0.72168
C	3.865347	-2.08377	-0.91223

Table 4.31. Mulliken spin-densities for the binuclear Ni_2 complexes.[a]

Complex	Ni(1)	Ni(2)	X(1)	X(2)
Ni_2[I,I]Cl_2 (**15**)	0.71	-0.75	0.05	-0.05
Ni_2[I,I]Br_2 (**16**)	0.82	-0.79	0.06	-0.06
Ni_2[I,0]Cl(CH_3CN) (**17**)	0.64	0.22	0.06	0.04
Ni_2[I,0]Br(CH_3CN) (**18**)	0.62	0.20	0.08	0.05
Ni_2[I,0]Cl(CF_3CN)	0.71	0.17	0.06	0.03

[a] All complexes with three bridging tfepma ligands. uB3LYP; 6-311+G(d) (Ni, X (=Br,Cl), and P); 6-31G(d) (F, O, C, H).

4.17 References

1 Cook, T. R.; Dogutan, D. K.; Reece, S. Y.; Surendranath, Y.; Teets, T. S.; Nocera, D. G. *Chem. Rev.* **2010**, *110*, 6474.

2 Rüttinger, W.; Dismukes, G. C. *Chem. Rev.* **1997**, *97*, 1.

3 Yagi, M.; Kaneko, M. *Chem. Rev.* **2001**, *101*, 21.

4 McEvoy, J. P.; Brudvig, G. W. *Chem. Rev.* **2006**, *106*, 4455.

5 Esswein, A. J.; Nocera, D. G. *Chem. Rev.* **2007**, *107*, 4022.

6 Lin, T.-P.; Gabbaï, F. P. *J. Am. Chem. Soc.* **2012**, *134*, 12230.

7 Karikachery, A. R.; Lee, H. B.; Masjedi, M.; Ross, A.; Moody, M. A.; Cai, X.; Chui, M.; Hoff, C. D.; Sharp, P. R. *Inorg. Chem.* **2013**, *52*, 4113.

8 Carrera, E. I.; McCormick, T. M.; Kapp, M. J.; Lough, A. J.; Seferos, D. S. *Inorg. Chem.* **2013**, *52*, 13779.

9 Lee, C. H.; Lutterman, D. A.; Nocera, D. G. *Dalton Trans.* **2013**, *42*, 2355.

10 Nocera, D. G. *Inorg. Chem.* **2009**, *48*, 10001.

11 Cotton, F. A.; Nocera, D. G. *Acc. Chem. Res.* **2000**, *33*, 483.

12 Heyduk, A. F.; Nocera, D. G. *Science* **2001**, *293*, 1639.

13 Esswein, A. J.; Veige, A. S.; Nocera, D. G. *J. Am. Chem. Soc.* **2005**, *127*, 16641.

14 Elgrishi, N.; Teets, T. S.; Chambers, M. B.; Nocera, D. G. *Chem. Commun.* **2012**, *48*, 9474.

15 Gray, T. G.; Veige, A. S.; Nocera, D. G. *J. Am. Chem. Soc.* **2004**, *126*, 9760.

16 Powers, D. C.; Chambers, M. B.; Teets, T. S.; Elgrishi, N.; Anderson, B. L.;Nocera, D. G. *Chem. Sci.* **2013**, *4*, 2880.

17 Norton, J. R. *Acc. Chem. Res.* **1979**, *12*, 139.

18 Halpern, J. *Inorg. Chim. Acta* **1982**, *62*, 31.

19 Norton, J. R. *Acc. Chem. Res.* **1979**, *12*, 139.

20 Martin, B. D.; Warner, K. E.; Norton, J. R. *J. Am. Chem. Soc.* **1986**, *108*, 33.

21 Kristjánsdóttir, S. S.; Norton, J. R. In *Transition Metal Hydrides.* Dedieu, A., Ed.; VCH: New York, 1992, Ch. 9, p 309.

22 Arndtsen, B. A.; Bergman, R. G.; Mobley, T. A.; Peterson, T. H. *Acc. Chem. Res.* **1995**, *28*, 154.

23 Esswein, A. J.; Veige, A. S.; Nocera, D. G. *J. Am. Chem. Soc.***2005**,*127*, 16641.

24 Cook, T. R.; Esswein, A. J.; Nocera, D. G. *J. Am. Chem. Soc.***2007**,*129*, 10094.

25 Teets, T. S.; Lutterman, D. A.; Nocera, D. G. *Inorg. Chem.***2010**,*49*, 3035.

26 Birkholz, M. *Thin Film Analysis by X-Ray Scattering;* Wiley-VCH, Germany. 2006. p 183.

27 Schmøkel, M. S. Kamiński, R.; Benedict, J. B.; Coppens, P. *Acta Cryst A* **2010**, *66*, 632.

28 Wallace, T. J.; Gritter, R. J. *J. Org. Chem.* **1962**, *27*, 3067.

29 Mignani, S.; Beaujean, M.; Janousek, Z.; Merenyi, R.; Viehe, H. G. *Tetrahedron* **1981**, *37*, 111.

30 Yamamoto, Y. *Coord. Chem. Rev.* **1980**, *32*, 193.

31 Robertson, M. J.; Angelici, R. J. *Langmuir* **1994**, *10*, 1488.

32 Malatesta, L.; Bonati, F. *Isocyanide Complexes of Metals*, John Wiley, New York, NY, 1969, 25.

33 Spessard, G. O.; Miessler, G. L. *Organometallic Chemistry*, Prentice-Hall, Upper Saddle River, NJ, 1997, 140.

34 Teets, T. S.; Nocera, D. G. *J. Am. Chem. Soc.* **2011**, *133*, 17796.

35 Lo, J. M. H.; Marriott, R. A.; Giri, B. R.; Roscoe, J. M.; Klobukowski, M. *Can. J. Chem.* **2010**, *88*, 1136.

36 Raamat, E.; Kaupmees, K.; Ovsjannikov, G.; Trummal, A.; Kütt, A.; Saame, J.; Koppel, I.; Kaljurand, I.; Lipping, L.; Rodima, T.; Pihl, V.; Koppel, I. A.; Leito, I. *J. Phys. Org. Chem.* **2013**, *26*, 162.

37 Kütt, J.; Rodima, T.; Saame, J.; Raamat, E.; Mäemets, V.; Kaljurand, I.; Koppel, I. A.; Garlyauskayte, R. Y.; Yagupolskii, Y. L.; Yagupolskii, L. M.; Bernhardt, E.; Willner, H.; Leito, I. *J. Org. Chem.* **2011**, *76*, 391.

38 Dibble, B. R.; Sigman, M. S.; Arif, A. M. *Inorg. Chem*. **2005**, *44*, 3774.

39 Lin, C.-Y.; Power, P. P. *Chem. Soc. Rev.* **2017**, *46*, 5347.

40 DeLaet, D. L.; Rosario, R. del.; Fanwick, P. E.; Kubiak, C. P. *J. Am. Chem. Soc.* **1987**, *109*, 754.

41 Ferrence, G. M.; Simón-Manso, E.; Breedlove, B. K.; Meeuwenberg, L.; Kubiak, C. P. *Inorg. Chem*. **2004**, *43*, 1071.

42 Laarhoven, L. J. J.; Mulder, P.; Wayner, D. D. M. *Acc. Chem. Res.* **1999**, *32*, 342.

43 Krogman, J. P.; Thomas, C. M. *Chem. Commun.***2014**,*50*, 5115.

44 Demas, J. N.; Bowman, W. D.; Zalewski, E. F.; Velapoldi, R. A. *J. Phys. Chem.* **1981**, *85*, 2766.

45. Kuhn, H.; Braslavasky, S. E.; Schmidt, R. *Pure Appl. Chem.* **2004**, *76*, 2105.

46. Manojlovic-Muir, L.; Muir, K. W.; Davis, W. M.; Mirza, H. A.; Puddephatt, R. J. *Inorg. Chem.* **1992**, *31*, 904.

47. Hwang, S. J.; Powers, D. C.; Maher, A. G.; Anderson, B. L.; Hadt, R. G.; Zheng, S.-L.; Chen, Y.-S.; Nocera, D. G. *J. Am. Chem. Soc.* **2015**, *137*, 6472.

48. Hwang, S. J.; Anderson, B. L.; Powers, D. C.; Maher, A. G.; Hadt, R. G.; Nocera, D. G. *Organometallics* **2015**, *34*, 4766.

49. Powers, D. C.; Anderson, B. L.; Nocera, D. G. *J. Am. Chem. Soc.* **2013**, *135*, 18876.

50. Powers, D. C.; Hwang, S. J.; Zheng, S.-L.; Nocera, D. G. *Inorg. Chem.***2014**,*53*, 9122.

51 Wickramasinghe, L. A.; Sharp, P. R. *Inorg. Chem.* **2014**, *53*, 1430.

52 Karikachery, A. R.; Lee, H. B.; Masjedi, M.; Ross, A.; Moody, M. A.; Cai, X.; Chui, M.; Hoff, C. D.; Sharp, P. R. *Inorg. Chem.* **2013**, *52*, 4113.

53 Lin, T.-P.; Gabbaï, F. P. *J. Am. Chem. Soc.* **2012**, *134*, 12230.

54 Carrera, E. I.; McCormick, T. M.; Kapp, M. J.; Lough, A. J.; Seferos, D. S. *Inorg. Chem.* **2013**, *52*, 13779.

55 Perera, T. A.; Masjedi, M.; Sharp, P. R. *Inorg. Chem.* **2014**, *53*, 7608.

56 Zheng, S.-L.; Wang, Y.; Yu, Z.; Lin, Q.; Coppens, P. *J. Am. Chem. Soc.* **2009**, *131*, 18036.

57 Ohashi, Y. *Crystalline State Photoreactions: Direct Observation of Reaction Processes and Metastable Intermediates;* Springer, Japan. 2014.

58 Coppens, P.; Zheng, S. L. in *Supramolecular Photochemistry: Controlling Photochemical Processes*, V. Ramamurthy, T. Inoue, Eds. John Wiley & Sons, Hoboken, NJ, USA. 2011, 155.

59 Coppens, P.; Sokolow, J.; Trzop, E.; Makal, A.; Chen, Y. *J. Chem. Phys. Lett.* **2013**, *4*, 579.

60 Makal, A.; Trzop, E.; Sokolow, J.; Kalinowski, J.; Benedict, J.; Coppens, P. *Acta Cryst. A* **2011**, *67*, 319.

61 Benedict, J. B.; Makal, A.; Sokolow, J. D. Trzop, E.; Scheins, S.; Henning, R.; Graber, T.; Coppens, P. *Chem. Commun*. **2011**, *47*, 1704.

62 Cook, T. R.; Surendranath, Y.; Nocera, D. G. *J. Am. Chem. Soc.* **2009**, *131*, 28.

63 Teets, T. S.; Nocera, D. G. *J. Am. Chem. Soc.* **2009**, *131*, 7411.

64 Yang, H.; Gabbaï, F. P. *J. Am. Chem. Soc.* **2014**, *136*, 10866.

65 Norton, J. R. *Acc. Chem. Res.* **1979**, *12*, 139.

66 Halpern, J. *Inorg. Chim. Acta* **1982**, *62*, 31.

67 Evans, J.; Okrasinski, S. J.; Pribula, A. J.; Norton, J. R. *J. Am. Chem. Soc.* **1977**, *99*, 5835.

68 Carter, W. J.; Okrasinski, S. J.; Norton, J. R. *Organometallics* **1985**, *4*, 1376.

69 Carter, W. J.; Kelland, J. W.; Okrasinski, S. J.; Warner, K. E.; Norton, J. R. *Inorg. Chem.* **1982**, *21*, 3955.

70 Wolczanski, P. T.; Threlkel, R. S.; Bercaw, J. E. *J. Am. Chem. Soc.* **1979**, *101*, 218.

71 Janowicz, A. H.; Bergman, R. G. *J. Am. Chem. Soc.* **1981**, *103*, 2488.

72 Jones, W. D.; Huggins, J. M.; Bergman, R. G. *J. Am. Chem. Soc.* **1981**, *103*, 4415.

73 Nappa, M. J.; Santi, R.; Halpern, J. *Organometallics* **1985**, *4*, 34.

74 Marsella, J. A.; Huffman, J. C.; Caulton, K. G.; Longato, B.; Norton, J. R. *J. Am. Chem. Soc.* **1982**, *104*, 6360.

75 Nappa, M. J.; Santi, R.; Halpern, J. *Organometallics* **1985**, *4*, 34.

76 Alemdaroğlu, N. H.; Penninger, J. L. M.; Oltay, E. *Monatsh. Chem.* **1976**, *107*, 1153.

77 Hebrard, F.; Kalck, P. *Chem. Rev.* **2009**, *109*, 4272.

78 Collman, J. P. *J. Organomet. Chem.* **1980**, *200*, 79.

79 Liu, G.; Li, C.; Guo, L.; Garland, M. *J. Catal.* **2006**, *237*, 67.

80 Feng, J.; Garland, M. *Organometallics* **1999**, *18*, 1542.

81 Mirbach, M. F. *J. Organomet. Chem.* **1984**, *265*, 205.

82 Broussard, M. E.; Juma, B.; Train, S. G.; Peng, W.-J.; Laneman, S. A.; Stanley, G. G. *Science* **1993**, *260*, 1784.

83 Li, C.; Chen, L.; Garland, M. *J. Am. Chem. Soc.* **2007**, *129*, 13327.

84 Gray, T. G.; Veige, A. S.; Nocera, D. G. *J. Am. Chem. Soc.* **2004**, *126*, 9760.

85 Pangborn, A. B.; Giardello, M. A.; Grubbs, R. H.; Rosen, R. K.; Timmers, F. J. *Organometallics* **1996**, *15*, 1518.

86 Teets, T. S.; Cook, T. R.; Nocera, D. G. *Inorg. Synth*. **2010**, *35*, 164.

87 Tao, J.; Tran, R.; Murphy, G. K. *J. Am. Chem. Soc.* **2013**, *135*, 16312.

88 Fulmer, G. R.; Miller, A. J. M.; Sherden, N. H.; Gottlieb, H. E.; Nudelman, A.; Stoltz, B. M.; Bercaw, J. E.; Goldberg, K. I. *Organometallics*, **2010**, *29*, 2176.

89 Bruker AXS (2009). Apex II. Bruker AXS, Madison, Wisconsin.

90 Sheldrick, G. M. *Acta Cryst.* **2010**, *D66*, 479.

91 Frisch, M.J.; Schlegel, H.B.; Scuseria, G.E.; Robb, M.A.; Cheeseman, J.R.; Scalmani, G.; Barone, V.; Mennucci, B.; Petersson, G.A.; Nakatsuji, H.; Caricato, M.; Li, X.; Hratchian, H.P.; Izmaylov, A.F.; Bloino, J.; Zheng, G.; Sonnenberg, J.L.; Hada, M.; Ehara, M.; Toyota, K.; Fukuda, R.; Hasegawa, J.; Ishida, M.; Nakajima, T.; Honda, Y.; Kitao, O.; Nakai, H.; Vreven, T.; Montgomery, J.A. Jr.; Peralta, J.E.; Ogliaro, F.; Bearpark, M.; Heyd, J.J.; Brothers, E.; Kudin, K.N.; Staroverov, V.N.; Keith, T.; Kobayashi, R.; Normand, J.; Raghavachari, K.; Rendell, A.; Burant, J.C.; Iyengar, S.S.; Tomasi, J.; Cossi, M.; Rega, N.; Millam, J.M.; Klene, M.; Knox, J.E.; Cross, J.B.; Bakken, V.; Adamo, C.; Jaramillo, J.; Gomperts, R.; Stratmann, R.E.; Yazyev, O.; Austin, A.J.; Cammi, R.; Pomelli, C.; Ochterski, J.W.; Martin, R.L.; Morokuma, K.; Zakrzewski, V.G.; Voth, G.A.; Salvador, P.; Dannenberg, J.J.; Dapprich, S.; Daniels, A.D.; Farkas, O.; Foresman, J.B.; Ortiz, J.V.; Cioslowski, J.; Fox, D.J. Gaussian 09 (Revision A.01), Gaussian, Inc., Wallingford, CT, 2009.

92 Becke, A. D. *J. Chem. Phys*. **1993**, *98*, 5648.

93 Francl, M. M.; Pietro, W. J.; Hehre, W. J.; Binkley, J. S.; Gordon, M. S.; DeFrees, D. J.; Pople, J. A. *J. Chem Phys.* **1982**, *77*, 3654.

94 Hariharan, P. C.; Pople, J. A. *Theor. Chim. Acta*, **1973**, *28*, 213.

95 Rassolov, V. A.; Pople, J. A.; Ratner, M. A.; Windus, T. L. *J. Chem. Phys.* **1998**, *109*, 1223.

96 Noodleman, L. *Chem. Phys.* **1981**, *74*, 5737.

97 Noodleman, L.; Case, D. A. *Adv. Inorg. Chem.* **1992**, *38*, 423.

98 Kieber-Emmons, M. T. β-Lumo, Version 0.9b; Burlingame, CA, 2011

99 Gorelsky, S. I.; Lever, A. B. P. *J. Organomet. Chem.* **2001**, *635*, 187.

100 Gorelsky, S. I. SWizard (http://www.sg-chem.net/); University of Ottawa, Ottawa, Canada, 2010

101 Miertus, S.; Scrocco, E.; Tomasi, J. *Chem. Phys.* **1981**, *55*, 117.

Chapter5

Effects of Secondary Coordination Interactions and Electronics on Halogen Photoelimination Chemistry in Monomeric Iron(III) Complexes

Parts of this chapter have been published:

Gygi, D.; Hwang, S. J.; Nocera D. G. "Scalable Syntheses of 4-Substituted Pyridine-Diimines" *J. Org. Chem.* **2017**, *82*, 12933.

5.1 Introduction

The activation of metal-halide bonds from first-row transition metal complexes is central to solar energy storage involving HX in the form of a redox flow battery[1] or chemical fuel,[2,3] and more recently in the development of methodologies for photoredox-mediated organic transformations of small molecules.[4–7] Whereas the kinetic inertness of the M–X bond may be overcome with a light input, the bond activation may be circumvented by the exergonic and facile back reaction of photogenerated products to reform the M–X bond. One approach to preventing the back reaction is to perform the photochemistry in the solid state where an X_2 photoproduct may be swept from the system.[8–12] Whereas this strategy has merit for HX splitting photocycles,[13] it is inapplicable for photoredox-mediated organic transformations, which rely on the generation of reactive halogen radicals in solution. We have therefore explored new strategies to bypass the back reaction of halogen radicals produced upon M–X bond photoactivation. Examination of the photochemistry of a family of monomeric Ni(III)X_3(LL) (LL = bidentate phosphine) complexes has suggested that the secondary coordination sphere may be a chaperone for guiding photogenerated halogen radicals from the metal center.[14] Nanosecond transient absorption (TA) spectra taken immediately after photoexcitation of the Ni(III)X_3(LL) complexes reveal spectral signatures of a halogen|arene charge transfer complex, suggesting that the halogen radical produced from M–X bond activation is captured by the pendant arenes of the ancillary bidentate phosphine.[15] The nature of this charge transfer complex has been under considerable debate[16,17] as the halogen|arene interaction has heretofore eluded structural characterization.

The free radical halogenation of alkanes has been regarded as one of the most important and basic organic transformations for the preparation of alky halides and the mechanism by

which it occurs has been well understood for at least six decades.[18] As depicted in Figure 5.1, the overall reaction converting C–H into C–X bonds with halogen undergoes a free radical chain reaction that involves the highly reactive and unselective halogen atom. The reactivity and selectivity of halogenation reaction varies depending on the nature of halogen atoms; Cl atoms shows high reactivity and moderate selectivity in hydrogen abstraction reactions from alkanes, 3°(4.2) > 2°(3.6) >1°(1), as compared to the significantly less reactive but more selective halogenation reaction with bromine 3°(25000) > 2°(700) >1°(1).[19,20]

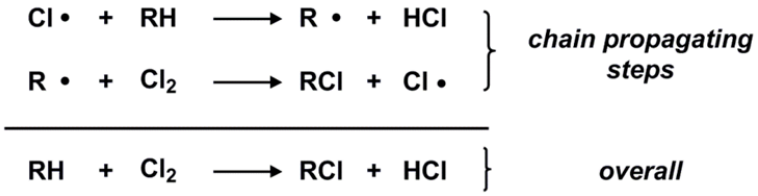

Figure 5.1. Overall mechanism of chlorination of alkane reactions.

In 1955 Russell studied the effects of aromatic solvents on the selectivity of the chlorination of 2,3-dimethylbutane (DMB) (Figure 5.2).[21] They discovered that the selectivity for tertiary relative to primary (3°/1°) (designated as r(3°/1°)) dramatically increased in the presence of aromatic hydrocarbons; r(3°/1°) = 59 in 8 M benzene and 4.2 in the absence of benzene.

Russell proposed the formation of a new complex between Cl atom and benzene (Cl•|benzene) as a η^6 π-type interaction which is less reactive and more selective than a free Cl atom during the chlorination reaction with DMB to account for its unique selectivity dependent on benzene concentration. Russell postulated that this π-type complex is in equilibrium with benzene and a free Cl atom since the selectivity of this chlorination reaction was independent of DMB concentration (Eq 1).[22–24]

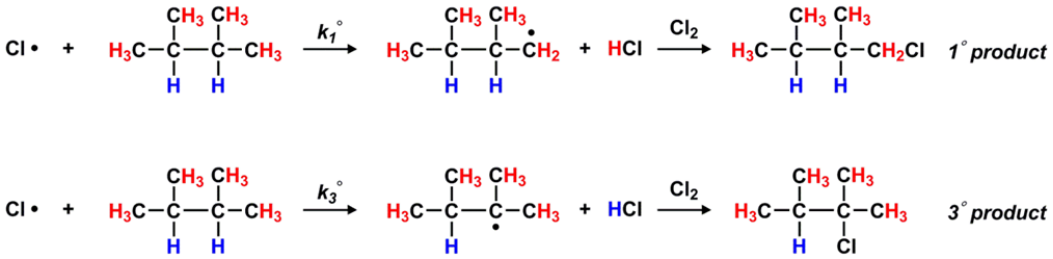

Figure 5.2. Two chlorination products (1° and 3°) with 2,3-dimethylbutane (DMB).

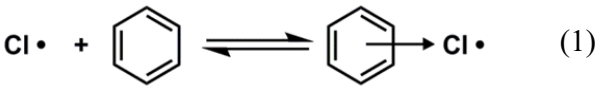

(1)

Russel considered two possible structures for the Cl•|arene complex, a hexahapto π-complex and a 6-chlorocyclohexadienyl radical σ complex. Russel finally assigned it as the π complex for the following reasons; (1) The Cl•|arene complex is believed to be in rapid equilibrium thus formation of a weak π complex would occur faster than that of σ complex. (2) The selectivity of halogenation correlated to the σ–bonding ability of the aromatic solvent but there was no connection to the rate of phenyl radical addition to the solvent.

However, In 1983, Skell and co-workers reintroduced the structural assignment of the Cl•|arene complex as a 6-chlorocyclohexadienyl radical σ–complex based on their studies for the r(3°/1°) over a much broader range of DMB concentrations where the Cl•|arene complex was not in equilibrium.[25] Specifically, they found that the observed selectivity approached that of a free Cl atom at high DMB concentration, whereas the selectivity was independent with DMB concentration at the lower concentrations Russel probed. The Skell group suggested that the highly selective intermediate might be better assigned as the σ complex, whereas the poorly selective intermediate was best described as a mixture of Cl atom and the Cl•|arene π complex.[25,26]

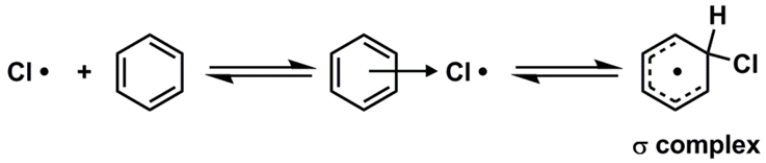

(2)

In 1985, Ingold and coworkers re-examined the issues raised by Skell, reporting the absolute rate constant for all reactions for both free and complexed Cl by laser flash photolysis.[27–30] They determined that the equilibrium constant for the formation of the Cl•|arene complex to be 200 M^{-1}. Ingold argued for the π-complex as the appropriate structure of the Cl•|arene complex based on the charge-transfer band at 490 nm that corresponded to earlier reports that assigned these spectra as the π complex.

However, the controversy over the structure of this Cl•|arene complex continues to this day. EPR spectroscopy has been utilized but did not appear to be conclusive since the Cl•|arene complex in the solid state suggested that it has an intermediate structure between a pure π-complex and a pure chlorocyclohexadienyl radical.[31] Recently, a range of halogen|arene complexes were examined by DFT and the η^1-Cl•|arene interaction was predicted to be most stable.[32]

The potential utility of a secondary interaction in engendering a productive M–X bond activation provides an imperative for a more detailed knowledge of these transient species. To this end, we now examine the halogen photoelimination chemistry of the five-coordinate Fe(III) complexes shown in Figure 5.3. These two families of compounds are isoelectronic but present distinct secondary coordination environments of the peripheral arene groups in square pyramidal and trigonal bipyramidal ligand fields. For the case of the former ligand field, we have made use of the popular pyridine diiimine (PDI) scaffold in which an arene may be presented over the top face of a [Fe(III)–Cl_{ax}] moiety by modification of the 4-position of the PDI ligand.[33] The trigonal

bipyramidal ligand field induced by the ancillary phosphines about [Fe(III)–Cl_{eq}] is the same as we have employed for the Ni(III)$X_3(LL)_2$ compounds, which serve as a benchmark for this study. Using photocrystallography,[34,35] we isolate and directly observe the Cl•|arene charge transfer intermediate generated as the primary event of M–X bond photoactivation and structurally establish the prevalence of a η^1-Cl•|arene interaction. We further observe that the solution quantum yield for M–X bond activation benefits from the Cl•|arene interaction in the secondary coordination sphere.

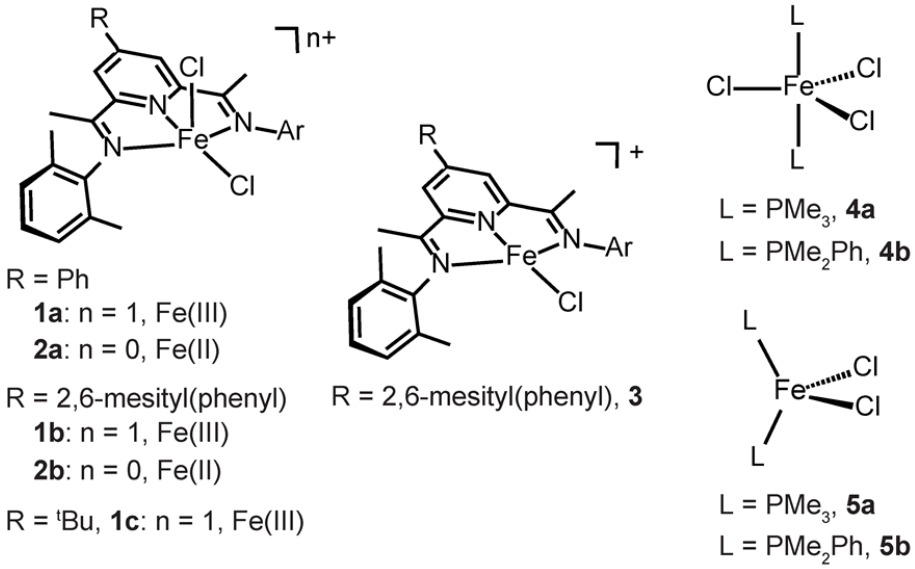

Figure 5.3. Fe complexes studied for secondary coordination sphere interactions.

5.2 Synthesis and Characterization of Mononuclear Fe(III) Complexes

A modified Minisci reaction and iterative Suzuki couplings detailed in Figure 5.4 allowed the PDI ligands to be synthesized with the 4-position of the PDI ligand derivatized with phenyl, 2,6-mesityl(phenyl) and *tert*-butyl groups. NMR spectra for the PDIs and their precursors are provided in Figures 5.34–5.41.

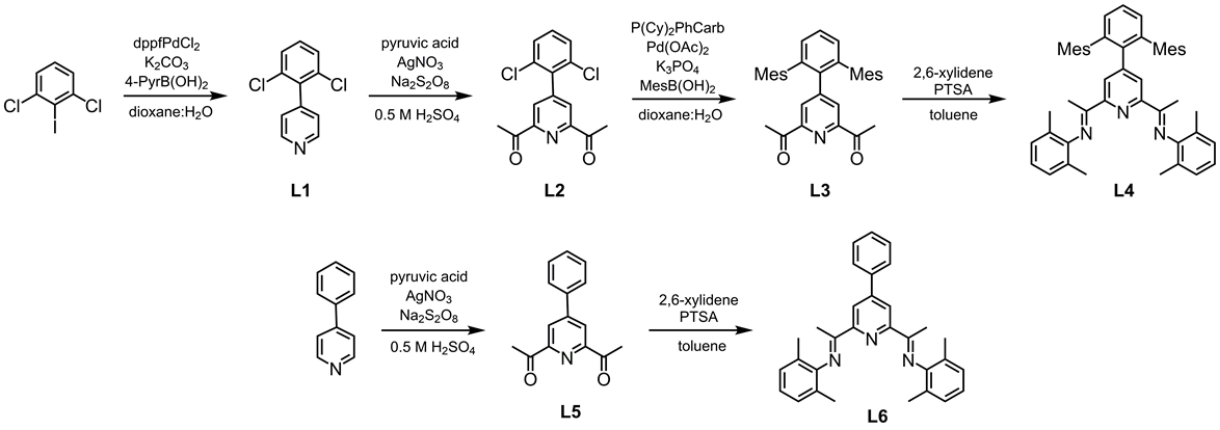

Figure 5.4. Synthetic scheme for PDI ligands.

The five-coordinate cationic $[Fe(III)Cl_2(PDI)]^+$ complexes **1a–1c** were synthesized by treatment of the parent PDI ligand with anhydrous $FeCl_3$ and an equivalent of $AgPF_6$ or $AgBF_4$. The $[FeCl_2(PDI)]PF_6$ complexes were isolated as dark red crystalline solids in high yield (60 – 70%). Each of the Fe(III) compounds exhibits an S = $^5/_2$ ground state as determined by the Evans method, resulting in the expected broadening of their ^{1}H NMR spectra (Figures 5.65–5.67). The ^{57}Fe Mössbauer spectra (Figures 5.5) of compounds **1a** and **1b** show broad asymmetric peaks supporting the presence of a single iron environment with parameters (isomer shift, δ = 0.53 and 0.39 mm s^{-1} and a quadrupole splitting, $|\Delta E_Q|$ = 1.25 and 0.89 mm s^{-1} for **1a** and **1b**, respectively) in line with other five-coordinate S = $^5/_2$ Fe(III) complexes.[36]

Complexes **1a**–**1c** were characterized by X-ray diffraction; representations of the solid-state structures are shown in Figures 5.6 and 5.7. Distorted square-pyramidal geometries were observed with two Cl atoms in apical and basal positions of the five-coordinate bis(imino)pyridine iron dihalide complexes. Complexes **1a** and **1b** exhibit near-identical metrical parameters (τ_5 = 0.19 for **1a**, τ_5 = 0.22 for **1b**)[37] that are similar to **1c** (Table 5.1), which displays almost perfect square-pyramidal geometry (τ_5 = 0.01), indicating that the arene groups of the PDI

ligand do not significantly alter the primary coordination sphere about the Fe(III) center. The secondary coordination sphere of **1b**, however is distinct. As evident in Figure 5.6, the bulky mesityl groups of an associated arene forces the ring to sit above the [Fe–Cl_{ax}] moiety.

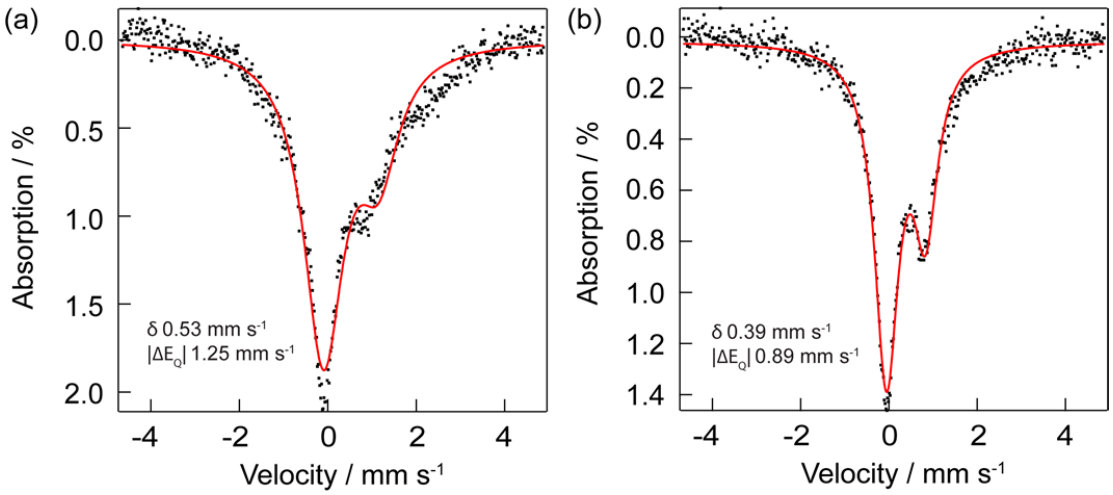

Figure 5.5. Zero-field ^{57}Fe Mössbauer spectrum of compound (a) **1a** and (b) **1b** recorded at 90 K. Isomer shift and quadrupole splitting are reported relative to Fe foil at room temperature.

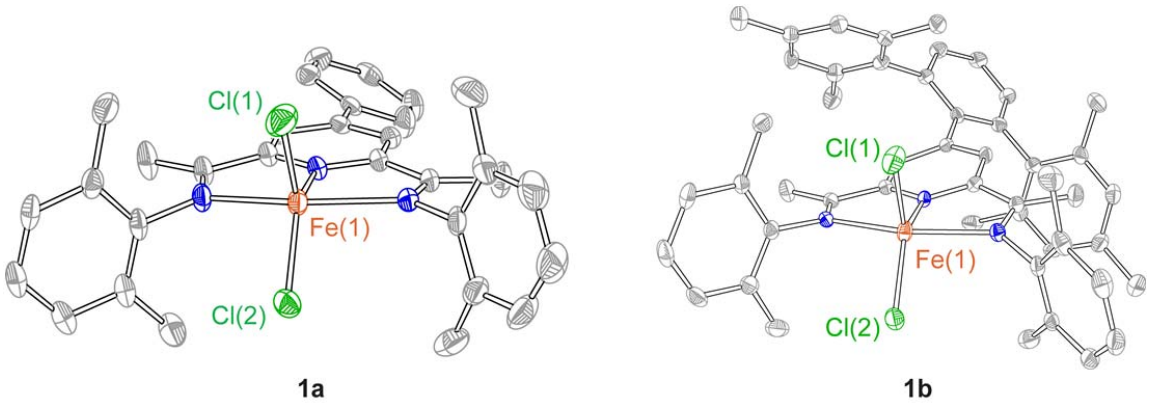

Figure 5.6. Solid-state structures of **1a** and **1b** at 100K and 20 K respectively with 50% probability ellipsoids. H atoms PF_6 anion, and solvent molecules have been omitted for clarity.

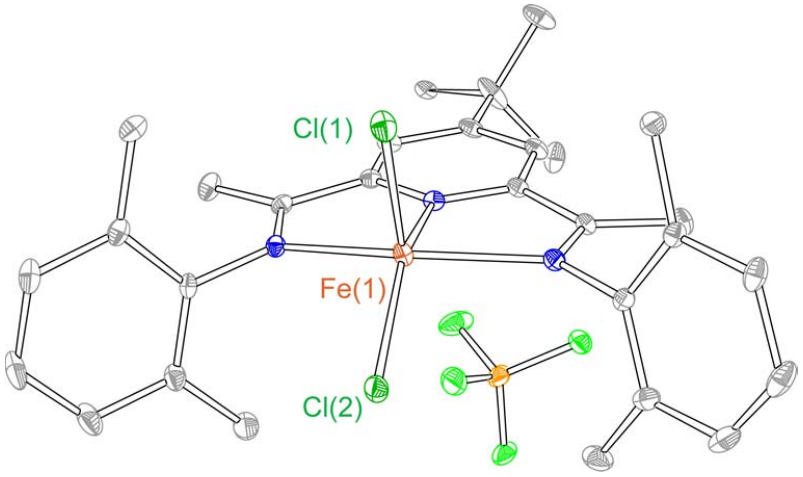

Figure 5.7. Thermal ellipsoid plots of $[FeCl_2(^tBuPDI)]BF_4$ (**1c**) drawn at the 50% probability level. H-atoms are omitted for clarity.

Table 5.1. Selected metrical parameters for **1a**, **1b** and **1c**.

	1a	**1b**	**1c**
Fe(1)–N(1)	2.058(2)	2.068(3)	2.0674(3)
Fe(1)–N(2)	2.180(2)	2.188(3)	2.1888(3)
Fe(1)–N(3)	2.183(2)	2.198(3)	2.1707(3)
Fe(1)–Cl(1)	2.1712(9)	2.1946(14)	2.20084(12)
Fe(1)–Cl(2)	2.1780 (8)	2.1715(13)	2.20544(13)
N(2)–C(6)	1.276(4)	1.300(5)	1.3003(5)
N(3)–C(8)	1.286(4)	1.298(5)	1.3004(5)
C(1)–C(6)	1.479(4)	1.482(6)	1.4935(6)
C(5)–C(8)	1.480(4)	1.501(6)	1.4892(5)
N(1)−Fe(1)−N(2)	73.88(9)	74.59(13)	74.121(13)
N(1)−Fe(1)−N(3)	74.42(8)	73.96(13)	74.831(13)
N(1)−Fe(1)−Cl(1)	113.91(7)	110.54(10)	104.690(8)
N(2)−Fe(1)−Cl(1)	99.08(7)	98.66(10)	98.838(7)
N(3)−Fe(1)−Cl(1)	100.40(7)	97.63(10)	100.700(8)
N(1)−Fe(1)−Cl(2)	135.96(7)	134.95(10)	146.143(8)
N(2)−Fe(1)−Cl(2)	98.49(6)	99.66(10)	99.38(1)
N(3)−Fe(1)−Cl(2)	98.98(7)	101.35(9)	99.457(9)
Cl(1)−Fe(1)−Cl(2)	110.13(4)	114.47(6)	109.154(4)

τ_5[a]	0.19	0.22	0.01

[a] τ_5 is a metric for five coordinate complexes. $\tau_5 = 0$ for a perfect square pyramid and $\tau_5 = 1$ for a perfect trigonal bipyramid.

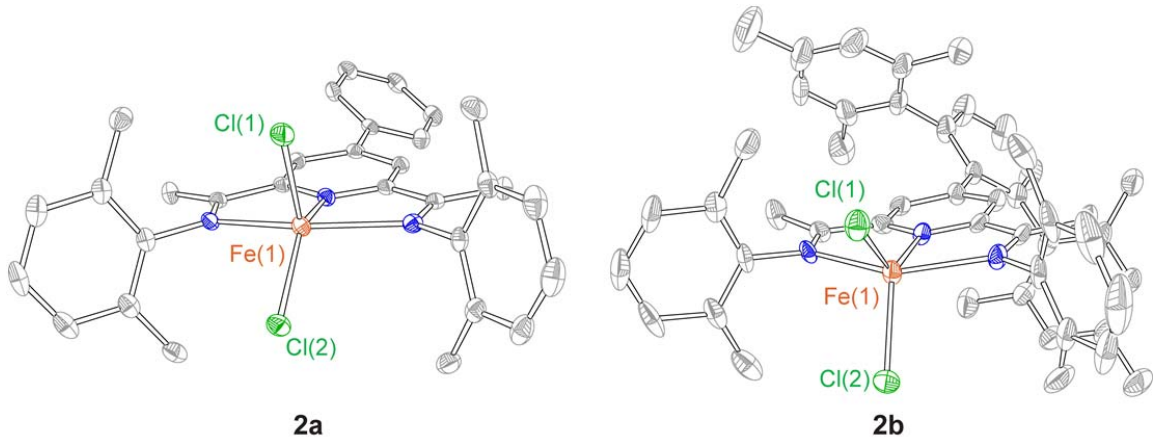

Figure 5.8. Thermal ellipsoid plots of $FeCl_2$(4-PhPDI) (**2a**) and $FeCl_2$(BisMesPDI) (**2b**) drawn at the 50% probability level. H-atoms and solvent are omitted for clarity.

The corresponding Fe(II)Cl_2(PDI) complexes (PDI = 4-phenylPDI (**2a**) and 4-(2,6-mestiyl(phenyl)PDI (**2b**)) were prepared from the parent PDI ligand and $FeCl_2$. Evan's method reveals a S = 2 ground state, but the ^{1}H NMR spectra exhibit sharper resonances (Figures 5.68 and 5.69) than their Fe(III) counterparts. The X-ray structures (Figure 5.8) show five coordinate distorted square pyramidal iron centers. For **2a**, the iron center sits inside the N_3 plane of the PDI with local C_{2v} symmetry whereas for **2b** the iron center resides slightly above the N_3 plane as for **1a**. The ^{57}Fe Mössbauer spectra of compounds **2a** and **2b** (Figure 5.9) are consistent with Fe(II) complexes of spin S = 2 (isomer shift, δ = 1.02 and 1.03 mm s^{-1} and quadrupole splitting, $|\Delta E_Q|$ = 2.69 and 2.72 mm s^{-1} for **2a** and **2b**, respectively).[38] The Fe(II) PDI complex with a single bound chloride, [FeCl(MeCN)(PDI)]PF_6 (**3**), is formed from the reaction of 2,6-mesityl(phenyl)PDI with $FeCl_2$ in the presence of $AgPF_6$ in acetonitrile. This cationic Fe(II)

complex possess a ^{1}H NMR spectrum (Figure 5.70) similar to its dichloride congener. The solid state structure of **3** (Figure 5.10) shows a five-coordinate iron congener with the coordination site previously occupied by the chloride now containing an N-bound acetonitrile molecule. Selected metrical parameters for the Fe(II) PDI complexes **2a**, **2b** and **3** are summarized in Table 5.2.

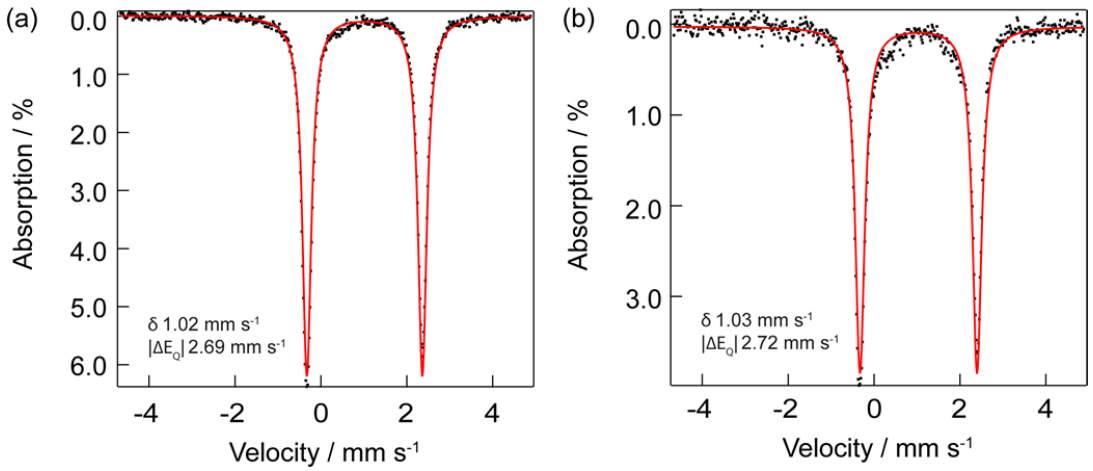

Figure 5.9. Zero-field ^{57}Fe Mössbauer spectrum of compound (a) **2a** and (b) **2b** recorded at 90 K. Isomer shift and quadrupole splitting are reported relative to Fe foil at room temperature.

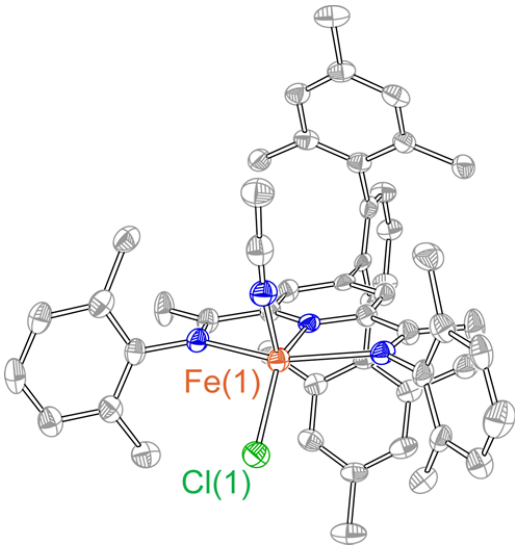

Figure 5.10. Thermal ellipsoid plots of [FeCl(BisMesPDI)]PF_6 (**3**) drawn at the 50% probability level. H-atoms and PF_6 anion are omitted for clarity.

Table 5.2. Selected metrical parameters for complexes **2a**, **2b** and **3**.

	2a	**2b**	**3**
Fe(1)–N(1)	2.1225(18)	2.122(4)	2.114(4)
Fe(1)–N(2)	2.2750(18)	2.267(4)	2.252(4)
Fe(1)–N(3)	2.2438(18)	2.270(4)	2.219(4)
Fe(1)–Cl(1)	2.3057(7)	2.3085(14)	2.2411(15)
Fe(1)–Cl(2)	2.2896(7)	2.2920(15)	-
N(2)–C(6)	1.281(3)	1.279(6)	1.279(7)
N(3)–C(8)	1.283(3)	1.272(6)	1.277(7)
C(1)–C(6)	1.497(3)	1.478(7)	1.494(7)
C(5)–C(8)	1.493(3)	1.480(7)	1.493(7)
N(1)−Fe(1)−N(2)	72.09(6)	72.39(14)	72.71(15)
N(1)−Fe(1)−N(3)	72.95(7)	72.85(13)	73.33(16)
N(1)−Fe(1)−Cl(1)	113.67(5)	120.37(12)	139.66(11)
N(2)−Fe(1)−Cl(1)	100.32(5)	100.81(11)	104.47(11)
N(3)−Fe(1)−Cl(1)	99.24(5)	102.21(10)	102.78(12)
N(1)−Fe(1)−Cl(2)	140.59(5)	131.70(12)	-
N(2)−Fe(1)−Cl(2)	99.53(5)	99.98(12)	-
N(3)−Fe(1)−Cl(2)	103.33(5)	98.06(11)	-
Cl(1)−Fe(1)−Cl(2)	105.69(2)	107.93(6)	-
τ_5	0.06	0.22	0.11

[a] τ_5 is a metric for five coordinate complexes. τ_5 = 0 for a perfect square pyramid and τ_5 = 1 for a perfect trigonal bipyramid.

The Fe(III) trichloride bisphosphine complexes $FeCl_3L_2$ (L = PMe_3 (**4a**) and PMe_2Ph (**4b**)) were prepared by treatment of anhydrous $FeCl_3$ with the corresponding phosphine ligand in $PhCF_3$, as described previously.[39,40] The molecular structures of the compounds, shown in Figure 5.11 for **4b** feature Fe(III) centers in a distorted trigonal bipyramidal geometry with the chlorides residing in the equatorial plane. The X-ray structures of the corresponding $Fe(II)Cl_2L_2$ complexes

(L = PMe_3 (**5a**) and PMe_2Ph (**5b**)), prepared from the reaction of the corresponding phosphine ligands with $FeCl_2$ in THF, show a distorted tetrahedral geometry at the iron center as previously observed for **5a**[41] and shown in Figure 5.11 for **5b**.

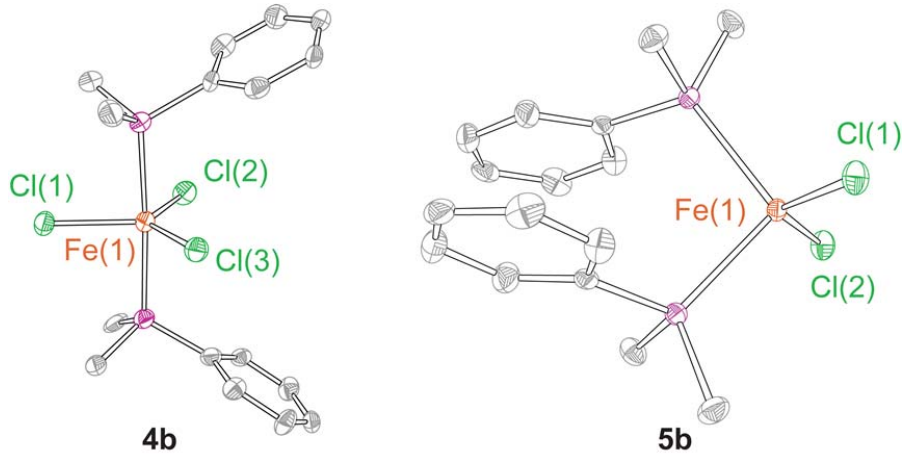

Figure 5.11. Thermal ellipsoid plot of $FeCl_3(PMe_2Ph)_2$ (**4b**) and $FeCl_2(PMe_2Ph)_2$ (**5b**) in which H-atoms have been removed for clarity. Ellipsoids are drawn at 50% probability.

The absorption profiles in the UV–vis spectra of the Fe(III) PDI and bisphosphine compounds are dominated by ligand-to-metal charge transfer (LMCT) transitions. Compounds **1a** and **1b** display significantly enhanced visible absorption as compared to their Fe(II) counterparts **2a** and **2b** (Figure 5.12). Similarly, the Fe(III) compounds of the bisphosphine series are intensely red to violet whereas the Fe(II) complexes are colorless (Figure 5.13). The photochemistry of the two series of compounds is consonant with their UV-vis spectra; whereas Fe(II) complexes are photochemically inert (λ_{exc} > 320 nm), the Fe(III) compounds are reactive under irradiation (λ_{exc} > 320 nm).

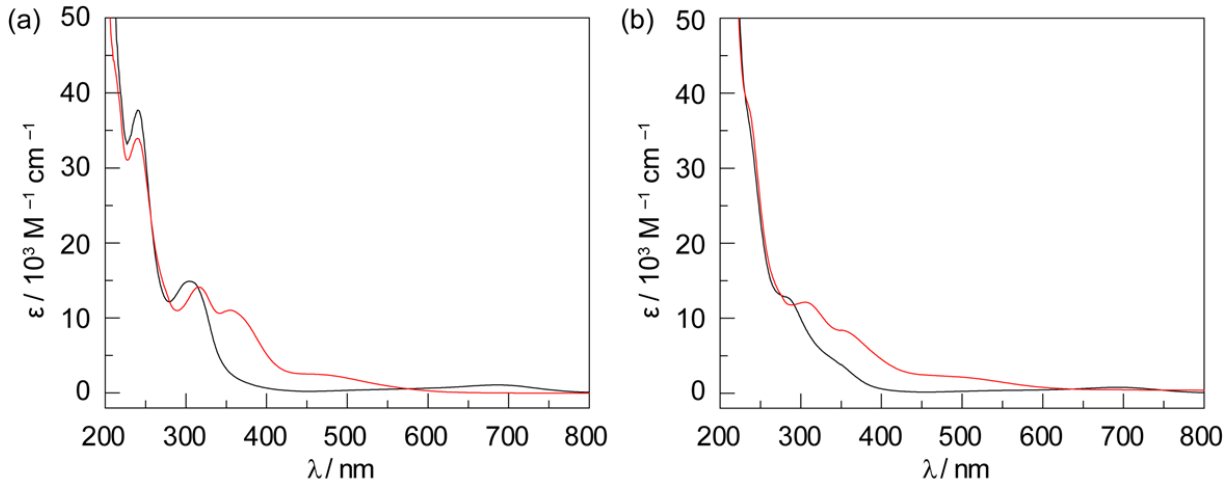

Figure 5.12. Extinction spectra of complexes (a) **1a** (—, red) and **2a** (—, black) and (b) **1b** (—, red) and **2b** (—, black).

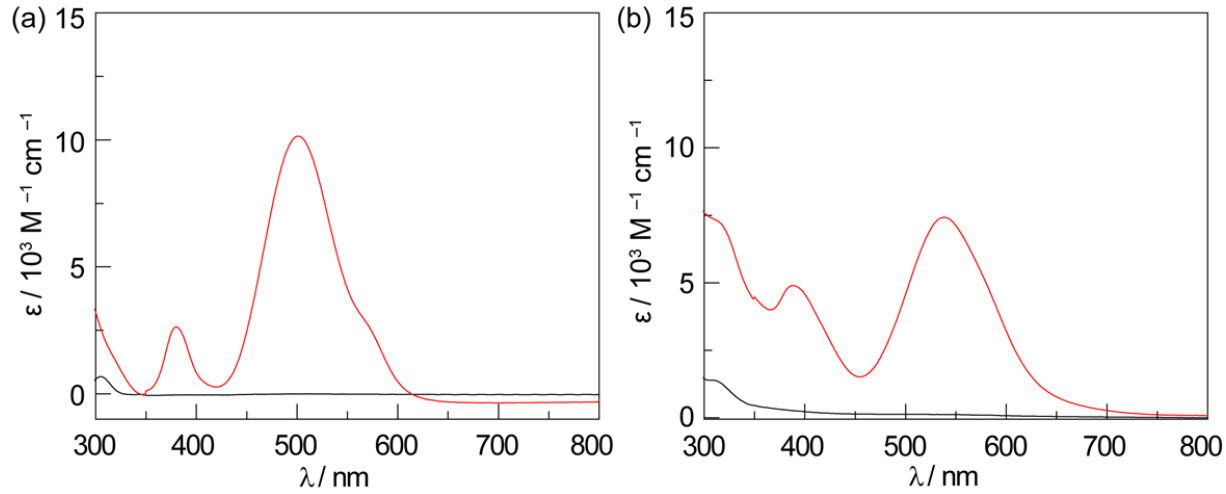

Figure 5.13. Extinction spectra of complexes (a) **4a** (—, red) and **5a** (—, black) and (b) **4b** (—, red) and **5b** (—, black).

5.3 Steady-state Photolysis in Solution

Figure 5.14 presents the spectral evolution of photolyzed (λ_{exc} > 320 nm) CH_3CN solutions of **1a** and **1b** in the presence of base (1,1-dimethyloxirane); in the absence of base, the photogenerated HCl leads to a deleterious dark reaction. The final spectrum matches that of

independently prepared samples of **2a** and **2b**, respectively. Photoreduction of the Fe center would be expected to generate a square-planar cationic Fe(II) intermediate. To verify this supposition, we have independently prepared this putative intermediate as compound **3**, which reacts smoothly with an equivalent of $^{n}Bu_4NCl$ to yield **2b**, as confirmed by ^{1}H NMR spectroscopy (Figure 5.15). Together these results establish an overall photoreaction corresponding to,

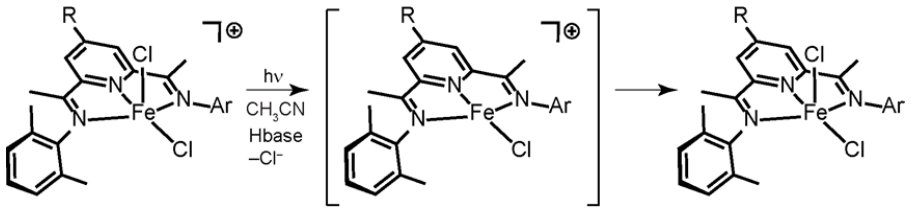

(3)

where the Fe(II) intermediate facilely reacts with chloride produced from the trapping of a photogenerated chlorine atom with solvent, as we have seen in halogen photoelimination reactions of numerous systems,[15, 42] and subsequent reaction with the oxirane base. The photochemical quantum yield for **1b** is greater by a factor of 1.5 than that for **1a** for excitation wavelengths spanning the near UV and visible (Table 5.3).

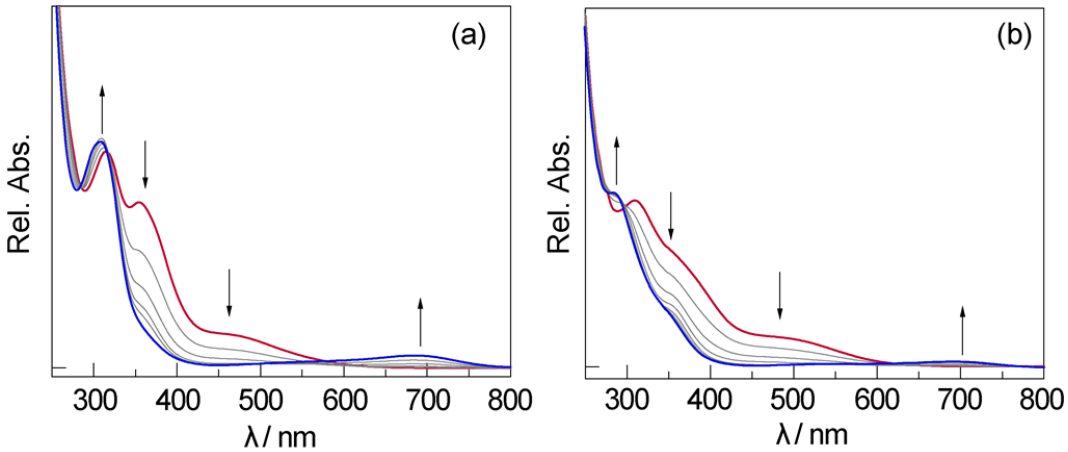

Figure 5.14. Spectra evolution during photolysis (λ > 320 nm) of PDI ferric complexes (a) **1a** and (b) **2a** in CH_3CN in the presence of 0.05 M 1,1-dimethyloxirane.

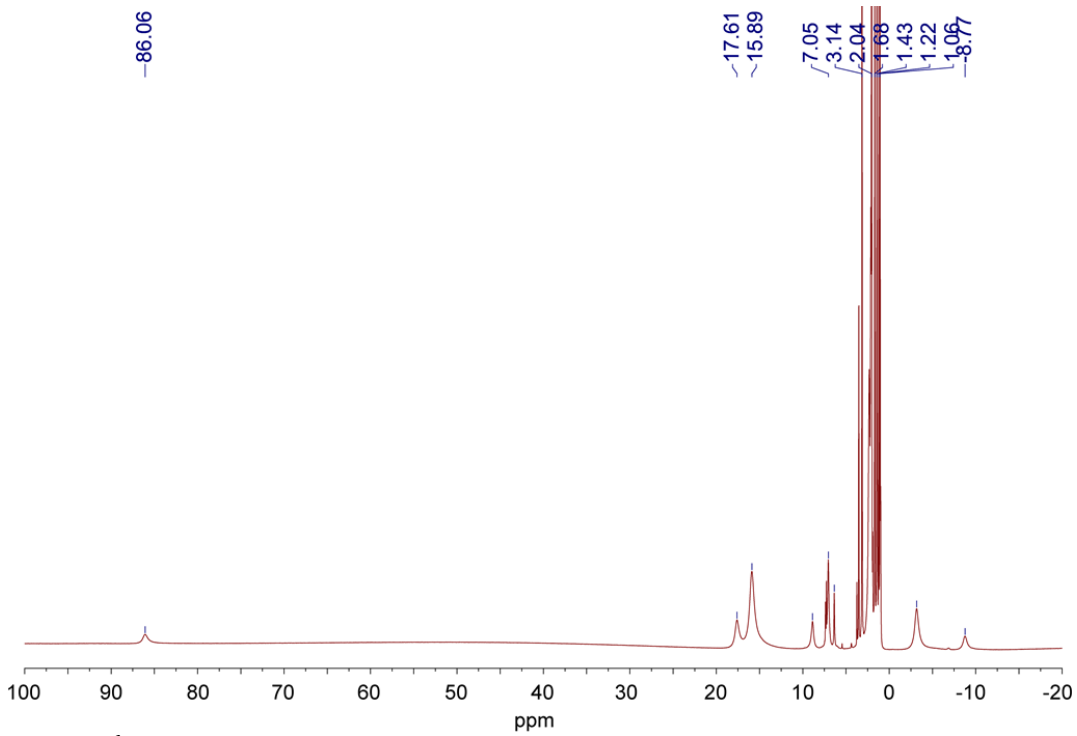

Figure 5.15. ^{1}H NMR spectrum of reaction of [FeCl(BisMesPDI)]PF_6 (**3**) with 1 equiv of $^{n}Bu_4NCl$ recorded in CD_3CN at 23 °C. The spectrum is identical to the spectrum of $FeCl_2$(BisMesPDI) (**2b**) with the addition of peaks attributable to $^{n}Bu_4N^{+}$.

Table 5.3. Summary of Photochemical Quantum Yield Data for **1a** and **1b**.

λ_{exc} (nm)	1a (%)	1b (%)
315	5.5 ± 0.2	8.5 ± 0.1
365	2.9 ± 0.1	4.4 ± 0.1
434	3.0 ± 0.1	4.2 ± 0.1

Wavelength-dependent quantum yield measurements (315, 365, and 434 nm) of halogen photoelimination from **1a** and **1b** in CH_3CN in the presence of 0.01 M 1,1,-dimethyloxirane. A potassium ferrioxalate standard actinometer was used to calculate quantum yields.[43,44]

Irradiation (λ_{exc} > 320 nm) of a CH_2Cl_2 solution of **4a** and **4b** in the presence of 1,1-dimethyloxirane gives rise to a LMCT photochemistry that is similar to that of the Fe(III) PDI complexes. The final photolysis spectrum is consistent with the one-electron reduced Fe(II)Cl_2L_2

photoproducts **5a** and **5b** (Figure 5.16).

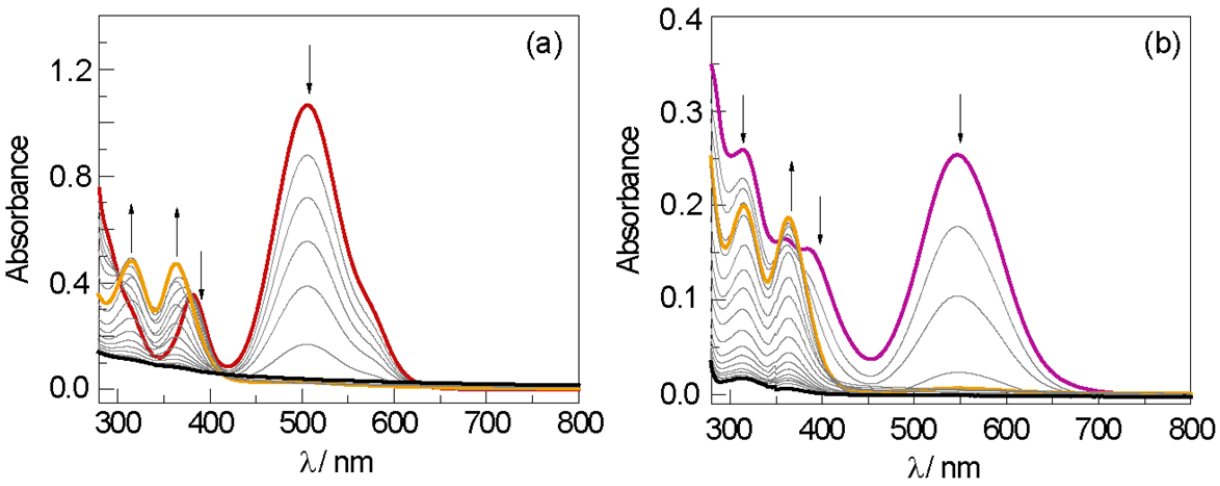

Figure 5.16. Spectral evolution during photolysis (λ_{exc} > 320 nm) of bisphosphine Fe(III) complexes (a) 4a (—) → [6 (—)] → 5a (—) and (b) 4b (—) → [6 (—)] → 5b (—) in CH_2Cl_2. The initial Fe(III) absorption profile evolves to that of Fe(III)Cl_3L and finally to the Fe(II) photoproduct. 6 is not isolated in the photolysis and hence is represented in brackets; the spectrum of the intermediate indicated by the yellow-orange trace (—) is similar to that of $FeCl_3$(XPhos), which was independently synthesized and characterized.

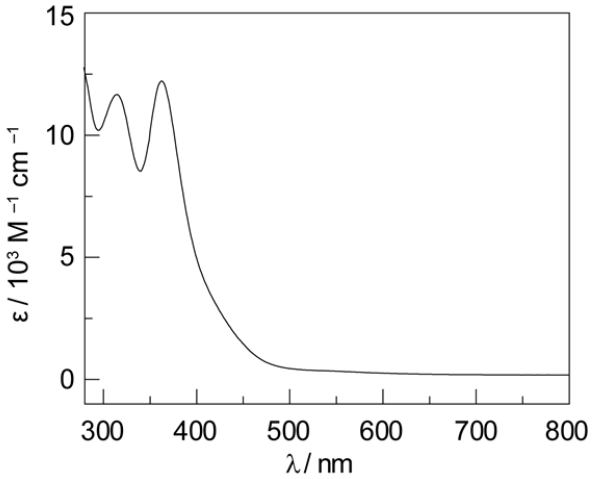

Figure 5.17. Extinction spectra of complex **6** (—, black).

However, unlike the PDI complexes, an absorption signature for an intermediate (λ_{max} = 320 nm) is observed during the photolysis that matches that of four-coordinate Fe(III)Cl_3L

complex (Figure 5.17), which has been independently prepared and isolated for bulky Xphos phosphine ligand, 2-dicyclohexylphosphino-2′,4′,6′-triisopropylbiphenyl (**6**) (^{1}H NMR spectrum, X-ray diffraction structure, and ^{57}Fe Mössbauer spectrum of **6** are presented in Figures 5.74, 5.18 and 5.19, respectively).

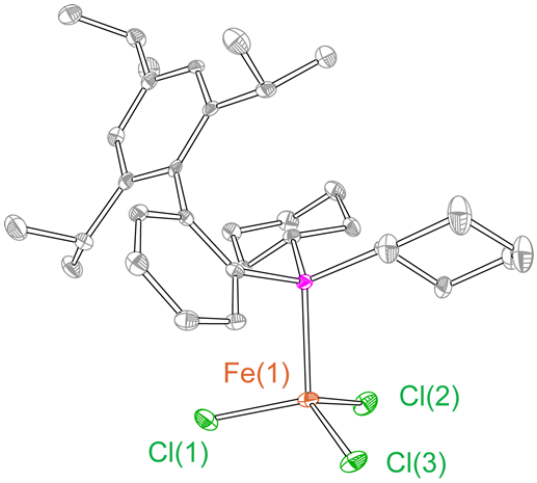

Figure 5.18. Thermal ellipsoid plot of $FeCl_3$XPhos (**6**) in which H-atoms have been removed for clarity. Ellipsoids are drawn at 50% probability.

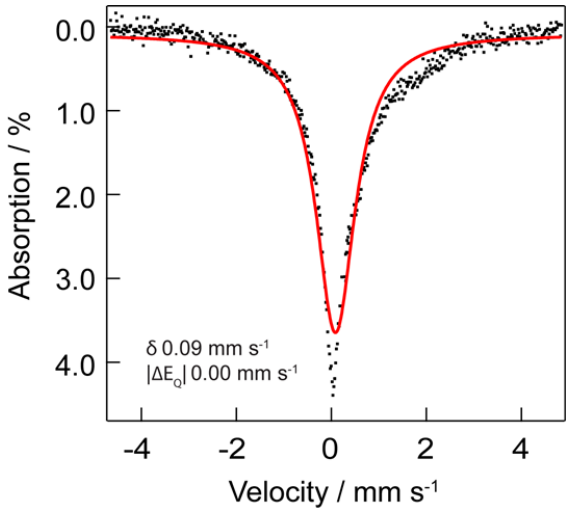

Figure 5.19. Zero-field ^{57}Fe Mössbauer spectrum of compound **6** recorded at 90 K. Isomer shift and quadrupole splitting are reported relative to Fe foil at room temperature.

The overall photochemical transformation is consistent with the reaction sequence,

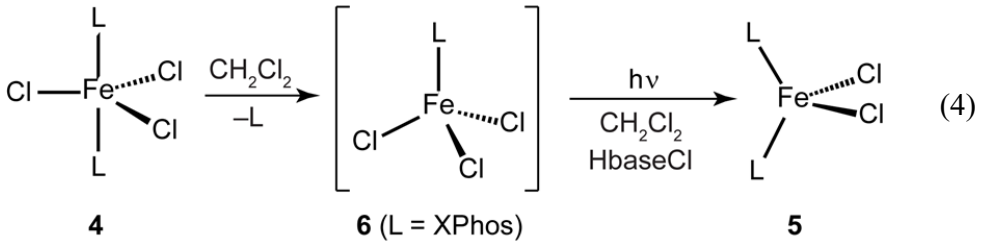

(4)

5.4. Time-Resolved Photochemistry

Based on the photolyses spectra, the primary photoevent for the Fe(III) PDI and bisphosphine compounds should be M–X bond homolysis to produce a chlorine atom. Nanosecond transient absorption (TA) spectra of **1b** support this contention. A prompt TA signal with a λ_{max} = 508 nm is observed immediately following excitation with a 355 nm laser pulse (Figure 5.20). The transient signal is spectrally similar to that of Cl•|arene charge transfer complexes generated by pulse-radiolysis and laser flash photolysis.[45]

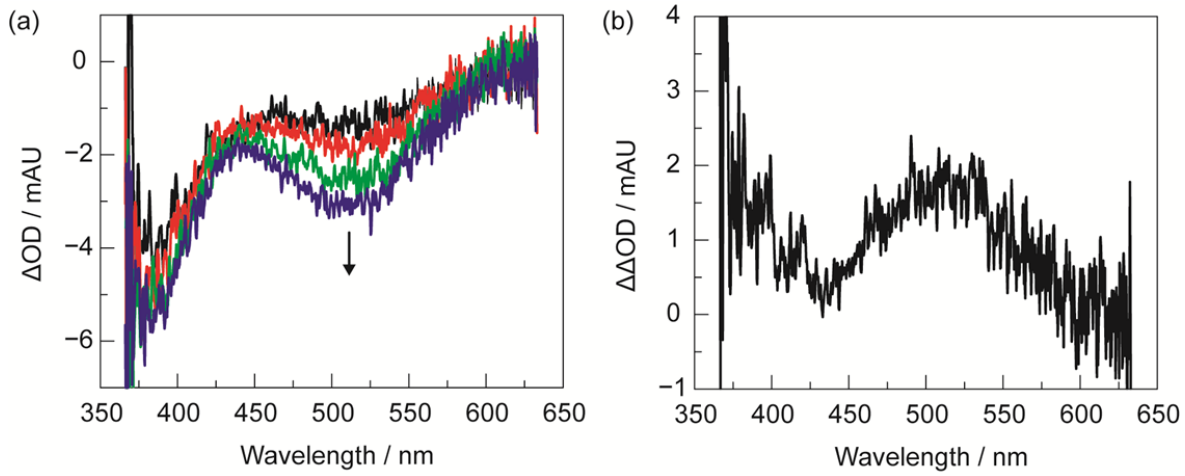

Figure 5.20. (a) Transient absorption spectra of a sample of **1b** in CH_3CN taken at the following time delays following excitation: 30 ns (—, black), 1.4 μs (—, red), 9.4 μs (—, green), and 20.0 μs (—, blue). (b) Difference spectrum generated by subtracting the TA spectrum taken at a 20 μs delay from the TA spectrum taken at a 30 ns delay. The 20 μs delay spectrum is that of the Fe(II) photoproduct; thus its subtraction from the 30-ns spectrum furnishes the primary photoproduct generated immediately after excitation.

5.5. Photocrystallographic Observation of M–X Bond Activation

The proposed Cl•|arene charge transfer complex is observed and structurally characterized by X-ray photocrystallography. Compound **1b** was subject to illumination with 300 nm laser light. Figure 5.21a shows the overlay of the crystal structure of **1b** in the absence (faded) and presence (solid) of laser irradiation. Only those atoms with an appreciable electron density (Fe and Cl) can be solved accurately in the photocrystallographic structure.

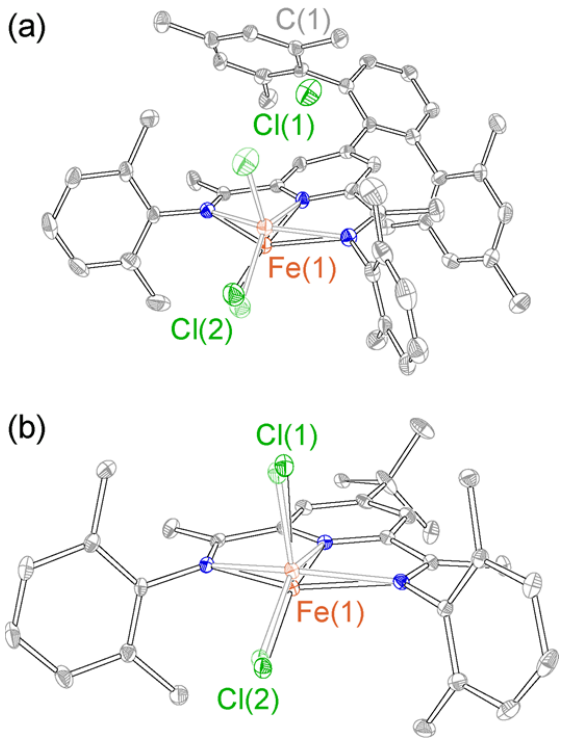

Figure 5.21. Photocrystallographic analysis of Fe(III) PDI complexes (a) **1b** and (b) **1c**. The photo-induced structure (solid) is superimposed on dark structure (faded). Δd(Fe–Cl1) = 1.896 Å (**1b**) and 0.473 Å (**1c**). H atoms, counter anions (BF_4 and PF_6), and solvent molecules have been omitted for clarity.

The two mesityl groups on the top and bottom of the pyridine ring in compound **1b** introduce a secondary coordination environment that promotes M–X photoactivation. For compound **1b**, 6.9% of the photoinduced structure was identified in the photodifference map in

which the basal Fe(1)–Cl(2) bond distance contracts from 2.1902(8) to 1.885(6) Å upon irradiation. A dramatic change is revealed for the apical Fe–Cl bond, which shows substantial elongation to the extent that the chlorine atom is dissociated from the Fe center (d(Fe(1)–Cl(1) = 2.1886(8) to 4.085(6) Å) and is associated to the mesityl ring sitting above the face of the PDI. The Cl• associates to the mesityl ring with a η^1 nearest contact distance of d(Cl(1)–C(1)) = 3.924 Å and a secondary distance to the next nearest carbon (d(Cl(1)–C(2)) = 4.010 Å) by virtue of the facial approach of the Cl• to the arene ring (Table 5.4).

Table 5.4. Selected metrical parameters for excited structure from complexes **1b**.

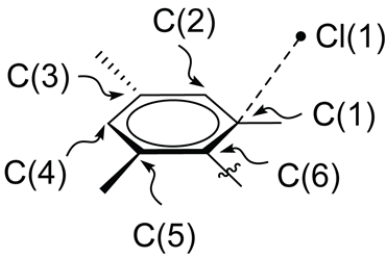

Bond	Distance / Å
Cl(1)–C(1)	3.924
Cl(1)–C(2)	4.010
Cl(1)–C(3)	5.158
Cl(1)–C(4)	6.000
Cl(1)–C(5)	5.974
Cl(1)–C(6)	5.015

Variable-temperature diffraction measurements (Figure 5.22 and Tables 5.5–5.8) establish that the bond length changes in the photodifference map are due to irradiation and not due to laser heating. The photocrystallographic solution of **1b** represents the first direct structural observation of a Cl•|arene charge transfer complex.

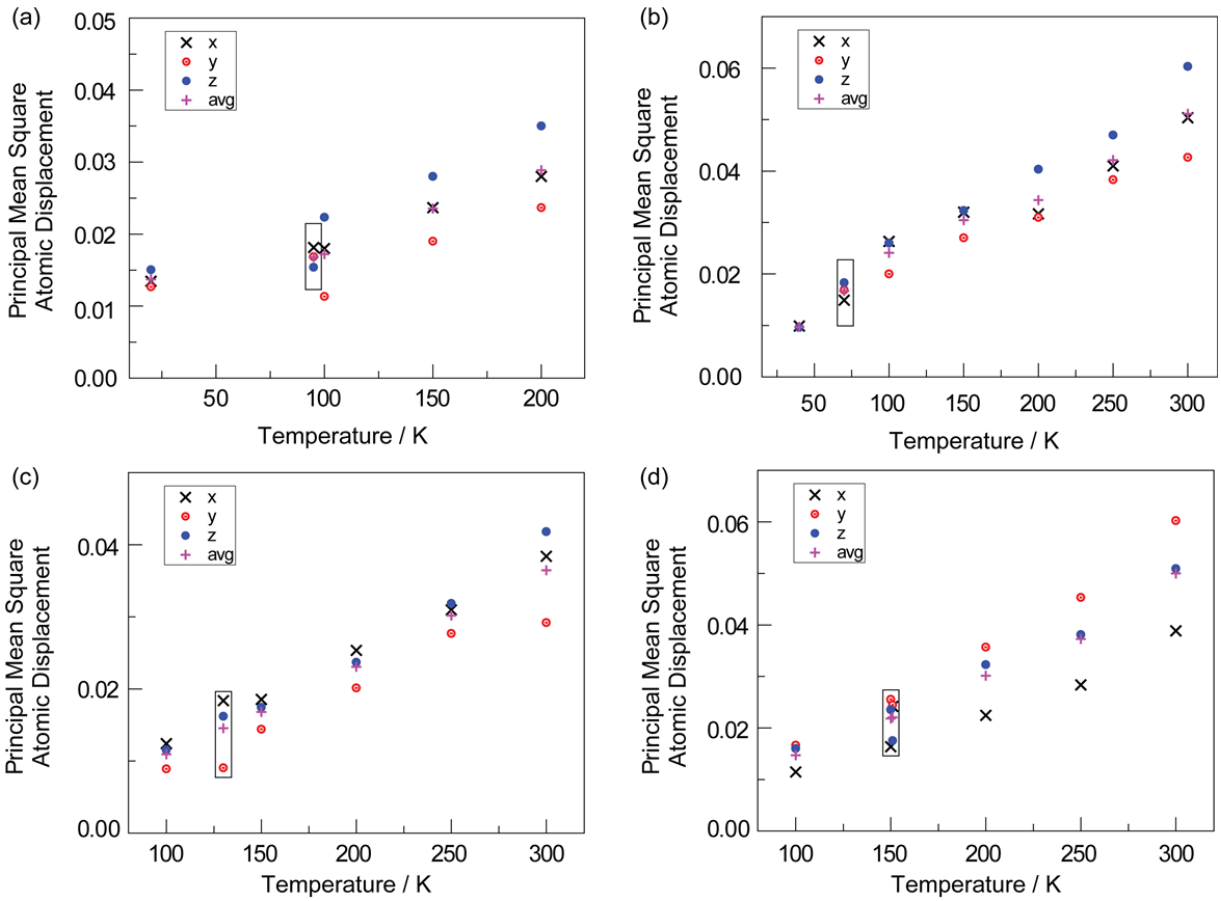

Figure 5.22. Principal mean square atomic displacements (U) for Complex (a) **1b** (b) **1c** (c) **4a**, and (d) **4b** as a function of temperature plotted for nitrogen and phosphorus atoms. Thermal parameters obtained during photocrystallography are highlighted in a box.

Table 5.5. Selected metrical parameters for complex **1b** as a function of temperature.

	Fe–Cl(1) (Å)	Fe–Cl(2) (Å)	Fe–N(1) (Å)	Fe–N(2) (Å)	Fe–N(3) (Å)
100 K	2.2368(19)	2.2216(19)	2.096(5)	2.213(5)	2.206(5)
150 K	2.2323(19)	2.2236(19)	2.091(5)	2.213(5)	2.201(5)
200 K	2.2367(19)	2.2191(19)	2.095(5)	2.215(5)	2.225(5)

Table 5.6. Selected metrical parameters for complex **1c** as a function of temperature.

	Fe–Cl(1) (Å)	Fe–Cl(2) (Å)	Fe–N(1) (Å)	Fe–N(2) (Å)	Fe–N(3) (Å)
20 K	2.20084(12)	2.20544(13)	2.0674(3)	2.1888(3)	2.1707(3)
100 K	2.194(3)	2.191(3)	2.051(6)	2.189(7)	2.166(7)
150 K	2.188(2)	2.187(2)	2.050(5)	2.161(6)	2.191(6)
200 K	2.186(2)	2.183(2)	2.060(5)	2.167(5)	2.184(5)
250 K	2.180(3)	2.175(2)	2.050(5)	2.187(5)	2.166(5)
300 K	2.177(3)	2.175(2)	2.058(5)	2.188(5)	2.172(5)

Table 5.7. Selected metrical parameters for complex **4a** as a function of temperature.

	Fe–Cl(1) (Å)	Fe–Cl(2) (Å)	Fe–Cl(3) (Å)	Fe–P(1) (Å)	Fe–P(2) (Å)
20 K	2.2491(3)	2.2678(2)	2.2678(2)	2.3338(3)	2.3474(3)
100 K	2.2375(10)	2.2525(6)	2.2526(6)	2.3217(10)	2.3346(10)
150 K	2.2342(9)	2.2498(6)	2.2498(6)	2.3212(9)	2.3336(9)
200 K	2.2353(9)	2.2480(6)	2.2480(6)	2.3231(9)	2.3344(9)
250 K	2.2251(12)	2.2372(9)	2.2372(9)	2.3170(12)	2.3296(13)
300 K	2.232(2)	2.2481(13)	2.2481(13)	2.3330(18)	2.3403(19)

Table 5.8. Selected metrical parameters for complex **4b** as a function of temperature.

	Fe–Cl(1) (Å)	Fe–Cl(2) (Å)	Fe–Cl(3) (Å)	Fe–P(1) (Å)	Fe–P(2) (Å)
20 K	2.2339(5)	2.2495(5)	2.2994(5)	2.3583(5)	2.3624(5)
100 K	2.2168(7)	2.2284(7)	2.2825(7)	2.3411(7)	2.3493(7)
150 K	2.2174(6)	2.2266(6)	2.2807(6)	2.3424(6)	2.3500(6)
200 K	2.2155(6)	2.2251(6)	2.2768(6)	2.3443(6)	2.3515(6)

250 K	2.2160(8)	2.2249(8)	2.2735(7)	2.3470(7)	2.3546(7)
300 K	2.2156(8)	2.2241(10)	2.2699(9)	2.3575(8)	2.3639(8)

To authenticate the effect of the secondary coordination sphere on halogen photoelimination, photocrystallography was undertaken on a PDI complex in which an arene proximate to the Fe-Cl_{ax} is absent. Complex **1a** could not be used in these experiments because of crystallographic disorder in the solid-state (dark) structure. Accordingly, **1c** was prepared so as to mimic the presence of steric bulk at the 4-position of the pyridine ring but in the absence of arene. The steady-state photocrystallographic structure with 2.6% photo–induced population (Figure 5.21b) shows elongation of the apical Fe–Cl(1a) bond from 2.1927(2) Å (faded) to 2.666(9) Å (solid) under illumination; no change is observed for the equatorial Fe–Cl bond (d = 2.2042(3) Å (dark) and 2.240(11) Å (photoinduced). Thus, in the absence of the arene ring, a dissociated Cl• atom is not observed in the photocrystallographic structure of **1c**.

The photocrystallography of Fe(III)$Cl_3(L)_2$ complexes **4a** and **4b** show that the chlorine Cl(1) and iron Fe(1) atoms move away from one another (Figure 5.23), towards the pseudotetrahedral structure of Fe(II)$Cl_2(L)_2$ (Figure 5.24). This photoinduced structural change is apparent in the changes to the P(1)–Fe(1)–P(2) bond angle (**4a**: 176.856(6) to 150.9(1)° and **4b**: 175.103(6) to 154.6(0)°). The solid-state photoreactivity of the Fe(III)$Cl_3(L)_2$ differs from the PDI system in that the Cl•|arene charge transfer interaction is intermolecular. As highlighted in Figure 4, one of the Fe–Cl bonds in the equatorial plane in complex **4b** elongates from 2.2480(2) to 3.53(3) Å. As observed for the Cl•|arene charge transfer interaction in **1b**, an η^1 interaction is observed for the photoeliminanted chlorine atom's approach (d(Cl(1)–C(1)) = 3.159 Å) to the phenyl ring of its neighboring molecule (Table 5.9).

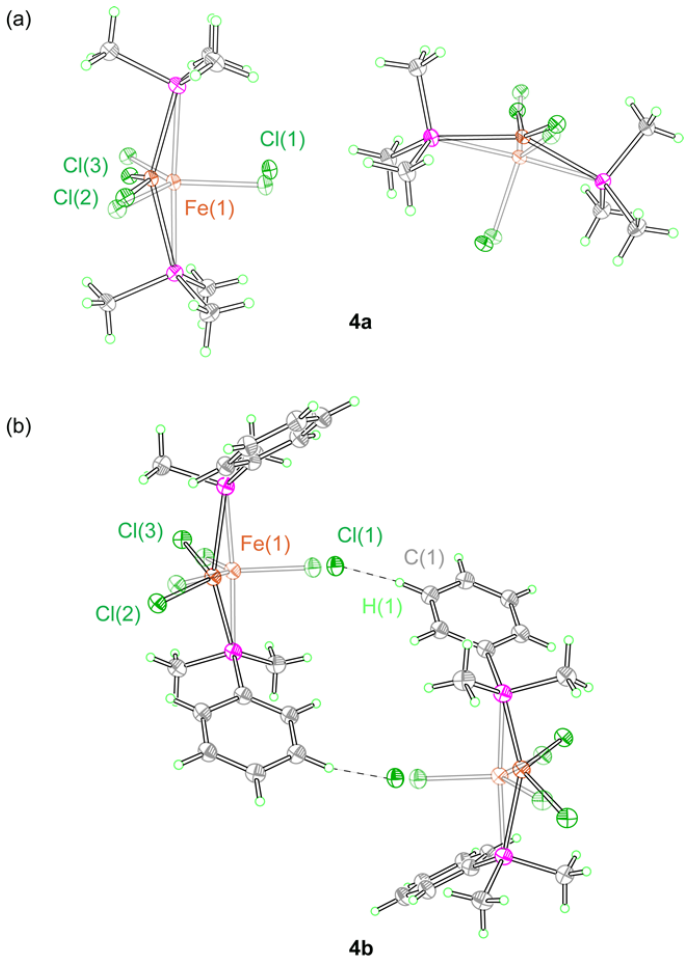

Figure 5.23. Photocrystallographic analysis of Fe(III) phosphine complexes (a) **4a** and (b) **4b**. The photo-induced structure (solid) is superimposed on dark structure (faded). $\Delta d(Fe–Cl_{eq})$ = 0.682 Å (**4a**) and 1.28 Å (**4b**) respectively.

The nature of the interaction between Cl• and arene rings is a longstanding issue[46,47] that has yet to be resolved owing to the reactivity of the Cl• atom. The interaction was initially postulated to be η^6,[48,49] followed by the contention of a σ complex (chlorocyclohexadienyl radical)[50] as well as intermediate structures between η^6 and σ complexes.[51] DFT studies examining a range structures showed the η^1 Cl•|arene interaction to be most stable,[32] as we have now observed by photocrystallography. An arene in the secondary coordination sphere provides a stabilizing element for the eliminating Cl• atom, thus suppressing its rapid back reaction with

the metal center as reflected in the greater photochemical quantum yields of **1b**. As the photogeneration of halogen atoms is finding increased utility in photoredox-mediated organic chemistry and is the primary photochemical event of M–X bond activation for energy conversion cycles, Cl•|arene stabilization via a secondary coordination sphere offers a new design concept for synthetic and energy conversion photochemistry.

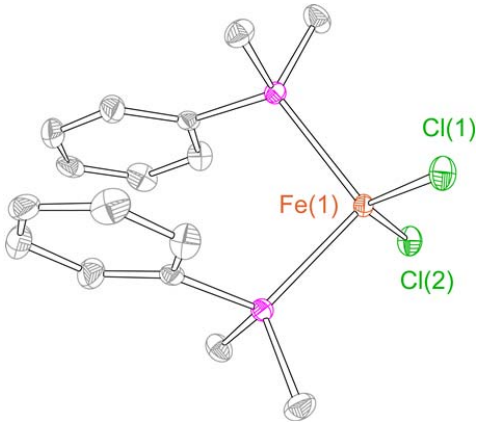

Figure 5.24. Thermal ellipsoid plot of $FeCl_2(PMe_2Ph)_2$ (**5b**) in which H-atoms have been removed for clarity. Ellipsoids are drawn at 50% probability.

Table 5.9. Selected metrical parameters for excited structure from complexes **4b**.

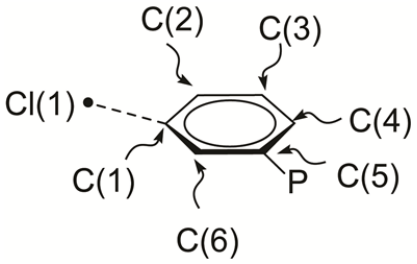

Bond	Distance / Å
Cl(1)–C(1)	3.165
Cl(1)–C(2)	4.391
Cl(1)–C(3)	5.523
Cl(1)–C(4)	5.696
Cl(1)–C(5)	4.805
Cl(1)–C(6)	3.446

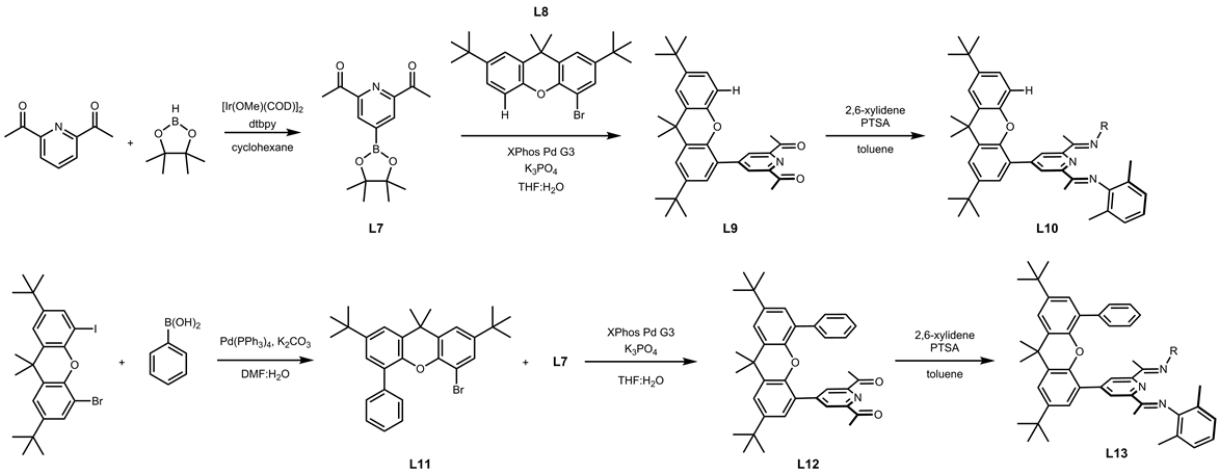

Figure 5.25. Synthetic scheme for new PDI ligands.

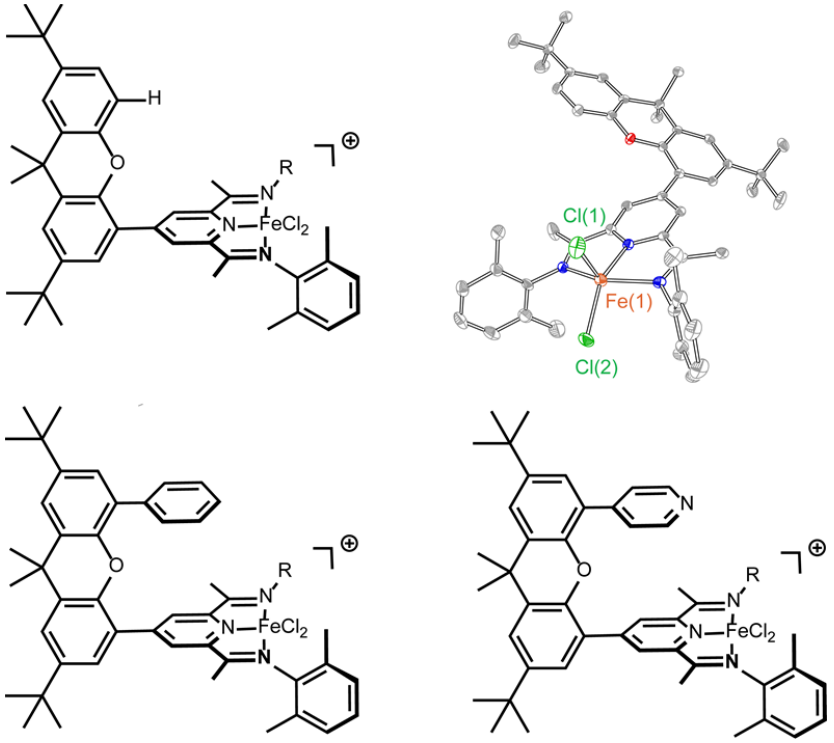

Figure 5.26. Three new class of Fe(III) complexes and Thermal ellipsoid plots.

The installation of acid/base groups on functionalized xanthene moieties called “hangman effect” has proven beneficial in numerous catalytic reactions. The Nocera group also designed the new set of PDI ligands in order to maximize the secondary coordination sphere effects for the

high reactivity of halogen photoelimination reactions motivated by our photocrystallograpic data described above. These new xanthene based PDI ligands were readily accessible by two sequential Pd-catalyzed cross-coupling reactions with commercially available dibromoxanthene (Figure 5.25). SP Fe(III) cationic complexes with new ligand set were prepared in a similar way as described before and one of the solid state structure was characterized by X-ray diffraction analysis (Figure 5.26). QY measurement as well as time-resolved transient absorption spectroscopy will be conducted to better understand the arene-hangman effect for M–X bond activation in a systematic way.

5.6. Evaluation of the Electronic Effects on Photohalogen Elimination Reactions

Fundamental understanding of electronic and geometric effects in the photoefficiency of halogen elimination reactions is still lacking. Given the well-defined redox activity of bis(imino)pyridines, we continued our efforts toward the systematic evaluation of the electronic effects of 4-substitued bis(imino)pyridine Fe(III) complexes on halogen photoelimination reactions.

5.6.1. Scalable and Efficient Method for Synthesizing 4-substitued PDI Ligands

Electronic structure studies of PDI metal complexes show that substitution in the 4-position is more profound than at the imine arene, which assumes an orthogonal π-orientation to the pyridine ring.[52] Owing to strong delocalization through the backbone of the pyridine ring, large shifts in the redox potential of PDI metal complexes span 600 mV with substitution in the 4-position.[53] However, the synthesis of 4-substituted pyridine-diiimines has long been hampered by lengthy syntheses that often require pyrophoric reagents and Schlenk techniques.[53] The ability to rapidly prepare 4-substituted PDI ligands in usable quantities from readily available starting

materials is therefore beneficial to expanding the utility of PDI chemistry.

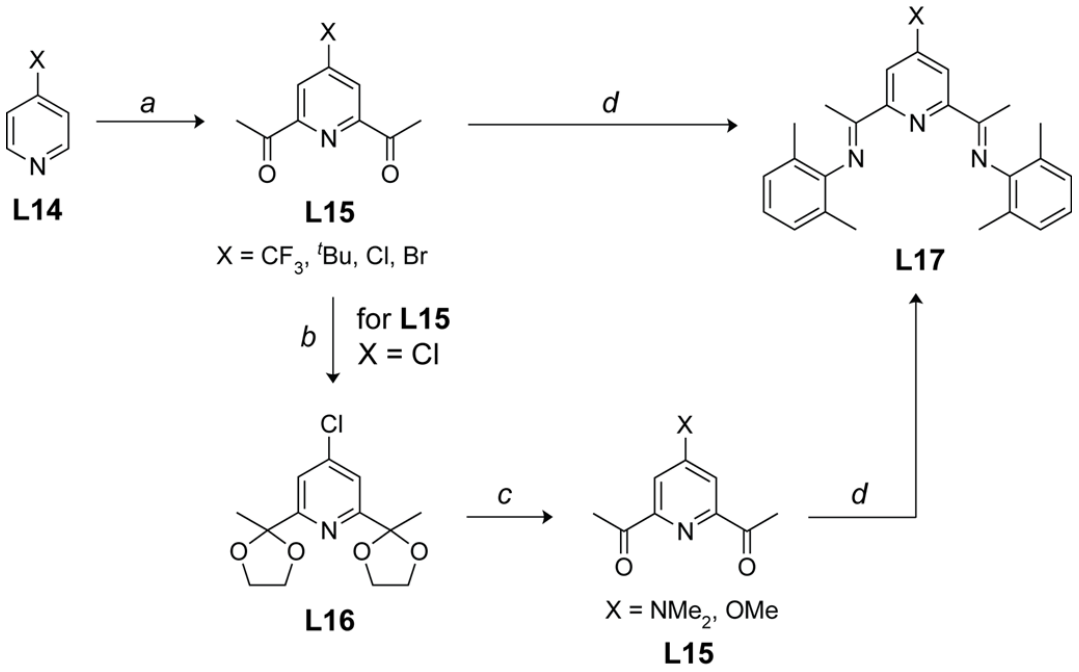

Figure 5.27. Synthetic route for the facile preparation of 4-subsituted PDIs: (a) $AgNO_3$, pyruvic acid, $Na_2S_2O_8$, 0.5 M H_2SO_4, RT. (b) ethylene glycol, PTSA, $PhCH_3$, 145 °C. (c) X = OMe: NaOMe, DMSO, 110 °C, HCl, 80 °C; X = NMe_2: 40% NMe_2 in H_2O, NaOH, DMSO, 110 °C, HCl, 80 °C. (d) 2,6 dimethylyaniline, PTSA, $PhCH_3$, 145°C.

In this section, we report a rapid, scalable, and general method for synthesizing PDI scaffolds with a range of electron donating and withdrawing groups at the 4-position. The PDI ligand is delivered from inexpensive commercial starting materials and purification of the ligand requires at most two columns, and one of these columns is run in neat CH_2Cl_2, allowing for solvent recycling. All steps are performed on the benchtop and do not require the use of Schlenk techniques, distillations, nor do they require the use of air or moisture sensitive reagents. Additionally, only one metal catalyzed step employing silver nitrate is needed, further reducing the cost and risk of contamination of the final ligand product. This latter feature is important for catalytic applications, particularly in the context of energy conversion reactions such as the hydrogen evolution reaction (HER) where trace Pd (used in cross coupling) may remain as a

contaminant,[54] which performs the HER.[55] Finally, the scalability of these synthetic routes and the use of inexpensive reagents pushes the accesibility of these PDIs to large scale synthesis.

Figure 5.27 summarizes the synthetic routes employed to deliver 4-substituted PDIs. Though the six diacetylpyridines shown in Figure 5.27 have been previously reported by other methods, their syntheses are not general and involve expensive, pyrophoric/toxic reagents and many lengthy steps.

A generalized synthesis of the PDIs begins with the key diacetylation step (a). A general method was developed for pyridine starting materials containing electron deficient (CF_3, Cl, and Br) or bulky groups (^{t}Bu) at the 4-position of the pyridine ring (**L14-X**) based on the Minisci reaction, which has been used previously to obtain the 4-chloro-2,6-diacetylpyridine **L15** (X = Cl, **L15-Cl**) and 4-cyano-2,6-diacetylpyridine.[56,57] Here, a simpler overall procedure resulted from the modification of the oxidant from ammonium persulfate to sodium persulfate and changes to the work up and purification such that **L14-Cl** does not need to be isolated, thus avoiding the complication of polymerization to insoluble and unreactive polypyridyl polymer. We began from the hydrochloride salts of **L14-X** (X = Cl, Br) compounds where polymerization was possible and generated the free base in solution, never allowing the solution to become concentrated. The diacetyl pyridines are directly furnished from the acyl Minisci reaction. The overall yields to arrive at the key diacetylpyridine intermediates **L15** and **L17** and the number of steps required are given in Table 5.10. In the case of **L14-Br** this synthetic method avoids the use of costly chelidamic acid and toxic PBr_5 to furnish an unstable intermediate that must be vacuum distilled under rigorously air free conditions.[58] Further, our method does not require the use of organo-lithium reagents.

Table 5.10. Yields for linear syntheses of 4-substituted diacetyl pyridines **L15** and the number of steps with the respective Hammett sigma parameters and λ_{max}. Yields represent isolated yields.

X	Yield[Steps][a]	Yield[Steps] [b]	σ_{para}[59]	λ_{max} [e] (nm)
CF_3	47%[1][d]	26%[5][53,c]	0.54	354
Cl	26%[1] [d]	25%[1][56,d]	0.23	351
Br	16%[1] [d]	41%[3][58,c]	0.23	351
^{t}Bu	17%[1] [d]	82%[1][60,c,d]	–0.20	340
OMe	20%[3] [d]	12.5%[6][61,c]	–0.27	338
NMe_2	17%[3] [d]	16%[5][53,c,d]	–0.83	334

[a] This work. [b] Previous work. [c] Pyrophoric/Toxic Reagents. [d] Multi–gram scale. [e] For compound 4–X.

That the 4-trifluoromethy-2,6-diacetylpyridine, **L15-CF_3**, was furnished in one step using the aforementioned acylation procedure represents a marked improvement over the current procedures, which begin from the expensive chelidamic acid and requires 5 steps, including a palladium catalyzed coupling, to arrive at the desired diacetyl product.[53] The method reported here begins from 4-trifluromethylpyridine **(L14-CF_3)** and requires only one step and no need for dry solvent, expensive metallic reagents, or pyrophoric reagents. The previous synthesis of the 4-*tert*-butyl-2,6-diacetylpyridine **(L15-^{t}Bu**) requires the expensive diacetylpyridine starting reagent, the use of chlorobenzene as a solvent and elevated temperatures in an inert atmosphere. Moreover, the product requires distillation and it is isolated as an oil.[60] Our method utilizes readily available **1-^{t}Bu** and arrives at the product as a white solid in one step using aqueous conditions at room temperature. In order to arrive at the **L15-OMe** and **L15-NMe_2**, we made use of the readily accessible **L15-Cl** and protected the reactive acyl group using ethylene glycol to generate the base and temperature stable cyclic ketal **L16**. Though propylene glycol has been used as a protecting group for a similar reaction, it tends to be more labile when compared to the 1,2 diol protecting group.[62] Compound **L16** is easily converted to the desired dimethylamino

(L15-NMe_2) and methoxy substituted pyridine **(L15-OMe)** in a sealed glass pressure flask by nucleophilic aromatic substitution in dimethylsulfoxide via the in-situ generation of sodium dimethylamide and sodium methoxide respectively. This transformation was achieved using 40% dimethylamine and sodium hydroxide to generate **L15-NMe_2** and methanol and sodium hydroxide to generate **L15-OMe**. The addition of the methoxy group can also be achieved by the direct addition of sodium methoxide in comparable yields. In both cases simple aqueous work-ups followed by acid hydrolysis in hydrochloric acid afforded **L15** (X=OMe, NMe_2) without any further purification necessary. Direct acylation was attempted for the electron rich 4-methoxypyridine (**L14-OMe**), yielding an inverse selectivity with the 3,5-diacetyl product obtained instead of the desired 2,6-diacetyl product. Meanwhile the 4-dimethylaminopyridine (**L14-NMe_2**) yielded no reaction at the desired ring positions. This synthetic protocol arrives at **L15-OMe** and **L15-NMe_2** in 6 and 5 steps, respectively, in lower yields utilizing harsh, toxic and air-sensitive reaction conditions.

With the 4-substituted diacetyl pyridines **L15** in hand, we sought to improve current methods for condensing the diacetyl-pyridine with dimethylaniline to yield the desired pyridine diimines **L17**. Current condensation methods involve refluxing in toluene or methanol for several days (36-72 h).[53] Approaches utilizing shorter reaction times (6 h) require the use of harsh solvents, which are difficult to remove such as acetic acid.[63] By using elevated temperatures (145 °C) and a larger volume of solvent (60 mL/mmol) as well as a short path Dean-Stark trap, we were able to promote the clean conversion to the desired PDIs in 12 h. Additionally, we found that a simple base work-up allowed for isolation of the pure material without further purification. Despite the use of excess toluene as a solvent, it can be recycled easily between reactions. The colors of the PDIs correlate with the electron withdrawing or

donating nature of the 4-substituent on the pyridine ring (Table 5.10), with the trifluoromethyl substituted PDI appearing bright yellow and the dimethylamino substituted PDI appearing bright white. This trend in compound color was corroborated by the UV-vis spectra (Figure 5.28).

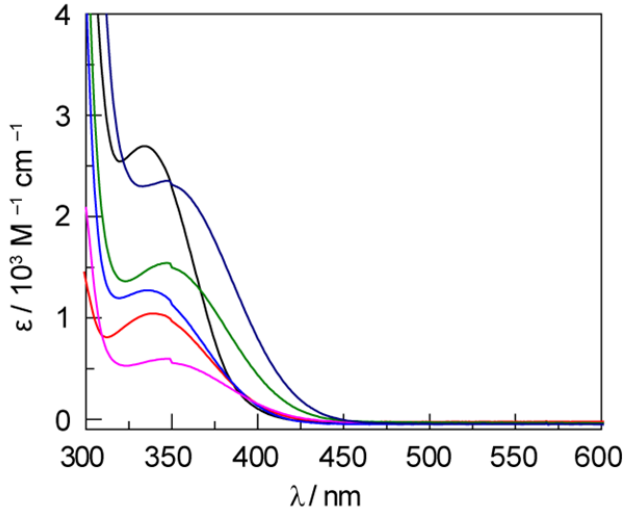

Figure 5.28. Extinction spectra of 4-X-pyridinediimines (**L17-X**) in CH_2Cl_2, X = NMe_2 (—, black), OMe (—, red), ^{t}Bu (—, blue), Br (—, magenta), Cl (—, green), and CF_3 (—, dark blue).

5.6.2. Synthesis and photochemistry of Fe(III) complexes with 4-substitued PDI ligands

Synthesis of the $[Fe(III)Cl_2(4R\text{-}PDI)]^+$ complexes **7a–7g** bearing each of the 4-substitued PDI ligands (R = CF_3, Cl, Br, H, ^{t}Bu, OMe, NMe_2) was accomplished by stirring the free ligand with anhydrous $FeCl_3$ and $AgPF_6$ salt in CH_3CN solution for 2 h followed by filtration of AgCl. Five examples (R = Cl, Br, ^{t}Bu, OMe, NMe_2) were characterized by X-ray diffraction, and representations of the solid-state structures are shown in Figure 5.29. Distorted square-pyramidal geometries were observed with two Cl atoms in the apical and basal positions from five-coordinate $[Fe(III)Cl_2(4R\text{-}PDI)]^+$ complexes. All five crystallographically characterized Fe(III) complexes exhibit near-identical metric parameters, indicating that modification of 4-substituent groups does not significantly alter the steric environment imparted by the PDI ligand (Table 5.11). A series of electrochemical and spectroscopic measurements were made on each of

compounds to determine the electronic influence on each of Fe metal centers.

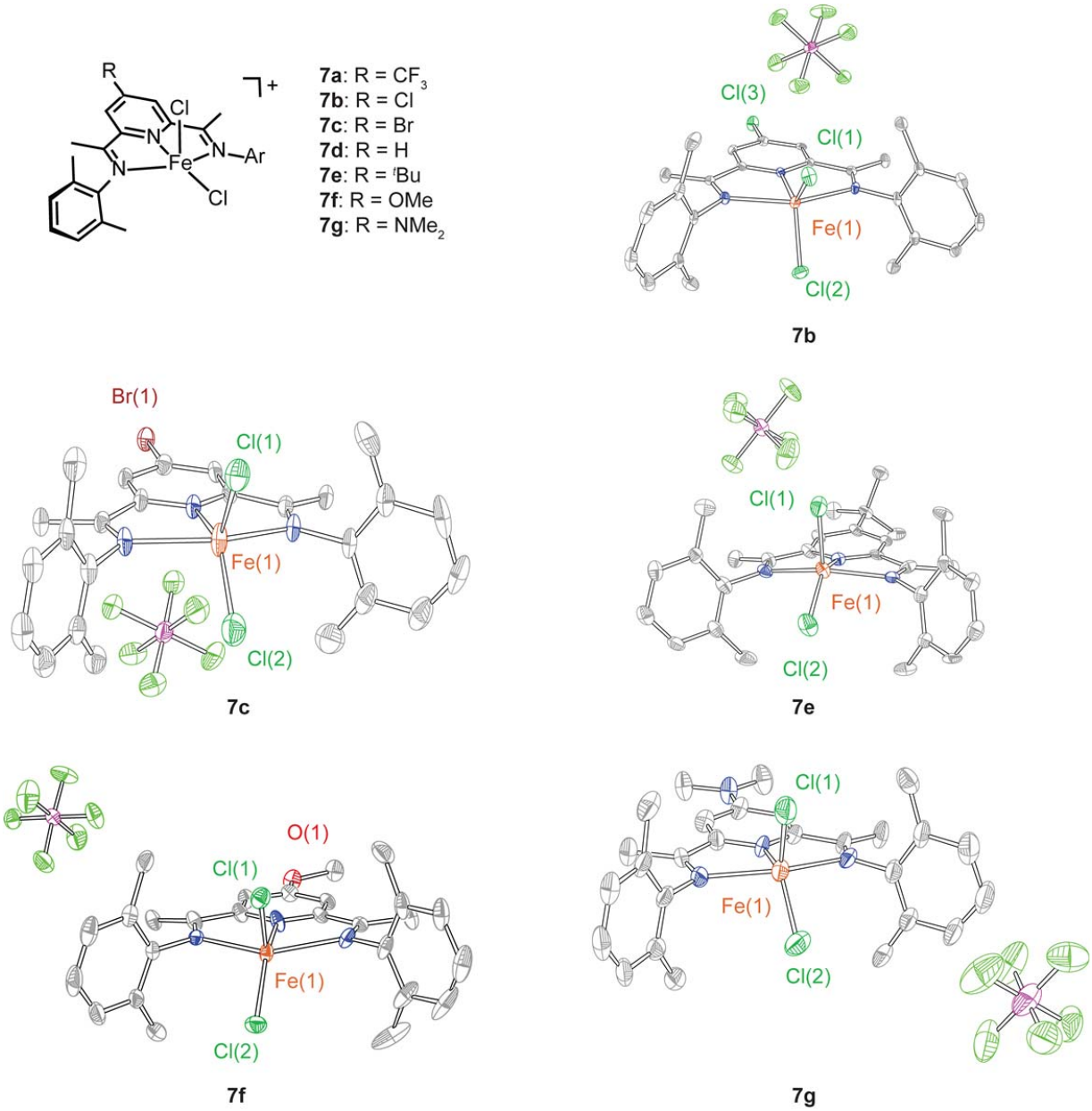

Figure 5.29. Thermal ellipsoid plots of $[Fe(III)Cl_2(4R\text{-}PDI)]^+$ complexes in which H-atoms and solvents have been removed for clarity. Ellipsoids are drawn at 50% probability.

Table 5.11. Selected metrical parameters for complexes **7b**, **7c**, **7e**, **7f**, and **7g**.

	7b	**7c**	**7e**	**7f**	**7g**
Fe(1)–N(1)	2.071(3)	2.087(4)	2.063(8)	2.027(7)	2.018(5)
Fe(1)–N(2)	2.194(3)	2.190(4)	2.164(8)	2.233(7)	2.188(4)
Fe(1)–N(3)	2.171(3)	2.179(4)	2.172(8)	2.124(7)	2.178(5)
Fe(1)–Cl(1)	2.1776(12)	2.1766(18)	2.178(3)	2.216(4)	2.1756(19)
Fe(1)–Cl(2)	2.1688(12)	2.209(2)	2.177(3)	2.210(6)	2.1745(18)
N(2)–C(6)	1.282(5)	1.277(7)	1.288(12)	1.275(5)	1.260(7)
N(3)–C(8)	1.291(5)	1.282(7)	1.289(12)	1.274(5)	1.277(8)
C(1)–C(6)	1.491(5)	1.490(8)	1.468(13)	1.485(5)	1.479(8)
C(5)–C(8)	1.485(5)	1.490(7)	1.490(13)	1.493(5)	1.521(8)
N(1)−Fe(1)−N(2)	74.05(12)	73.70(17)	73.5(3)	73.5(2)	74.47(18)
N(1)−Fe(1)−N(3)	74.21(12)	73.82(17)	74.1(3)	75.8(2)	74.80(19)
N(1)−Fe(1)−Cl(1)	111.35(9)	115.92(13)	108.9(2)	113.1(2)	114.04(15)
N(2)−Fe(1)−Cl(1)	100.41(9)	100.40(13)	102.2(2)	89.62(17)	98.61(15)
N(3)−Fe(1)−Cl(1)	99.33(9)	99.51(13)	100.5(2)	93.6(2)	99.46(14)
N(1)−Fe(1)−Cl(2)	138.70(9)	136.24(14)	140.7(2)	146.5(2)	137.02(15)
N(2)−Fe(1)−Cl(2)	97.19(9)	97.30(14)	97.5(2)	108.1(3)	98.97(14)
N(3)−Fe(1)−Cl(2)	100.60(9)	101.48(14)	99.1(2)	102.7(2)	99.12(13)
Cl(1)−Fe(1)−Cl(2)	109.92(5)	107.79(7)	110.40(13)	100.4(2)	108.94(8)
τ_5	0.45	0.34	0.51/0.39	0.56	0.38

[a] τ_5 is a metric for five coordinate complexes. $\tau_5 = 0$ for a perfect square pyramid and $\tau_5 = 1$ for a perfect trigonal bipyramid.

Electrochemical studied were carried out on the crystalline materials of $[Fe(III)Cl_2(4R\text{-}PDI)]^+$ complexes and cyclic voltammogram recorded in CH_3CN is presented in Figure 5.30a. The redox potentials of Fe(III/II) couple become increasingly negative moving from Br to NMe_2 substituent group that is consistent with a more electron rich metal center as electron donating groups are introduced into 4-position of pyridine. Figure 5.30b displays the electronic spectra for

the $[Fe(III)Cl_2(4R\text{-}PDI)]^+$ complexes; spectra for all other 4-substitued complexes show very similar features except **7g** exhibit a distinct and intense bathochromic low-energy absorption band that tails into the visible spectral region around 580 nm.

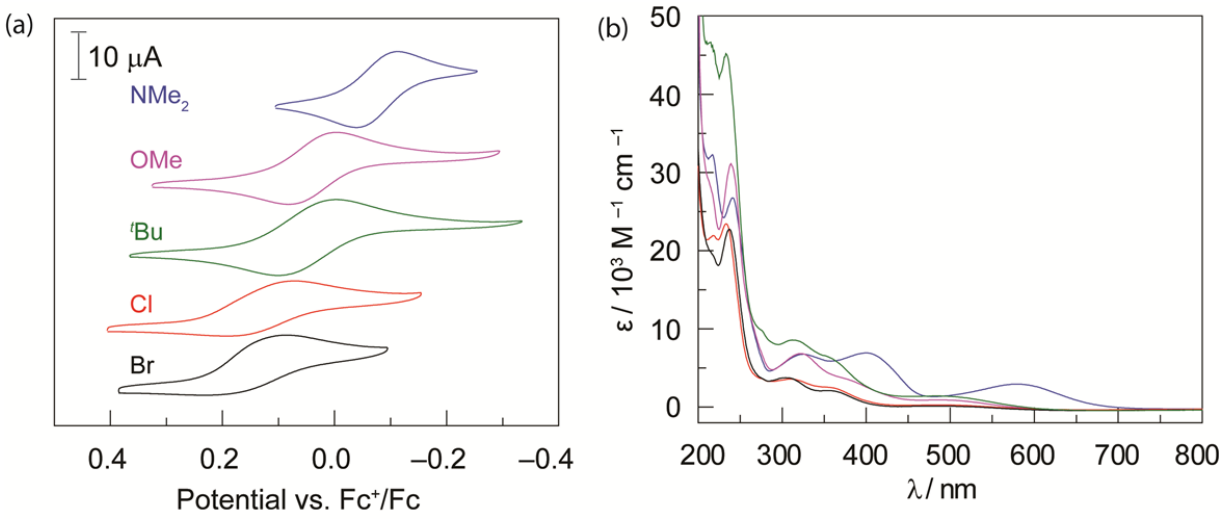

Figure 5.30. (a) Cyclic voltammograms of 1 mM $[Fe(III)Cl_2(4R\text{-}PDI)]^+$ complexes **7b** (—, red), **7c** (—, black), **7e** (—, green), **7f** (—, purple), and **7g** (—, blue) with 0.1 M $^nBu_4PF_6$ as a electrolyte CH_3CN solution with a scan rate of 100 mV/s. Glassy carbon working electrode, $Ag/AgNO_3$ reference, and Ag wire counter electrode were used. (b) Overlaid electronic absorption spectra of $[Fe(III)Cl_2(4R\text{-}PDI)]^+$ complexes measured in CH_3CN at room temperature (Same colors were used for assigning complexes).

The corresponding $[Fe(II)Cl(4R\text{-}PDI)]^+$complexes **8a–8g** were prepared from the parent PDI ligands with $FeCl_2$ in the presence of $AgPF_6$ in acetonitrile and were characterized by X-ray diffraction analysis (Figure 5.31). The solid state structures of **8a**, **8c**, **8e**, **8e**, and **8g** shows a five-coordinate Fe environment with coordination of one N-bound acetonitrile molecule. In the case of complexes **8b** and **8d**, two acetonitrile molecules were bound to the coordination site to make Fe in an octahedral environment. Selected metrical parameters for the seven Fe(II) PDI complexes are summarized in Tables 5.12 and 5.13. Each of the Fe(II) complexes exhibits an S = 2 ground state determined by the Evans method.

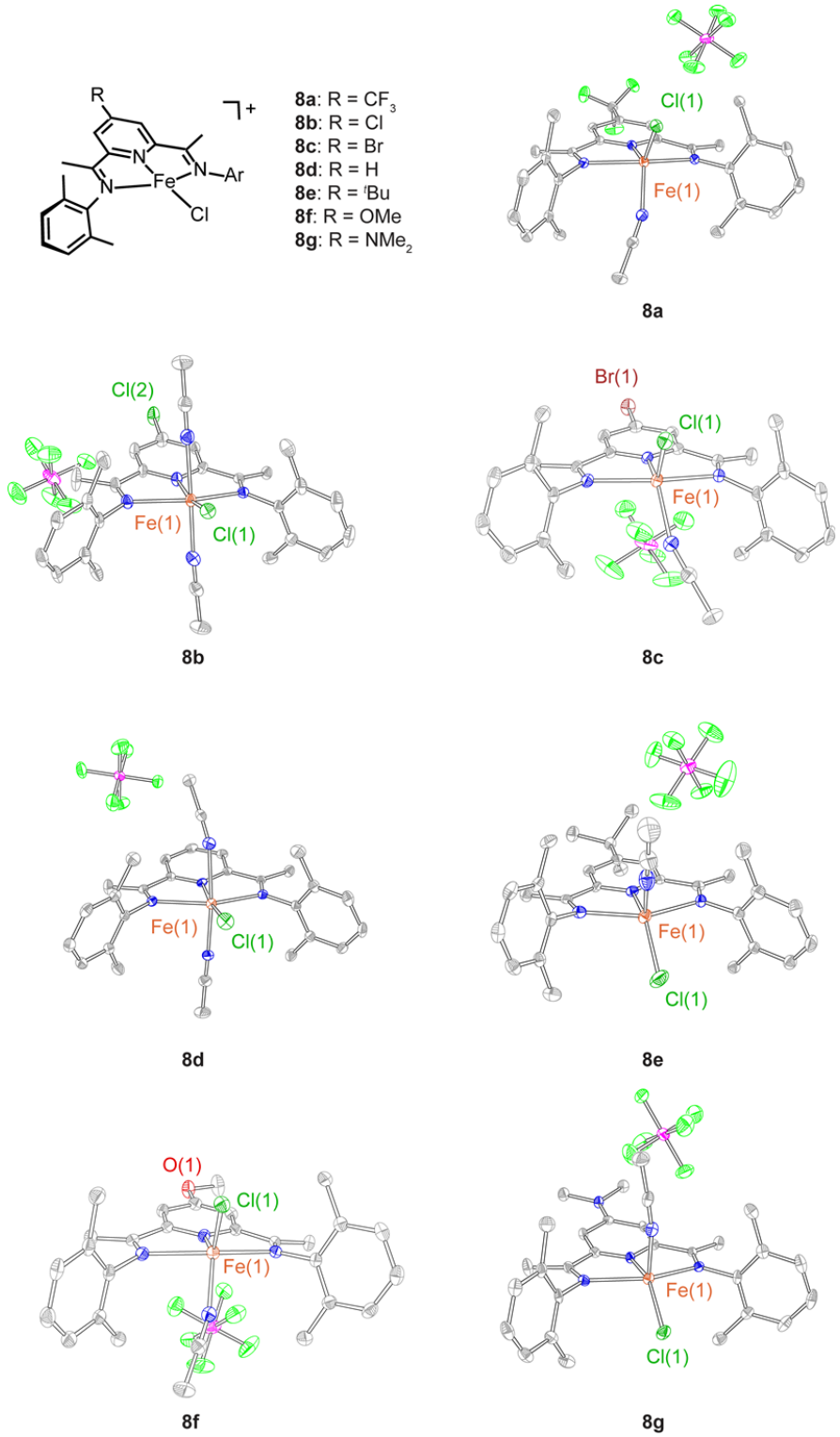

Figure 5.31. Thermal ellipsoid plots of SP cationic Fe(II) complexes in which H-atoms and solvents have been removed for clarity. Ellipsoids are drawn at 50% probability.

Table 5.12. Selected metrical parameters for complexes **8a**, **8c**, **8e**, **8f**, and **8g**.

	8a	**8c**	**8e**	**8f**	**8g**
Fe(1)–N(1)	2.1028(16)	2.095(2)	2.090(3)/2.088(2)	2.0861(19)	2.060(2)
Fe(1)–N(2)	2.2402(16)	2.218(2)	2.218(3)/2.214(3)	2.2454(19)	2.221(3)
Fe(1)–N(3)	2.2138(16)	2.242(2)	2.219(3)/2.196(3)	2.2019(19)	2.249(3)
Fe(1)–Cl(1)	2.2438(6)	2.2411(7)	2.2480(11)/2.2514(11)	2.2480(7)	2.2620(9)
Fe(1)–N(4)	2.0771(17)	2.078(2)	2.068(3)/2.072(3)	2.075(2)	2.067(3)
N(2)–C(6)	1.279(3)	1.284(3)	1.281(4)/1.282(4)	1.280(3)	1.286(4)
N(3)–C(8)	1.289(2)	1.279(3)	1.284(4)/1.284(4)	1.284(3)	1.287(4)
C(1)–C(6)	1.490(3)	1.496(3)	1.496(4)/1.496(4)	1.495(3)	1.491(4)
C(5)–C(8)	1.491(3)	1.499(3)	1.498(4)/1.501(4)	1.496(3)	1.489(4)
N(1)−Fe(1)−N(2)	72.91(6)	74.29(7)	73.55(10)/73.2(1)	73.00(7)	74.01(10)
N(1)−Fe(1)−N(3)	74.15(6)	73.01(7)	73.29(10)/73.93(10)	74.10(7)	73.63(10)
N(1)−Fe(1)−Cl(1)	128.23(5)	127.85(6)	137.32(8)/136.52(8)	125.91(6)	148.41(8)
N(2)−Fe(1)−Cl(1)	105.80(4)	102.63(5)	100.26(8)/102.32(7)	104.48(5)	105.91(7)
N(3)−Fe(1)−Cl(1)	101.55(4)	104.24(5)	106.70(8)/103.50(8)	102.11(5)	100.13(7)
N(1)−Fe(1)−N(4)	128.05(6)	128.35(8)	119.40(11)/119.84(11)	130.58(8)	103.67(11)
N(2)−Fe(1)−N(4)	88.96(6)	89.78(8)	100.74(11)/96.08(11)	90.03(7)	97.24(10)
N(3)−Fe(1)−N(4)	104.38(6)	103.73(8)	91.99(11)/97.47(11)	104.52(8)	92.97(10)
Cl(1)−Fe(1)−N(4)	103.33(5)	103.33(6)	119.40(11)/103.62(9)	103.03(6)	107.61(8)
τ_5	0.29	0.29	0.15/0.17	0.25	0.01

[a] τ_5 is a metric for five coordinate complexes. $\tau_5 = 0$ for a perfect square pyramid and $\tau_5 = 1$ for a perfect trigonal bipyramid.

Table 5.13. Selected metrical parameters for complexes **8b** and **8d**.

	8b	**8d**
Fe(1)–N(1)	2.148(3)	2.134(2)
Fe(1)–N(2)	2.274(3)	2.254(2)
Fe(1)–N(3)	2.257(3)	2.287(2)
Fe(1)–Cl(1)	2.3017(10)	2.2699(8)
Fe(1)–N(4)	2.255(4)	2.170(2)
Fe(1)–N(5)	2.158(4)	2.311(2)
N(2)–C(6)	1.275(5)	1.279(3)
N(3)–C(8)	1/280(5)	1.275(3)
C(1)–C(6)	1.492(5)	1.488(3)
C(5)–C(8)	1.492(5)	1.489(3)
N(1)−Fe(1)−N(2)	72.24(11)	73.16(7)
N(1)−Fe(1)−N(3)	72.44(11)	73.03(7)
N(1)−Fe(1)−N(4)	78.45(12)	90.76(8)
N(2)−Fe(1)−N(4)	89.08(12)	92.25(8)
N(3)−Fe(1)−N(4)	91.29(11)	86.29(8)
N(1)−Fe(1)−Cl(1)	167.50(9)	172.25(6)
N(1)−Fe(1)−N(5)	98.91(13)	76.85(8)
N(2)−Fe(1)−N(5)	89.95(12)	87.44(8)
N(3)−Fe(1)−N(5)	88.05(12)	86.84(8)
Cl(1)−Fe(1)−N(5)	93.57(9)	95.88(6)

When $[Fe(III)Cl_2(4R\text{-}PDI)]^+$ complexes in CH_3CN solution are irradiated with light ($\lambda >$ 365 nm), clean conversion to the corresponding one electron reduced $[Fe(III)Cl(4R\text{-}PDI)]^+$ species is observed as depicted in Figure 5.32 as representative. Although in the case of 4-OMe, side products were formed by reaction of reduced Fe(II) with HCl, clean conversation to the neutral $FeCl_2$ complex was obtained when additional external base was employed as we described in the previous section. Single wavelength quantum yield (QY) measurements will be

employed to assay the effects of electronic perturbation on photoefficiency of halogen photoelimination reactions of Fe metal complexes.

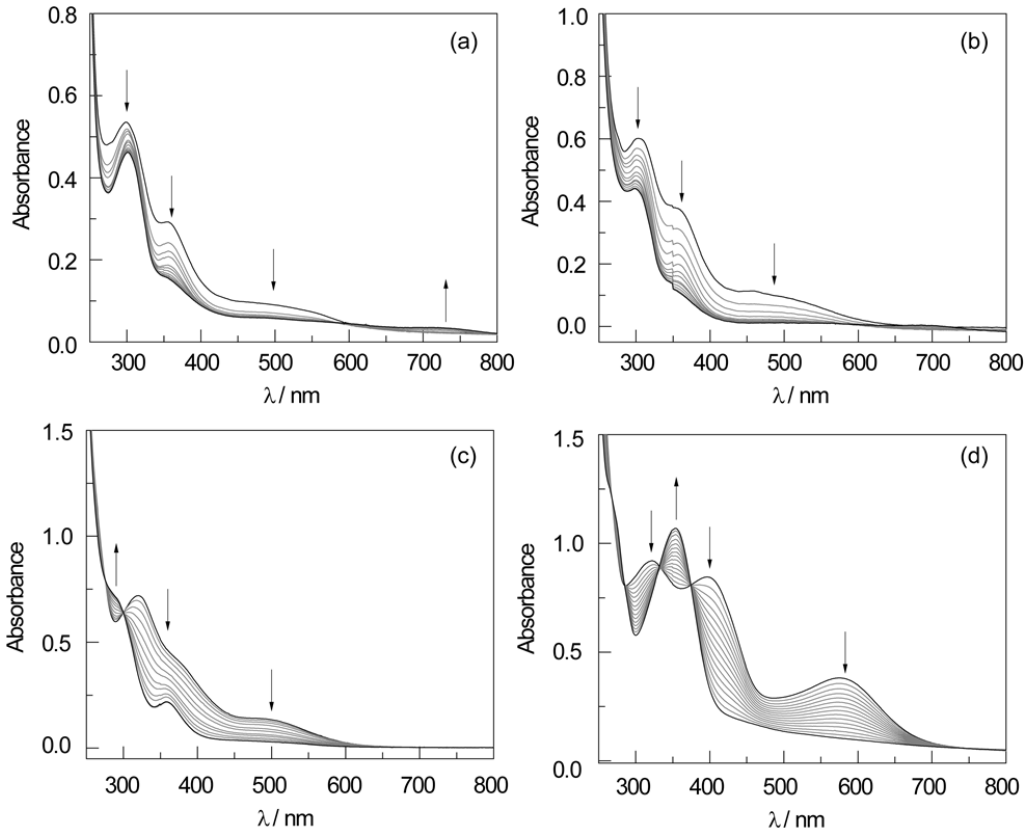

Figure 5.32. Spectra evolution for the photolysis of (a) **7a** (b) **7c** (c) **7f**, and (d) **7g** Fe(III) complexes in CH_3CN (λ_{exc} > 365 nm).

5.7. Attempts for the Observation of Cl–Cl Bond Formation

Motivated by our successful observation of dissociation of Cl• from Fe(III)-PDI systems, we have sought to better understand the formation of Cl_2 that occurs when no chemical trap is present. Since we have determined that the axial Fe–Cl bond is the bond that is cleaved photochemically, we have put effort toward synthesizing a dimeric system where two axial Fe–Cl are oriented toward each other with the ultimate goal of being able to directly observe the formation of Cl_2 via photocrystallography. To this end, we have synthesized ligand precursors

with two different backbones—dimethylxanthene and dibenzofuran—that possess distinct bite angles, which will allow us to modulate and optimize the orientation and spacing of the Fe–Cl bonds (Figure 5.33). Although fully condensed dimethylxanthene based PDI ligand from **L18** was not realized due to its steric constrains, full condensation of dibenzofuran (DBF) based bis(diacetylpyridine) (**L17**) which has larger bite angle, was successfully achieved for desired DBF based PDI ligand (**L19**).

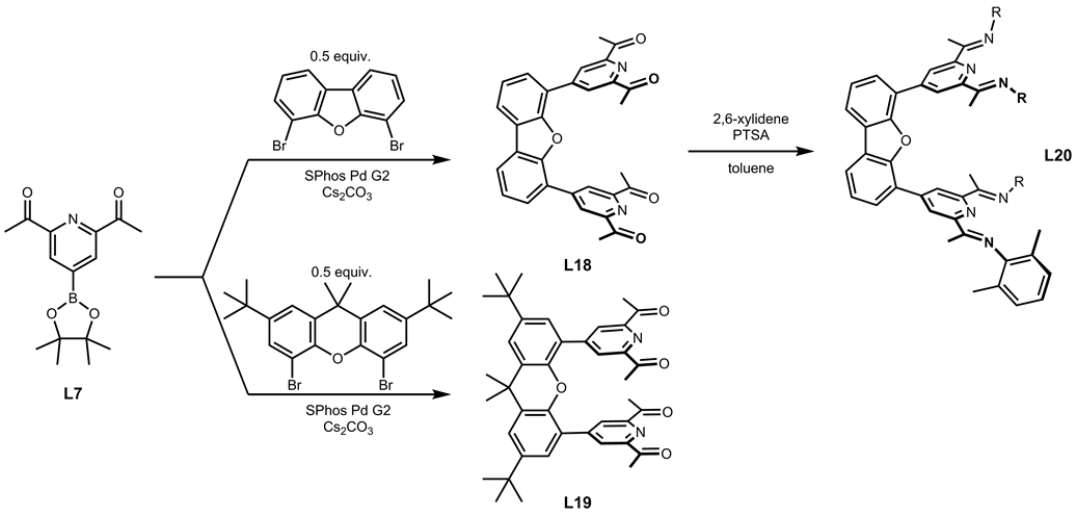

Figure 5.33. Synthetic route for DBF based PDI ligands.

Preliminary attempts to synthesize $(FeCl_3)_2$-DBF dimers have led to the intriguing formation of salts **9**, consistent with what we observe for monomeric complexes when there is a non-hydrogen atom in the 4-position of the pyridine ring (Figure 5.34). The formation of these salts coincides with the twisting of one face of the dimer as one anion sits proximal to the two ligated metal centers. We are currently exploring numerous methods to enforce cofacial dimer orientation, such as substituting for a larger anion (BPh_4, BAr_F, or carboranes) that cannot fit between the metal centers and by modifying the ligand scaffold such as putting bulkier alpha carbons. However, because of the propensity for these complexes to form salts, we are also

interested in exploring the possibility of performing photochemical reactions with tightly bound anions situated in the pocket between the two faces of the dimer.

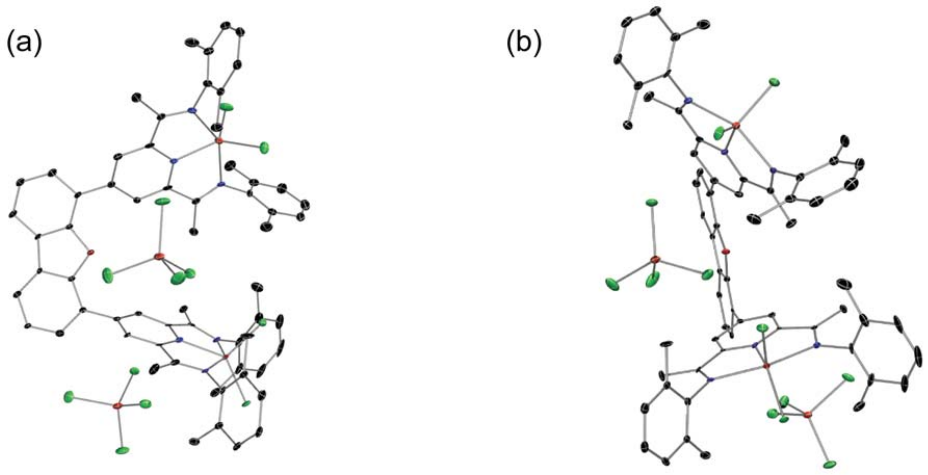

Figure 5.34. Thermal ellipsoid plots of $[Fe(III)Cl_2(DBF\text{-}PDI)]_2^{2+}$ complex **9**.

5.8 Conclusions

In summary, we have introduced two families of five-coordinate Fe(III) complexes to evaluate secondary coordination sphere effects of arenes on photohalogen elimination reactions both in the solid and solution state. Notably, we have found that the presence of additional arenes facilitates halogen atom radical formation in the solid-state, presumably by efficient stabilization of photochemically generated Cl•. We also report the first structural observation of the reactive Cl•|arene charge transfer complex by steady-state photocrystllography. The increased solution state photoefficency of **2a** compared to **1a** further supports the hypothesis that secondary coordination sphere interactions are crucial for efficient photohalogen elimination.

We also have prepared 4-functionalized Fe(III) complexes for the understanding of electronic effects on the halogen photoelimination reaction. We have developed a concise and

scalable synthesis of 4-pyridine diimines ligand framework from a Minisci reaction using pyruvic acid, silver nitrate and persulfate. Of pertinence to the scalability and ease of synthesis of PDI ligands, acylation and work-up conditions are consistent across a general series of compounds. The only identified side products of the reaction are the starting material and the mono-acylated product, consistent with what was originally observed by Minisci.[64] As the PDI ligand scaffold has been adopted for a range of catalytic applications, the ability to modulate the electronic properties of the ligand with facility may be useful to optimizing a variety of catalytic transformations.

5.9 Experimental Details

5.9.1. Materials and Synthetic Details

All reactions were carried out on the benchtop inside a fume hood. Silver hexafluorophosphate was obtained from Strem Chemical. 2,6-dichloroiodobenzene, 4-Trifluoromethyl-pyridine, 4-bromopyridine hydrochloride, and Pyridine-4-boronic acid hydrate were obtained from Oakwood Chemical, and 4-Phenylpyridine, mesityl boronic acid, 2,6 xylidene, 9-[2-(Dicyclohexylphosphino)phenyl]-9H-carbazole, iron trichloride, palladium(II) acetate, potassium carbonate, phenyl boronic acid, PddppfCl$_2$, 4-chloropyridine hydrochloride, 4-*tert*-butyl-pyridine, silver nitrate, pyruvic acid, sodium persulfate, tetrabutylammonium chloride (^{n}Bu$_4$NCl), and solvents were obtained from Sigma Aldrich. All chemicals were used without further purification. $FeCl_2(PMe_3)_2$ were prepared as previously reported.[65] Cross couplings were carried out in sealed heavy-walled reaction flasks (Chemglass Part # CG-1880-R-03) fitted with perfluoro O-rings (Chemglass part #CG-309-220). The solvent was degassed using a medium micro gas dispersion tube (Chemglass part #CG-207-02). Condensations utilized a short path Dean-Stark trap (Chemglass Part# CG-1258-01). Silica pads were run using Sigma Aldrich silica

gel pore size 60 Å 230-400 mesh particle size 40-63 μm. Columns were dry-loaded using Silicycle SiliaSphere PC 60A and run on a Biotage Isolera One Instrument using Snap Ultra Column Cartridges. Thin layer chromatography was performed using Analtech aluminum backed fluorescent silica gel (UV254). All reactions were heated in temperature controlled silicone oil baths where the oil level reached at least ¾ of the reaction volume at any time. All yields are isolated yields of purified products. All metalation chemistry and handling of the resulting compounds was performed in a VAC-Atmospheres Nexus II nitrogen filled glovebox. All solvents in the glove box were taken from a Pure Process Technologies System utilizing alumina columns and solvents degassed/stored under argon gas. All vials and pipettes in the glovebox were heated to 180°C for a minimum of 24 h in an oven before being brought into the glovebox.

4-(2,6-dichlorophenyl)pyridine (L1). To a 200 mL heavy walled pressure flask equipped with a stir bar was added 1,4-dioxane (200 mL) and water (40 mL). This solvent mixture was degassed with argon using a medium fritted gas dispersion tube by bubbling though the solution for 45 min. While under a blanket of argon gas, 2,6-dichloroiodobenzene (7.60 g, 27.9 mmol, 1.00 eq), pyridine-4-boronic acid hydrate (10.3 g, 83.6 mmol, 3.00 eq), potassium phosphate (17.6 g, 83.6 mmol, 3.00 eq) and $PddppfCl_2$ (2.04 g, 2.79 mmol, 10 mol%) were added. The reaction was sealed and heated at 95 °C for 12 h, cooled to room temperature, and added to 500 mL of distilled water. The reaction was extracted with ethyl acetate (3 × 150 mL), the organics combined, and dried over sodium sulfate, and dry loaded onto silica. A column was charged with the dry-loaded compound on silica and the compound was purified using Ethyl Acetate/Hexanes (1 column volume (CV) Hex, 3 CV 0→25% EtOAc in Hex, 10 CV 25% EtOAc). The appropriate fractions (See TLC below) were collected and evaporated to dryness yielding (**L1)** as a white powder (4.35 g, 70.0% yield). ^{1}H NMR (CD_2Cl_2-d_2, 23 °C) δ (ppm):

8.70 (d, 2H), 7.45 (d, 2H), 7.31 (m, 1H), 7.21 (d, 2H).

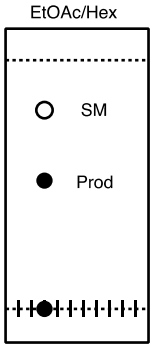

4-(2,6-dichlorophenyl)-2,6-diacetylpyridine (L2). (**L1**) (2.34 g, 10.4 mmol, 1.00 equiv) was dissolved in 500 mL of 0.5 M sulfuric acid. While stirring, pyruvic acid (4.6 g, 52.2 mmol, 5.00 equiv) and silver nitrate (354 mg, 2.09 mmol, 20.0 mol% dissolved in 200 mL of deionized water) were added. Finally, sodium persulfate (12.4 g, 52.2 mmol, 5.00 equiv) was added all at once with vigorous stirring. After approximately 15 min, carbon dioxide was seen evolving from the reaction. The reaction was allowed to stir overnight resulting in a dark green precipitate and yellow-green solution. The reaction was filtered and the precipitate washed with 150 mL of dichloromethane which is later combined with the extraction washes. The resulting filtrate was extracted (3 × 150 mL) with CH_2Cl_2. The combined washes were dried over sodium sulfate and dry-loaded onto silica. A column was charged with the dry-loaded compound on silica and the compound was purified by column chromatography using neat CH_2Cl_2. The first compound to come off the column was the desired product. The fractions were evaporated to dryness to yield **L2** as a white solid (1.64 g, 51.2% yield). ^{1}H NMR (CD_2Cl_2-d_2, 23 °C) δ (ppm): 8.14 (s, 2H), 7.49 (s, 2H), 7.37 (m, 1H), 2.83 (s, 6H).

4-(2,6-dimesitylphenyl)-2,6-diacetylpyridine (L3). To a 200 mL heavy walled pressure flask equipped with a stir bar was added 1,4-dioxane (50 mL) and water (10 mL). This solvent

mixture was degassed with argon using a medium fritted gas dispersion tube by bubbling though the solution for 30 min. While under a blanket of argon gas, **(L2)**(1.04 g, 3.37 mmol, 1.00 eq), mesityl boronic acid (3.32 g, 20.2 mmol, 6.00 eq), potassium phosphate (2.15 g, 10.1 mmol, 3.00 eq), palladium acetate (151 mg, 0.674 mmol, 20 mol%), 9-[2-(Dicyclohexylphosphino)phenyl]-9H-carbazole (888 mg, 2.02 mmol, 60 mol%), and phenyl boronic acid (5 mg as an initial palladium reductant) were added. The reaction was sealed and heated at 110 °C for 48 h, cooled to room temperature, and added to 500 mL of distilled water. The reaction was extracted with ethyl acetate (3 × 150 mL), the organics combined, dried over sodium sulfate, and dry loaded onto silica. A column was charged with the dry-loaded compound on silica and the compound was purified using Ethyl Acetate/Hexanes (1 column volume (CV) Hex, 2 CV 0→10% EtOAc in Hex, 15 CV 10% EA). The appropriate fractions (see TLC below) were collected and evaporated to dryness yielding an impure oil which was dissolved in CH_2Cl_2 and wet loaded onto another identical silica column and purified using neat CH_2Cl_2. The second column was run at a much slower rate of 50 mL/min vs. 100 mL/min for the first column in order to achieve a better separation. The appropriate fractions (see TLC below) were collected and evaporated to yield (**L3)** as a white powder (560 mg, 35.0% yield). ^{1}H NMR (CD_2Cl_2-d_2, 23 °C) δ (ppm): 7.66 (s, 2H), 7.56 (t, 1H), 7.23 (d, 2H), 2.55 (s, 6H), 2.17 (s, 6H), 1.98 (s, 12H).

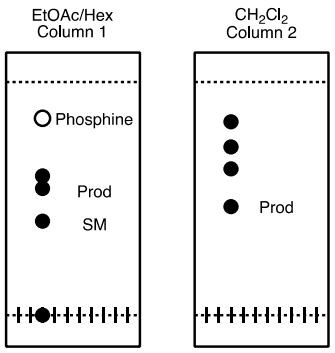

4-(2,6-dimesitylphenyl)pyridine-2,6-diimine (L4). A 500 mL round bottom flask

equipped with a stir bar was charged with **L3** (560 mg, 1.17 mmol, 1.00 eq), *p*-toluenesulfonic acid (22.3 mg, 0.117 mmol, 10.0 mol%), 2,6-dimethylaniline (427 mg, 3.53 mmol, 3.00 eq), and toluene (300 mL). This mixture was heated at 145 °C using a short path Dean-Stark apparatus with a reflux condenser attached to the top. The top of the condenser was sealed with a septum and a gentle nitrogen flow via a syringe needle was maintained during the reaction. The reaction was allowed to run for 12 h causing a gradual color change to yellow. The reaction was cooled to room temperature, the solvent removed, and the resulting thick oil re-dissolved in CH_2Cl_2 (100 mL). This solution was washed with saturated $NaHCO_3$. The CH_2Cl_2 layer was then dried over sodium sulfate and evaporated to yield a yellow oil that immediately begins to crystallize. A small amount (50 mL) of methanol was added to cause total precipitation of an off–white powder. The solid was isolated by filtration to yield **L4** (600 mg, 75.1% yield) as an off–white powder. ^{1}H NMR ($CDCl_3$-d_1, 23 °C) δ (ppm): 8.07 (s, 2H), 7.53 (t, 1H), 7.24 (d, 2H), 7.08 (d, 4H), 6.95 (t, 2H), 6.76 (s, 4H), 2.21 (s, 6H), 2.05 (s, 18H), 1.95 (s, 12H). ^{13}C NMR ($CDCl_3$-d_1, 23 °C) δ (ppm): 166.65, 153.90, 149.05 (d), 142.49, 140.96, 138.65, 137.70, 137.48, 136.34, 135.08, 130.13, 129.75, 128.88, 128.44, 127.85, 127.19, 126.00, 125.56, 122.92, 21.31, 21.21, 17.99, 16.37. MS(+ESI): calcd for $C_{49}H_{51}N_3$, $[M+H]^+$, *m/z* 682.408; found, *m/z* 682.41.

4-Phenyl-2,6-diacetylpyridine (L5). 4-Phenylpyridine (10.0 g, 64.4 mmol, 1.00 equiv) was dissolved in 1 L of 0.5 M sulfuric acid. While stirring, pyruvic acid (22.6 g, 257 mmol, 4.00 equiv) and silver nitrate (1.64 g, 9.66 mmol, 15.0 mol% dissolved in 200 mL of deionized water) were added. Finally, sodium persulfate (61.2 g, 257 mmol, 4.00 equiv) was added all at once with vigorous stirring. After approximately 15 min, carbon dioxide was seen evolving from the reaction. The reaction is allowed to stir overnight resulting in a yellow solution with a white precipitate. The solution was filtered to remove the precipitate, and the filtrate was extracted (3 ×

300 mL) with CH_2Cl_2 and the extracts combined, dried over sodium sulfate and dry-loaded onto silica. A column was charged with the dry-loaded compound on silica and the compound was purified by column chromatography using neat CH_2Cl_2 at a reduced flow rate of 75 mL/min. The first compound to come off the column was the desired product. The fractions were evaporated to dryness to yield a white solid that could be recrystallized from pentane at −60 °C to yield **L5** (1.13 g, 7.33% yield). ^{1}H NMR (CD_2Cl_2-d_2, 23 °C) δ (ppm): 8.45 (s, 2H), 7.79(m, 2H), 7.53(m, 23), 2.82(s, 6H).

4-phenylpyridine-2,6-diimine (L6). A 250 mL round bottom flask equipped with a stir bar was charged with **L5** (255 mg, 1.07 mmol, 1 eq), *p*-toluenesulfonic acid (20.2 mg, 0.107 mmol, 10.0 mol%), 2,6-dimethylaniline (395 mg, 3.26 mmol, 3.00 eq), and toluene (150 mL). This mixture was heated at 145 °C using a short path Dean-Stark apparatus with a reflux condenser attached to the top. The top of the condenser was sealed with a septum and a gentle nitrogen flow via a syringe needle was maintained during the reaction. The reaction was allowed to run for 24 h causing a gradual color change to pale yellow. The reaction was cooled to room temperature, the solvent removed, and the resulting thick oil re-dissolved in CH_2Cl_2 (100 mL). This solution was washed with saturated $NaHCO_3$. The CH_2Cl_2 layer was then dried over sodium sulfate and evaporated to yield a yellow oil that immediately begins to crystallize. A small amount (50 mL) of methanol was added to cause total precipitation of a pale yellow powder. The solid was isolated by filtration to yield **L6** (400 mg, 84.3% yield) as a pale yellow powder. ^{1}H NMR (CD_2Cl_2-d_2, 23 °C) δ (ppm): 8.78 (s, 2H), 7.89 (d, 2H), 7.52 (m, 3H), 7.10 (d, 4H), 6.95 (m, 3H), 2.28 (s, 6H), 2.07 (s, 12H). ^{13}C NMR (CD_2Cl_2-d_2, 23 °C) δ (ppm): 167.76, 156.34, 149.50 (d), 138.69, 129.62, 128.35, 127.82, 125.91, 123.44, 120.42, 18.22, 16.95. MS(+ESI): calcd for $C_{31}H_{31}N_3$, $[M+H]^+$, *m/z* 446.252; found, *m/z* 446.25.

4-hydroxycarbonyl-5-(4-(2,6-diacetylpyridyl))-2,7-di-*tert*-butyl-9,9-dimethyl xanthene (L7). 4,4'-Di-*tert*-butyl-bipyridyl (11.8 mg, 0.044 mmol, 2.93 mol%) was added to a 3-neck flask equipped with a condenser and the flask was transferred to a glovebox. $[Ir(OMe)(cod)]_2$ (14.6 mg, 0.022 mmol, 1.47 mol%) was dispersed in 40 mL of cyclohexane and the mixture was added to the flask. Pinacolborane (192 mg, 1.50 mmol, 1.0 equiv) was added to the mixture via syringe. The diacetylpyridine (245 mg, 1.50 mmol, 1.0 equiv) was added to the mixture, the flask was removed from the glovebox and the mixture was stirred at 100 ^{o}C for 3 h under a N_2 atmosphere. The mixture was cooled to ambient temperature and dried in vacuo and purified by flash silica gel column chromatography, eluting with a gradient of 1–25% ethyl acetate in hexanes. The fractions containing the major product by TLC were combined and concentrated to afford **L7** as a white solid (230.0 mg, 53.1% yield). ^{1}H NMR ($CDCl_3$-d_1, 23 °C) δ (ppm): 8.54 (s, 2H), 2.28 (s, 6H), 1.35 (s, 12H). ^{13}C NMR ($CDCl_3$-d_1, 23 °C) δ (ppm): 199.83, 152.17, 130.11, 85.16, 25.84, 25.03.

4-bromo-2,7-di-*tert*-butyl-9,9-dimethyl-9H-xanthene (L8). 4,5-dibromo-2,7-di-*tert*-butyl-9,9-dimehtylxanthene (423 mg, 0.880 mmol, 1.0 equiv) was dissolved in dry THF (30 mL) and cooled to −78 ^{o}C. The THF solution of 2.0 M solution of phenyllithium in dibutyl ether (0.440 mL, 0.880 mmol, 1.0 equiv) was added dropwise to the solution followed by stirring at −78 ^{o}C for 1h. The MeOH (10 mL) was then added slowly, as indicated by a slight discoloration of the solution on addition. The slightly brown mixture was stirred for an additional 2 h while warming to room temperature. The organic solvent was removed and the resulting precipitate was filtered, washed with water and a small amount of hexane, and dried under vacuo to afford **L8** as a white solid (283 mg, 80% yield).

1,1'-(4-(2,7-di-*tert*-butyl-9,9-dimethyl-9H-xanthen-4-yl)pyridine-2,6-diyl)bis(ethan-1-

one) (L9). To a 50 mL heavy walled pressure flask equipped with a stir bar was added THF (4 mL) and water (8 mL). This solvent mixture was degassed with argon using a medium fritted gas dispersion tube by bubbling though the solution for 30 min. While under a blanket of argon gas, **L7** (145 mg, 0.50 mmol, 1.00 eq), **L8** (201 mg, 0.50 mmol, 1.00 eq), potassium phosphate (106 mg, 0.50 mmol, 1.00 eq), XPhosPdG3 (13.0 mg, 0.015 mmol, 3.0 mol%), were added. The reaction was sealed and heated at 80 °C for 24 h, cooled to room temperature, and added to 100 mL of distilled water. The reaction was extracted with ethyl acetate (3 × 50 mL), the organics combined, dried over sodium sulfate, and purified by flash silica gel column chromatography, eluting with a gradient of 1–2% ethyl acetate in hexanes. The appropriate fractions by TLC were collected and evaporated to dryness yielding **L9** as a white powder (130 mg, 61.9% yield). ^{1}H NMR ($CDCl_3$-d_1, 23 °C) δ (ppm): 8.52 (s, 2H), 7.55 (d, *J* = 2.40 Hz, 1H), 7.44 (d, *J* = 2.40 Hz, 1H), 7.30 (d, *J* = 2.40 Hz, 1H), 7.23 (dd, *J* = 2.40, 8.80 Hz, 1H), 6.92 (d, *J* = 2.40, 8.00 Hz, 1H), 2.87 (s, 6H), 1.70 (s, 6H), 1.38 (s, 9H), 1.34 (s, 9H). ^{13}C NMR ($CDCl_3$-d_1, 23 °C) δ (ppm): 199.92, 152.89, 148.90, 148.21, 146.36, 146.05, 146.02, 131.27, 129.49, 125.70, 125.35, 124.89, 124.71, 124.38, 122.35, 115.96, 35.05, 34.79, 34.69, 32.00, 31.73, 31.69, 25.99. MS(+ESI): calcd for $C_{32}H_{37}NO_3$, $[M+H]^+$, *m/z* 484.277; found, *m/z* 484.287.

(1E,1'E)-1,1'-(4-(2,7-di-*tert*-butyl-9,9-dimethyl-9*H*-xanthen-4-yl)pyridine-2,6-diyl)bis(*N*-(2,6-dimethylphenyl)ethan-1-imine) (L10). A 500 mL round bottom flask equipped with a stir bar was charged with **L9** (130 mg, 0.267 mmol, 1.00 eq), *p*-toluenesulfonic acid (14.6 mg, 0.085 mmol, 31.7 mol%), 2,6-dimethylaniline (68.2 mg, 0.668 mmol, 2.50 eq), and toluene (50 mL). This mixture was heated at 145 °C using a short path Dean-Stark apparatus with a reflux condenser attached to the top. The top of the condenser was sealed with a septum and a gentle nitrogen flow via a syringe needle was maintained during the reaction. The reaction was

allowed to run for 24 h causing a gradual color change to yellow. The reaction was cooled to room temperature, the solvent removed, and the resulting thick oil re-dissolved in CH_2Cl_2 (40 mL). This solution was washed with saturated $NaHCO_3$. The CH_2Cl_2 layer was then dried over sodium sulfate and evaporated to yield yellow oil that immediately begins to crystallize. A small amount (20 mL) of methanol was added to cause total precipitation of a yellow powder. The solid was isolated by filtration to yield **L10** (138 mg, 75.0% yield) as a yellow powder. ^{1}H NMR ($CDCl_3$-d_1, 23 °C) δ (ppm): 8.79 (s, 2H), 7.52 (d, *J* = 2.40 Hz, 1H), 7.40 (dd, *J* = 2.40, 3.40 Hz, 2H), 7.16 (d, *J* = 2.00 Hz, 1H), 7.14 (m, 4H), 6.95 (m, 3H), 2.32 (s, 6H), 2.10 (s, 12H), 1.69 (s, 6H), 1.38 (s, 9H), 1.32 (s, 9H). ^{13}C NMR ($CDCl_3$-d_1, 23 °C) δ (ppm): 167.42, 155.24, 149.25, 148.42, 147.53, 146.06, 145.81, 130.91, 129.50, 128.04, 126.25, 125.63, 124.53, 123.76, 123.38, 123.03, 122.44, 115.90, 35.03, 34.79, 34.68, 32.22, 31.74, 18.20, 16.83, 1.21. MS(+ESI): calcd for $C_{48}H_{55}N_3O$, $[M+H]^+$, *m/z* 690.435; found, *m/z* 690.466.

4-bromo-2,7-di-tert-butyl-9,9-dimethyl-5-phenyl-9H-xanthene (L11). 4-bromo-2,7-di-tert-butyl-5-iodo-9,9-dimethyl-9H-xanthene (343 mg, 0.650 mmol, 1.08 equiv), phenylboronic acid (73.2 mg, 0.60 mmol, 1.00 equiv), K_2CO_3 (249 mg, 1.80 mmol, 3.00 equiv) and $Pd(PPh_3)_4$ (83.2 mg, 0.07 mmol, 0.12 equiv) were added to 100 mL of a 9:1 DMF:water mixture in a 250 mL round-bottom flask. The mixture was heated at reflux overnight under N_2 and then cooled to room temperature after which 400 mL of distilled water was added to the flask. The product was extracted with dichloromethane (DCM), and a solid was obtained upon drying under vacuum. The DPX product was purified by column chromatography (hexanes) to deliver a white solid (194 mg, 67.7%) ^{1}H NMR (400 MHz, $CDCl_3$): δ 7.67 (m, 1H), 7.66 (m, 1H), 7.40 (t, 2H), 7.36 (t, 2H), 7.30 (m, 2H), 7.25 (m, 1H), 1.62 (s, 6H), 1.31 (s, 9H), 1.25 (s, 9H).

1,1'-(4-(2,7-di-tert-butyl-9,9-dimethyl-5-phenyl-9H-xanthen-4-yl)pyridine-2,6-

diyl)bis(ethan-1-one) (L12). To a 50 mL heavy walled pressure flask equipped with a stir bar was added THF (4 mL) and water (8 mL). This solvent mixture was degassed with argon using a medium fritted gas dispersion tube by bubbling though the solution for 30 min. While under a blanket of argon gas, **L7** (117 mg, 0.41 mmol, 1.00 eq)**, L11** (194 mg, 0.41 mmol, 1.00 eq), potassium phosphate (86.9 mg, 0.41 mmol, 1.00 eq), XPhosPdG3 (10.7 mg, 0.012 mmol, 3.0 mol%), were added. The reaction was sealed and heated at 80 °C for 24 h, cooled to room temperature, and added to 100 mL of distilled water. The reaction was extracted with ethyl acetate (3 × 50 mL), the organics combined, dried over sodium sulfate, and purified by flash silica gel column chromatography, eluting with a gradient of 1–3% ethyl acetate in hexanes. The appropriate fractions by TLC were collected and evaporated to dryness yielding **L12** as a white powder (126 mg, 55.5% yield). ^{1}H NMR ($CDCl_3$-d_1, 23 °C) δ (ppm): 8.12 (s, 2H), 7.54 (d, J = 2.00 Hz, 1H), 7.44 (d, J = 2.40 Hz, 1H), 7.15 (m, 5H), 6.95 (m, 2H), 2.74 (s, 6H), 1.75 (s, 6H), 1.36 (s, 9H), 1.35 (s, 9H). ^{13}C NMR ($CDCl_3$-d_1, 23 °C) δ (ppm): 199.42, 152.39, 148.76, 146.09, 145.93, 145.78, 145.24, 138.24, 130.89, 129.99, 129.73, 129.43, 127.49, 126.33, 125.80, 125.73, 125.15, 123.93, 121.83, 35.25, 34.80, 34.73, 32.15, 31.71, 25.90, 1.21.

(1E,1'E)-1,1'-(4-(2,7-di-tert-butyl-9,9-dimethyl-5-phenyl-9H-xanthen-4-yl)pyridine-2,6-diyl)bis(N-(2,6-dimethylphenyl)ethan-1-imine) (L13). A 500 mL round bottom flask equipped with a stir bar was charged with **L12** (126 mg, 0.225 mmol, 1.00 eq), *p*-toluenesulfonic acid (12.3 mg, 0.072 mmol, 31.7 mol%), 2,6-dimethylaniline (57.5 mg, 0.563 mmol, 2.50 eq), and toluene (50 mL). This mixture was heated at 145 °C using a short path Dean-Stark apparatus with a reflux condenser attached to the top. The top of the condenser was sealed with a septum and a gentle nitrogen flow via a syringe needle was maintained during the reaction. The reaction was allowed to run for 24 h causing a gradual color change to yellow. The reaction was cooled to

room temperature, the solvent removed, and the resulting thick oil re-dissolved in CH_2Cl_2 (40 mL). This solution was washed with saturated $NaHCO_3$. The CH_2Cl_2 layer was then dried over sodium sulfate and evaporated to yield yellow oil that immediately begins to crystallize. A small amount (20 mL) of methanol was added to cause total precipitation of an yellow powder. The solid was isolated by filtration to yield **L13** (82.7 mg, 48.0% yield) as a yellow powder. ^{1}H NMR ($CDCl_3$-d_1, 23 °C) δ (ppm): 8.43 (s, 2H), 7.54 (d, *J* = 4.00 Hz, 1H), 7.47 (d, *J* = 4.00 Hz,1H), 7.28 (m, 1H), 7.20 (m, 5H), 6.97 (m, 4H), 2.27 (s, 6H), 1.98 (s, 12H), 1.73 (s, 6H), 1.56 (s, 6H), 1.36 (s, 9H), 1.34 (s, 9H). ^{13}C NMR ($CDCl_3$-d_1, 23 °C) δ (ppm): 167.44, 154.89, 148.95, 148.18, 146.34, 146.19, 145.80, 145.78, 138.11, 130.97, 130.91, 129.55, 129.09, 127.97, 127.60, 127.27, 126.16, 126.10, 125.65, 125.04, 123.61, 123.06, 122.59, 121.54, 35.48, 34.81, 34.73, 31.78, 31.73, 31.37, 18.21, 16.86, 1.22. MS(+ESI): calcd for $C_{48}H_{55}N_3O$, $[M+H]^+$, *m/z* 766.466; found, *m/z* 766.481.

4-Chloro-2,6-diacetylpyridine (L15-Cl). 4-Chloropyridine hydrochloride **(L14-Cl•HCl)** (200 mmol, 30.0 g, 1.00 equiv) was dissolved in 300 mL of deionized water. The solution was then basified using saturated sodium carbonate to a pH of 9. The resulting basified mixture was extracted (3 × 150 mL) with dichloromethane, which was then extracted (3 × 330 mL) with 0.5 M sulfuric acid. This sulfuric acid solution was added to a 2 L two-neck flask equipped with a large magnetic stir bar. While stirring, pyruvic acid (800 mmol, 70.5 g, 4.00 equiv) and silver nitrate (20.0 mmol, 3.40 g, 10.0 mol% dissolved in 300 mL of deionized water) were added. If a thick white precipitate forms (AgCl), the reaction should be started over and greater care should be taken to exclude all chloride in the anion exchange steps described above. Finally, sodium persulfate (800 mmol, 190 g, 4.00 equiv) was added all at once with vigorous stirring. After approximately 15 min, carbon dioxide was observed to evolve from the reaction. The reaction

was allowed to stir overnight resulting in a dark green precipitate and yellow-green solution. The solution was filtered and the precipitate was washed with 150 mL of dichloromethane. The resulting filtrate was basified to pH 10 using saturated sodium hydroxide. This leads to a warming of the solution and a change in color to dark red/brown. Once cooled to room temperature, the solution was extracted (3 × 300 mL) with CH_2Cl_2 and the extracts combined with the previous wash of the precipitate and filtered through a short silica pad (3′′). The filtrate was dried over sodium sulfate and dry-loaded onto silica. A column was charged with the dry-loaded compound on silica and the compound was purified by column chromatography using neat CH_2Cl_2. The first compound to come off the column is the desired product. The fractions were evaporated to dryness to yield **L15-Cl** as a white solid that could be recrystallized from pentane at –20 °C to yield white needles (10.2 g, 26.1 % yield). ^{1}H NMR (CD_2Cl_2-d_2, 23 °C) δ (ppm): 8.16 (s, 2H), 2.76 (s, 6H). Matched literature report.[56]

4-Chloro-2,6-bis(2-methyl-1,3-dioxolan-2-yl)pyridine (L16). A 500 mL round bottom flask was charged with **2-Cl** (6.45 g, 32.6 mmol, 1.00 equiv), ethylene glycol (28.0 mL, 490 mmol, 10.0 equiv), *p*-toluenesulfonic acid (2.28 mmol, 435 mg, 7.00 mol%), and toluene (300 mL). The flask was equipped with a large Dean-Stark trap (25 mL collection volume) and a reflux condenser. The top of the condenser was sealed with a septum and a gentle nitrogen flow via a syringe needle was maintained during the reaction. The reaction was heated at 145 °C for 24 h, and then the solution was cooled to room temperature, the solvent was evaporated, and the remaining oil was dissolved in CH_2Cl_2. This solution was washed with saturated $NaHCO_3$, dried over sodium sulfate and the solvent was evaporated to furnish a clear oil that was loaded onto a silica column and purified using CH_2Cl_2/EtOAc (1 column volume (CV) CH_2Cl_2, 10 CV 0→20% EtOAc in CH_2Cl_2, 2 CV 20% EtOAc). The product elutes as the second spot. Residual toluene

will give a false positive during the first column volume. The desired fractions were isolated and evaporated to yield **L16** (7.74 g, 83.1% yield) as a white powder. ^{1}H NMR (CH_2Cl_2-d_2, 23 °C) δ (ppm): 7.50 (s, 2H), 4.07 (m, 4H), 3.89 (m, 4H), 1.68 (s, 6H). Matched literature report.[56]

4-Bromo-2,6-diacetylpyridine (L15-Br). 4-Bromopyridine hydrochloride **(L14-Br•HCl)** (38.9 g, 200 mmol, 1.00 equiv) was dissolved in 300 mL of deionized water. The solution was then basified using saturated sodium carbonate to a pH of 9. The resulting basified mixture was extracted (3 × 100 mL) with dichloromethane, which in turn was then extracted (3 × 330 mL) with 0.5 M sulfuric acid. This sulfuric acid solution was added to a 2 L two-neck flask equipped with a large stir bar. While stirring, pyruvic acid (70.8 g, 800 mmol, 3.00 equiv) and silver nitrate (3.40 g, 20.0 mmol, 10.0 mol% dissolved in 200 mL of deionized water) were added. Should a thick white precipitate form at this point (AgCl) the reaction needs to be started over and greater care needs to be taken in the anion exchange steps described above to exclude all chloride. Finally, sodium persulfate (143 g, 600 mmol, 3.00 equiv) was added all at once with vigorous stirring. After approximately 15 min, carbon dioxide was seen evolving from the reaction. The reaction is allowed to stir overnight resulting in a dark green precipitate and yellow-green solution. The reaction is filtered and the precipitate is washed with 150 mL of dichloromethane. The resulting filtrate is basified to pH 10 using saturated sodium hydroxide. This leads to a warming of the solution and a change in color to dark red/brown. Once cooled to room temperature the solution was extracted (3 × 300 mL) with CH_2Cl_2 and the extracts combined with the previous wash of the precipitate and filtered through a short silica pad (3´´). The filtrate was dried over sodium sulfate and dry-loaded onto silica. A column was charged with the dry-loaded compound on silica and the compound was purified by column chromatography using neat CH_2Cl_2. The first compound to come off the column is the desired

product. The fractions were evaporated to dryness to yield **L15-Br** (7.50 g, 16.2% yield) as a white solid. ^{1}H NMR (CD_2Cl_2-d_2, 23 °C) δ (ppm): 8.33 (s, 2H), 2.75 (s, 6H). HRMS(+ESI–TOF) m/z: $[M+H]^+$ calcd for $C_9H_9BrNO_2$ 241.9811; found 241.9807. Matched literature report.[58]

4-Trifluoromethyl-2,6-diacetylpyridine (L15-CF_3). 4-Trifluoro-methylpyridine **(L14-CF_3)** (25.0 g, 170 mmol, 1.00 equiv) was dissolved in 1 L of 0.5 M sulfuric acid. While stirring, pyruvic acid (44.9 g, 510 mmol, 3.00 equiv) and silver nitrate (2.90 g, 16.9 mmol, 10.0 mol% dissolved in 200 mL of deionized water) were added. Finally, sodium persulfate (122 g, 510 mmol, 3.00 equiv) was added all at once with vigorous stirring. After approximately 15 min, carbon dioxide was seen evolving from the reaction. The reaction is allowed to stir overnight resulting in a yellow-green solution. The reaction was basified to pH 10 using saturated sodium hydroxide. This leads to a warming of the solution and a change in color to dark red/brown and an iridescent sheen due to the formation of silver byproducts. Once cooled to room temperature, the solution was extracted (3 × 300 mL) with CH_2Cl_2 and the extracts combined and filtered through a short silica pad (3´´). Note, the CH_2Cl_2 layer may contain dredges of silver byproducts, however they are removed by the silica pad. The red/orange filtrate was dried over sodium sulfate and dry-loaded onto silica. A column was charged with the dry-loaded compound on silica and the compound was purified by column chromatography using neat CH_2Cl_2. The first compound to come off the column was the desired product. The fractions were evaporated to dryness to yield **L15-CF_3** as a white solid that was recrystallized from pentane at –20 °C to yield white colorless needles (18.3 g, 47.8% yield). ^{1}H NMR (CD_2Cl_2-d_2, 23 °C) δ (ppm): 8.42 (s, 2H), 2.83 (s, 6H). ^{19}F NMR (CD_2Cl_2-d_2, 23 °C) δ (ppm): -65.10 (s, 3F). Matched literature report.[53]

4-tert-Butyl-2,6-diacetylpyridine (L15-^{t}Bu). 4-tert-Butyl-pyridine **(L14-^{t}Bu)** (25.0 g, 185 mmol, 1.00 equiv) was dissolved in 1 L of 0.5 M sulfuric acid. While stirring, pyruvic acid

(48.9 g, 555 mmol, 3.00 equiv) and silver nitrate (3.15 g, 18.5 mmol, 10.0 mol% dissolved in 200 mL of deionized water) were added. Finally, sodium persulfate (133 g, 555 mmol, 3.00 equiv) was added all at once with vigorous stirring. After approximately 15 min, carbon dioxide was seen evolving from the reaction. The reaction is allowed to stir overnight resulting in a yellow-green solution. The reaction was basified to pH 10 using saturated sodium hydroxide. This leads to a warming of the solution and a change in color to dark red/brown and an iridescent sheen due to the formation of silver byproducts. Once cooled to room temperature the solution was extracted (3 × 300 mL) with CH_2Cl_2 and the extracts combined and filtered through a short silica pad (3′′). Note, the CH_2Cl_2 layer may contain dredges of silver byproducts, however they are removed by the silica pad. The red/orange filtrate was dried over sodium sulfate and dry-loaded onto silica. A column was charged with the dry-loaded compound on silica and the compound was purified by column chromatography using neat CH_2Cl_2. The first compound to come off the column was the desired product. The fractions were evaporated to dryness to yield **L15-^{t}Bu** as a white solid (6.70 g, 17.3% yield). ^{1}H NMR (CD_2Cl_2-d_2, 23 °C) δ (ppm): 8.21 (s, 2H), 2.76(s, 6H), 1.37 (s, 12H). Matched literature report.[60]

4-Methoxy-2,6-diacetylpyridine (L15-OMe). To a 200 mL heavy walled pressure flask equipped with a stir bar was added **L16** (3.00 g, 10.5 mmol, 1.00 eq), sodium methoxide (10.0 g, 185 mmol, 17.0 equiv) and dimethylsulfoxide (75 mL). The reaction was sealed and heated at 110 °C for 12 h, cooled to room temperature and added to 400 mL of distilled water. The reaction was extracted with CH_2Cl_2 (3 × 150 mL), the organics combined and dried over sodium sulfate and evaporated to dryness. This oil was then dissolved in stock hydrochloric acid and water (20 mL) was added, and the solution placed in 200 mL heavy walled pressure flask. The reaction mixture was stirred at 80 °C for 4 h. The reaction was basified to pH 10 with saturated

sodium carbonate and extracted with CH_2Cl_2 (3 × 150 mL). The combined organic fractions were filtered through a short silica pad (2′′), dried over sodium sulfate, and evaporated to yield a clear oil that crystallizes upon standing. The isolation of solid can be accelerated by re-dissolving the oil in pentane and re-evaporating the solution to azeotrope off the CH_2Cl_2, yielding **L15-OMe** as a white powder (1.87 g, 92.0% yield). ^{1}H NMR (DCM-d_2, 23 °C) δ (ppm): 7.68 (s, 2H), 3.95 (s, 3H), 2.74(s, 6H). ^{13}C NMR (CD_2Cl_2-d_2, 23 °C) δ (ppm): 199.7, 168.1, 155.2, 110.7, 56.6, 26.1. HRMS(+ESI–TOF) m/z: $[M+H]^+$ calcd for $C_{10}H_{12}NO_3$ 194.0812; found 194.0806. Matched literature report.[61]

4-Dimethylamino-2,6-diacetylpyridine (L15-NMe$_2$). To a 200 mL heavy walled pressure flask equipped with a stir bar was added **L16** (3.00 g, 10.5 mmol, 1.00 eq), sodium hydroxide (6 g, 150 mmol), 40% dimethylamine in water (30 mL) and dimethylsulfoxide (50 mL). The reaction was sealed and heated at 110 °C for 12 h, cooled to room temperature and added to 400 mL of distilled water. The reaction was extracted with DCM (3 × 150 mL), the organics combined and dried over sodium sulfate and evaporated to dryness. This oil was then dissolved in stock hydrochloric acid and water (20 mL) was added, and the solution placed in 200 mL heavy walled pressure flask. The reaction mixture was stirred at 80 °C for 4 h. The reaction was basified to pH 10 and extracted with CH_2Cl_2 (3 × 150 mL). The combined organic fractions were filtered through a short silica pad (2′′), dried over sodium sulfate, and evaporated to yield a clear oil that crystallizes upon standing. The isolation of solid can be accelerated by re-dissolving the oil in pentane and re-evaporating the solution to azeotrope off the CH_2Cl_2, yielding **L15-NMe$_2$** as an off-white powder (1.71 g, 79.0% yield). ^{1}H NMR (CD_2Cl_2-d_2, 23 °C) δ (ppm): 7.38 (s, 2H), 3.09 (s, 6H), 2.71 (s, 6H). Matched literature report.[53]

4-Trifluoromethylpyridine-2,6-diimine (L17-CF$_3$). A 500 mL round bottom flask

equipped with a stir bar was charged with **L15-CF_3** (1.08 g, 4.67 mmol, 1.00 eq), *p*-toluenesulfonic acid (0.470 mmol, 10.0 mol%), 2,6-dimethylaniline(14.0 mmol, 3.00 eq), and toluene (300 mL). This mixture was heated at 145 °C using a short path Dean-Stark apparatus with a reflux condenser attached to the top. The top of the condenser was sealed with a septum and a gentle nitrogen flow via a syringe needle was maintained during the reaction. The reaction was allowed to run for 12 h causing a gradual color change to bright yellow. The reaction was cooled to room temperature, the solvent removed, and the resulting thick oil re-dissolved in CH_2Cl_2 (100 mL). This solution was washed with saturated $NaHCO_3$. The CH_2Cl_2 layer was then dried over sodium sulfate and evaporated to yield a yellow oil that immediately begins to crystallize. A small amount (100 mL) of methanol was added to cause total precipitation of a bright yellow powder. The solid was isolated by filtration to yield **L17-CF_3** (1.51 g, 73.0% yield) as a bright yellow powder. ^{1}H NMR (CD_2Cl_2-d_2, 23 °C) δ (ppm): 8.73 (s, 2H), 7.08 (d, 4H), 6.97 (t, 2H), 2.25 (s, 6H), 2.04 (s, 12H). ^{13}C NMR (CD_2Cl_2-d_2, 23 °C) δ (ppm): 166.8, 157.2, 149.0, 140.0 (d), 128.5, 125.8, 123.8, 118.3, 18.2, 16.9. ^{19}F NMR (CD_2Cl_2-d_2, 23 °C) δ (ppm): –64.73 (m, 3F). HRMS(+ESI–TOF) m/z: $[M+H]^+$ calcd for $C_{26}H_{27}F_3N_3$ 438.2152; found 438.2143.

4-Chloropyridine-2,6-diimine (L17-Cl). A 500 mL round bottom flask equipped with a stir bar was charged with **L15-Cl** (1.03 g, 5.18 mmol), *p*-toluenesulfonic acid (0.520 mmol, 10.0 mol%), 2,6-dimethylaniline(15.5 mmol, 3.00 eq), and toluene (300 mL). This mixture was heated at 145 °C using a short path Dean-Stark apparatus with a reflux condenser attached to the top. The top of the condenser was sealed with a septum and a gentle nitrogen flow via a syringe needle was maintained during the reaction. The reaction was allowed to run for 12 h causing a gradual color change to bright yellow. The reaction was cooled to room temperature, the solvent removed, and the resulting thick oil re-dissolved in CH_2Cl_2 (100 mL). This solution was washed

with saturated $NaHCO_3$. The CH_2Cl_2 layer was then dried over sodium sulfate and evaporated to yield a yellow oil that immediately begins to crystallize. A small amount (100 mL) of methanol was added to cause total precipitation of a bright yellow powder. The solid was isolated by filtration to yield **L17-Cl** (1.54 g, 74.4% yield) as a bright yellow powder. ^{1}H NMR (CD_2Cl_2-d_2, 23 °C) δ (ppm): 8.49 (s, 2H), 7.08 (d, 4H), 6.95 (3, 2H), 2.21 (s, 6H), 2.03 (s, 12H). ^{13}C NMR (CD_2Cl_2-d_2, 23 °C) δ (ppm): 166.8, 157.2, 149.1, 145.7, 128.4, 125.8, 123.7, 122.8, 18.2, 16.9. HRMS(+ESI–TOF) m/z: $[M+H]^+$ calcd for $C_{25}H_{27}ClN_3$ 404.1888; found 404.1883.

4-Bromopyridine-2,6-diimine (L17-Br). A 500 mL round bottom flask equipped with a stir bar was charged with **L15-Br** (1.13 g, 4.70 mmol, 1.00 equiv), *p*-toluenesulfonic acid (0.470 mmol, 10.0 mol%), 2,6-dimethylaniline (14.1 mmol, 3.00 equiv), and toluene (300 mL). This mixture was heated at 145 °C using a short path Dean-Stark apparatus with a reflux condenser attached to the top. The top of the condenser was sealed with a septum and a gentle nitrogen flow via a syringe needle was maintained during the reaction. The reaction was allowed to run for 12 h causing a gradual color change to bright yellow. The reaction was cooled to room temperature, the solvent removed, and the resulting thick oil re-dissolved in CH_2Cl_2 (100 mL). This solution was washed with saturated $NaHCO_3$. The CH_2Cl_2 layer was then dried over sodium sulfate and evaporated to yield a yellow oil that immediately begins to crystallize. A small amount (100 mL) of methanol was added to cause total precipitation of a bright yellow powder. The solid was isolated by filtration to yield **L17-Br** (1.50 g, 71.2% yield) as a bright yellow powder. ^{1}H NMR (CD_2Cl_2-d_2, 23 °C) δ (ppm): 8.65 (s, 2H), 7.08 (d, 4H), 6.95 (d, 2H), 2.20 (s, 6H), 2.03 (s, 12H). ^{13}C NMR (CD_2Cl_2-d_2, 23 °C) δ (ppm): 166.7, 156.9, 149.1, 134.4, 128.4, 125.8, 123.7, 18.2, 16.8. HRMS(+ESI–TOF) m/z: $[M+H]^+$ calcd for $C_{25}H_{27}BrN_3$ 448.1383; found 448.1375.

4-tert-Butylpyridine-2,6-diimine (L17-^{t}Bu). A 500 mL round bottom flask equipped

with a stir bar was charged with **L15-^{t}Bu** (1.41 g 6.43 mmol), *p*-toluenesulfonic acid (0.330 mmol, 10.0 mol%), 2,6-dimethylaniline (19.3 mmol, 3.00 equiv), and toluene (300 mL). This mixture was heated at 145 °C using a short path Dean-Stark apparatus with a reflux condenser attached to the top. The top of the condenser was sealed with a septum and a gentle nitrogen flow via a syringe needle was maintained during the reaction. The reaction was allowed to run for 12 h causing a gradual color change to bright yellow. The reaction was cooled to room temperature, the solvent removed, and the resulting thick oil re-dissolved in CH_2Cl_2 (100 mL). This solution was washed with saturated $NaHCO_3$. The CH_2Cl_2 layer was then dried over sodium sulfate and evaporated to yield a yellow oil that immediately begins to crystallize. A small amount (100 mL) of methanol was added to cause total precipitation of a pale yellow powder. The solid was isolated by filtration to yield **L17-^{t}Bu** (1.92 g, 71.0% yield) as a pale yellow powder. ^{1}H NMR (CD_2Cl_2-d_2, 23 °C) δ (ppm): 8.52 (s, 2H), 7.08 (d, 4H), 6.93 (d, 2H), 2.22 (s, 6H), 2.05 (s, 12H), 1.45 (s, 9H). ^{13}C NMR (CD_2Cl_2-d_2, 23 °C) δ (ppm): 168.0, 161.7, 155.8, 149.6, 128.4, 125.9, 123.4, 119.7, 35.8, 31.1, 18.3, 17.0. HRMS(+ESI–TOF) m/z: $[M+H]^+$ calcd for $C_{29}H_{36}N_3$ 426.2904; found 426.2898. Matched literature report.[60]

4-Methoxypyridine-2,6-diimine (L17-OMe). A 500 mL round bottom flask equipped with a stir bar was charged with **L15-OMe** (1.10 g, 5.69 mmol), *p*-toluenesulfonic acid (0.570 mmol, 10.0 mol%), 2,6-dimethylaniline (17.1 mmol, 3.00 equiv), and toluene (300 mL). This mixture was heated at 145 °C using a short path Dean-Stark apparatus with a reflux condenser attached to the top. The top of the condenser was sealed with a septum and a gentle nitrogen flow via a syringe needle was maintained during the reaction. The reaction was allowed to run for 12 h causing a gradual color change to dark yellow. The reaction was cooled to room temperature, the solvent removed, and the resulting thick oil re-dissolved in CH_2Cl_2 (100 mL). This solution

was washed with saturated $NaHCO_3$. The CH_2Cl_2 layer was then dried over sodium sulfate and evaporated to yield a dark yellow/orange oil that was dissolved in minimal methanol and cooled to –20 °C yielding dark yellow crystals. The crystals were isolated by filtration to yield **L17-OMe** (1.62 g, 70.5% yield) as a dark yellow powder. ^{1}H NMR (CD_2Cl_2-d_2, 23 °C) δ (ppm): 8.02 (s, 2H), 7.07 (d, 4H), 6.93 (d, 2H), 4.00 (s, 3H), 2.20 (s, 6H), 2.03 (s, 12H). ^{13}C NMR (CD_2Cl_2-d_2, 23 °C) δ (ppm): 167.6, 157.6, 149.4, 128.4, 125.9, 123.5, 108.5, 56.3, 18.2, 17.0. HRMS(+ESI–TOF) m/z: $[M+H]^+$ calcd for $C_{26}H_{30}N_3O$ 400.2383; found 400.2379.

4-Dimethylaminopyridine-2,6-diimine (L17-NMe$_2$). A 500 mL round bottom flask equipped with a stir bar was charged with **L15-NMe$_2$** (1.48 g, 7.17 mmol), *p*-toluenesulfonic acid (0.720 mmol, 10.0 mol%), 2,6-dimethylaniline (21.5 mmol, 3.00 equiv), and toluene (300 mL). This mixture was heated at 145 °C using a short path Dean-Stark apparatus with a reflux condenser attached to the top. The top of the condenser was sealed with a septum and a gentle nitrogen flow via a syringe needle was maintained during the reaction. The reaction was allowed to run for 12 h causing a gradual color change to pale yellow. The reaction was cooled to room temperature, the solvent removed, and the resulting thick oil re-dissolved in CH_2Cl_2 (100 mL). This solution was washed with saturated $NaHCO_3$. The CH_2Cl_2 layer was then dried over sodium sulfate and evaporated to yield a pale yellow oil that immediately begins to crystallize. A small amount (100 mL) of methanol was added to cause total precipitation of a white powder. The solid was isolated by filtration to yield **L17-NMe$_2$** (2.21 g, 74.2% yield) as a white powder. ^{1}H NMR (CD_2Cl_2-d_2, 23 °C) δ (ppm): 7.76 (s, 2H), 7.07 (d, 4H), 6.92 (d, 2H), 3.14 (s, 6H), 2.19 (s, 6H), 2.04 (s, 12H). ^{13}C NMR (CD_2Cl_2-d_2, 23 °C) δ (ppm): 168.5, 156.1, 149.7, 128.3, 126.0, 123.2, 105.2, 39.9, 18.2, 17.1. HRMS(+ESI–TOF) m/z: $[M+H]^+$ calcd for $C_{27}H_{33}N_4$ 413.2700; found 413.2693.

1,1',1'',1'''-(dibenzo[b,d]furan-4,6-diylbis(pyridine-4,2,6-triyl))tetrakis(ethan-1-one) (L18). To a 50 mL heavy walled pressure flask equipped with a stir bar was added DMF (20 mL) and water (3 mL). This solvent mixture was degassed with argon using a medium fritted gas dispersion tube by bubbling though the solution for 30 min. While under a blanket of argon gas, 4,6-dibromodibenzofuran (511 mg, 1.57 mmol, 1.00 eq), **L7** (954 mg, 3.30 mmol, 2.10 eq), cesium carbonate (1.01 g, 3.10 mmol, 2.00 eq), SPhosPdG2 (115 mg, 0.16 mmol, 10.0 mol%), were added. The reaction was sealed and heated at 90 °C for 44 h, cooled to room temperature, and added to 50 mL of distilled water. The reaction was extracted with CH_2Cl_2 (2 × 15 mL), the organics combined, dried over sodium sulfate, and purified by flash silica gel column chromatography, eluting with CH_2Cl_2. The appropriate fractions by TLC were collected and evaporated to dryness yielding **xx** as a white powder (259 mg, 33.6% yield). ^{1}H NMR ($CDCl_3$-d_1, 23 °C) δ (ppm): 8.84 (s, 4H), 8.13 (d, *J* = 5.00 Hz, 2H), 7.95 (d, *J* = 10.0 Hz, 2H), 7.57 (t, *J* = 10.0 Hz, 2H), 2.87 (s, 12H).

1,1',1'',1'''-((2,7-di-tert-butyl-9,9-dimethyl-9H-xanthene-4,5-diyl)bis(pyridine-4,2,6-triyl))tetrakis(ethan-1-one) (L19). To a 50 mL heavy walled pressure flask equipped with a stir bar was added DMF (20 mL) and water (3 mL). This solvent mixture was degassed with argon using a medium fritted gas dispersion tube by bubbling though the solution for 30 min. While under a blanket of argon gas, 4,5-dibromo-2,7-di-tert-butyl-9,9-dimethyl-9H-xanthene (745 mg, 1.55 mmol, 1.00 eq), **L7** (941 mg, 3.26 mmol, 2.10 eq), cesium carbonate (1.01 g, 3.10 mmol, 2.00 eq), SPhosPdG2 (115 mg, 0.16 mmol, 10.0 mol%), were added. The reaction was sealed and heated at 90 °C for 24 h, cooled to room temperature, and added to 50 mL of distilled water. The reaction was extracted with CH_2Cl_2 (2 × 15 mL), the organics combined, dried over sodium sulfate, and purified by flash silica gel column chromatography, eluting with CH_2Cl_2. The

appropriate fractions by TLC were collected and evaporated to dryness yielding **L19** as a white powder (549 mg, 58.0% yield).

1,1',1'',1'''-(dibenzo[b,d]furan-4,6-diylbis(pyridine-4,2,6-triyl))tetrakis(N-(2,6-dimethylphenyl)ethan-1-imine) (L20). A 500 mL round bottom flask equipped with a stir bar was charged with **L18** (113 mg, 0.230 mmol, 1.00 eq), *p*-toluenesulfonic acid (12.3 mg, 0.065 mmol, 28.1 mol%), 2,6-dimethylaniline (226 mg, 1.87 mmol, 8.12 eq), and toluene (50 mL). This mixture was heated at 145 °C using a short path Dean-Stark apparatus with a reflux condenser attached to the top. The top of the condenser was sealed with a septum and a gentle nitrogen flow via a syringe needle was maintained during the reaction. The reaction was allowed to run for 5 days causing a gradual color change to yellow. The reaction was cooled to room temperature, the solvent removed, and the resulting thick oil re-dissolved in CH_2Cl_2 (40 mL). This solution was washed with saturated $NaHCO_3$. The CH_2Cl_2 layer was then dried over sodium sulfate and evaporated to yield yellow oil that immediately begins to crystallize. A small amount (20 mL) of methanol was added to cause total precipitation of a yellow powder. The solid was isolated by filtration to yield **L20** (150 mg, 72.0% yield) as a yellow powder. ^{1}H NMR ($CDCl_3$-d_1, 23 °C) δ (ppm): 8.90 (s, 4H), 8.15 (d, J = 10.0 Hz, 2H), 7.81 (d, J = 5.00 Hz, 2H), 7.56 (t, J = 10.0 Hz, 2H), 7.02 (m, 8H), 6.90 (m, 4H), 2.27 (s, 12H), 1.88 (s, 24H).

[$FeCl_2$(4-PhPDI)]PF_6 (1a). To a 20 mL scintillation vial was added **L6** (110 mg, 0.246 mmol, 1.00 eq), $FeCl_3$ (40.0 mg, 0.246 mmol, 1.00 eq), and $AgPF_6$ (62.19 mg, 0.246 mmol, 1.00 eq)., and MeCN (5.00g) The reaction immediately turned deep red and a white AgCl precipitate was observed. The reaction was stirred using a small Teflon coated magnetic stir bar at ambient temperature for 1 hr, pipette filtered through glass paper, and concentrated to leave approximately 1 mL of solution. The resulting solution was filtered again through a tightly

packed glass paper pipette filter and placed in an ether diffusion chamber to grow red plate shaped crystals. If upon complete diffusion of ether into the solution the crystal yield is low, the vial was placed in a freezer at −35 °C for 24 hrs prior to crystal collection. The supernatant was removed and the crystals washed with additional diethyl ether. The crystals were then dried under vacuum to yield **1a** (118 mg, 68.1% yield) as a dark red powder. ^{1}H NMR (500 MHz, C_6F_2, 23 ^{o}C) δ (ppm): 63.99 (br s), 32.37 (br s), 11.30, 3.50, 2.33, 1.36, 0.99, −0.66 (br s), −3.87 (br s), −38.10 (br s). μ_{eff} (295 K, CH_3CN) 6.02 μB. Zero-field ^{57}Fe Mössbauer (100 K) (δ, $|\Delta E_Q|$ (mm/s)): 0.53, 1.25. Crystals suitable for single-crystal diffraction analysis were obtained from CH_3CN solution layered with Et_2O at −35 ^{o}C.

[$FeCl_2$(BisMesPDI)]PF_6 (1b). To a 20 mL scintillation vial was added **L4** (130 mg, 0.191 mmol, 1.00 eq), $FeCl_3$ (31.0 mg, 0.191 mmol, 1.00 eq), and $AgPF_6$ (48.3 mg, 0.191 mmol, 1.00 eq), and MeCN (5.00g). The reaction immediately turned deep red and a white AgCl precipitate was observed. The reaction was stirred using a small Teflon coated magnetic stir bar at ambient temperature for 1 hr, pipette filtered through glass paper, and concentrated to leave approximately 1 mL of solution. The resulting solution was filtered again through a tightly packed glass paper pipette filter and placed in an ether diffusion chamber to grow red plate shaped crystals. The supernatant was removed and the crystals washed with additional diethyl ether. If upon complete diffusion of ether into the solution the crystal yield is low, the vial was placed in a freezer at −35 °C for 24 hrs prior to crystal collection. The crystals were then dried under vacuum to yield **1b** (121 mg, 64.2% yield) as a dark red powder. ^{1}H NMR (500 MHz, C_6F_2, 23 ^{o}C) δ (ppm): 62.17 (br s), 33.06 (br s), 12.19, 7.04, 3.16, 2.34, 2.23, 1.64, 1.22, 0.82, 0.55, −39.46 (br s). μ_{eff} (295 K, CH_3CN) 6.16 μB. Zero-field ^{57}Fe Mössbauer (100 K) (δ, $|\Delta E_Q|$ (mm/s)): 0.39, 0.89. Crystals suitable for single-crystal diffraction analysis were obtained from

CH_3CN solution layered with Et_2O at −35 ^oC.

[$FeCl_2$(4-^{t}BuPDI)]BF_4 (1c). To a 20 mL scintillation vial was added 4-tert-butylpyridine-2,6-diimine (35 mg, 0.082 mmol, 1.00 eq), $FeCl_3$ (13.3 mg, 0.082 mmol, 1.00 eq), and $AgPF_6$ (16.0 mg, 0.082 mmol, 1.00 eq)., and MeCN (2.00g) The reaction immediately turned deep red and a white AgCl precipitate was observed. The reaction was stirred using a small Teflon coated magnetic stir bar at ambient temperature for 1 hr, pipette filtered through glass paper, and concentrated to leave approximately 1 mL of solution. The resulting solution was filtered again through a tightly packed glass paper pipette filter and placed in an ether diffusion chamber to grow red plate shaped crystals. If upon complete diffusion of ether into the solution the crystal yield is low, the vial was placed in a freezer at −35 °C for 24 hrs prior to crystal collection. The supernatant was removed and the crystals washed with additional diethyl ether. The crystals were then dried under vacuum to yield **1a** (21.5 mg, 71.0% yield) as a dark red powder. ^1H NMR (500 MHz, CD_3CN, 23 ^oC) δ (ppm): 64.79 (br s), 59.14 (br s), 33.18, 4.79, −38.18 (br s). μ_{eff} (295 K, CH_3CN) 6.33 μB. Crystals suitable for single-crystal diffraction analysis were obtained from CH_3CN solution layered with Et_2O at −35 ^oC.

$FeCl_2$(4-PhPDI) (2a). To a 20 mL scintillation vial was added **L6** (99.5 mg, 0.220 mmol, 1.00 eq), $FeCl_2$ (28.3 mg, 0.220 mmol, 1.00 eq), and MeCN (5.00 g). The reaction immediately turned deep blue. The reaction was stirred using a small Teflon coated magnetic stir bar at ambient temperature for 1 hr, pipette filtered through glass paper, and concentrated to leave approximately 1 mL of solution. The resulting solution was filtered again through a tightly packed glass paper pipette and placed in an ether diffusion chamber to grow blue plate shaped crystals. The supernatant was removed and the crystals washed with additional diethyl ether. The crystals were then dried under vacuum to yield **2a** (96.7 mg, 76.6 % yield) as a blue powder. ^1H

NMR (500 MHz, CD_3CN-d_3, 23 ^oC) δ (ppm): 89.76, 17.28, 14.79, 8.69, 7.29, 6.04, −4.83, −9.56. μ_{eff} (295 K, CH_2Cl_2) 5.02 μB. Zero-field ^{57}Fe Mössbauer (100 K) (δ, $|\Delta E_Q|$ (mm/s)): 1.02, 2.69. Crystals suitable for single-crystal diffraction analysis were obtained from CH_3CN solution layered with Et_2O at −35 ^oC.

$FeCl_2$(BisMesPDI) (2b). To a 20 mL scintillation vial was added **L4** (50.0 mg, 0.073 mmol, 1.00 eq), $FeCl_2$ (9.30 mg, 0.073 mmol, 1.00 eq), and MeCN (3.00 g). The reaction immediately turned deep blue. The reaction was stirred using a small Teflon coated magnetic stir bar at ambient temperature for 1 hr, pipette filtered through glass paper, and concentrated to leave approximately 1 mL of solution. The resulting solution was filtered again through a tightly packed glass paper pipette and placed in an ether diffusion chamber to grow blue plate shaped crystals. The supernatant was removed and the crystals washed with additional diethyl ether. The crystals were then dried under vacuum to yield **2b** (48.3 mg, 81.4% yield) as a blue powder. ^1H NMR (500 MHz, CD_3CN-d_3, 23 ^oC) δ (ppm): 86.06, 17.62, 15.91, 8.65, 6.85, 6.30, −3.21, −8.80. μ_{eff} (295 K, CH_3CN) 5.06 μB. Zero-field ^{57}Fe Mössbauer (100 K) (δ, $|\Delta E_Q|$ (mm/s)): 1.03, 2.72. Crystals suitable for single-crystal diffraction analysis were obtained from CH_3CN solution layered with Et_2O at −35 ^oC.

[FeCl(BisMesPDI)]PF_6 (3). To a 20 mL scintillation vial was added **L4** (107mg, 0.156 mmol, 1.00 eq), $FeCl_2$ (19.7 mg, 0.156 mmol, 1.00 eq), and $AgPF_6$ (39.4 mg, 0.156 mmol, 1.00 eq), and MeCN (5.00g). The reaction immediately turned deep red and a white AgCl precipitate was observed. The reaction was stirred using a small Teflon coated magnetic stir bar at ambient temperature for 4 hr, pipette filtered through glass paper, and concentrated to leave approximately 1 mL of solution. The resulting solution was filtered again through a tightly packed glass paper pipette filter and placed in an ether diffusion chamber to grow red plate

shaped crystals. The supernatant was removed and the crystals washed with additional diethyl ether. If upon complete diffusion of ether into the solution the crystal yield is low, the vial was placed in a freezer at −35 °C for 24 hrs prior to crystal collection. The crystals were then dried under vacuum to yield **3** (62.7 mg, 64.2% yield) as a light red powder. ^{1}H NMR (500 MHz, CD_3CN, 23 ^{o}C) δ (ppm): 94.89 (br s), 14.06, 13.21 (br s), 10.47, 7.79, 5.43, 3.41, 3.02, 2.51, 1.93, 1.79, 1.29, −5.68, −12.14. Crystals suitable for single-crystal diffraction analysis were obtained from CH_3CN solution layered with Et_2O at −35 ^{o}C.

$FeCl_2(PMe_2Ph)_2$ (5b). To a 20 mL scintillation vial was added anhydrous $FeCl_2$ (100 mg, 0.789 mmol, 1.00 eq) and PMe_2Ph (218 mg, 1.58 mmol, 2.00 eq), and 6 mL THF. The reaction was stirred at 23 ^{o}C for 12 hr, during which time a white precipitate was observed. The mixture was concentrated to dryness and the residue was washed with pentane and dried in vacuo to afford title compound as an off white solid (286 mg, 90% yield). ^{1}H NMR (500 MHz, C_6D_6-d_6, 23 ^{o}C) δ (ppm): 81.38 (br s), 14.68, −3.87. μ_{eff} (295 K, C_6H_6) 5.41 μB. Zero-field ^{57}Fe Mössbauer (100 K) (δ, $|\Delta E_Q|$ (mm/s)): 0.70, 2.79. Crystals suitable for single-crystal diffraction analysis were obtained from diflurobenzene solution layered with pentane at −35 ^{o}C.

$FeCl_3$XPhos (6). Anhydrous $FeCl_3$ (123 mg, 0.757 mmol, 1.00 eq) was dissolved in 2 mL Et_2O and added into a solution of XPhos (361 mg, 0.757 mmol, 1.00 eq) in 5 mL of benzene, immediately turned a red solution. The mixture was stirred for 0.5 hr, at which time the solution was filtered through glass fiber, layered with pentane, and stored at −35°C for 24 hrs. The supernatant was decanted, and complex **6** was isolated as a yellow crystalline solid (319 mg, 49.9% yield). ^{1}H NMR (500 MHz, C_6D_6-d_6, 23 ^{o}C) δ (ppm): 46.83 (br s), 15.12 (br s), 9.68 (br s), 8.36, 3.27, 2.90, 2.11, 1.28, −15.25 (br s). μ_{eff} (295 K, CH_2Cl_2) 5.72 μB. Zero-field ^{57}Fe Mössbauer (100 K) (δ, $|\Delta E_Q|$ (mm/s)): 0.09, 0.00. Crystals suitable for single-crystal diffraction analysis

were obtained from $PhCH_3$ solution layered with pentane at −35 ^oC.

[$FeCl_2$(4-CF_3-PDI)]PF_6 (7a). To a 20 mL scintillation vial was added **L17-CF_3** (110 mg, 0.251 mmol, 1.00 eq), $FeCl_3$ (40.7 mg, 0. 251 mmol, 1.00 eq), and $AgPF_6$ (63.5 mg, 0.251 mmol, 1.00 eq)., and MeCN (5.00g) The reaction immediately turned deep red and a white AgCl precipitate was observed. The reaction was stirred using a small Teflon coated magnetic stir bar at ambient temperature for 1 hr, pipette filtered through glass paper, and concentrated to leave approximately 1 mL of solution. The resulting solution was filtered again through a tightly packed glass paper pipette filter and placed in an ether diffusion chamber to grow red plate shaped crystals. If upon complete diffusion of ether into the solution the crystal yield is low, the vial was placed in a freezer at −35 °C for 24 hrs prior to crystal collection. The supernatant was removed and the crystals washed with additional diethyl ether. The crystals were then dried under vacuum to yield **7a** (110 mg, 62% yield) as a dark red powder.

[$FeCl_2$(4-Cl-PDI)]PF_6 (7b). To a 20 mL scintillation vial was added **L17-Cl** (115 mg, 0.284 mmol, 1.00 eq), $FeCl_3$ (46.1 mg, 0. 284 mmol, 1.00 eq), and $AgPF_6$ (71.8 mg, 0.284 mmol, 1.00 eq)., and MeCN (5.00g) The reaction immediately turned deep red and a white AgCl precipitate was observed. The reaction was stirred using a small Teflon coated magnetic stir bar at ambient temperature for 1 hr, pipette filtered through glass paper, and concentrated to leave approximately 1 mL of solution. The resulting solution was filtered again through a tightly packed glass paper pipette filter and placed in an ether diffusion chamber to grow red plate shaped crystals. If upon complete diffusion of ether into the solution the crystal yield is low, the vial was placed in a freezer at −35 °C for 24 hrs prior to crystal collection. The supernatant was removed and the crystals washed with additional diethyl ether. The crystals were then dried under vacuum to yield **7b** (130 mg, 68% yield) as a dark red powder. ^1H NMR (500 MHz,

CD_3CN, 23 ^oC) δ (ppm): 57.77 (br s), 32.50 (br s), 13.45, 8.68, 7.23, −37.19 (br s). Crystals suitable for single-crystal diffraction analysis were obtained from CH_3CN solution layered with Et_2O at −35 ^oC.

[$FeCl_2$(4-Br-PDI)]PF_6 (7c). To a 20 mL scintillation vial was added **L17-Br** (113 mg, 0.251 mmol, 1.00 eq), $FeCl_3$ (40.7 mg, 0.251 mmol, 1.00 eq), and $AgPF_6$ (63.5 mg, 0.251 mmol, 1.00 eq)., and MeCN (5.00g) The reaction immediately turned deep red and a white AgCl precipitate was observed. The reaction was stirred using a small Teflon coated magnetic stir bar at ambient temperature for 1 hr, pipette filtered through glass paper, and concentrated to leave approximately 1 mL of solution. The resulting solution was filtered again through a tightly packed glass paper pipette filter and placed in an ether diffusion chamber to grow red plate shaped crystals. If upon complete diffusion of ether into the solution the crystal yield is low, the vial was placed in a freezer at −35 °C for 24 hrs prior to crystal collection. The supernatant was removed and the crystals washed with additional diethyl ether. The crystals were then dried under vacuum to yield **7c** (124 mg, 67% yield) as a dark red powder. ^1H NMR (500 MHz, CD_3CN, 23 ^oC) δ (ppm): 58.23 (br s), 32.35 (br s), 12.25, 7.23, −36.96 (br s). Crystals suitable for single-crystal diffraction analysis were obtained from CH_3CN solution layered with Et_2O at −35 ^oC.

[$FeCl_2$(4-H-PDI)]PF_6 (7d). To a 20 mL scintillation vial was added **L17-H** (105 mg, 0.284 mmol, 1.00 eq), $FeCl_3$ (46.1 mg, 0. 284 mmol, 1.00 eq), and $AgPF_6$ (71.8 mg, 0.284 mmol, 1.00 eq)., and MeCN (5.00g) The reaction immediately turned deep red and a white AgCl precipitate was observed. The reaction was stirred using a small Teflon coated magnetic stir bar at ambient temperature for 1 hr, pipette filtered through glass paper, and concentrated to leave approximately 1 mL of solution. The resulting solution was filtered again through a tightly

packed glass paper pipette filter and placed in an ether diffusion chamber to grow red plate shaped crystals. If upon complete diffusion of ether into the solution the crystal yield is low, the vial was placed in a freezer at −35 °C for 24 hrs prior to crystal collection. The supernatant was removed and the crystals washed with additional diethyl ether. The crystals were then dried under vacuum to yield **7d** (106 mg, 58% yield) as a dark red powder.

[$FeCl_2$(4-^{t}Bu-PDI)]PF_6 (7e). To a 20 mL scintillation vial was added **L17-^{t}Bu** (114 mg, 0.267 mmol, 1.00 eq), $FeCl_3$ (43.4 mg, 0.267 mmol, 1.00 eq), and $AgPF_6$ (67.5 mg, 0.267 mmol, 1.00 eq)., and MeCN (5.00g) The reaction immediately turned deep red and a white AgCl precipitate was observed. The reaction was stirred using a small Teflon coated magnetic stir bar at ambient temperature for 1 hr, pipette filtered through glass paper, and concentrated to leave approximately 1 mL of solution. The resulting solution was filtered again through a tightly packed glass paper pipette filter and placed in an ether diffusion chamber to grow red plate shaped crystals. If upon complete diffusion of ether into the solution the crystal yield is low, the vial was placed in a freezer at −35 °C for 24 hrs prior to crystal collection. The supernatant was removed and the crystals washed with additional diethyl ether. The crystals were then dried under vacuum to yield **7e** (136 mg, 73% yield) as a dark red powder. ^{1}H NMR (500 MHz, CD_3CN, 23 ^oC) δ (ppm): 64.91 (br s), 58.97 (br s), 33.20 (br s), 13.80, 4.79, −38.09 (br s). Crystals suitable for single-crystal diffraction analysis were obtained from CH_3CN solution layered with Et_2O at −35 ^oC.

[$FeCl_2$(4-OMe-PDI)]PF_6 (7f). To a 20 mL scintillation vial was added **L17-OMe** (103 mg, 0.257 mmol, 1.00 eq), $FeCl_3$ (41.7 mg, 0. 257 mmol, 1.00 eq), and $AgPF_6$ (65.0 mg, 0. 257 mmol, 1.00 eq)., and MeCN (5.00g) The reaction immediately turned deep red and a white AgCl precipitate was observed. The reaction was stirred using a small Teflon coated magnetic stir bar

at ambient temperature for 1 hr, pipette filtered through glass paper, and concentrated to leave approximately 1 mL of solution. The resulting solution was filtered again through a tightly packed glass paper pipette filter and placed in an ether diffusion chamber to grow red plate shaped crystals. If upon complete diffusion of ether into the solution the crystal yield is low, the vial was placed in a freezer at −35 °C for 24 hrs prior to crystal collection. The supernatant was removed and the crystals washed with additional diethyl ether. The crystals were then dried under vacuum to yield **7f** (123 mg, 71% yield) as a dark red powder. ^{1}H NMR (500 MHz, CD_3CN, 23 ^oC) δ (ppm): 61.71 (br s), 59.17 (br s), 33.16 (br s), 24.20 (br s), 12.79, −38.15 (br s). Crystals suitable for single-crystal diffraction analysis were obtained from CH_3CN solution layered with Et_2O at −35 ^oC.

[$FeCl_2$(4-NMe_2-PDI)]PF_6 (7g). To a 20 mL scintillation vial was added **L17-NMe_2** (108 mg, 0.260 mmol, 1.00 eq), $FeCl_3$ (42.3 mg, 0.260 mmol, 1.00 eq), and $AgPF_6$ (66.0 mg, 0. 260 mmol, 1.00 eq)., and MeCN (5.00g) The reaction immediately turned deep red and a white AgCl precipitate was observed. The reaction was stirred using a small Teflon coated magnetic stir bar at ambient temperature for 1 hr, pipette filtered through glass paper, and concentrated to leave approximately 1 mL of solution. The resulting solution was filtered again through a tightly packed glass paper pipette filter and placed in an ether diffusion chamber to grow red plate shaped crystals. If upon complete diffusion of ether into the solution the crystal yield is low, the vial was placed in a freezer at −35 °C for 24 hrs prior to crystal collection. The supernatant was removed and the crystals washed with additional diethyl ether. The crystals were then dried under vacuum to yield **7g** (139 mg, 78% yield) as a dark red powder. ^{1}H NMR (500 MHz, CD_3CN, 23 ^oC) δ (ppm): 119.30 (br s), 102.51 (br s), 57.25 (br s), 51.10 (br s), 33.46 (br s), −38.27 (br s). Crystals suitable for single-crystal diffraction analysis were obtained from CH_3CN

solution layered with Et_2O at −35 °C.

[FeCl(4-CF_3-PDI)]PF_6 (8a). To a 20 mL scintillation vial was added **L17-CF_3** (101 mg, 0.231 mmol, 1.00 eq), $FeCl_2$ (29.3 mg, 0.231 mmol, 1.00 eq), and $AgPF_6$ (58.4 mg, 0.231 mmol, 1.00 eq), and MeCN (5.00g). The reaction immediately turned deep red and a white AgCl precipitate was observed. The reaction was stirred using a small Teflon coated magnetic stir bar at ambient temperature for 4 hr, pipette filtered through glass paper, and concentrated to leave approximately 1 mL of solution. The resulting solution was filtered again through a tightly packed glass paper pipette filter and placed in an ether diffusion chamber to grow red plate shaped crystals. The supernatant was removed and the crystals washed with additional diethyl ether. If upon complete diffusion of ether into the solution the crystal yield is low, the vial was placed in a freezer at −35 °C for 24 hrs prior to crystal collection. The crystals were then dried under vacuum to yield **8a** (127 mg, 82% yield) as a light red powder. ^{1}H NMR (500 MHz, CD_3CN, 23 °C) δ (ppm): 92.44 (br s), 14.27 (br s), 13.54, −10.39 (br s), −12.37. μ_{eff} (295 K, CH_3CN) 5.23 μB. Crystals suitable for single-crystal diffraction analysis were obtained from CH_3CN solution layered with Et_2O at −35 °C.

[FeCl(4-Cl-PDI)]PF_6 (8b). To a 20 mL scintillation vial was added **L17-Cl** (118 mg, 0.292 mmol, 1.00 eq), $FeCl_2$ (37.0 mg, 0.292 mmol, 1.00 eq), and $AgPF_6$ (74.0 mg, 0.292 mmol, 1.00 eq), and MeCN (5.00g). The reaction immediately turned deep red and a white AgCl precipitate was observed. The reaction was stirred using a small Teflon coated magnetic stir bar at ambient temperature for 4 hr, pipette filtered through glass paper, and concentrated to leave approximately 1 mL of solution. The resulting solution was filtered again through a tightly packed glass paper pipette filter and placed in an ether diffusion chamber to grow red plate shaped crystals. The supernatant was removed and the crystals washed with additional diethyl

ether. If upon complete diffusion of ether into the solution the crystal yield is low, the vial was placed in a freezer at −35 °C for 24 hrs prior to crystal collection. The crystals were then dried under vacuum to yield **8b** (132 mg, 71% yield) as a light red powder. ^{1}H NMR (500 MHz, CD_3CN, 23 ^oC) δ (ppm): 96.57 (br s), 13.89 (br s), −6.89, −12.04. μ_{eff} (295 K, CH_3CN) 5.67 μB. Crystals suitable for single-crystal diffraction analysis were obtained from CH_3CN solution layered with Et_2O at −35 ^oC.

[FeCl(4-Br-PDI)]PF_6 (8c). To a 20 mL scintillation vial was added **L17-Br** (104 mg, 0.233 mmol, 1.00 eq), $FeCl_2$ (29.5 mg, 0.233 mmol, 1.00 eq), and $AgPF_6$ (58.8 mg, 0.233 mmol, 1.00 eq), and MeCN (5.00g). The reaction immediately turned deep red and a white AgCl precipitate was observed. The reaction was stirred using a small Teflon coated magnetic stir bar at ambient temperature for 4 hr, pipette filtered through glass paper, and concentrated to leave approximately 1 mL of solution. The resulting solution was filtered again through a tightly packed glass paper pipette filter and placed in an ether diffusion chamber to grow red plate shaped crystals. The supernatant was removed and the crystals washed with additional diethyl ether. If upon complete diffusion of ether into the solution the crystal yield is low, the vial was placed in a freezer at −35 °C for 24 hrs prior to crystal collection. The crystals were then dried under vacuum to yield **8c** (122 mg, 77% yield) as a light red powder. ^{1}H NMR (500 MHz, CD_3CN, 23 ^oC) δ (ppm): 92.82 (br s), 13.88 (br s), −6.64, −12.09. μ_{eff} (295 K, CH_3CN) 5.62 μB. Crystals suitable for single-crystal diffraction analysis were obtained from CH_3CN solution layered with Et_2O at −35 ^oC.

[FeCl(4-H-PDI)]PF_6 (8d). To a 20 mL scintillation vial was added **L17-H** (114 mg, 0.307 mmol, 1.00 eq), $FeCl_2$ (39.0 mg, 0.307 mmol, 1.00 eq), and $AgPF_6$ (77.6 mg, 0.307 mmol, 1.00 eq), and MeCN (5.00g). The reaction immediately turned deep red and a white AgCl

precipitate was observed. The reaction was stirred using a small Teflon coated magnetic stir bar at ambient temperature for 4 hr, pipette filtered through glass paper, and concentrated to leave approximately 1 mL of solution. The resulting solution was filtered again through a tightly packed glass paper pipette filter and placed in an ether diffusion chamber to grow red plate shaped crystals. The supernatant was removed and the crystals washed with additional diethyl ether. If upon complete diffusion of ether into the solution the crystal yield is low, the vial was placed in a freezer at −35 °C for 24 hrs prior to crystal collection. The crystals were then dried under vacuum to yield **8d** (123 mg, 66% yield) as a light red powder. ^{1}H NMR (500 MHz, CD_3CN, 23 ^oC) δ (ppm): 97.57 (br s), 13.74 (br s), 7.04, −1.93, −12.52. μ_{eff} (295 K, CH_3CN) 5.16 μB. Crystals suitable for single-crystal diffraction analysis were obtained from CH_3CN solution layered with Et_2O at −35 ^oC.

[FeCl(4-^{t}Bu-PDI)]PF_6 (8e). To a 20 mL scintillation vial was added **L17-^{t}Bu** (146 mg, 0.343 mmol, 1.00 eq), $FeCl_2$ (43.5 mg, 0.343 mmol, 1.00 eq), and $AgPF_6$ (86.7 mg, 0.343 mmol, 1.00 eq), and MeCN (5.00g). The reaction immediately turned deep red and a white AgCl precipitate was observed. The reaction was stirred using a small Teflon coated magnetic stir bar at ambient temperature for 4 hr, pipette filtered through glass paper, and concentrated to leave approximately 1 mL of solution. The resulting solution was filtered again through a tightly packed glass paper pipette filter and placed in an ether diffusion chamber to grow red plate shaped crystals. The supernatant was removed and the crystals washed with additional diethyl ether. If upon complete diffusion of ether into the solution the crystal yield is low, the vial was placed in a freezer at −35 °C for 24 hrs prior to crystal collection. The crystals were then dried under vacuum to yield **8e** (154.4 mg, 68% yield) as a light red powder. ^{1}H NMR (500 MHz, CD_3CN, 23 ^oC) δ (ppm): 96.71 (br s), 14.18, 13.78 (br s), 4.71, −12.23. μ_{eff} (295 K, CH_3CN)

5.15 μB. Crystals suitable for single-crystal diffraction analysis were obtained from CH_3CN solution layered with Et_2O at −35 °C.

[FeCl(4-OMe-PDI)]PF_6 (8f). To a 20 mL scintillation vial was added **L17-OMe** (138 mg, 0.345 mmol, 1.00 eq), $FeCl_2$ (43.8 mg, 0.345 mmol, 1.00 eq), and $AgPF_6$ (75.4 mg, 0.345 mmol, 1.00 eq), and MeCN (5.00g). The reaction immediately turned deep red and a white AgCl precipitate was observed. The reaction was stirred using a small Teflon coated magnetic stir bar at ambient temperature for 4 hr, pipette filtered through glass paper, and concentrated to leave approximately 1 mL of solution. The resulting solution was filtered again through a tightly packed glass paper pipette filter and placed in an ether diffusion chamber to grow red plate shaped crystals. The supernatant was removed and the crystals washed with additional diethyl ether. If upon complete diffusion of ether into the solution the crystal yield is low, the vial was placed in a freezer at −35 °C for 24 hrs prior to crystal collection. The crystals were then dried under vacuum to yield **8f** (171 mg, 75% yield) as a light red powder. ^{1}H NMR (500 MHz, CD_3CN, 23 °C) δ (ppm): 94.87 (br s), 15.18, 14.55, 13.06 (br s), 0.28, −11.86. μ_{eff} (295 K, CH_3CN) 5.61 μB. Crystals suitable for single-crystal diffraction analysis were obtained from CH_3CN solution layered with Et_2O at −35 °C.

[FeCl(4-NMe_2-PDI)]PF_6 (8g). To a 20 mL scintillation vial was added **L17-NMe_2** (113 mg, 0.273 mmol, 1.00 eq), $FeCl_2$ (34.6 mg, 0.273 mmol, 1.00 eq), and $AgPF_6$ (45.8 mg, 0.273 mmol, 1.00 eq), and MeCN (5.00g). The reaction immediately turned deep red and a white AgCl precipitate was observed. The reaction was stirred using a small Teflon coated magnetic stir bar at ambient temperature for 4 hr, pipette filtered through glass paper, and concentrated to leave approximately 1 mL of solution. The resulting solution was filtered again through a tightly packed glass paper pipette filter and placed in an ether diffusion chamber to grow red plate

shaped crystals. The supernatant was removed and the crystals washed with additional diethyl ether. If upon complete diffusion of ether into the solution the crystal yield is low, the vial was placed in a freezer at −35 °C for 24 hrs prior to crystal collection. The crystals were then dried under vacuum to yield **8g** (145 mg, 82% yield) as a light red powder. ^{1}H NMR (500 MHz, CD_3CN, 23 ^{o}C) δ (ppm): 85.97 (br s), 44.84, 15.16, 12.24 (br s), 1.04, −12.01. μ_{eff} (295 K, CH_3CN) 5.71 μB. Crystals suitable for single-crystal diffraction analysis were obtained from CH_3CN solution layered with Et_2O at −35 ^{o}C.

[Fe(III)Cl$_2$(DBF-PDI)]$_2$(FeCl$_4$)$_2$ (9). To a 20 mL scintillation vial was added **L20** (34.4 mg, 0.038 mmol, 1.00 eq), $FeCl_3$ (12.3 mg, 0.076 mmol, 2.00 eq), and THF (7 mL) The reaction immediately turned deep red. The reaction was stirred using a small Teflon coated magnetic stir bar at ambient temperature for 1 hr, and dried under vacuum to yield red powder. The compounds were redissolved in 1,2-difluorobenzene layered with pentane and placed in a freezer at −35 °C for 24 hrs prior to crystal collection. The crystals were then dried under vacuum to yield **9** (12 mg, 35% yield) as a dark red powder. Crystals suitable for single-crystal diffraction analysis were obtained from 1,2-difluorobenzene solution layered with pentane at −35 ^{o}C.

5.9.2. X-ray crystallographic details

X-ray structures of complexes **1a**, **2a**, **2b**, **3**, **5b**, **6**, **7b, 7c, 7e, 7f, 7g, 8a–8g**, **9**, and variable-temperature (VT) X-ray data were collected on a Bruker three-circle platform goniometer equipped with an Apex II CCD and an Oxford cryostream cooling device operating between 100-300 K. Radiation was from a graphite fine focus sealed tube Mo Kα (0.71073 Å) source. Crystals were mounted on a glass fiber pin using Paratone N oil. Data was collected as a series of φ and/or ω scans. Data was integrated using SAINT and scaled with multi-scan

absorption correction using SADABS.[66] The structures were solved by intrinsic phasing using SHELXT (Apex3 program suite v2016.1.0) and refined against F^2 on all data by full matrix least squares with SHELXL-97.[67] All non-hydrogen atoms were refined anisotropically. H atoms were placed at idealized positions and refined using a riding model.

X-ray structures and photocrystallography data of complexes **1b**, **1c**, **4a**, and **4b** were collected using 0.41328 Å radiation at temperature of 20 K (Oxford Diffraction Helijet) on a vertical mounted Bruker D8 three-circle platform goniometer equipped with an Apex II CCD at ChemMatCARS located at Advances Photon Source (APS), Argonne National Laboratory (ANL). Illumination was provided by a Thor Labs 300 nm LED (M300F2) and was delivered to the sample via a 200 μm ID fiber optic. Dark structures were solved and refined as described above. For data sets obtained during irradiation, non-H atoms of the product were located in difference-Fourier maps, calculated with coefficients F_0(irradiated)–F_0(dark), and then refined with restraints on the product molecule's bond lengths and constraints of the atomic displacement parameters to the corresponding values of the reactant molecule (SADI and EADP instructions of SHELXL97). The percentage of the reactant in the crystal was treated as a variable in the refinements.

5.9.3. Physical measurements

NMR spectra were recorded on a Varian Mercury 400 NMR spectrometer at the Harvard University Department of Chemistry and Chemical Biology Laukien-Purcell Instrumentation Center. ^{1}H spectra were internally referenced to the residual solvent signal (δ = 1.72 and 3.58 for THF in THF-d_8),[68] while $^{31}P\{^1H\}$ and ^{19}F NMR spectra were externally referenced to 85% H_3PO_4 and 1:1 solution of $CFCl_3$ and $CDCl_3$ respectively. Solution magnetic moments were determined using the Evans method in solvent and measured using ^{19}F NMR (hexafluorobenzene

added); diamagnetic corrections were estimated from Pascal constants.[69] UV–vis absorption spectra were acquired at 293 K in quartz cuvettes using a Cary 5000 spectrometer (Agilent) and were blanked against the appropriate solvent. Steady-state photochemical reactions were performed using a 1000 W high-pressure Hg/Xe arc lamp (Oriel). The beam was passed through a water-jacketed filter holder containing the appropriate long pass filter then through an iris and collimating lens before entering the sample, which was in a quartz cuvette placed in a water-jacketed sample holder to maintain a constant temperature. ^{57}Fe Mossbauer spectra were measured with a constant-acceleration mode on a spectrometer (SEE Co, Minneapolis, MN) at 90 K. Isomer shifts are quoted relative to Fe foil at room temperature. Data were analyzed and simulated with Igor Pro 6 software using Lorentzian fitting functions. Samples were prepared by suspending 30-40 mg of crystalline compound in sufficient Paratone N oil and immobilizing by rapid freezing in liquid N_2.

Nanosecond-resolved transient absorption (TA) spectroscopic experiments were carried out using a modified version of a home-built system described previously.(ref) The pump excitation (λ = 355 nm, 8-10 ns at FWHM) was produced by a 10 Hz Spectra-Physics Lab-190 Nd:YAG pulsed laser and attenuated to 3.0 mJ/pulse using neutral density filters. Probe light was provided by a Xe arc lamp (PTI) in pulsed mode (30 A, 2.5 ms duration). The probe light was coupled into a Horiba iHR320 spectrometer (entrance slit set to 0.24 mm/3.0 nm resolution) and dispersed using a 500-nm blazed grating (300 grooves/mm). Full spectra were detected using an iCCD with a gate time set to 40 ns for all experiments. Each spectrum shown is an average of 100 four-spectrum sequences, and fluctuations in the baseline were corrected by pinning all spectra to 0.000 mAU at wavelengths greater than 625 nm, where no bleaches or growths are expected. The sample solution was prepared in a Schlenk flask in an N_2-atmosphere glovebox

and flowed through a 3-mm diameter, 1-cm path length flow cell (Starna, type 585.2) using a peristaltic pump and positive N_2 pressure.

5.9.4 NMR data

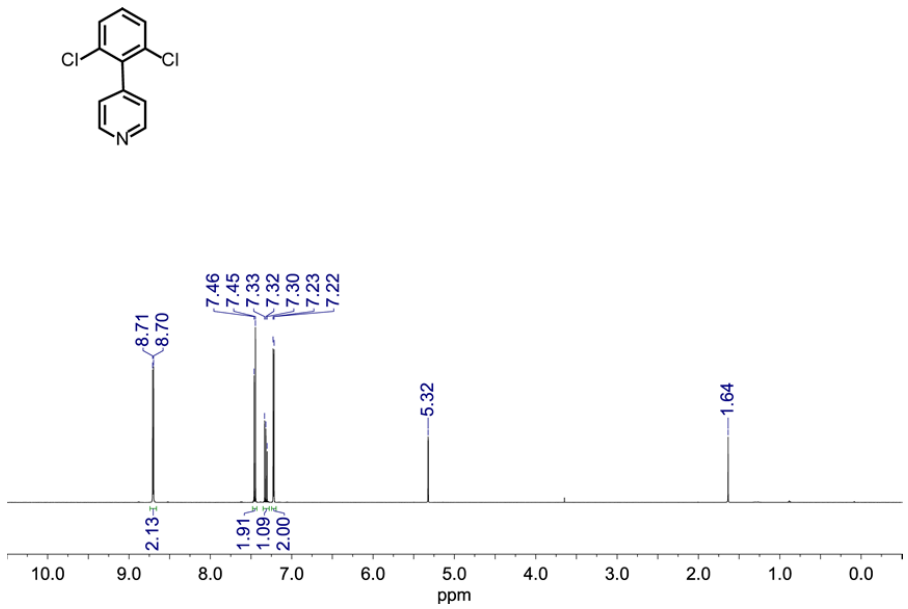

Figure 5.35. ^{1}H NMR spectrum of 4-(2,6-dichlorophenyl)pyridine **(L1)** recorded in CD_2Cl_2-d_2 at 23 °C**.**

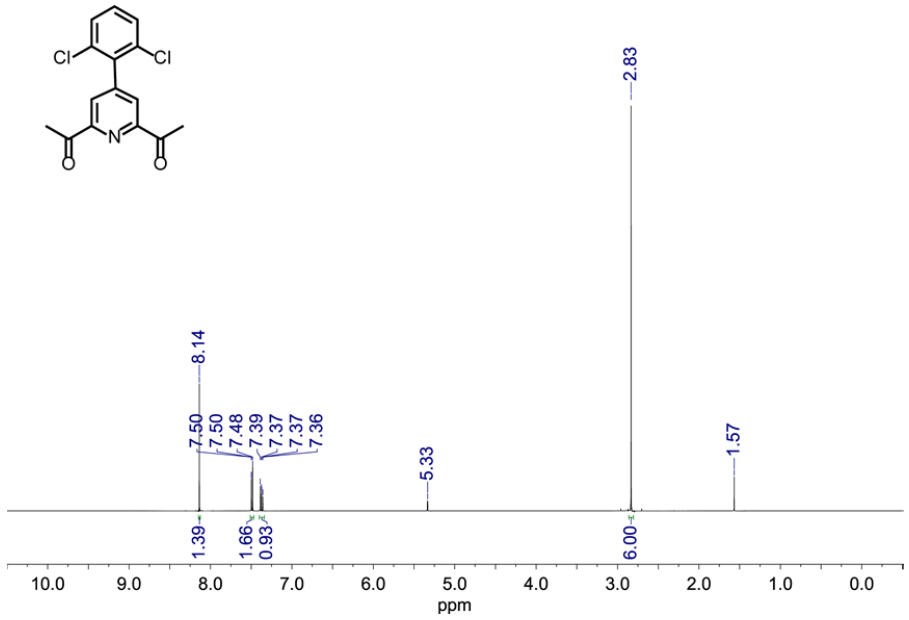

Figure 5.36. ^{1}H NMR spectrum of 4-(2,6-dichlorophenyl)-2,6-diacetylpyridine **(L2)** recorded in CD_2Cl_2-d_2 at 23 °C**.**

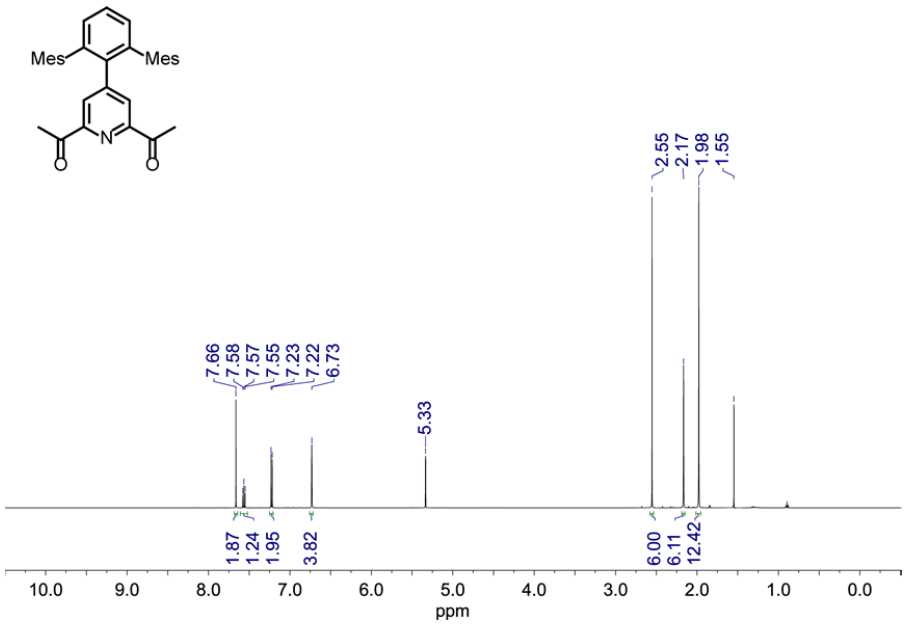

Figure 5.37. ^{1}H NMR spectrum of 4-(2,6-dimesitylphenyl)-2,6-diacetylpyridine **(L3)** recorded in CD_2Cl_2-d_2 at 23 °C**.**

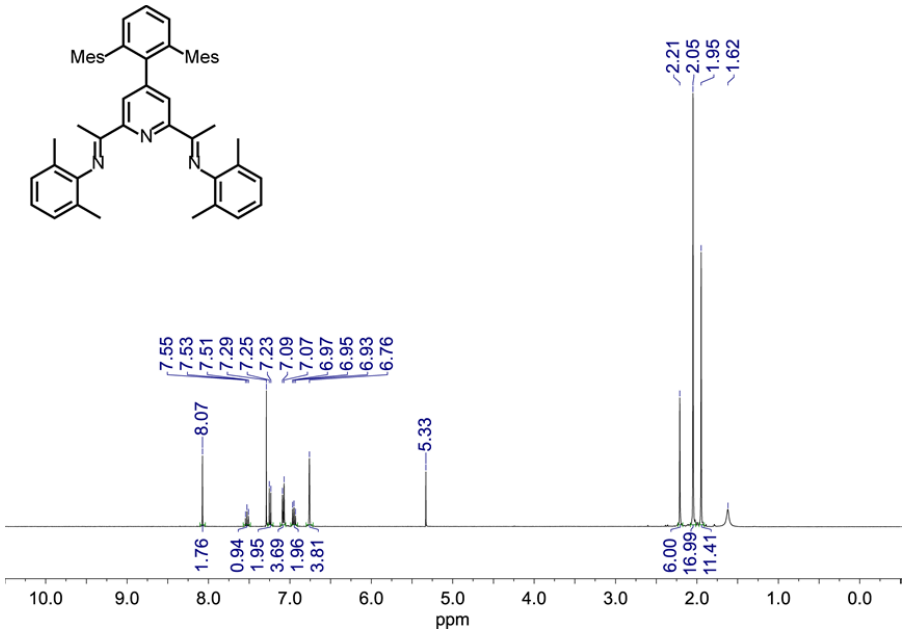

Figure 5.38. ^{1}H NMR spectrum of 4-(2,6-dimesitylphenyl)pyridine-2,6-diimine **(L4)** recorded in $CDCl_3$-d_1 at 23 °C**.**

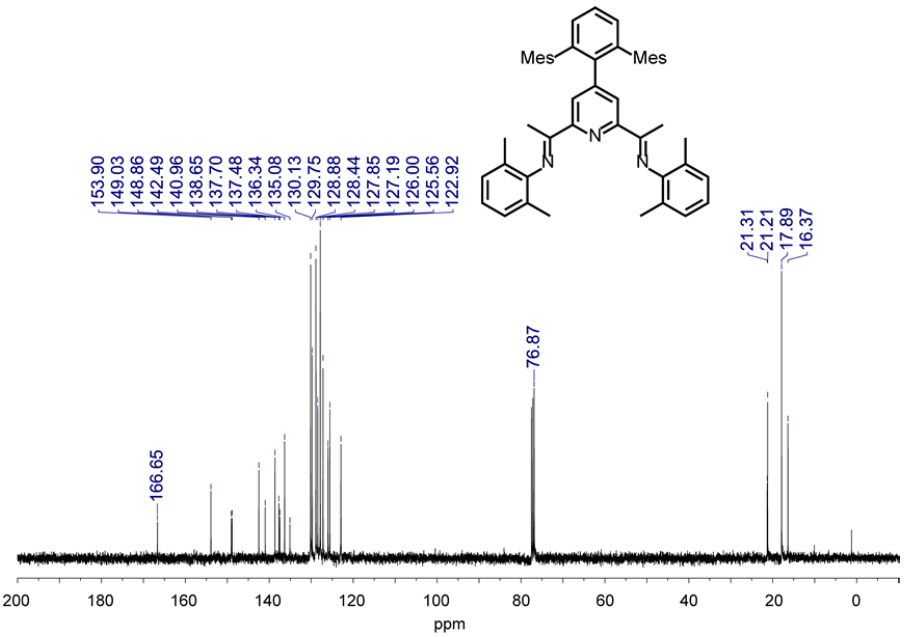

Figure 5.39. ^{13}C NMR spectrum of 4-(2,6-dimesitylphenyl)pyridine-2,6-diimine **(L4)** recorded in $CDCl_3$-d_1 at 23 °C**.**

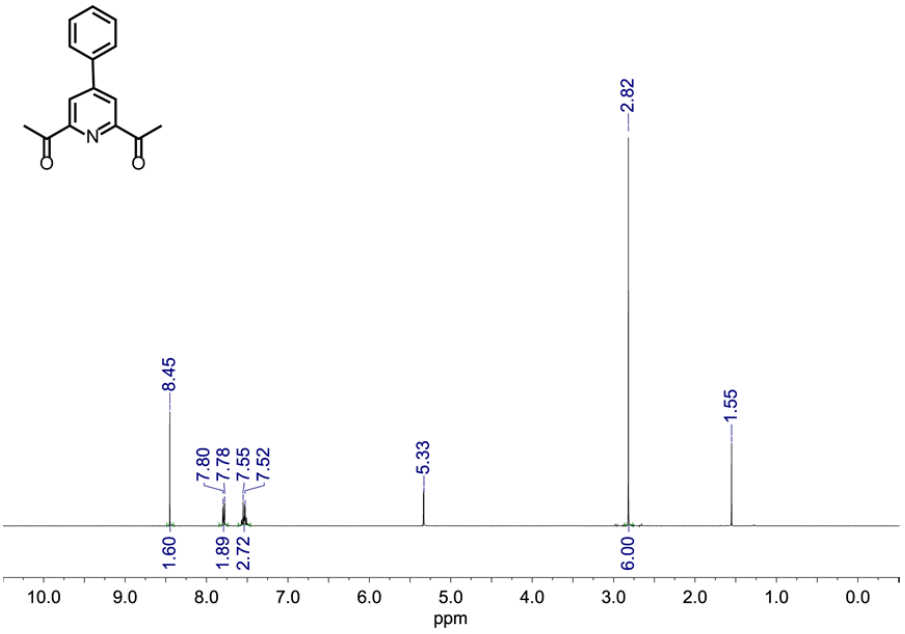

Figure 5.40. ^{1}H NMR spectrum of 4-Phenyl-2,6-diacetylpyridine **(L5)** recorded in CD_2Cl_2-d_2 at 23 °C**.**

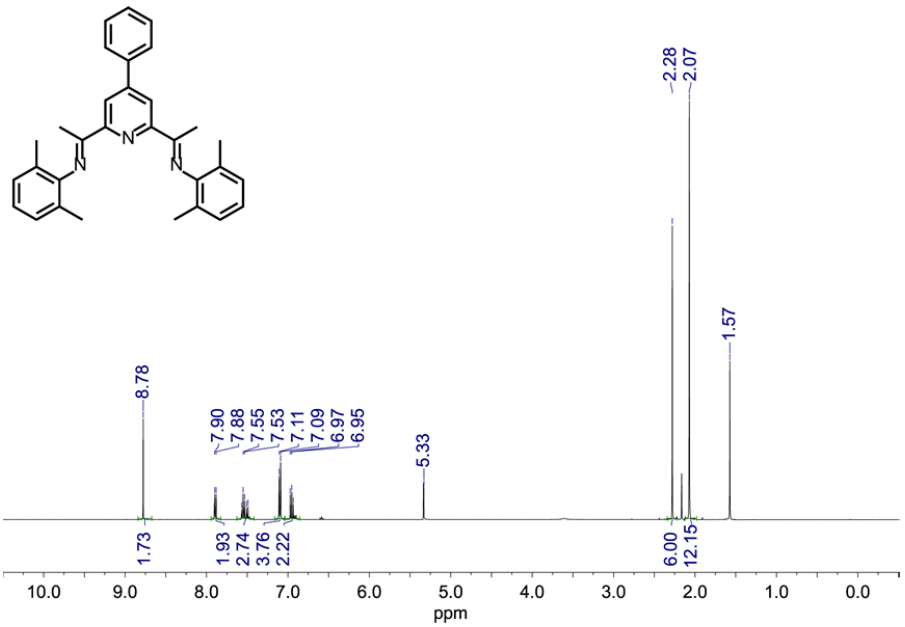

Figure 5.41. ^{1}H NMR spectrum of 4-phenylpyridine-2,6-diimine **(L6)** recorded in CD_2Cl_2-d_2 at 23 °C.

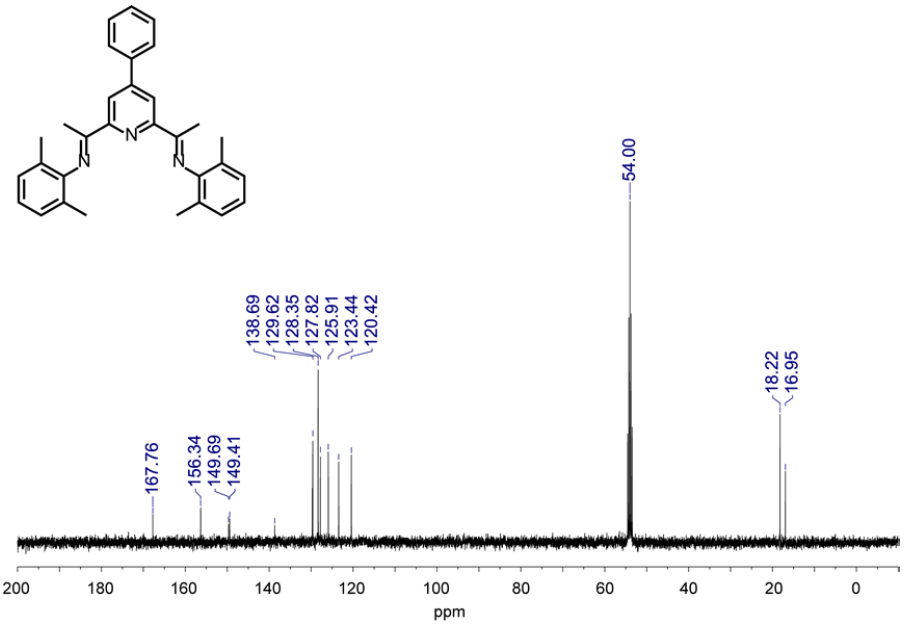

Figure 5.42. ^{13}C NMR spectrum of 4-phenylpyridine-2,6-diimine **(L6)** recorded in CD_2Cl_2-d_2 at 23 °C.

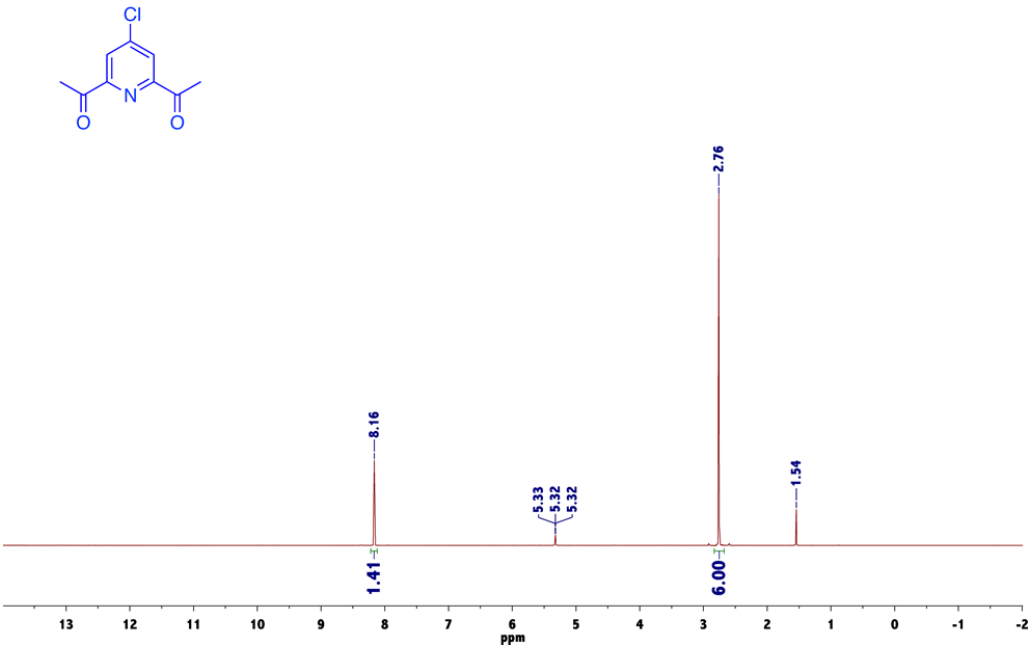

Figure 5.43. ^{1}H NMR spectrum of compound **L15-Cl** recorded in CD_2Cl_2 at 23 °C.

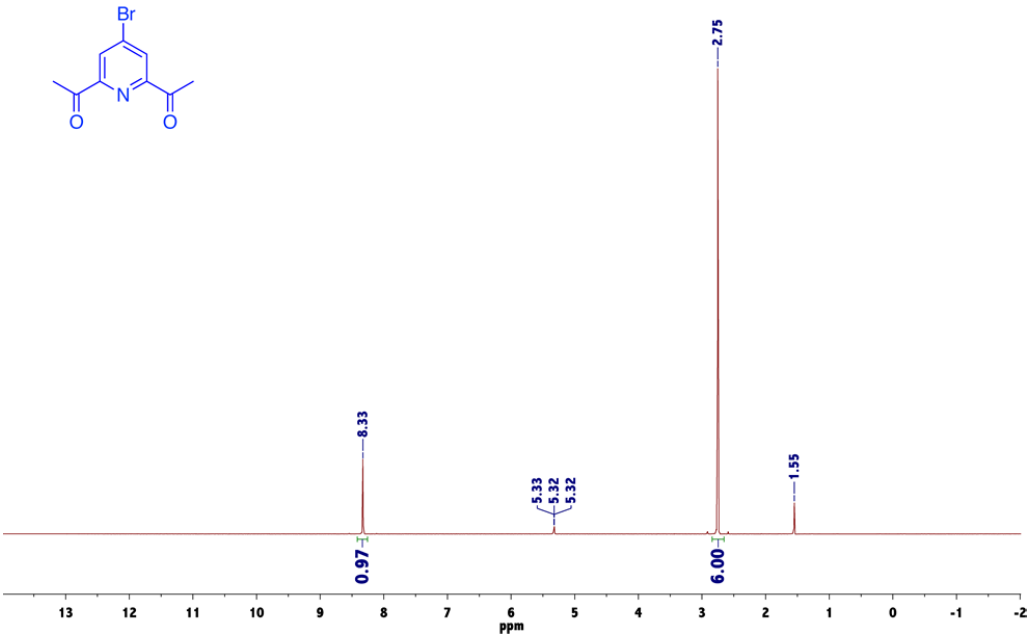

Figure 5.44. ^{1}H NMR spectrum of compound **L15-Br** recorded in CD_2Cl_2 at 23 °C.

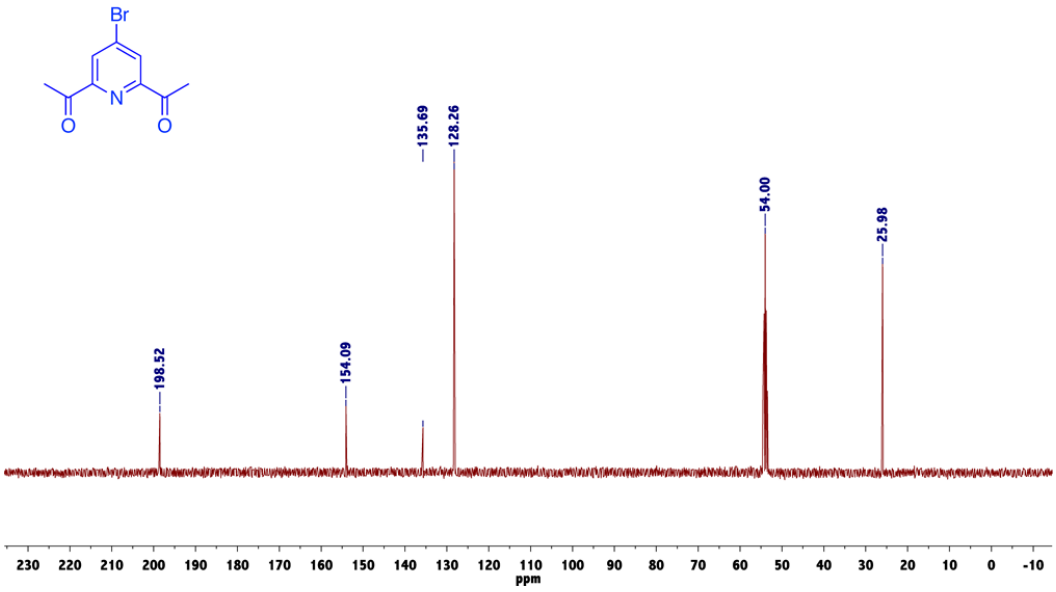

Figure 5.45. ^{13}C NMR spectrum of compound **L15-Br** recorded in CD_2Cl_2 at 23 °C.

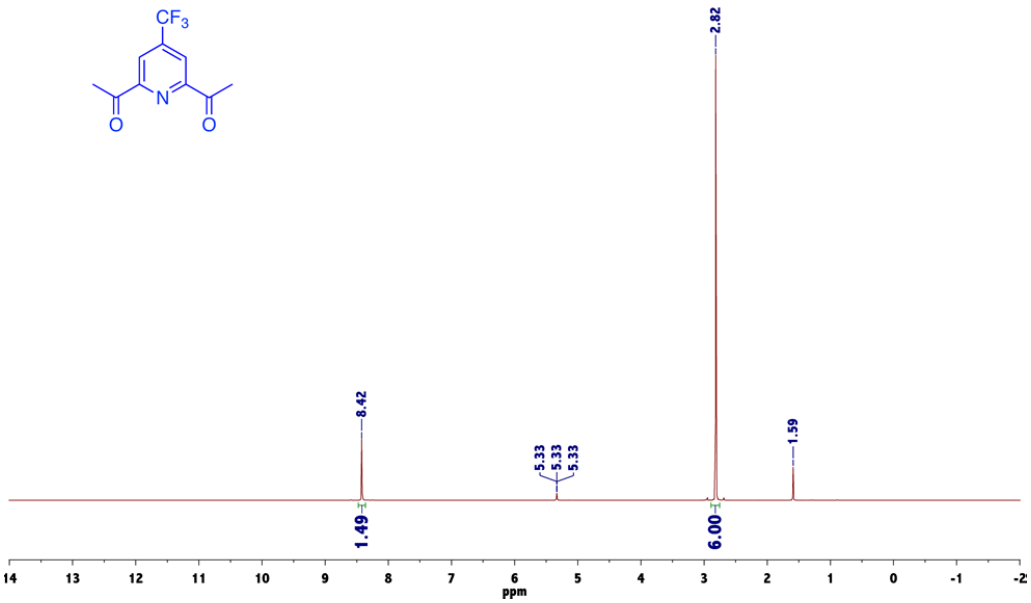

Figure 5.46. ^{1}H NMR spectrum of compound **L15-CF$_3$** recorded in CD_2Cl_2 at 23 °C.

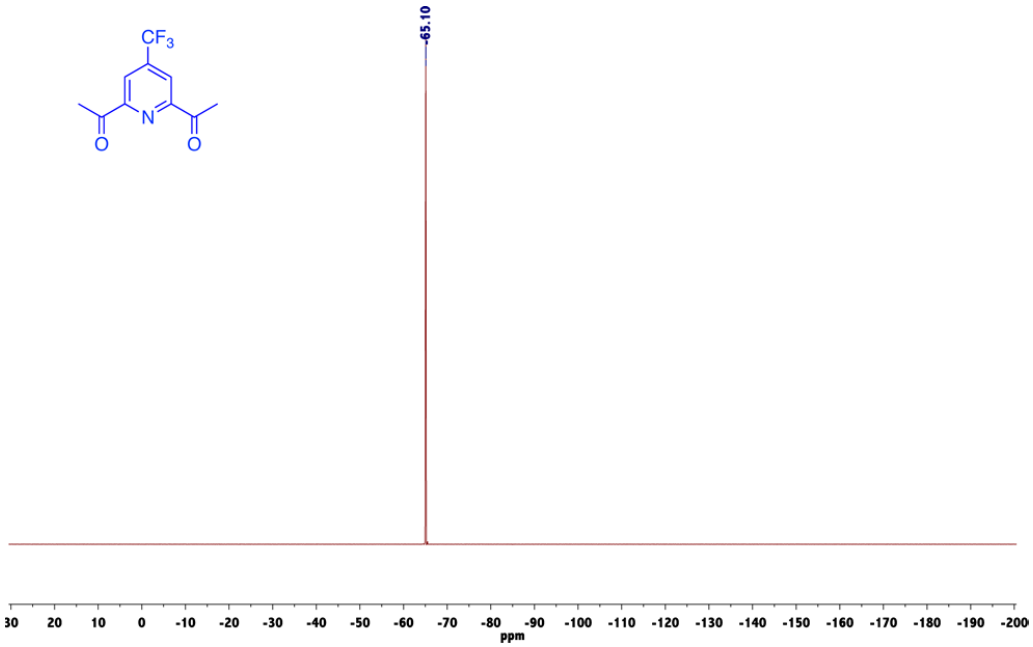

Figure 5.47. ^{19}F NMR spectrum of compound **L15-CF$_3$** recorded in CD_2Cl_2 at 23 °C.

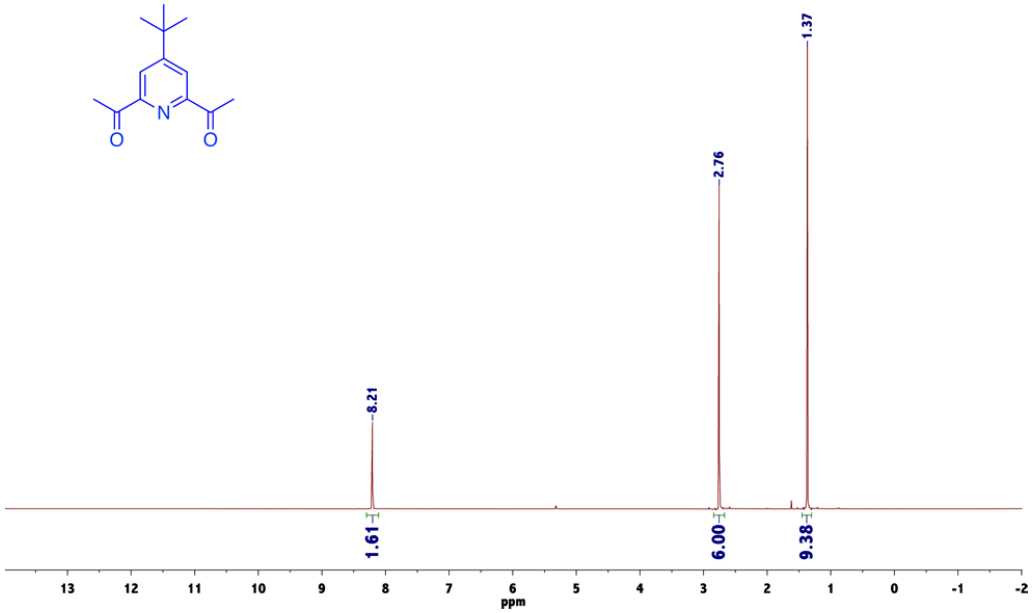

Figure 5.48. ^{1}H NMR spectrum of compound **L15-^{t}Bu** recorded in CD_2Cl_2 at 23 °C.

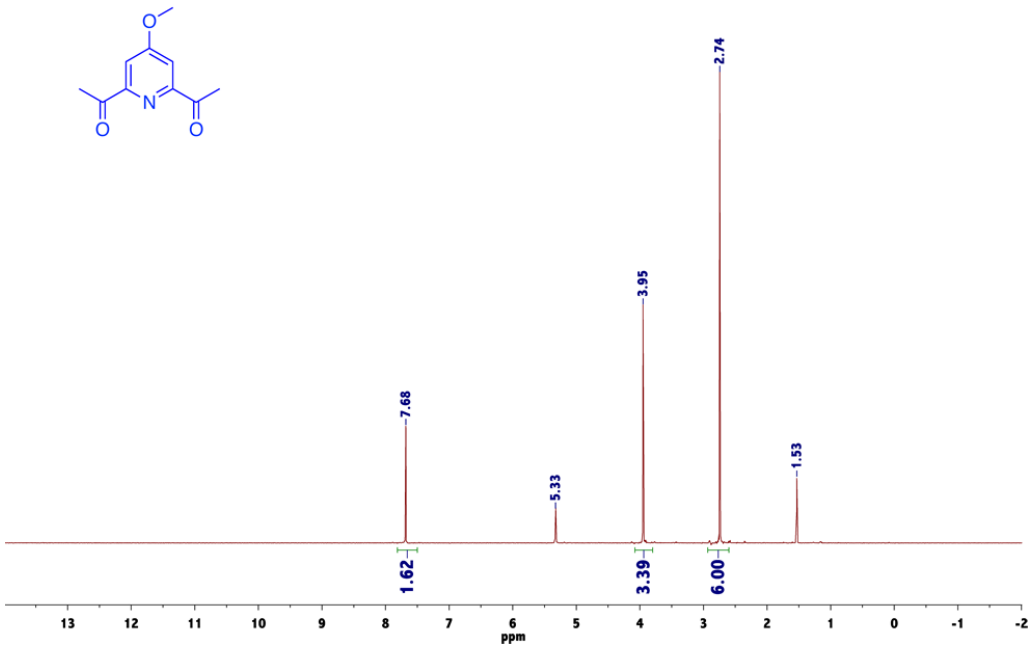

Figure 5.49. ^{1}H NMR spectrum of compound **L15-OMe** recorded in CD_2Cl_2 at 23 °C.

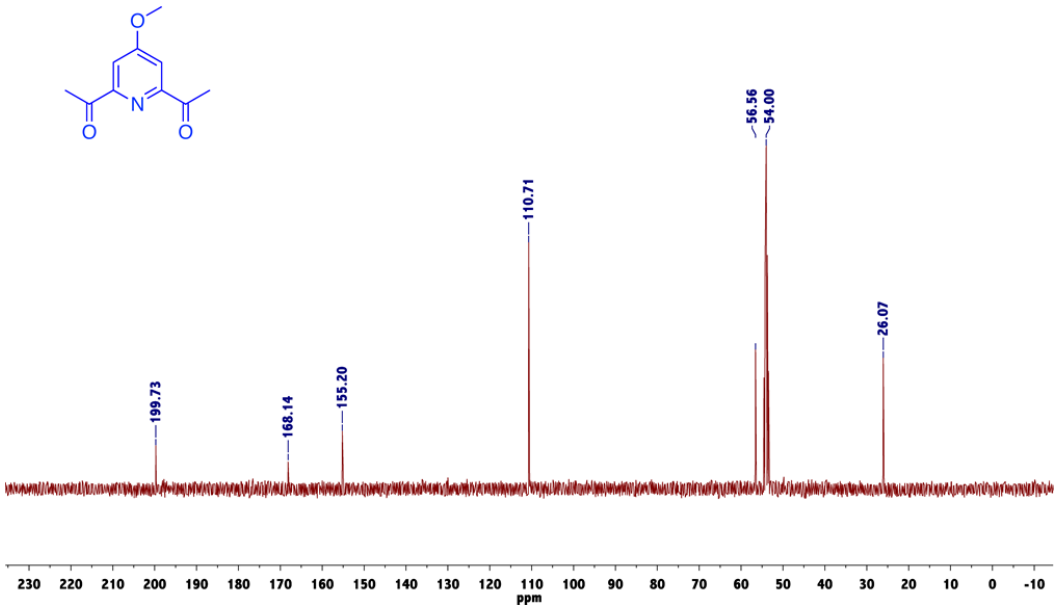

Figure 5.50. ^{13}C NMR spectrum of compound **L15-OMe**recorded in CD_2Cl_2 at 23 °C.

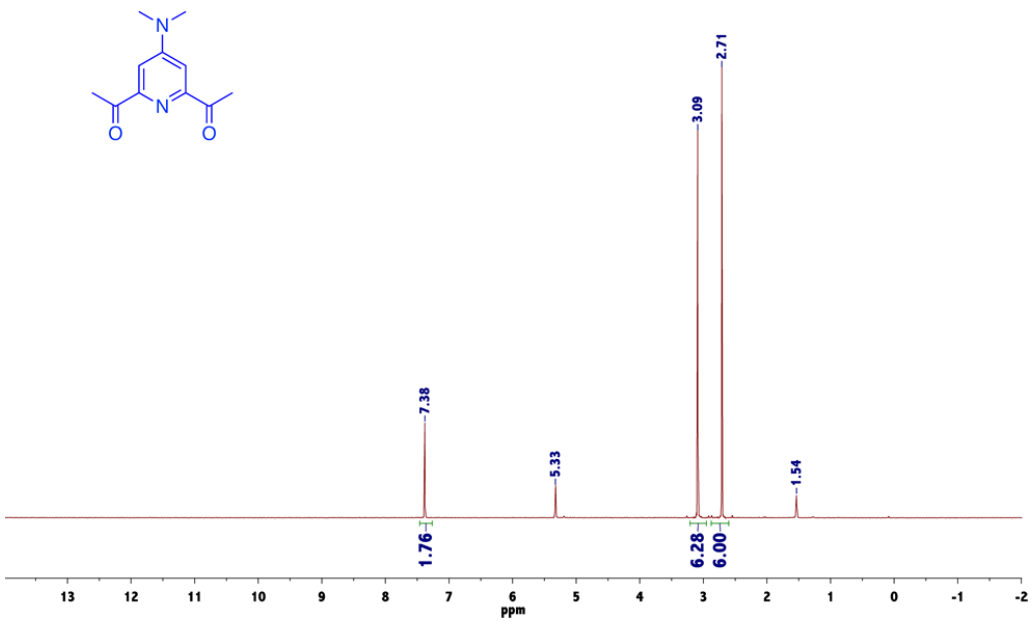

Figure 5.51. ^{1}H NMR spectrum of compound **L15-NMe$_2$** recorded in CD_2Cl_2 at 23 °C.

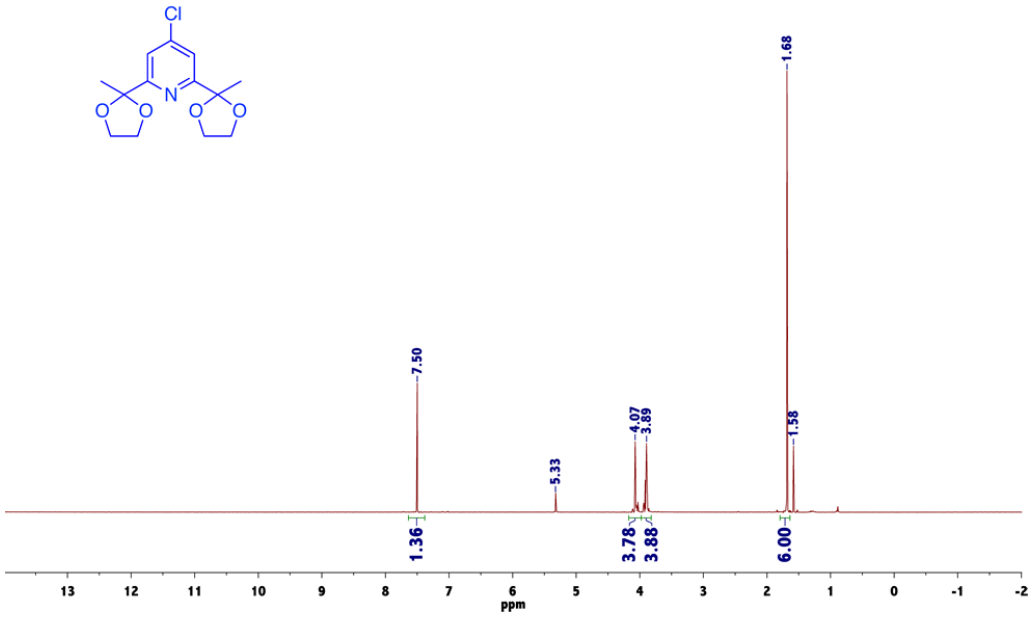

Figure 5.52. ^{13}C NMR spectrum of compound **L16** recorded in CD_2Cl_2 at 23 °C.

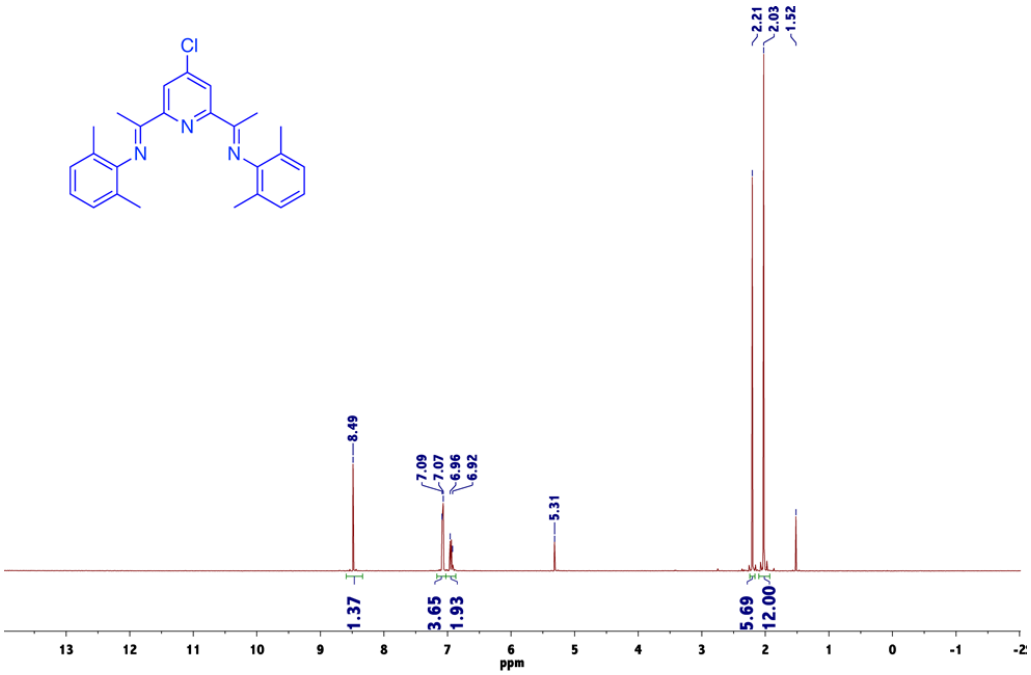

Figure 5.53. ^{1}H NMR spectrum of compound **L17-Cl** recorded in CD_2Cl_2 at 23 °C.

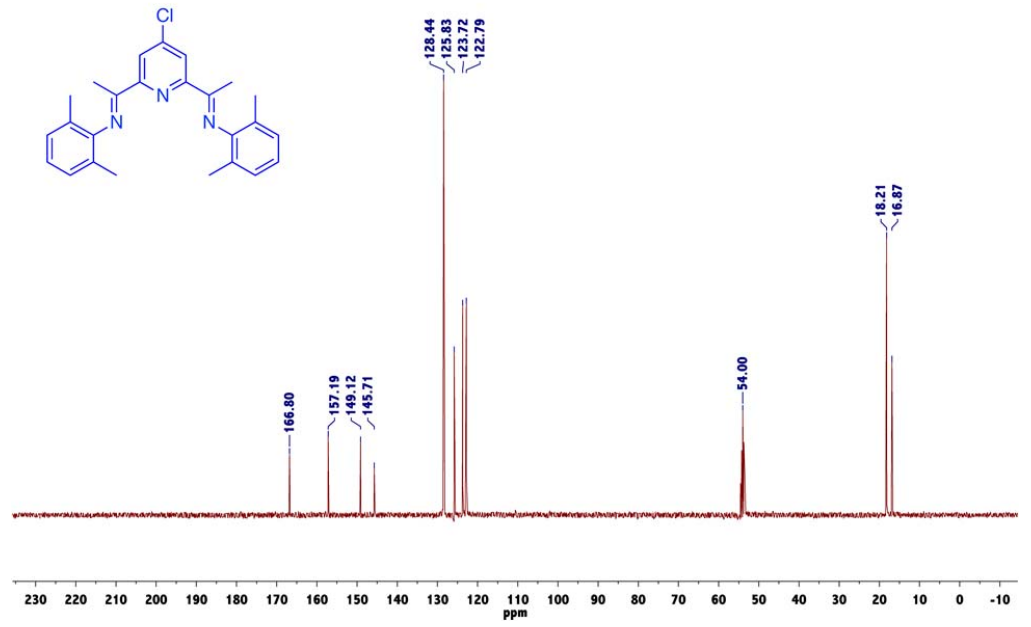

Figure 5.54. ^{13}C NMR spectrum of compound **L17-Cl** recorded in CD_2Cl_2 at 23 °C.

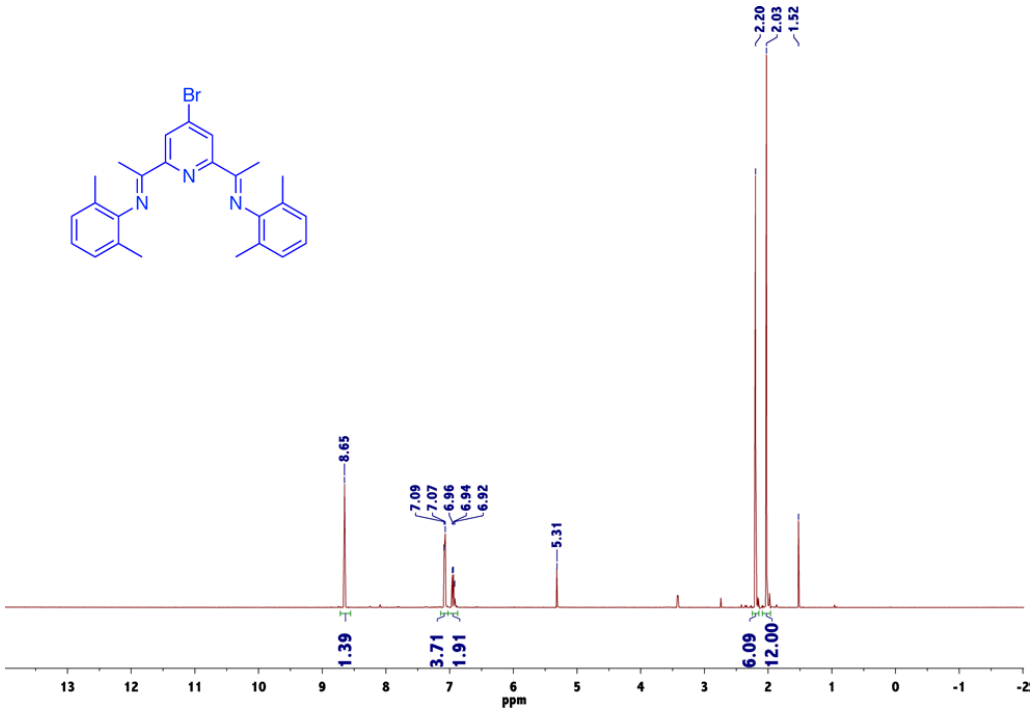

Figure 5.55. ^{1}H NMR spectrum of compound **L17-Br** recorded in CD_2Cl_2 at 23 °C.

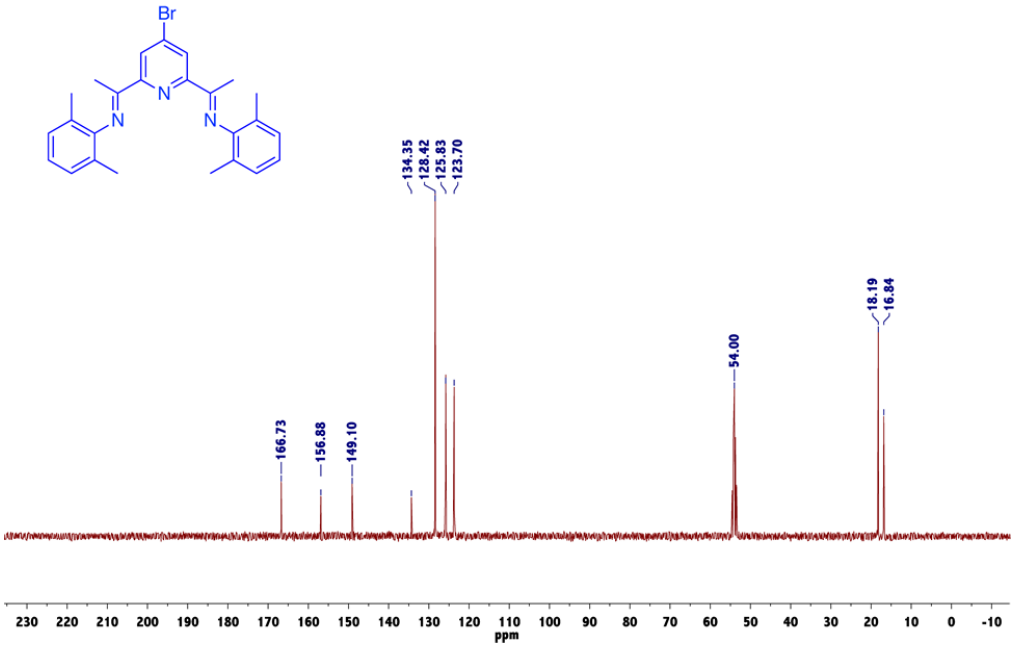

Figure 5.56. ^{13}C NMR spectrum of compound **L17-Br** recorded in CD_2Cl_2 at 23 °C.

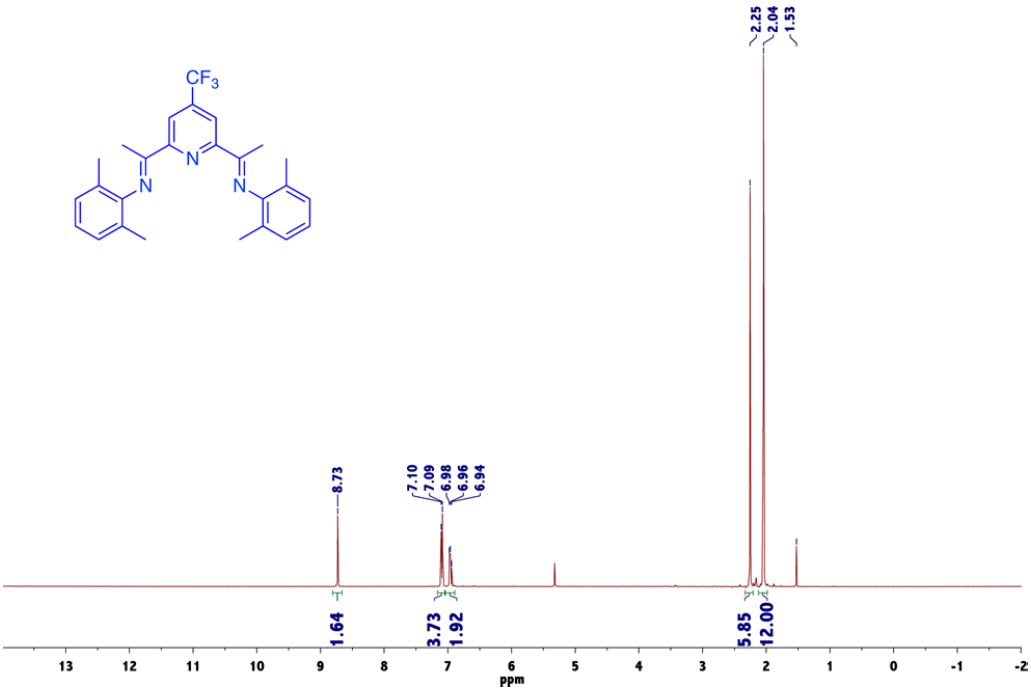

Figure 5.57. ^{1}H NMR spectrum of compound **L17-CF$_3$** recorded in CD_2Cl_2 at 23 °C.

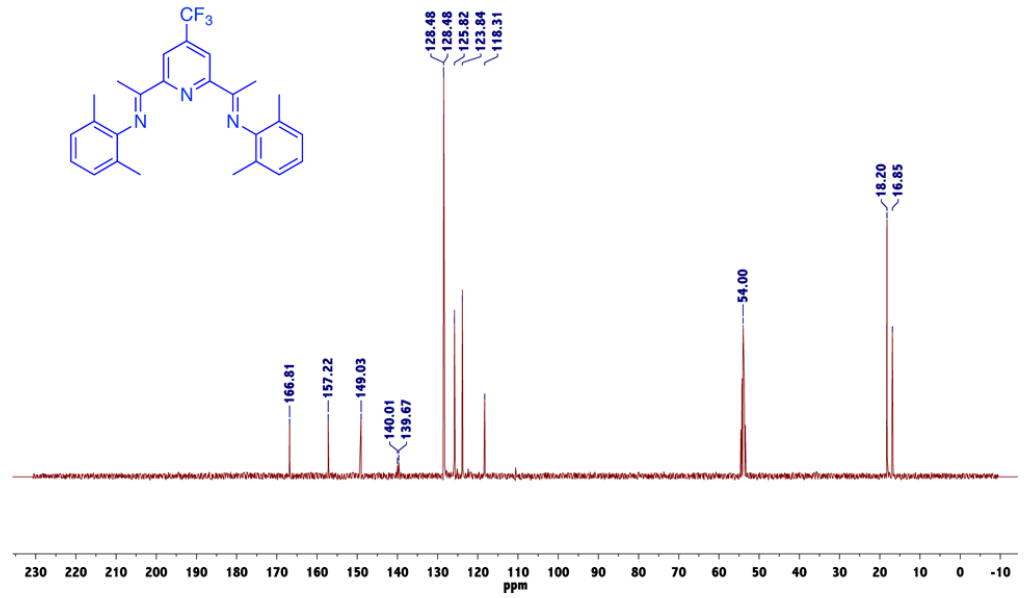

Figure 5.58. ^{13}C NMR spectrum of compound **L17-CF$_3$** recorded in CD_2Cl_2 at 23 °C.

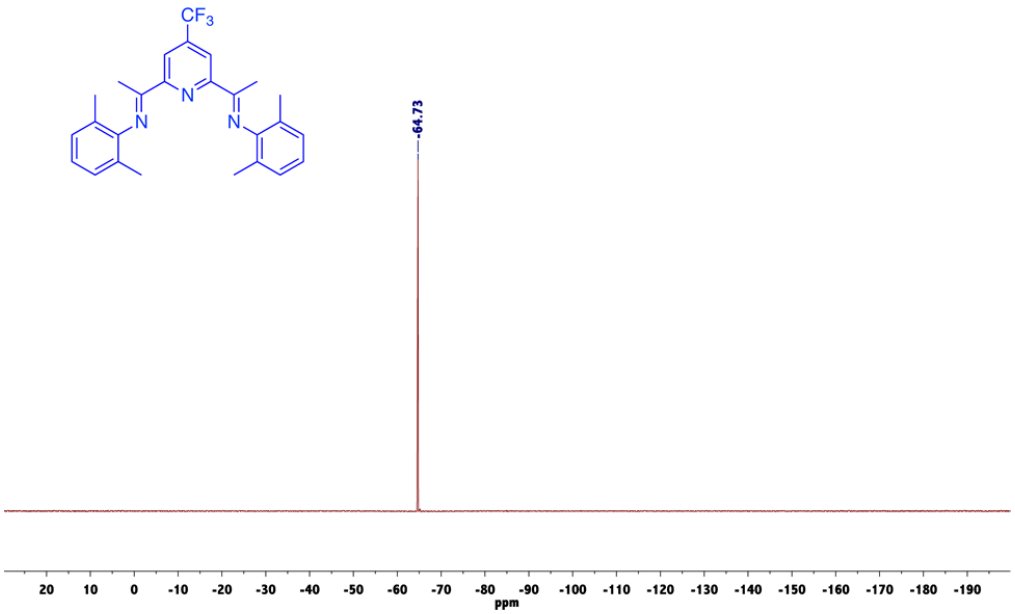

Figure 5.59. ^{19}F NMR spectrum of compound **L17-CF$_3$** recorded in CD_2Cl_2 at 23 °C.

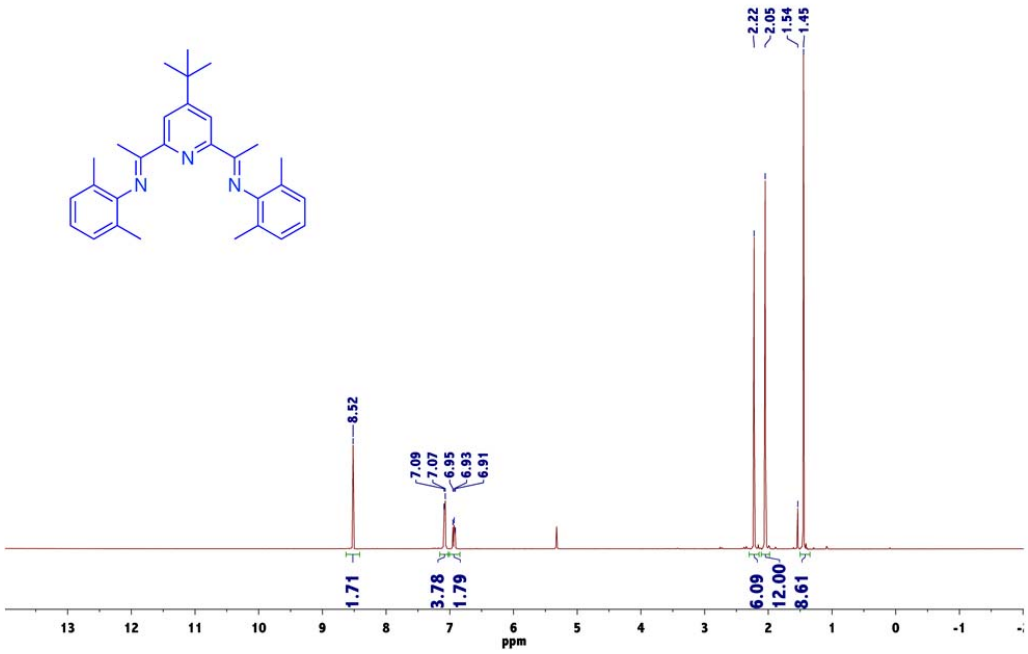

Figure 5.60. ^{1}H NMR spectrum of compound **L17-^{t}Bu** recorded in CD_2Cl_2 at 23 °C.

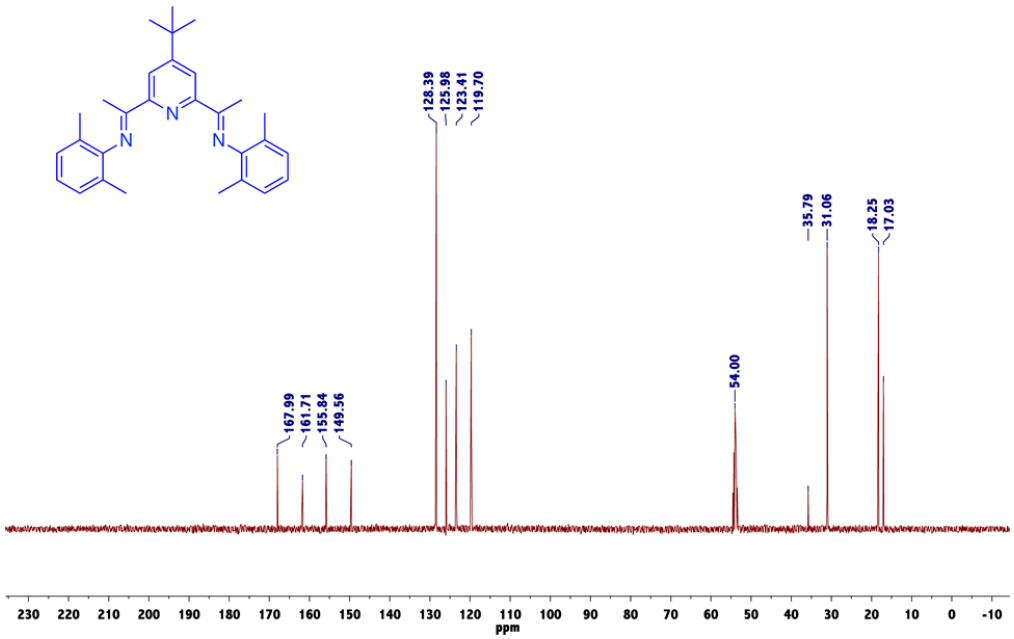

Figure 5.61. ^{13}C NMR spectrum of compound **L17-^{t}Bu** recorded in CD_2Cl_2 at 23 °C.

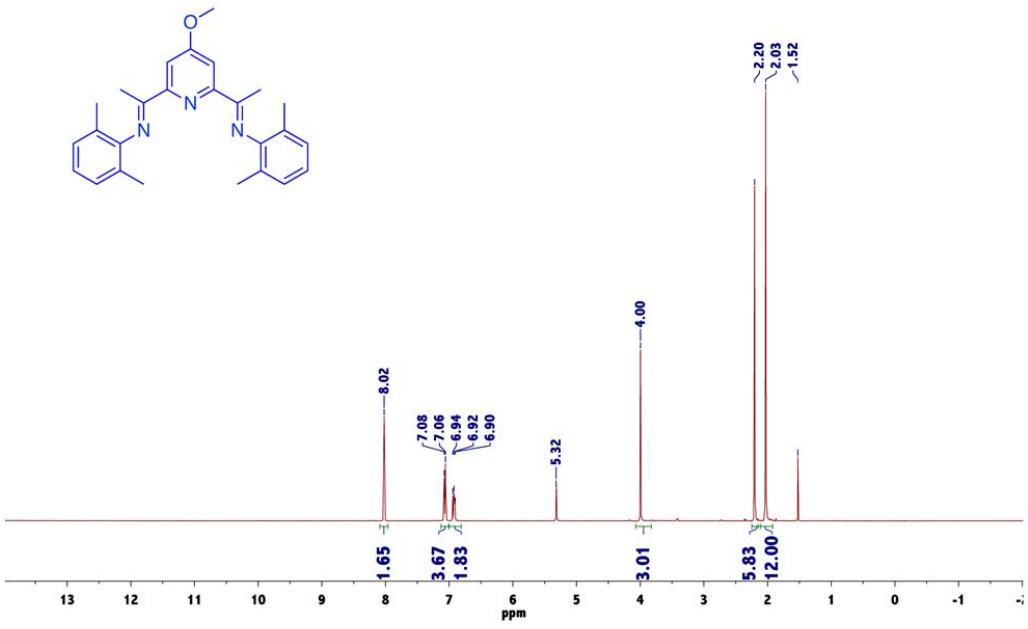

Figure 5.62. ^{1}H NMR spectrum of compound **L17-OMe** recorded in CD_2Cl_2 at 23 °C.

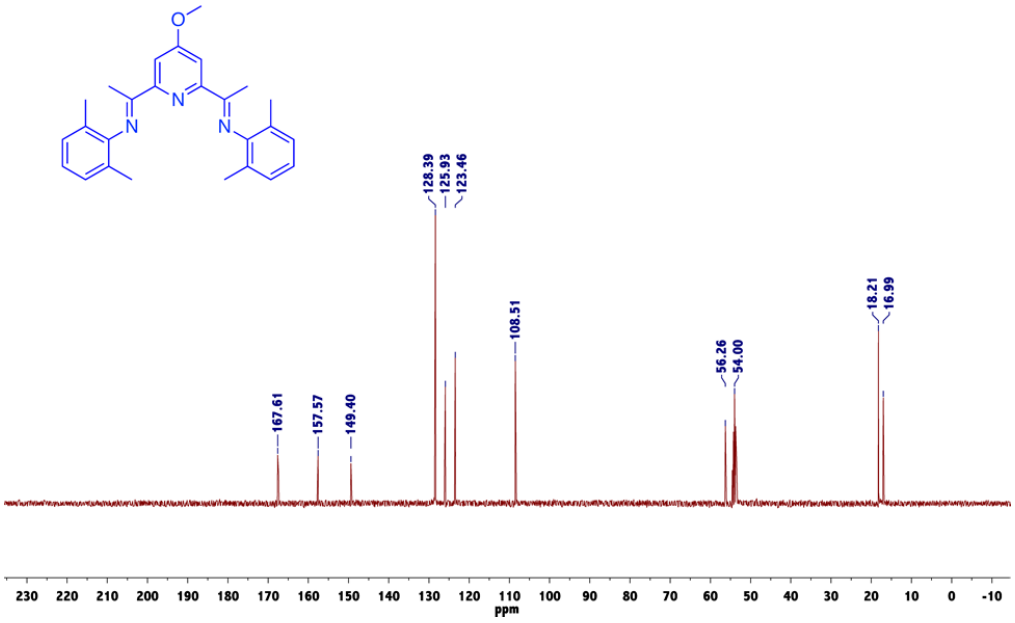

Figure 5.63. ^{13}C NMR spectrum of compound **L17-OMe** recorded in CD_2Cl_2 at 23 °C.

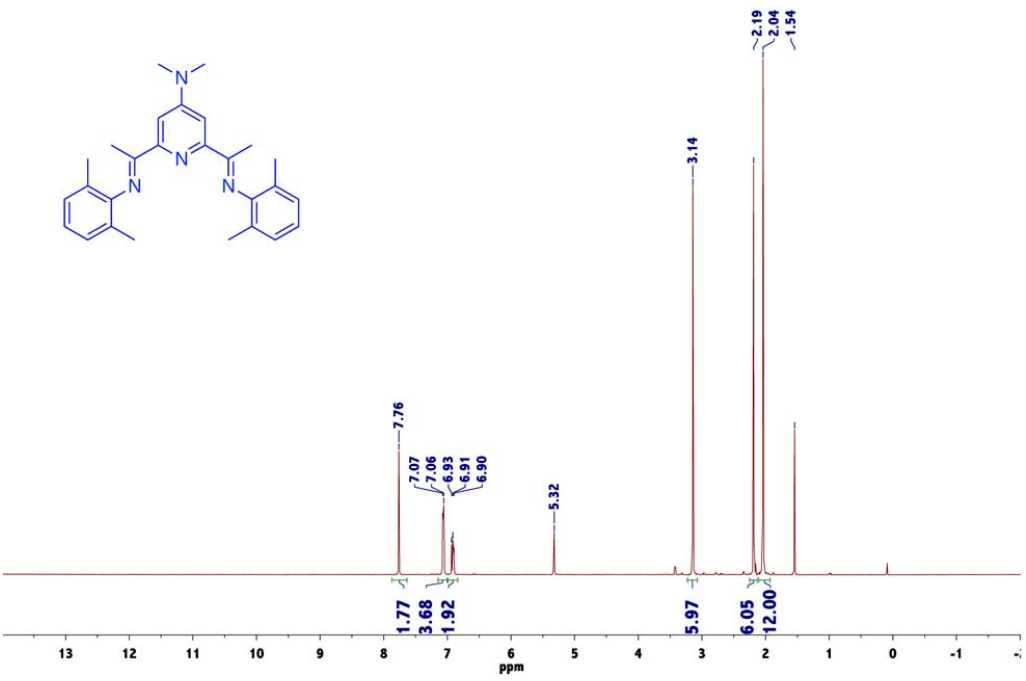

Figure 5.64. ^{1}H NMR spectrum of compound **L17-NMe$_2$** recorded in CD_2Cl_2 at 23 °C.

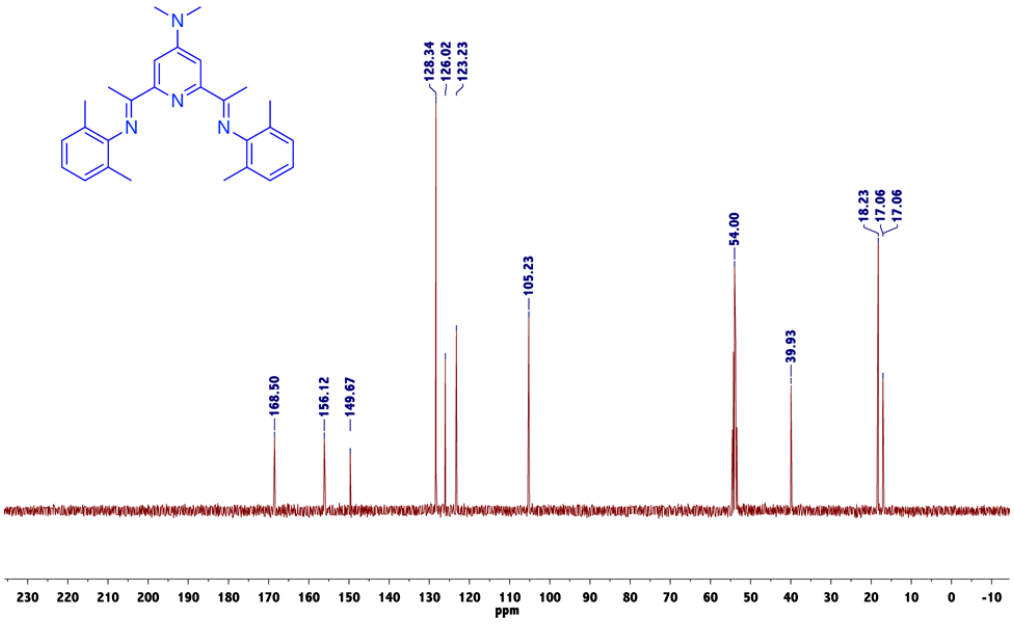

Figure 5.65. ^{13}C NMR spectrum of compound **L17-NMe$_2$** recorded in CD_2Cl_2 at 23 °C.

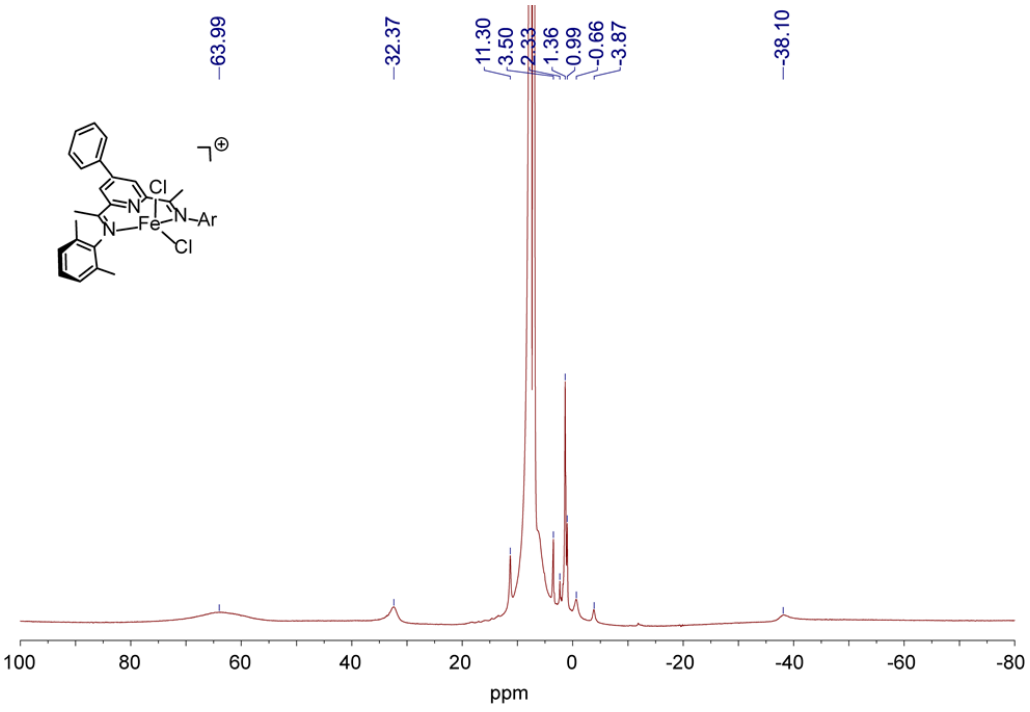

Figure 5.66. ^{1}H NMR spectrum of [$FeCl_2$(4-PhPDI)]PF_6 **(1a)** recorded in 1,2-difluorobenzene (solvent suppression) at 23 °C.

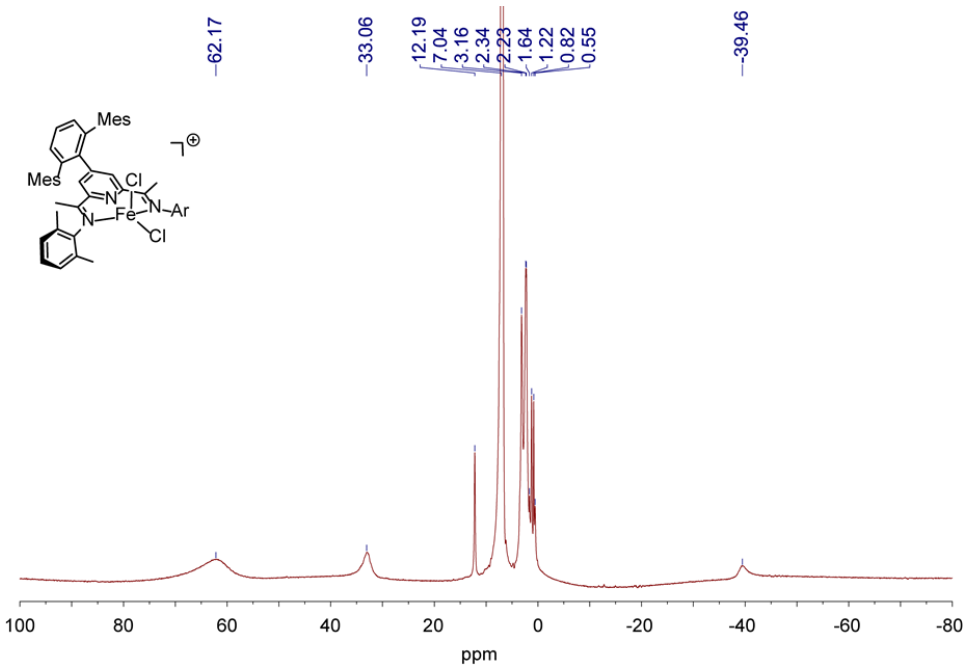

Figure 5.67. ^{1}H NMR spectrum of [$FeCl_2$(BisMesPDI)]PF_6 **(1b)** recorded in 1,2-difluorobenzene (solvent suppression) at 23 °C.

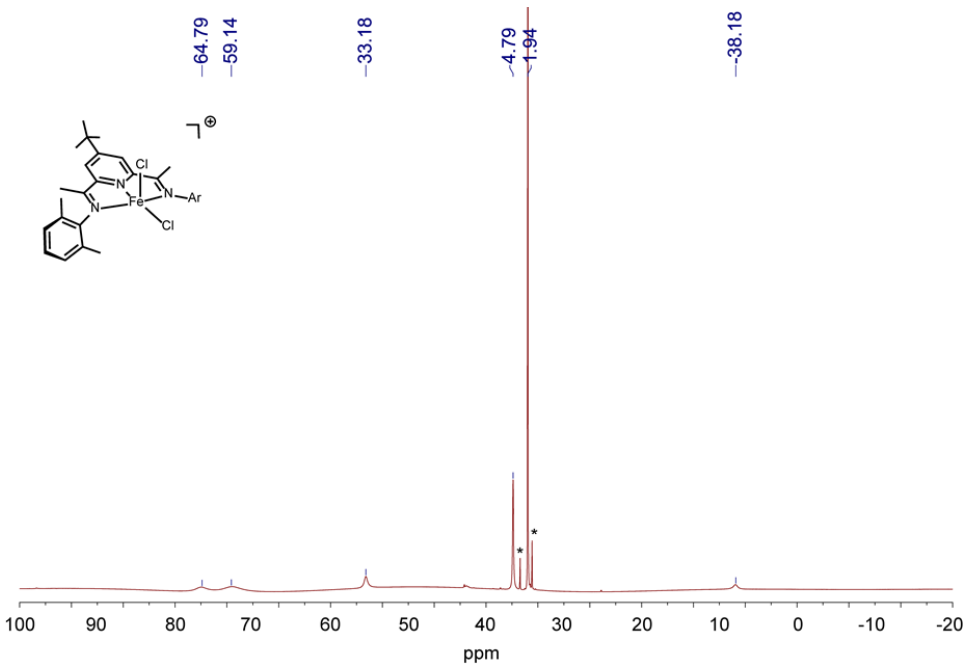

Figure 5.68. ^{1}H NMR spectrum of [$FeCl_2$(4-^{t}BuPDI)]BF_4 (**1c**) recorded in CD_3CN at 23 °C. Asterisk symbol (*) denotes residual ^{1}H peak of small amounts of Et_2O from crystallization.

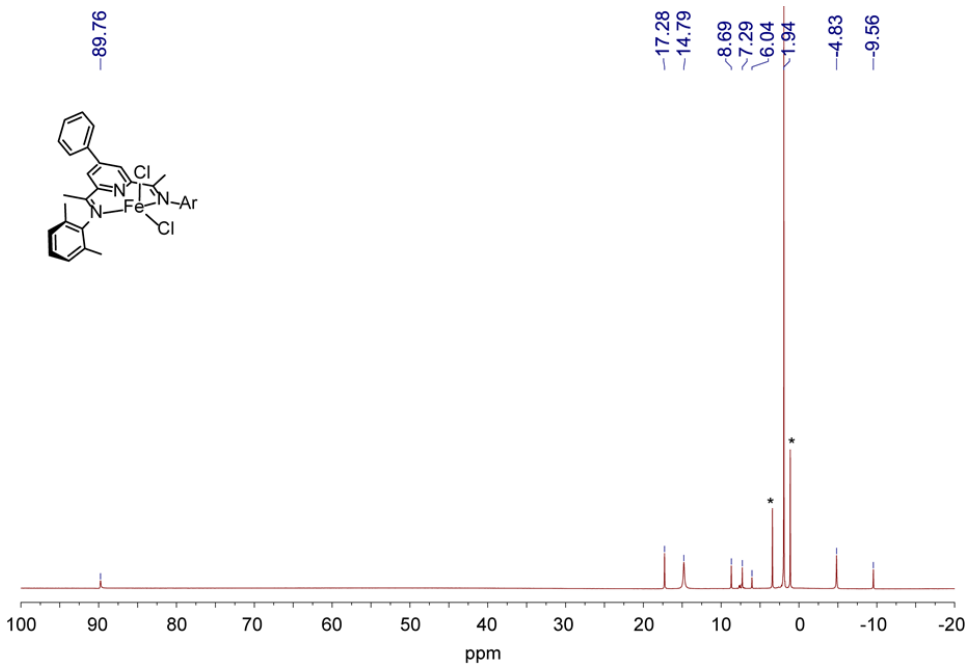

Figure 5.69. ^{1}H NMR spectrum of $FeCl_2$(4-PhPDI) **(2a)** recorded in CD_3CN at 23 °C. Asterisk symbol (*) denotes residual ^{1}H peak of small amounts of Et_2O from crystallization.

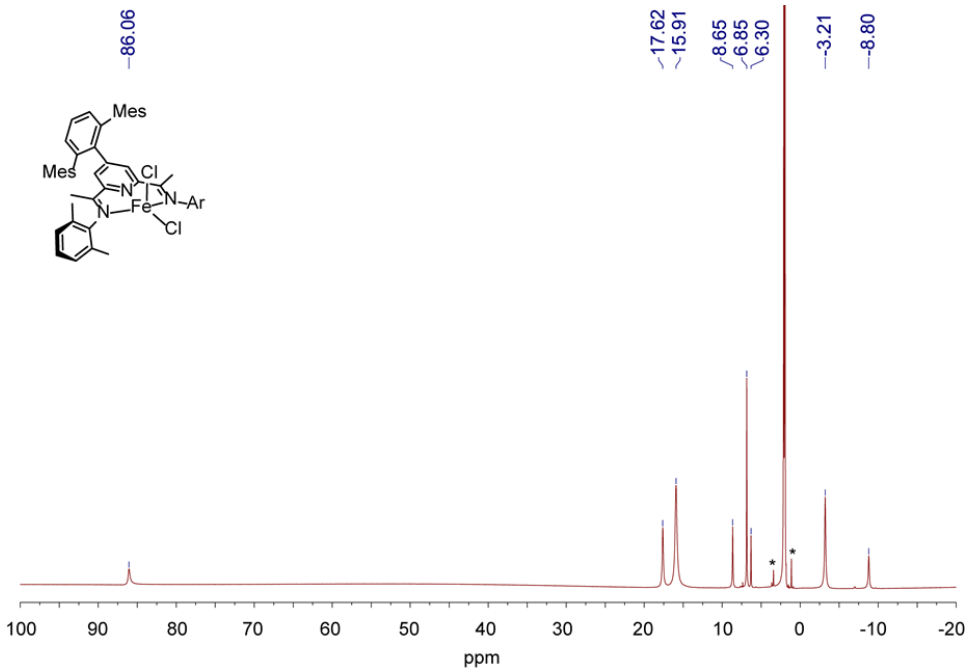

Figure 5.70. ^{1}H NMR spectrum of $FeCl_2$(BisMesPDI) **(2b)** recorded in CD_3CN at 23 °C. Asterisk symbol (*) denotes residual ^{1}H peak of small amounts of Et_2O from crystallization.

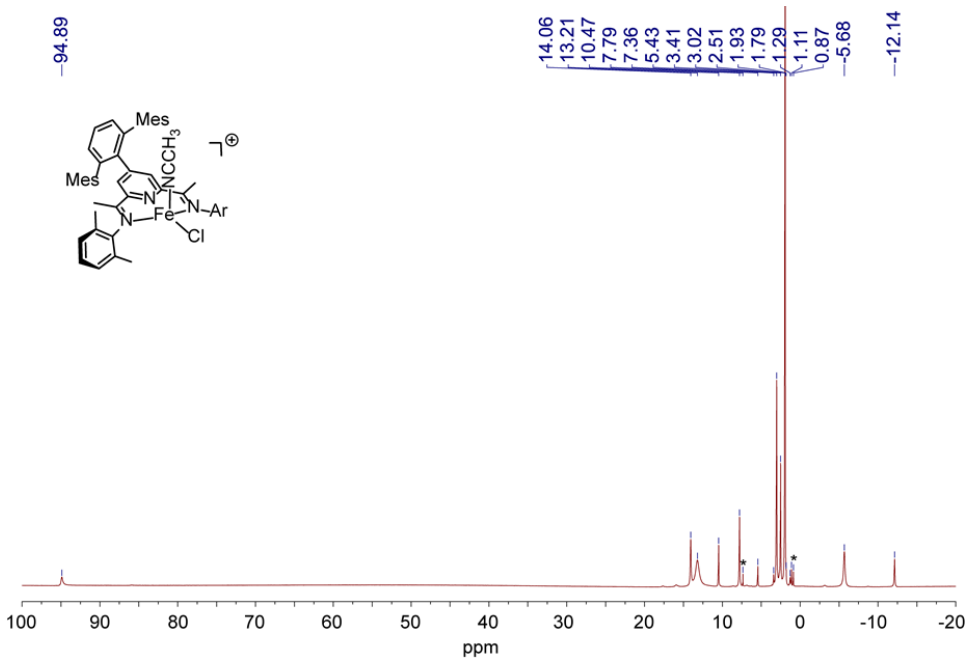

Figure 5.71. ^{1}H NMR spectrum of [FeCl(CH_3CN)(BisMesPDI)]PF_6 **(3)** recorded in CD_3CN at 23 °C. Asterisk symbol (*) denotes residual ^{1}H peak of small amounts of pentane and benzene from work up.

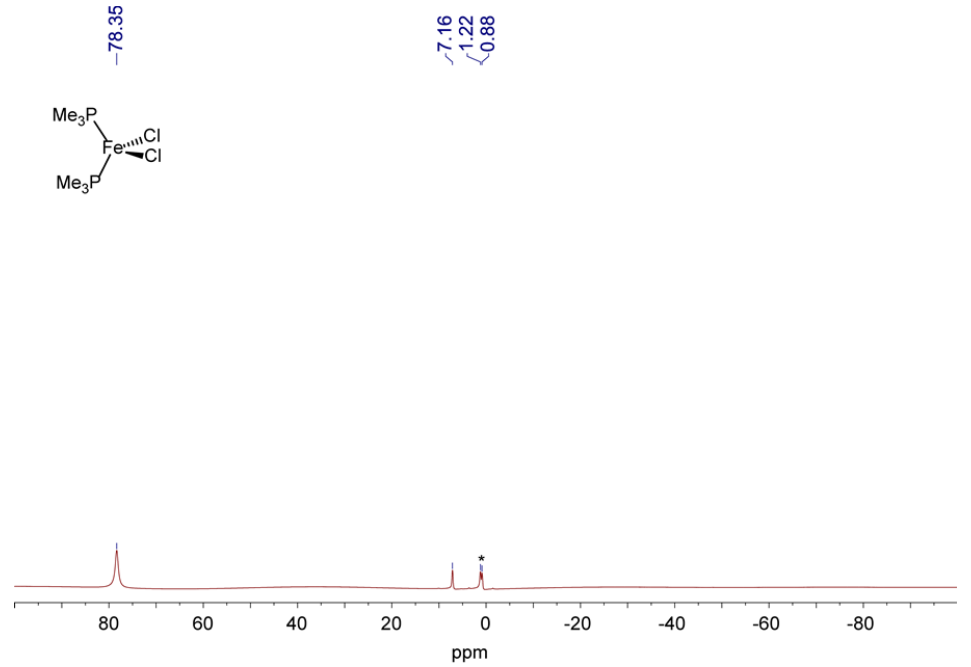

Figure 5.72. ^{1}H NMR spectrum of $FeCl_2(PMe_3)_2$ **(5a)** recorded in C_6D_6 at 23 °C. Asterisk symbol (*) denotes residual ^{1}H peak of small amounts of pentane from crystallization.

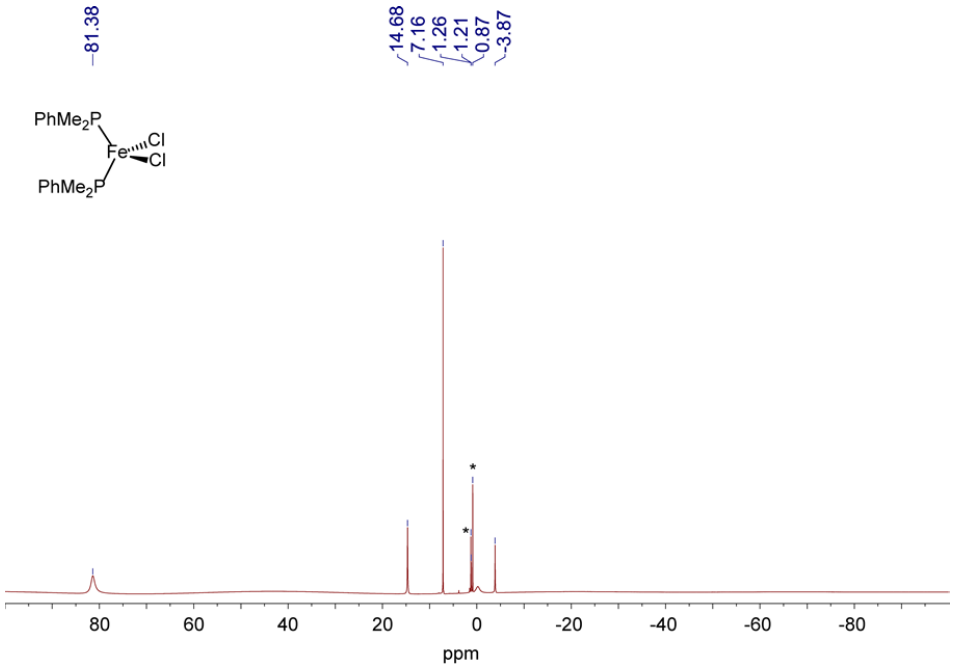

Figure 5.73. ^{1}H NMR spectrum of $FeCl_2(PMe_2Ph)_2$ **(5b)** recorded in C_6D_6 at 23 °C. Asterisk symbol (*) denotes residual ^{1}H peak of small amounts of pentane from crystallization.

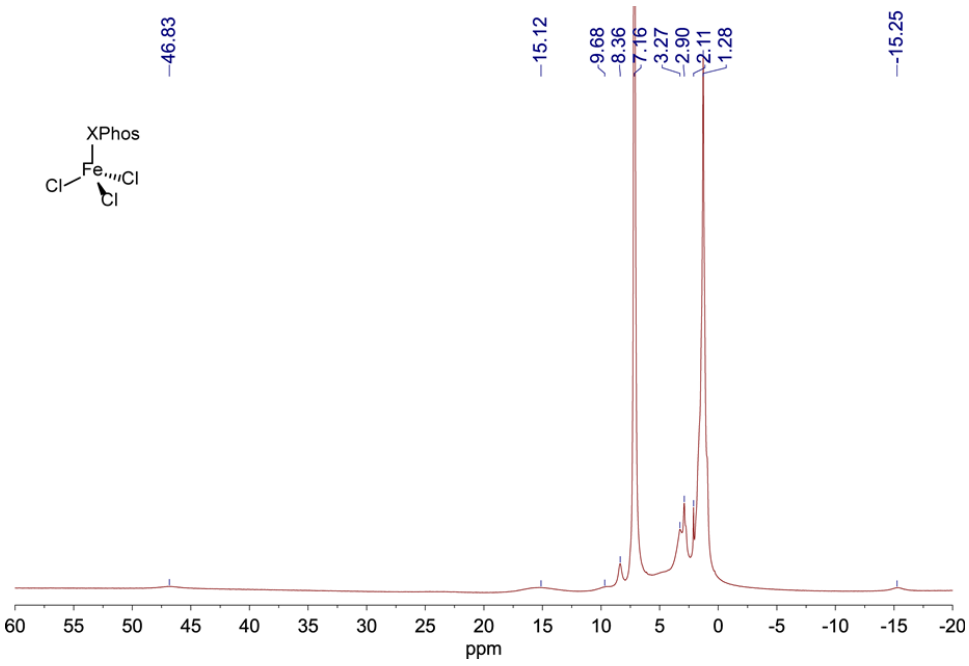

Figure 5.74. ^{1}H NMR spectrum of $FeCl_3$XPhos **(6)** recorded in C_6D_6 at 23 °C.

5.9.5 X-Ray Data Analysis

Table 5.14. X-ray experimental details for complex **1a** (CCDC 1582371).

Crystal Data	
Chemical formula	$C_{31}H_{31}Cl_2F_6FeN_3P$
Fw, g/mol	717.31
Crystal system, space group	monoclinic, *C2/c*
Temperature (K)	100(2)
a, *b*, *c* (Å)	33.907(3), 15.4446(12), 14.1732(11)
α, β, γ (°)	90, 109.235(2), 90
V (Å^3)	7007.8(9)
Z	8
Radiation type	Mo *Kα*
μ (mm^{-1})	0.685
Crystal size (mm)	0.23 × 0.12 × 0.09
Data collection	
Diffractometer	Bruker *APEX*-II CCD
Absorption correction	Multi-scan, *SADABS*
T_{min}, T_{max}	0.8567, 0.9390
No. of measured, independent and observed [$I > 2\sigma(I)$] reflections	6250, 6250, 4962
R_{int}	0.0580
$(\sin \theta/\lambda)_{max}$ (Å^{-1})	0.597
Refinement	
$R[F^2 > 2\sigma(F^2)]$, $wR(F^2)$, S	0.0419, 0.1128, 1.085
No. of reflections	6250
No. of parameters	403
No. of restraints	0
H-atom treatment	H atoms treated by a mixture of independent and constrained refinement
Dr_{max}, Dr_{min} (e Å^{-3})	0.151, –0.439

Table 5.15. X-ray experimental details for complex **1b** (CCDC 1582372).

Crystal Data	
Chemical formula	$C_{29}H_{30}ClF_3Fe_{0.5}N_{1.5}P_{0.5}$
Fw, g/mol	535.40
Crystal system, space group	Triclinic, *P-1*
Temperature (K)	20(2)
a, *b*, *c* (Å)	11.4777(10), 11.5059(10), 22.921(2)
α, β, γ (°)	85.294(2), 77.999(2), 67.583(2)
V (Å^3)	2737.1(4)
Z	4
Radiation type	synchrotron
μ (mm^{-1})	0.115
Crystal size (mm)	0.01 × 0.01 × 0.01
Data collection	
Diffractometer	Bruker *APEX*-II CCD
Absorption correction	Multi-scan, *SADABS*
T_{min}, T_{max}	0.9989, 0.9989
No. of measured, independent and observed [$I > 2\sigma(I)$] reflections	30251, 9544, 6550
R_{int}	0.1065
$(\sin\theta/\lambda)_{max}$ (Å^{-1})	0.607
Refinement	
$R[F^2 > 2\sigma(F^2)]$, $wR(F^2)$, S	0.0671, 0.1734, 1.040
No. of reflections	9544
No. of parameters	652
No. of restraints	0
H-atom treatment	H atoms treated by a mixture of independent and constrained refinement
Dr_{max}, Dr_{min} (e Å^{-3})	1.872, –0.911

Table 5.16. X-ray experimental details for **1c** (CCDC 1582375).

Crystal Data	
Chemical formula	$C_{29}H_{35}BCl_2F_4FeN_3$
Fw, g/mol	639.16
Crystal system, space group	Monoclinic, *P2(1)/c*
Temperature (K)	20(2)
a, *b*, *c* (Å)	13.2860(5), 17.7025(6), 14.4220(5)
α, β, γ (°)	90, 116.545(1),90
V (Å^3)	3034.42(19)
Z	4
Radiation type	synchrotron
μ (mm^{-1})	0.170
Crystal size (mm)	0.01 × 0.01 × 0.01
Data collection	
Diffractometer	Bruker *APEX*-II CCD
Absorption correction	Multi-scan, *SADABS*
T_{min}, T_{max}	0.998, 0.998
No. of measured, independent and observed [$I > 2\sigma(I)$] reflections	96480, 9259, 8097
R_{int}	0.0389
$(\sin \theta/\lambda)_{max}$ (Å^{-1})	0.712
Refinement	
$R[F^2 > 2\sigma(F^2)]$, $wR(F^2)$, S	0.0327, 0.0847, 1.059
No. of reflections	9259
No. of parameters	491
No. of restraints	103
H-atom treatment	H atoms treated by a mixture of independent and constrained refinement
Dr_{max}, Dr_{min} (e Å^{-3})	0.691, – 0.581

Table 5.17. X-ray experimental details for complex **2a** (CCDC 1582373).

Crystal Data	
Chemical formula	$C_{33}H_{34}Cl_2FeN_4$
Fw, g/mol	613.39
Crystal system, space group	monoclinic, *P2(1)/n*
Temperature (K)	100(2)
a, *b*, *c* (Å)	12.8622(18), 14.846(2), 17.262(2)
α, β, γ (°)	90, 111.789(2), 90
V (Å^3)	3060.6(7)
Z	4
Radiation type	Mo *Kα*
μ (mm^{-1})	0.696
Crystal size (mm)	0.38 × 0.07 × 0.07
Data collection	
Diffractometer	Bruker *APEX*-II CCD
Absorption correction	Multi-scan, *SADABS*
T_{min}, T_{max}	0.7784, 0.9542
No. of measured, independent and observed [$I > 2\sigma(I)$] reflections	40764, 5411, 4269
R_{int}	0.0507
$(\sin\theta/\lambda)_{max}$ (Å^{-1})	0.595
Refinement	
$R[F^2 > 2\sigma(F^2)]$, $wR(F^2)$, S	0.0335, 0.0741, 1.014
No. of reflections	5411
No. of parameters	368
No. of restraints	0
H-atom treatment	H atoms treated by a mixture of independent and constrained refinement
Dr_{max}, Dr_{min} (e Å^{-3})	0.299, –0.318

Table 5.18. X-ray experimental details for complex **2b** (CCDC 1582374).

Crystal Data	
Chemical formula	$C_{26.5}H_{28.5}ClFe_{0.5}N_{2.5}$
Fw, g/mol	445.39
Crystal system, space group	monoclinic, *P2(1)/c*
Temperature (K)	100(2)
a, *b*, *c* (Å)	13.6446(13), 19.9168(19), 21.468(2)
α, β, γ (°)	90, 107.654(3), 90
V (Å^3)	5559.3(9)
Z	8
Radiation type	Mo *Kα*
μ (mm^{-1})	0.402
Crystal size (mm)	0.20 × 0.20 × 0.15
Data collection	
Diffractometer	Bruker *APEX*-II CCD
Absorption correction	Multi-scan, *SADABS*
T_{min}, T_{max}	0.9239, 0.9421
No. of measured, independent and observed [$I > 2\sigma(I)$] reflections	9819, 9819, 6699
R_{int}	0.1162
$(\sin \theta/\lambda)_{max}$ (Å^{-1})	0.596
Refinement	
$R[F^2 > 2\sigma(F^2)]$, $wR(F^2)$, S	0.0817, 0.2055, 1.060
No. of reflections	9819
No. of parameters	564
No. of restraints	0
H-atom treatment	H atoms treated by a mixture of independent and constrained refinement
Dr_{max}, Dr_{min} (e Å^{-3})	0.895, –0.727

Table 5.19. X-ray experimental details for complex **3** (CCDC 1582378).

Crystal Data	
Chemical formula	$C_{51}H_{54}ClF_6FeN_4P$
Fw, g/mol	959.25
Crystal system, space group	Monoclinic, *C2/c*
Temperature (K)	100(2)
a, *b*, *c* (Å)	20.028(3), 19.250(3), 24.652(4)
α, β, γ (°)	90, 101.756(2), 90
V (Å^3)	9305(3)
Z	8
Radiation type	Mo *Kα*
μ (mm^{-1})	0.480
Crystal size (mm)	0.36 × 0.19 × 0.13
Data collection	
Diffractometer	Bruker *APEX*-II CCD
Absorption correction	Multi-scan, *SADABS*
T_{min}, T_{max}	0.8454, 0.9420
No. of measured, independent and observed [$I > 2\sigma(I)$] reflections	46177, 8297, 5611
R_{int}	0.1189
$(\sin\theta/\lambda)_{max}$ (Å^{-1})	0.596
Refinement	
$R[F^2 > 2\sigma(F^2)]$, $wR(F^2)$, *S*	0.0847, 0.2188, 1.081
No. of reflections	8297
No. of parameters	591
No. of restraints	0
H-atom treatment	H atoms treated by a mixture of independent and constrained refinement
Dr_{max}, Dr_{min} (e Å^{-3})	3.197, –0.638

Table 5.20. X-ray experimental details for complex **5b** (CCDC 1582376).

Crystal Data	
Chemical formula	$C_{16}H_{22}Cl_2FeP_2$
Fw, g/mol	403.03
Crystal system, space group	Monoclinic, *C2/c*
Temperature (K)	100(2)
a, *b*, *c* (Å)	13.0174(13), 9.7951(10), 16.060(2)
α, β, γ (°)	90, 110.2950(10), 90
V (Å^3)	1920.6(4)
Z	4
Radiation type	Mo *Kα*
μ (mm^{-1})	1.221
Crystal size (mm)	0.61 × 0.60 × 0.34
Data collection	
Diffractometer	Bruker *APEX*-II CCD
Absorption correction	Multi-scan, *SADABS*
T_{min}, T_{max}	0.5234, 0.6844
No. of measured, independent and observed [$I > 2\sigma(I)$] reflections	13500, 1694, 1649
R_{int}	0.0197
$(\sin\theta/\lambda)_{max}$ (Å^{-1})	0.595
Refinement	
$R[F^2 > 2\sigma(F^2)]$, $wR(F^2)$, S	0.0192, 0.0524, 1.080
No. of reflections	1694
No. of parameters	98
No. of restraints	0
H-atom treatment	H atoms treated by a mixture of independent and constrained refinement
Dr_{max}, Dr_{min} (e Å^{-3})	0.374, –0.196

Table 5.21. X-ray experimental details for complex **6** (CCDC 1582377).

Crystal Data	
Chemical formula	$C_{22}H_{32.67}Cl_2Fe_{0.67}P_{0.67}$
Fw, g/mol	425.93
Crystal system, space group	Monoclinic, *P2(1)/n*
Temperature (K)	100(2)
a, *b*, *c* (Å)	14.3035(6), 11.8427(4), 25.2650(10)
α, β, γ (°)	90, 103.6770(10), 90
V (Å^3)	4158.3(3)
Z	6
Radiation type	Mo *Kα*
μ (mm^{-1})	0.610
Crystal size (mm)	0.29 × 0.16 × 0.12
Data collection	
Diffractometer	Bruker *APEX*-II CCD
Absorption correction	Multi-scan, *SADABS*
T_{min}, T_{max}	0.8424, 0.9293
No. of measured, independent and observed [$I > 2\sigma(I)$] reflections	7315, 7315, 5595
R_{int}	0.0604
$(\sin \theta/\lambda)_{max}$ (Å^{-1})	0.595
Refinement	
$R[F^2 > 2\sigma(F^2)]$, $wR(F^2)$, S	0.0435, 0.1162, 1.138
No. of reflections	7315
No. of parameters	349
No. of restraints	0
H-atom treatment	H atoms treated by a mixture of independent and constrained refinement
Dr_{max}, Dr_{min} (e Å^{-3})	0.368, –0.348

Table 5.22. X-ray experimental details for complex **7b**.

Crystal Data	
Chemical formula	$C_{50}H_{52}Cl_6F_{12}Fe_2N_6P_2$
Fw, g/mol	1351.32
Crystal system, space group	orthorhombic, *Pbca*
Temperature (K)	100(2)
a, *b*, *c* (Å)	8.2826(3), 23.9456(9), 57.660(2)
α, β, γ (°)	90, 90, 90
V (Å^3)	11435.8(8)
Z	15
Radiation type	Mo *Kα*
μ (mm^{-1})	0.924
Crystal size (mm)	0.18 × 0.20 × 0.20
Data collection	
Diffractometer	Bruker *APEX*-II CCD
Absorption correction	Multi-scan, *SADABS*
T_{min}, T_{max}	0.8367, 0.8513
No. of measured, independent and observed [$I > 2\sigma(I)$] reflections	63537, 10076, 7975
R_{int}	0.0766
$(\sin \theta/\lambda)_{max}$ (Å^{-1})	0.593
Refinement	
$R[F^2 > 2\sigma(F^2)]$, $wR(F^2)$, S	0.0533, 0.0921, 1.118
No. of reflections	10076
No. of parameters	716
No. of restraints	0
H-atom treatment	H atoms treated by a mixture of independent and constrained refinement
Dr_{max}, Dr_{min} (e Å^{-3})	0.603, –0.567

Table 5.23. X-ray experimental details for complex **7c**.

Crystal Data	
Chemical formula	$C_{25}H_{26}BrCl_2F_6FeN_3P$
Fw, g/mol	720.12
Crystal system, space group	Monoclinic, *P2(1)/n*
Temperature (K)	100(2)
a, *b*, *c* (Å)	8.3854(6), 12.3400(9), 28.268(2)
α, β, γ (°)	90, 98.4380(10), 90
V (Å^3)	2893.4(4)
Z	4
Radiation type	Mo *Kα*
μ (mm^{-1})	2.202
Crystal size (mm)	0.10 × 0.13 × 0.15
Data collection	
Diffractometer	Bruker *APEX*-II CCD
Absorption correction	Multi-scan, *SADABS*
T_{min}, T_{max}	0.7307, 0.8066
No. of measured, independent and observed [$I > 2\sigma(I)$] reflections	25774, 5107, 3965
R_{int}	0.0796
$(\sin \theta/\lambda)_{max}$ (Å^{-1})	0.595
Refinement	
$R[F^2 > 2\sigma(F^2)]$, $wR(F^2)$, S	0.0582, 0.1287, 1.071
No. of reflections	5107
No. of parameters	358
No. of restraints	0
H-atom treatment	H atoms treated by a mixture of independent and constrained refinement
Dr_{max}, Dr_{min} (e Å^{-3})	1.305, –1.271

Table 5.24. X-ray experimental details for complex **7e**.

Crystal Data	
Chemical formula	$C_{30.25}H_{37.83}Cl_2F_6FeN_{3.14}O_{0.24}P$
Fw, g/mol	721.02
Crystal system, space group	Triclinic, *P-1*
Temperature (K)	100(2)
a, *b*, *c* (Å)	9.6203(15), 18.787(3), 18.809(3)
α, β, γ (°)	82.424(2), 88.231(2), 79.928(3)
V (Å^3)	3317.8(9)
Z	4
Radiation type	Mo *Kα*
μ (mm^{-1})	0.724
Crystal size (mm)	0.06 × 0.13 × 0.20
Data collection	
Diffractometer	Bruker *APEX*-II CCD
Absorption correction	Multi-scan, *SADABS*
T_{min}, T_{max}	0.8711, 0.9572
No. of measured, independent and observed [$I > 2\sigma(I)$] reflections	47711, 11739, 7968
R_{int}	0.1444
$(\sin \theta/\lambda)_{max}$ (Å^{-1})	0.594
Refinement	
$R[F^2 > 2\sigma(F^2)]$, $wR(F^2)$, S	0.1003, 0.2450, 1.079
No. of reflections	11739
No. of parameters	841
No. of restraints	111
H-atom treatment	H atoms treated by a mixture of independent and constrained refinement
Dr_{max}, Dr_{min} (e Å^{-3})	1.844, –0.892

Table 5.25. X-ray experimental details for complex **7f**.

Crystal Data	
Chemical formula	$C_{28}H_{32}Cl_2F_6FeN_4OP$
Fw, g/mol	712.30
Crystal system, space group	Monoclinic, *P2(1)/c*
Temperature (K)	100(2)
a, *b*, *c* (Å)	14.644(2), 15.843(3), 14.658(2)
α, β, γ (°)	90, 113.414(4), 90
V (Å^3)	3120.8(9)
Z	4
Radiation type	Mo *Kα*
μ (mm^{-1})	0.771
Crystal size (mm)	0.07 × 0.25 × 0.30
Data collection	
Diffractometer	Bruker *APEX*-II CCD
Absorption correction	Multi-scan, *SADABS*
T_{min}, T_{max}	0.8027, 0.9509
No. of measured, independent and observed [$I > 2\sigma(I)$] reflections	77641, 4499, 5541
R_{int}	0.0799
$(\sin \theta/\lambda)_{max}$ (Å^{-1})	0.596
Refinement	
$R[F^2 > 2\sigma(F^2)]$, $wR(F^2)$, S	0.0609, 0.1249, 1.078
No. of reflections	5541
No. of parameters	407
No. of restraints	3
H-atom treatment	H atoms treated by a mixture of independent and constrained refinement
Dr_{max}, Dr_{min} (e Å^{-3})	0.708, –0.792

Table 5.26. X-ray experimental details for complex **7g**.

Crystal Data	
Chemical formula	$C_{27}H_{32}Cl_2F_6FeN_4P$
Fw, g/mol	684.29
Crystal system, space group	Hexagonal, *P6(1)*
Temperature (K)	100(2)
a, *b*, *c* (Å)	22.2358(8), 22.2358(8), 11.5937(6)
α, β, γ (°)	90, 90, 120
V (Å^3)	4964.3(4)
Z	6
Radiation type	Mo *Kα*
μ (mm^{-1})	0.722
Crystal size (mm)	0.02 × 0.09 × 0.18
Data collection	
Diffractometer	Bruker *APEX*-II CCD
Absorption correction	Multi-scan, *SADABS*
T_{min}, T_{max}	0.8792, 0.9857
No. of measured, independent and observed [$I > 2\sigma(I)$] reflections	29637, 5862, 4381
R_{int}	0.0975
$(\sin \theta/\lambda)_{max}$ (Å^{-1})	0.596
Refinement	
$R[F^2 > 2\sigma(F^2)]$, $wR(F^2)$, S	0.0637, 0.1475, 1.077
No. of reflections	5862
No. of parameters	432
No. of restraints	173
H-atom treatment	H atoms treated by a mixture of independent and constrained refinement
Dr_{max}, Dr_{min} (e Å^{-3})	0.628, –0.324

Table 5.27. X-ray experimental details for complex **8a**.

Crystal Data	
Chemical formula	$C_{28}H_{29}ClF_9FeN_4P$
Fw, g/mol	714.82
Crystal system, space group	Monoclinic, *P2(1)/c*
Temperature (K)	100(2)
a, *b*, *c* (Å)	8.5840(7), 27.783(2), 12.7587(11)
α, β, γ (°)	90, 92.6550(10), 90
V (Å^3)	3039.6(4)
Z	4
Radiation type	Mo *Kα*
μ (mm^{-1})	0.719
Crystal size (mm)	0.05 × 0.10 × 0.10
Data collection	
Diffractometer	Bruker *APEX*-II CCD
Absorption correction	Multi-scan, *SADABS*
T_{min}, T_{max}	0.9316, 0.9650
No. of measured, independent and observed [$I > 2\sigma(I)$] reflections	27838, 5370, 4617
R_{int}	0.0375
$(\sin \theta/\lambda)_{max}$ (Å^{-1})	0.595
Refinement	
$R[F^2 > 2\sigma(F^2)]$, $wR(F^2)$, S	0.0310, 0.0761, 1.049
No. of reflections	5370
No. of parameters	404
No. of restraints	0
H-atom treatment	H atoms treated by a mixture of independent and constrained refinement
Dr_{max}, Dr_{min} (e Å^{-3})	0.515, –0.335

Table 5.28. X-ray experimental details for complex **8b**.

Crystal Data	
Chemical formula	$C_{68}H_{83}Cl_4F_{12}Fe_2N_{13}OP_2$
Fw, g/mol	1641.91
Crystal system, space group	Monoclinic, *Cc*
Temperature (K)	100(2)
a, *b*, *c* (Å)	17.8731(10), 18.4160(10), 24.1007(13)
α, β, γ (°)	90, 97.8320(10), 90
V (Å^3)	7858.8(7)
Z	4
Radiation type	Mo *Kα*
μ (mm^{-1})	0.624
Crystal size (mm)	0.12 × 0.17 × 0.20
Data collection	
Diffractometer	Bruker *APEX*-II CCD
Absorption correction	Multi-scan, *SADABS*
T_{min}, T_{max}	0.8854, 0.9289
No. of measured, independent and observed [$I > 2\sigma(I)$] reflections	52481, 13757, 13307
R_{int}	0.0426
$(\sin \theta/\lambda)_{max}$ (Å^{-1})	0.596
Refinement	
$R[F^2 > 2\sigma(F^2)]$, $wR(F^2)$, *S*	0.0412, 0.1121, 1.117
No. of reflections	13757
No. of parameters	940
No. of restraints	2
H-atom treatment	H atoms treated by a mixture of independent and constrained refinement
Dr_{max}, Dr_{min} (e Å^{-3})	0.595, –0.454

Table 5.29. X-ray experimental details for complex **8c**.

Crystal Data	
Chemical formula	$C_{27}H_{29}BrClF_6FeN_4P$
Fw, g/mol	725.72
Crystal system, space group	Monoclinic, *P2(1)/c*
Temperature (K)	100(2)
a, *b*, *c* (Å)	8.4689(8), 27.812(3), 12.6960(12)
α, β, γ (°)	90, 91.989(2), 90
V (Å^3)	2988.6(5)
Z	4
Radiation type	Mo *Kα*
μ (mm^{-1})	2.047
Crystal size (mm)	0.05 × 0.11 × 0.12
Data collection	
Diffractometer	Bruker *APEX*-II CCD
Absorption correction	Multi-scan, *SADABS*
T_{min}, T_{max}	0.7913, 0.9046
No. of measured, independent and observed [$I > 2\sigma(I)$] reflections	43711, 5271, 4513
R_{int}	0.0386
$(\sin \theta/\lambda)_{max}$ (Å^{-1})	0.595
Refinement	
$R[F^2 > 2\sigma(F^2)]$, $wR(F^2)$, S	0.0303, 0.0702, 1.033
No. of reflections	5271
No. of parameters	377
No. of restraints	0
H-atom treatment	H atoms treated by a mixture of independent and constrained refinement
Dr_{max}, Dr_{min} (e Å^{-3})	0.638, –0.530

Table 5.30. X-ray experimental details for complex **8d**.

Crystal Data	
Chemical formula	$C_{29}H_{33}ClF_6FeN_5P$
Fw, g/mol	687.87
Crystal system, space group	Orthorhombic, *P212121*
Temperature (K)	100(2)
a, *b*, *c* (Å)	7.8744(8), 19.270(2), 20.784(2)
α, β, γ (°)	90, 90, 90
V (Å^3)	3153.8(6)
Z	4
Radiation type	Mo *Kα*
μ (mm^{-1})	0.677
Crystal size (mm)	0.13 × 0.19 × 0.57
Data collection	
Diffractometer	Bruker *APEX*-II CCD
Absorption correction	Multi-scan, *SADABS*
T_{min}, T_{max}	0.6984, 0.9183
No. of measured, independent and observed [$I > 2\sigma(I)$] reflections	47112, 5607, 5220
R_{int}	0.0348
$(\sin \theta/\lambda)_{max}$ (Å^{-1})	0.594
Refinement	
$R[F^2 > 2\sigma(F^2)]$, $wR(F^2)$, S	0.0304, 0.0711, 1.035
No. of reflections	5607
No. of parameters	396
No. of restraints	0
H-atom treatment	H atoms treated by a mixture of independent and constrained refinement
Dr_{max}, Dr_{min} (e Å^{-3})	0.625, –0.217

Table 5.31. X-ray experimental details for complex **8e**.

Crystal Data	
Chemical formula	$C_{31}H_{38}ClF_6FeN_4P$
Fw, g/mol	702.92
Crystal system, space group	Monoclinic, *P2(1)/c*
Temperature (K)	100(2)
a, *b*, *c* (Å)	10.527(4), 18.713(6), 34.328(9)
α, β, γ (°)	90, 94.554(19), 90
V (Å^3)	6741(4)
Z	16
Radiation type	Mo *Kα*
μ (mm^{-1})	0.634
Crystal size (mm)	0.10 × 0.10 × 0.14
Data collection	
Diffractometer	Bruker *APEX*-II CCD
Absorption correction	Multi-scan, *SADABS*
T_{min}, T_{max}	0.9164, 0.9393
No. of measured, independent and observed [$I > 2\sigma(I)$] reflections	48885, 11943, 7461
R_{int}	0.0970
$(\sin \theta/\lambda)_{max}$ (Å^{-1})	0.593
Refinement	
$R[F^2 > 2\sigma(F^2)]$, $wR(F^2)$, S	0.0455, 0.0910, 1.009
No. of reflections	11943
No. of parameters	813
No. of restraints	0
H-atom treatment	H atoms treated by a mixture of independent and constrained refinement
Dr_{max}, Dr_{min} (e Å^{-3})	0.655, –0.415

Table 5.32. X-ray experimental details for complex **8f**.

Crystal Data	
Chemical formula	$C_{28}H_{32}ClF_6FeN_4OP$
Fw, g/mol	676.85
Crystal system, space group	Monoclinic, *P2(1)/c*
Temperature (K)	100(2)
a, *b*, *c* (Å)	8.4230(8), 27.937(3), 12.9042(13)
α, β, γ (°)	90, 92.399(2), 90
V (Å^3)	3033.9(5)
Z	4
Radiation type	Mo *Kα*
μ (mm^{-1})	0.704
Crystal size (mm)	0.11 × 0.16 × 0.46
Data collection	
Diffractometer	Bruker *APEX*-II CCD
Absorption correction	Multi-scan, *SADABS*
T_{min}, T_{max}	0.7359, 0.9247
No. of measured, independent and observed [$I > 2\sigma(I)$] reflections	33947, 5356, 4308
R_{int}	0.0493
$(\sin\theta/\lambda)_{max}$ (Å^{-1})	0.596
Refinement	
$R[F^2 > 2\sigma(F^2)]$, $wR(F^2)$, S	0.0354, 0.0843, 1.041
No. of reflections	5356
No. of parameters	387
No. of restraints	0
H-atom treatment	H atoms treated by a mixture of independent and constrained refinement
Dr_{max}, Dr_{min} (e Å^{-3})	0.593, –0.456

Table 5.33. X-ray experimental details for complex **8g**.

Crystal Data	
Chemical formula	$C_{29}H_{35}ClF_6FeN_5P$
Fw, g/mol	689.89
Crystal system, space group	Monoclinic, *P2(1)/c*
Temperature (K)	100(2)
a, *b*, *c* (Å)	13.6986(8), 17.1010(10), 14.1783(8)
α, β, γ (°)	90, 105.8630(10), 90
V (Å^3)	3194.9(3)
Z	4
Radiation type	Mo *Kα*
μ (mm^{-1})	0.669
Crystal size (mm)	0.12 × 0.14 × 0.20
Data collection	
Diffractometer	Bruker *APEX*-II CCD
Absorption correction	Multi-scan, *SADABS*
T_{min}, T_{max}	0.8801, 0.9229
No. of measured, independent and observed [$I > 2\sigma(I)$] reflections	37966, 5654, 3783
R_{int}	0.0925
$(\sin \theta/\lambda)_{max}$ (Å^{-1})	0.594
Refinement	
$R[F^2 > 2\sigma(F^2)]$, $wR(F^2)$, S	0.0485, 0.0849, 1.014
No. of reflections	5654
No. of parameters	397
No. of restraints	0
H-atom treatment	H atoms treated by a mixture of independent and constrained refinement
Dr_{max}, Dr_{min} (e Å^{-3})	0.425, –0.345

Table 5.34. Selected metrical parameters for complexes **4b** and **6a**.

	5b	**6**
Fe(1)–P(1)	2.4282(4)	2.4649(8)
Fe(1)–P(2)	2.4282(4)	NA
Fe(1)–Cl(1)	2.2382(4)	2.1769(8)
Fe(1)–Cl(2)	2.2382(4)	2.1690(8)
Fe(1)–Cl(3)	NA	2.1739(8)
Cl(1)−Fe(1)−Cl(2)	126.18(2)	112.67(3)
P(1)−Fe(1)−P(2)	100.03(2)	NA
P(1)−Fe(1)−Cl(1)	106.491(14)	109.5(3)
P(1)−Fe(1)−Cl(2)	107.324(15)	101.19(3)
P(2)−Fe(1)−Cl(1)	107.323(15)	NA
P(2)−Fe(1)−Cl(2)	106.490(14)	NA
Cl(1)−Fe(1)−Cl(3)	NA	110.60(3)
Cl(2)−Fe(1)−Cl(3)	NA	115.54(3)
P(1)−Fe(1)−Cl(3)	NA	106.62(3)
τ_4	1.0	0.9

[a] τ_4 is a metric for four coordinate complexes. $\tau_4 = 0$ for a perfect square planar and $\tau_4 = 1$ for a perfect tetrahedron.

5.10. References

1. Yang, Z.; J. Zhang, J.; Kintner-Meyer, M. C. W.; Lu, X.; Choi, D.; Lemmon, J. P.; Liu, J. *Chem. Rev.* **2011**, *111*, 3577.

2. Esswein, A. J.; Nocera, D. G. *Chem. Rev.* **2007**, *107*, 4022.

3. Cook, T.R.; Dogutan, D. K.; Reece, S. Y.; Surendranath, Y.; Teets, T. S.; Nocera, D. G. *Chem. Rev.* **2010**, *110*, 6474.

4. Twilton, J.; Le, C.; Zhang, P.; Shaw, M. H.; Evans, R. W.; MacMillan, D. W. C. *Nat. Rev. Chem.* **2017**, *1*, 1.

5. Romero, N. A.; Nicewicz, D. A. *Chem. Rev.* **2016**, *116*, 10075.

6. Shields, B. J.; Doyle, A. G. *J. Am. Chem. Soc.* **2016**, *138*, 12719.

7. Heitz, D. R.; Tellis, J. C.; Molander, G. A. *J. Am. Chem. Soc.* **2016**, *138*, 12715.

8. Cook, T. R.; Surendranath, Y.; Nocera, D. G. *J. Am. Soc. Chem.* **2009**, *131*, 28.

9. Teets, T. S.; Nocera, D. G. *J. Am. Chem. Soc.* **2009**, *131*, 7411.

10. Power, D. C.; Chambers, M. B.; Teets, T. S.; Elgrishi, N.; Anderson, B. L.; Nocera, D. G. *Chem. Sci.* **2013**, *4*, 2880.

11. Karikachery, A. R.; Lee, H. B.; Masjedi, M.; Ross, A.; Moody, M. A.; Cai, X.; Chui, M.; Hoff, C. D.; Sharp, P. R. *Inorg. Chem.* **2013**, *52*, 4113.

12. Yang, H.; Gabbaï, F. P. *J. Am. Chem. Soc.* **2014**, *136*, 10866.

13. Nocera, D. G. *Inorg. Chem.* **2009**, *48*, 10001.

14. Hwang, S. J.; Powers, D. C.; Maher, A. G.; Anderson, B. L.; Hadt, R. G.; Zheng, S.-L.; Chen, Y.-S.; Nocera, D. G. *J. Am. Soc. Chem.* **2015**, *137*, 6472.
15. Hwang, S. J.; Anderson, B. L.; Powers, D. C.; Maher, A. G.; Hadt, R. G.; Nocera, D. G. *Organometallics* **2015**, *34*, 4766.

16. Walling, C. *J. Org. Chem*. **1988**, *53*, 305.

17. Benson, S. W. *J. Am. Chem. Soc*. **1993**, *115*, 6969.

18. Poutsma, M. L. In *Methods in Free Radical Chemistry*, Vol. 1, E. S. Huyser, ed., Marcel Dekker: New York, 1969.

19. Russell, G. A. In *Free Radicals*, Vol. 1, Kochi, J. K., ed., Wiley, New York, 1973.

20. Lüning, U.; Skell, P. S. *Tetrahedron*, **1985**, *41*, 4289.

21. Russell, G. A.; Brown, H. C. *J. Am. Chem. Soc*. **1955**, *77*, 4031.

22. Russell, G. A. *J. Am. Chem. Soc*. **1957**, *79*, 2977.

23. Russell, G. A. *J. Am. Chem. Soc*. **1958**, *80*, 4987.

24. Russell, G. A. *J. Am. Chem. Soc*. **1958**, *80*, 4997.

25. Skell, P. S.; Baxter, H. N., III; Tayer, C. K. *J. Am. Chem. Soc*. **1983**, *105*, 120.

26. Skell, P. S.; Baxter, H. N., III; Tanko, J. M.; Chebolu, V. *J. Am. Chem. Soc*. **1986**, *108*, 6300.

27. Bunce, N. J.; Ingold, K. U.; Landers, J. P.; Lusztyk, J.; Scaiano, J. C. *J. Am. Chem. Soc*. **1985**, *107*, 5464.

28. Ingold, K. U.; Lusztyk, J.; Raner, K. D. *Acc. Chem. Res*. **1990**, *23*, 219.

29. Rander, K. D.; Lusztyk, J.; Ingold, K. U. *J. Phys. Chem*. **1989**, *93*, 564.

30. Rander, K. D.; Lusztyk, J.; Ingold, K. U. *J. Am. Chem. Soc*. **1989**, *110*, 3519.

31. Sergeev, G. B.; Pukhovskii, A. V.; Smirnov, V. V. *Russ. J. Phys. Chem.* **1983**, *57*, 589.

32. Tsao, M.-L.; Hadad, C. M.; Platz, M. S. *J. Am. Chem. Soc*. **2003**, *125*, 8390.

33. Gygi, D.; Hwang, S. J.; Nocera, D. G. *J. Org. Chem*. **2017**, *82*, 12933.

34. Coppens, P. *J. Phys. Chem. Lett.* **2011**, *2*, 616.

35. Coppens, P. *Struct. Dyn.* **2017**, *4*, 032102.

36. Sakai, T.; Ohgo, Y.; Hoshino, A.; Ikeue, T.; Saitoh, T.; Takahashi, M.; Nakamura, M. *Inorg. Chem.* **2004**, *43*, 5034.

37. Addison, A. W.; Rao, T. N.; Reedijk, J.; van Rijn, J.; Verschoor, G. C. *J. Chem. Soc., Dalton Trans.,* **1984**, *0*, 1349.

38. Bart, S. C.; Chłopek, K.; Bill, E.; Bouwkamp, M. W.; Lobkovsky, E.; Neese, F.; Wieghardt, K.; Chirik, P. J. *J. Am. Chem. Soc.* **2006**, *128*, 13901.

39. Walker, J. D.; Poli, R. *Inorg. Chem*. **1989**, *28*, 1793.

40. Feng, X.; Hwang, S. J.; Liu, J.-L.; Chen, Y.-C.; Tong, M.-L.; Nocera, D. G. *J. Am. Chem. Soc.* **2017**, *139*, 16474.

41. Fillman, K. L.; Przyojski, J. A.; Al-Afyouni, M. H.; Tonzetich, Z. J.; Neidig, M. L. *Chem. Sci*. **2015**, *6*, 1178.

42. Powers, D. C.; Hwang, S. J.; Zheng, S.-L.; Nocera, D. G. *Inorg. Chem*. **2014**, *53*, 9122.

43. Demas, J. N.; Bowman, W. D.; Zalewski, E. F.; Velapoldi, R. A. *J. Phys. Chem.* **1981**, *85*, 2766.

44. Kuhn, H.; Braslavasky, S. E.; Schmidt, R. *Pure Appl. Chem.* **2004**, *76*, 2105.

45. Raner, K. D.; Lusztyk, J.; Ingold, K. U. *J. Phys. Chem.* **1989**, *93*, 564.

46. Ingold, K. U.; Lusztyk, J.; Raner, K. D. *Acc. Chem. Res.* **1990**, *23*, 219.

47. Tanko, J. M.; Suleman, N. K. In Energetics of Organic Free Radicals; Simões, J. A. S., Greenberg, A., Liebman, J. F., Eds.; Chapman & Hall: New York, 1996; Chapter 8.

48. Russell, G. A. *J. Am. Chem. Soc.* **1958**, *80*, 4987.

49. Bunce, N. J.; Ingold, K. U.; Landers, J. P.; Lusztyk, J.; Scaiano, J. C. *J. Am. Chem. Soc.* **1985**, *107*, 5464.

50. Skell, P. S.; Baxter, H. N., III; Tanko, J. M.; Chebolu, V. *J. Am. Chem. Soc.* **1986**, *108*, 6300.

51. Sergeev, G. B.; Pukhovskii, A. V.; Smirnov, V. V. *Russ. J. Phys. Chem.* **1983**, *57*, 589.

52. Tondreau, A. M.; Stieber, S. C. E.; Milsmann, C.; Lobkovsky, E.; Weyhermüller, T.;

Semproni, S. P.; Chirik, P. J. *Inorg. Chem.* **2013**, *52*, 635

53. Darmon, J. D.; Turner, Z. R.; Lobkovsky, E.; Chirik, P. J. *Organometallics* **2012**, *31*, 2275.

54. Handa, S.; Andersson, M. P.; Gallou, F.; Reilly. J.; Lipshutz, B. H. *Angew. Chem. Int. Ed.* **2016**, *55*, 4914.

55. Lee, C. H.; Villágran, D.; Cook, T. R.; Peters, J. C.; Nocera, D. G. *ChemSusChem* **2013**, *6*, 1541.

56. Lieb, D.; Kenkell, I.; Miljković, J. L.; Moldehauer, D.; Weber, N.; Filipović, M. R.; Gröhn, F.; Ivanović-Burmazović, I. *Inorg. Chem* **2014**, *53*, 1009.

57. Weekley, C. M.; Kenkel, I.; Lippert, R.; Wei, S.; Lieb, D.; Cranwell, T.; Wedding, J. L.; Zillmann, A. S.; Rhor, R.; Filpovic, M. R.; Ivanović-Burmazović, I.; Harris, H. H. *Inorg. Chem* **2017**, *56*, 6076.

58. Ivchenko, P. V.; Nifant'ev, I. E.; Bulsov, I. V. *Tetrahedron Lett.* **2013**, *54*, 217.

59. Hansch, C.; Leo, A. *Substituent Constants for Correlation Analysis in Chemistry and Biology*; Wiley-Interscience: New York, 1979.

60. Nückel, S.; Burger, P. *Organometallics* **2001**, *20*, 4345.

61. Zohuri, G. H.; Seyedi, S. M.; Sandaroos, R.; Damavandi, S.; Mohammadi, A. *Catal. Lett.* **2010**, *140*, 160.

62. Dumont, A.; Jaques, V.; Desreux, J. F. *Tetrahedron* **2000**, *56*, 2043.

63. Appukuttan, V. K.; Liu, Y.; Son, B. C.; Ha, C.; Suh, H.; Kim, I. *Organometallics* **2011**, *30*, 2285.

64. Fontana, F.; Minisci, F.; Claduia, M.; Barbosa, N.; Vismara. *J. Org. Chem.* **1991**, *56*, 2866.

65. Jacobs, B. P.; Wolczanski, P. T.; Lobkovsky, E. B. *Inorg. Chem*. **2016**, *55*, 4223.

66. Bruker AXS (2009). Apex II. Bruker AXS, Madison, Wisconsin.

67. Sheldrick, G. M. *Acta Cryst.* **2010**, *D66*, 479–485.

68. Fulmer, G. R.; Miller, A. J. M.; Sherden, N. H.; Gottlieb, H. E.; Nudelman, A.; Stoltz, B. M.; Bercaw, J. E.; Goldberg, K. I. *Organometallics*, **2010**, *29*, 2176.

69. Bain, G. A.; Berry, J. F. *J. Chem. Ed.*, **2008**, *85*, 532.

Chapter 6

Slow Magnetic Relaxation in Intermediate Spin S = $^3/_2$ Mononuclear Fe(III) Complexes

Parts of this chapter have been published:

Feng, X.; Hwang, S. J.; Liu, J.-L.; Chen, Y.-C.; Tong, M.-L.; Nocera D. G. "Slow Magnetic Relaxation in Intermediate Spin S = 3/2 Mononuclear Fe(III) Complexes" *J. Am. Chem. Soc.* **2017**, *139*, 16474.

6.1 Introduction

Paramagnetic molecules displaying single-molecule magnet (SMM) behavior exhibit slow magnetic relaxation at low temperatures.[1–3] This phenomenon arises from an energy barrier (U_{eff}) to spin inversion, generated by magnetic anisotropy (D) acting on a high spin ground state (S). The capacity of SMMs to maintain their magnetization at higher temperatures leads to potential applications in high-density information storage and quantum computing.[4–10] To this end, SMMs made from noncritical elements is a beneficial goal for their implementation as materials for large-scale information storage.

Efforts to increase U_{eff} have centered on synthesizing polynuclear transition metal complexes possessing high S.[11] However, theoretical and experimental studies suggest that an increase of S is compensated by a corresponding decrease in overall D.[12–15] To overcome this problem, molecules containing highly anisotropic lanthanide ions have been introduced as spin centers owing to their strong spin-orbit coupled ground state; [16–25] energy barriers exceeding 1837 K (1277 cm^{-1}) have been reported, an order of magnitude larger than that of the original Mn_{12} SMMs. [26,27] As an alternative to the critical f-block elements, interest has turned to mononuclear complexes of non-critical first-row transition metals with large magnetic anisotropies where orbital angular momentum is left unquenched.[28–30] Additionally, in the first-row, fast quantum tunneling due to the mixing of ground states can be circumvented by utilizing non-integer spin systems as predicted by Kramers' theorem.[31] Mononuclear transition metals of $S = {}^3/_2$ are promising systems for such an approach.[32–36] For example, a linear two-coordinate Fe(I) complex displays an energy barrier of 354 K (246 cm^{-1}) and magnetic hysteresis at temperatures of 6.5 K, comparable to highest SMM performing lanthanide complexes.[37] To date, systems with $S = {}^3/_2$ mononuclear transition metal ions have been largely confined to Co(II)

systems, which exhibit moderate magnetic anisotropy, and in this body of work, a Co(II) complex with three-fold symmetry establishes control of the local symmetry as a good strategy to design SMMs with large anisotropy.[38] Along these lines, (PNP)$FeCl_2$ (PNP = N[2-P($CHMe_2$)$_2$-4-methylphenyl]$_2^-$) is a notable exception as an iron-based $S = {}^3/_2$ system that exhibits slow magnetic relaxation with $D = -11$ cm^{-1}.[33] This finding suggests the opportunity for realizing an iron-based intermediate spin $S = {}^3/_2$ SMMs with large anisotropy for ligand fields that enforce the appropriate local symmetry. Herein we show this to be the case with the observation of slow magnetic relaxation for the $S = {}^3/_2$ mononuclear Fe(III) complex, (PMe_3)$_2FeCl_3$ (**1**), which possesses almost perfect three-fold symmetry. The compound displays an energy barrier of 116 K (81 cm^{-1}) arising from a zero-field splitting parameter of $D = -50(2)$ cm^{-1}, which represents the largest magnetic anisotropy for any Fe(III) molecule yet reported. More fundamentally, the system reported herein elegantly demonstrates the criticality of local symmetry on the magnetic anisotropy. By breaking three-fold symmetry of the complex by substitution the axial PMe_3 ligands with PMe_2Ph, the (PMe_2Ph)$_2FeCl_3$ (**2**) complex shows a significantly reduced magnetic anisotropy, highlighting the influence of local symmetry on the overall anisotropy of SMMs.

6.2 Synthesis and Characterization of Mononuclear Fe(III) Complexes

Fe(III) trichloride complexes **1** and **2** were prepared by modifying the method reported by Poli[39] with the treatment of $FeCl_3$ in $PhCF_3$ solution with 2.5 equiv of corresponding phosphines, PMe_3 and PMe_2Ph, respectively. The molecular structures of **1** and **2** have been determined by X-ray diffraction and they are shown in Figure 6.1. The mononuclear Fe(III) center resides in a

5-coordinate trigonal bipyramid (TBP) as defined by the five-coordinate geometric parameter τ (τ_5 = 0.90 for **1**, τ_5 = 0.83 for **2**) ligand field.[40]

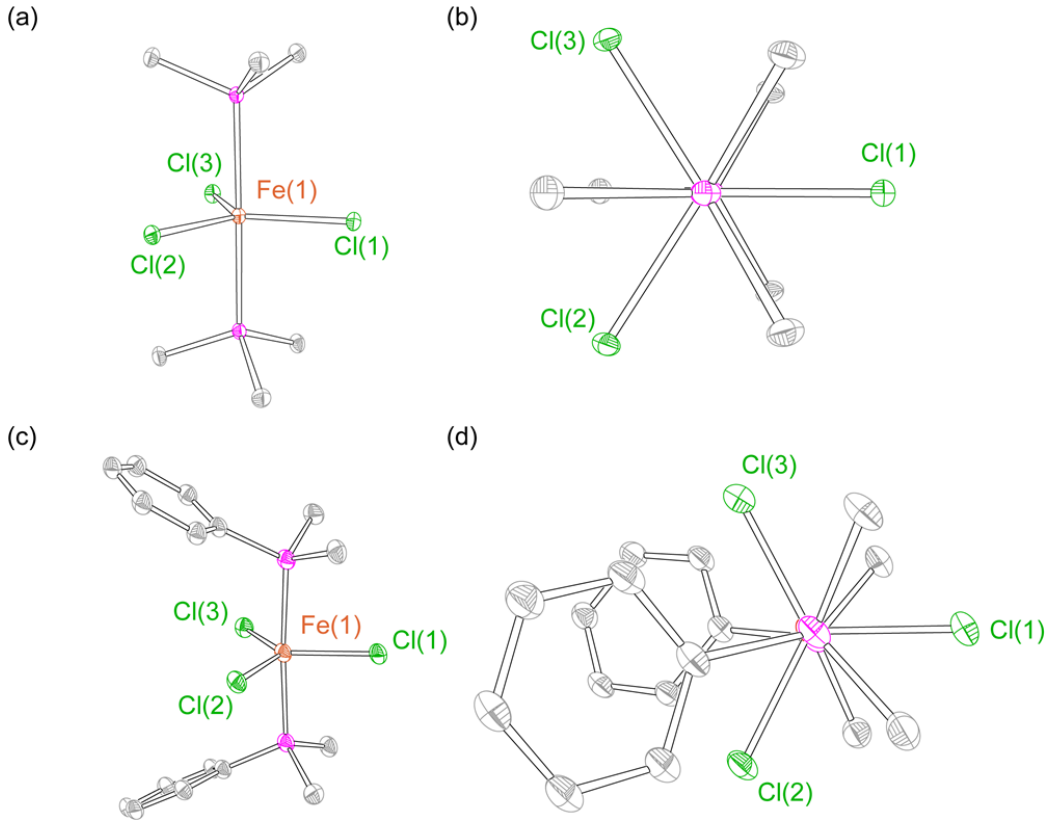

Figure 6.1. (a) Side view and (b) top view thermal ellipsoid plots of $FeCl_3(PMe_3)_2$ (**1**) drawn at the 50% probability level. H-atoms are omitted for clarity. (c) Side view and (d) top view thermal ellipsoid plots of $FeCl_3(PMe_2Ph)_2$ (**2**) drawn at the 50% probability level. H-atoms omitted for clarity.

Complex **1** has almost perfect three-fold local symmetry as demonstrated by Cl–Fe–Cl angles of 122.475(6)°, 115.023(12)°, and 122.476(6)°. This local three-fold symmetry is broken in **2** by the presence of the unique phenyl ring on the phosphine ligand. Whereas the PMe_3 groups in **1** are perfectly eclipsed with a P–Fe–P angle of 176.604(12)°, the structure of **2** shows the PMe_2Ph groups to be slightly staggered (20°) with a P–Fe–P angle of 175.11(2)°. In **1** and **2**, one of the Fe–Cl bonds is longer than the others; in **1** this lengthening is 0.0187 Å as compared to 0.0577 Å)

in **2**. Selected bond distances and angles for **1** and **2** are summarized in Table 6.1. Zero-field ^{57}Fe Mössbauer analysis of **1** and **2** in Figures 6.2 and 6.3, respectively, revealed the presence of a single iron environment with parameters (isomer shift, δ = 0.46 and 0.48 mm s^{-1} and a quadrupole splitting, $|\Delta E_Q|$ = 1.93 and 2.22 mm s^{-1} for **1** and **2**, respectively), in line with other intermediate spin $S = {}^3/_2$ Fe(III) complexes previously synthesized.[41,42] The larger quadrupole splitting of **2** is consistent with a significant symmetry distortion about Fe, as observed in solid-state structure.

Table 6.1. Selected bond distance [Å] and angles [°] for compounds **1** and **2**.

	1	**2**
Fe(1)–Cl(1)	2.2491(3)	2.2994(5)
Fe(1)–Cl(2)	2.2678(2)	2.2339(5)
Fe(1)–Cl(3)	2.2678(2)	2.2495(5)
Fe(1)–P(1)	2.3474(3)	2.3624(5)
Fe(1)–P(2)	2.3338(3)	2.3583(5)
Cl(1)−Fe(1)−Cl(2)	122.476(6)	117.45(2)
Cl(1)−Fe(1)−Cl(3)	122.475(6)	117.103(19)
Cl(2)−Fe(1)−Cl(3)	115.023(12)	125.425(19)
P(1)−Fe(1)−Cl(1)	88.795(11)	88.691(19)
P(1)−Fe(1)−Cl(2)	91.462(8)	89.095(18)
P(1)−Fe(1)−Cl(3)	91.462(8)	93.58(2)
P(2)−Fe(1)−Cl(1)	87.809(12)	87.690(19)
P(2)−Fe(1)−Cl(2)	90.362(8)	89.657(19)
P(2)−Fe(1)−Cl(3)	90.361(8)	90.992(19)
P(1)−Fe(1)−P(2)	176.604(12)	175.11(2)
τ_5[a]	0.90	0.83

[a]τ_5 is defined as (β-α)/60, with α and β being the two largest angles within the five-coordinate complex (τ_5 = 0 for square pyramidal and τ_5 = 1 for trigonal bipyramidal).

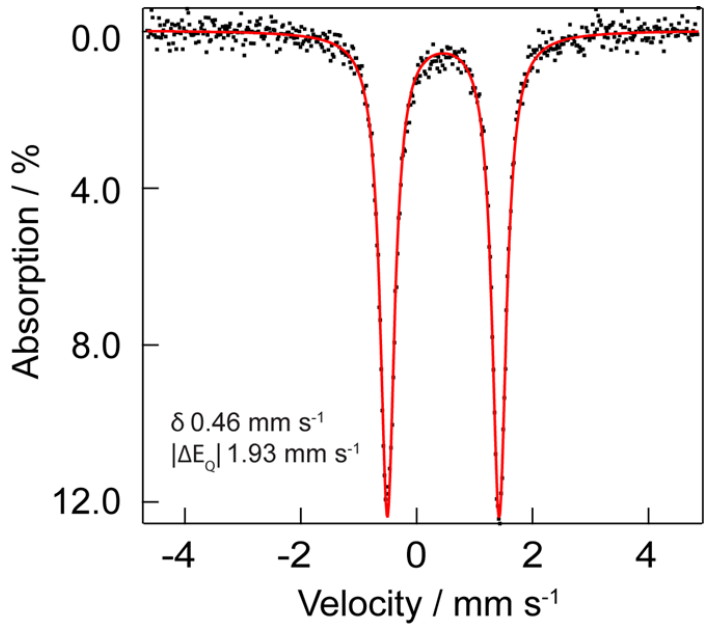

Figure 6.2. Zero-field ^{57}Fe Mössbauer spectrum of compound **1** recorded at 90 K. Isomer shift and quadrupole splitting are reported relative to Fe foil at room temperature.

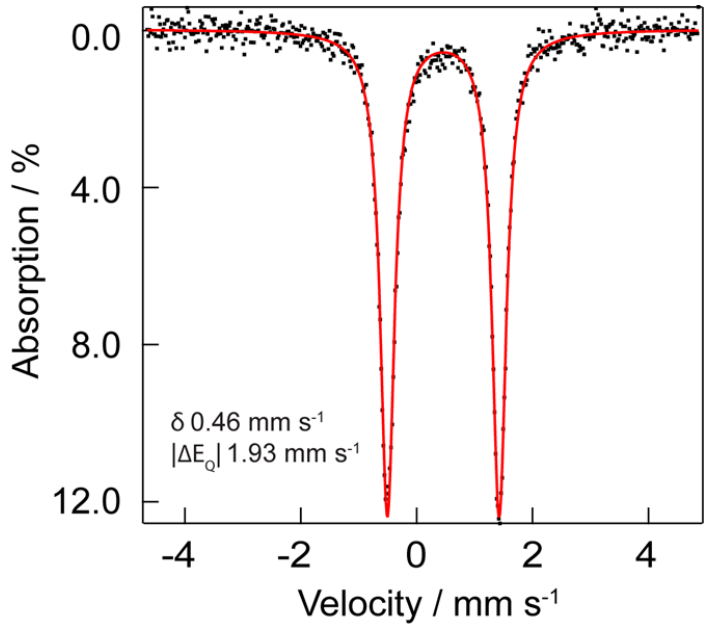

Figure 6.3. Zero-field ^{57}Fe Mössbauer spectrum of compound **2** recorded at 90 K. Isomer shift and quadrupole splitting are reported relative to Fe foil at room temperature.

6.3 Magnetic Properties

6.3.1 Dc susceptibility measurements

The influence of local symmetry on magnetic anisotropy was examined by performing *dc* susceptibility measurements under an applied field of 5000 Oe. For **1**, at 300 K, the value of $\chi_M T$ (Figure 6.4 (a)) yields 2.29 cm^3 K mol^{-1}, corresponding to a $S = {}^3/_2$ spin ground state. As temperature decreases, the value of $\chi_M T$ remains constant until 40 K, before dropping off at lower temperatures. In contrast, the value of $\chi_M T$ for **2** in Figure 6.4 (b) shows a significant temperature dependence over the range of 50 to 300 K, indicative of gradual $S = {}^3/_2$ to $S = {}^5/_2$ thermal spin crossover behavior.[33]

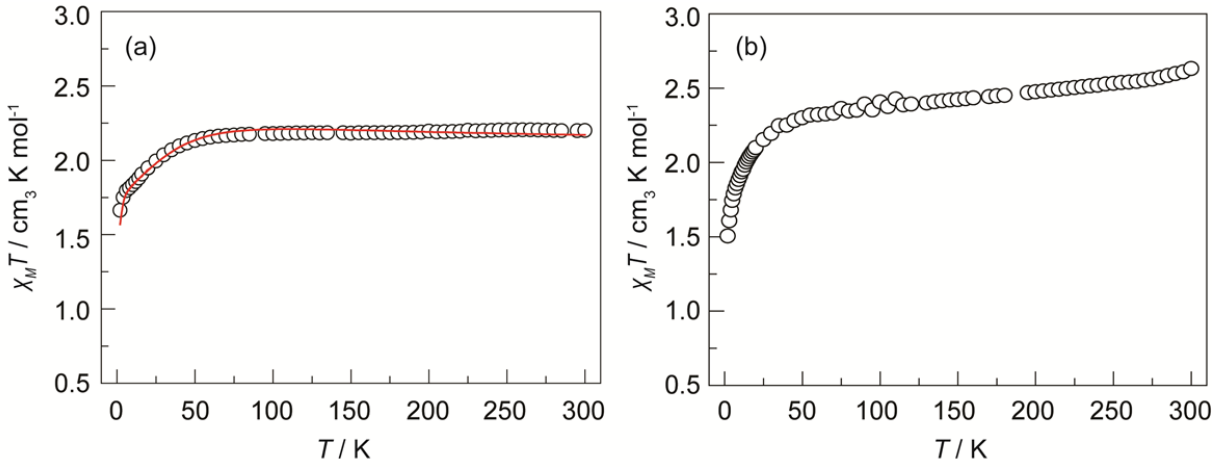

Figure 6.4. Variable-temperature magnetic susceptibility data collected for (a) **1** and (b) **2** under an applied *dc* field of 1000 Oe.

6.3.2 Variable field magnetization measurements

The magnetic anisotropy of the ground states of **1** and **2** was probed with variable field magnetization measurements collected from 2 to 20 K. The resulting magnetization plot (Figure 6.5) exhibits separated iso-field curves, and saturation behavior at 1.94 $N\beta$ for **1** and 2.40 $N\beta$ for **2** under an applied field of 7 T. The magnetization would be expected to saturate at 3 $N\beta$ ($M = gS$)

for a spin-only $S = {}^3/_2$ ion; deviation from this value arises from the presence of magnetic anisotropy. That saturation in **1** occurs at a significantly lower value than 3 $N\beta$, indicates a highly anisotropic spin ground state. To quantify the zero-field splitting parameter further, variable temperature, variable field magnetization was fit to the spin Hamiltonian,[43]

$$\hat{H} = D\hat{S}_z^2 + \beta(g_x\hat{S}_x + g_y\hat{S}_y + g_z\hat{S}_z)\mathbf{H} \quad (1)$$

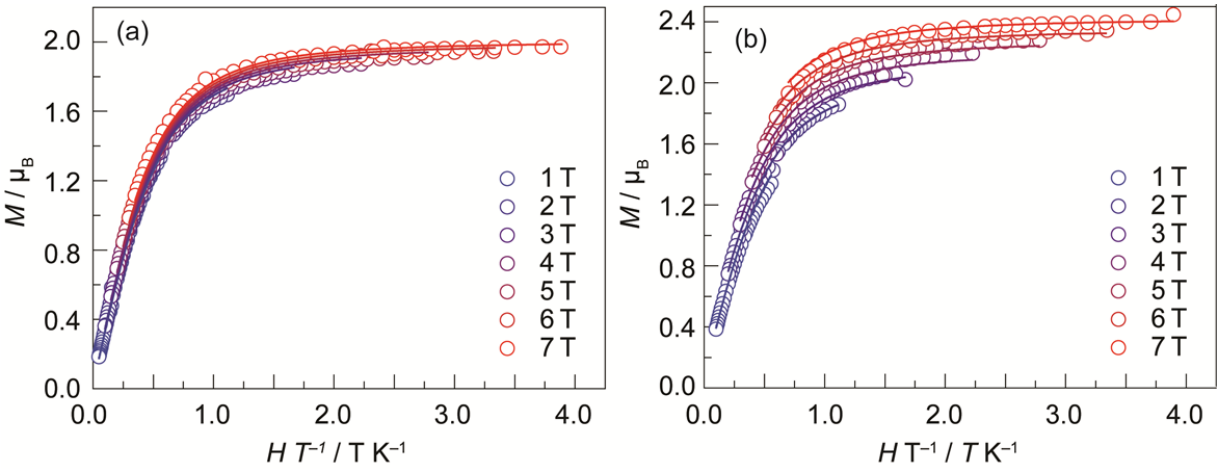

Figure 6.5. Variable field magnetization data collected at 7 fields (1−7 T) over the temperature range 2.0 to 20 K for (a) complex **1** and (b) complex **2**. Solid lines are the best fits to the experimental data. Magnetization fit parameters obtained with PHI: $g = 2.49(1)$, $D = -17(1)$ cm^{-1}.

For **2**, an isotropic g tensor sufficiently fit the data, yielding $D = -17(1)$ cm^{-1} and $g_x = g_y = g_z = 2.49(1)$ where an isotropic g value was used so as not to overfit the observed data; spin crossover in **2** prevents the use of *dc* susceptibility to provide constraints on g values. This is not the case for **1** where spin crossover is not observed thus allowing both $\chi_M T$ (Figure 6.4 (a)) and magnetization data (Figure 6.5 (a)) be used to fit eq (1), yielding an anisotropic g tensor ($g_x = g_y = 1.91(1)$ and $g_z = 2.49(1)$) and $D = -50(2)$ cm^{-1}. These magnetic data were fit to high temperatures (1.8–20 K for M vs HT^{-1} and 2–300 K for $\chi_M T$ vs T) to account for the magnetic contribution arising from thermal population of the doublet excited state. The much larger

magnitude of D in **1** results from three electrons in the doubly degenerate (e″) orbital set, resulting in unquenched orbital contribution and thus magnetic anisotropy (Figure 6.7).[29,30] In comparison, due to the local distortion from three-fold symmetry in **2**, the degeneracy of the e″ orbitals is removed, leading to a significantly reduced zero-field splitting parameter. These results emphasize the sensitivity of the magnetic anisotropy to subtle changes in local symmetry, which may be further accentuated by second-order spin-orbit coupling effects,[35,44,45] though the small differences in bond lengths between the primary coordination spheres (<0.04 A) suggests such effects to perturb D to be attenuated. To the best of our knowledge, the zero-field splitting parameter $D = -50(2)$ cm^{-1} in **1** represents the highest value yet observed for an Fe(III) ion.

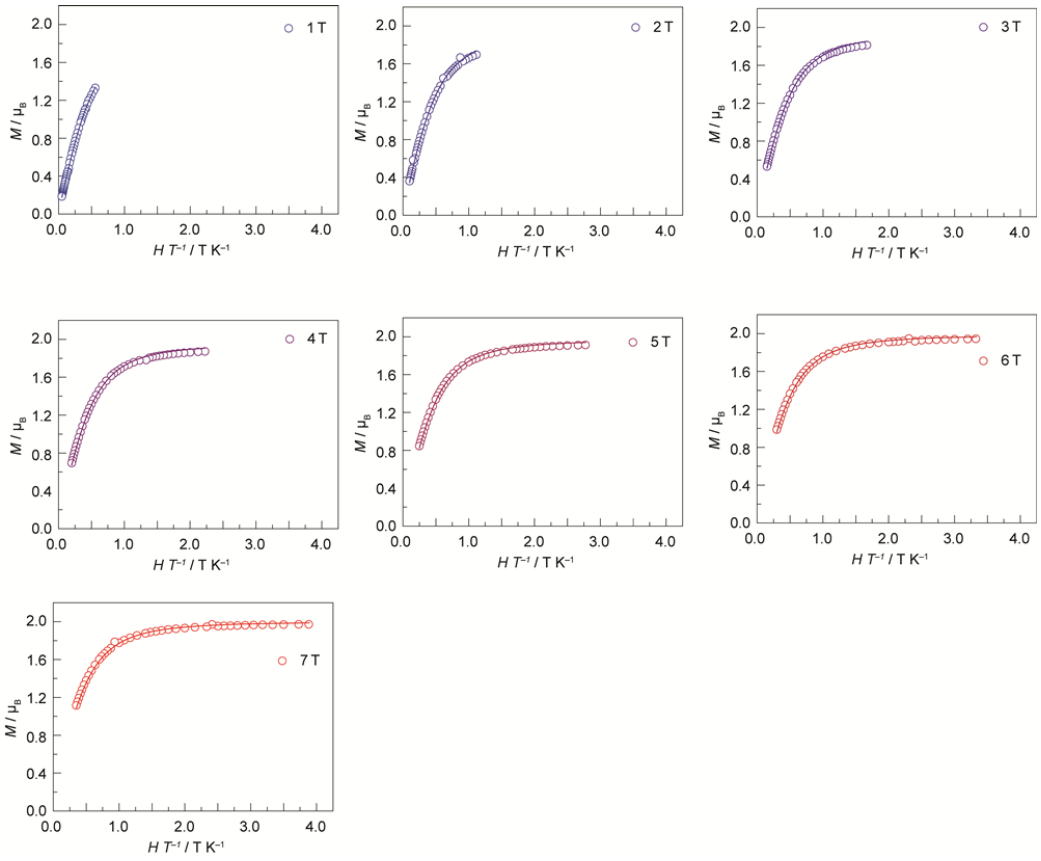

Figure 6.6. Magnetization data of **1** collected at 7 fields (1−7 T) and fits of each of the individual traces presented in Figure 6.5 (a).

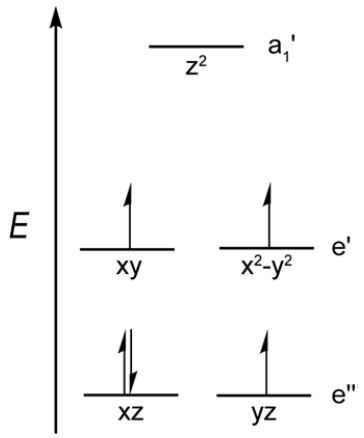

Figure 6.7. Qualitative *d*-orbital splitting diagram for a trigonal bipyramidal $FeCl_3L_2$ complex of intermediate spin $S = {}^3/_2$.

6.3.3 Ac susceptibility measurements

The large negative *D* value of **1** suggests the possibility of slow magnetic relaxation with a large spin reversal energy barrier. To assess this contention, the magnetization dynamics of **1** and **2** were probed with variable frequency *ac* susceptibility measurements at various temperatures. In the absence of an applied external magnetic field, χ_M''–frequency plots show only small shoulders for frequencies up to 1500 Hz and temperatures down to 1.8 K. The response is likely due to fast quantum tunneling through intermolecular dipolar interactions (6.762 Å intermolecular Fe–Fe distance for **1**). For systems with significant quantum tunneling, application of an external *dc* field helps eliminate these pathways to reveal thermal relaxation processes.[28,46–49] Indeed, application of a *dc* magnetic field, led to the appearance of clear frequency-and temperature-dependent peaks. To further probe the effect of magnetic field on relaxation time, variable *ac* frequency dependent measurements were performed at 4 K. Relaxation times slowed with increasing external magnetic field, attaining a maximum at an applied field of 4000 Oe for both **1** and **2** (Figure 6.8).

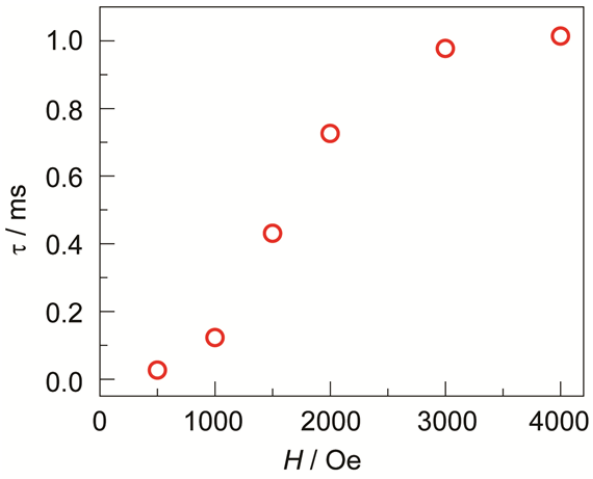

Figure 6.8. *Dc* field dependence of relaxation time for $FeCl_3(PMe_3)_2$ (**1**) at 7 K.

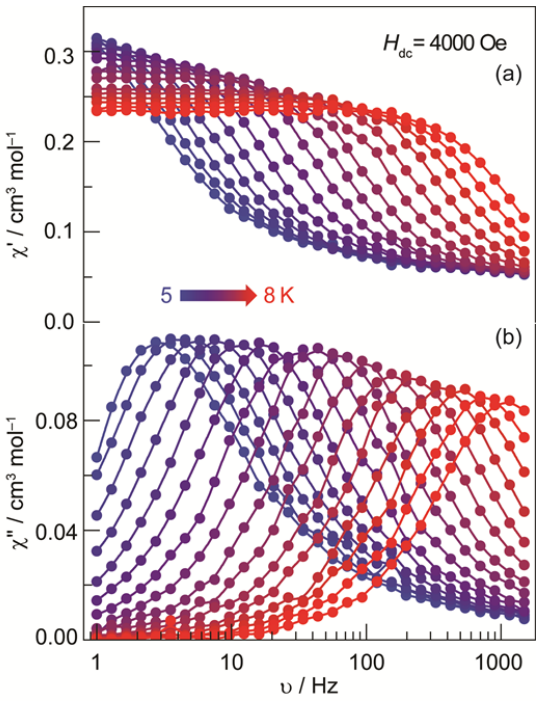

Figure 6.9. Variable-temperature, variable frequency (a) in-phase (χ_M') and (b) out-of-phase (χ_M'') components of the *ac* magnetic susceptibility data collected for **1** under a 4000 Oe applied *dc* field from 5 to 8 K. The solid lines are guides to the eye.

To extract the slow relaxation behavior of **1**, variable frequency *ac* susceptibility measurements were conducted under the optimized static field of 4000 Oe from 5 to 8 K (Figures

6.9). From these data, Cole–Cole plots of χ_M' vs χ_M'' were constructed (Figure 6.10) and fit to a generalized Debye model to furnish temperature-dependent relaxation times (τ).[50 – 52] The resulting Arrhenius plot of ln(τ) vs 1/T features a linear regime at high temperatures (Figure 6.11). A fit to these data furnishes a spin reversal barrier of U_{eff} = 110 K and a pre-exponential factor of $\tau_0 = 1.1\times10^{-10}$ s. The value of τ_0 is in line with previously reported SMMs,[1,16–28,32,37] consistent with the presence of a thermally activated slow relaxation pathway.

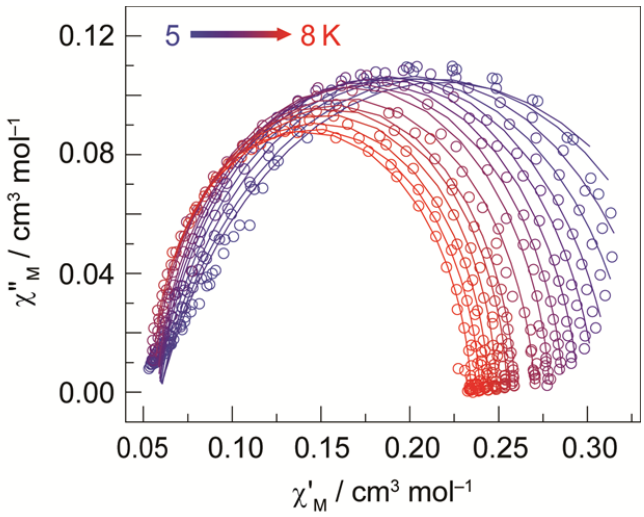

Figure 6.10. Cole-Cole plots for compound **1**, obtained from variable frequency ac susceptibility data under 4000 Oe *dc* field in the temperature range 5 (—, blue) to 8 (—, red) K. Solid lines represent fits to the data using a generalized Debye model.

Figure 6.11 shows that low temperatures relaxation times deviate from Arrhenius behavior. To fit the entire temperature range (as opposed to the linear regime of Figure 6.12), the presence of additional faster relaxation mechanism should be considered. Raman and/or direct fast relaxation processes at low temperatures, respectively, may arise from nonresonant two-

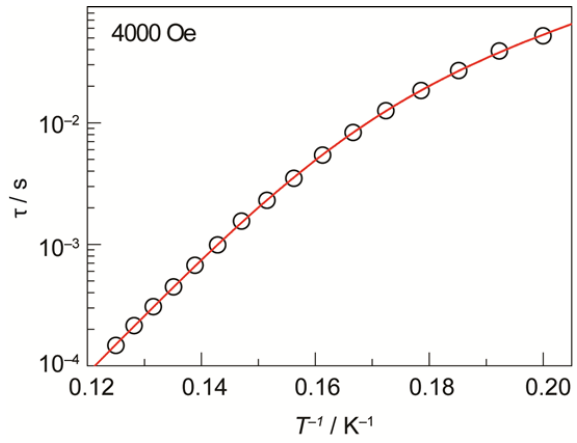

Figure 6.11. Arrhenius plot of the natural log of the relaxation time, τ, versus inverse temperature. Red solid line is the best fit to the data.

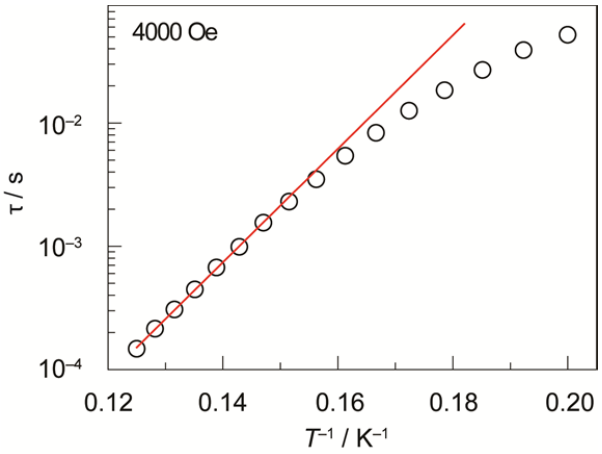

Figure 6.12. Arrhenius plot for the relaxation time, τ, of $FeCl_3(PMe_3)_2$ (**1**). Linear fit to data between 6.0 to 8.0 K (▬, red).

phonon spin-lattice relaxation and the one-phonon spin-lattice relaxation; both mechanisms give rise to a n^{th} power dependence of the relaxation times with inverse temperature.[53,54] The Raman process does not appear to be solely operative because a fit of the temperature-dependent relaxation times gives an n = 14, which greatly exceeds a physically reasonable exponent (n ≈ 9 for a Kramers' system).[53,54] Noting that a thermally activated relaxation process dominates at

high temperature (linear region of Figure 6.11), the relaxation dynamics were fit over the full temperature ranges to account for an Orbach contribution by using,[53–57]

$$\tau^{-1} = CT^{n} + \tau_0^{-1}\exp(-U_{eff}/T) \quad (2)$$

The best fit, shown in Figure 6.11, reveals that Raman (n = 7.3(4), C = 1.4(7) × 10^{-4} s^{-1} $K^{-7.3}$) and Orbach processes (τ_0 = 1.1(3) × 10^{-10} s, and U_{eff} = 116(2) K (81cm^{-1})) can well reproduce the relaxation times.

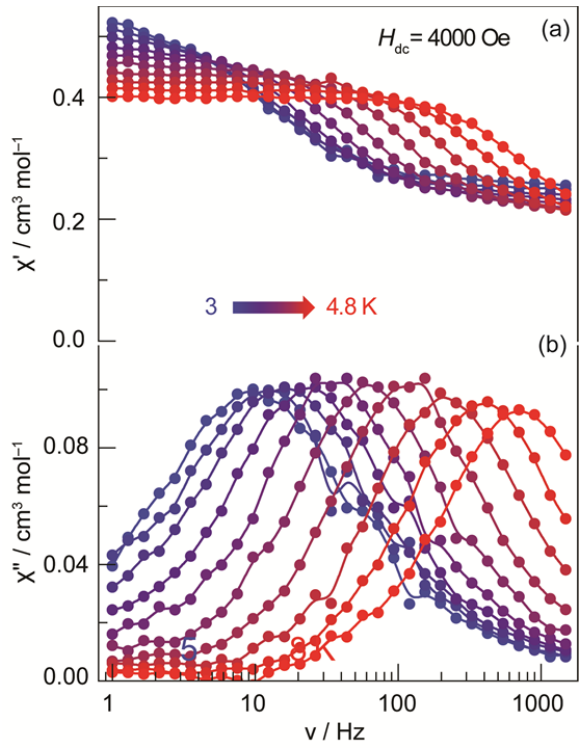

Figure 6.13. Variable-temperature, variable frequency (a) in-phase (χ_M') and (b) out-of-phase (χ_M'') components of the *ac* magnetic susceptibility data collected for **2** under a 4000 Oe applied *dc* field from 3 to 4.8 K.

A similar analysis performed on **2**, shown in Figures 6.13−6.15, gives a much-reduced energy barrier of U_{eff} = 67(2) K (46 cm^{-1}). These experimentally determined energy barriers are consonant with those calculated from the direct-current magnetic data (i.e., |2D| for **1** (100 cm^{-1})

and **2** (34 cm^{-1})). As observed for *D*, to the best of our knowledge, **1** also displays the highest U_{eff} among all Fe(III)-based SMMs.

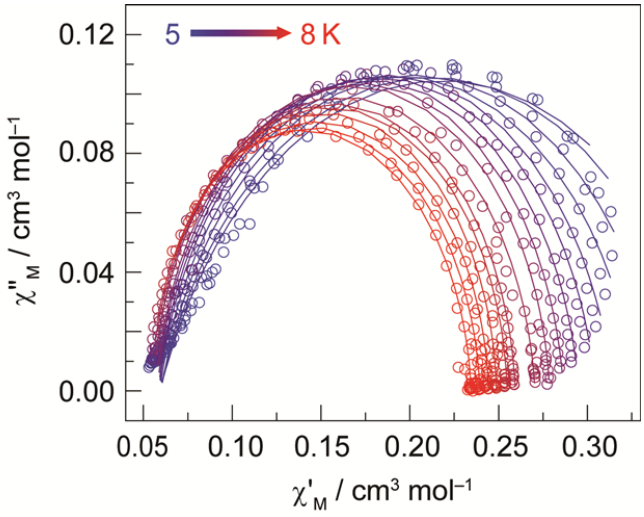

Figure 6.14. Cole-Cole plots for compound **2**, obtained from variable frequency ac susceptibility data under 4000 Oe *dc* field in the temperature range 3 (—, blue) to 4.8 (—, red) K. Solid lines represent fits to the data using a generalized Debye model.

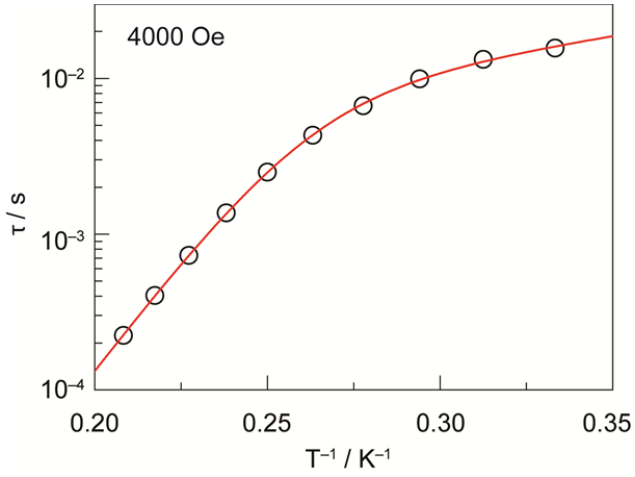

Figure 6.15. Natural log of the relaxation time, τ, versus inverse temperature. The direct, Raman, and Orbach processes were all included in the fitting model. The resulting fit afforded $C = 2.5(9)$ s^{-1} $K^{-2.9}$, $n = 2.9(3)$, $\tau_0 = 2.2(7) \times 10^{-10}$ s, and $U_{eff} = 67(2)$ K.

6.3.4 THz frequency measurements

Although, the fitting of the reduced magnetization is mature methodology and widely used to extract the zero-field splitting, especially for many 3*d* mononuclear single-molecule magnets with a well-defined spin,[32,38] a precise quantification of the *D* parameter by conducting high-field EPR would be desirable to further strengthen our work. However, 3 THz radiation is minimally required, to account for a large zero-field splitting (*ca.* 100 cm^{-1}) for complex **1**. Such a high frequency falls in the upper limit of high-frequency EPR range, not to mention the measurement under applied field. To overcome this challenge, we turned to subject our samples to THz Frequency ESR technique as reported by Keith Nelson.[58] However, strong far-infrared absorbance of the lattice vibrations obviated the measurement (Figure 6.16).

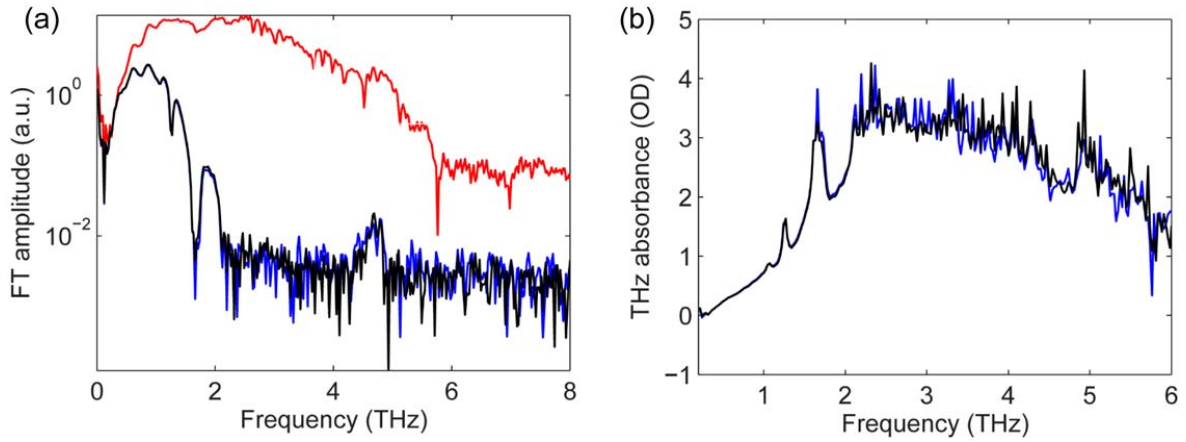

Figure 6.16. (a) THz Fourier-transform spectra recorded at 30 K (—, blue), and at 8 K (—, black), and THz reference (—, red) and (b) THz absorbance spectra recorded at 30 K (—, blue), and at 8 K (—, black) for complex **1**.

6.3.5 Variable-field magnetization plot

Considering the high barrier to magnetic relaxation in **1**, variable-field magnetization data were collected from 2 to 4 K under an applied external field (up to 2 T) with a sweep rate of 200 Oe s^{-1} to probe for magnetic hysteresis. Figure 6.17 displays waist-restricted magnetic hysteresis

plots. The collapse of magnetic hysteresis at zero field indicates the presence of a quantum tunneling pathway, consistent with the presence of fast relaxation at zero applied field in *ac* measurements. This observation is similar to that of the waist-restricted hysteresis observed from 2 to 6.5 K for the linear Fe(I) complex, [K(crypt-222)][Fe(C-($SiMe_3$)$_3$)$_2$]. Compound **1** and [K(crypt-222)][Fe(C-($SiMe_3$)$_3$)$_2$] are among the few examples of a first row transition metal mononuclear SMM displaying magnetic hysteresis.[34–37]

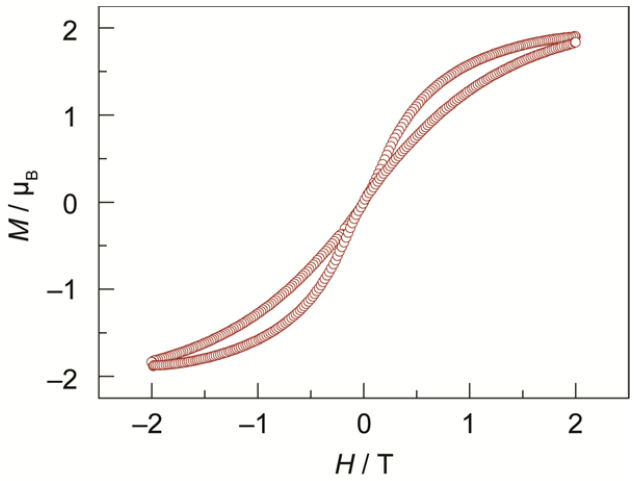

Figure 6.17. Variable-field magnetization plot for complex **1** with sweep rate of 200 Oe s^{-1}.

6.3.6 Heavy atom effects to maximize energy barrier

We sought to maximize the energy barrier by preparing isostructural Fe(III) complexes with increased relative heavy atom effect arising from the halides (Cl to Br) and apical ligands (PMe_3 to $AsMe_3$). Synthesis of this modified series of compounds was analogous to that already described with the substitution of Fe(III)Cl_3 by Fe(III)Br_3 and PMe_3 by $AsMe_3$. Figure 6.18 describes the molecular structure of complex **3**, Fe(III)Br_3(PMe_3)$_2$ by X-ray diffraction analysis, shows its isostructural in trigonal bipyramidal geometry (τ_5 = 0.93) to chloride analog complex **1**. Nonetheless, the preliminary magnetic analysis of complex **3** shows a much reduced energy

barrier of U_{eff} = 19 K (13 cm^{-1}), compared to 116(2) K (81 cm^{-1}) obtained for complex **1**, suggesting that axial anisotropy has more significantly influence to the overall magnetic anisotropy. Unfortunately, isostructural Fe complexes with heavier main group axial ligand, $AsMe_3$ was not realized. When 2.5 equiv of $AsMe_3$ was treated with the solution of $FeCl_3$, the constitutional isomer $[FeCl_4][FeCl_2(AsMe_3)_4]$ (**4**) was obtained instead of desired neutral five-coordinate Fe arsenic compound, presumably due to pi-accepting nature of arsenic ligand as compared to that of phosphine ligand (Figure 6.19). This contention was supported by the isolation of isostructural $FeCl_4][FeCl_2(^tBuNC)_4]$ (**5**) when pi-accepting *tert*-butyl isocyanide was employed as a ligand (Figure 6.20).

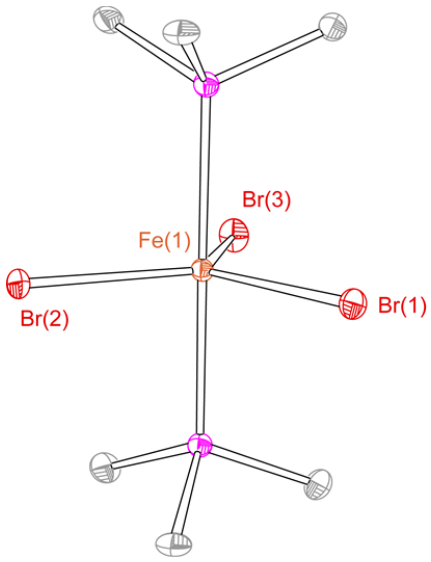

Figure 6.18. Thermal ellipsoid plots of $FeBr_3(PMe_3)_2$ (**3**) drawn at the 50% probability level. H-atoms are omitted for clarity.

Table 6.2. Selected bond distance [Å] and angles [°] for compounds **3**.

	3
Fe(1)–Br(1)	2.3752(6)
Fe(1)–Br(2)	2.3930(4)
Fe(1)–Br(3)	2.3930(4)
Fe(1)–P(1)	2.3267(11)
Fe(1)–P(2)	2.3375(11)
Br(1)−Fe(1)−Br(2)	121.959(12)
Br(1)−Fe(1)−Br(3)	121.959(12)
Br(2)−Fe(1)−Br(3)	116.06(2)
P(1)−Fe(1)−Br(1)	88.16(3)
P(1)−Fe(1)−Br(2)	90.286(19)
P(1)−Fe(1)−Br(3)	90.297(19)
P(2)−Fe(1)−Br(1)	89.43(3)
P(2)−Fe(1)−Br(2)	90.985(19)
P(2)−Fe(1)−Br(3)	90.984(19)
P(1)−Fe(1)−P(2)	177.60(4)
τ_5[a]	0.93

[a]τ_5 is defined as (β-α)/60, with α and β being the two largest angles within the five-coordinate complex (τ_5 = 0 for square pyramidal and τ_5 = 1 for trigonal bipyramidal).

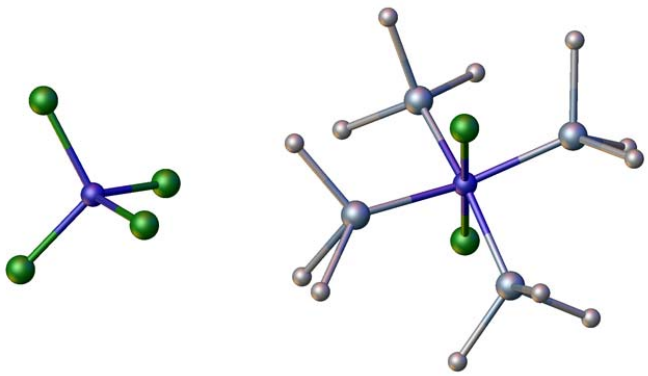

Figure 6.19. Crystal structure of Fe complex $[FeCl_4][FeCl_2(AsMe_3)_4]$ (**4**). H-atoms are omitted for clarity.

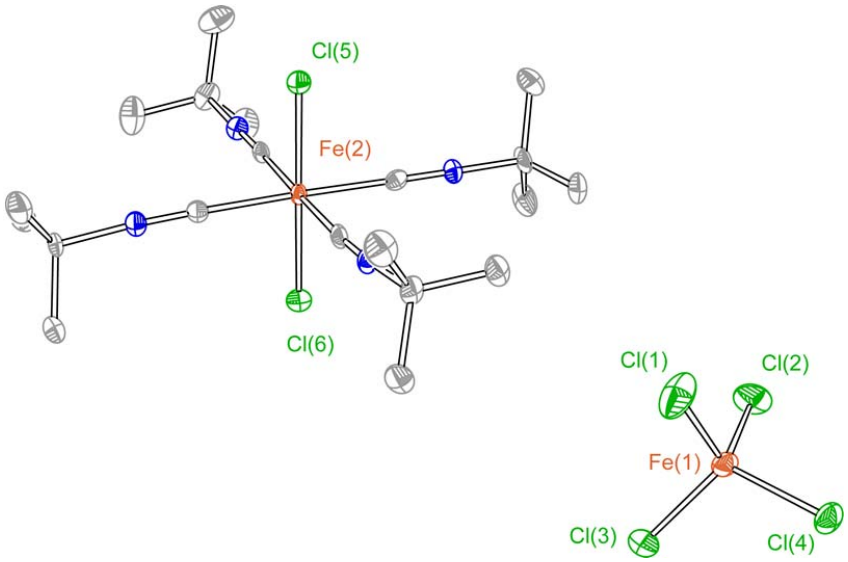

Figure 6.20. Thermal ellipsoid plots of $[FeCl_4][FeCl_2(^tBuNC)_4]$ (**5**) drawn at the 50% probability level. H-atoms and solvent molecule are omitted for clarity.

6.4 Summary/Conclusions

Fe(III) is one of the most common ions in bulk magnets. How to tune single ion of magnetic anisotropy on Fe(III) is not only of interest for single-molecule magnet community but also for the field of solid-state and materials science. A fundamental understanding of how to tune magnetic anisotropy by local symmetry in Fe(III) complexes may serve as a guide to develop better bulk magnet materials. Along these lines, two intermediate spin $S = {}^3/_2$ Fe(III) SMMs reported in this Chapter reveal the effectiveness of symmetry in tuning magnetic anisotropy for the benefit of SMM behavior. The nearly perfect local three-fold symmetry in **1** engenders the largest zero-field splitting parameters ($D = -50(2)$ cm^{-1}) yet observed for an Fe(III) complex, resulting in slow magnetic relaxation (U_{eff} = 116 K (81 cm^{-1})) and hysteresis. Though SMM with intermediate spin $S = {}^3/_2$ Fe(III) centers remains relatively unexplored, these observations suggest that $S = {}^3/_2$ Fe(III) complexes with appropriate high local symmetry can

provide large magnetic anisotropy and accordingly lead to wider applications of noncritical first-row transition metals as SMMs.

6.5 Experimental Details

6.5.1 Materials and Synthetic Details

All reactions were carried out in an N_2-filled glovebox. Anhydrous solvents were obtained from drying columns.[59] Anhydrous $FeCl_3$, PMe_3, PMe_2Ph, and anhydrous $PhCF_3$ solvents were obtained from Sigma Aldrich. All chemicals were used without purification. Compound **1** was prepared using a modified procedure based on a published procedure.[39]

$FeCl_3(PMe_3)_2$ (1). To a pre-cooled $PhCF_3$ solution of anhydrous $FeCl_3$ (100 mg, 0.616 mmol, 1.00 equiv) at −30 °C (6 mL), 1.0 M THF solution of PMe_3 (1.54 mL, 1.54 mmol, 2.50 equiv) was added. The dark red reaction solution was stirred at 23 °C for 2 h. The reaction mixture was filtered using a medium frit. The red solid was washed with pentane to afford 159 mg of the title complex (82.1% yield) as a red solid. Crystals suitable for single-crystal diffraction analysis were obtained from a $PhCF_3$ solution of the complex layered with pentane at –30 °C. ^{1}H NMR (600 MHz, C_6D_6) δ (ppm): −47.9 (br); **1** is silent in $^{31}P\{^1H\}$ NMR.

$FeCl_3(PMe_2Ph)_2$ (2). To a pre-cooled $PhCF_3$ solution of anhydrous $FeCl_3$ (100 mg, 0.616 mmol, 1.00 equiv) at −30 °C (6 mL), PMe_2Ph (213 mg, 1.54 mmol, 2.50 equiv) was added. The dark violet reaction solution was stirred at 23 C for 2 h. The reaction mixture was filtered using a medium frit, and the filtrate was layered with pentane to afford 120 mg of **2** (44.4% yield) as a violet crystalline solid. Crystals suitable for single-crystal diffraction analysis were obtained from a $PhCF_3$ solution of the complex layered with pentane at –30 °C. ^{1}H NMR (500 MHz, C_6D_6) δ (ppm): 26.9 (br), 13.5(br), 0.900 (br); **2** is silent in $^{31}P\{^1H\}$ NMR.

$FeBr_3(PMe_3)_2$ (3). To a pre-cooled $PhCF_3$ solution of anhydrous $FeBr_3$ (100 mg, 0.338 mmol, 1.00 equiv) at −30 °C (6 mL), 1.0 M THF solution of PMe_3 (0.846 mL, 0.846 mmol, 2.50 equiv) was added. The dark black reaction solution was stirred at 23 °C for 2 h. The reaction mixture was filtered using a medium frit. The black solid was washed with pentane to afford 127 mg of the title complex (84.0% yield) as a dark black solid. Crystals suitable for single-crystal diffraction analysis were obtained from a $PhCF_3$ solution of the complex layered with pentane at –30 °C.

$[FeCl_4][FeCl_2(AsMe_3)_4]$ (4). To a pre-cooled $PhCF_3$ solution of anhydrous $FeCl_3$ (100 mg, 0.617 mmol, 1.00 equiv) at −30 °C (6 mL), $PhCF_3$ solution of $AsMe_3$ (185 mg, 1.54 mmol, 2.50 equiv) was added. The green reaction solution was stirred at 23 °C for 2 h. The reaction mixture was filtered using a medium frit. The purple solid was washed with pentane to afford 199 mg of the title complex (40.0% yield) as a purple solid. Crystals suitable for single-crystal diffraction analysis were obtained from a $PhCF_3$ solution of the complex layered with pentane at –30 °C.

$[FeCl_4][FeCl_2(^tBuNC)_4]$ (5). To a pre-cooled $PhCF_3$ solution of anhydrous $FeCl_3$ (100 mg, 0.617 mmol, 1.00 equiv) at −30 °C (6 mL), $PhCF_3$ solution of ^{t}BuNC (128 mg, 1.54 mmol, 2.50 equiv) was added. The green reaction solution was stirred at 23 °C for 2 h. The reaction mixture was filtered using a medium frit. The purple solid was washed with pentane to afford 170 mg of the title complex (42.0% yield) as a purple solid. Crystals suitable for single-crystal diffraction analysis were obtained from a 1,2-difluorobenzene solution of the complex layered with pentane at –30 °C.

6.5.2 Physical Measurements

^{1}H NMR spectra were recorded on Agilent DD2 600 MHz or Varian Unity/Inova 500 MHz spectrometers at the Harvard University Department of Chemistry and Chemical Biology Laukien-Purcell Instrumentation Center. ^{1}H spectra were internally referenced to the residual solvent signal (δ = 7.16 for C_6H_6 in C_6D_6),[60] while $^{31}P\{^{1}H\}$ was externally referenced to 85% H_3PO_4. ^{57}Fe Mossbauer spectra were measured with a constant-acceleration mode on a spectrometer (SEE Co, Minneapolis, MN) at 90 K. Isomer shifts are quoted relative to Fe foil at room temperature. Data were analyzed and simulated with Igor Pro 6 software using Lorentzian fitting functions. Samples were prepared by suspending 70−90 mg of crystalline compound in sufficient Paratone N oil and immobilizing by rapid freezing in liquid N_2.

X-ray Crystallographic Details. X-ray structure of complexes **1** and **2** were collected using 0.41328 Å radiation at temperature of 20 K (Oxford Diffraction Helijet) on a vertical mounted Bruker D8 three-circle platform goniometer equipped with an Apex II CCD at ChemMatCARS located at Advances Photon Source (APS), Argonne National Laboratory (ANL). X-ray structures of complexes **3**, **4**, and **5** X-ray data were collected on a Bruker three-circle platform goniometer equipped with an Apex II CCD and an Oxford cryostream cooling device. Radiation was from a graphite fine focus sealed tube Mo Kα (0.71073 Å) source. Crystals were mounted on a glass fiber pin using Paratone N oil. Data was collected as a series of φ and/or ω scans. Data was integrated using SAINT and scaled with multi-scan absorption correction using SADABS.[61] The structures were solved by intrinsic phasing using SHELXT (Apex3 program suite v2016.1.0) and refined against F^2 on all data by full matrix least squares with SHELXL-97.[62] All non-hydrogen atoms were refined anisotropically. H atoms were placed at idealized positions and refined using a riding model. Crystal data and refinement statistics are

summarized in Tables 6.3–6.5 and thermal ellipsoid plots are collected in Figure 6.1 and Figure 6.18–6.20.

Magnetic Susceptibility Measurements. Magnetic data were collected on a Quantum Design MPMS-XL SQUID magnetometer and PPMS-9 susceptometer. These instruments work between 1.80 and 400 K with applied dc fields ranging from −7 to 7 T (MPMS). Dc susceptibility, dc magnetization and ac susceptibility measurements were obtained for a microcrystalline powder within a sealed gelatin capsules. Ac magnetic susceptibility data were collected in the temperature range 1.8–10 K, under an *ac* field of 4 Oe oscillating at frequencies in the range 0.5000–1488 Hz. All data were corrected for diamagnetic contributions from the sample holder, as well as for the core diamagnetism of each sample (estimated using Pascal's constants).[63] The magnetic hysteresis loops were measured using a Quantum Design PPMS with the VSM option. The data were continuously collected at intervals of 1 sec with the field ramping speed of 200 Oe sec^{-1}.

6.5.3 NMR data

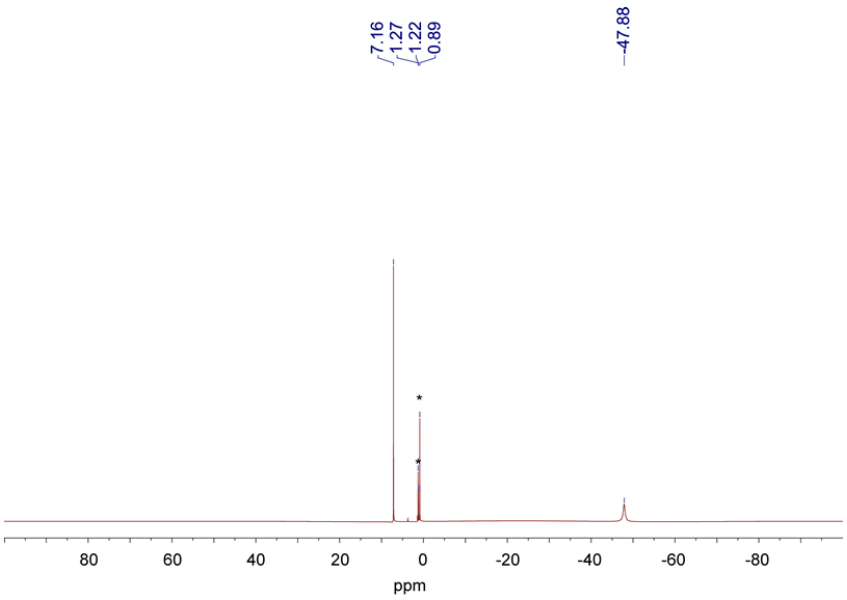

Figure 6.21. ^{1}H NMR spectrum of compound **1** recorded in C_6D_6 at 23 °C. Asterisk symbol (*) denotes residual ^{1}H peak of small amounts of pentane from crystallization.

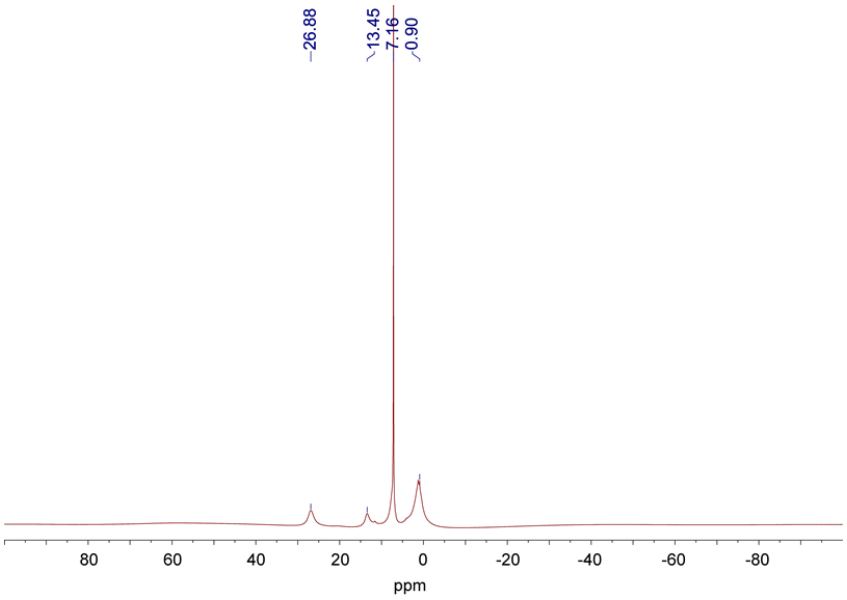

Figure 6.22. ^{1}H NMR spectrum of compound **2** recorded in C_6D_6 at 23 °C.

6.5.4 X-Ray Data Analysis

Table 6.3. X-ray experimental details for complex **1** (CCDC 1565911).

Crystal Data	
Chemical formula	$C_6H_{18}Cl_3FeP_2$
Fw, g/mol	314.34
Crystal system, space group	Orthorhombic, *Pnma*
Temperature (K)	20(2)
a, *b*, *c* (Å)	9.7630(3), 10.5338(3), 13.3513(4)
α, β, γ (°)	90, 90, 90
V (Å^3)	1373.07(7)
Z	4
Radiation type	synchrotron
μ (mm^{-1})	0.405
Crystal size (mm)	0.01 × 0.01 × 0.01
Data collection	
Diffractometer	Bruker *APEX*-II CCD
Absorption correction	Multi-scan, *SADABS*
T_{min}, T_{max}	0.9960, 0.9960
No. of measured, independent and observed [$I > 2\sigma(I)$] reflections	32245, 2183, 2103
R_{int}	0.0152
$(\sin \theta/\lambda)_{max}$ (Å^{-1})	0.714
Refinement	
$R[F^2 > 2\sigma(F^2)]$, $wR(F^2)$, S	0.0144, 0.0401, 1.138
No. of reflections	2183
No. of parameters	68
No. of restraints	0
H-atom treatment	H atoms treated by a mixture of independent and constrained refinement
Dr_{max}, Dr_{min} (e Å^{-3})	0.766, –0.334

Table 6.4. X-ray experimental details for complex **2** (CCDC 1565912).

Crystal Data	
Chemical formula	$C_{16}H_{22}Cl_3FeP_2$
Fw, g/mol	438.48
Crystal system, space group	Monoclinic, *P2(1)/c*
Temperature (K)	20(2)
a, *b*, *c* (Å)	16.7477(17), 8.6634(10), 14.6030(16)
α, β, γ (°)	90, 108.678(2), 90
V (Å^3)	2007.2(4)
Z	4
Radiation type	synchrotron
μ (mm^{-1})	0.288
Crystal size (mm)	0.01 × 0.01 × 0.01
Data collection	
Diffractometer	Bruker *APEX*-II CCD
Absorption correction	Multi-scan, *SADABS*
T_{min}, T_{max}	0.9971, 0.9971
No. of measured, independent and observed [$I > 2\sigma(I)$] reflections	63860, 6150, 5373
R_{int}	0.0502
$(\sin \theta/\lambda)_{max}$ (Å^{-1})	0.718
Refinement	
$R[F^2 > 2\sigma(F^2)]$, $wR(F^2)$, S	0.0444, 0.1171, 1.038
No. of reflections	6150
No. of parameters	199
No. of restraints	0
H-atom treatment	H atoms treated by a mixture of independent and constrained refinement
Dr_{max}, Dr_{min} (e Å^{-3})	1.281, –0.940

Table 6.5. X-ray experimental details for complex **3**.

Crystal Data	
Chemical formula	$C_6H_{18}Br_3FeP_2$
Fw, g/mol	447.72
Crystal system, space group	Orthorhombic, *Pnma*
Temperature (K)	100(2)
a, *b*, *c* (Å)	9.9027(6), 10.6907(7), 13.6452(9)
α, β, γ (°)	90, 90, 90
V (Å^3)	1444.57(16)
Z	4
Radiation type	Mo *Kα*
μ (mm^{-1})	9.523
Crystal size (mm)	0.10 × 0.14 × 0.16
Data collection	
Diffractometer	Bruker *APEX*-II CCD
Absorption correction	Multi-scan, *SADABS*
T_{min}, T_{max}	0.3042, 0.4617
No. of measured, independent and observed [$I > 2\sigma(I)$] reflections	24719, 1360, 1194
R_{int}	0.0266
$(\sin \theta/\lambda)_{max}$ (Å^{-1})	0.597
Refinement	
$R[F^2 > 2\sigma(F^2)]$, $wR(F^2)$, S	0.0197, 0.0376, 1.150
No. of reflections	1360
No. of parameters	68
No. of restraints	0
H-atom treatment	H atoms treated by a mixture of independent and constrained refinement
Dr_{max}, Dr_{min} (e Å^{-3})	0.481, –0.511

Table 6.6. X-ray experimental details for complex **5**.

Crystal Data	
Chemical formula	$C_{26}H_{40}Cl_6F_2Fe_2N_4$
Fw, g/mol	771.02
Crystal system, space group	Monoclinic, *P2(1)/n*
Temperature (K)	100(2)
a, *b*, *c* (Å)	12.2910(6), 20.8733(12), 14.6853(12)
α, β, γ (°)	90, 93.9680(10), 90
V (Å^3)	3758.5(4)
Z	4
Radiation type	Mo *Kα*
μ (mm^{-1})	1.230
Crystal size (mm)	0.10 × 0.10 × 0.15
Data collection	
Diffractometer	Bruker *APEX*-II CCD
Absorption correction	Multi-scan, *SADABS*
T_{min}, T_{max}	0.8370, 0.8869
No. of measured, independent and observed [$I > 2\sigma(I)$] reflections	39929, 6640, 5093
R_{int}	0.0726
$(\sin \theta/\lambda)_{max}$ (Å^{-1})	0.596
Refinement	
$R[F^2 > 2\sigma(F^2)]$, $wR(F^2)$, S	0.0477, 0.0914, 1.088
No. of reflections	6640
No. of parameters	373
No. of restraints	0
H-atom treatment	H atoms treated by a mixture of independent and constrained refinement
Dr_{max}, Dr_{min} (e Å^{-3})	0.880, –0.506

6.6 References

1. Gatteschi, G.; Sessoli, R.; Villain, J. *Molecular Nanomagnets*; Oxford University Press, Oxford, **2006**.

2. Sessoli, R.; Tsai, H. L.; Schake, A. R.; Wang, S.; Vincent, J. B.; Folting, K.; Gatteschi, D.; Christou, G.; Hendrickson, D. N. *J. Am. Chem. Soc.* **1993**, *115*, 1804.

3. Sessoli, R.; Gatteschi, D.; Caneschi, A.; Novak, M. A. *Nature* **1993**, *365*, 141.

4. Garanin, D. A.; Chudnovsky, E. M. *Phys. Rev. B* **1997**, *56*, 11102.

5. Leuenberger, M. N.; Loss, D. *Nature* **2001**, *410*, 789.

6. Jo, M.-H.; Grose, J. E.; Liang, W.; Baheti, K.; Deshmukh, M. M.; Sokol, J. J.; Rumberger, E. M.; Hendrickson, D. N.; Long, J. R.; Park H.; Ralph, D. C. *Nano Lett*. **2006**, *6*, 2014.

7. Ardavan, A.; Rival, O.; Morton, J. J. L.; Blundell, S. J.; Tyryshkin, A. M.; Timco, G. A.; Winpenny, R. E. P. *Phys. Rev. Lett*. **2007**, *98*, 57201.

8. Bogani, L.; Wernsdorfer, W. *Nat. Mater*. **2008**, *7*, 179.

9. Stamp, P. C. E.; Gaita-Arino, A. *J. Mater. Chem*. **2009**, *19*, 1718.

10. Loth, S.; von Bergmann, K.; Ternes, M.; Otte, A. F.; Lutz, C. P.; Heinrich, A. J. *Nature Phys*. **2010**, *6*, 340.

11. Milios, C. J.; Vinslava, A.; Wernsdorfer, W.; Moggach, S.; Parsons, S.; Perlepes, S. P.; Christou, G.; Brechin, E. K. *J. Am. Chem. Soc*. **2007**, *129*, 2754.

12. Neese, F.; Solomon, E. I. *Inorg. Chem.* **1998**, *37*, 6568.

13. Waldmann, O. *Inorg. Chem.* **2007**, *46*, 10035.

14. Ruiz, E.; Cirera, J.; Cano, J.; Alvarez, S.; Loose, C.; Kortus, J. *Chem. Commun.* **2008**, *52.*

15. Neese, F.; Pantazis, D. A. *Faraday Discuss.* **2011**, *148*, 229.

16. Ishikawa, N.; Sugita, M.; Ishikawa, T.; Koshihara, S. Y.; Kaizu, Y. *J. Am. Chem. Soc.* **2003**, *125*, 8694.

17. Branzoli, F.; Caretta, P.; Filibian, M.; Zoppellaro, G.; Graf, M. J.; Galan-Mascaros, J. R.; Fuhr, O.; Brink, S.; Ruben, M. *J. Am. Chem. Soc.* **2009**, *131*, 4387.

18. Jiang, S.-D.; Wang, B.-W.; Sun, H.-L.; Wang, Z.-M.; Gao, S. *J. Am. Chem. Soc.* **2011**, *133*, 4730.

19. Liu, J.-L.; Chen, Y.-C.; Zheng, Y.-Z.; Lin, W.-Q.; Ungur, L.; Wernsdorfer, W.; Chibotaru, L. F.; Tong, M.-L. *Chem. Sci.* **2013**, *4*, 3310.

20. Rinehart, J. D.; Long, J. R. *J. Am. Chem. Soc.* **2009**, *131*, 12558.

21. Meihaus, K. R.; Rinehart, J. D.; Long, J. R. *Inorg. Chem.* **2011**, *50*, 8484.

22. Gregson, M.; Chilton, N. F.; Ariciu, A.-M.; Tuna, F.; Crowe, I. F.; Lewis, W.; Blake, A. J.; Collison, D.; McInnes, E. J. L.; Winpenny, R. E. P.; Liddle, S. T. *Chem. Sci.* **2016**, *7*, 155.

23. Baldovı, J. J.; Cardona-Serra, S.; Clemente-Juan, J. M.; Coronado, E.; Gaita-Arino, A. *Chem. Sci.* **2013**, *4*, 938.

24. Ungur, L.; Le Roy, J. J.; Korobkov, I.; Murugesu, M.; Chibotaru, L. F. *Angew. Chem. Int. Ed.* **2014**, *53*, 4413.

25. Liu, J.; Chen, Y.-C.; Liu, J.-L.; Vieru, V.; Ungur, L.; Jia, J.-H.; Chibotaru, L. F.; Lan, Y.; Wernsdorfer, W.; Gao, S.; Chen, X.-M.; Tong, M.-L. *J. Am. Chem. Soc.* **2016**, *138*, 5441.

26. Guo, F.-S.; Day, B. M.; Chen, Y.-C.; Tong, M.-L.; Mansikkamaki, A.; Layfield, R. A. *Angew. Chem. Int. Ed*. **2017**, *56*, 11445.

27. Goodwin, C. A. P.; Ortu, F.; Reta, D.; Chilton, N. F.; Mills, D. P. *Nature* **2017**, *548*, 439.

28. Freedman, D. E.; Harman, W. H.; Harris, T. D.; Long, G. J.; Chang, C. J.; Long, J. R. *J. Am. Chem. Soc.* **2010**, *132*, 1224.

29. Harman, W. H.; Harris, T. D.; Freedman, D. E.; Fong, H.; Chang, A.; Rinehart, J. D.; Ozarowski, A.; Sougrati, M. T.; Grandjean, F.; Long, G. J.; Long, J. R.; Chang, C. J. *J. Am. Chem. Soc.* **2010**, *132*, 18115.

30. Craig, G. A.; Murrie, M. *Chem. Soc. Rev.* **2015**, *44*, 2135.

31. Kramers, H. A. *Proc. R. Acad. Sci. Amsterdam* **1930**, *33*, 959.

32. Zadrozy, J. M.; Long, J. R. *J. Am. Chem. Soc*. **2011**, *133*, 20732.

33. Mossin, S.; Tran, B. L.; Adhikari, D.; Pink, M.; Heinemann, F. W.; Sutter, J.; Szilagyi, R. K.; Meyer, K.; Mindiola, D. J. *J. Am. Chem. Soc.* **2012**, *134*, 13651.

34. Rechkemmer, Y.; Breitgoff, F. D.; van der Meer, M.; Atanasov, M.; Hakl, M.; Orlita, M.; Neugebauer, P.; Neese, F.; Sarkar, B.; van Slageren, J. *Nat. Commun.* **2016**, *7*, 10467.

35. Yao, X.-N.; Du, J.-Z.; Zhang, Y.-Q.; Leng, X.-B.; Yang, M.-W.; Jiang, S.-D.; Wang, Z.-X.; Ouyang, Z.-W.; Deng, L.; Wang, B.-W.; Gao, S. *J. Am. Chem. Soc*. **2017**, *139*, 373.

36. Zhu, Y.-Y.; Liu, F.; Liu, J.-J.; Meng, Y.-S.; Jiang, S.-D.; Barra, A.-L.; Wernsdorfer, W.; Gao, S. *Inorg. Chem.* **2017**, *56*, 697.

37. Zadrozny, J. M.; Xiao, D. J.; Atanasov, M.; Long, G. J.; Grandjean, F.; Neese, F.; Long, J. R. *Nature Chem.* **2013**, *5*, 577.

38. Zhu, Y.-Y.; Chi, C.; Zhang, Y.-Q.; Jia, J.-H.; Guo, X.; Gao, C.; Qian, K.; Jiang, S.-D.; Wang, B.-W.; Wang, Z.-M.; Gao, S. *Chem. Sci.* **2013**, *4*, 1802.

39. Walker, J. D.; Poli, R. *Inorg. Chem*. **1989**, *28*, 1793.

40. Addison, A. W.; Rao, T. N.; Reedijk, J.; van Rijn, J.; Verschoor, G. C. *J. Chem. Soc., Dalton Trans.,* **1984**, 1349.

41. Ray, K.; Bill, E.;Weyhermüller, T.;Wieghardt, K. *J. Am. Chem. Soc*. **2005**, *127*, 5641.

42. Gütlich, P., Bill, E.; Trautwein, A. X. *Mossbauer Spectroscopy and Transition Metal Chemistry*; Springer: Berlin, 2011.

43. Chilton, N. F.; Anderson, R. P.; Turner, L. D.; Soncini, A.; Murray, K. S. *J. Comput. Chem.* **2013**, *34*, 1164.

44. Karunadasa, H. I.; Arquero, K. D.; Berben, L. A.; Long, J. R. *Inorg. Chem.* **2010**, *49*, 4738.

45. Coste, S. C.; Vlaisavljevich, B.; Freedman, D. E. *Inorg. Chem.* **2017**, *56*, 8195.

46. Harman, W. H.; Harris, T. D.; Freeman, D. E.; Fong, H.; Chang, A.; Rinehart, J. D.; Ozarowski, A.; Sougrati, M. T.; Grandjean, F.; Long, G. J.; Long, J. R.; Chang, C. J. *J. Am. Chem. Soc*. **2010**, *132*, 18115.

47. Lin, P. H.; Smythe, N. C.; Gorelsky, S. I.; Maguire, S.; Henson, N. J.; Korobkov, I.; Scott, B. L.; Gordon, J. C.; Baker, R. T.; Murugesu, M. *J. Am. Chem. Soc*. **2011**, *133*, 15806.

48. Weismann, D.; Sun, Y.; Lan, Y.; Wolmershauser, G.; Powell, A. K.; Sitzmann, H. *Chem. Eur. J.* **2011**, *17*, 4700.

49. Zadrozny, J. M.; Atanasov, M.; Bryan, A. M.; Lin, C.-Y.; Rekken, B. D.; Power, P. P.; Neese, F.; Long, J. R. *Chem. Sci.* **2012**, *4*, 125.

50. Cole, K. S.; Cole, R. H. *J. Chem. Phys.* **1941**, *9*, 341.

51. Boettcher, C. J. F. Theory of Electric Polarisation; Elsevier: Amsterdam, **1952**.

52. Aubin, S. M.; Sun, Z.; Pardi, L.; Krzystek, J.; Folting, K.; Brunel, L.-J.; Rheingold, A. L.; Christou, G.; Hendrickson, D. N. *Inorg. Chem*. **1999**, *38*, 5329.

53. Abragam, A.; Bleaney, B. *Electron Paramagnetic Resonance of Transition Ions*; Dover, New York, **1986**.

54. Shrivastava, K. N. *Phys. Stat. Sol. (b)* **1983**, *117*, 437.

55. Singh, A.; Shrivastava, K. N. *Phys. Stat. Sol. (b)* **1979**, *95*, 273.

56. Finn, C. B. P.; Orbach, R.; Wolf, W. P. *Proc. Phys. Soc.* **1961**, *77*, 261.

57. Feng, X.; Liu, J.; Pedersen, K. S.; Nehrkorn, J.; Schnegg, A.; Holldack, K.; Bendix, J.; Sigrist, M.; Mutka, H.; Samohvalov, D.; Aguila, D.; Tong, M.; Long, J. R.; Clerac, R. *Chem. Commun.* **2016**, *52*, 12905.

58. Lu, J.; Ozel, I. O.; Belvin, C. A.; Li, X.; Skorupskii, G.; Sun, L.; Ofori-Okai, B. K.; Dincă, M.; Gedik, N.; Nelson, K. A. *Chem. Sci.* **2017**, *8*, 7312.

59. Pangborn, A. B.; Giardello, M. A.; Grubbs, R. H.; Rosen, R. K.; Timmers, F. J. *Organometallics* **1996**, *15*, 1518.

60. Fulmer, G. R.; Miller, A. J. M.; Sherden, N. H.; Gottlieb, H. E.; Nudelman, A.; Stoltz, B. M.; Bercaw, J. E.; Goldberg, K. I. *Organometallics*, **2010**, *29*, 2176.

61. Bruker AXS (2009). Apex II. Bruker AXS, Madison, Wisconsin.

62. Sheldrick, G. M. *Acta Cryst.* **2010**, *D66*, 479.

63. Bain, G. A.; Berry, J. F. *J. Chem. Ed.*, **2008**, *85*, 532.